UNIVERSITÄT BERN

Graduate School for Cellular and Biomedical Sciences

University of Bern

SLC transporter-mediated transfer of iron and amino acids across the placenta

PhD Thesis submitted by

Jonas Zaugg

from Lützelflüh BE

for the degree of

PhD in Biochemistry and Molecular Biology

Supervisor

Prof. Dr. Christiane Albrecht

Institute of Biochemistry and Molecular Medicine

Faculty of Medicine of the University of Bern

Co-advisor

Prof. Dr. med. Martin Müller

Department of Obstetrics and Gynecology

Faculty of Medicine of the University of Bern

Accepted by the Faculty of Medicine, the Faculty of Science and the Vetsuisse Faculty of the University of Bern at the request of the Graduate School for Cellular and Biomedical Sciences

Bern, Dean of the Faculty of Medicine

Bern, Dean of the Faculty of Science

Bern, Dean of the Vetsuisse Faculty Bern

Abstract

A successful pregnancy and the birth of a healthy baby depends to a great extent on the controlled supply of essential nutrients via the placenta. Inspired by clinical observations and in close collaborations with clinical obstetricians, we focused on the implementation of biochemical and cell biological *in vitro* models to mimick and investigate physiological relationships between the human placenta and gestational diseases.

This work is structured into two clinically based sections studying solute carrier (SLC)-mediated materno-fetal transport of amino acids and iron across the placenta. The third methodologically oriented part describes the attempt to generate placental SLC knockout cells.

The first clinically oriented part investigated the contribution of amino acid transporters of the SLC7 family in transplacental transfer of essential amino acids. Na^+-independent placental leucine transport is mainly attributed to the System L-transporters LAT1/SLC7A5 and LAT2/SLC7A8. We determined physiological amino acid gradients of paired maternal and fetal serum samples by ion exchange chromatography. Subsequently, we assessed their importance by performing Spearman correlation analysis between materno-fetal gradients determined *in vivo* and anthropometric parameters. We found significant associations between reduced materno-fetal amino acid gradients with maternal gestational weight gain and maternal blood pressure suggesting a potential role of amino acid gradients in reduced intrauterine growth or even in hypertensive diseases like preeclampsia. Functional effects of a physiological gradient versus equimolar leucine concentrations were tested using *in vitro* uptake and Transwell®-based transfer assays. Interestingly, materno-fetal leucine transfer was significantly stimulated against a counter-directed gradient. These results suggest a currently underestimated effect of transplacental amino acid gradients on leucine transfer efficiency and underline their potential impact in pregnancy diseases associated with impaired fetal growth. Moreover, we investigated the relevance of SLC7 transporter in placental leucine transfer by applying the LAT1-specific inhibitor JPH203 and the System L-specific inhibitor JX009 synthesized by our collaborators in the NCCR TransCure network. These studies identified LAT1 as the major accumulative transporter in the placenta, but other System L-transporters like LAT2 as rate-limiting for leucine efflux to the fetus.

Abstract

The second clinical part of this thesis focused on investigating the molecular mechanisms of materno-fetal iron transport. Clinical studies suggest that pregnancies with elevated iron levels are more vulnerable to develop gestational diabetes mellitus (GDM), but the underlying mechanisms are unknown. We found differential regulation of iron transporters (DMT1/FPN1/ZIP8), receptors (TfR1), sensors (IRP1), regulators (HEPC) and oxidoreductases (HEPH/Zp) by RT-qPCR and by LC-MS/MS-based protein quantification in placental tissue from GDM compared to healthy pregnancies. Newly established hyperglycemic and hyperlipidemic trophoblast cell models, but also obesogenic HFHS diet in wildtype mice, mimicked to a great extent the expression results found in the clinical specimens of GDM patients. By expressional and functional assessment of normo-glycemic, hyperglycemic and hyperglycemic-hyperlipidemic BeWo choriocarcinoma cells, we found altered cellular morphology, differential expression of iron transporters and reduced iron uptake confirming the impact of hyperglycemia on iron transport as observed in GDM patients. Iron depletion by the iron chelator deferoxamine (DFO) revealed a bidirectional relationship between placental glucose and iron homeostasis. Pathway analysis and rescue experiments indicated that dysregulated oxidative stress and autophagy contribute to reduced placental iron transport under hyperglycemic conditions. These adaptations are likely mediated by ferroptosis and could represent a protective mechanism preventing oxidative damage for both fetus and placenta caused by highly oxidative iron levels or hyperglycemia. Thus, in pregnancies with increased risk for GDM, antioxidant treatment and controlled iron supplementation could help to protect mother and fetus from impaired iron and glucose homeostasis.

Within the last methodologically oriented part, we aimed to establish an efficient protocol to generate CRISPR/Cas9-mediated trophoblast knockout cell lines. Trophoblast cells lacking the function of single nutrient transporters would help to unravel their role in physiological nutrient transfer or in gestational diseases affecting fetal growth. To date, we were not able to successfully generate knockout cell lines by CRISPR/Cas9-mutagenesis. However, the achieved optimization of target site validation, BeWo transfection and characterization procedures of potential CRISPR/Cas9-mutant candidates created an advanced toolbox suitable to successfully continue the CRISPR/Cas9-mediated mutagenesis approach in future placental studies.

Acknowledgements

Foremost, I would like to thank Prof. Christiane Albrecht for giving me the opportunity to enter into the fascinating field of placentology and nutrient transport, but also to make my first experience in academic teaching of human medicine students and to grow into the international family of placental research. She even managed getting me excited about writing manuscripts and patiently answer to challenging feedback of colleges and reviewer. On the experimental side, I thank Prof. Christiane Albrecht for the offered freedom in the lab work and in the development of my project. She invested endless hours correcting and shortening my abstracts and manuscripts, but also pushed me to continuous challenge my results and supported me with personal guidance, not only in my project, but also to find my way in academic life.

I would like to thank my PhD committee, namely my co-advisor Prof. Dr. med. Martin Müller, my Graduate School for Cellular and Biomedical Sciences (GCB) mentor Prof. Dr. med. Andrea De Gottardi and my external expert Dr. Amanda Sferruzzi-Perri from the University of Cambridge, UK.

I am particularly thankful to the core group accompanying me during the years of this PhD project including Dr. Sampada Kallol, Dr. Xiao Huang, Michael Lüthi and Dr. Corneille Edgar Ontsouka for incorporating me so familiarly into the Albrecht lab and for the excellent support to conduct my experiments. I thank my former lab mates Hassan Melhem, Line Zurkinden, Nithya Venkateswaran, Alexandra Eppstein, Saira Shahnawaz, Rona Karahoda and Regina Berchtold. I also thank former BSc and MSc students for allowing me to be their co-supervisor, namely Kevin Muli, Fabian Burri, Fabian Ziegler, Thuvaraga Kalakaran, Daniela Ramp, Martyna Kazimierczak and Roman Bächler. Further thanks go to Barbara Järmann our expert for administrative questions.

Further, a big thank goes to PD Dr. med. Meike Körner, who initially introduced me the Prof. Albrecht when I was still working with her as medical laboratory assistant in pathology institute Bern, but also for her help with histological quantification of transporter expression. I would like to thank Dr. med. Ruedi Moser-Hässig and midwives of Lindenhof Hospital in Bern for coordinating and providing the placentae, while a special thank goes to all the women who donated placentae and blood for my studies, this work would be nowhere without their help!

Many thanks go to PD Dr. med Jean-Marc Nuoffer Senior physician for metabolic analysis at the university hospital Bern for finding time to discuss putative relationships between gestational concentrations of amino acids and their metabolites. Furthermore, I would like to thank Dr. Christian Trachsel, Dr. Witold Wolski and Dr. Paolo Nanni form the Functional Genomics Center (FGC) at the Swiss Federal Institute of Technology in Zurich (ETH) Zurich for their guidance and help in MS/MS-based protein quantification experiments and analysis.

Acknowledgements

I'd like to thank also Dr. Julien Graff and Jennifer Müller in the lab of Prof. Karl-Heinz Altmann at the ETH in Zurich for the synthesis on the small molecule inhibitors and corresponding help with questions concerning chemistry. As another member of NCCR TransCure and collaborator for characterization of SLC7 inhibitor, I'd like to thank Prof. Jürg Gertsch, also for critically revising the SLC7 inhibitor manuscript. I am thankful for the uncomplicated collaboration with Dr. Stefan Muller. He supported me with all issues with flow cytometry analysis and he did a great job with FACSorting in the CRISPR/Cas9-mutagenesis project.

My thanks also go to Carolin Anders for providing us with high-quality Cas9 protein and Prof. Dr. Martin Jinek for advanced help with the Cas9 protein application.

I am indebted to my funders, the Swiss National Science Foundation (SNF) and National Centre of Competence in Research (NCCR) TransCure for providing grant and financial support to conduct the research. It was a great experience to be together with Barbara Preti, Jennifer Müller and Saurav Subedi part of the TransCure fellow committee and organizing several meetings and events to support networking among research fellows.

I am grateful to the graduate school for GCB graduate school at the University of Bern, who supported me with the admission of the PhD program and financially helped to travel to international conferences.

Finally, I would like to say a big thank to my wife Karin Zaugg-Ammon. Thank you for your endless patience, infinite understanding, support and help in graphical questions and to my family for their moral support.

Once again, many thanks to you all,

Jonas

Index

Abbreviations

1 Introduction

The placenta is a vital tissue during pregnancy as it is the connecting organ between the fetus and the *ex utero* world. Furthermore, it is a fetal organ and temporary enables the mutual exchange between the embryo and mother. Besides its main function of physiological materno-fetal exchange of nutrients and waste products, the placenta is also responsible for the prevention of maternal immune rejection as well as for maintaining pregnancy through the secretion of gestational hormones. The placenta maintains the balance between nutrition and growth control of the fetus through selective and regulated supply of macronutrients such as carbohydrates, protein, lipids and critical micronutrients like minerals and vitamins (Roos, Powell, and Jansson 2009). The placental nutrient transport does not just play a role in fetal development, but also affects the newborn's life by metabolic programming until adulthood (Burton, Fowden, and Thornburg 2016).

This work was focusing mainly on solute carrier (SLC) -mediated materno-fetal transport of essential amino acids like leucine and iron as most abundant trace element in the human body. Both parts of the current project (amino acid and iron transport) are embedded in and profit from the TransCure scientific network (www.nccr-transcure.ch/research/), in which we tightly collaborate with chemists, structural biologists, and physiologists in the field of membrane transporters.

1.1 The role of the placenta in gestational pathologies

The latest report published by the Swiss Federal Statistical Office revealed that, the prevalence of pregnancies resulting in abnormal fetal growth has been increased by 1.3% from 5.9% in 1979 to 7.2% in 2017 (**Figure 1**). Such altered fetal development has a fundamental impact on lifelong health and wellbeing and may contribute by fetal programming to later prevalence for cardiovascular disease and diabetes/adiposity (Harder et al. 2007; Eriksson et al. 2003; Boney et al. 2005; Leon et al. 1998). Appropriate *in utero* fetal growth is largely dictated by the availability of nutrients in the maternal circulation, which is ensured during pregnancy by the capacity of the placenta to transfer these nutrients into the fetal circulation. In the framework of the current work, we

focused on gestational diabetes mellitus (GDM). Therefore, the hallmarks and consequences of this disease will be introduced in detail (see next chapter).

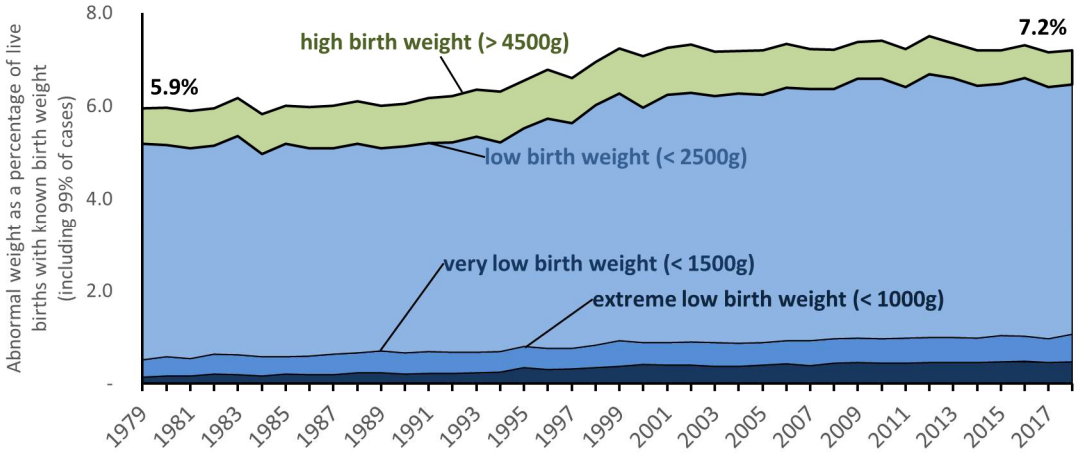

Figure 1: Prevalence of abnormal weight in life births in Switzerland from 1979 until 2017. Source: Federal Statistical Office (Bundesamt für Statistik, BSF) - Statistics of Natural Population Movement (Statistik der natürlichen Bevölkerungsbewegung, BEVNAT), 2019

1.2 Link between GDM and iron homeostasis

GDM, defined as any degree of glucose intolerance with onset or first recognition during pregnancy, is one of the most common pregnancy complications and has a prevalence of 4.8% in Switzerland (Orecchio et al. 2014) and 9.2% in the US (DeSisto, Kim, and Sharma 2014), respectively. Within a swiss cohort study (n= 1042), GDM was strongly associated with short-term complications of fetal development and its early life (Crowther et al. 2005). They observed high birth complication rate, e.g. 6.3% neonatal hypoglycemia, 9.4% respiratory distress syndrome and 9.4% jaundice that was far above the incidence in the control group and in the general population. Despite considerable progress in diagnosis and treatment of GDM, it has still substantial adverse health effects on the mother and her offspring. The etiology of GDM is multifactorial. Well known modifiable risk factors for GDM include obesity, high fat diet, high blood pressure, excess weight gain in pregnancy, endocrine dysfunction and sedentary life style (Lappas et al. 2011). Several clinical studies ascertain a positive association between increased serum iron levels and increased risk to develop GDM (Bo et al. 2009; Zein et al. 2015; Rawal et al. 2017; Fu et al. 2016; Afkhami-Ardekani and Rashidi 2009). Zein et al. found ferritin levels at early pregnancy correlating positively with glucose levels in oral glucose tolerance tests (oGTTs) (Zein et al. 2015). More recently, Rawal et al. associated in a longitudinal and prospective study increased

ferritin levels already in gestational week 10-14 with increased risk to develop GDM (Rawal et al. 2017). These findings raise potential concerns for the recommendation of routine iron supplementation among iron-replete pregnant women. However, the pathophysiological association of GDM and elevated maternal iron plasma levels reported in clinical studies as well as the underlying mechanism are still unclear.

Association of GDM-mediated hyperglycemia and placenta iron homeostasis

Both the hyperglycemic environment and increased levels of iron may play a role in the generation of oxidative stress during pregnancy. Oxidative stress occurs when the delicate balance between generation of reactive oxygen species (ROS) and production of antioxidant neutralizing species, such as nicotinamide adenine dinucleotide phosphate (NADPH) and glutathione (GSH), is disturbed. Hyperglycemia raises oxidative stress levels through different metabolic pathways. For example, glucose is converted under intracellular hyperglycemic conditions to the polyalcohol sorbitol by utilizing intracellular NADPH and GSH. Consequently, hyperglycemia induces an overrepresentation of ROS by antioxidant depletion (Brownlee 2001). On the other side, excessive iron supplementation might expose women to increased lipid peroxidation and protein carbonylation by intracellular generation of ROS (Papanikolaou and Pantopoulos 2005; Ziaei et al. 2007). Notably, whether hyperglycemia could alter placental iron homeostasis in the placenta and increased antioxidant intake could reduce the complications of GDM in both mother and fetus has not been explored yet.

1.3 Development and structure of human placenta

The placenta is the first organ to be formed in humans and other mammals (Maltepe and Fisher 2014). It has a discoidal, flat and round to oval macroscopic appearance. At term, which represents the time at the end of pregnancy, approx. 40 weeks post fertilization, the average diameter of a human placenta is 22 cm, reaches a thickness of 2.5 cm and has a weight of approx. 470 g (Baergen 2005).

The development of the placenta begins following the attachment of the blastocyst to the uterine endometrium of the uterine wall within 6-7 days after fertilization (**Figure 2A**). At the blastocyst stage, the inner cell mass (ICM) and the blastocoel are enveloped by mononucleated trophoblasts also called trophectoderm cells at this stage (Cha, Dey, and

Lim 2015). The trophoblasts that get direct contact to the maternal endometrium immediately start to fuse with the neighboring uterine cells to form the first multinucleated syncytiotrophoblasts (STB) (**Figure 2A**). This process continues until day 11 after fertilization (**Figure 2B**), when a complete syncytium surrounds the fully implanted blastocyst (**Figure 2C**) (Sadovsky and Jansson 2015; Turco and Moffett 2019). At this stage of human embryonic development, the lacunar stage starts with the formation of fluid-filled spaces (lacunas) within the STB cell mass (**Figure 2C**). These lacunas will form the intervillous spaces after further proliferation, branching and filling with maternal blood. In parallel, the endometrium proliferates to cover the entire implantation site and the ICM cells differentiate to form the embryonal germ layers such as the ectoderm, the mesoderm and endoderm that will ultimately form the developing fetus, but also the extraembryonic layer of cells that will form stromal structures of the placenta (**Figure 2D**).

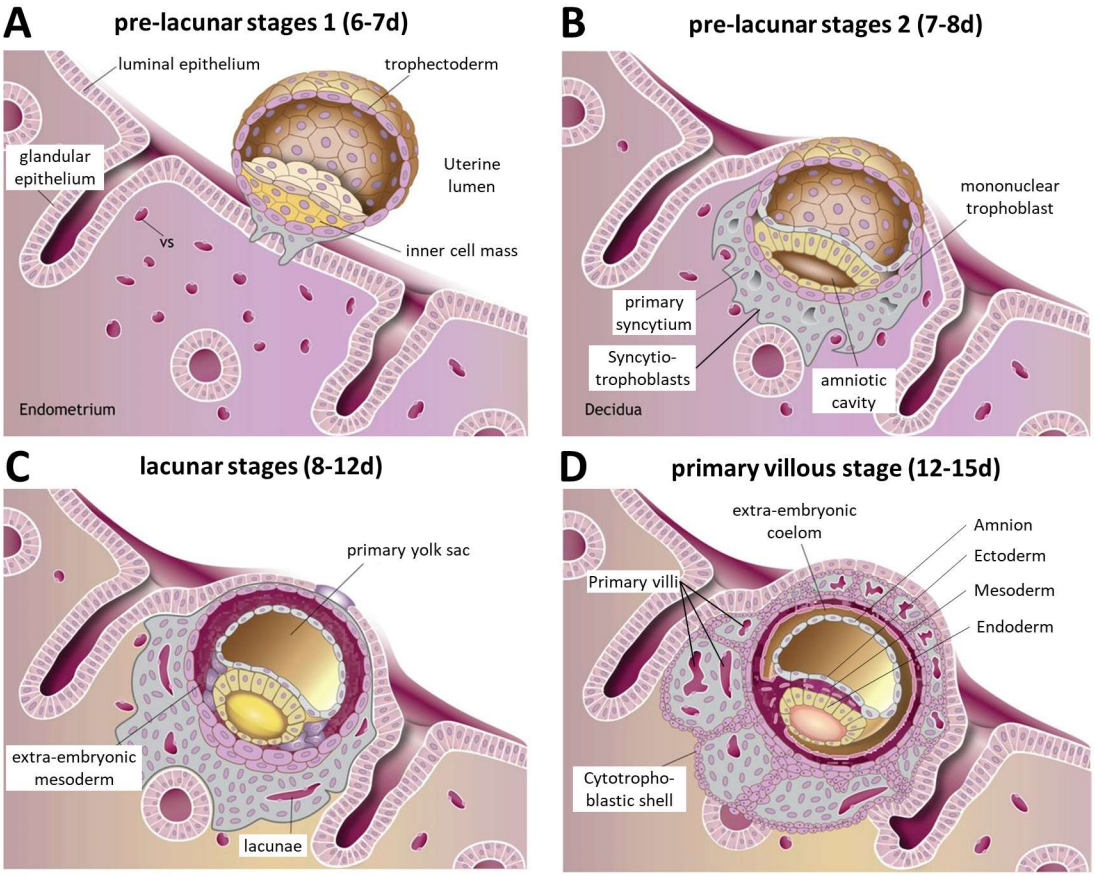

Figure 2: The early stages of human placental development. The development of the human placenta starts with the implantation of the blastocyst at pre-lacunar stage at approx. 1 week after fertilization (**A**). During the pre-lacunal stage extraembryonic trophoblasts syncytialize and invade the endometrium of the uterine wall (**B**). Syncytiotrophoblasts (STB) completely surround the implanted early embryo, while lacunae, the intervillous space precursors, are formed and uterine

glands get invaded for histotroph nutrition in the lacunar stage (**C**). STB grow further into the decidua basalis (basal plate) toward the maternal vessels and get penetrated by cytotrophoblasts to form primary villi (**D**). Modified from Turco and Moffett 2019.

Following implantation, the primary syncytium quickly invades through the surface epithelium into the underlying endometrium. These invasive extravillous cytotrophoblasts penetrate the uterine glands and cells around and within the spiral arteries, forming the endovascular trophoblast and transform the contractile spiral arteries into noncontractile, constantly dilated arteries (Sadovsky and Jansson 2015). The invaded uterine glands secrete vital nutrients and become the first nutrient source for the conceptus during the histotrophic first trimester, before the establishment of maternal blood flow to the intervillous space of the placenta occurs (Filant and Spencer 2014). To connect the early placenta to the circulation of the mother, the STBs interfere with maternal capillaries to form a direct connection between the lacunas and maternal blood vessels, but they maintain feto-placental hypoxia until the end of the first trimester (Jauniaux et al. 2000). Once fully functional, the intra-arterial plug lyses and the intervillous space fills with maternal blood and enables oxygenation and hemotrophic nutrient transport from the maternal blood to the fetus at around 4 months after conception (Turco and Moffett 2019). With the connection of the lacunas to the maternal circulation the lacunar stage ends and placental development progresses to the villous stage (**Figure 2D**). First primary villi are formed by cytotrophoblast (CTB) proliferation at the wall of the lacunas. Cells of the extraembryonic mesoderm move out (purple cells, **Figure 2D**) and penetrate the primary villi to form the villous cores (secondary villi). Proliferating hemangioblastic progenitors of hematopoietic and endothelial cells (EC) differentiate within the extraembryonic mesoderm to form the early first fetal capillaries and blood cells (Demir et al. 1989). By the third week of gestation tertiary villi have formed consisting of an outer monolayer of STB, invaded by an inner layer of CTB cells and vascularized with fetal capillaries (Huppertz 2008). Tertiary villi containing differentiated blood vessels will eventually form the placental barrier representing the site of nutrient exchange until term.

1.4 The human placental barrier

As soon as a feto-placental circulation is established within the placental villi towards the end of the first trimester, fetal and maternal blood come into close contact with each other. The two bloodstreams are always separated by the placental barrier (Baergen 2005). The placental or chorionic villi increase the effective surface area and represent the functional unit of the placenta, where most transport, metabolic and endocrine activities are localized (**Figure 3A** left panel). Virtually all materno-fetal and feto-maternal exchange takes place across the placental barrier of the chorionic villi (**Figure 3A** middle panel with magnification to the right). The chorionic villi are surrounded by STB, a multinuclear epithelial surface layer that is in direct contact with the maternal blood (**Figure 3A** right panel and STB in **Figure 3D**). Between STB and the basal lamina (trophoblastic basement membrane) are the villous CTB. CTB are the stem cells of the syncytium, supporting its growth and regeneration (**Figure 3A** violet cells). The basal lamina separates the trophoblast from the villous stroma (**Figure 3A** orange lamina). The stroma (intercellular space, pink in **Figure 3A**) is composed of connective tissue cells, such as first mesenchymal cells that differentiate to fibroblasts in the last trimester, connective tissue fibers, tissue macrophages (Hofbauer cells) and fetal vessels (**Figure 3D**) (Baergen 2005). Interestingly, it is speculated that Hofbauer cells play a role in iron storage and homeostasis as described in 1.5.2 on p.19ff.

There are two important cell layers in the chorionic villi to coordinate the nutrient transfer, namely the fetal capillary EC and the STB. The EC form the fetal vessels, which allow the unrestricted diffusion of the molecules like glucose and amino acids (peptides <204 Da) through the paracellular channels (Edwards et al. 1993; R. M. Lewis et al. 2013). In contrast, STB represent the limiting barrier for charged macro- and microelements due to the syncytium composed of two polarized plasma membranes, the microvillous plasma membrane (MVM) facing towards the maternal side and the basal membrane (BM) directed towards the fetal capillary (**Figure 3A**). However, strikingly little information has been published on the molecular transport mechanisms and regulations involved in controlling the crucial interface between mother and fetus. Therefore, this project investigated the physiology of fetal nutrition, mainly focusing on the STB-mediated

materno-fetal transfer of fundamental macromolecules (amino acids) and the most abundant trace element (iron).

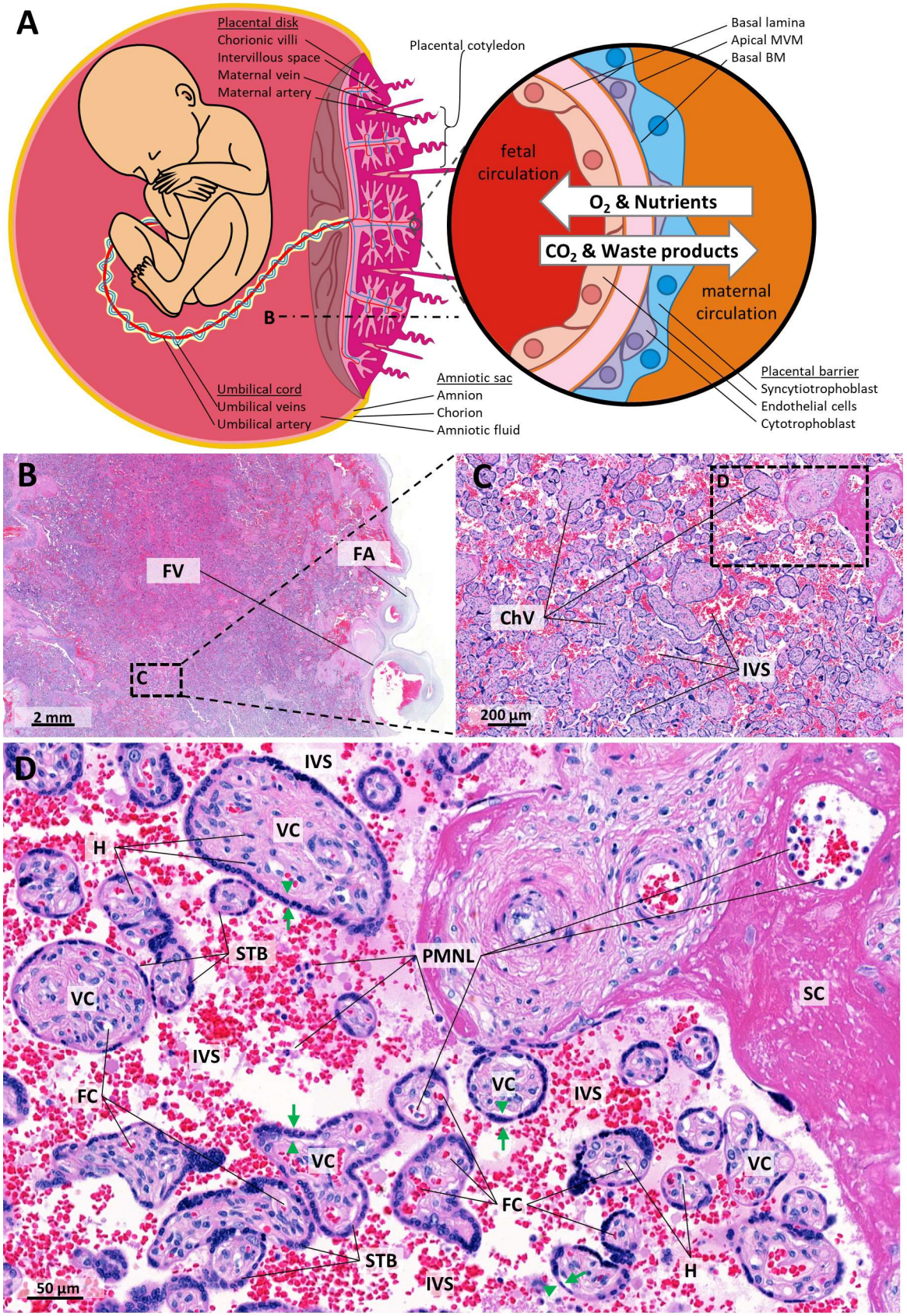

Figure 3: Simplified representation and histological pictures of the human placenta as connection between the developing fetus and the maternal circulation separated through the placental barrier. Scheme a developing fetus connected via umbilical cord to the placenta (**A**, left panel). Cross section of the placental disk revealing fetal villous structures and the maternal interface connecting the intervillous space via spiral arteries and maternal veins to the uterine blood supply. **A**, right panel, closeup of the placental barrier in a chorionic villous as hemochorial interface between the fetal capillaries (fetal blood compartment in red) and the maternal circulation (maternal blood compartment in orange). The human placental barrier involves three different cell types: endothelial cells (EC) lining the fetal capillaries, single-nucleated cytotrophoblasts (CTB, violet) and syncytiotrophoblasts (STB, blue) forming a multi-nucleated monolayer. The STB are in direct contact with maternal blood and mainly responsible for materno-fetal nutrient and feto-maternal CO_2 and waste product exchange. **B**-**D**, histological pictures of haematoxylin and eosin (HE) stained placental tissue at term with increasing magnification as indicated by the dashed boxes (placental tissue from Malia Zaugg, *20.12.2019). **B**, section through the chorionic plate at the fetal side with macroscopically visible superficial fetal artery (vessel cross section with thicker wall) and vein (larger vessel with thinner wall) still containing erythrocytes (purple cells) to the right of the picture. **C**, with a 5 x magnification the intervillous space (IVS) filled with erythrocytes and the hierarchy of chorionic villi becomes visible. There are large villi with condensed collagen fibers (fibers in magenta) in the stroma histologically called stem villi (upper right structure in C and D) making about 20-25% of the placental volume at term, but also small and intermediate villi that are long and slender with numerous capillaries. **D**, beside the large stromal villi to the right with completely fibrotic stromal core (magenta), single placental cells are visible with 20 x magnification. There are small and intermediate villi with multinucleated STB at the borders and fetal capillaries (nuclei in dark blue), stromal and Hofbauer cells in the stromal core, but also numerous erythrocytes in the IVS. Green arrows indicate the apical microvillous membrane (MVM), i.e. maternal blood orientated side; arrowheads depict the basal membrane (BM) of the STB. As is typical for term placentae, the trophoblastic cover of the stem villi is partly replaced by fibrinoid. The stromal core is completely fibrotic. Abbreviations: FV, fetal vein; FA fetal artery; MV, microvilli; IVS, intervillous space; STB, syncytiotrophoblast; VC, villous core; PMNL, polymorphonuclear leukocytes; H, Hofbauer cell; FC, fetal capillary; SC, stromal core.

1.5 Nutrient transport across the placenta

Human hemochorial placenta represents the structural barrier and prevents the direct contact between maternal and fetal blood as explained before in 1.4, which highlights the importance of diffusion, endocytosis/exocytosis and transporter-, channel- or facilitator-mediated mechanisms for nutrient exchange across the materno-fetal interface (**Figure *4***).

Passive transport

Nutrients can be transferred across epithelial barriers either between STB cells via intercellular water-filled pores (paracellular transport) or through cells (transcellular transport) by diffusion (**Figure 4**, left panel). Simple diffusion is the adenosine triphosphate (ATP) -independent passage of molecules across lipid bilayers of the cell

membranes and the cytoplasm in-between. For small uncharged molecules, the rate of diffusion is governed by Fick's Law of diffusion, being proportional to the surface area for exchange and inversely proportional to the thickness of the placental barrier. Small hydrophobic molecules cross cell membranes easily, so their transplacental flux depends principally on the concentration and electrochemical gradient. The main factor maintaining such a gradient is the rate of blood circulation on both sides of the membrane, refreshing and depleting the donating and receiving pools respectively (Burton, Fowden, and Thornburg 2016). Hence, exchange of molecules such as the respiratory gas O_2 and lipophilic drugs are flow-limited, thus changes in maternal or fetal blood flow have a strong impact on their net flux (Wilkening and Meschia 1992).

Since the STB represent a true syncytium, no intercellular spaces exist in the transporting epithelium of the human placenta. However, there are evidences for transtrophoblastic channels (**Figure 4**, second from left), pores filled with water traversing the syncytiotrophoblast revealed by electron microscopy and by physiological data obtained in several species with hemochorial placentae, demonstrating that the transplacental flux of small inert hydrophilic molecules is proportional to their water diffusion coefficients (Kertschanska, Kosanke, and Kaufmann 1997). Although STB are able to generate and maintain significant concentration differences for a large variety of molecules across the placental barrier, including Ca^{2+} and amino acids, the transfer of large molecules such as alpha-fetoprotein across perfused placental cotyledons *ex vivo* are confirming the existence of transtrophoblastic channels (Brownbill et al. 1995). Occasional membrane clefts and ruptures resembling intercellular spaces have been reported, but may represent areas of repair associated with fibrin deposits. However, the primary route of transport across the placental barrier for nutrients and important ions is in most cases conveyed by specific solute carrier-mediated transport mechanisms (Sadovsky and Jansson 2015).

Active transport

The transplacental transfer of most nutrients and ions is dependent on carrier proteins spanning the cell membranes to facilitate the passage of highly hydrophilic molecules (**Figure 4**, middle panel). They are characterized similar to enzymes by features such as substrate specificity, saturation kinetics, and the ability to be inhibited. When mediated

membrane transport does not require energy, the transport is termed facilitated transport, while active transport implies that energy is consumed usually by ATP hydrolysis. Transport mechanisms are generally classified as direct primary active transport, indirect secondary active or indirect tertiary active transport. The most common pathway for regulated nutrient transport in the placental barrier is via transporter proteins in the STB plasma membranes. Materno-fetal glucose transfer mediated by facilitative glucose transporters (GLUT1) expressed in the MVM and BM of the STB is an example of facilitated transport (such as depicted in green **Figure 4**). Calcium efflux across the BM, mediated by calcium (Ca^{2+})-ATPase, is an example of primary active transport. Sodium (Na^{+})-dependent transport systems for amino acids, such as System A, represent a secondary active transport mechanism and hence the tertiary active like System L transport of large neutral amino acids is maintained by System A dependent amino acids gradients (see 1.5.1 on p.12). Transplacental transport may also be facilitated by the expression of substrate binding proteins such as fatty acid-binding proteins in the STB cytosol (Sadovsky and Jansson 2015). Of note, there is evidence of great clinical relevance indicating that expression of transporter systems is responsive to nutritional and hormonal stimuli. This flexibility allows the placenta to adapt functionally by insertion of transporter proteins into the appropriate membrane (Winterhager and Gellhaus 2017; Thomas Jansson and Powell 2007).

Transcytosis

Receptor-mediated or passive intracellular vesicle formation occurs by invagination of the apical or basolateral side plasma membrane of STB. Subsequently, vesicles may be transported to the opposite side of the cell, where the vesicle content can be released into the extracellular space following fusion of the vesicles with the plasma membrane (**Figure 4**, right panel). In non-mediated endocytosis and transcytosis vesicles are formed at the plasma membrane incorporating fluid and any dissolved solute. Vesicles from non-mediated endocytosis are transferred across the syncytium via Brownian movement (Sadovsky and Jansson 2015). Mediated endocytosis involves the binding of a specific ligand to a receptor in the plasma membrane, which initiates the clathrin-mediated invagination of the plasma membrane. Transfer of vesicles formed by mediated endocytosis across the cytoplasm is guided by intracellular trafficking and specific

cytoskeletal components, respectively (R. Fuchs and Ellinger 2004). Transcytosis plays an important role in the transfer of immunoglobulin G (IgG), iron (see 1.5.2 on p.19), and lipoproteins across the placental barrier. Large molecules such as IgG and cholesterol are transported by transcytosis as third class of mechanisms for transplacental transport (**Figure 4**). IgG binds to the MVM of the STB surface, concentrates in clathrin-coated pits or is internalized through non-mediated endocytosis, and delivered to early endosomes (Henning Schneider and Miller 2010). Uptake of maternal proteins by endocytosis has been described for megalin-mediated albumin endocytosis in the human STB (Lambot et al. 2006) and is particularly prominent during the histotrophic period in the first trimester when maternal glycoproteins are secreted by the endometrial glands (Burton et al. 2002).

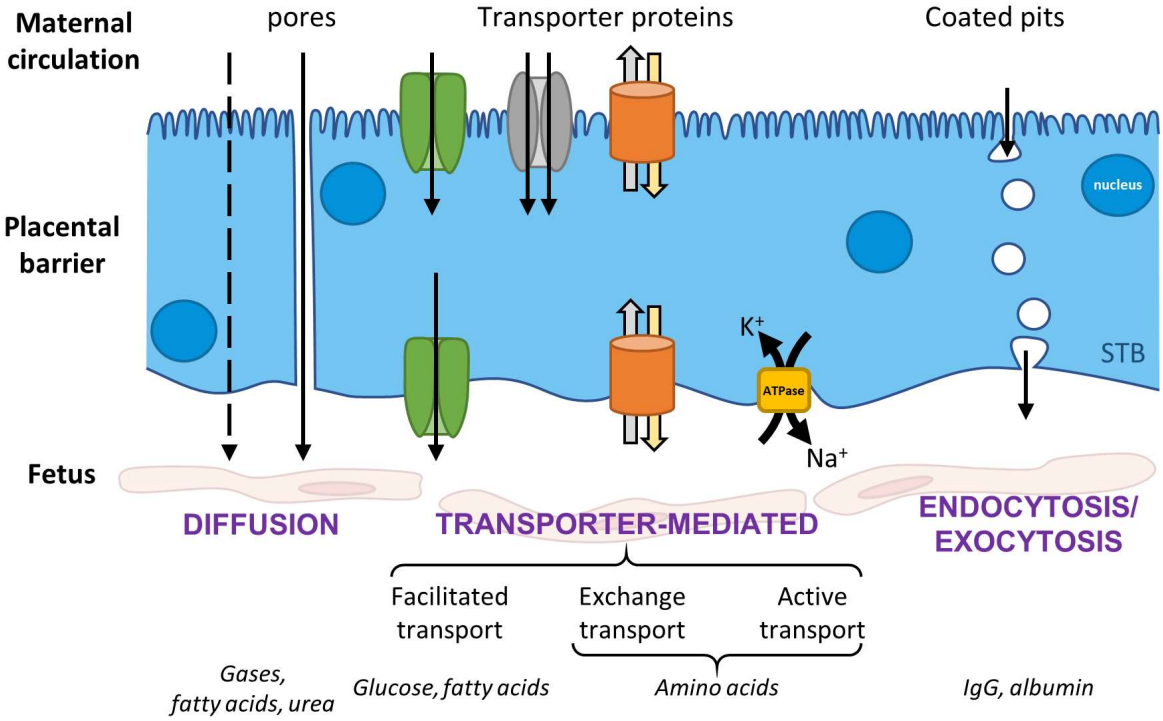

Figure 4: Schematic representation of the general nutrients transport mechanisms in the human placenta. The three main processes by which materials such as gases, ions, water, sugars, amino acids, lipids, vitamins and minerals, but also drugs and xenobiotics can cross the placental barrier: diffusion, transporter-mediated, and endo-/exocytosis. Transcellular non-mediated (dashed arrow) and transtrophoblastic channel-facilitated diffusion are depicted to the left. Solute carrier- or transporter-mediated transport often form interactive transport systems, that are composed of channels or facilitators (green), co-transporter (grey) and gradient-dependent exchanger (orange), which are ultimately driven by ATPase activity (yellow). Transcytosis is mediated by clathrin-dependent endocytosis, intracellular trafficking, and exocytosis (right panel). Modified from (Burton, Fowden, and Thornburg 2016).

1.5.1 Amino acid transport

Beside representing the fundamental building components required for fetal protein synthesis, amino acids constitute critical precursors for the biosynthesis of porphyrins, nitric oxide, neurotransmitters and nucleotides. It is estimated that 32% of the energy requirement of well-nourished fetal sheep is derived from amino acid oxidation and used as fetal energy source (Faichney and White 1987). Comparable amino acid oxidation estimates were published in humans. In two studies healthy pregnant women received continuous stable isotope infusions of the essential amino acids ^{13}C-leucine, ^{13}C-valine, ^{15}N-phenylalanine and ^{13}C-methionine 4 h before elective cesarean section. Then the enrichment and concentration of amino acids and carbon dioxide was measured in cord blood. Fetal whole-body accretion of leucine carbon was 69% of the umbilical uptake. Both studies estimated that 33-40% of total leucine carbon uptake is oxidized, although whole-body protein synthesis was much faster in the fetus than in adults (Van Den Akker et al. 2011; Chien et al. 1993).

The role of amino acid concentrations in placental transport

Appropriate fetal growth is largely dictated by the availability of amino acids in the maternal circulation, which is ensured during pregnancy by the capacity of the placenta to transfer amino acids from the maternal into the fetal circulation (Frederick C. Battaglia and Meschia 1988; Vaughan et al. 2017). For most amino acids, the concentrations in the umbilical vein are two- to threefold higher than in the uterine vein, demonstrating that the transfer of amino acids is an active energy-dependent process against counter-directed feto-maternal gradients (Philipps et al. 1978; Irene Cetin et al. 1990; Thomas Jansson 2001; Jane K. Cleal and Lewis 2008). This is also supported by the observation that placental concentrations of amino acids are, in general, much higher than in the blood on either side of the placental barrier (Philipps et al. 1978). Already in 1973 Hill et al. demonstrated in placenta perfusion experiments in guinea pigs that System L-mediated materno-fetal leucine transfer was two-fold increased after application of feto-maternal gradients (Hill and Young 1973). However, extrapolation of results from animal experiments to humans must be done with caution, specifically as the structure and anatomy of the human placenta is quite unique among mammals (Schmidt et al. 2015). To our knowledge, no human trophoblast studies have assessed the functional effect of

counter-directed amino acid gradients on transplacental amino acid transfer *in vitro*. There are few studies that investigated materno-fetal amino acid transfer under different physiological and pathological conditions *in vivo.* This was performed by measuring amino acid concentration differences between fetal arterial and fetal venous sera obtained from umbilical cord blood and/or from the uteroplacental unit in the maternal circulation (Pohlandt 1978; Malinow et al. 1998; McIntosh, Rodeck, and Heath 1984; Irene Cetin et al. 1988; Karsdorp et al. 1994; Irene Cetin et al. 2005; Bajoria et al. 2001; Cockburn et al. 1971). Such observational correlation studies revealed interesting associations by comparing paired amino acid concentrations in maternal radial artery and uterine vein with fetal umbilical vein and artery sides with each other (Holm et al. 2017). However, potential relationships between amino acid gradients and demographic data such as maternal constitution or fetal growth have not been reported yet.

Transplacental amino acid transport

Amino acid transporters expressed in human placenta are categorized into accumulative transporters, exchangers and facilitators (**Table 1**). Accumulative transporters mediate cellular uptake, resulting in increased intracellular amino acid concentrations. Amino acid exchangers exchange one amino acid for another, resulting in altered amino acid composition without changing total concentration (S. Bröer 2002). The primary driving force for amino acid uptake across the MVM mediated by accumulative cotransporters is the extra-intracellular directed Na^+ gradient exploited by Na^+-dependent System A and taurine transporter families (see **Table 1**). The difference of the membrane potential is the driving force mediating uptake of the cationic amino acids (arginine, histidine, and lysine) by System y^+, y^+L or $b^{0,+}$ families (see first section in **Table 1**). The System L-amino acid transporters LAT1, LAT2, LAT3 and LAT4 are exchangers using the outwardly directed concentration gradients of nonessential amino acids as tertiary active mechanism to drive the uptake of essential amino acids (e.g. leucine), against its counter-directed concentration gradient (**Figure 5**). The energy for the uphill transport of amino acids is ultimately generated by the Na^+K^+-ATPase, which extrudes sodium in exchange for potassium, thereby maintaining a low intracellular Na^+ concentration and creating a potential difference across the plasma membrane (Johansson, Jansson, and Powell 2000). Subsequently, amino acids are transferred across the BM by non-mediated or facilitated

diffusion driven by the intra-extracellular directed concentration gradient (see more details in the next paragraph). Although the amino acid uptake mechanisms and interactions across the MVM into the STB are well studied, the mechanisms by which amino acids are transported out of the STB towards the fetal circulation across the BM and the ratio to which amino acids are metabolized by the human placenta are not well elucidated yet (Jane K. Cleal and Lewis 2008; J. K. Cleal et al. 2011). The asymmetric distribution of amino acid transporters between the STB MVM and BM is critical to generate a net materno-fetal flux of amino acids. Of note, the human STB expresses at least 20 different amino acid transporters (**Table 1**), with each transporter mediating the uptake of several amino acids, and each amino acid can be transported by multiple transport systems (Sadovsky and Jansson 2015). Computational modelling of amino acid transfer demonstrated the importance and interrelation of amino acid gradients by considering separate maternal and fetal compartments and specific kinetic properties of accumulative and exchanging amino acid transporter systems (Sengers, Please, and Lewis 2010). Although there is a well-known interdependence between Na^+ and different amino acid transport systems depending on co-substrate gradients, no human trophoblast studies have assessed the functional effect of counter-directed materno-fetal amino acid gradients on transplacental transfer of essential amino acid so far.

Table 1: Amino acid transport systems in the human placenta, modified and updated from (Sadovsky and Jansson 2015)

System	Activity	Protein	Gene	Transport type*	Localization	Substrates	Ref.
Na^+-dependent transporters for neutral amino acids							
A	MVM ≫ BM	SNAT1	*SLC38A1*	CoT / Na^+	MVM	(Gly), Ala, Ser, Cys, Gln, Asn, His, (Met), MeAIB	[1-3]
		SNAT2	*SLC38A2*	CoT / Na^+	MVM	Gly, Pro, Ala, Ser, Cys, Gln, Asn, His, Met, MeAIB	[4]
		SNAT4	*SLC38A4*	CoT / Na^+	MVM, BM	Gly, (Pro), Ala, Ser, Cys, Asn, (Met), (MeAIB)	[4]
ASC	BM MVM?	ASCT1	*SLC1A4*	CoT / Na^+, ExT / AA		Ala, Ser, Cys, Thr	[1]
		ASCT2	*SLC1A5*	CoT / Na^+, ExT / AA		Ala, Asn, Ser, Cys, Thr, Gln	[3]
B^0	?	B^0AT1	*SLC6A19*		nd	neutral amino acids; Ala, Asn, Cys, Gln, Gly, Ile, Leu, Met, Phe, Pro, Ser, Thr, Trp, Tyr, Val	[5,6]
		B^0AT2	*SLC6A15*		nd	large, neutral amino acids	
N	MVM?	SNAT3	*SLC38A5*	CoT / Na^+, ExT / H^+	nd	Ala, His, Gln, Asn	[7]
		SNAT5	*SLC39A3*	CoT / Na^+, ExT / H^+	nd	Asn, Gln, His, Ser	[8]
Gly	MVM	XT2	*SLC6A18*		nd	Gly	[9]
β	MVM ≫ BM	TauT	*SLC6A6*		MVM, BM	Tau, β-ala	[10,11]
Na^+-independent transporters for neutral amino acids							
L	MVM, BM	LAT1	*SLC7A5*	ExT	MVM	(Gln), His, Met, Leu, Iso, Val, Phe, Tyr, Trp, BCH, T3, T4, L-DOPA	[1]
		LAT2	*SLC7A8*	ExT	MVM (50 kD) BM (30 kD)	Ala, Ser, Cys, Thr, Asn, Gln, His, Met, Leu, Iso, Val, Phe, Tyr, Trp, T3, T4, BCH	[3]
	BM?	LAT3	*SLC43A1*	FaT	BM	L-BCAAs, amino alcohols	[12,13]
	BM?	LAT4	*SLC43A2*	FaT	BM	Phe, Leu, Iso, met, BCH	[14]
	BM?	TAT1	SLC16A10	FaT	BM	Phe, Leu, T3, T4	[13]
Transporters for cationic amino acids							
y^+	MVM>BM	CAT1	*SLC7A1*	FaT (non-obligatory ExT)	BM	Arg, Lys, His	[15]
		CAT2B	*SLC7A2*	FaT	nd	Arg, Lys, His	[16]
		CAT3	*SLC7A3*	FaT	nd	Arg, Lys	
		CAT4	*SLC7A4*	OrT	nd	Arg, Lys, ornithine	
y^+L	BM>MVM	y^+LAT1	*SLC7A7*	ExT / Na^+, Arg, Lys, His	nd	Arg, Lys, His (Na^+ indep.); Gln, Met, Leu (Na^+ dep.)	[15]
		y^+LAT2	*SLC7A6*	ExT / Na^+, Arg, Lys, His	nd	Lys, Arg, Gln, His, met, Leu,a Ala, Cys	[16]
$b^{0,+}$	BM?	$b^{0,+}$ AT	SLC7A9		nd	Lys, Arg, Ala, Ser, Cys, Thr, Asn, Gln, His, Met, Iso, Leu, Val, Phe, Tyr, Trp	
Transporters for anionic amino acids							
X^-_{AG}	MVM, BM	EAAT1	*SLC1A3*	CoT / Na^+, H^+, K^+	nd	Glu, Asp, Cys	[17]
		EAAT2	*SLC1A2*	CoT / Na^+, H^+, K^+	nd	Glu, Asp	[18]
		EAAT3	*SLC1A1*	CoT / Na^+, H^+, K^+	nd	Glu, Asp	

References: [1] (L. W. Johnson and Smith 1988), [2] (Michelle Desforges et al. 2009), [3] (Hoeltzli and Smith 1989), [4] (Schiöth et al. 2013), [5] (Pramod et al. 2013), [6] (Lassance et al. 2015), [7] (Peter I. Karl, Tkaczevski, and Fisher 1989), [8] (Novak and Beveridge 1997), [9] (Dicke et al. 1993), [10] (Miyamoto et al. 1988), [11] (Norberg, Powell, and Jansson 1998), [12] (Kudo and Boyd 2001), [13] (J. K. Cleal et al. 2011), [14] (Jane K. Cleal et al. 2007), [15] (Furesz, Moe, and Smith 1995), [16] (Ayuk et al. 2000), [17] (Hoeltzli et al. 1990), [18] (Moe and Smith 1989); *Abbreviations for transport type: CcT: Cotransporter; ExT: Exchanger; FaT: Facilitated transporter; OrT: Orphan transporter.

System L mediated leucine transport across the placenta

The System L amino acid transporters are a Na^+-independent exchanger family that mediates cellular uptake of essential amino acids, such as leucine, methionine and tryptophan. Since no accumulative transporters that transport essential amino acids are expressed in the MVM, System L exchange of nonessential amino acids in the STB cytosol with extracellular essential amino acids is critical for the uptake of essential amino acids across the MVM (Sadovsky and Jansson 2015). The Na^+-independent System L-transporters expressed in the human placenta are heterodimeric exchangers consisting of the light chain L-type amino acid transporter 1 (LAT1 / *SLC7A5*) or L-type amino acid transporter 2 (LAT2 / *SLC7A8*), responsible for amino acid transport, covalently attached to the heavy chain 4F2 (*SLC3A2*), important for trafficking of the light chain to the plasma membrane (Fotiadis, Kanai, and Palacín 2013). Moreover, the SLC43-family members LAT3 (*SLC43A1*) and LAT4 (*SLC43A2*), known to be involved in facilitated amino acid diffusion (Bodoy et al. 2013; J. K. Cleal et al. 2011), are expressed at the BM (**Table 1**). As depicted in **Figure 5**, LAT1 and LAT2 are predominantly localized at the MVM of human term placenta, LAT2 is also present at the BM and in endothelial cells lining the fetal capillaries (Gaccioli et al. 2015). Kudo and Boyd have suggested that LAT1 expression at the MVM mediates System L activity across the placental barrier (Kudo and Boyd 2001), whereas Lewis et al. have shown LAT2 as the predominant transporter in the MVM (R. M. Lewis et al. 2007). The efflux transporters LAT3 and LAT4 are expressed in the placenta, and LAT4 has been demonstrated to be functional in isolated perfused human placental cotyledons, suggesting that the System L facilitators LAT4 and probably also LAT3 may also play a role in the efflux of certain essential amino acids across the BM (Jane K. Cleal et al. 2007).

In the last decade, increasing evidence suggests a tight link between the reduced activity of placental System L-transporters and intrauterine growth restriction (IUGR) (Paolini et al. 2001; Lager and Powell 2012), and their upregulation in placentae of large for gestational age (LGA) infants (Thomas Jansson et al. 2002). Such altered fetal development has a fundamental impact on lifelong health and wellbeing, and may contribute by fetal programming to an increased prevalence for cardiovascular disease and diabetes/adiposity later in life (Harder et al. 2007; Eriksson et al. 2003; Boney et al. 2005; Leon et al. 1998). Notably, it has been reported that LAT1 or its associated

glycoprotein 4F2hc is involved in placenta decidualization and fusogenic trophoblast differentiation (Ohgaki et al. 2017). This could imply that the diminished leucine uptake found in knock-down cell models (Balthasar et al. 2017) results rather from failure in trophoblast differentiation than from reduced SLC7 transport activity. Hence, small molecules which induce only short-term inhibition of transporter activity are a valuable experimental tool to study placental transfer mechanisms as they will not affect trophoblast differentiation and associated processes like trophoblast fusion. Therefore, studying placental amino acid transfer by using specific small molecule inhibitors of amino acid transporters instead of silencing or knock-out could help to reveal the relevance of LAT1 or LAT2 in materno-fetal leucine transfer without affecting cell differentiation. Since LAT1 was found to be selectively expressed and upregulated in various rapidly proliferative cancer types (Häfliger and Charles 2019; B. C. Fuchs and Bode 2005; Kaira et al. 2008) and has a putative role in drug delivery across the blood-brain barrier (Peura et al. 2011), efforts have been made to pharmaceutically target this transporter using substrate-mimicking or virtual screening approaches (Singh et al. 2019; Augustyn et al. 2016; Geier et al. 2013; Kongpracha et al. 2017; Scalise et al. 2018). The substrate-mimicking tyrosine analog JPH203 (also known as KYT-0353) was tested in several *in vitro* and *in vivo* cancer cell proliferation experiments and described as potent LAT1-specific inhibitor (Enomoto et al. 2019; Cormerais et al. 2019; Muto et al. 2019; Häfliger et al. 2018; Yothaisong et al. 2017). To delineate the contribution of LAT1 from LAT2 in materno-fetal leucine transport, the collaborating chemists within the NCCR TransCure network synthesized the LAT1-specific inhibitor JPH203, the structurally closely related inhibitor JG336 and two other small molecule inhibitors (JX009, JX020) with high leucine uptake inhibition efficiency but lower LAT1-specificity (structures see **Figure 22** on p.85). To our knowledge, no human trophoblast studies have tried to dissect transporter interplay by application of transporter selective small molecule inhibitors or transporter targeted Clustered Regularly Interspaced Short Palindromic Repeats (CRISPR) /CRISPR-associated endonuclease (Cas9) mutagenesis for the generation of SLC knockout cell lines.

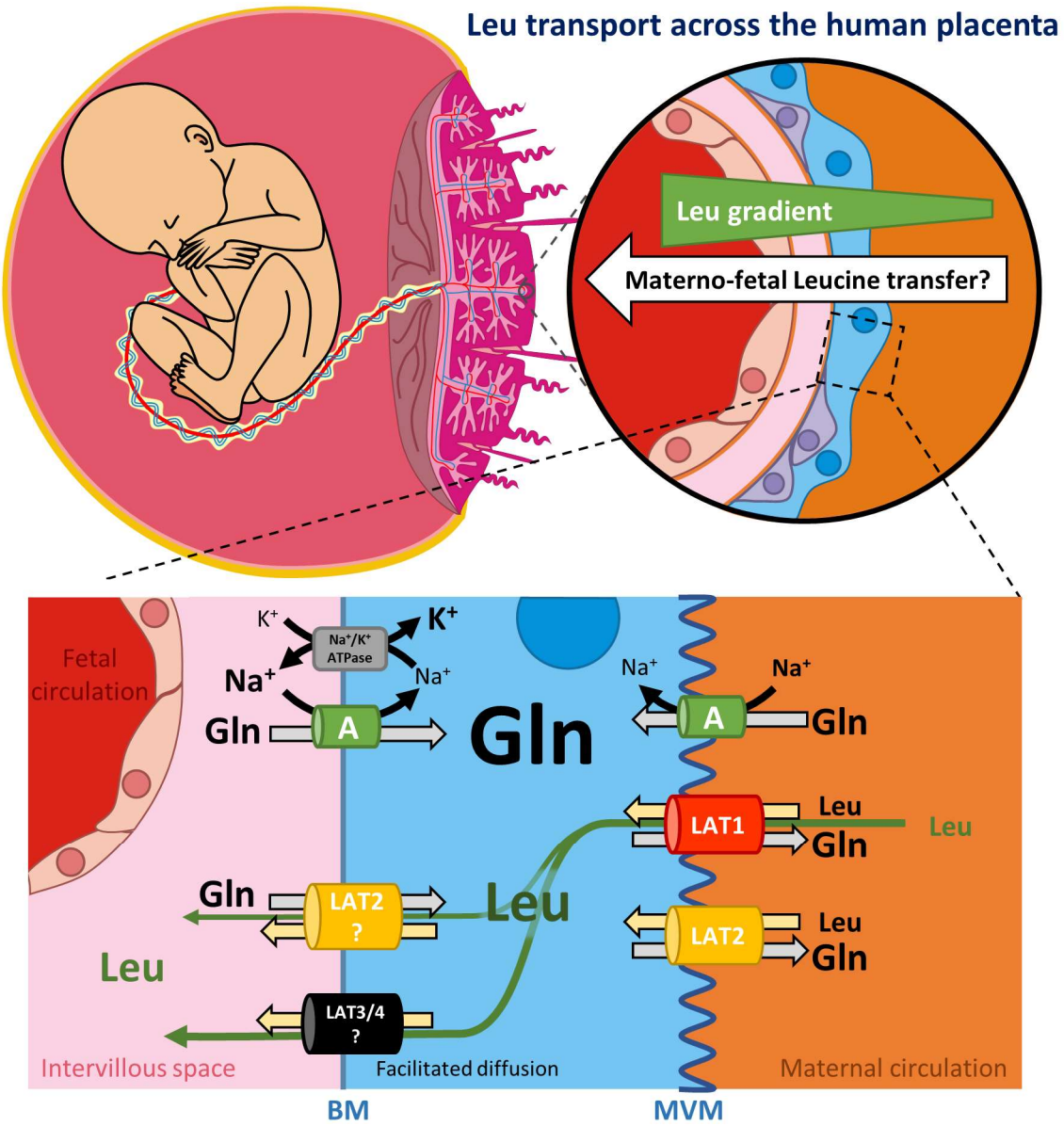

Figure 5: Asymmetric expression of amino acid transporters allows leucine transfer across the human placenta against a counter-directed gradient. The uptake of the essential amino acid leucine (Leu) from the maternal circulation across the microvillous membrane (MVM) into the syncytiotrophoblast (STB) represents the active step of amino acid transport and is mediated by accumulative System A transporters (green) in the interplay with amino acid exchangers (LAT1/*SLC7A5* in red, LAT2/*SLC7A8* in yellow). System A transporters mediate cellular uptake across the MVM, resulting in increased intracellular concentrations of non-essential amino acid like glutamine (Gln). On the other hand, amino acid exchangers like LAT1 and LAT2, both expressed at the MVM, exchange one branched-chain amino acids (BCAA, like Leu) for another (in this case Gln), resulting in altered amino acid composition without changing the total intra-extracellular concentration. The driving forces for the amino acid uptake mediated by accumulative transporters are the inwardly directed Na^+ gradient that is ultimately maintained by the Na^+/K^+-ATPase (grey). System L exchangers use the extracellularly directed concentration gradient of nonessential amino acids (NEAA) to drive the uptake of Leu against its materno-fetal concentration gradient. Finally, Leu is transferred across the BM by facilitators like LAT3-, LAT4- or potentially TAT1-mediated diffusion driven by the extracellularly directed concentration gradient on the fetal side. The font size of the amino acid in the 3-letter code represents an

estimation of their relative concentration in the fetal (left in pink and red), intracellular (middle in blue) and maternal (right in orange) compartment.

1.5.2 Iron transport

In humans, the iron requirement during pregnancy is significantly higher in comparison to the nonpregnant state to fulfill fetal and placental iron needs (**Figure 6**). As pregnancy progresses, iron requirements for fetal growth rise steadily in proportion to the weight of the fetus. Although, the requirements of iron are even lower in the first trimester, if compared to the nongravid state, around 80% of the gestational iron requirements are accumulating during the third trimester upon term (Thomas H. Bothwell 2000). All iron homeostasis genes known to be expressed in human placenta are listed in **Table 11** on p.91.

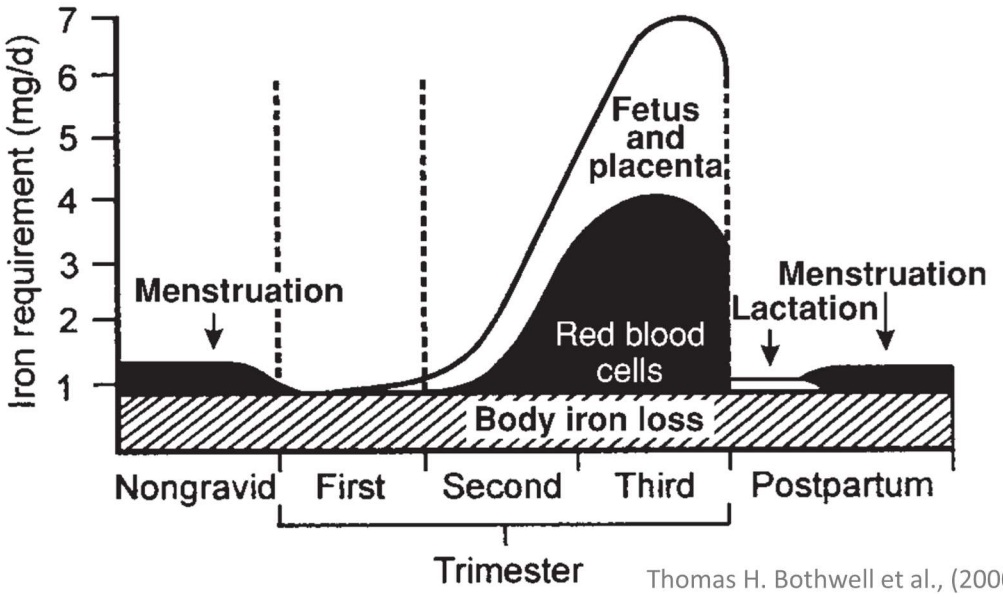

Thomas H. Bothwell et al., (2000)

Figure 6: Estimated daily iron requirements during pregnancy in a 55 kg woman from (Thomas H. Bothwell 2000)**.** Although reduced during the first trimester, iron requirements rise to 4-6 mg in the second and third trimesters, respectively. Major changes in the red blood cell mass start in the middle of the second trimester, iron requirements may reach as much as 10 mg/d during the last 6-8 weeks of pregnancy (T H Bothwell et al. 1979). Irrespective of the exact value, it is apparent that daily iron requirements cannot be met from dietary absorption alone in the latter part of pregnancy, even from the most optimal diet. In diets containing large quantities of bioavailable iron, e.g. diets with generous quantities of meat, poultry, fish and foods containing high amounts of ascorbic acid, overall iron absorption is usually 3-4 mg/d and, at most, 5 mg/d (T H Bothwell et al. 1979). The amount of iron absorbed is much lower when the diet contains only small amounts of bioavailable iron, as is often the case in many developing countries where the staple food is cereal and the intake of meat and ascorbic acid is limited (Thomas H. Bothwell 2000).

Iron uptake at the maternal side across the microvillous membrane

Since there is no possibility in human placenta to secrete iron across the MVM into the maternal circulation, placenta mediated fetal iron homeostasis is controlled exclusively by regulating iron uptake. **Figure 7** depicts the pathways of transplacental iron transport in humans. Transferrin (Tf) -iron is the major, if not the only maternal iron source for placental transfer. Tf receptor 1 (TfR1) is a homodimeric transmembrane protein with high affinity for diferric Tf ($2Fe^{3+}$-Tf). Expressed in virtually all cells except mature erythrocytes, TfR1 is found at extraordinarily high levels in STB. This is probably the reason, why TfR1 was first isolated in placental tissue (Seligman, Schleicher, and Robert 1979). Despite the likely importance of TfR1, the mechanism of iron transport in the placenta remains poorly characterized, partly because of the lack of *in vitro* models that mimic the polar iron physiology of the placental STB (C. Cao and Fleming 2016). Immunohistochemical studies have localized TfR1 and Tf to the apical membrane of syncytiotrophoblasts in clathrin-coated endosomes (Booth and Wilson 1981). The disruption of endosomal acidification after endocytosis by the weak base chloroquine inhibits placental accumulation (promoting H^+-dependent DMT1) and fetal transfer of Tf-iron, demonstrating the requirement of acidification in Tf-iron utilization in the classic Tf cycle (Contractor and Eaton 1986).

In endosomes of erythrocytes, ferric iron (Fe^{3+}) is reduced to ferrous iron (Fe^{2+}) by the ferrireductase six-transmembrane epithelial antigen of the prostate 3 (STEAP3) and is subsequently transported across the endosomal membrane by divalent metal transporter 1 (DMT1/*SLC11A2*). Although there is still a lack of experimental proof, STEAP3 and DMT1 play probably essential roles in the placenta (C. Cao and Fleming 2016). Of note, the alternative ferrireductase candidate STEAP4, a homolog of STEAP3, is also highly expressed in the human placenta (Ohgami et al. 2006).

Beside DMT1 there are also alternative ferrous iron transporter that mediate endosomal iron export from the endosome into the cytosol. DMT1 is critical for endosomal iron release in erythrocytes and in enterocytes (Veuthey and Wessling-Resnick 2014). There are *in vivo* studies suggesting DMT1 as not exclusive endosomal iron exporter, as demonstrated in the two DMT1 mutant animal models microcytic anemia (mk) -mouse and Belgrade-rat (Tabuchi et al. 2000; Veuthey and Wessling-Resnick 2014; Farcich and

Morgan 1992). Due to viable but severely anemic birth of Dmt1-null mice, the role of DMT1 in placental iron transport requires further experimental confirmation (Gunshin et al. 2005). Other potential endosomal iron transporters with high expression in the human placenta are Zrt- and Irt-like protein 8 (ZIP8/*SLC39A8*) and Zrt- and Irt-like protein 14 (ZIP14/*SLC39A14*), both members of the SLC39 zinc (Zn^{2+}/$(HCO_3^-)_2$) transporter family that also transport ferrous iron (Fe^{2+}) (Jenkitkasemwong et al. 2012). ZIP14 has been shown to mediate plasma membrane uptake of non-Tf-bound iron (Liuzzi et al. 2006) as well as Tf-iron from endosomes (Zhao et al. 2010). Targeted Zip14 mutants have no abnormal birth phenotype except lower birth weight (Hojyo et al. 2011), while deletion of Zip8 in mice leads to complete mortality before birth (Wang et al. 2011). Despite different pH-dependence, ZIP14 and ZIP8 together with DMT1 probably play redundant roles in placental endosomal iron export.

Finally, there is discrepancy of ferritin expression in STB. There are reports showing a lack of expression (Bastin et al. 2006; Maymon et al. 2000), while others demonstrate some staining for a placental-specific ferritin heavy chain (FHC) homolog (Brown et al. 1979; Yasemin et al. 2011). This discrepancy may be due to the use of inadequate antibodies reacting differentially with each ferritin isoform. However, fetal villous stromal cells consistently show pronounced ferritin staining in all studies cited above (Bastin et al. 2006; Maymon et al. 2000; Brown et al. 1979; Yasemin et al. 2011). This raises the possibility that the villous stroma may serve as a buffer between the STB and fetal circulation to ensure adequate, but not excessive, iron supply. Whether synthesis and degradation of ferritin in the stromal cells respond to fetal iron demand is unknown (C. Cao and Fleming 2016). The function of the villous macrophages, known as Hofbauer cells (see in histological picture **Figure 3** on p.8), is not well defined but may include the support of trophoblast differentiation, stromal development, angiogenesis and erythroid cell maturation (Tang et al. 2011; Van Handel et al. 2010). Interestingly, Hofbauer cells express most of the major heme and nonheme iron transporters and storage proteins (Bastin et al. 2006; Georgieff et al. 2000), suggesting a role in iron transport and/or regulation (Van Handel et al. 2010). Therefore, Hofbauer cells may serve as the temporary iron storage buffer in the villous stroma, storing iron when maternal supply exceeds fetal demands and releasing iron when iron supply is low.

Although, it can be inferred that TFR1, DMT1, STEAP3, ZIP8 and ZIP14 are essential for iron uptake in the placenta, experiments designed to exactly localize and functionally test this hypothesis are still lacking.

Iron efflux at the fetal side across the basal membrane

Iron export from the STB to the fetal stroma is mediated by the iron exporter ferroportin 1 (FPN1/*SLC40A1*). FPN1 is abundantly expressed along the BM of human STB (Bastin et al. 2006) Mouse embryos with a hypomorphic mutation leading to a reduced expression of Fpn1 are severely iron deficient at embryonic day 12.5 (E12.5) 12.5 and exhibit defects in neural tube closure and forebrain patterning (Mao et al. 2010), strongly suggesting a role of Fpn1 in materno-fetal iron transport. Additionally, an iron-responsive elements (IREs) deletion in the Fpn1 untranslated region (UTR) results in dysregulation of Fpn1 in organogenesis of multiple organs and markedly reduced FPN1 protein expression in the mouse placenta, causing severe anemia and iron deficiency in embryonic tissue at birth (Mok et al. 2004). These results strongly suggest that Fpn1 expression and function at the materno-fetal interface is essential for normal embryonic development. Although all mouse studies suggest an essential role of Fpn1 in placental iron transfer, to our knowledge, there are no articles investigating iron efflux across the BM of STB towards the fetal circulation.

Iron must be re-oxidized to the ferric state (Fe^{3+}) before being able to be bound by Tf. The three multicopper ferroxidases ceruloplasmin (CP), hephaestin (HEPH), and zyklopen (Zp/*HEPHL1*) have been detected in placental tissue (see **Table 11** on p.91). CP is a soluble copper-dependent ferroxidase that facilitates iron efflux and was detected by immunohistochemical staining in STB and fetal capillaries (Guller et al. 2008). Unexpectedly, Cp-null animals exhibit a normal phenotype at birth, suggesting that Cp is not essential for placental iron transfer (Harris et al. 1999). HEPH has not been localized to human placenta, but expression of *HEPH* mRNA has been detected and quantified in BeWo cells (Y. Q. Li et al. 2012). In 2010, an international group with scientists from the US, UK, China and Lebanon identified a placenta-specific ferroxidase in connection with sex-linked anemia (SLA) -mice harboring a mutation in Heph. Interestingly, they proposed the name “zyklopen” (Zp) after the mythical one-eyed iron workers called *cyclops* in Greek mythology who helped Hephaestus, Hera's parthenogens child and blacksmith of the gods

in Olympia (Chen et al. 2010). Zp has approximately 50% protein identity with CP and HEPH, and contains a transmembrane domain and an extracellular ferroxidase domain with appropriate topology to interact with FPN1 (Chen et al. 2010). Absent in liver and intestine, Zp is abundantly expressed in the placenta and has been localized to the labyrinth, spongiotrophoblasts and yolk sac of mouse placenta (Chen et al. 2010). Furthermore, the intracellular iron chaperone protein poly(rC)-binding protein 2 (PCBP2) was suggested to act as a recipient of iron from DMT1 and as a donor of iron to FPN1 based on localization using confocal microscopy and binding studies using pulldown techniques (Yanatori et al. 2016). Since iron is potentially toxic because it catalyzes the generation of ROS, the carrying-over of iron by chaperons like PCBP2 could be relevant for protection of fetal tissue from putative oxidative ferrous iron and for iron release at the placental barrier across the BM (C. Cao and Fleming 2016). Stunningly, there are evidences that all 3 ferroxidases and the chaperon PCBP2 are expressed in the human placenta, but little has been experimentally investigated regarding their functions in the iron transport mechanism across the placenta.

Non-transferrin-bound iron transport

As indicated before, there is no proof whether Tf-mediated iron uptake is the exclusive pathway for placental iron acquisition. Therefore, other circulating forms of iron such as free non-Tf-bound iron and heme iron could be taken up by the placenta as well. Although global deletion of Tfr1 in mice leads to embryonic lethality by day of embryonic development (E)12.5, some $Tfr1^{-/-}$ embryos were still able to develop hemoglobin-containing erythrocytes upon E10.5 (Levy et al. 1999), suggesting that the Tf cycle may not be essential for erythropoiesis during early development. Furthermore, it is unclear whether anemia in $Tfr1^{-/-}$ embryos is due to insufficient placental iron transport or to defects in erythroid iron uptake or both. Tissue-specific knockout of Tfr1 in the placenta would be needed to answer this question.

Electron microscopy of placental villi from radio-labeled ferritin-injected animals showed ferritin-containing endosomes (Lamparelli et al. 1989) and ferritin accumulation in the basement membranes (Thornburg and Faber 1976) suggesting ferritin endocytosis and transport in the placenta. Li et al. found that scavenger receptor class A member 5 (SCARA5) conveys serum ferritin binding and then stimulates its endocytosis from the cell

surface with consequent iron delivery into ureteric bud tips of the kidney (J. Y. Li et al. 2009). However, the molecular mechanism of ferritin endocytosis by STB the relevance of this process to maternal delivery of iron to the fetus is unknown yet.

Finally, the placenta may be able to utilize heme iron sources, as suggested by its high expression of heme iron transporters and heme catabolic enzymes (see **Table 11** on p.91). The recent finding that the placenta represents a major hematopoietic organ that supports hematopoietic stem cell development, was shedding light on placental heme pathways (Lee et al. 2010). Therefore, several heme iron homeostasis proteins, including lipoprotein receptor-related protein 1 (LRP1), heme carrier protein 1 (HCP1), heme oxygenase 1 and 2 (HO1 / HO2), have been localized to the STB and/or stroma. Very recently scientist found that HO1 overexpression in human placenta-derived mesenchymal stem cell (hPMSC) decreased apoptosis and enhanced migration properties by improving the balance of angiogenic factors *in vitro* (Wu et al. 2020). The improved placental vascularization by HO1-hPMSC motivates the authors to further studying this as an alternative treatment for preeclampsia. However, data are lacking on placental localization of the more recently identified heme transporters such as feline leukemia virus subgroup C receptor 1 (FLVCR1) and heme-responsive gene 1 (HRG1).

As depicted with numerous ? in **Figure 7**, experimental prove of placental heme-iron transfer, the relevance of chaperones, ferritin uptake, endosomal or MVM localization of several iron transporter and the putative redundancy of ferroxidases is missing. Furthermore, mechanisms like ferritin capturing, heme transport and expression of alternative transporter like ZIP8 / ZIP14 might explain relatively mild effect of the TfR1 and DMT1 knockout in mouse (Levy et al. 1999; Gunshin et al. 2005). Pioneer research is needed to characterize alternative iron transport pathways across the placenta.

Regulation of placental iron transport

The iron regulatory hormone hepcidin (HEPC) is highly expressed by the human liver and in placental tissue, but also in mouse embryos in the second trimester (Yoon et al. 2006). HEPC binding results in rapid ubiquitination of FPN1 causing its internalization and degradation (Qiao et al. 2012). Thus, HEPC negatively regulates cellular iron export via FPN1 across the BM towards the fetal circulation. Furthermore, HEPC may play a role in fetal sensing of the placental iron status and hence in signaling fetal demand to the

mother (C. Cao and Fleming 2016). The anemic, iron-deficient phenotype of transgenic mouse embryos overexpressing Hepc further supports this notion (Nicolas et al. 2002). More research is needed to reveal the role of HEPC in regulating placental iron homeostasis and to identify other fetal factors regulating placental iron transport, such as those related to growth and pathology. Another protein that is expressed in placenta and regulates iron metabolism is the hemochromatosis Factor HFE (Parkkila et al., 1997). HFE is an MHC class I-like glycoprotein that assembles with β2-microglobulin to form a heterodimeric complex. A mutation in the HFE gene results in the autosomal iron-overload disease hereditary hemochromatosis (Feder et al., 1996). HFE associates with TfR (Feder et al., 1998; Gross et al., 1998; Salter-Cid et al., 1999) and DMT1 (Gruper et al. 2005).

Of note, the relative resistance of fetal hemoglobin levels to maternal anemia highlights the ability of the placenta to respond to altered maternal iron supply. Stable isotope data in human pregnancies has shown that more iron from maternal diet is transferred to the fetus when the maternal stores are low (O'Brien et al. 2003). This is probably a consequence of intestinal and placental iron transporters and TFR1 upregulation (Young et al. 2010; Gambling et al. 2001). The mechanisms underlying this regulation are not well characterized and may involve placental iron regulatory protein 1 and 2 (IRP1 / IRP2) and intracellular iron. In brief, during cellular iron deficiency, IRPs bind to the stem-loop structure of IREs within the UTR of iron-regulated genes including *TfR1*, *ferritin*, *FPN1* and *DMT1*. The binding of IRPs to of 3'-IREs promotes stabilization of mRNAs mediating increased iron uptake mainly via TfR1, whereas binding to 5'-IREs prevents translation of mRNAs involved in iron storage and export via ferritin and FPN1 (Wilkinson and Pantopoulos 2014). Both IRP1 and IRP2 activity have been detected in human placentae (Bradley et al. 2004). IRP regulation of placental FPN1 is less clear (C. Cao and Fleming 2016).

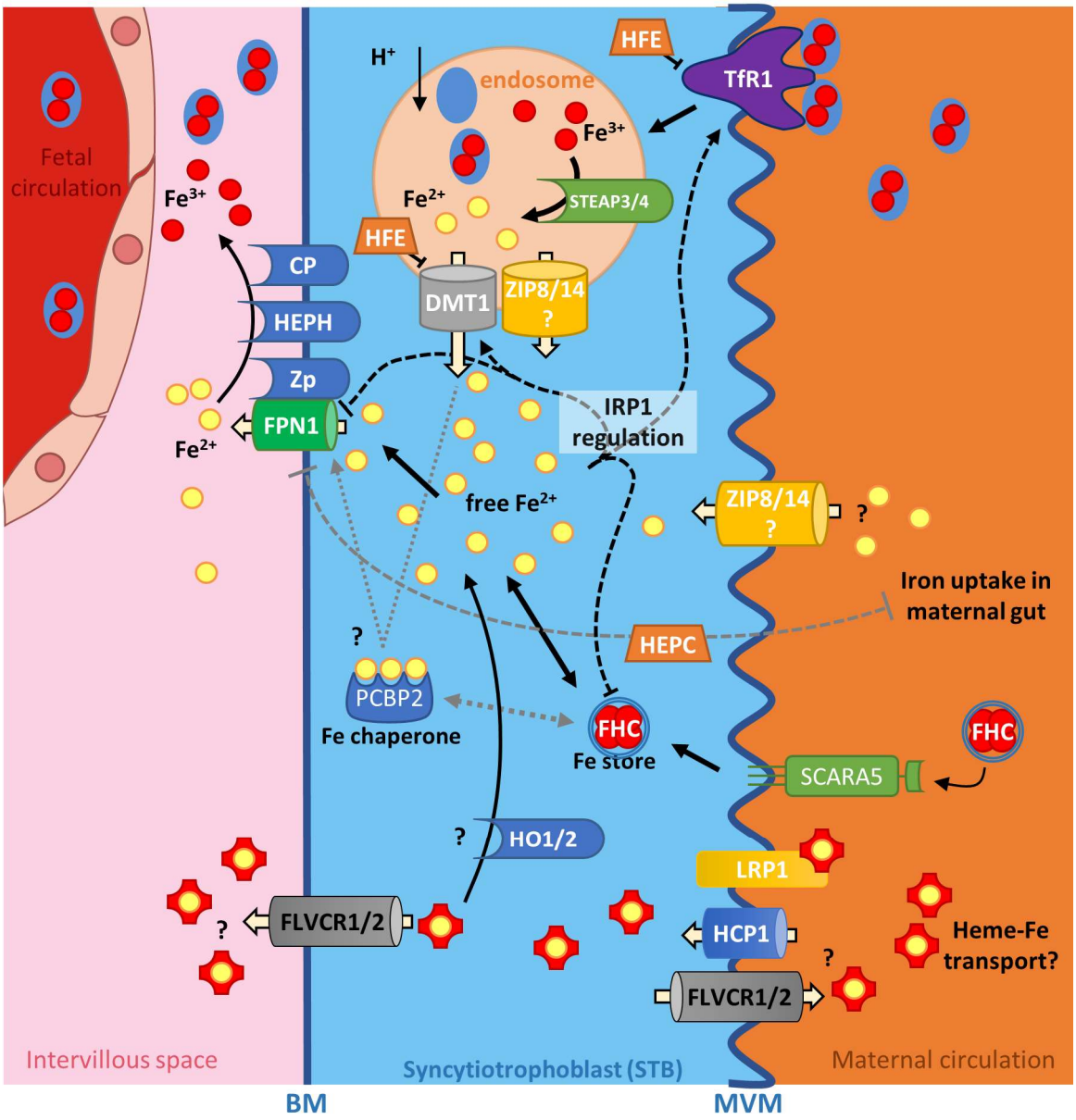

Figure 7: Schematic representation of the mechanisms and regulation of materno-fetal iron transfer across the placenta. Iron (Fe) is transferred from the mother to the fetus across the blood-placenta barrier (right to left). The placenta is in direct contact with the maternal blood circulation via a monolayer of syncytialized trophoblast cells (blue). After transferrin receptor (TfR1)-mediated uptake ferric iron (Fe^{3+}, red) by clathrin-dependent endocytosis at the maternal side of the syncytiotrophoblasts (villous membrane, MVM) into endosomes, divalent metal transporter 1 (DMT1) is supposed to release divalent iron (Fe^{2+}, yellow) from endosomes into the cytosol. Transferrin (Tf) and TfR1 return to the apical microvillous membrane (MVM) to be used for further cycles. Cytosolic iron is transferred to the fetal circulation presumably through the iron exporter ferroportin (FPN1) or stored intracellularly in oxidized form bound to ferritin heavy chain (FHC). The exact mechanisms as well as the role of other transporters such as the Zrt- and Irt-like proteins (ZIP) ZIP8 or ZIP14 in transplacental iron transfer are currently still unclear. Although the lipoprotein receptor-related protein 1 (LRP1), heme carrier protein 1 (HCP1) and feline leukemia virus subgroup C receptor 1 (FLVCR1) were found to be apically expressed, the relevance of heme iron transport across the placenta and the possibility of reverse transfer of iron into the maternal circulation need more investigation. Similar speculative is the function of scavenger receptor class A member 5 (SCARA5) maybe mediating the binding and endocytosis of serum ferritin. Furthermore, human poly (rC) binding protein 1 (PCBP1) is an iron chaperone that probably

protects fetal tissue by delivery of oxidative ferrous iron from DMT1 to FPN1 or ferritin (dotted gray lines). Regulatory wise, HEPC likely act as sensor of the placental iron status and initiates FPN1 degradation at placental BM and in enterocytes of the mother (dashed gray lines). The binding of IRP1 to of 3'-IRE promotes mRNAs expression of *TfR1* and *DMT1*, whereas binding to 5'-IREs prevents mRNA translation of iron storage and export via FHC and FPN1.

Adverse effects of imbalanced iron homeostasis for gestation

Maternal iron stores are generally improved by iron supplementation, but often no changes are observed in cord ferritin and maternal ferritin levels. Preziosi et al. found in a small observational studies only a weak relationship with neonatal ferritin levels (Preziosi et al. 1997). In contrast, a study from the Institute of Food Science, Swiss Federal Institute of Technology in Zurich, Switzerland including pregnant women (n=381) in the second and third trimester showed a clear benefit of iron supplementation (Hess et al. 2001). 65% of women were taking iron supplements and had significantly higher serum ferritin concentrations compared to those not taking an iron-containing supplement. Of note, the success of folate supplementation was clearly higher compared to iron supplementation. Furthermore, a more recent study in China including 3702 mother-newborn pairs, detected a strong correlation between maternal and neonatal ferritin levels in women whose plasma ferritin levels fell below a threshold of depletion (13.6 µg/L serum ferritin). Below this threshold very unit of decrease in maternal serum ferritin was corresponding to a 2.4-unit drop in cord ferritin (Shao et al. 2012), suggesting a "broken stick" relationship between maternal and fetal iron parameters. However, most studies are based on healthy pregnancy, neglecting that conditions with underlying placental abnormalities, such as intrauterine growth restriction (IUGR) and GDM, may disrupt the normal regulatory mechanism of the placenta and negatively affect fetal iron transfer (C. Cao and Fleming 2016). GDM is another common pregnancy complication associated with decreased infant iron stores at birth (further information in 1.2 on p.2). Unlike expression of placental TFR1 in IUGR, expression of placental TFR1 in GDM shows a significant relationship between fetal iron stores and placental IRP1 (Georgieff et al. 1999).

These findings were an incentive for us to mechanistically investigate changes in placental iron homeostasis as consequence of hyperglycemic stress and to identify involved iron transport pathways and cellular response mechanisms (see specific aims in 1.6.2 on p.30).

1.5.3 Glucose transport

Glucose is the main energy source for the growing fetus, but due to the limited gluconeogenesis ability of the unborn most glucose is provided by the mother (Desoye, Gauster, and Wadsack 2011). Due to very low permeability of glucose across the placental barrier formed by the STB, a carrier mediated transport system through transporters is needed. Glucose is taken up by transporters embedded in the MVM. Glucose transporter proteins from the GLUT family play a crucial role in the transport mechanism. Previous studies revealed that 6 isoforms of the GLUT family are expressed on mRNA level during pregnancy, but the composition, distribution and localization changes throughout pregnancy (N.P. Illsley 2000). The glucose transporter 1 (GLUT1) is responsible for glucose transport during pregnancy. It acts sodium independent and is the major isoform expressed in the placental STB and CTB (Baumann, Deborde, and Illsley 2002; Carter 2012). The glucose concentration in the blood of the mother is a key factor in the maternal-fetal transport mechanism as it determines the net transport across the placental barrier. GLUT1 has a higher expression level in MVM than in the BM (T. Jansson et al. 2002). The asymmetric expression leads to higher transport capacity in the MVM whereas the BM indicates the rate-limiting step in the glucose homeostasis during pregnancy (Gallo, Barrett, and Dekker Nitert 2017). Therefore, transplacental glucose transfer represents a typically non-mediated and transporter facilitated mechanism as depicted green in **Figure 4** on p.11. The GLUT1 expression level increases with progressing pregnancy as the demand for glucose in the fetus increases as well. Previous studies have shown that the expression of GLUT1 on the basal side is increased in GDM patients compared to healthy pregnancies (Baumann, Deborde, and Illsley 2002). To our knowledge, there are no studies yet that investigated the effect of changing iron levels on GLUT1-mediated glucose transport across the placenta.

1.6 Hypotheses and specific aims of the thesis

The placenta is a temporary fetal organ serving as the only connection of the developing fetus to the *ex utero* world. It maintains the balance between nutrition and growth control of the fetus through selective and regulated supply of macronutrients such as carbohydrates, protein, lipids and critical micronutrients like minerals and vitamins for fetal development. This work focused mainly on the SLC-mediated materno-fetal transport of essential amino acids like leucine and iron as most abundant trace element in human body. Therefore, the hypotheses and specific aims of this PhD project are divided into two parts, namely amino acid transport (**A**) and iron transport (**B**).

1.6.1 Amino acid transport

The placental amino acid transport is maintained by a complex interplay between accumulative transporter, facilitating channels and exchanger systems. The exchanger-mediated transfer of leucine is mainly maintained by the heteromeric System L transporters LAT1 and LAT2. However, whether amino acid gradients affect transplacental amino acid transport and how important the highly expressed leucine transporter LAT1 is for uptake and transfer across the placental barrier, still needs to be answered.

Hypotheses:

1. **Materno-fetal amino acid gradients are crucial for transplacental amino acid transport and correlate with selected maternal and fetal parameters.**
2. **Counter-directed amino acid gradients *in vivo* affect leucine uptake into trophoblasts and transfer across the placental barrier.**
3. **Specific inhibition of SLC7 transporters or knockout of single transporter genes can reveal the relevance of single solute carriers in placental nutrient acquisition.**

The specific aims in the amino acid transport part were:

A1) To determine maternal and fetal amino acid concentrations in healthy term pregnancies.
A2) To perform correlation analysis between materno-fetal amino acid gradients and parameters characterizing the maternal nutritional condition and fetal growth.
A3) To study the effect of substrate concentrations on System L-mediated leucine uptake into trophoblasts and leucine transport across the placental barrier *in vitro*.
A4) To characterize the effect of trophoblast differentiation on expression and function of placental leucine transporters.
A5) To investigate small molecule inhibitors as tool compounds for modulating placental leucine uptake by acting on SLC7 transporters.
A6) To generate and characterize trophoblast knockout cell lines for nutrient transporters by CRISPR/Cas9 mutagenesis.

1.6.2 Iron transport

In contrast to the materno-fetal amino acid transfer, the transport of non-heme iron across the placenta is largely underinvestigated. GDM has been associated with elevated iron concentrations in sera (Bo et al. 2009; Zein et al. 2015; Afkhami-Ardekani and Rashidi 2009; Fu et al. 2016), but a potential impact of GDM on placental iron transport has never been investigated.

Hypotheses:

1. **The expression of placental iron-transporters and iron-regulatory proteins is altered in GDM.**
2. **Simulation of hyperglycemic and hyperlipidemic conditions in trophoblasts induces cellular stress and affects iron uptake.**
3. **The reduction of cellular stress levels recues placental iron homeostasis.**

The specific aims in the iron transport part were:

B1) To characterize expressional changes of iron homeostasis genes in GDM-affected placental tissues.
B2) To establish and characterize trophoblast models mimicking human GDM and investigate the effect of hyperglycemic and hyperlipidemic conditions on transplacental iron transfer.
B3) To identify cellular stress pathways responsible for altered placental iron homeostasis under hyperglycemic and hyperlipidemic conditions.
B4) To test whether increasing antioxidative potential rescues the hyperglycemic effect on placental iron homeostasis.
B5) To analyze expression patterns of placental iron homeostasis genes in an obesogenic mouse model that develops GDM-like symptoms.

2 Materials and Methods

2.1 Human placental collection and processing

2.1.1 Tissue and paired materno-fetal sera sampling for free amino acids profiling

Placentae from normal healthy pregnancies were collected after elective Caesarean section at the Division of Gynecology and Obstetrics, Lindenhofgruppe, Bern, Switzerland. The study was conducted in accordance with the Declaration of Helsinki, and the protocol was approved by the Ethics Committee of the Canton of Bern (Basec Nr. 2016-00250). Anthropometric characteristics of healthy donors of placentae for this study are shown in **Table 7** on p.62. A graphical summary of the sera sampling is depicted in **Figure 8**. Maternal venous whole blood samples were prospectively sampled before administration of the spinal anesthesia from 22 inconspicuous pregnancies approx. 5 min prior to parturition by caesarean section. The corresponding fetal blood (n=22) was sampled from placental arteries and veins within 20 min after delivery. Contamination with maternal blood was impossible. After collection of the whole blood sample in a S-Monovette with clotting activator (Sarstedt Group, Nümbrecht, DE), the blood was allowed to clot for 15-30 min at room temperature (RT). The clot was removed by centrifugation with 1000 rcf for 10 min at 4°C. The supernatants (=sera) were aliquoted and stored at -20°C upon analysis.

The acquisition of the full amino acid spectra was carried out in serum by ion exchange chromatography. The concentrations of 20 amino acids were determined in the Centre of laboratory medicine (ISO 17025 accredited) at the University Hospital of Bern by ion exchange chromatography with post column derivatization with Ninhydrin on an automated Biochrom 30+ Series amino acid analyzer (Biochrom, Cambridge, UK). Norleucin (5.24 mg/100 mL sulfosalicylic acid) was used as internal standard and calibration was obtained using amino acid standards from Laborservice Onken (Art. Nr. 5.403.151) and Sigma (Art. Nr. A-9906). The inter-assay coefficient of variation of the analysis was 7%.

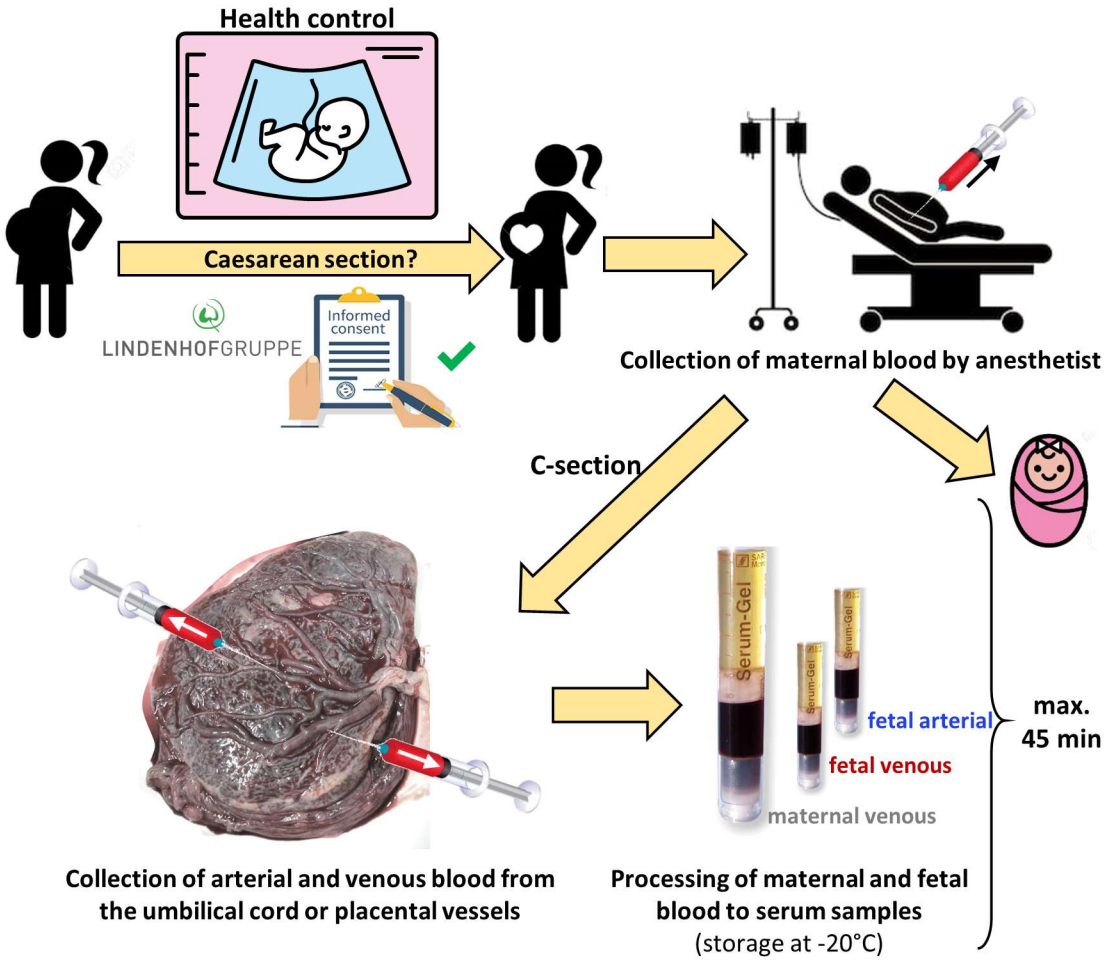

Figure 8: Schematic summary of the standardized collection of mother-fetal paired blood sera from Caesarean sections in collaboration with the Lindenhof Hospital, Bern, Switzerland. After unsuspicious pregnancy women, who want to deliver by caesarian section, were informed about our studies and recruited by our collaborating clinicians at the Lindenhof hospital in Bern. Maternal venous blood samples were prospectively collected from healthy patients approx. 5 min prior to parturition by caesarian section. The corresponding fetal blood was sampled from placental arteries and veins within 20 min after delivery of the placenta. The acquisition of the full amino acid spectra was carried out in maternal and fetal serum samples by ion exchange chromatography. There are passing about 45 min from blood collection until the processed serum samples are stored in -20°C upon analysis.

2.1.2 Patient selection and tissue collection to compare healthy and GDM diseased placental tissue

For the characterization of GDM-specific alternation in placental iron homeostasis 22 women with elective Caesarean section at the Department of Obstetrics and Gynaecology, University Hospital Bern, Switzerland were enrolled. Anthropometric characteristics of healthy and GDM-affected placentae for this study are shown in **Table 10** on p. 90. To minimize blood contamination, each piece of tissue was intensively washed

in Dulbecco's phosphate buffered saline (DPBS). Tissue samples were immediately snap-frozen in liquid nitrogen and stored at -80°C upon further analysis. GDM was diagnosed in 11 pregnancies according to the criteria of the American Diabetes Association based on pathologic glucose plasma values following a 75 g oral glucose tolerance test (OGTT) performed between the 24^{th}-28^{th} gestational week and normal OGTT values at the 6^{th} *postpartum* week (Basevi et al. 2011). The control group (n=11) consisted of pregnancies without pathologies and terminated at term by elective primary caesarean section upon patient's request or due to breech presentation. All GDM-affected women did not show glucose intolerance before pregnancy. None of the subjects included in the study showed iron excess or deficiency or any type of hematological abnormalities. This study was approved by the cantonal ethical committee, Bern, Switzerland, and written informed consent was obtained from all participants.

2.1.3 Primary trophoblast isolation

Placentae from normal healthy pregnancies were collected after elective Caesarean section at the Division of Gynecology and Obstetrics, Lindenhofgruppe, Bern, Switzerland. The study was conducted in accordance with the Declaration of Helsinki, and the protocol was approved by the Ethics Committee of the Canton of Bern (Basec Nr. 2016-00250). The collected tissue was used to isolate primary CTB cells by three consecutive digestions with trypsin followed by a Percoll® density gradient centrifugation as previous described (Nikitina et al. 2011; Xiao Huang et al. 2016; Kallol, Moser-Haessig, et al. 2018). Freshly isolated cells were cultured on Cell-BIND plates in Dulbecco's modified Eagle's medium containing 4.5 g/L glucose (DMEM-highGlucose, Gibco, Paisley, UK) and characterized by analyzing the expression of cytokeratin-7 and vimentin as previously described (Kallol, Huang, et al. 2018). Primary trophoblasts were evaluated for leucine uptake at the CTB (after 12 h of culture) and STB stage (after 48 h of culture) when spontaneous differentiation and fusion has occurred (Kallol, Moser-Haessig, et al. 2018; Shi et al. 1993).

2.1.4 Placental membrane protein isolation

Placental tissues from healthy pregnancies were used to simultaneously isolate microvillous membranes (MVM) and basal membranes (BM) by Mg^{2+} precipitation based on a previously published method (Nicholas P. Illsley et al. 1990). In brief, approximately 100 g villous tissue from central and lateral areas of the placenta was washed 3-times with

NaCl 0.9% to remove blood. All following steps were performed at 4°C or on ice. After the final wash, the tissue was homogenized in Buffer H (250 mM sucrose, 10 mM Hepes, adjusted pH to 6.95, supplemented with protease inhibitor cocktail) for 2 min with a Polytron homogenizer (Kinematica AG). The crude homogenate was centrifuged with 1000 rcf to remove cellular debris. Two differential centrifugation steps at 10'000 rcf for 15 min at 4°C (Optima L-90K ultracentrifuge with TFT70.38 rotor) were performed. The supernatants of both centrifugations were combined and filtered through 4 layers of gauze on ice and then centrifuged at 125'000 rcf for 30 min at 4°C (TFT 70.38 rotor). The pellets containing all cellular membranes were homogenized with a Teflon homogenizer and diluted with Buffer H, followed by Mg^{2+} precipitation applying a final Mg^{2+} concentration of 12 mM by adding 240 mM $MgCl_2$ and slowly stirring for 20 min. The centrifugation with 2500 rcf for 10 min separates MVM in the supernatant and all other membranes in the pellet. To isolate the BM-fraction from the pellet by ultracentrifugation on a 2 step gradient, it was first washed, then resuspended with Buffer E (0.1% bovine serum albumin in 1 mM Titriplex® III, Merck, Darmstadt, Germany) and homogenized using a Teflon homogenizer. A two-step sucrose gradient was prepared in a thin-walled ultra-centrifuge Beckman SW28 tube (Beckman Coulter, Brea, CA, USA) by applying a bottom layer with 1.192 g/cm^3 density, a middle layer with 1.162 g/cm^3 density and on top the homogenized membrane-fraction. This gradient was centrifuged at 100'000 rcf for 60 min using a Beckman SW28 swing-out rotor (Beckman Coulter, Brea, CA, USA). The BM deposit between the bottom and the middle layer was removed. Finally, the BM-fraction and the MVM pellets were resuspended in buffer E and homogenized with a Teflon homogenizer. MVM and BM were centrifuged at 125'000 rcf for 30 min for a final clean-up. The pellets were resuspended in buffer H, snap frozen in liquid nitrogen and stored at -80°C. Anthropometric characteristics of healthy donors of placentae for this study are shown in **Table 2**. The total membrane isolation (TMI) fraction was collected prior to MVM/BM separation.

Table 2: Anthropometric characteristics of healthy patients donating placental tissue and their offspring.

	Characteristics	Healthy controls	
Mother	Number of individuals	11	
	Maternal age (years)	33.9	± 3.48
	Parity	1.8	± 0.60
	Gestational age at *partum*	39 3/7	± 6/7
Newborn	Weight of placenta (g)	569.3	± 86.1
	Weight of baby (g)	3367.3	± 284.0
	Sex of baby	3♂ /	6♀

2.2 Analysis of placental transmembrane proteins

2.2.1 Immunoblotting

Cells were lysed by adding hypotonic lysis buffer (10 mM Tris-HCl, Sigma T5941; 10 mM NaCl, Sigma 71376; 1.5 mM $MgCl_2$, Millipore 1.05833; 1% Triton X-100, Sigma T8787; 1 bottle/100 mL protease inhibitor cocktail, Sigma P2714; adjusted pH to 7.4). The samples were vortexed in hypotonic lysis buffer every 5 min during 30 min on ice for thorough lysis of the cells. Subsequently, the cell lysates were centrifuged with 1000 rcf for 10 min at 4°C to remove cellular debris and stored upon analysis at -80°C. Protein content was measured using the Pierce™ BCA Protein Assay Kit. 50 µg cell lysates were loaded on 10% acrylamide gels and separated by sodium dodecyl sulfate polyacrylamide gel electrophoresis (SDS-PAGE) using the Biorad minigel system. The immobilized bands were then semi-dry transferred to nitrocellulose membranes (GE Healthcare). Blots were blocked with 5% non-fat milk in Tris Buffered Saline with 0.1% Tween-20 (TBST). The primary polyclonal rabbit anti-LAT1 antibody (KE026/TG170215 Transgenic Inc.), Anti-LAT2/*SLC7A8* antibody produced in rabbit (Sigma AV43930), anti-DMT1/*SLC11A2* antibody clone 4C6 (Sigma WH0004891M1), anti-FPN1 antibody (Thermo Fisher Scientific PA5-22993), Anti ZIP8/*SLC39A8* (Sigma HPA038833), purified Mouse Anti-BiP/*GRP78* (BD Transduction Lab. 610978), SQSTM1/p62 Antibody (Cell Signaling Technology 5114S), Anti-LC3-I/II Antibody (Millipore ABC929), Anti-GLUT-1 (Millipore 07-1401) and in a second staining round for the reference signal (loading control) the mouse anti-beta-actin antibody (Sigma A2228) were incubated overnight at 4°C, followed by 4 times washing with TBST, and incubation with DyLight 680 or 800 fluorescence conjugated secondary antibodies (Thermo Scientific™). The immunoreactive bands were quantified with the

OdysseyW Sa Infrared Imaging System (LI-COR) to obtain relative densitometry values without signal saturation.

The effect of LAT2 glycosylation on SDS-PAGE segregation was tested by Peptide N-glycosidase F (PNGase F) treatment according to the protocol from Promega V4831. In brief, 40 µg lysate of knockout candidate clones was incubated with 1% Nonidet P-40 and 50 mM sodium phosphate (pH 7.5, 25°C) and PNGase F at 37°C for 2 h. Samples were then denatured with SDS-PAGE loading buffer without boiling and further quantified by immunoblotting and densitometry as explained above.

2.2.2 Membrane protein isolation for MS/MS-based protein quantification

Due to insufficient antibody specificity in the iron transporter project, we started a service collaboration with the FGCZ at the University of Zurich to develop a liquid chromatography tandem mass spectrometry (LC-MS/MS) -based quantification method for 12 genes of interest (**Figure 27** on p.94). The workflow, graphically visualized in **Figure 9**, started with the tissue collection from placenta donors at the Lindenhof hospital, continued with sample preparation, tryptic digestion and mass determination by tandem mass spectrometry. Finally, peptides suitable for MS-analysis were identified selected by MASCOT-search.

Table 3: Genes of interest chosen for selected reaction monitoring (SRM) method used to quantitatively asses protein levels by tandem mass spectrometry in collaboration with Functional Genomics Center in Zurich (FGCZ).

Gene ID	Gene name	Protein name	project assignment
Q01650	*SCL7A5*	LAT1	Amino acid transport project
Q9UHI5	*SLC7A8*	LAT2	
P08195	*SLC3A2*	4F2hc	
P02786	*TFRC*	TFR1	iron transport project
P49281	*SLC11A2*	DMT1	
Q9NP59	*SLC40A1*	FPN1	
Q9C0K1	*SLC39A8*	ZIP8	
Q15043	*SLC39AE*	ZIP14	
P04406	*GAPDH*	G3P	reference genes
P63104	*YWHAZ*	1433Z	
Q15365	*PCBP1*	PCBP1	
O95477	*ABCA1*	ABCA1	

Prior to proteomic analysis TMI from placental tissues was performed to deplete highly abundant proteins (e.g. albumin). Approx. 50 mg of snap-frozen tissue was homogenized

in lysis buffer (250 mM Sucrose; 10 mM Hepes; protease inhibitor cocktail, all reagents from Sigma; pH adjusted to 6.95) with a Polytron® homogenizer (Kinematica AG, Switzerland) on wet ice. Large cellular debris was removed by a first centrifugation step at 4°C and with 1000 rcf for 5 min. The supernatants were collected and subjected to two consecutive centrifugation steps at 10'000 rcf for 15 min at 4°C. The pellets were discarded, and the two combined supernatants were subjected to a final ultra-centrifugation step at 125'000 rcf for 30 min at 4°C. The pellets were consecutively washed with 1 mL ice cold 1M KCl and 1 mL 100 mM Na_2CO_3. The final TMI pellets were resuspended in 200 µL 50 mM Tris-HCl (pH 8) ice cold buffer using a glass-teflon homogenizer. The TMI homogenates were aliquoted for protein measurement using Pierce™ BCA Protein Assay Kit (Thermo Scientific™) and stored at -80°C until proteomic analysis.

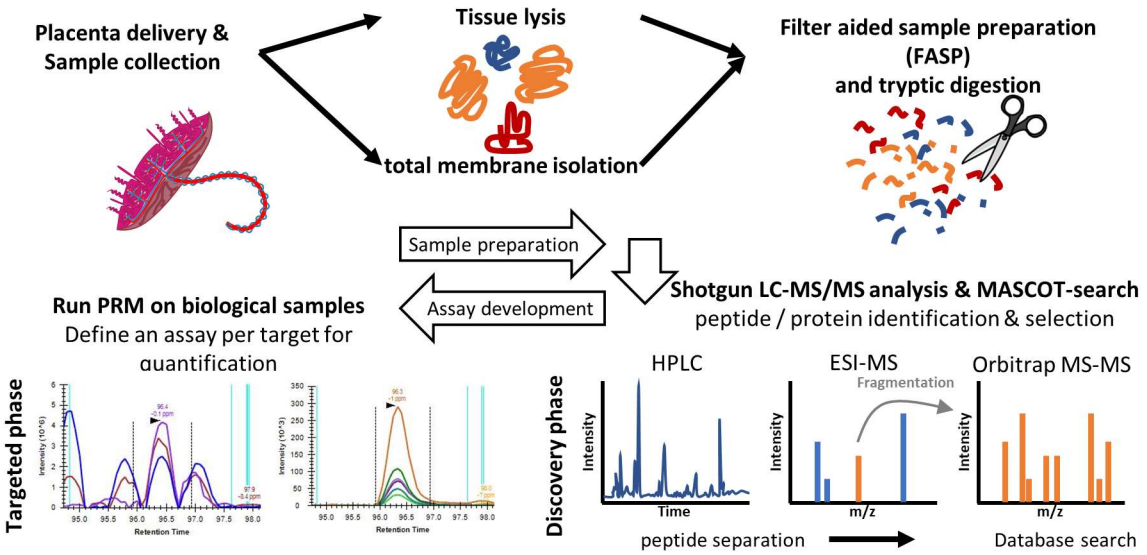

Figure 9: Schematic representation of the mass spectrometry-based approach to quantify placental membrane proteins.

2.2.3 Development of a Parallel Reaction Monitoring (PRM) assay

For the development of the quantification assay, preliminary experiments were performed to optimize the sample preparation and to select the proteotypic peptides of each target protein. 30 µg protein of TMI samples were subjected to filter-assisted sample preparation (FASP) and tryptic digested (Wiśniewski et al. 2009) with a subsequent desalting step by C18 solid phase extraction columns (Sep-Pak Fenisterre; Waters Corp., Milford, MA, USA). The dried samples were re-solubilized in 15 µL 3% acetonitrile, 0.1% formic acid and spiked with iRT peptides (Biognosys, Switzerland) for mass spectrometry

(MS) analysis which was performed on a QExactive mass spectrometer coupled to a nano EasyLC 1000 (Thermo Fisher Scientific). Solvent composition at the two channels was 0.1% formic acid for channel A and 0.1% formic acid, 99.9% acetonitrile for channel B. For each sample 1µL of peptides were loaded on a commercial Acclaim PepMapTM Trap Column (75 µm x 20 mm, Thermo Scientific™) followed by a PepMapTM RSLC C18 Snail Column (75 µm×500 mm, Thermo Scientific™). The peptides were eluted at a flow rate of 300 nL/min by a gradient from 2 to 30% B in 115 min, 47% B in 4 min and 95% B in 4 min. The mass spectrometer was operated in data-dependent mode (DDA), acquiring a full-scan MS spectrum (300−1700 m/z) at a resolution of 70'000 at 200 m/z after accumulation to a target value of 3'000'000, followed by HCD (higher-energy collision dissociation) fragmentation on the twelve most intense signals per cycle. HCD spectra were acquired at a resolution of 35'000 using a normalized collision energy of 25 and a maximum injection time of 120 ms. The automatic gain control (AGC) was set to 50'000 ions. Charge state screening was enabled and singly and unassigned charge states were rejected. Precursor masses previously selected for MS/MS measurement were excluded from further selection for 30 s, and the exclusion window was set at 10 ppm. The samples were acquired using internal lock mass calibration on m/z 371.1010 and 445.1200.

The acquired raw MS data were processed by MaxQuant (version 1.4.2.1) (Cox and Mann 2008), followed by protein identification using the integrated Andromeda search engine. Spectra were searched against a uniprot Homo Sapiens (taxonomy 9606) reference proteome (canonical version from 2016-12-09), concatenated to its reversed decoyed fasta database and common protein contaminants. Carbamidomethylation of cysteine was set as fixed, while methionine oxidation and N-terminal protein acetylation were set as variable modifications. MaxQuant Orbitrap default search settings were used. Enzyme specificity was set to trypsin/P.

The mass spectrometry proteomics data were handled using the local laboratory information management system (LIMS) (Türker et al. 2010) and all relevant data have been deposited to the ProteomeXchange Consortium via the PRIDE (http://www.ebi.ac.uk/pride) partner repository with the data set identifier o3022: MaxQuant 1.4.2.1 (WU146123) and o3176 : MaxQuant 1.4.2.1 (WU148929).

Based on these experiments, a set of proteotypic peptides was selected for 8 protein targets and 4 housekeeping proteins excluding, whenever possible, peptides containing cysteine, methionine, asparagine and glutamine (**Table 3**). For proteins with no or less than three proteotypic peptides, additional peptides were selected from the SRM Atlas (http://www.srmatlas.org) (**Table 4**). Stable isotope-labeled standard peptides corresponding to the proteotypic peptides and containing either a C-terminal (13C(6) 15N(4)) arginine or a (13C(6) 15N(2)) lysine residue were chemically synthesized via SPOT synthesis (JPT Peptide Technologies, Germany) and used in unpurified form for PRM analysis. In total, the scheduled PRM assay targets 85 peptides (12 proteins, 37 peptides in Light/Heavy (L/H) form and 11 iRT peptides). The MS/MS spectra of these peptides were used for the generation of spectral libraries using Mascot (Matrixscience) according to the parameters previously described for MaxQuant (with, in addition, 13C(6) 15N(4) arginine and 13C(6) 15N(2) lysine as variable modifications) Finally, both the MaxQuant and the Mascot search results (dat. files) were imported into the Skyline software (v2.6.0) (MacLean et al. 2010) and spectral libraries were built using the BiblioSpec algorithm (Frewen and MacCoss 2007).

Table 4: List of peptide sequences used to quantify proteins of iron homeostasis and reference genes by LC-MS/MS. All represented peptides had positive polarity.

Mass [m/z]	CS [z]	Start [min]	End [min]	NCE	Comment	Protein
385.72402	2	14.71	16.71	27	M[-131.0404]VLGPEQK (light)	DMT1
389.73112	2	14.71	16.71	27	M[-131.0404]VLGPEQK (heavy)	
882.40090	2	39.15	41.15	27	ISIPEEEYSC[+57.021464]FSFR (light)	
887.40503	2	39.15	41.15	27	ISIPEEEYSC[+57.021464]FSFR (heavy)	
415.97925	4	30.72	32.72	27	LGVVTGLHLAEVC[+57.021464]HR (light)	
418.48132	4	30.72	32.72	27	LGVVTGLHLAEVC[+57.021464]HR (heavy)	
754.90823	4	50.08	52.08	27	TPQIEQAVGIVGAVIMPHNMYLHSALVK (light)	
756.91178	4	50.08	52.08	27	TPQIEQAVGIVGAVIMPHNMYLHSALVK (heavy)	
629.82495	2	38.48	40.48	27	DWIVVVAGEDR (light)	FPN1
634.82909	2	38.48	40.48	27	DWIVVVAGEDR (heavy)	
350.22361	2	19.49	21.49	27	TPALAVK (light)	
354.23071	2	19.49	21.49	27	TPALAVK (heavy)	
496.76162	2	16.59	18.59	27	FAQNTLGNK (light)	
500.76872	2	16.59	18.59	27	FAQNTLGNK (heavy)	
664.58471	4	42.46	44.46	27	FSVIC[+57.021464]PAVLQQLNFHPC[+57.021464]EDRPK (light)	ZIP8
666.58826	4	42.46	44.46	27	FSVIC[+57.021464]PAVLQQLNFHPC[+57.021464]EDRPK (heavy)	
420.21090	2	14.67	16.67	27	VDSYVEK (light)	
424.21800	2	14.67	16.67	27	VDSYVEK (heavy)	
749.99826	3	19.40	21.40	27	TYGQNGHTHFGNDNFGPQEK (light)	
752.66966	3	19.40	21.40	27	TYGQNGHTHFGNDNFGPQEK (heavy)	
726.37246	2	30.69	32.69	27	YGEGDSLTLQQLK (light)	ZIP14
730.37956	2	30.69	32.69	27	YGEGDSLTLQQLK (heavy)	
421.91045	3	30.42	32.42	27	ALLNHLDVGVGR (light)	
425.24654	3	30.42	32.42	27	ALLNHLDVGVGR (heavy)	
835.70816	3	36.71	38.71	27	NLSTC[+57.021464]FSSGDLFTAHNFSEQSR (light)	
839.04425	3	36.71	38.71	27	NLSTC[+57.021464]FSSGDLFTAHNFSEQSR (heavy)	
873.42830	2	43.36	45.36	27	SAFSNLFGGEPLSYTR (light)	TfR1
878.43244	2	43.36	45.36	27	SAFSNLFGGEPLSYTR (heavy)	
781.35246	2	16.96	18.96	27	LAVDEEENADNNTK (light)	
785.35956	2	16.96	18.96	27	LAVDEEENADNNTK (heavy)	
717.41614	2	44.83	46.83	27	VSASPLLYTLIEK (light)	
721.42324	2	44.83	46.83	27	VSASPLLYTLIEK (heavy)	
706.39882	2	31.59	33.59	27	GALQNIIPASTGAAK (light)	GAPDH
710.40592	2	31.59	33.59	27	GALQNIIPASTGAAK (heavy)	
435.25819	2	23.47	25.47	27	VIPELNGK (light)	
439.26528	2	23.47	25.47	27	VIPELNGK (heavy)	
882.40483	2	38.68	40.68	27	LISWYDNEFGYSNR (light)	
887.40896	2	38.68	40.68	27	LISWYDNEFGYSNR (heavy)	
774.86045	2	18.38	20.38	27	SVTEQGAELSNEER (light)	YWHAZ
779.86458	2	18.38	20.38	27	SVTEQGAELSNEER (heavy)	
1020.99728	2	36.61	38.61	27	GIVDQSQQAYQEAFEISK (light)	
1025.00438	2	36.61	38.61	27	GIVDQSQQAYQEAFEISK (heavy)	
711.33544	3	51.13	53.13	27	TAFDEAIAELDTLSEESYK (light)	
714.00683	3	51.13	53.13	27	TAFDEAIAELDTLSEESYK (heavy)	
694.91103	2	40.37	42.37	27	IITLTGPTNAIFK (light)	PCBP1
698.91813	2	40.37	42.37	27	IITLTGPTNAIFK (heavy)	
507.76998	2	18.95	20.95	27	QGANINEIR (light)	
512.77411	2	18.95	20.95	27	QGANINEIR (heavy)	
543.78054	2	17.82	19.82	27	IANPVEGSSGR (light)	
548.78468	2	17.82	19.82	27	IANPVEGSSGR (heavy)	

2.2.4 Protein quantification of placental membrane proteins by mass spectrometry

Prior to proteomic analysis TMI from placental tissues was performed as described in 2.2.2 and a PRM assay was developed as described in 2.2.3. After assay development, protein digestion for the 22 TMI samples was further improved by using a commercial iST Kit (PreOmics, Germany) with an adapted version of the protocol. Briefly, 30 µg of protein were solubilized in lysis buffer, boiled at 95°C for 10 min and processed with High Intensity Focused Ultrasound (HIFU) for 30 s setting the ultrasonic amplitude to 85%. Then the samples were transferred to the cartridge and digested by adding 50 µL of the digestion solution. After 60 min of incubation at 37°C the digestion was stopped with 100 µL of stop solution. The solutions in the cartridge were removed by centrifugation at 3800 rcf, while the peptides were retained by the iST-filter. Finally, the peptides were washed, eluted, dried and re-solubilized in LC-Load buffer for MS-Analysis. For PRM quantification, samples were analyzed on a Q Exactive HF mass spectrometer (Thermp Scientific) equipped with a Digital PicoView source (New Objective) and coupled to a M-Class UPLC (Waters). Solvent composition at the two channels was 0.1% formic acid for channel A and 0.1% formic acid, 99.9% acetonitrile for channel B. For each sample 1 µL of peptides were loaded on a commercial MZ Symmetry C18 Trap Column (100 Å, 5 µm, 180 µm x 20 mm, Waters) followed by nanoEase MZ C18 HSS T3 Column (100 Å, 1.8 µm, 75 µm x 250 mm, Waters). The peptides were eluted at a flow rate of 300 nL/min by a gradient from 5 to 35% B in 50 min and 98% B in 5 min. The Q Exactive HF performed MS1 scans (350–1250 m/z) followed by 16 MS/MS acquisitions in PRM mode. The full scan event was collected at a resolution of 15000 (at m/z 200) and an AGC value of $3e^6$ and a maximum injection time of 15 ms. The PRM scan events used an Orbitrap resolution of 120000, maximum fill time of 200 ms with an isolation width of 1.4 m/z, an isolation offset of 0.5 m/z and an AGC value of $2e^5$. HCD fragmentation was performed at a normalized collision energy (NCE) of 27. The whole method included 74 L/H peptide precursors and 11 Biognosys iRT standard peptides. Based on the spiked iRTs, the retention time of the target peptides was normalized and transformed into iRT values (Escher et al. 2012) allowing to set the scan windows to 4 min for each peptide in the final PRM method (**Table 4**). This ensured the measurement of 6–10 points per LC peak per transition. The results were calculated as fold changes relative to spiked peptides. GDM (n=11) and controls (n=11) were normalized to the reference gene glyceraldehyde-3-phosphate

dehydrogenase (GAPDH) (sp|P04406|G3P_HUMAN). The normalization was executed by subtracting. the protein value of GAPDH from the value of the target protein.

2.3 Placenta histology

2.3.1 Immunohistochemistry

Tissues from 11 GDM- and 11 control-placentae were embedded in Tissue-Tek® optimum cutting temperature (O.C.T.) medium, cut at 5 µm thickness and mounted on Superfrost plus slides (Menzel, Germany). The frozen tissue blocks were stored at -80°C upon sectioning. The tissue sections were fixed in pre-cooled acetone (-20°C) for 10 min and washed 2 times for 5 min in 10 mM phosphate buffered saline (PBS, pH 7.4). Fixed sections were incubated in H_2O_2-Block (Dako S2023) at room temperature for 10 min to block endogenous peroxidase activity and again washed 2-times in PBS. The primary antibodies were diluted in PBS with 0.5% bovine serum albumin (DMT1 1:1000; FPN1 1:1000). Diluted primary antibodies (100 µL per slide) were added to cover the tissue on the slides and incubated in a humidified chamber (DMT1 for 2 h; FPN1 for 1.5 h) at 4°C. For the visualization of the antigens on the next day UltraVision LP Detection System (Thermo Scientific™ TL-015-HAS) was used according to the manufacturer's instructions. Slides were washed with PBS and incubated with Antibody Enhancer solution for 20 min. After an additional washing step with PBS, the horseradish peroxidase (HRP) polymer was added for 30 min, the slides were washed again, and AEC chromogen was applied for 5 min in the dark. Sections were washed in distilled water, counterstained with Gill's hematoxylin (Merck, 105174) and mounted with Aquatex® (EMD Millipore 1.08562). Negative controls were stained without prior incubation with the primary antibody. Immunohistochemical images were prepared with a DM6000 B microscope (Leica Microsystems, Germany). The staining intensity of DMT1 and FPN1 expression in all specimens was semi-quantitatively scored by a blinded expert (PD Dr. med. Meike Körner, Pathology Laenggasse, Bern, Switzerland). Staining intensity was rated on a scale of 0–3, with 0=negative, 1=weak, 2=moderate, and 3=strong and statistically assessed by Pearson's χ^2 test.

2.3.2 Special staining for lipid storage visualization in trophoblasts

Oil red O staining and counter-stained with hematoxylin was performed as described on http://www.ihcworld.com/_protocols/special_stains/oil_red_o.htm. In brief, after 32

days of adaptation of previously in low-glucose cultured BeWo cells to the 3 hyperglycemic conditions (see 2.4), cells were seeded on double chamber slides by avoiding 100% confluency. Then the slides were air dried for 30 min at room temperature and then fix in ice cold 10% formalin (22.0 mL 7% Formaline in 58.0 mL PBS, pH 7.4) for 5 min, followed by rinsing in 3 changes of distilled water and repeated air drying for another 30 min. Before the actual staining the cells were equilibrated in absolute propylene glycol (1,2-Propanediol, Sigma, 398039) for 5 min to avoid carrying water into Oil Red O. Lipid stores in the cells were stained in pre-warmed 0.5% Oil Red O (Sigma, 102419) in 100% propylene glycol solution for 10 min in 60°C oven differentiated in 85% propylene glycol in distilled water solution for 5 min, followed by rinsing in 2 changes of distilled water. In a second step the cells were counter-stained in Gill's hematoxylin for 30 s and washed thoroughly in running tap water for 3 min and finally covered by cover-glass and Aquatex®. Cells were visualized via inverted light microscopy and photographed.

2.4 BeWo cell culture

As primary cultures of trophoblasts do not proliferate *in vitro,* the choriocarcinoma-derived BeWo cell line (clone b30; donated by Dr. Alan L. Schwartz, Washington University School of Medicine, USA) was used as trophoblast cell model. BeWo cells are conventionally cultured in Dulbecco's modified Eagle's medium containing 25 mM glucose (DMEM-HG, Gibco, Switzerland) with 10% fetal bovine serum (LabForce, Basel, Switzerland) and antibiotic-antimycotic (Gibco 15240062) in a humidified incubator under a 5% pCO_2 atmosphere at 37°C. To adapt BeWo cells to physiological glucose concentrations, they were grown in medium containing 5.5 mM glucose (DMEM-low glucose, Gibco, Switzerland) for 28 passages. These low glucose BeWo cells were used for all Leucine uptake (see 2.7.1) and Transwell (see 2.7.4) assays, but also to establish cell models mimicking different grades of diabetic severity in the iron project. Beside the normoglycemic condition (**N**; DMEM 5.5 mM glucose) the cells were exposed to a hyperglycemic (**H**; DMEM 25 mM glucose) and a hyperglycemic/hyperlipidemic condition (**HL**; H + 100 µM palmitic acid). The stock solution of palmitic acid was prepared by conjugation with bovine serum albumin (BSA). In brief, palmitic acid was dissolved in pre-heated 0.1 M NaOH and diluted 1:10 in pre-warmed 12% BSA solution to obtain a final

concentration of 10 mM. N and H media contained same amounts of 0.1 M NaOH and BSA without lipid (Sinha et al. 2004).

2.4.1 Induction of oxidative stress and rescue by antioxidant treatment

For oxidative stress induction following antioxidant treatment, BeWo cells were seeded in DMEM 5.5 mM glucose medium with 10% fetal bovine serum (FBS, Seraglob, Schaffhausen, Switzerland) till they reach approx. 80% confluency, followed by incubation in serum-free DMEM 5.5 mM glucose medium and different oxidative stress conditions using 0.8 µM Rotenone (Sigma, R8875) or 1 mM tert-Butyl hydroperoxide (tert-BOOH; Sigma, 458139). We tested 0.1 µM sodium selenite (NaSe) inducing GSH-dependent antioxidative pathways in trophoblasts (A. Khera, Vanderlelie, and Perkins 2013) and 50 µM quercetin as well-known dietary antioxidant (Bach et al. 2010). Finally, we aimed to use the best method for the rescue experiment by antioxidants treatment. See the results in **Figure 36D** on p.107.

2.5 CRISPR/Cas9-mutagenesis of single placental nutrient transporter

Sequence specific gene knockout by CRISPR/Cas9-mutagenesis, allows to assess the role of a single transporter in complex nutrient transport pathway such as materno-fetal amino acid or iron transport. Trophoblast cells lacking the expression and function of a single nutrient transporter by specifically and CRISPR/Cas9-mediated knockout, would reveal its role at the materno-fetal barrier in the placenta. The strategy adapted for CRISPR/Cas9-mutagenesis of placental nutrient transporter is depicted in **Figure 39** on p.114.

2.5.1 Design of target sites and synthesis of sgRNA

Four nutrient transporter and the trophoblast hormone human choriogonadotropin (*hCG*) as reference target (J. Li et al. 2018) were selected to be targeted by CRISPR/Cas9-mutagenesis: LAT1 (*SLC7A5*), LAT2 (*SLC7A8*), DMT1 (*SLC11A2*), ZIP8 (*SLC39A8*) and beta subunit 3 of the human chorionic gonadotropin (*hCGB3*). The genomic sequence for each target was downloaded from National Center for Biotechnology Information (NCBI) GENE database. Potential target sites were independently generated using the online target site searching and analysis webpages CRISPOR (http://crispor.tefor.net) and CHOPCHOP (http://chopchop.cbu.uib.no). The integrated bioinformatics tool software (UGENE

software from NCBI, US, freeware) was used to annotate sequences essential for gene expression, such as the initial ATG or splice sites of the target gene and the final target sites inclusive protospacer adjacent motif (PAM) -sequence. This information was used to plan the double-strand-break location with an effect on gene expression and function as devastating as possible. Three different target sites per target gene were designed. The target site is defined by 20 nucleotides each with <5'-20bp-NGG-3'>-structure. Both target site searching tools CRISPOR and CHOPCHOP generated additionally to the target sites sequence, primer pairs flanking the proximity of the respective target sites. We further used the NCBI- Basic Local Alignment Search Tool (BLAST) online tool to analyze the target sites for off-targets. The PAM sequence (=NGG) on the 3'-end of the target site, which does not count to the 20 bp of the target site nucleotides, but is essential for Cas9-mediated cleavage (Jinek et al. 2012). The G or GG at the 5'-end of the target site is required since these are the last nucleotides of the T7-transcriptase recognition site, but also the first nucleotides transcribed to ribonucleic acid (RNA) and hence already part of the guide RNA. We added another G, if there was only one G at the 5'-end of the target site to get a more efficient transcription (Bassett et al. 2013). The final versions of designed target sites are listed in **Table 5**.

Table 5: List of target sequences designed for CRISPR/Cas9-mutagenesis with respective primer pairs to amplify the flanking target sequence for sequencing.

Name target site	Sequence target site (5'-3')	Forward primer (5'-3')	Reverse primer (5'-3')	fragment length
LAT1 MK1	GATGCTGTCGTCCGAGGCCG	TGACCAACCTGGCCTACTTC	GTAGGGGAGGCTTAGAGATGTG	170 bp
LAT1 MK2	GCAGGCTTACCGTGAACACG	GTCTGTCCACAGGCTCTTCTTC	ACATTTGAGCTGTCACCCAGT	229 bp
LAT1 MK3	GCTGCCCGTCTACTTCTTCG	CTGCCTGTGTTCTTCATCCTG	GAGATACTCACAGATGCCCTGG	177 bp
LAT2 142	GGATGTGGGGAACATTGTGC	TGTAAGGCTACACGCATGCA	AAAGTGAGTGGGGCTACAGC	305 bp
LAT2 184	GGAGCTTCTCTCCAAAAGTC	GTTCTGCTTGTGTGCCTTGG	GGGGAAATCTCAGGGTGTGG	306 bp
LAT2 1539	GGCATCCAACGCCGTCGCTG	ACATCCAGATGCCCACACAG	CCAGAGTGAAGTGGGAGCTG	293 bp
DMT1_92	GGCCTGCTGCACTCTACATT	AGGCAGAGAAACGAAGGAGC	CATGGTGGAGCTCTGTCCTG	304 bp
DMT1_1312	GGCCCTCACATTTGGATATG	TAAGGAGAGCGGGAATGGGA	TTTAAACCTGGGAGCCCCTG	387 bp
ZIP8_567	GTGGAGTCAAAATCAATCCG	ACATCATTTGGTTCCTTGCTCT	TAGCCAACATCCTTACCTCTGG	244 bp
ZIP8_694	GCTTGGGCCGATCCTCACAT	CTCTGTCATCTGTCCAGCAGTC	GCAATAAAGCAGAAAAAGAGGC	182 bp
hCGB3	GATCCCGACTCCCGGGGCCCT	CCTCAGGTGGTGTGCAACT	AGAAGCCTTTATTGTGGGAGGA	290 bp
hCGB3_1	GCCACGGCGTAGGAGACCAC	CCTCAGGTGGTGTGCAACT	AGAAGCCTTTATTGTGGGAGGA	290 bp

Before continuing with "single guide"-RNA (sgRNA) synthesis the target sites were validated by amplification of the target site from the BeWo genome by GoTag G2 hot start polymerase (Promega, M7401), oligo cleaning using "ReliaPrep DNA clean-up and concentration system" kit (Promega, A2892) and subsequent sequencing using

Microsynth oligo sequencing service (Microsynth AG, Switzerland: https://srvweb.microsynth.ch/SingleTubeSequencing). All kits mentioned above were used according to the protocols provided by manufacturers.

The synthesis of target site-specific sgRNA was done as described before in (Burger et al. 2016). In brief, before we were able to perform the *in vitro* transcription (IVT) for sgRNA generation, the double strand deoxyribonucleic acid (DNA) template for each target had to be prepared. To reduce oligo synthesis costs, we profit from the hybridization ability of DNA oligos and ordered one 63 bp long target-specific oligo per target site called CRISPRfwd (green sequence in **Figure 10**) and only one 80 bp long oligo called sgRNArev with a 20 bp overlap with all CRISPRfwd ordered shown as red sequence in **Figure 10**. Therefore, only a single CRISPRfwd oligo was needed to be ordered per target site, while the sgRNArev oligo was used for all sgRNA IVT templates.

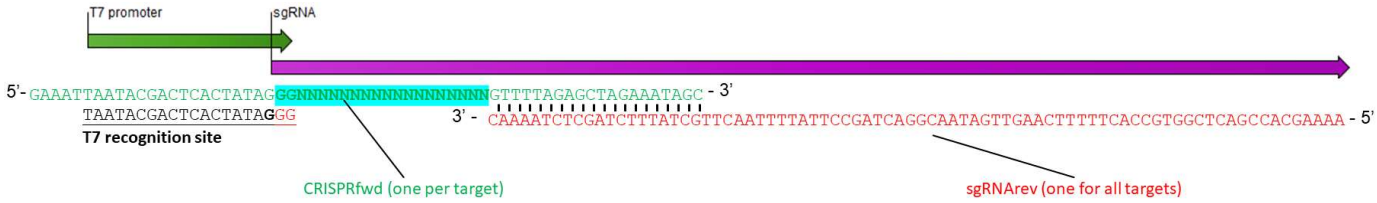

Figure 10: Schematic annealing of the target-specific CRISPRfwd and sgRNArev oligonucleotide as template for sgRNA synthesis. After thermal annealing, the CRISPRfwd and sgRNArev oligos expose two 3'-ends allowing sequence elongation. Subsequent elongation was performed by running a standard PCR using the GoTaq® G2 Hot Start polymerase (Promega) to get a linear *in vitro* transcription (IVT) template; 4 µL of 10 µM sgRNArev oligo, 4 µL 10 µM CRISPRfwd oligo and 42 µL nuclease free water were mixed with the 2 x master mix followed by standard PCR. The CRISPRfwd sequence (green) was bearing the T7 promotor sequence (underlined) ending with a GG. This GG represented the start of the target site designed for target gene binding (blue background) and the start of the final sgRNA, respectively. The sgRNArev oligonucleotide (red) includes the whole sgRNA sequence downstream of the target site responsible for Cas9 recognition.

After polymerase chain reaction (PCR) -elongation (**Figure 10**), the double stranded template DNA was precipitated in 10% sodium acetate (3 M) and 40% isopropanol with subsequent ethanol (95%) wash on ice, to remove reagents from elongation reaction. The target site-specific DNA template was transcribed using the MAXIscript™ T7 Transcription Kit (Invitrogen AM1312) optimized for sgRNA synthesis. In brief, the reaction was composed as follows: 8 µL of 10 mM NTPs (Thermo Fischer 18109017), approx. 300 ng of purified template DNA, 2 µL T7 Polymerase, 2 µL 10 x transcription buffer and nuclease free water to adjust total volume to 20 µL. Transcription

components were mixed well by pipetting and incubating at 37°C overnight (not in water bath to avoid condensation on the cap). The synthesized sgRNA were purified first by protein precipitation with chloroform by adding 80 µL of RNase free water per 20 µL reaction and chloroform with a 1:2 (v/v) ratio and followed by centrifugation for 5 min at 10'000 rcf at 4°C. The upper organic phase (sgRNA) was transferred into a fresh 1.5 mL tube, while the lower aqueous phase was discarded. The sgRNA was further washed 3-times by replacing the supernatant volume with ice-cold 95% ethanol and again precipitated overnight at -20°C. The sgRNA samples were then centrifuged with 10'000 rcf for 60 min at 4°C, to carefully discard the supernatant, followed by drying the RNA pellet for 10 min below a laminar flow bench. The pellet was resuspended in 30 µL RNase free water and stored at -80°C until transfection. Concentration of the sgRNA was measured with Nanodrop (Thermo Fischer). For several samples, the quality of the RNA was measured on a Bioanalyzer (Agilent) chip according to protocol provided by the company.

2.5.2 Transfection methods for sgRNA and Cas9 into trophoblasts

Two different transfection strategies were tested for bringing finally active sgRNA and Cas9 protein into trophoblasts (**Figure 11**). The first strategy **A** includes simultaneous transfection of previously transcribed sgRNA and Cas9 plasmid, bearing promotor sequences for instant expression in each transfected trophoblast cell. The second strategy **B** was to directly deliver active preassembled sgRNA-Cas9 ribonucleoprotein complexes (RNPs) into trophoblasts. Both strategies should lead to sequence-specific binding of the nuclease Cas9 and mutation of the targeted placental nutrient transporter gene. Multiple methods were tested for sgRNA-Cas9-plasmid and sgRNA-Cas9- ribonucleoprotein (RNP) transfection, followed by fluorescence-activated cell sorting (FACS) sorting and characterization of potential emerged new knockout cell candidates.

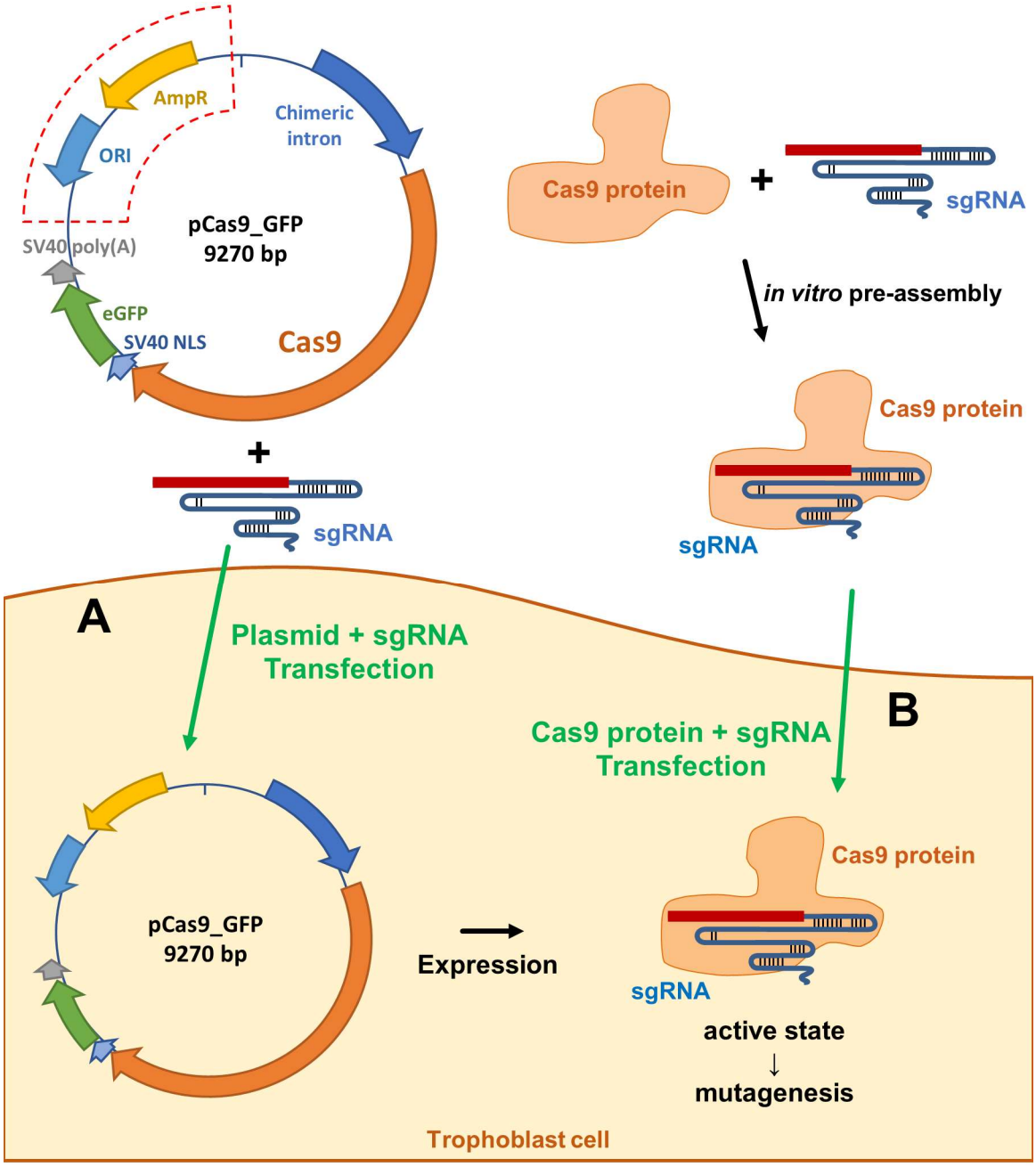

Figure 11: Two strategies to generate nutrient transporter knockout trophoblast lines by CRISPR/Cas9 mutagenesis. Either simultaneous transfection of sgRNA and pCas9_green fluorescent protein (GFP) plasmid (**A**) or direct transfection of active sgRNA-Cas9 ribonucleoprotein complexes (RNPs) into trophoblasts (**B**) were performed to generate target sites-specific destructive mutations in placental nutrient transporter genes. Strategy A requires expression of the Cas9-GFP gene on the transfected plasmid and sgRNA-Cas9 protein assembly through the target cell itself, while in strategy B already reactive and *in vitro* preassembled RNPs should convey efficient CRISPR/Cas9 mutagenesis immediately after RNP transfection. **A**, The pCas9_GFP plasmid (Addgene ID 41824) includes a chimeric intron (blue), which significantly increase transgene expression, a Cas9 gene (orange), followed by a SV40 nuclear localization signal (NLS, bright blue) for cellular transport of Cas9 into the nucleus. Furthermore, the Cas9 gene is fused to an enhanced green fluorescent protein (Cas9-2A-eGFP) reporter gene sequence for post-transfectional selection by flow cytometry. The SV40 poly(A) signal after the gene sequences on the plasmid convey mRNA stability in the targeted cell. The sequences in the red dashed box were

used for bacterial cloning of the pCas9_GFP plasmid. **B**, highly pure GFP labeled Cas9-NLS protein (MJ922, orange) was kindly provided by the group of Prof. Dr. Martin Jinek (Department of Biochemistry, University of Zurich).

For all transfection experiments, BeWo and HEK-293 (human embryonic kidney 293) cells were seeded one day before starting the transfection experiment into conventional 96-well plates using DMEM low glucose (Gibco, 21885) for BeWo or EMEM (Gibco, 15240-062) for HEK-293 respectively, but both with 10% FBS and 1 x antibiotics. They were incubated overnight at 37°C and 5% pCO_2. The transfection of both cell lines was performed according to the same protocol. The seeding density for BeWo was 42'000 cells/well and 60'000 cells/well for HEK-293.

2.5.2.1 Transfection strategy A: sgRNA-Cas9-plasmid

Three different transfection reagents were tested to simultaneously transfer sgRNA and pCas9_GFP plasmid (Addgene ID 41824, see **Figure 11**) into trophoblasts to generate knockout cell lines by sgRNA delivery and Cas9 expression in the targeted cells. Finally, the Xfect™ Transfection Reagent from TAKARA was selected for further experiment (see description of the method below), due to better performance compared to DharamFECT™ Duo from Horizon or XtremeGENE9 DNA transfection reagent from Roche.

Xfect™ Transfection Reagent (TAKARA PT5003-2) was used to transfect BeWo and HEK-293 cells with Cas9 plasmid and sgRNA in a molar ratio of 1:2. The manufacturer's protocol was adapted as follows: Cas9 plasmid and sgRNA were mixed with the transfection reagent and incubated 15 min at room temperature before adding to the cells. The cells were incubated together with transfection complex reagent for 18 h, followed by medium change to complete medium with 10% FBS. Further analysis was done 48 h post transfection.

2.5.2.2 Transfection strategy B: sgRNA-Cas9-RNP transfection

Transfection Reagents from two companies were used to transfect the BeWo cells with the Cas9-GFP protein together with the sgRNA as a preassembled RNP complex. The aim was to attain fast and efficient knockout after transfection of already active sgRNS-Cas9protein-RNPs as done before in the framework of a Master of Science Project at the University of Zurich "Maximizing mutagenesis with solubilized CRISPR-Cas9

ribonucleoprotein complexes" in Danio rerio embryos by microinjection (Burger et al. 2016).

Xfect™ Protein Transfection Reagent (Takara PT5166-2) is a modified peptide with cell-penetrating activity, whose amino acid composition enables an interaction with a protein cargo and transport across a cell membrane barrier. The manufacturer's protocol was adapted as follows: 350'000 BeWo and 550'000 HEK-293 cells were seeded 18 h before transfection in a 12-well plate. In step 2b 0.8 - 2 µg of Cas9 protein (2 µg Cas9=10.4 pmol) were mixed with 10.4 pmol of sgRNA, then Xfect protein buffer was added to bring the volume to 40 µL. The rest was done according to protocol (www.takarabio.com/assets/-documents/User%20Manual/PT5166-2_032712.pdf).

jetCRISPR (Polyplus 502-01) was used, similar to Xfect™ Protein before, to transfect BeWo and HEK-293 cells with the Cas9 protein together with the sgRNA in an RNP complex. jetCRISPR® is especially designed after a confidential principle to deliver RNP in a CRISPR/Cas9 experiments. 350'000 BeWo and 550'000 HEK-293 cells/well were seeded 18 h before transfection in a 12 well plate. The manufacturer's protocol was linearly scaled to a 12 well plate leading to the following amounts: 1 mL of total volume, 31,3 µL serum free medium, 30,4 pmol of Cas9 and 30,4 pmol of sgRNA. Add 92 µL of final RNP solution to 828 µL of cell medium (www.polyplus-transfection.com/wp-content/-uploads/2017/09/Short-Protocol-jetCRISPR-RNP.pdf).

2.5.3 Sorting of transfected cells with flow cytometry

After transfection, the cells were washed once with DPBS then trypsinized using 0.05% Trypsin-ethylenediaminetetraacetic acid (EDTA) (Gibco 25300). The cells were resuspended in DPBS with 1% FBS. Then GFP-positive cells were sorted into a 96-well plate containing 100 µL DMEM low glucose, 10% FBS and 1 x antibiotics using a flow cytometer (BD FACSAria™ III sorter) operated by Dr. Stefan Müller at the FACSLab of the University of Bern. The transfected cells were sorted according to further analysis as single cells, 100 cells or 200 cells per 96-well. The sorted cells were cultured at 37°C and 5% pCO_2. The medium was carefully exchanged one week after the sorting to avoid the loss of mutant cells. Apart from that, the medium was exchanged 1-2 times per week. After formation of tight colonies, the cells were redistributed by trypsinization within the well and subsequently transferred into a bigger well format up to a T75 flask. Cell mutant

candidates were frozen in FBS containing 10% dimethyl sulfoxide (DMSO, Merck, Darmstadt, Germany) and stored in liquid nitrogen. Every mutant candidate line was tested for loss of target gene expression by immunoblotting and functionally according to the target gene function by leucine (2.7.1 on p.57) respectively iron uptake assay (2.7.2 on p.57). For direct analysis of the mutation rate after transfection the treated cells (GFP-positive and GFP-negative) were sorted directly into PCR tubes prefilled with PCR-mastermix and corresponding primer pair to amplify the target site DNA for sequencing. The Single-Tube Sequencing service of Microsynth AG in Switzerland was used for sequencing, while the resulting sequence trace chromatogram was analyzed using the UGENE software from NCBI, US.

2.5.4 Determination of mutation rate by T7 Endonuclease 1 assay

Purified genomic DNA from CRISPR/Cas9-targeted cells was analyzed with EnGen Mutation Detection Kit (NEB E3321) also known as T7 endonuclease 1 assay to estimate the mutation rate by genome editing. This assay is based on the property of the T7 Endonuclease 1 which cleaves non-perfectly matched respectively hybridized DNA. Leading to a shedding of mutated DNA. The resulting DNA pieces with different sizes of a PCR product after digestion which are analyzed on an 1% agarose gel. Purification of genomic DNA was done with the ReliaPrep DNA Clean-Up and Concentration System (Promega A2892) and directly after stopping the digestion with 0.25 M EDTA (Sigma) the samples were loaded with BenchTop 100 bp DNA ladder (Promega G8291) on an 1% agarose gel containing RedSafe (Intron Biotechnology) as substitute for EtBr (ethidium bromide). The gels were running with 60 mV for 40 min.

2.6 Biochemical investigation of placental tissue and cell lysates

TRI Reagent (Sigma, T9424) was used for the isolation of RNA from various cell lines and placental tissue, as for example BeWo or primary trophoblasts, but also from fresh or frozen tissue samples. Therefore, approximately 50-100 mg of placental tissue or up to 1×10^7 cells (T75-flask with confluent BeWo) were subjected to RNA isolation as previously described (X. Huang et al. 2013). This procedure is an improvement of the single-step method for total RNA isolation reported by (Chomczynski and Sacchi 2006). TRI Reagent is a mixture of guanidine thiocyanate and phenol in a monophase solution, effectively dissolves DNA, RNA, and protein on homogenization or lysis of tissue sample.

After adding chloroform or 1-bromo-3-chloropropane and centrifuging, the mixture separates into 3 phases: an aqueous phase containing the RNA, the interphase containing DNA, and an organic phase containing proteins. Briefly, approx. 50 mg of frozen or fresh placental tissue were subjected to homogenization in 1 mL TRI Reagent 2-times for 30 s on ice with a Polytron® homogenizer (Kinematica AG, Switzerland) followed by centrifugation at 12000 rcf for 10 min at 4°C (optional step 2 in the Invitrogen protocol). Phase separation was performed with 200 µL 1-bromo-3-chloropropane followed by centrifugation at 12000 rcf for 15 min at 4°C. The RNA was precipitated from the water phase by adding 500 µL isopropanol (100%), incubated for 10 min at room temperature and centrifuged with 12000 rcf for 10 min at 4°C. After washing the pellet with 1 mL EtOH (75%) and centrifugation at 7500 rcf for 5 min at 4°C, the RNA pellet was partially air dried below the laminar flow hood and redissolved in RNase free water, followed by incubation at 55°C for 10 min. Total RNA concentration was measured by NanoDrop 1000 (Thermo Scientific). All RNA samples included in the study had an OD260/280 ratio >1.8. Structural RNA integrity was measured for all samples in the iron project using a microchip electrophoresis system on an AGILENT 2100 Bioanalyzer© (Agilent Technologies). Chips were prepared and loaded according to the manufacturer's instructions using the Agilent RNA 6000 Nano Kit (Agilent Technologies). Total RNA degradation was expressed as RNA Integration Numbers (RIN) (Schroeder et al. 2006).

Cell lysis with hypotonic buffer with protease inhibitor is another quick method to isolate proteins and protecting them from degradation. In brief, *in vitro* cultured cells were lysed by adding hypotonic lysis buffer (10 mM Tris-HCl; 10 mM NaCl; 1.5 mM $MgCl_2$, 1% Triton X-100; protease inhibitor cocktail, Sigma P2714; pH 7.4). The samples were vortexed in hypotonic lysis buffer every 5 min during 30 min on ice for thorough lysis of the cells. Alternatively, hypotonic lysis buffer was directly added to adherent cell and scraped using Techno Plastic Products AG (TPP) cell scrapers followed by thorough vortexing as explained before. Subsequently, the cell lysates were centrifuged at 1000 rcf for 10 min at 4°C to remove cellular debris and stored upon analysis at -20°C. Protein content in any case was measured using a commercial Pierce™ BCA Protein Assay Kit.

2.6.1 Quantitative RT-PCR

First-strand cDNA was synthesized from 2 µg of total RNA with Oligo(dT)$_{15}$ primers and GoScript™ Reverse Transcriptase (Promega, Switzerland) according to the manufacturer's instructions. The reverse transcription-quantitative polymerase chain reaction (RT-qPCR) reaction in SYBR® Green reagent was performed in a volume of 10 µL which contained 0.5 µM primers, 2 x GoTaq®qPCR Master Mix (Promega, Switzerland) and 1 µL cDNA. Primer nucleotide sequences are described in **Table 6**. Amplification reactions were performed as duplicates in 384-well plates (Applied Biosystem, USA) with the ViiA7 system (Applied Biosystem, USA). Melting curves were analyzed to exclude the presence of additional unspecific PCR products.

Table 6: Primer sequences used to quantify amino acid transporter, iron homeostasis and reference genes by RT-qPCR.

Protein	Gene	Forward sequence, 5'-3'	Reverse sequence, 5'-3'	Length [bp]
β-actin	*ACTG1*	AACTCCATCATGAAGTGTGACG	GATCCACATCTGCTGGAAGG	234
GAPDH	*GAPDH*	ACCACAGTCCATGCCATCAC	TCCACCACCCTGTTGCTGTA	452
UBI	*UbC*	TCGCAGCCGGGATTTG	GCATTGTCAAGTGACGATCACA	64
1433Z	*YWHAZ*	CCGTTACTTGGCTGAGGTTG	AGTTAAGGGCCAGACCCAGT	143
LAT1	*SLC7A5*	CAGGGCATCTTCTCCACGAC	TGGGTTCGAGGAGGTGATCTA	137
LAT2	*SLC7A8*	AGGCCCTCCTCTGTGGCTGG	GTGCAGCAGGAGTGGCTGGG	106
4F2hc	*SLC3A2*	AGCTGGAGTTTGTCTCAGGC	GGCCAATCTCATCCCCGTAG	127
DMT1#	*SLC11A2*	TGCTATCAATCTTCTGTCT	ACTGTAACATACTCATATCCA	177
ZIP8#	*SLC39A8*	GACAGTTATGTTGAGAAGG	TGACCATTCTGACCATAT	107
CP#	*CP*	CACTTACACCGTTCTACA	GTATGCTTCCAGTCTTCT	170
HEPH#	*HEPH*	GCTGAGATGGTGCCCTGGGAAC	AGGAGGGGCCATGGAGCAAGAC	117
Zp#	*HEPHL1*	AAGATTCAGAAGGAGCCCTATACCCAG	CGTCGATGTGCGAATGGTACACCC	171
TfR1#	*TFRC*	GTAGATGGCGATAACAGT	CCAATCATAAATCCAATCAAGA	167
FPN1#	*SLC40A1*	AGATCACAACCGCCAGAGAG	CACATCCGATCTCCCCAAGT	111
Zip14#	*SLC39A14*	CTGCTGCTCTACTTCATA	CAGACTTGGAGACATAATAATC	118
MFRN1#	*SLC25A37*	AACACTCAGGAGAACGTGGC	AAGCAATTTCTCGCTCCCCT	467
FTH#	*FTH1*	TTGAGACACATTACCTGAA	AAGAGATATTCCGCCAAG	112
HEPC#	*HAMP*	TCCCACAACAGACGGGACAACTTG	GCAGATGGGGAAGTGGGTGTCTC	119
IRP1#	*IREB1*	ACAAGCAGGCACCACAGACTATCC	GCACCGTACTCTTTGCCAGCCAG	124
IRP2#	*IREB2*	GGTGGATTTTGCTGCTATGAGGGAG	CACCTCCAGGATTTGGTGCATTCTG	155
HIF-1α#	*HIF1A*	TCCATGTGACCATGAGGAAA	CCAAGCAGGTCATAGGTGGT	251
GLUT1#	*SLC2A1*	GAACTCTTCAGCCAGGGTCC	ACCACACAGTTGCTCCACAT	114
TRFE#	*TF*	AGCCTGCACTTTCCGTAGAC	AACCACTTGGGCCAGTGAAA	112
HFE#	*HFE*	ATTGGAGAGCAGCAGAACCC	TGGTAGGTCCCATCCCCATT	334
TfR2#	*TFR2*	CAATCACAGGACCTCCACCC	GTTGTCCAGGCTCACGTACA	322

Table 6 (continued)

STEAP3#	*STEAP3*	GAAAACCACACTGGCTCCAAC	CACAGGGGAAGTAAGCTAGAGTC	207
HCP1#	*SLC46A1*	CGCTCACCACGCAGTATCTG	GTGGGAGGTAAGGGTCTCCAC	131
HRG1#	*SLC48A1*	TTCTCAGAGTGCCCTTGCTG	GCTGATACAAATGGCCGCTG	327
FLVC1#	*FLVCR1*	CTCGCGAAAGGATACCTCCC	CTGGATCCACTGAAAGGCGT	330
FLVC2#	*FLVCR2*	CCCAACATTGAAGACCGGGA	AGCATTCACTTCTTCCCCCG	327
LRP1#	*LRP1*	CAGCAAACGAGGCCTAAGTC	CATGGGTTGGTCACTTCGGG	201
SCARA5#	*SCARA5*	TCTGAGGGGACAAGGCTCTA	CTTGCCCGCCGTTTGTGAC	195
HO1#	*HMOX1*	ATGACACCAAGGACCAGAGC	GTCGCCACCAGAAAGCTGAG	172
HO2#	*HMOX2*	GGAAACCTCAGAGGGGGTAG	TGTGAAGTAAAGTGCCGTGG	317
ATFX	*ATF5*	ACCTTCTTTCTTCAGCCGAGG	GAGTTTCCCATAGTCTACGAGC	262
BiP (GRP78)	*HSPA5*	TGTGCAGCAGGACATCAAGT	TCCCAAATAAGCCTCAGCGG	166
GRP94 (Endoplasmin)	*HSP90B1*	GCCAGTTTGGTGTCGGTTTC	GGGTAATTGTCGTTCCCCGT	168
iNOS	*NOS2*	GGAGCCAGCTCTGCATTATC	GTGCACTCAGCAGCAAGTTC	251
Nrf2	*NR2F1*	ATCGTGCTGTTCACGTCAGAC	TGGCTCCTCACGTACTCCTC	104

Legend: #, iron homeostasis proteins know to be expressed in human placental tissue.

2.6.2 Colorimetric ferrozine-based assay for iron quantitation

50 mg placental tissue from the same localization as the samples for mRNA and protein quantification was lysed in 50 mM NaOH (200 µL for 24 well-plate cultures). 100 mM NaOH with a ratio of 1:2 was used to reach 50 mM NaOH in samples lysed in hypotonic buffer with protease inhibitor. Tissue lysates were homogenized for 2 min with a Polytron® homogenizer in iced water or alternatively for adherent cells were lysed for 2 h on a shaker in a humidified atmosphere. $FeCl_3$ standard dilutions with concentrations from 1.562 – 300 µM were prepared in 10 mM HCl (Sigma 258148) diluent. 50 mM NaOH (S8045 Sigma) solution was added with equal volume to standard dilutions to reach 50 mM NaOH/ 5 mM HCl. Accordingly, 100 mM NaOH solution and 10 mM HCl was added with 1:2 volume/volume (v/v) ratio to 50 µL tissue or cell lysates to reach the same NaOH and HCl concentration as in standard dilutions. Aliquots of these lysates were used for iron quantitation and protein measurement (Pierce™ BCA Protein Assay, Thermo Scientific™). To the lysates and standard dilutions, respectively, freshly prepared iron releasing reagent (solution of equal volumes of 1.4M HCl and 4.5% weight/volume (w/v) $KMnO_4$, Sigma 31404 in distilled water) was added 1:1 v/v. Samples were incubated for 2 h at 60°C. After cooling the samples to RT, 30 µL of the iron-detection reagent (6.5 mM ferrozine; 6.5 mM neocuproine; 2.5 M ammonium acetate; and 1 M ascorbic acid (VWR, Switzerland); all dissolved in distilled water) was added to 300 µL sample volume. Samples were further incubated at RT for 30 min. The absorbance was measured in duplicates at

550 nm using the microplate reader (VMax® Kinetic ELISA Microplate Reader with Softmax® Pro Software, Molecular Devices LLC, USA). Absorbance of samples was compared to the absorbance of equally treated $FeCl_3$ standard multiplied by dilution factor 2. The iron content was normalized to the protein concentration of the sample.

2.6.3 Determination of oxidative damage and antioxidative potential of trophoblasts

To measure oxidative stress levels in the BeWo cell models (N, H and HL), we determined products of the lipid peroxidation cycle and protein carbonylation. Furthermore we assessed the antioxidant potential of BeWo cells by quantifying GSH levels according to (Rahman, Kode, and Biswas 2007).

2.6.3.1 Lipid peroxidation assay

The products of lipid peroxidation, such as malondialdehyde (MDA), were measured using a thiobarbituric acid reactive substances (TBARS) assay in cell culture supernatant. MDA combines with thiobarbituric acid (TBA) in a 1:2 stoichiometry to form a fluorescent adduct. TBARS are expressed as MDA equivalents and normalized to total cellular protein concentration (Potter, Neun, and Stern 2011). Cell media were collected after 30 days of treatment and stored upon analysis at -20°C. For the other oxidative stress assays the cells were trypsinized, washed in cold PBS and stored at -20°C. 15% w/v trichloroacetic acid (TCA, Merck, Germany), sample or MDA standard (1,1,3,3 Tetraethoxypropane) and 0.67% w/v TBA (VWR, Switzerland) in 2.5 M HCl were mixed in a 4:5:8 ratio, vortexed and boiled for 20 min at 95°C. The MDA standard curve was prepared as a 1:2 dilution series from 2 – 0.007 nmol/mL. After cooling the samples to RT, 2 mL 1-butanol was added and gently mixed. Spinning the samples for 1 min at 1000 rcf speeded up the phase separation. For the measurement, the butanol phase (top) was transferred to a black-wall 96-well plate and measured using Flex Station II fluorescence microplate reader (Thermo Fisher Scientific, Switzerland) at an excitation/emission wavelength of 530/550 nm, respectively. MDA equivalents were calculated by interpolation to the MDA standard curve.

2.6.3.2 Protein carbonylation assay

Carbonyl groups (aldehydes and ketones) are produced on protein side chains when they are oxidized. The detection of protein carbonyl groups involves their reaction with 2,4-dinitrophenylhydrazine (DNP), which leads to the formation of a stable 2,4-dinitrophenyl-hydrazone product, followed by its spectrophotometric quantification (Levine et al. 2009).

The cell pellets were resuspended with 2.5% w/v TCA and centrifuged at 11'000 rcf for 3 min. 500 µL of 10 mM DNP in 2 M HCl was added to the precipitates and allowed to stand for 1 h at room temperature, with vortexing every 10-15 min. Thereafter, 20% w/v TCA was added for precipitation, followed by three washing steps with ethanol-ethylacetate (1:1) to remove free reagent. The precipitated proteins were dissolved in 600 µL of 6 M guanidine solution. The carbonyl content was calculated from the $OD_{405\ nm}$ measured by V_{max} Kinetic Enzyme-linked Immunosorbent Assay (ELISA) Microplate Reader (VWR) using a molar absorption coefficient of 22'000 M^{-1} cm^{-1}. Carbonyl contents were normalized to the protein concentration.

2.6.3.3 Measurement of total glutathione levels

The assay to estimate the antioxidant potential of cultured trophoblasts is based on the reaction of GSH with 5,5'-dithio-bis-2-nitrobenzoic acid (DTNB) forming the chromophore 5-thio-2-nitrobenzoic acid (TNB). The rate of TNB formation was measured at 405 nm using V_{max} Kinetic ELISA Microplate Reader and is proportional to the concentration of GSH in the sample. The determination of total-GSH concentration detects both forms of glutathione, the reduced sulfhydryl form (GSH) and the oxidized glutathione disulfide (GSSG). The assay was performed according to the protocol from Rahman et al. 2007 (Rahman, Kode, and Biswas 2007). The total-GSH concentration was calculated from the linear standard curve based on a 1:2 dilution series ranging from 125 - 1.96 nmol/mL.

2.7 Placental nutrient uptake and transfer

Trophoblasts are in direct contact with the maternal circulation, act as main transport unit and are responsible for tightly controlled nutrient acquisition for the vulnerable intra uterine growth. Therefore, nutrient uptake assays are used to investigate the first and crucial step in materno-fetal transport of leucine and iron respectively transfer assays to study transplacental leucine transport *in vitro*. As first, BeWo cells were seeded at a density of 100'000 cells/cm^2. The isolated primary trophoblasts were seeded at a density of 1'000'000 cells/cm^2 on 96-well plates which were coated with 430 µL per Transwell with 4.3 cm^2 (or 55 µL per 96-well resp. 92 µL per 12-well) of 1:30 diluted Matrigel™ basement membrane matrix (VWR 734-1100) per 96-well. Trophoblasts were cultured until they reached their assigned differentiation stage and then washed 3-times with buffer depending on further procedure to leucine or iron uptake. Unstimulated BeWo

cells (BeWo-CTB) were investigated after overnight culturing. To obtain the syncytiotrophoblast (BeWo-STB) stage, BeWo cells were cultured overnight followed by stimulation with 100µM forskolin (Sigma F3917) for 48 h as described in (Azar et al. 2018).

2.7.1 Leucine uptake

The recently published leucine uptake method (Häfliger et al. 2018) was adapted to test the effect of different substrate concentrations on leucine uptake kinetics. In brief, cultured BeWo cells were cultured in complete growth medium (DMEM-lowGlucose, Gibco, Paisley, UK) containing 10% FBS and 1 x antibiotic-antimycotic and washed 3-times after culturing according to their assigned differentiation stage with pre-warmed Na^+-free Hank's buffer (125 mM choline chloride, 25 mM HEPES, 4.8 mM KCl, 1.2 mM $MgSO_4$, 1.2 mM KH_2PO_4, 1.3 mM $CaCl_2$, 5.6 mM glucose, adjusted pH to 7.4). After equilibration by incubation in Hank's buffer at 37°C for 7 min in a humidified incubator under 5% pCO_2 atmosphere, the cells were incubated for 3 min with pre-warmed Hank's buffer containing L-Leu substrate including 1 µCi/mL respective 20 nM radioactive L-[3,4,5-^{3}H(N)]-leucine (PerkinElmer, Waltham, MA, USA). leucine uptake was stopped by three washing steps with ice-cold Na^+-free Hank's buffer to remove the substrate. Cells were lysed by intense shaking for 1.5 h in MicroScint™-20 (PerkinElmer, Waltham, MA, USA). Finally, leucine uptake was quantified by a TopCount® NXT™ Scintillation and Luminescence Counter (PerkinElmer, Waltham, MA, USA).

2.7.2 Iron uptake

The different BeWo cell lines N, H and HL (see 2.4) were seeded 2 h before starting the experiment into 96-well plates (Corning® 96 Wellplate Flat Clear Bottom White Polystyrene TC-Treated, #3610) at a density of 60'000 cells/well and incubated with the respective medium. The preparation of Tf, the experimental procedure and calculation of iron-uptake was adapted from (Gambling et al. 2001). In brief, to prepare $^{55}FeCl_3$ (PerkinElmer, Germany)-labelled the uptake solution, human apo-Tf was dissolved in balanced salt solution (BSS; 136 mM NaCl, 5 mM KCl, 1 mM $CaCl_2$, 1 mM $MgCl_2$ and 18 mM 4-(2-hydroxyethyl)-1-piperazineethanesulfonic acid (HEPES), pH 7.4) and added to 7.5% w/v $NaHCO_3$. The previously mixed hot and cold iron was added for Tf binding at 37°C for 2 h. The concentrated iron-transferrin (Fe-Tf) solution with the concentration of 45 nmol/mL Tf, 90 nmol/mL $^{55}FeCl_3$ and 243 µmol/mL $NaHCO_3$ was diluted in BSS buffer

to final iron concentration of 179.8 pmol/mL. Binding of Fe^{3+} to Tf was confirmed by measuring $E_{470\,nm}$ /$E_{280\,nm}$ absorption ratio (data not shown). The cells were washed 3 x with BSS and incubated 30 min at 37°C for equilibration before 100 µL of the diluted uptake solution was added. Iron uptake was stopped at defined time points (1.5 min – 2 h) by washing 3 x with BSS. 10% of uptake solution volume was measured separately to obtain dosage control (DC) values. For cell lysis and ^{55}Fe detection 100 µL scintillation solution MicroScint-20 was added and the wells were shaken for 1.5 h at RT. The uptake data was acquired by TopCount Microplate Scintillation and Luminescence Counter (PerkinElmer, Germany). Counts per minute (cpm) were determined for each timepoint and then transformed into iron-uptake in % of total dose using the following equation:

$$\text{Iron uptake in \%} = \frac{\text{count/well(cpm) of samples} - \text{count/well(cpm) of background}}{\text{mean of dosa} \quad \text{control (DC)} \times 10} \times 100$$

To monitor the time-dependent adaptation processes on a functional level, iron-uptake time courses in BeWo cells were performed for 30 d under N, H and HL conditions.

2.7.3 Glucose uptake

Glucose uptake was measured using 2-Deoxy-D-glucose (2-DG; Sigma D8375) to study the effect of iron depletion on placental glucose uptake. 2-DG is a glucose analog that inhibits glycolysis via its actions on hexokinase, the rate limiting step of glycolysis. It is phosphorylated by hexokinase to 2-DG-P which cannot be further metabolized by phosphoglucose isomerases. This leads to the accumulation of 2-DG-P in the cell and is therefore the substrate of choice to study glucose uptake into trophoblasts as previously shown in competitive uptake assays using different glucose analogs (Larry W. Johnson and Smith 1985). In brief, 60'000 cells per well were seeded on a white-walled 96-well plates. BeWo cells were treated 18 h after seeding with FBS free medium with deferoxamine (DFO) (0, 15 and 30 µM) for 48 h in 7 replicates. BeWo cells were washed once with 100 µL KRH buffer (Krebs-Ringer-HEPES buffer; 50 mM HEPES, 137 mM NaCl, 4.7 mM KCl, 1.85 mM $CaCl_2$, 1.3 mM Mg_SO_4; adjusted to a pH 7.4 with 0.5 M NaOH). Radiolabeled 2-[1,2-^{3}H (N)]-DG (^{3}H-2-DG; 1 mCi, Perkin Elmer NET328001MC) was used for uptake quantification. 50 µL KRH buffer containing 2-DG and ^{3}H-2-DG was added to each well (6.5 mM 2-DG and 0.5 µCi/well ^{3}H-2-DG). Uptake was measured at different time points with a range from 0-120 min. Uptake was stopped by washing three times with ice cold

KRH buffer. For glucose uptake quantification 100 µL/well scintillation MicroScint™-20 cocktail was added. In one row of the assay plate 55 µL lysis buffer for each time point was added to measure protein concentration using Pierce™ BCA Protein Assay Kit. Plate was mixed for 1.5 h on shaker (Edmund Bühler, type KS10) at 250 rpm and measured on TopCount NXT scintillation and luminescence counter. Uptake was normalized to protein concentration.

2.7.4 Leucine transfer across placental barrier using Transwell technique

Trophoblast monolayers with verified tightness were selected after 7 days of culturing on Transwell® membranes and randomly assigned to leucine transfer time courses and inhibition experiments. The inserts with cultured BeWo cells and an insert without cells (non-cell control) were placed in 12-well plates and washed 3-times with pre-warmed Na^+-free Hank's buffer. Prior to starting the time course, the cells were equilibrated in Hank's buffer for 30 min at 37°C. Leucine transfer from the upper (maternal) towards the lower (fetal) compartment was started by simultaneously replacing the buffer in both compartments. The buffer in the lower chamber was replaced with Na^+-free Hank's containing 300 µM glutamine and 167 µM unlabeled L-leucine to obtain a physiological counter-directed leucine gradient. Consecutively the buffer in the upper compartment was replaced with Hank's containing 30 µM leucine (labeled with 3.7 nM L-[3,4,5-^{3}H(N)]-leucine), 300 µM glutamine and either vehicle DMSO or a constant 10 µM-dose of JPH203, JG336, JX020 or JX009, respectively. Inhibitors were applied in the upper compartment which is comparable to previous *in vivo* experiments (Wempe et al. 2012). At defined time points between 5 min and 6 h, 50 µL samples were taken from the maternal and fetal compartment. At the end of the experiment, all membranes were washed twice with DPBS and sampled to determine intracellular leucine levels. The medium and membrane samples including non-cell controls were collected in 3 mL of scintillation cocktail (Zinsser Analytic, Frankfurt, Germany). Radioactivity was quantified using Tri-carb 2100TR Liquid Scintillation Counter (PerkinElmer, Waltham, US).

2.8 Leucine transport inhibition by small molecules

JPH203, JG336, JX020 and JX009 were synthesized by our collaborators within the NCCR TransCure project (group of Prof. Karl-Heinz Altmann, ETH Zurich) following the routes described in the European Patent Application EP 2-959-918-A1, 2014. Compounds were

obtained as hydrochlorides, dissolved in DMSO and applied in the concentration range from 0.001-31.6 µM. JPH203 has been characterized as highly LAT1-specific; JX009 is described as LAT1 and LAT2-specific inhibitor (Endo et al. 2008). JG336 is a derivate of JPH203 with an additional methoxy group at the peripheral phenyl moiety residue, but unknown efficiency and specificity. JX009 is a meta-tyrosine in which the hydroxyl group at the phenol residue has been extended with a bulky side chain, while the amino acid of the other meta-tyrosine derivate called JX020 was fixed with a second ring. Meta-tyrosine would probably be a substrate itself, but the side chains in JX009 and JX020 prevents System L transport. Compound structures are depicted in **Figure 22** on p.85.

2.9 Statistics

Data are expressed as mean ± standard deviation (SD) for or median with interquartile range. Transcript and protein levels were usually presented as fold-change or relative abundance and plotted as boxplots with Tukey whiskers (1.5-times interquartile range (IQR)) depicting mean (+), median (-). Of note, the chosen statistical test is mentioned in each Figure legend. In general, data sets were first tested, whether they came from Gaussian distribution by Shapiro-Wilk normality test. Hence, parametric statistical analysis was applied only if the values were following a normal distribution. Statistics comparing maternal-vein, fetal-artery and fetal-vein amino acid profiles were performed using paired two-way Analysis of variance (ANOVA) with Tukey's correction. Spearman correlation was performed to test associations between physiological amino acid levels and anthropometric values. Differences between various uptake and transfer conditions and the difference in MS/MS-determined protein quantities between GDM and control were tested by Sidak's multiple comparisons test. For the detection of intracellular leucine retention in leucine transfer experiments by System L inhibition were statistically tested using a parametric one-way ANOVA analysis. Paired student T-tests were performed to detect differences in mRNA levels between CTBs and STBs or unstimulated BeWo-CTB or stimulated BeWo-STB. Expression changes of iron homeostasis genes in placental tissue, the analysis of sex dimorphism of iron homeostasis genes and in asymmetric System L transporter expression in MVM / BM membrane protein fractions were compared by using nonparametric Mann-Whitney test. Anthropometric and clinical data were compared between GDM and controls by unpaired two-tailed Student's t-test. For

immunohistochemistry the non-parametric chi-square (χ^2)-test was used to compare semi-quantitative protein expression between control and GDM placentae. A p-value <0.05 was considered as statistically significant and shown as asterisk in figures next to the data points, *p<0.05, **p<0.01, ** p<0.001, ****p<0.0001. For collection and arrangement of numeric data we used Excel from Microsoft Office, while statistical comparisons were performed using GraphPad Prism (GraphPad).

3 Results

The following results part is divided into two sections investigating first the specific aims A1-A5 (1.6.1 on p.29) regarding the effect of counter-directed amino acid gradients on transplacental leucine transport, the expression of the System L transporter LAT1 and LAT2 in differentiating trophoblasts, the role of these singe transporter in placental leucine transport using small molecule inhibitors. In the second part of the results, the specific aims B1-B6 (1.6.2 on p.30) are elucidated concerning the relation between GDM-mediated hyperglycemia and disturbed placental iron homeostasis. Herein expressional comparisons of iron homeostasis genes in placental tissues from GDM patients and healthy control were analyzed to identify affected iron transport pathways under GDM-mediated hyperglycemia. Moreover, newly developed hyperglycemic *in vitro* models were applied to reveal functional disturbances and underlying cellular mechanisms and an obesogenic diet during mouse pregnancy was tested as alternative *in vivo* model system.

3.1 Amino acid transport

3.1.1 Relevance of physiological amino acid concentrations on gestation and fetal growth

3.1.1.1 Determination of maternal and fetal amino acid spectra

Maternal vein (MV) serum and the corresponding fetal vein (FV)/ fetal artery (FA) serum samples were prospectively collected from 22 clinically unsuspicious patients by Caesarian section at term (**Table 7**).

The concentrations of the 20 standard proteinogenic amino acids are shown in Figure 12 and **Table 8**. Brackets represent expected physiological ranges of amino acid concentrations in adults (>15 years) and newborns (0-1 month), respectively, based on

internally measured standard values at the University Hospital Bern. Particularly essential amino acids like Thr, Val, Trp and Lys and some conditionally essential amino acids such as Gly and Tyr were significantly higher concentrated in both fetal FA and FV compartments compared to MV. There was no difference between maternal and fetal concentrations for Cys and Asn. Ser and Gln showed significant greater concentrations in FA compared to MV. For Cys all quantitative measurements (4 µM in FV and 5 µM in MV) were clearly below the expected range of 25-80 µM for FV and 20-85 µM for MV. Due to the discrepancy to published data (Irene Cetin et al. 1988; Hayashi et al. 1978; Velazquez et al. 1976), Cys concentrations and gradients were excluded in the follow-up correlation analysis .There was no significant difference between female and male babies.

Table 7: Anthropometric characteristics of healthy patients and their offspring.

	Characteristics	Control
Mother	Number (n)	22
	Delivery mode	cesarean sections
	Maternal age (years)	34.36 ± 3.74
	Preconceptional weight (kg)	67.52 ± 11.47
	Weight at *partum* (kg)	82.05 ± 14.30
	Height (cm)	163.95 ± 7.50
	Preconceptional BMI (kg/m^2)	25.04 ± 4.76
	BMI at *partum* (kg/m^2)	30.53 ± 5.06
	Weight gain (kg)	15.86 ± 5.83
	Gravidity	2.55 ± 1.34
	Parity	1.82 ± 0.85
	Gestational age at *partum*	38 3/4 ± 1
	Systolic blood pressure	117.36 ± 9.33
	Diastolic blood pressure	69.91 ± 10.05
	Placental weight (g)	644.18 ± 112.80
Newborn	Gender	9 ♂ / 13 ♀
	Weight (g)	3410.23 ± 456.95
	Percentile[#] (%)	47.45 ± 28.56

Data are presented as mean ± standard deviation (SD). Abbreviations: BMI, body mass index. [#] Percentile were calculated by using child growth standards published by WHO (www.who.int/childgrowth/standards/weight_for_age); March 2020).

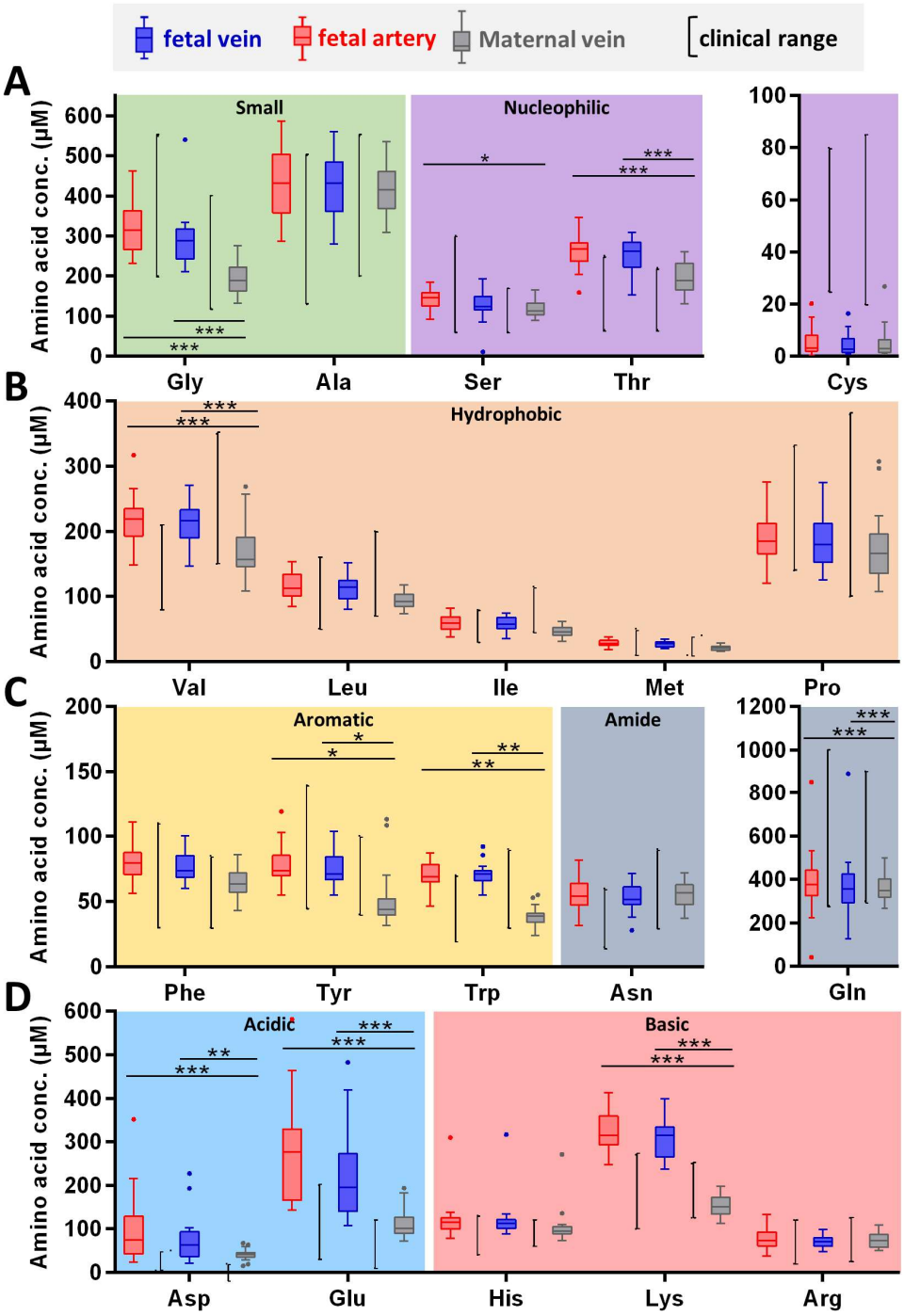

Figure 12: Full proteinogenic amino acid profile of maternal-fetal matched blood samples. The concentrations of the 20 standard proteinogenic amino acids (AA) were measured in prospectively collected blood sera from clinically unsuspicious woman and the placenta of their newborns (n=22) within 20 min after elective Caesarian section. The AA concentrations were measured by ion exchange chromatography in three different compartments, namely in blood sera from maternal vein (grey), in fetal artery (red) and fetal vein (blue). Data are depicted as Boxplots with Tukey whiskers. The various AA are classified according to their chemical structure and properties (see colored backgrounds). Brackets represent expected physiological ranges of AA concentrations of adults (>15 years) and newborns (0-1 month), respectively. The maternal-fetal matched blood samples were compared using paired two-way ANOVA with Tukey's correction; * p<0.05, ** p<0.01, *** p<0.001. AA concentrations in sera from healthy mother-baby pairs at birth were significantly different by comparing maternal vein *versus* fetal artery for Gly, Ser, Thr, Val, Tyr, Trp, Gln, Asp, Glu and Lys. An overview on all results is presented in **Table 8**.

Table 8: Paired materno-fetal amino acid concentrations and materno-fetal gradients.

Amino acid / classification		Fetal arterial (FA) [µM]	Fetal venous (FV) [µM]	Maternal venous (MV) [µM]	FA-MV Gradients [µM]	FV-MV Gradients [µM]	FV-FA Difference [µM]
		mean ± SD	mean ± SD	mean ± SD	mean ± SD	mean ± SD	mean ± SD
Small	Gly(!)	324 ± 67	290 ± 68	195 ± 38	129 ± 73 ***	95 ± 64 ***	-34 ± 56 ***
	Ala	429 ± 88	425 ± 77	421 ± 65	8 ± 87	5 ± 86	-4 ± 52
Nucleophilic	Ser	141 ± 26	124 ± 35	118 ± 18	23 ± 26 *	6 ± 32	-17 ± 32
	Thr!	260 ± 41	252 ± 39	194 ± 35	66 ± 27 ***	58 ± 30 ***	-8 ± 23
	Cys(!)	5 ± 5	4 ± 4	5 ± 6	0 ± 3	-1 ± 3	-1 ± 2
Hydrophobic	Val!	216 ± 38	212 ± 33	170 ± 39	46 ± 30 ***	42 ± 34 ***	-4 ± 22
	Leu!	116 ± 21	113 ± 19	94 ± 13	22 ± 21	18 ± 20	-4 ± 17
	Ile!	60 ± 13	59 ± 10	46 ± 8	14 ± 11	13 ± 10	-1 ± 8
	Met!	28 ± 5	27 ± 4	21 ± 4	7 ± 5	6 ± 5	-1 ± 3
	Pro(!)	189 ± 45	184 ± 42	173 ± 52	16 ± 25	11 ± 33	-5 ± 19
Aromatic	Phe!	79 ± 12	76 ± 10	64 ± 11	15 ± 13	12 ± 12	-3 ± 9
	Tyr(!)	77 ± 15	75 ± 13	50 ± 21	27 ± 25 *	25 ± 24 *	-2 ± 7
	Trp!	70 ± 10	71 ± 8	39 ± 7	31 ± 11 **	32 ± 10 **	1 ± 8
Amide	Asn	55 ± 13	54 ± 11	55 ± 10	0 ± 13	-2 ± 11	-1 ± 11
	Gln(!)	391 ± 145	376 ± 144	362 ± 62	29 ± 171 **	14 ± 167	-16 ± 55
Acidic	Asp	98 ± 81	74 ± 51	41 ± 13	57 ± 82 ***	33 ± 56 **	-24 ± 75 *
	Glu	279 ± 116	218 ± 99	111 ± 34	168 ± 115 ***	107 ± 104 ***	-61 ± 100 ***
Basic	His!	122 ± 45	120 ± 46	104 ± 39	18 ± 16	15 ± 16	-2 ± 11
	Lys!	320 ± 48	311 ± 48	152 ± 23	168 ± 35 ***	159 ± 38 ***	-9 ± 29
	Arg(!)	79 ± 23	72 ± 14	74 ± 17	5 ± 24	-2 ± 19	-7 ± 14

Legend: Statistical comparison between different blood compartments, e.g. FA *versus* MV, FV *versus* MV and FV *versus* FA were performed in 22 healthy controls using 2 way ANOVA and multiple comparison with Tukey testing; α=0.05, * p<0.05, ** p<0.01, *** p<0.001. Amino acids are abbreviated according to 3-letter amino acid code. Fetal arterial (FA); Fetal venous (FV); Maternal venous (MV); !, essential amino acids; (!), Conditionally essential amino acids.

3.1.1.2 Individual and amino acid-specific differences in materno-fetal gradients

The difference between FA and MV was selected as AA-gradient relevant for materno-fetal transfer. We found significant FA-MV differences for the small AA Gly, the nucleophilic AA Ser and Thr, the hydrophobic AA Val, and the aromatic AA Tyr and Trp. Similar differences were also found when comparing the FA-MV against FV-MV gradients. Of note, large differences were found for essential AA. The non-essential AA Ser, Asp and Gln additionally showed highly negative veno-arterial (FV-FA) differences (**Table 8**), i.e. they disappear in placental capillaries and are secreted into the placenta towards maternal circulation, respectively (Holm et al. 2017). Although there were negative means of FV-FA differences for all AA except Trp (**Table 8**), 7 out of 22 individuals showed predominantly positive FV-FA differences (Figure 13). Thus, the placentae included in our studies can be classified into either accumulative (positive FV-FA difference; 45.5%) or secretive (negative FV-FA difference; 54.5%) tissues. Of note, only four placentae (18%) exposed a mixture of accumulation and secretion mode, which could be a transient state.

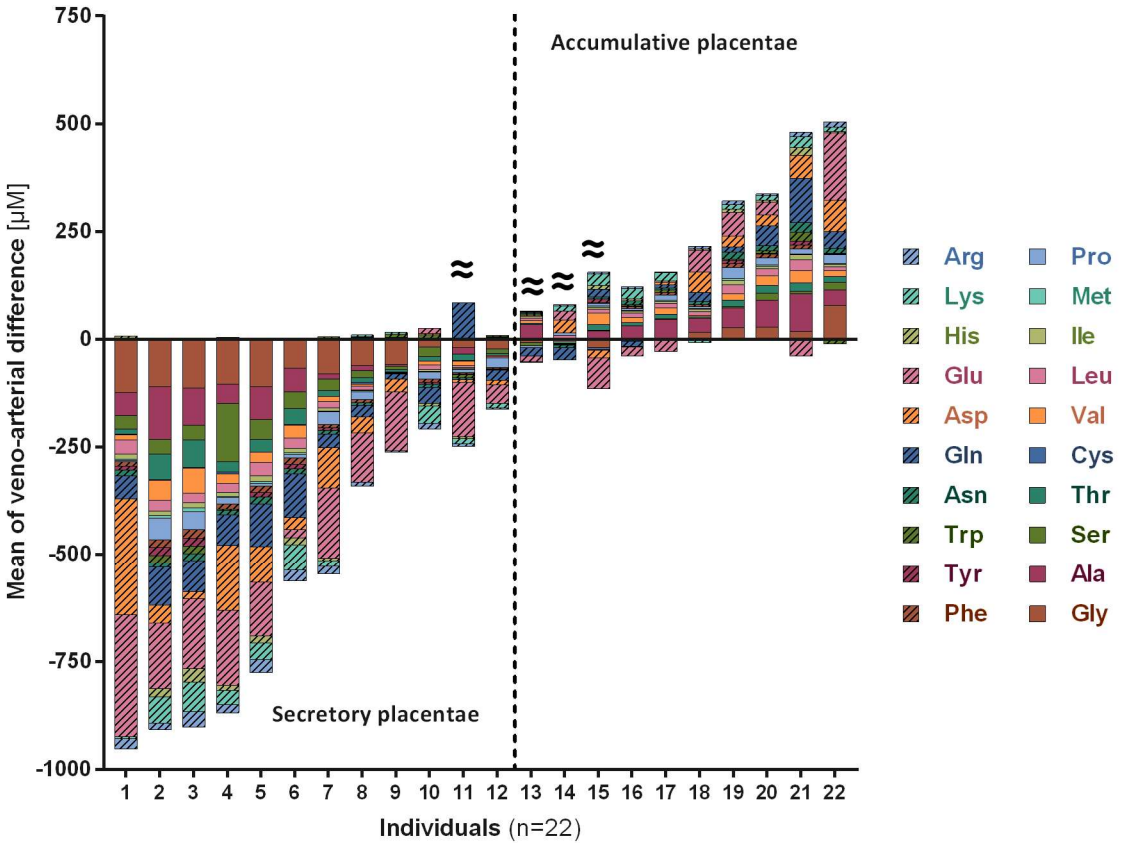

Figure 13: Individual differences in fetal net amino acid accumulation and secretion. The means of veno-arterial (FV-FA) differences of 20 amino acids (AA) are represented in a stacked bar diagram. The analyzed individuals are depicted on the x axis in ascending order. 12 out of 22 individuals showed a negative, while 7 out of 22 individuals showed a clear positive sum of veno-arterial differences. Of note, only four placentae (18%) exposed a mixture of accumulation and

secretion (≈). In general, the 22 individuals can be classified based on their veno-arterial differences in either accumulative placentae, performing fetal AA uptake or in secretory placentae, performing fetal AA efflux. Since there were more secretory placentae present in this study, the total FV-FA difference as listed in Table 8 is negative.

3.1.1.3 Amino acid concentrations and materno-fetal gradients correlate with selected anthropometric data

Next, the concentrations of all 20 amino acids, their materno-fetal gradients and fetal veno-arterial differences were correlated to the corresponding anthropometric data listed in **Table 7**. The summary of all significant Spearman's correlations is shown in **Table 9**, negative correlations are marked with (↓). In general, 79% of all Spearman's correlations between the different sera compartments and clinical parameters concerning maternal constitution, fetal growth or maternal blood pressure were positively associated. Interestingly, 36 out of 85 (42%) significant positive Spearman's correlations were associated with amino acid concentrations in the MV, which is affected by the diet and fasting time of the mother. In contrast, all negative correlations were associated to fetal amino acid concentrations. 69% of all and 56% of MV correlations, respectively, were associations between LAT1 substrates and anthropometric parameters. Based on the latter results, we focused in this study specially on LAT1 substrates as highlighted in **Table *9***.

Table 9: Spearman correlations between amino acid concentrations, materno-fetal gradients and corresponding anthropometric data

		Gly(!)	Ala	Ser	Thr!	Cys(!)	Val!	Leu!	Ile!	Met!	Pro(!)	Phe!	Tyr(!)	Trp!	Asn	Gln(!)	Asp	Glu	His!	Lys!	Arg(!)
Mother	**Age**	FV											↓FA								
	preconception Weight		MV				FA MV	MV	FV MV		FA MV MV-FV	MV-FV	MV-FV				MV	MV			
	Weight at *partum*		MV				MV	MV	MV	MV	FA MV	MV	MV MV-FV			MV		MV	MV		
	Weight gain	FA FV ↓MV-FV	FV											↓FV MV-FA MV-FV							
	Height					↓FV MV-FA MV-FV			MV-FA										MV-FA MV-FV		
	BMI mother at *partum*		MV				MV	MV	FA FV MV	MV	FA MV							MV MV-FV	MV		
	preconception BMI						FA MV	FV MV	FA FV MV		FA MV							MV	MV		
	Gravidity																	MV			
	BP Syst mother	↓FA ↓FV MV-FV	↓FA	↓FA	MV-FA MV-FV		↓FA MV-FA	↓FA ↓FV		↓FV		↓FA ↓FV MV-FA			↓FA ↓FV MV-FA		↓FV MV-FV			↓FA	
	BP Diast mother		MV-FA		MV-FA		MV-FA					MV-FA		FV-FA				↓FV MV-FV			MV-FA MV-FV
Fetus	**Gestational age**					↓FV-FA										↓MV-FV	↓MV-FA				
	Weight placenta	MV-FV	MV-FV	MV		FV-FA											MV-FV	MV MV-FV			
	Weight offspring	FV											↓FA								
	Gender offspring														MV						

Legend: Statistical significant correlations between different blood compartments, e.g. FA *versus* MV, FV *versus* MV and FV *versus* FA were performed in 22 healthy controls by Spearman correlations; α=0.05; !, essential amino acids; (!), conditionally essential amino acids; Green, LAT1 substrates; orange, Glutamine (Gln) as LAT1 co-substrate; ↓, negative correlations.

3.1.1.4 Associations between amino acid concentrations in maternal and fetal compartments with clinical data

The correlations between clinical data with amino acid concentrations in maternal and fetal sera, but also with materno-fetal gradients are listed in **Table 9**. There were positive correlations between preconceptional weights and the MV concentrations for Ala, Val, Leu, Ile, Pro, Asp and Glu (**Table 9**), but also FA concentrations for Val and Pro respectively FV concentration of Ile. All MV concentrations correlating with preconceptional weights were also correlating with maternal weight at *partum* but also to Met, Phe, Tyr, Gln and His (**Table 9**). Figure 14 shows Spearman correlation with maternal weights and body mass index (BMI) as scatter plot for Leu, that seems to persist throughout pregnancy. The group of hydrophobic amino acids and LAT substrates Val, Leu and Ile were showing similar correlation patterns. For maternal weight gain as parameter combining the weight before pregnancy and at term only fetal amino acid concentrations such as for Gly Ala and Trp were correlating significantly (**Table 9**). Analogous to the relation between preconceptional weights and the weights at *partum*, there were comparable correlations between amino acid concentrations and preconceptional BMI and BMI at term **(**Figure ***14***).

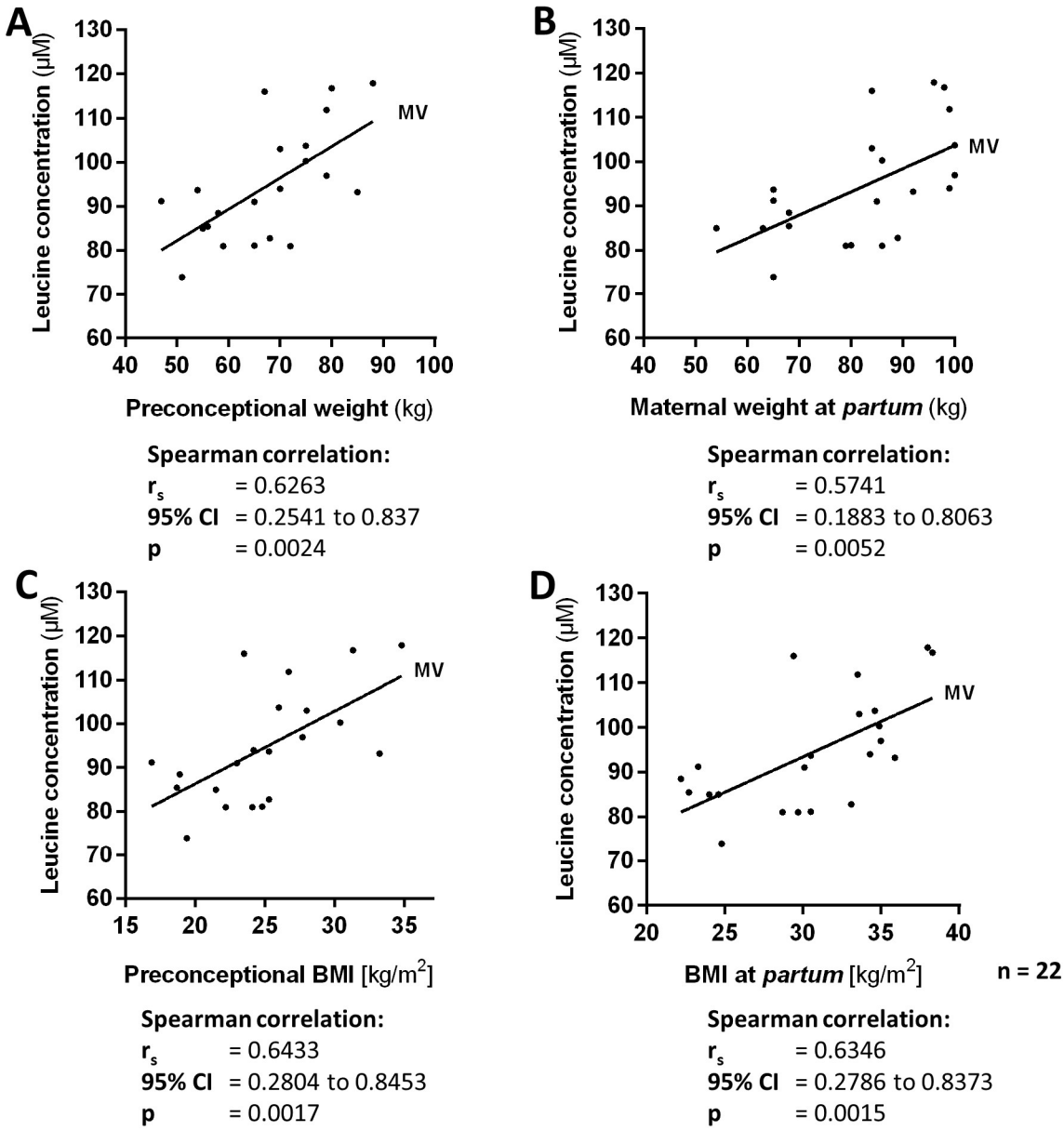

Figure 14: Linear relation between leucine concentrations and maternal anthropometric data. The relation between measured leucine (Leu) concentrations in maternal venous sera (MV) and (**A)** maternal preconceptional weights, **(B)** maternal weights at *partum* (**C)** preconceptional body mass index (BMI) and (**D**) BMI at *partum* was analyzed by Spearman correlation for 22 healthy controls (n=22). Data are presented as scatter plots with the anthropometric parameters on the x-axis and AA concentrations in the maternal vein (MV) on the y-axis. Preconceptional weights, maternal weights at *partum* and BMI were mainly correlating with MV concentrations of AA which are LAT1 substrates. The results of all significant correlations are listed in **Table 9**. Statistical values describing the linear relationship between two parameters are denoted to the right of the scatter plots: r_s, Spearman correlation coefficient; CI, confidence interval; p, two-tailed p value.

3.1.1.5 Correlations of the amino acid gradients and veno-arterial differences with clinical data

Amino acid gradients across the materno-fetal barrier were calculated as difference between MV and FV or FA. Positive correlations were detected between materno-fetal

amino acid gradients and maternal weights of Pro, Phe and Tyr before conception and Tyr at *partum* as well (**Table 9**). Furthermore, amino acid gradients of Ile, His were correlating with maternal heights, while putting weights and height into relation Glu MV-FV was correlating with BMI at *partum*. Negative correlations were found between amino acid gradients and clinical data of Gly MV-FV with maternal weight gain, but also of Gln and Asp with gestational age (**Table 9**). The MV-FV gradients of the three aromatic amino acids Phe, Tyr and Trp were correlating with the different maternal weight parameters like preconceptional weight, weight at *partum* and weight gain (see ***Figure 4*** for Tyr and Trp). For the veno-arterial (FV-FA) difference only few positive correlations with anthropometric data were detected, namely between maternal diastolic blood pressure and Trp (see, 3.1.1.7) respectively between placental weight and Cys, whereas FV-FA difference for Cys were negatively related to gestational age (**Table 9**).

3.1.1.6 Placental weight correlates with MV-FV gradients of non-essential amino acids

MV-FV gradients of the non-essential small amino acids Gly and Ala, but also the two acidic amino acids Asp and Glu, as well as MV levels of Ser and Glu were positively associated with placental weight (**Table 9**). However, Fetal gender and birth weight were largely independent of the amino acid concentrations. As exceptions there were correlations for weights of offspring with Gly concentration in FV and the negative relation with Tyr in FA, whereas only Asn in MV was correlating with fetal sex (**Table 9**).

3.1.1.7 Association between maternal blood pressure and fetal amino acid concentrations

The concentrations of Gly, Ala, Ser, Val, Leu, Met, Phe, Asn, Asp and Lys in fetal vein and artery were significantly decreasing with increasing systolic blood pressures values (**Table 9**). The decreasing fetal amino acid levels relative to the elevation in systolic blood pressure resulted in a positive correlation with materno-fetal gradients and systolic blood pressure. MV-FV gradients for Gly, Thr, Asp, Glu and Arg and MV-FA gradients for Ala, Thr, Val, Phe, Asn, and Arg were positively correlating with diastolic and systolic blood pressure (**Table 9**).

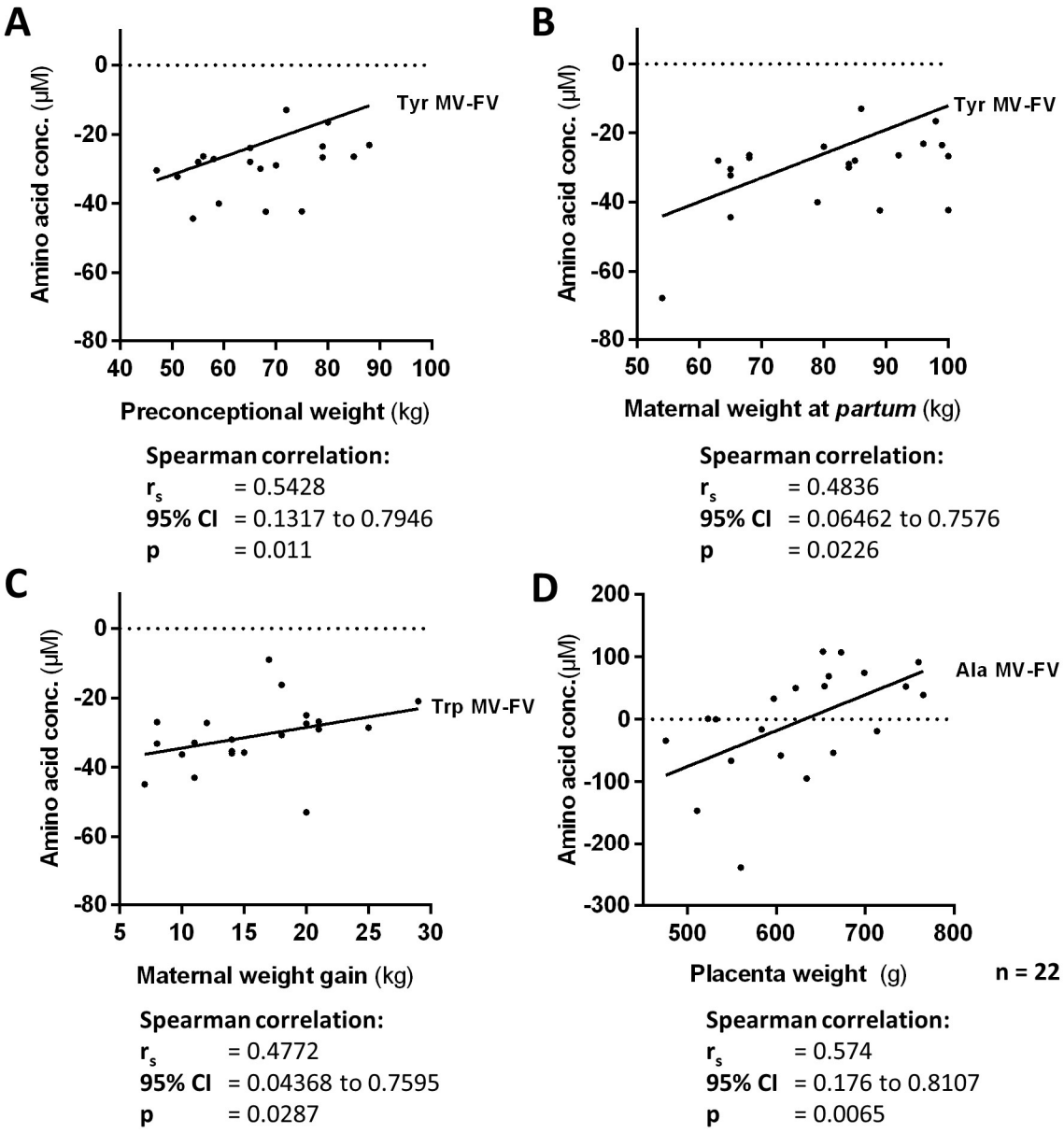

Figure 15: Representative correlations between tyrosine and tryptophan gradients across materno-fetal barrier and anthropometric data. Amino acid (AA) gradients across the materno-fetal barrier were calculated as difference between concentrations in maternal vein (MV) and fetal artery (FA) or fetal vein (FV) for 22 mother-fetus paired serum samples (n=22). Since AA levels are generally higher in the fetal as compared to the maternal circulation, AA gradients are negative values and therefore represent counter-directed materno-fetal gradients. Significant Spearman correlations were found between (**A**) tyrosine (Tyr) gradients and maternal preconceptional weights, (**B**) Tyr gradients and maternal weights at *partum*, (**C**) Trp gradients and maternal weight gain (defined as maternal weight at *partum* minus preconceptional weight) and (**D**) Alanine (Ala) gradients and placental weight. Results are presented as scatter plots with anthropometric data on the x-axis and AA gradients on the y-axis. Additional significant correlations for other significant correlations (**Table 9**). Statistical parameters describing the linear relationship are denoted below the scatter plots: r_s, Spearman correlation coefficient; CI, confidence interval; p, two-tailed p value.

3.1.2 Effects of counter-directed gradients on placental leucine transfer

3.1.2.1 Increased extracellular leucine levels facilitate leucine uptake into trophoblast cells

Two different extracellular leucine concentrations were applied to test the effect of amino acid gradients on leucine uptake efficiency into the choriocarcinoma cell line BeWo and the colon carcinoma cell line HT-29. A leucine concentration in the upper clinical range (167 µM) was selected and compared to a lower concentration of 30 µM leucine. 30 µM leucine corresponds to approx. 1/3 of the mean leucine -MV concentration. As shown in **Figure 7A**, increased extracellular leucine levels facilitated uptake of leucine into undifferentiated BeWo-CTB from 15.9 to 47.3 nmol/mg protein (mean difference and standard error = 31.4 ± 3.5 nmol/mg protein), and into differentiated BeWo-STB from 30.7 to 103.4 nmol/mg protein (mean difference and standard error = 72.8 ± 8.5 nmol/mg protein). In comparison, the uptake into HT-29 cells increased from 32.7 to 66.2 nmol/mg protein (mean difference and standard error = 33.5 ± 5.0 nmol/mg protein). Therefore, for trophoblasts a 2-times higher basic leucine uptake rate was found in BeWo-STB compared to BeWo-CTB. A comparable leucine uptake capacity was observed in BeWo-STB and HT-29 cells under low substrate conditions, but a clearly enhanced uptake capacity of trophoblasts was detected under high extracellular leucine concentrations (**Figure 16A**). The LAT1-specific inhibitor JPH203 was applied to assure that leucine uptake in Na^+-free conditions was mediated by LAT1. LAT1-specific inhibition in a dose-response experiment resulted in a dramatic reduction of leucine uptake into both BeWo-CTB with 85% and into BeWo-STB 76% reduction with half maximal effective concentration (EC_{50}) values in the nanomolar range (**Figure 16B**), suggesting an only minor involvement of other System L transporters like LAT2 at exceeding leucine concentrations. These results indicate a primarily LAT1-mediated leucine uptake process in trophoblasts with high dependency on extracellular substrate availability.

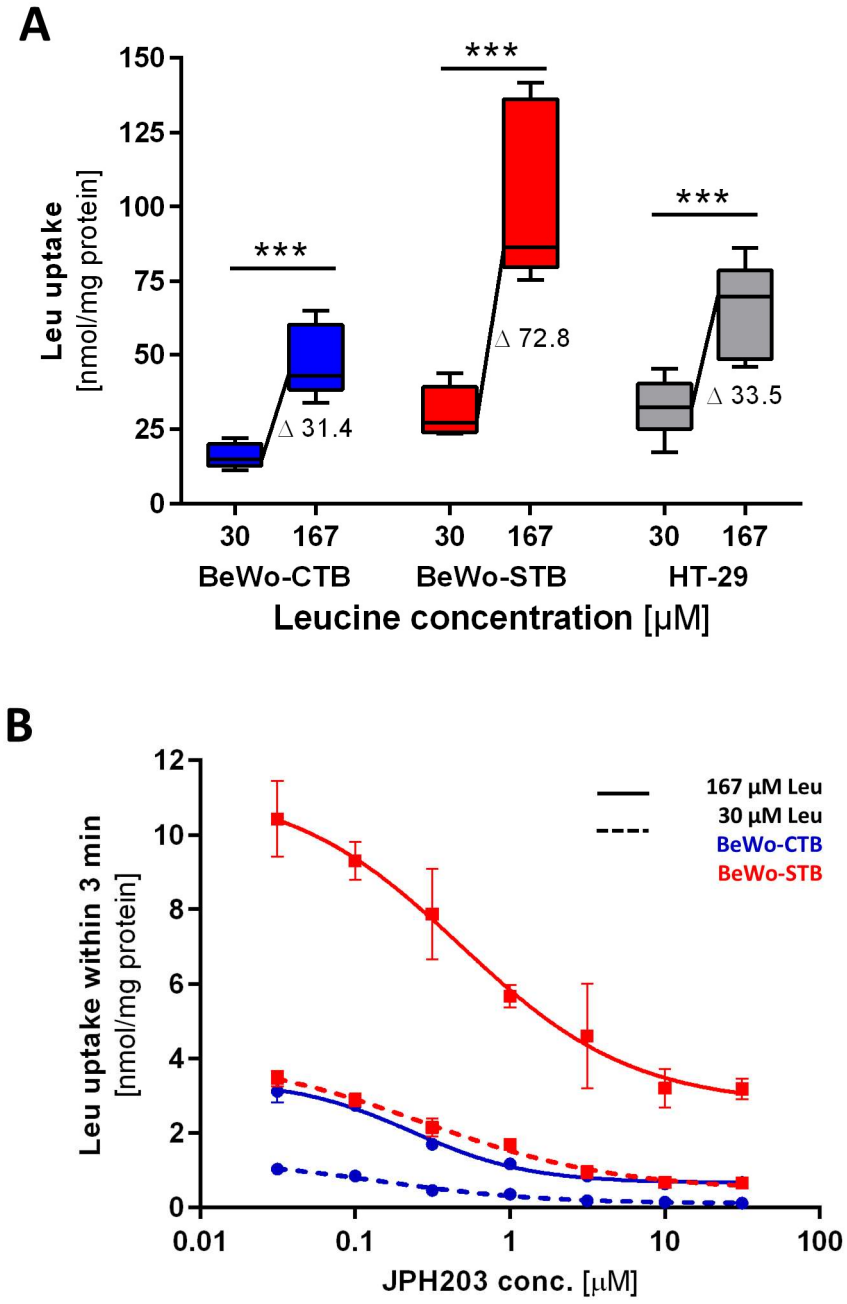

Figure 16: Amino acid concentration influences LAT1-mediated leucine uptake in the BeWo cell model. (**A**) The effect of extracellular leucine (Leu) concentrations on the Leu uptake capacity into BeWo trophoblasts was assessed and compared to the frequently used colon cancer cell model HT-29 cell. Leu uptake assays were performed with Leu concentrations of 167 µM, reflecting an upper clinical range, and a lower concentration of 30 µM. Moreover, the uptake capacity between syncytiotrophoblasts (STB) and cytotrophoblasts (CTB) was compared by stimulating undifferentiated BeWo cells (BeWo-CTB) with 100 µM forskolin for 48 h (BeWo-STB). For all cell types Leu uptake was measured within 3 min and normalized to the total protein concentration. BeWo-CTB are depicted in blue, BeWo STB in red and HT-29 in grey (**A-B**). Differences were tested by Sidak's multiple comparisons test; * $p<0.05$, ** $p<0.01$, *** $p<0.001$. Of note, the stimulation of Leu uptake through increased extracellular Leu concentration was more then 2-times higher in BeWo-STB, as compared to the other undifferentiated cell types. The results of 3 individual experiments with 4 replicates each are presented as mean (+), median (-) and Tukey whiskers (1.5-times IQR). (**B**) To verify the presence of LAT1/*SLC7A5*-mediated Leu uptake and its susceptibility to different substrate concentrations, a dose-response experiment with the LAT1-specific inhibitor

JPH203 was performed. Leu uptake under high Leu concentration (167 µM Leu) are depicted as solid lines and lower (30 µM Leu) as dashed lines (**B**). BeWo-STB with high Leu levels showed significantly higher Leu uptake rates, but also a much higher susceptibility to inhibition by JPH203 compared to BeWo-CTB. Interestingly, even high doses of JPH203 did not inhibit Leu uptake in BeWo-STB at 167 µM Leu as markedly as in BeWo-CTB. Differences were tested by Sidak's multiple comparisons test; * p<0.05, ** p<0.01, *** p<0.001. Error bars represent standard deviation (SD) of a representative experiment with 4 replicates each.

3.1.2.2 Counter-directed leucine gradient promotes leucine transfer across the materno-fetal barrier

The materno-fetal leucine transfer was measured by applying either equimolar leucine concentrations (30 µM each) in the upper (maternal) and lower (fetal) compartment (Leu materno-fetal gradient = 0 µM) or by applying a counter-directed gradient with 30 µM leucine in the maternal and 167 µM leucine in the fetal compartment (counter-directed leucine materno-fetal gradient = 137 µM). **Figure 17B** shows the experimental setup and the concentration changes of radio-labeled leucine measured in the upper (Maternal venous (Mv)) compartment and in the receiving lower (Fetal arterial (Fa)) compartment from a representative Transwell® experiment over 6 h. The application of a counter-directed leucine gradient of 137 µM significantly stimulated the materno-fetal transfer of leucine by 47.2% in average within the last three time points (4 – 6 h). Moreover, leucine transfer was significantly reduced by applying 10 µM of LAT-specific inhibitor JPH203 (**Figure 17A**, dashed line), indicating that mainly LAT1-mediated leucine transfer across the materno-fetal barrier occurs. Within three successively and independently performed Transwell® experiments (n=3), there were significant differences detected from 120 min transfer time onwards (**Figure 17C**). The intracellular leucine content measured at the end of the experiment (**Figure 17D**) was not significantly different between equimolar leucine concentrations and counter-directed leucine gradient. Intracellular leucine retainment would be a sign for leucine efflux limitations forwards the lower fetal compartment.

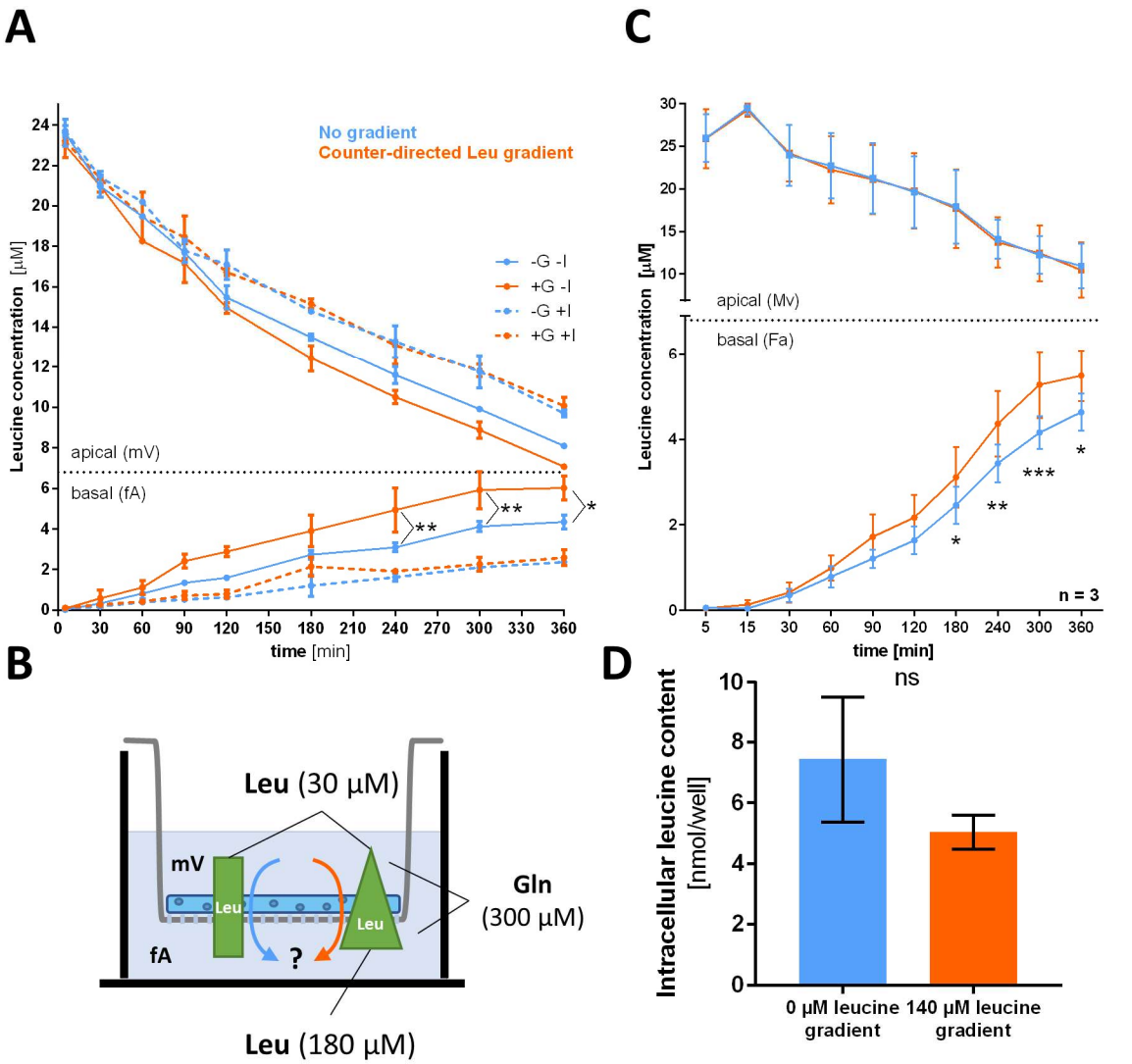

Figure 17: Counter-directed leucine gradient increases amino acid transfer across the placental barrier. (**A**) Materno-fetal leucine (Leu) transfer across a tight trophoblast monolayer was studied using the Transwell® system. BeWo cells were cultured on a semi-permeable membrane and differentiated by stimulation with 100 µM forskolin 24 h after seeding. Leu transfer was measured by simultaneous sampling and measurement of diminishing radiolabeled Leu (L-[3,4,5-^{3}H(N)]-leucine) in the upper maternal vein (Mv) compartment and appearing radiolabeled Leu in the lower compartment representing the fetal artery (Fa) over 360 min (**A**). Two different conditions were compared: materno-fetal Leu transfer in the condition with 30 µM Leu both in the Mv and the Fa compartment (no gradient, blue) or against a counter-directed Leu gradient with 30 µM Leu in Mv and 167 µM Leu in the Fa compartment (orange). In all conditions there was 300 µM Gln as exchange partner in both compartments. The schematic representation of the experimental setup is shown in panel **B**. Leu transfer across the placental barrier was increased against a counter-directed 137 µM Leu-gradient. **A**, shows results of a representative dataset from 3 independent experiments. The combination of the 3 independent Transwell® experiments (n=3) are shown in panel **C**. Measured accumulation of intracellular Leu at the end of the experiment is presented in panel **D**. Differences were tested by 2 way ANOVA with Tukey's multiple comparisons test; * p<0.05, ** p<0.01, *** p<0.001.

3.1.3 Trophoblast differentiation affects placental amino acid uptake

3.1.3.1 LAT1, LAT2 and 4F2hc are asymmetrically expressed in the human placenta

Before MVM- and BM-fractions were used for protein localization studies, the enrichment of MVM and BM samples was approved by determining alkaline phosphatase activity and FPN1 expression for each isolation as shown in **Figure 18**.

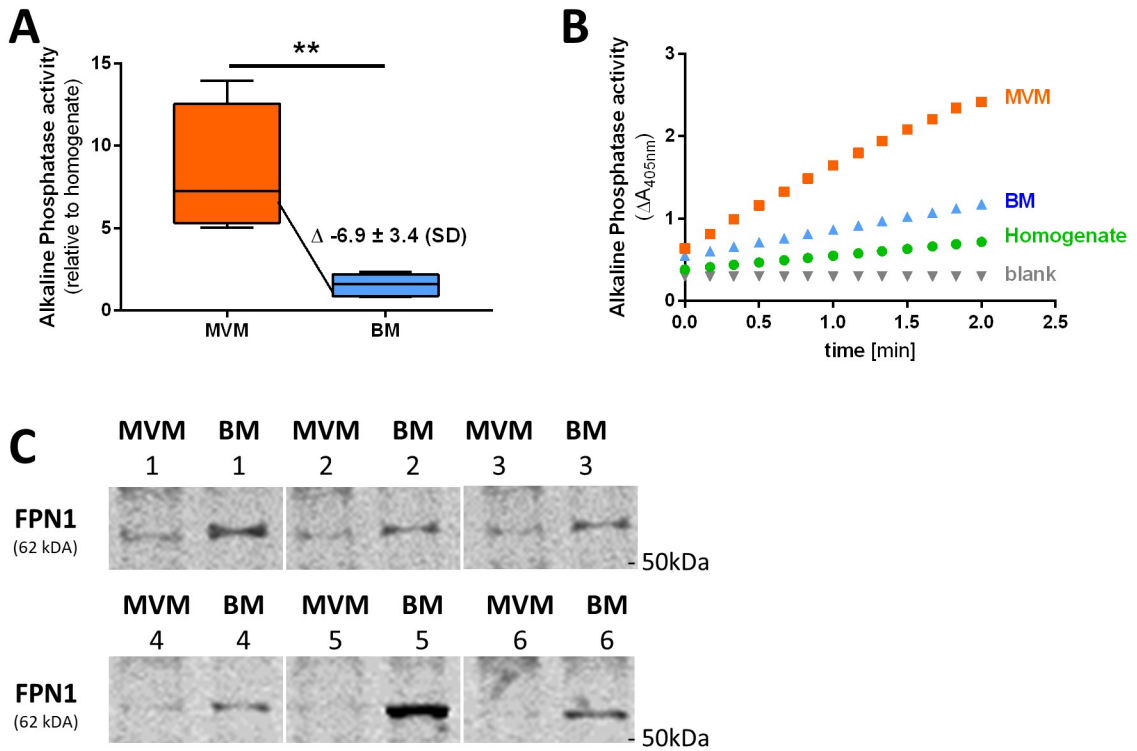

Figure 18: Characterization of MVM/BM enrichment by determining alkaline phosphatase activity as MVM-marker and FPN1 as BM-marker expression. Alkaline phosphatase is a marker enzyme for the syncytiotrophoblast (STB) apical membrane/microvillous membrane (MVM) (Nicholas P. Illsley et al. 1990), while Ferroportin 1 (FPN1) as iron exporter is expressed in the basal membrane (BM) (Bastin et al. 2006). Alkaline phosphatase activity in MVM and BM samples from membrane isolations were compared to their corresponding homogenate fraction before MVM/BM enrichment using a parametric paired t-test. Alkaline phosphatase activity relative to homogenate as depicted in **A** was 7.0-times higher in MVM (9.6-times enrichment) compared to BM (1.6-times enrichment). **B** left panel shows p-nitrophenyl phosphate (pNPP) hydrolysis (colorless) to p-nitro-phenol (yellow, $\lambda_{abs.}$=405 nm) by alkaline phosphatase activity of a representative experiment during 2 min. FPN1 expression was analyzed by immunoblotting (**C**). BM-marker FPN1 was increased in BM compared to MVM fractions. **A-C**, Characterization of MVM/BM enrichment was performed for 6 out of 11 isolations (n=6).

Histological investigation of healthy placental tissue demonstrated strong expression of LAT1 at the apical membrane of STB (arrows in **Figure 19A**), if compared to almost no signal at the basal membrane of STB (arrowheads in **Figure 19A**). Very similar asymmetric LAT1 expression was found by comparing the strong signal in the MVM *versus* BM fraction,

both compared to total membrane homogenate from 11 MVM/BM isolation experiments (**Figure 19B**). The investigation of the asymmetric expression was expanded from LAT1 to LAT2 and 4F2hc by immunoblot analysis in paired MVM/BM isolated fractions from term control placentae. LAT1 was predominantly expressed at the MVM as reflected in a mean MVM to BM ratio of 6.9 (range 3.5 – 14.9*;* **Figure 19B**). Western blot analysis of MVM and BM pairs revealed a significantly higher expression of LAT1 in MVM compared to BM ($p=0.0015$; **Figure 19C**). The results of these two independent experimental approaches suggest almost exclusive LAT1 expression at the apical membrane which is in direct contact with maternal blood. In contrast, LAT2 was found to be expressed in both MVM and BM (**Figure 19C**), with an apparent predominance of the two LAT2 variants (30 and 50 kDa) in BM as reported before(Rosario et al. 2013). Expression of 4F2hc, the heavy chain partner protein of LAT1 and LAT2, was higher in MVM as compared to BM (**Figure 19C**).

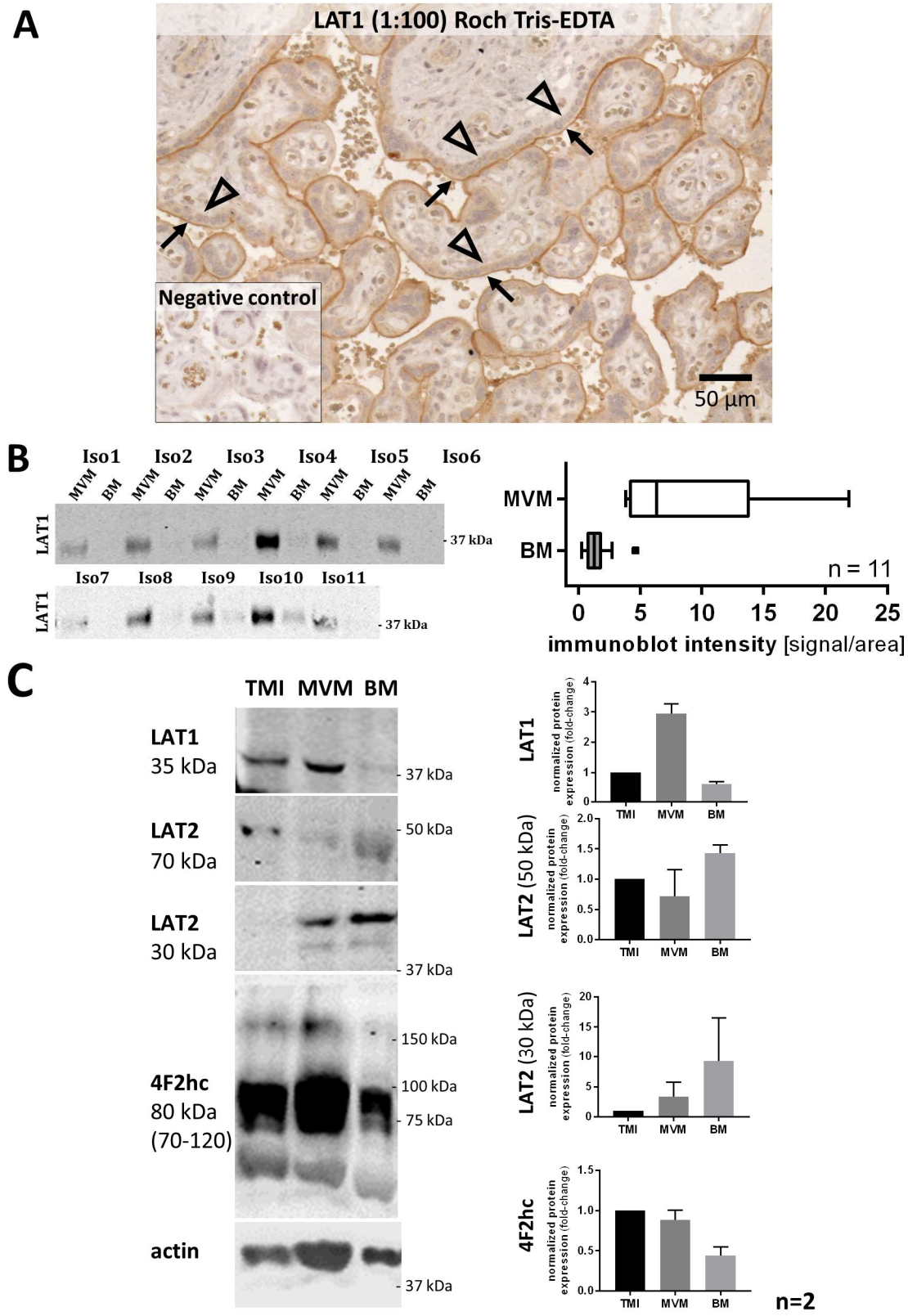

Figure 19: Asymmetric expression of the Na^+-independent leucine transporters LAT1 and LAT2 at the placental barrier. A, Representative picture showing apical LAT1 localization in immunohistochemistry performed on human term placenta. Arrows indicate the apical MVM, i.e. maternal blood orientated side; arrowheads depict the BM of the STB. There was no signal in negative control. **B**, Left panel, representative immunoblot from a total of 11 human term placentae. **B**, Right panel, LAT1 was highly expressed in MVM, but negligible in BM protein fractions. The data are shown as boxplots with Tukey whiskers (Mann-Whitney test, α=0.05;

p<0.0001). Densitometric analysis was corrected for actin signal. **C**, The expression of LAT1 (*SLC7A5*), LAT2 (*SLC7A8*) and 4F2hc (*SLC3A2*) was analyzed in total membrane isolation (TMI), microvillous membrane (MVM) and basal membrane (BM) fractions in two independent experiments (n=2) by immunoblotting. In the left panels, images of a representative immunoblot are shown with corresponding densitometric quantification on the right. In the right panels the densitometric analyses and consecutive statistics for both experiments are shown. LAT1 was almost exclusively expressed in MVM, while LAT2 was found in both MVM and BM. 4F2hc, the heavy chain partner protein of LAT1 and LAT2, was higher expressed in MVM as compared to BM. Beta-actin was used as reference gene.

3.1.3.2 Trophoblast differentiation induces upregulation of LAT1 and 4F2hc expression

To study the role of LAT1 at the placental barrier on the cellular level, *LAT1* expression during trophoblast differentiation was analyzed in both primary human trophoblast cells and in the BeWo cell line model on mRNA and protein level. Forskolin-stimulated differentiation in BeWo cells resulted in a significant upregulation of *LAT1* and *4F2hc*, but no significant changes for *LAT2* were observed (**Figure 20A**). Spontaneously occurring trophoblast differentiation in primary trophoblasts tended to increase *LAT1* and *4F2hc* mRNA levels, but due to the high variation between the individual placental cell isolations this effect did not reach statistical significance (**Figure 20B**). Interestingly, protein analysis by immunoblotting revealed a clear difference in the protein expression pattern between LAT1 and LAT2 depending on the differentiation state: while LAT2 was predominantly found in undifferentiated primary CTB and BeWo-CTB, LAT1 protein levels were clearly increased in differentiated primary STB and BeWo-STB (**Figure 20C**). Furthermore, increased 4F2hc expression was detected after differentiation in both primary and BeWo cells. 4F2hc protein expression was identified in the form of multiple bands ranging from 70-120 kDa under reducing conditions. The shattered expression pattern of 4F2hc was found previously and is presumably due to dimerization with itself, with LAT1 or LAT2 (Okamoto et al. 2002; Ohgaki et al. 2017; Costa et al. 2013). BeWo cells exhibited higher expression levels, but comparable expression changes during differentiation as primary trophoblasts.

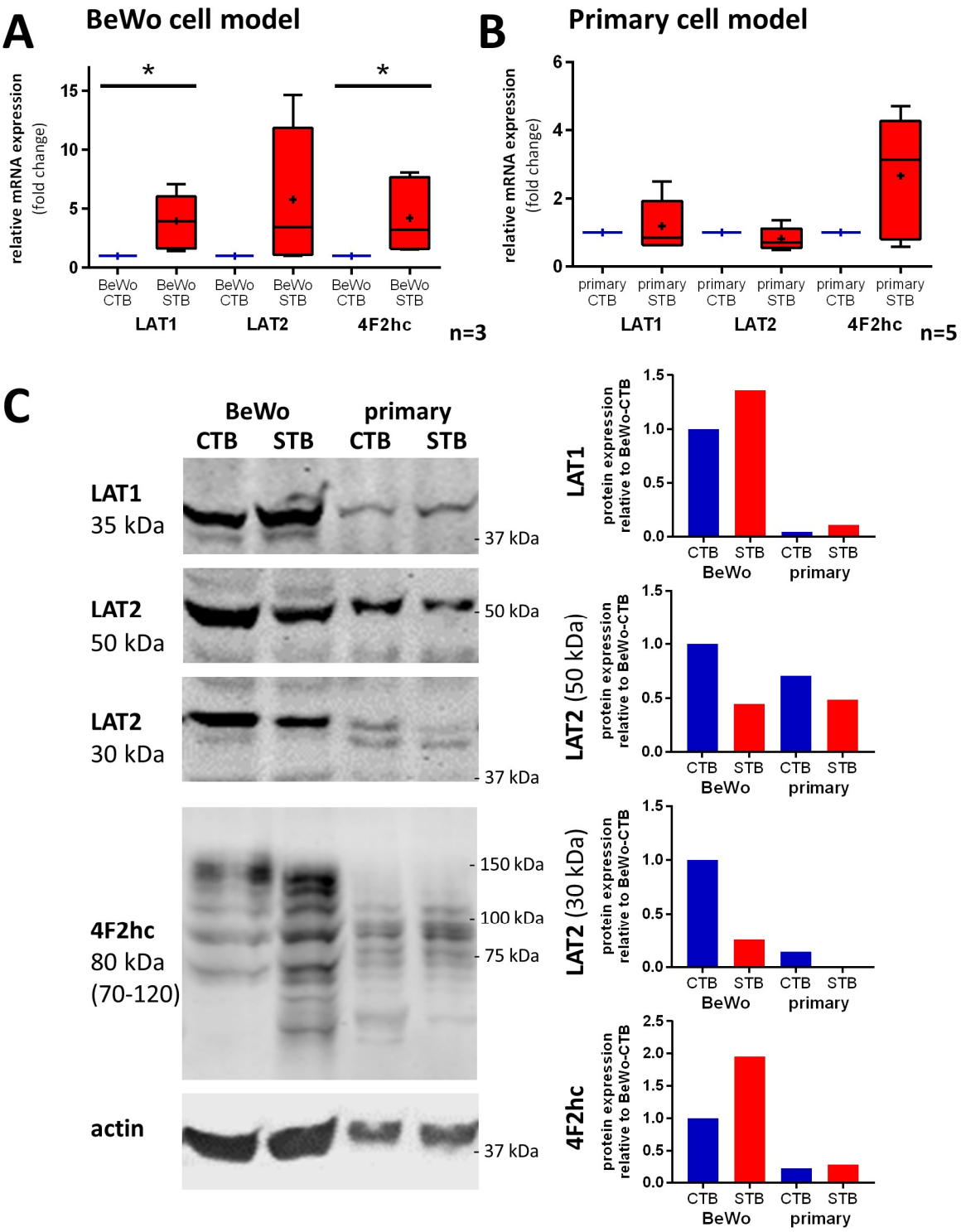

Figure 20: Expression patterns of the placental System L-transporters in primary trophoblasts and BeWo cells depend on their differentiation stage. Comparison of the choriocarcinoma derived BeWo cell line (**A**) and primary trophoblasts (**B**) was performed with respect to LAT1 (*SLC7A5*), LAT2 (*SLV7A8*) and 4F2hc (*SLC3A2*, CD98) mRNA levels at the undifferentiated cytotrophoblast (CTB) and differentiated syncytiotrophoblast (STB) stage. **A**, *LAT1* and *LAT2* transcript levels of primary trophoblasts were not significantly increased in STB as compared to the CTB counterpart (paired T-test), while *4F2hc* was upregulated after cell differentiation. Primary trophoblasts were harvested from 5 individual trophoblast isolations (n=5). They were lysed for mRNA isolation and quantitative RT-qPCR after 12 h at the CTB stage and after 72 h of culturing at the STB stage. **B**, *LAT1* was upregulated, while *LAT2* and *4F2hc* expression in BeWo-

STB cells were not significantly increased relative to their BeWo-CTB control (paired T-test of 3 independent experiments). BeWo-CTB were sampled after 24 h of culturing and BeWo-STB were analyzed after stimulation with 100µM forskolin for 48 h. **A/B**, Expression results were normalized to the mean of the reference genes YWHAZ, GAPDH and β-actin. Transcript data are presented as fold-change ($2^{-\Delta\Delta Ct}$) and plotted as Tukey whiskers (1.5-times IQR) with mean (+), median (-), α=0.05, * p<0.05. **C**, Representative immunoblot (left panel) and densitometric analysis of both cell types revealed increased LAT1 protein expression after cell differentiation (CTB<STB). Generally higher LAT1 protein expression levels were found in the BeWo cell line compared to primary cells (BeWo-CTB/STB>pCTB/STB). The expression of the two LAT2 variants (50 kD; 30 kD) were decreased after trophoblast differentiation in both cell types (primary trophoblasts and BeWo cells). 4F2hc was increased in both primary trophoblasts and BeWo-STB as compared to the corresponding CTB-stage. Densitometric analysis in the right panel was corrected for actin signal.

3.1.3.3 Leucine uptake increases with trophoblast differentiation

We further investigated whether the expression changes caused by trophoblast differentiation resulted also in an increased leucine uptake efficiency in both primary (n=3; **Figure 21A**) and BeWo cells (n=3; **Figure 21B**). Indeed, both spontaneously differentiated primary trophoblasts (pCTB-V_{max}=1.05 nmol/mg protein *versus* pSTB-V_{max}=2.34 nmol/mg protein=2.2-fold) and forskolin-stimulated BeWo cells (BeWo-CTB-V_{max}=4.96 nmol/mg protein *versus* BeWo-STB-V_{max}=13.41 nmol/mg protein=2.7-fold) reached more than 2-times higher maximal uptake levels after 6 min compared to the undifferentiated stage. By comparing maximal leucine uptake levels between BeWo and primary cells, a 4.7-fold greater uptake capacity for the BeWo-CTB and 5.7-fold difference for the BeWo-STB stage was observed. However, the half-maximal leucine uptake time, calculated as Kd from the time course curve fit, for primary cells (pCTB-Kd=1.45 nmol/min; pSTB-hillslope=1.36 nmol/min) and BeWo cells (BeWo-CTB-Kd=1.19 nmol/min; BeWo-STB-Kd=1.42 nmol/min) was similar between the differentiation stages. Thus, in accordance to expressional changes, also on functional level leucine uptake capacity was higher in BeWo cells compared to primary trophoblasts, but the kinetic changes due to cell differentiation were similar in both cell models (**Figure 21**).

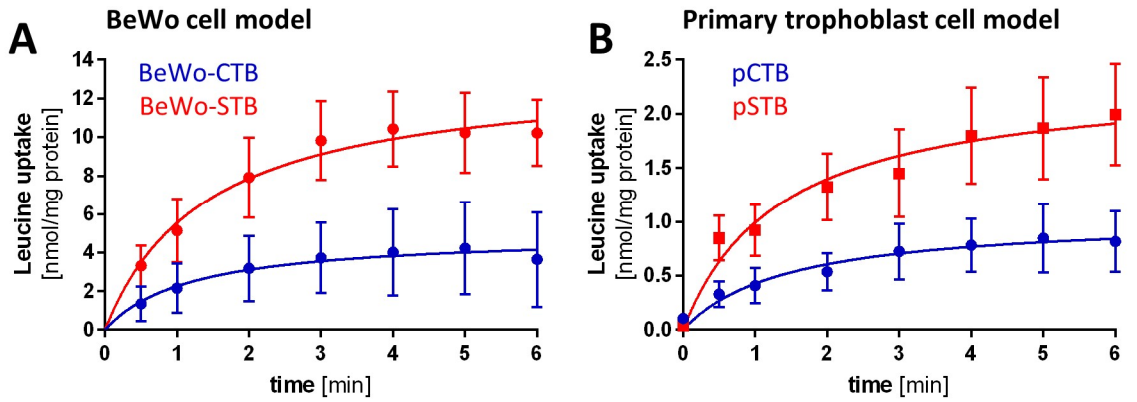

Figure 21: Similar leucine uptake kinetics were detected for primary trophoblast and BeWo cells. **A**, In the BeWo cell model significantly increased Na^+-independent leucine maximal uptake capacity (V_{max}) was found in 3 independent experiments (n=3). Leucine uptake increased from 4.96 nmol/mg protein in BeWo-CTBs to 13.41 nmol/mg protein in BeWo-STBs (2 way-ANOVA, α=0.05; p=0.018). Leucine uptake for BeWo-CTB was performed after 24 h of culturing and for BeWo-STB after stimulation with 100 µM forskolin for 48 h. **B**, Primary trophoblasts isolated from 3 individual control placentae (n=3) significantly increased their V_{max} over 6 min from 1.046 nmol/mg protein in pCTB to 2.345 nmol/mg protein in pSTB stage (2 way-ANOVA, α=0.05; p<0.0001). The maximal leucine uptake capacity (V_{max}) and half-maximal uptake time (Kd) was calculated using a saturation model curve fitting (y = Vmax*X/(Kd + x). The final concentration of leucine in all experiments was 167 nmol/mL including 1 µCi/mL ^{3}[H]-L-leucine for detection. Error bars represent standard deviation (SD) of 3 individual experiments with 6 replicates each.

3.1.4 Small molecule inhibitors reveal relevance of LAT1- and LAT2-mediated amino acid transport

3.1.4.1 Leucine uptake is modulated by System L-specific small molecule inhibitors

Based on the high leucine uptake capacity and the high expression levels of functional LAT1, the BeWo cell model was selected to test different LAT1 or LAT1/LAT2-specific small molecular inhibitors in dose-response experiments. Two new alternative compounds, JG336 and JX009 (**Figure 22B,C**), were investigated and compared in two separate experiments to the already established potent LAT1-specific inhibitor JPH203 (**Figure 22A**). In BeWo-CTB all three inhibitors reached a maximal inhibition of less than 0.8 nmol/mg protein at a concentration of 10 µM (corresponding to the bottom value of a four-parameter nonlinear fit with variable slope; kinetic parameters are listed in the panels on the right). The leucine analog 2-amino-2-norbornane-carboxylic acid (BCH) completely inhibited leucine uptake at a concentration of approx. 1 mM regardless of the differentiation stage (**Figure 22E**). This observation further verifies the relevance of SLC7-mediated leucine uptake in trophoblasts. Although there was profound leucine uptake inhibition in BeWo-CTB, 10 µM of JPH203 and JG336 showed a residual uptake of 3.8

(56.3% inhibition) and 3.2 nmol/mg protein (62.4% inhibition), respectively. JX009 and JX020 (10 µM) blocked leucine uptake regardless of the trophoblast differentiation stage. In BeWo-STB leucine uptake was inhibited by 87% suggesting inhibition of most Na^+-independent SLC7-transporters by JX009 and JX020. While the dose-response experiments with the less specific inhibitors JX009 and JX020 revealed an EC_{50} of 3.9 µM/0.62 µM for BeWo-CTB and 2.3 µM/2.5 µM for BeWo-STB, which is comparable with JPH203 (EC_{50}=3.1 µM for BeWo-CTB and 2.6 µM for BeWo-STB), JG336 was identified as the most efficient inhibitor (EC_{50}=0.8 µM for BeWo-CTB and 2.0 µM for BeWo-STB) in both differentiation stages of BeWo cells. Compared to the dose response curve of BCH, JX009 and JX020 showed both comparable efficiency but >180-times higher potency (**Figure 22C/D**). The new inhibitors JG336 and JX009 as well as JPH203 reached maximal inhibition (first concentration without significant difference to the bottom value) at a concentration of 10 µM, JG336 required 1 µM for maximal inhibition in BeWo-CTB. Of note, comparable inhibition patterns were also found in the colorectal adenocarcinoma cell line HT-29 (**Figure 23**). Lower substrate concentrations (30 µM instead of 167 µM leucine) lead to lower EC_{50} values (**Figure 23** to the right of each curve). The LAT1 overexpressing HT-29 cell line with an uptake dose of 30 µM leucine was previously used as model in structure–activity relationship studies in the NCCR TransCure network. In summary, the dose-response analysis of the three inhibitors suggested that JG336 inhibits LAT1-specific placental leucine transport with similar LAT1-specificity as JPH203, but exhibits an almost 4-times higher efficiency. JX009 represents a potent inhibitor of all active System L-transporters in trophoblasts; JX020 mediated 6-times higher efficiency in BeWo-CTB.

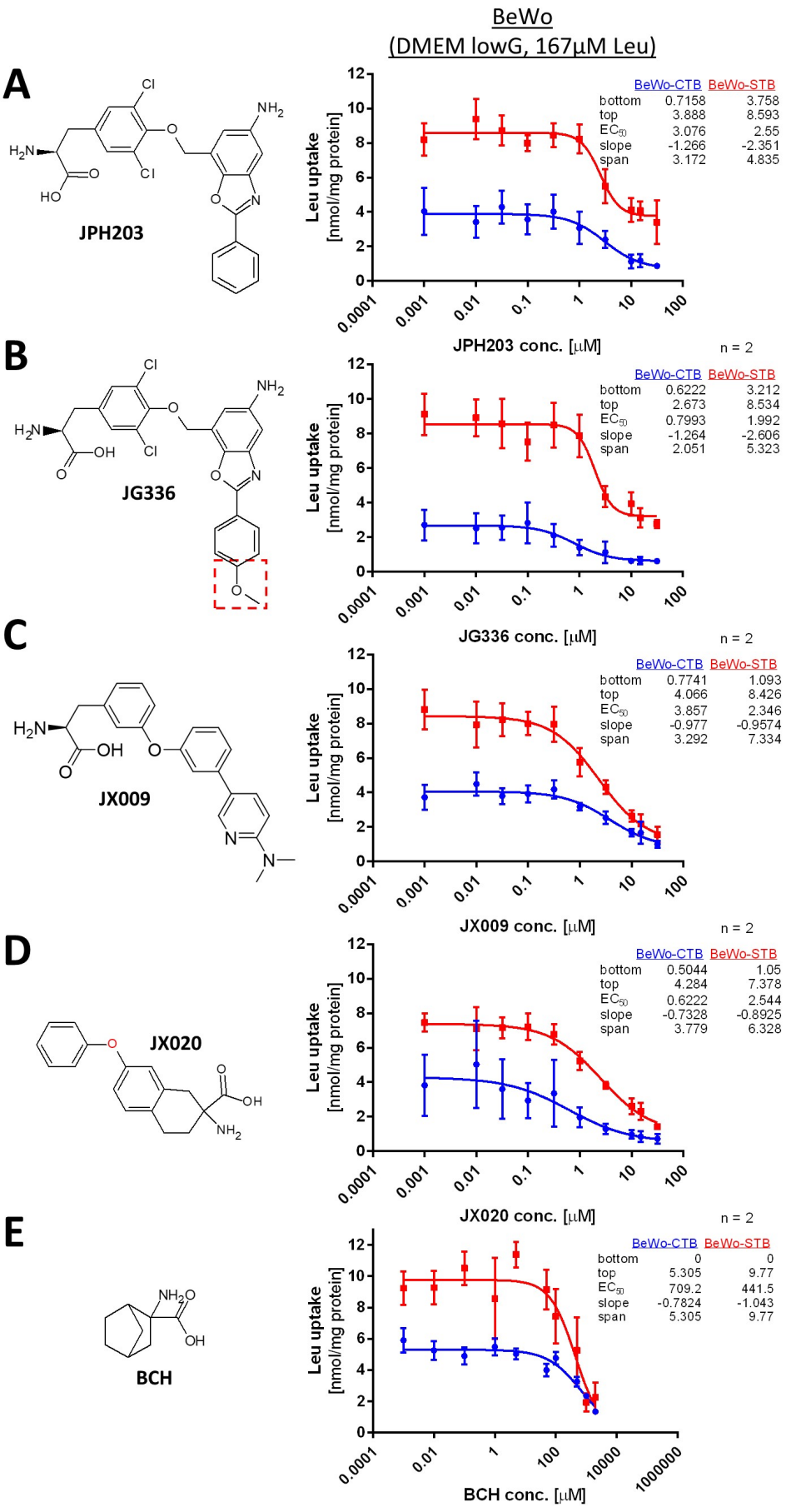
BeWo
(DMEM lowG, 167µM Leu)
A
JPH203
B
JG336
C
JX009
D
JX020
E
BCH
Leu uptake [nmol/mg protein]
JPH203 conc. [µM]
JG336 conc. [µM]
JX009 conc. [µM]
JX020 conc. [µM]
BCH conc. [µM]
n = 2
BeWo-CTB BeWo-STB
bottom 0.7158 3.758
top 3.888 8.593
EC50 3.076 2.55
slope -1.266 -2.351
span 3.172 4.835
bottom 0.6222 3.212
top 2.673 8.534
EC50 0.7993 1.992
slope -1.264 -2.606
span 2.051 5.323
bottom 0.7741 1.093
top 4.066 8.426
EC50 3.857 2.346
slope -0.977 -0.9574
span 3.292 7.334
bottom 0.5044 1.05
top 4.284 7.378
EC50 0.6222 2.544
slope -0.7328 -0.8925
span 3.779 6.328
bottom 0 0
top 5.305 9.77
EC50 709.2 441.5
slope -0.7824 -1.043
span 5.305 9.77

Figure 22: Inhibition of leucine uptake in BeWo cells using small molecule inhibitors with different specificities. Dose-response experiments in BeWo-cytotrophoblasts (BeWo-CTB) and forskolin-stimulated BeWo- syncytiotrophoblasts (BeWo-STB) for the established LAT1-specific inhibitor JPH203 (**A**) and for the alternative compound JG336 which carries an additional methoxy-group as marked in the dashed red box (**B**). The results showed that both compounds conveyed a significant inhibition (JPH203=56%, JG336=62%), but suggest also that approximately 40 % of Na^+-independent leucine uptake is LAT1 independent. **C**, Application of JX009 and JX020, inhibitors of both LAT1 and LAT2, resulted in almost complete leucine uptake inhibition in BeWo-STB; JX020 exhibited a higher efficiency in BeWo-CTB. Compared to the dose response performance of the leucine analog 2-amino-2-norbornane-carboxylic acid (BCH, **E**), JX009 shows comparable efficiency but >180-times higher potency. BCH is a widely accepted inhibitor blocking all System L transport. BCH completely blocked leucine uptake in BeWo-CTB with an EC_{50} of 709 µM and BeWo-STB with an EC_{50} of 442 µM (**D**). **A**-**D**, The new inhibitors JG336, JX020 and JX009 as well as JPH203 reached maximal inhibition (first concentration without significant difference to the bottom value) at a concentration of 10 µM, JG336 required 1 µM for maximal inhibition in BeWo-CTB. BCH reached maximal inhibition with 1 mM in both differentiation stages. **A**-**E** All uptake assays were performed in two individual experimental setups (n=2) for 3 min, under the same conditions in Na^+-free Hanks buffer with 167.2 µM leucine (1 µCi/mL ^{3}H-L-leucine). The chemical structures of the small molecule compounds are depicted to the left of each dose-respond curve. Dose-response kinetics were calculated using the nonlinear four-parameter model [Y=Bottom+(Top-Bottom)/ (1+10^((LogEC$_{50}$-X)*HillSlope))] and ordinary fit with GraphPad Prism software. Best-fit values of the including EC_{50} values are shown to the right of the dose-response curve. Error bars represent standard deviation (SD) of 2 experiments with 6 replicates each.

3.1.4.2 Transfer of leucine across the placental barrier is reduced by inhibitors of System L-transporters

The small molecule inhibitors JPH203, JG336, JX009 and JX020 were also used to assess the relevance of LAT1 and LAT2 in leucine transport across the placental barrier using the Transwell® system (**Figure 24**). Leucine transfer experiments were performed in the presence or absence of the individual inhibitors with a fixed concentration of 10 µM applied at the upper compartment. This concentration was chosen as it showed in dose-response experiments maximal inhibition for all three compounds (see **Figure 22**). **Figure 24B** shows the experimental setup and the applied leucine concentrations in the upper compartment (corresponding to the maternal side of the placental barrier) and the lower chamber (corresponding to the fetal side) of the Transwell® system. Gradually diminishing radioactive signal ^{3}[H]-leucine on the maternal side and increasing radioactivity on the fetal side was considered to represent leucine transfer across the trophoblast monolayer. Treatment with JPH203, JG336, JX009 and JX020 at the apical (maternal) side caused significant reduction of leucine transfer by 58%, 60%, 55% and48, respectively. All inhibitors significantly decreased leucine transfer from the apical towards the basal compartment from 60 min onwards. Measurement of intracellular ^{3}[H]-leucine content in

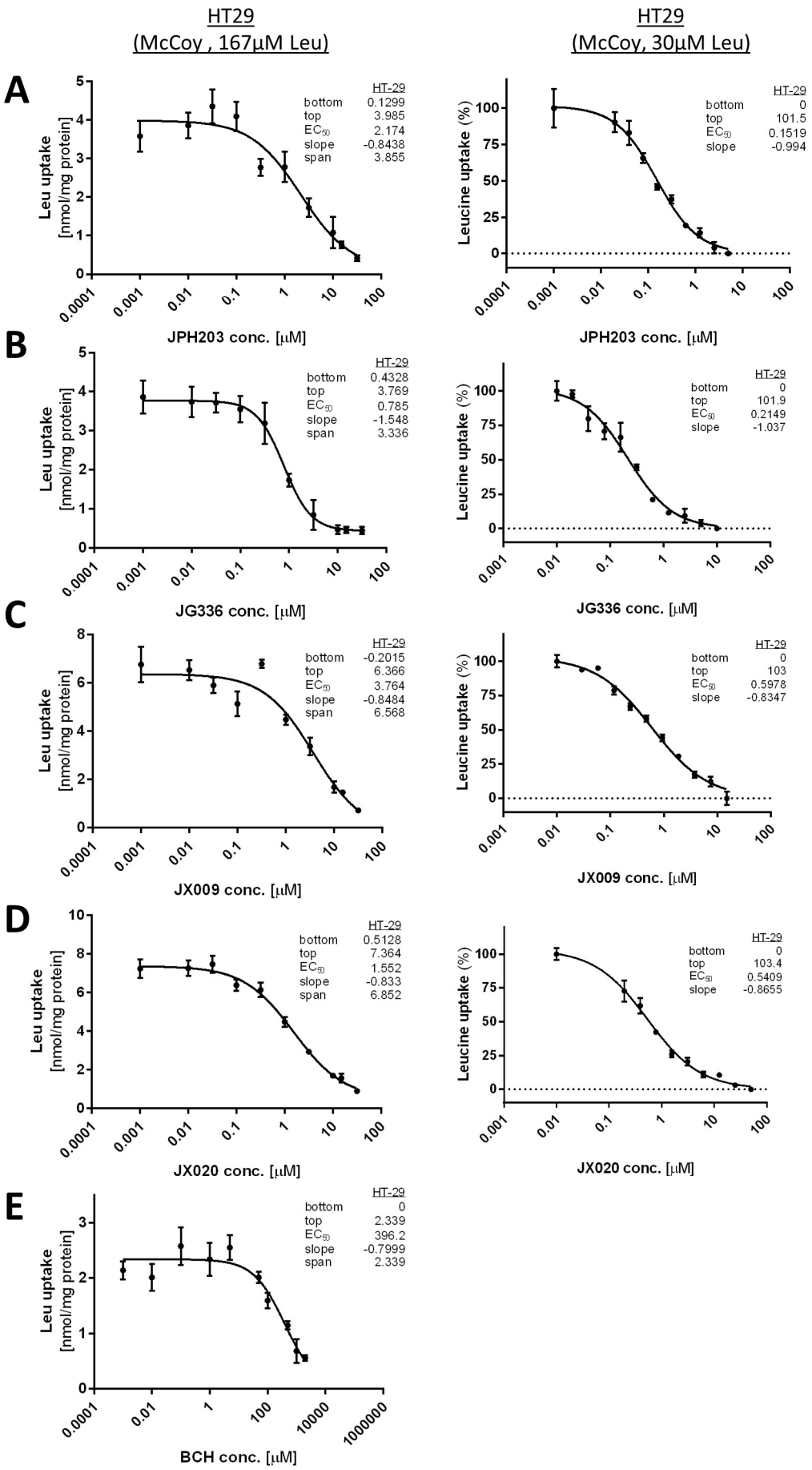
HT29
(McCoy , 167µM Leu)
HT29
(McCoy, 30µM Leu)
A
Leu uptake [nmol/mg protein]
HT-29
bottom 0.1299
top 3.985
EC50 2.174
slope -0.8438
span 3.855
JPH203 conc. [µM]
Leucine uptake (%)
HT-29
bottom 0
top 101.5
EC50 0.1519
slope -0.994
JPH203 conc. [µM]
B
Leu uptake [nmol/mg protein]
HT-29
bottom 0.4328
top 3.769
EC50 0.785
slope -1.548
span 3.336
JG336 conc. [µM]
Leucine uptake (%)
HT-29
bottom 0
top 101.9
EC50 0.2149
slope -1.037
JG336 conc. [µM]
C
Leu uptake [nmol/mg protein]
HT-29
bottom -0.2015
top 6.366
EC50 3.764
slope -0.8484
span 6.568
JX009 conc. [µM]
Leucine uptake (%)
HT-29
bottom 0
top 103
EC50 0.5978
slope -0.8347
JX009 conc. [µM]
D
Leu uptake [nmol/mg protein]
HT-29
bottom 0.5128
top 7.364
EC50 1.552
slope -0.833
span 6.852
JX020 conc. [µM]
Leucine uptake (%)
HT-29
bottom 0
top 103.4
EC50 0.5409
slope -0.8655
JX020 conc. [µM]
E
Leu uptake [nmol/mg protein]
HT-29
bottom 0
top 2.339
EC50 396.2
slope -0.7999
span 2.339
BCH conc. [µM]

Figure 23: Leucine uptake inhibition and substrate-dependence of EC_{50} values in HT-29 cells using SLC7- inhibitors. Dose-response experiments for leucine uptake inhibition in the colorectal adenocarcinoma cell line HT-29 were performed in Na^+-free Hanks buffer with 167 µM leucine and 1 µCi/mL ^{3}H-L-leucine (left panels **A**, **B** and **C**) and in Na^+-free Hanks buffer with 30 µM leucine and 1 µCi/mL ^{3}H-L-leucine (right panels **A**, **B** and **C**). HT-29 cells and a substrate concentration of 30µM L-leucine were used to compare EC_{50} values in structure–activity relationship studies as performed in the NCCR TransCure network. Dose-response experiments demonstrated complete leucine uptake inhibition with JPH203 (**A** left panel, EC_{50} 2.17 µM) and the three novel SLC7-targeting inhibitors JG336 (**B** left panel, EC_{50} 0.73 µM), JX009 (**C** left panel, EC_{50} 3.76 µM) and JX020 (**D** left panel, EC_{50} 1.55 µM) under physiological 167 µM leucine concentrations. JG336 was the most efficient inhibitor being 2.6-times more efficient than the LAT1-specific inhibitor JPH203. All tested inhibitors show markedly lower EC_{50} values at the lower substrate concentration of 30 µM, i.e. for JPH203 (**A** right panel) EC_{50}=0.15 µM, JG336 (**B** right panel), EC_{50}=0.21 µM and JX009 (**C** right panel), EC_{50}=0.60 µM. The leucine uptake experiments were performed during 3 min in Na^+-free Hanks buffer with 167 µM leucine (1 µCi/mL ^{3}H-L-leucine) and are shown as representative experiments of two independent experiments (n=2). Dose-response kinetics were calculated using same statistical tools as explained in Figure 22. EC_{50} values are shown to the right of the dose-response curve. Error bars represent standard deviation (SD) of 2 experiments with 6 replicates each.

the trophoblast cell layer at the end of the transfer experiment (6 h) indicated significantly decreased intracellular leucine concentrations of 24% for JPH203, 41% for JG336 and 35% for JX020, respectively (**Figure 24C**). In contrast, JX009 had no effect on the intracellular ^{3}[H]-leucine concentration within the tested time course. The higher retention of leucine in JX009 treated cells suggests inhibition of leucine secretion likely towards the lower fetal compartment.

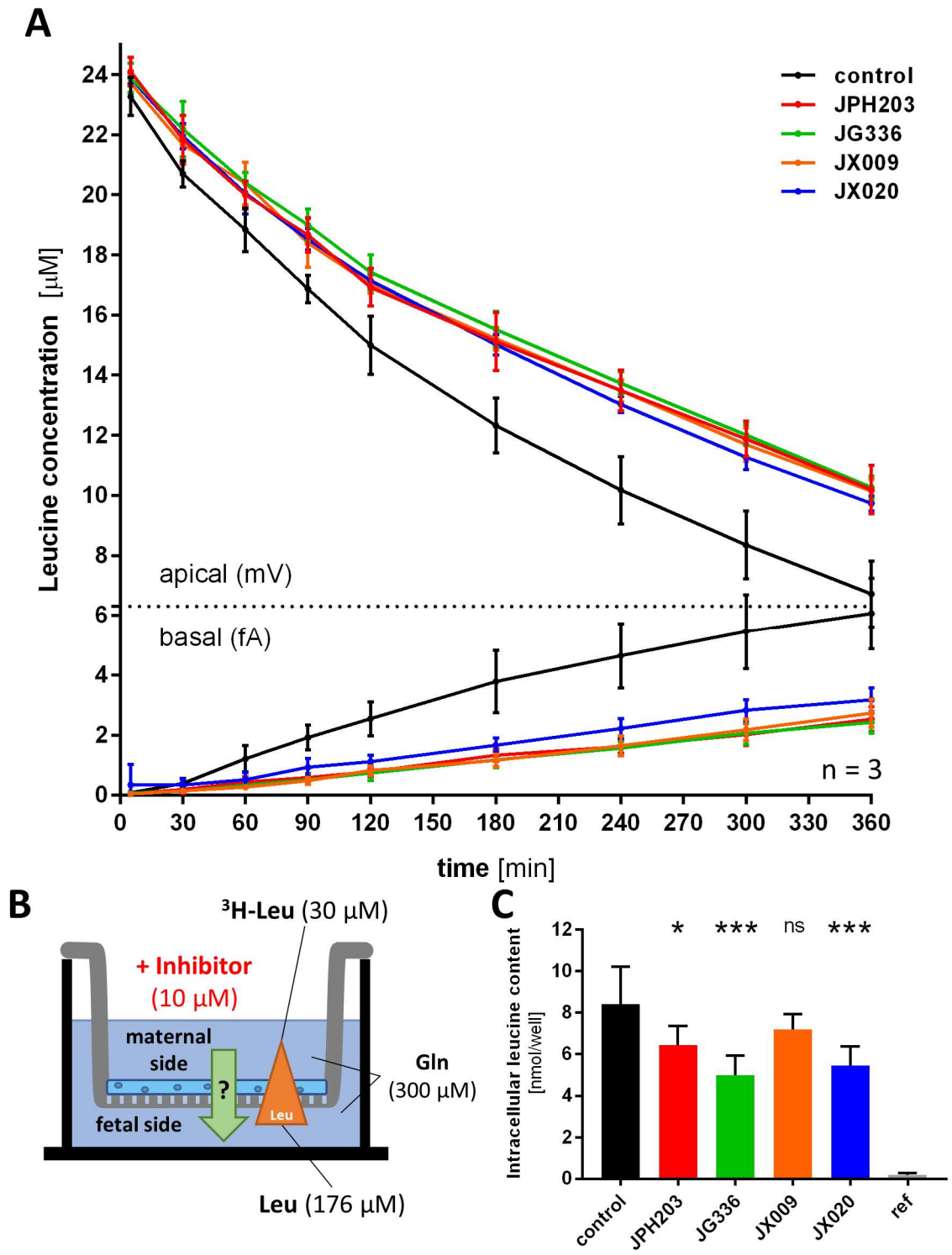

Figure 24: Relevance of LAT1- and System L-inhibition in leucine transfer across the placental barrier *in vitro*. A, Leucine (Leu) transfer across a tight BeWo monolayer was measured from the apical (i.e. upper compartment) towards the basal side (i.e. lower compartment) during 6 h using the Transwell® system. Leu transfer was significantly reduced by the System L inhibitor JX009 (orange) and JX020 (blue), and the LAT1-specific inhibitors JPH203 (red) and JG336 (green) compared to the DMSO-control (black) already after 1 h. Equal concentrations (10 µM) of each inhibitor and DMSO as vehicle control were applied in three experiments (n=3) with two replicates per condition. **B**, The experimental setup represented as schematic illustration. All Leu transfer assays were performed against a counter-directed gradient of 137 µM (30→167 µM) Leu, in the presence of 300 µM glutamine (Gln) in both compartments. The Leu in the upper compartment

was spiked with 1 µCi/mL ^{3}H-L-leucine for transfer quantification. **C**, The intracellular leucine content was measured after washing the cell layers with DPBS at the end of the experiment (after 6 h). A significant reduction of intracellular Leu contents was detected for JPH203 (p=0.017), JG336 (p=0.0001) and JX020 (p=0.0003), but not for the System L-inhibitor JX009 (p=0.215). The detected intracellular leucine retention caused through LAT1 and LAT2 inhibition by JX009 suggests a System L-dependent Leu efflux across the BM as rate limiting step. Statistical analyses were performed in three individual experiments (n=3) using a parametric one-way ANOVA analysis (α=0.05).

3.2 Iron transport

3.2.1 Influence of GDM on transplacental iron transport

3.2.1.1 GDM affects clinical parameters of newborns and iron homeostasis genes

To investigate the impact of GDM on placental iron homeostasis, we collected placental tissue from 11 diagnosed GDM and 11 healthy pregnancies according to the criteria of the ADA (American Diabetes Association 2007). As shown in **Table 10** the mothers with GDM exhibited under comparable demographic characteristics significantly increased BMI before pregnancy and increased hemoglobin values at the day of delivery. Increased hemoglobin levels were detected in maternal sera, but no changes in the fetal iron status was documented. Upon exclusion of unequal gender distribution, the corresponding offspring of GDM pregnancies are born LGA as demonstrated by increased weight and body length of the newborns (**Table 10**).

The RT-qPCR screening of 24 placental iron homeostasis genes (# marked primer pairs in **Table 6**) in the two cohorts revealed significant downregulation of the iron-transporters *DMT1* and *FPN1*, upregulation of the ferroxidases *HEPH* and *Zp*, and of the iron-entry regulator *HEPC* in GDM (**Table 11**; **Figure 25**).

Table 10: Anthropometric and clinical characteristics of gestational diabetes mellitus (GDM) and control patients including their offspring

	Characteristics	control	GDM	p value	
	Number of individuals	11	11		
	Delivery mode	Cesarean section	Cesarean section		
	Age (years)	30.91 ± 5.43	31.91 ± 7.66	0.7276	
	BMI (pre-conceptional)	23.14 ± 3.92	29.53 ± 5.16	0.0038	**
	Parity	2.36 ± 0.67	2.09 ± 0.83	0.4080	
	Gestational age at *partum*	39.00 ± 0.60	39.06 ± 1.29	0.8814	
Mother	Glucose (mmol/l)	4.92 ± 0.74	5.25 ± 1.51	0.5190	
Mother	Treatment	-	8 insulin/3 diabetes diet		
Mother	Creatinine (µmol/l)	46.82 ± 7.90	51.09 ± 10.67	0.2985	
Mother	RBC (T/l)	3.86 ± 0.35	4.10 ± 0.34	0.1201	
Mother	Hemoglobin (g/l)	115.27 ± 6.96	124.82 ± 10.90	0.0237	*
Mother	MCV (fl)	88.64 ± 5.61	88.36 ± 3.96	0.8965	
Mother	MCH (pg)	30.00 ± 2.14	30.55 ± 2.07	0.5505	
Mother	MCHC (g/l)	337.82 ± 3.76	344.18 ± 9.45	0.0512	
Mother	Hematocrit (%)	0.34 ± 0.02	0.36 ± 0.03	0.0640	
Baby	Weight (g)	3182 ± 242	3787 ± 419	0.0005	***
Baby	Length (cm)	48.4 ± 1.8	50.6 ± 2.0	0.0095	**
Baby	Sex of baby	5♂, 6♀	5♂, 6♀		

Data are represented as mean ± standard deviation (SD). Differences between GDM and the control group were analyzed by two-way Student's T-test; α=0.05, * p<0.05, ** p<0.01, *** p<0.001. Abbreviations: BMI, body mass index; MCH, mean corpuscular hemoglobin; MCHC, mean corpuscular hemoglobin concentration; MCV, mean corpuscular volume; PCV, packed cell volume; RBC, Red Blood Cells.

Table 11: Expression analysis of iron homeostasis genes in placentae from GDM patients and controls

Accession No.	Protein	Name	p value	
Iron endocytosis				
P02787	Tf	Serotransferrin	0.6047	
P02786	TfR1	Transferrin receptor protein 1	0.9725	
Q07954	LRP1	Lipoprotein receptor-related protein 1	0.3494	
Q6ZMJ2	SCARA5	Scavenger receptor class A member 5	0.6539	
Iron transmembrane transporters				
P49281	DMT1	Divalent metal transporter 1	0.0139	* ↓
Q9C0K1	Zip8	Zrt- and Irt-like protein 8	0.7564	
Q15043	Zip14	Zrt- and Irt-like protein 14	0.1545	
Q9NP59	FPN1	Ferroportin-1	0.0032	** ↓
Q9NYZ2	MFRN1	Mitoferrin-1	0.8633	
Q9Y5Y0	FLVCR1	Feline leuk. virus subg. C receptor 1	0.5516	
Q9UPI3	FLVCR2	Feline leuk. virus subg. C receptor 2	0.8238	
Q96NT5	HCP1	Heme carrier protein 1	0.2230	
Q6P1K1	HRG1	Heme transporter HRG1	0.1971	
Fe-storage				
P02794	FHC	Ferritin heavy chain	0.2816	
Oxidoreductases				
P00450	CP	Ceruloplasmin	0.3144	
Q9BQS7	HEPH	Hephaestin	0.0242	* ↑
Q6MZM0	Zp	Zyklopen	0.0201	* ↑
P09601	HO1	Heme oxygenase 1	0.6539	
P30519	HO2	Heme oxygenase 2	0.1517	
Q658P3	STEAP3	Metalloreductase STEAP3	0.4679	
Regulators				
P81172	HEPC	Hepcidin	0.0242	* ↑
Q30201	HFE	Hereditary hemochromatosis protein	0.2512	
Iron sensing, mRNA binding				
P21399	IRP1	Iron regulatory protein 1	0.0251	* ↓
P48200	IRP2	Iron regulatory protein 2	0.5116	

Quantitative RT-PCR analysis of placental tissues from GDM (n=11) and control (n=11) patients was performed in two independent experiments and normalized to the mean of the reference genes 14-3-3 protein zeta/delta (*YWHAZ*), *GAPDH* and ubiquitin (*UBC*). The results of the comparison between GDM and controls are represented by target-specific p-values and arrows displaying up- (↑) or downregulation (↓) in GDM. Statistical significance was determined using two-tailed Mann-Whitney test; α=0.05, * p<0.05, ** p<0.01, *** p<0.001. Genes were selected upon proven placental expression in literature or according to data from protein atlas (www.proteinatlas.org).

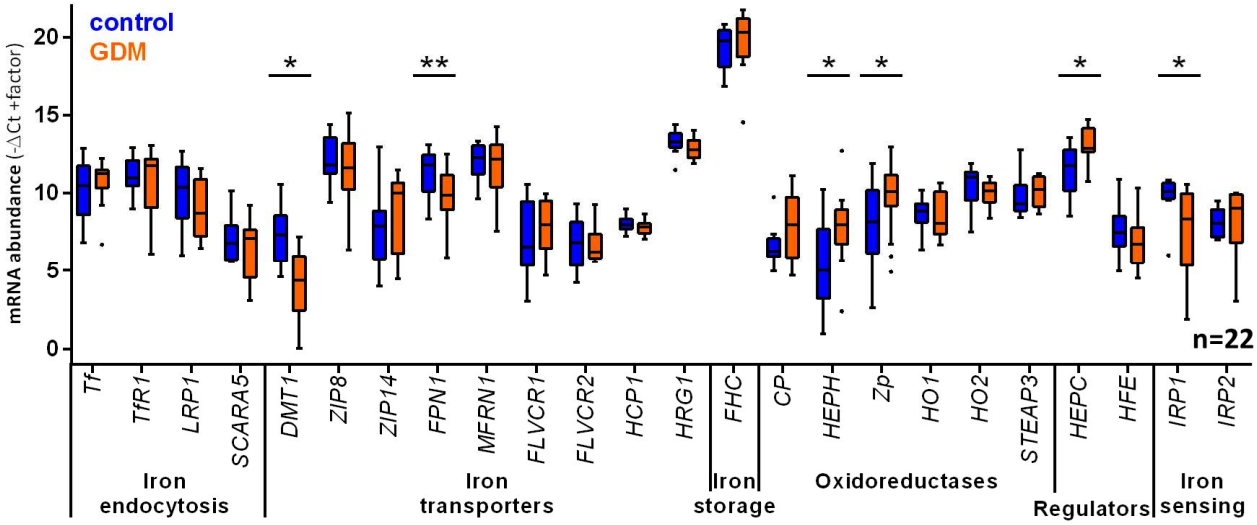

Figure 25: Expression changes iron homeostasis genes in placental tissue affected by gestational diabetes mellitus (GDM) on mRNA level. Transcript levels of Divalent metal transporter 1 (*DMT1*), Zrt- and Irt-like protein 8 (*ZIP8*), Ferroportin-1 (*FPN1*) and Transferrin receptor protein 1 (*TfR1*) were analyzed in placental tissues of GDM patients (orange) and term controls (blue). Expression results were determined in two independent experiments and normalized to the mean of the reference genes Tyrosine 3-monooxygenase/tryptophan 5-monooxygenase activation protein, zeta polypeptide (*YWHAZ*), Glyceraldehyde-3-phosphate dehydrogenase (*GAPDH*) and ubiquitin (*UBC*). Comparative transcript data are presented as mRNA abundance ($\Delta Ct = Ct_{reference\ gene} - Ct_{target\ gene}$) from placental tissues from GDM (n=11) and control (n=11) patients using the mean of the 3 reference genes *YWHAZ*, *GAPDH* and *UBQ*). Statistical significance was determined as described in Table 10 using two-tailed Mann-Whitney test, $\alpha=0.05$, * $p<0.05$, ** $p<0.01$, *** $p<0.001$. Data are presented as mean (x), median (-) and Tukey whiskers (1.5 times the IQR).

We analyzed the difference between male and female placentae for all 24 iron homeostasis genes. Since the data did not pass the normality tests, the nonparametric multiple T-test was used for statistical evaluation. There were no significant gender differences between male and female placentae within all 22 placentae (10♂ and 12♀) that would explain the detected difference between control and GDM for any of the 24 genes (**Figure 26A**). There were no significant gender differences for any of the 24 analyzed iron homeostasis genes using a nonparametric Mann-Whitney test. Of note, there were significant differences in the male-female comparison within the control cohort for Zp on mRNA and TfR1 on protein levels (**Figure 26B/C**).

A

	♂ vs. ♀	
	p values	
Gene#	**mRNA**	**protein**
DMT1	0.8336	>0.9999
Zip8	0.6770	0.6005
CP	0.4929	
HEPH	0.2614	
Zp (HEPHL1)	0.1493	
TfR	0.2441	0.1264
FPN1	0.4445	0.6005
Zip14	0.1545	
Mitoferrin	0.8030	
FTH	0.7833	
HAMP	0.2954	
IREB1	0.4552	
IREB2	0.6216	
FLVCR1	0.8171	
FLVCR2	0.7821	
LRP1	0.4974	
SCARA5	0.1681	
HMOX1	0.2811	
HMOX2	0.2276	
HCP1	0.6849	
HRG1	0.9296	
Tf	0.6217	
Hfe	0.2923	
Steap3	0.4294	
SLC19A1	0.7012	
SLC19A2	0.4629	
SLC19A3	0.0659	

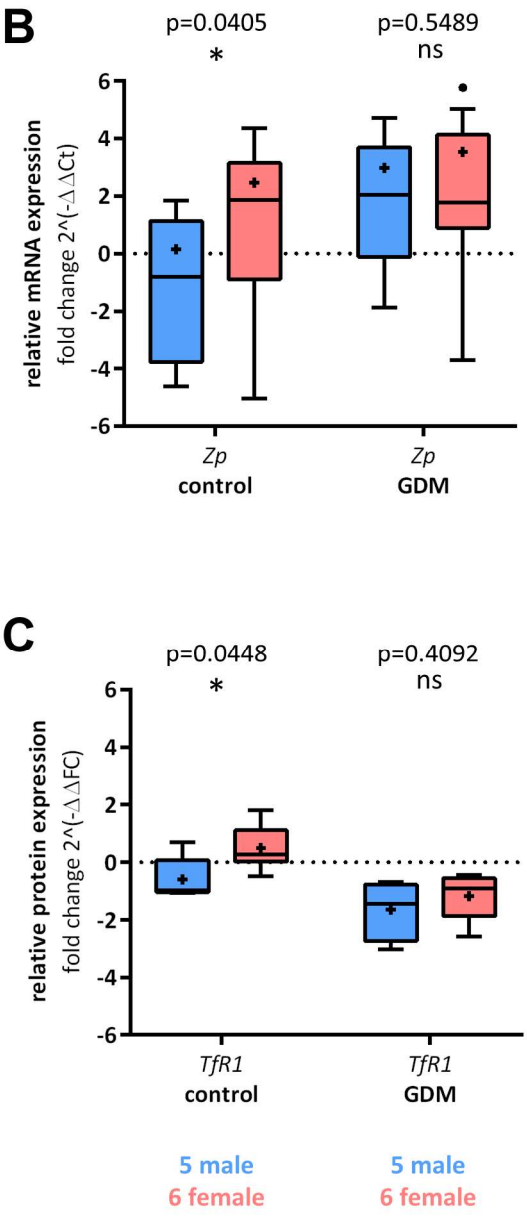

Figure 26: Analysis of sex dimorphism of iron homeostasis genes expression in placentae from gestational diabetes mellitus (GDM) patients and controls. List of p values from 10 male and 12 female placentae on mRNA (**A**, middle column) and protein data comparison (**A**, right column) by nonparametric Mann-Whitney test, α=0.05. Differential analysis of sex dimorphism separated in control and GDM for the ferroxidase zyklopen (Zp, *HEPHL1*) on mRNA (**B**) and for Transferrin receptor (*TfR1*) on protein level (**C**). **A**-**C** mRNA levels from male and female placentae of each gene was statistically compared using nonparametric Mann-Whitney test. # names of measured placental iron homeostasis genes.

For the quantification on protein level the target genes TfR1 as sensitive indicator of changes in placental iron homeostasis and the three iron transporters DMT1, ZIP8 and FPN1 were selected. Since it was not possible to quantify the three iron-transporters by LC-MS/MS analysis in placental tissue lysates, we reduced the sample complexity by

isolating membrane proteins (TMI assay) for all 22 placentae. In collaboration with the FGCZ, we developed a method for LC-MS/MS-based protein quantification in TMI samples (see 2.2.2 on p.36 until 2.2.4 on p. 41ff). **Figure 27** shows the results of all selected proteins (as defined in **Table 3** on p.36) as raw values and after normalization with GAPDH allowing the comparison between GDM and control TMI samples.

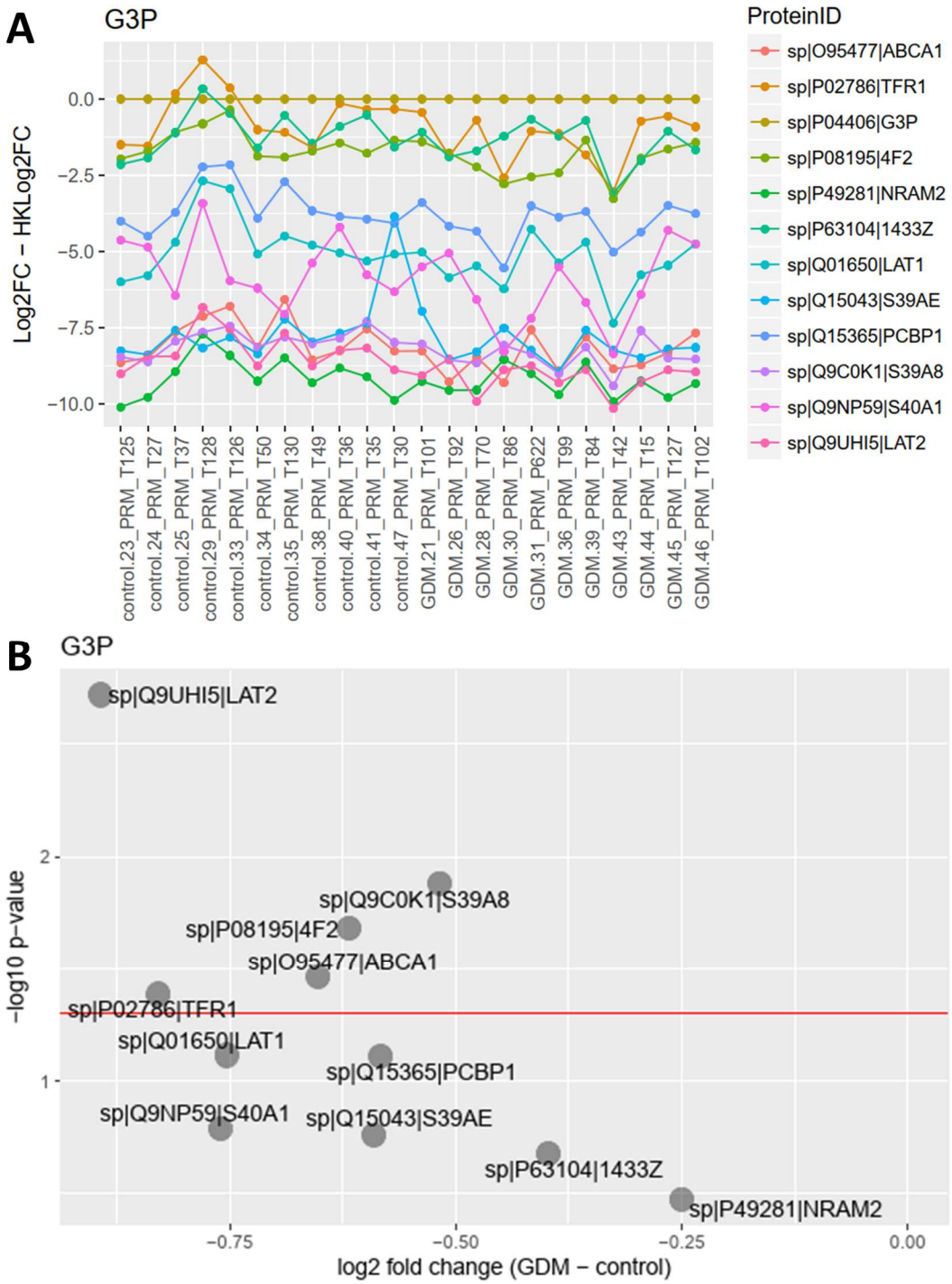

Figure 27: Placental membrane protein quantification in total membrane isolation (TMI) samples by mass spectrometry provided by the specialists from the Functional Genomics Center Zurich (FGCZ). The relative protein levels of 11 control and 11 GDM samples were normalized to GAPDH (G3P, dark gold color). Statistical significance determined by parametric t-test using the

Holm-Sidak method, α=0.05. Panel **A** is showing the protein level in a line plot for all individual samples in the x-axis and the relative protein levels as logarithmic 2-fold change in the y-axis. Panel **B** depicts the results of the comparison between the GDM *versus* control group as volcano plot. Here the mean logarithmic 2-fold changes are presented in x-axis and the p-values in y-axis. The red line indicates α=0.05 (-log10(α)= 1.3010). Therefore, all values above the red line were significantly different in GDM relative to the control group. In summary, ZIP8 (S39A8), 4F2hc (4F2), ABCA1, TfR1 (TFR1) and LAT2 were significantly (above red line) downregulated (negative log2 fold change) in GDM total membrane samples.

The MS/MS-based PRM quantification and the comparison of protein level in GDM and healthy control revealed a GDM-specific downregulation of the iron transporter ZIP8 and holo-Tf binding receptor TfR1, while the downregulation of *DMT1* and *FPN1* on mRNA level could not be confirmed in the proteomic approach (**Figure 28**).

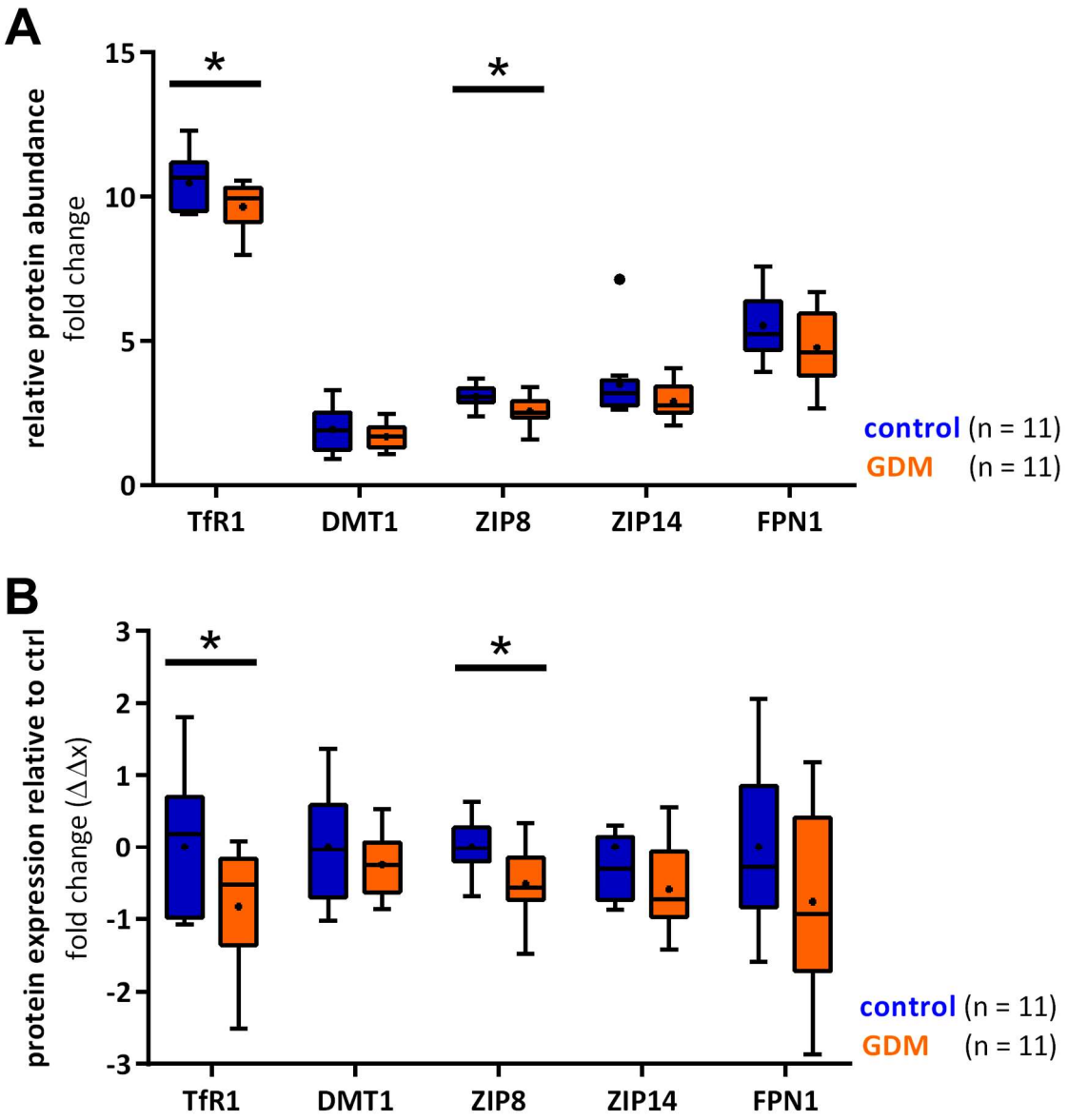

Figure 28 Expression changes of selected iron homeostasis genes in placental tissue from gestational diabetes mellitus (GDM) patients and controls on protein level. Altered expression

of iron homeostasis genes critical for transplacental iron transport, which were regulated in GDM either on mRNA Table 11 or protein level. Results of LC-MS/MS-based protein quantification in total membrane isolations of placental tissues from the same patient cohort and for the same targets as presented in **Figure 25**. Protein levels were calculated as fold changes relative to spiked peptides and subsequently relative to the reference gene GAPDH. **A**, protein data of 11 control and 11 GDM samples are comparatively presented as protein abundance fold changes relative to spiked peptides of target gene and normalized to GAPDH (abundance = reference gene – target gene). **B**, for easier comparison between GDM and control the same data are presented as delta-delta FC values (ΔΔFC = fold changes (FC) relative to spiked peptides of target gene – FC relative to spiked peptides of GAPDH) and normalized to the mean of controls. Statistical significance was determined by two-tailed Student's T-test, α=0.05.

3.2.1.2 GDM-specific changes in placental DMT1 localization

To follow up the discrepancy of significantly decreased *DMT1* mRNA levels, but unchanged protein levels, blind semi-quantitative immunohistochemical analysis for DMT1 and FPN1 was performed in 22 placental tissues (**Figure 29**). Placental tissue samples from central localization (close to umbilical cord attachment) were stained for DMT1 and FPN1 and semi-quantitatively analyzed by an experienced external collaborator in a blinded trial (**Figure 29C**). The intense STB-specific staining mediated by the anti-FPN1 antibody was restricted to basal/basolateral structures and did not show any differences between GDM and control (χ^2 (2) =3.21, p=0.201, α<0.05). In contrary, the apically accentuated expression pattern of DMT1 in control was significantly shifted towards the cytoplasm of the STB in GDM (χ^2 (2) =7.62, p=0.022, α<0.05).

3.2.1.3 Unchanged iron levels in placental tissue from GDM pregnancies

Based on the results showing GDM-specific downregulation and changes of expression patterns of iron transporters and the iron receptor TfR1, we measured and compared iron contents between GDM and control placentae. Although decreased iron levels were expected, the total iron contents measured by colorimetric ferrozine-based assay were similar between control and GDM placentae (**Figure 30**).

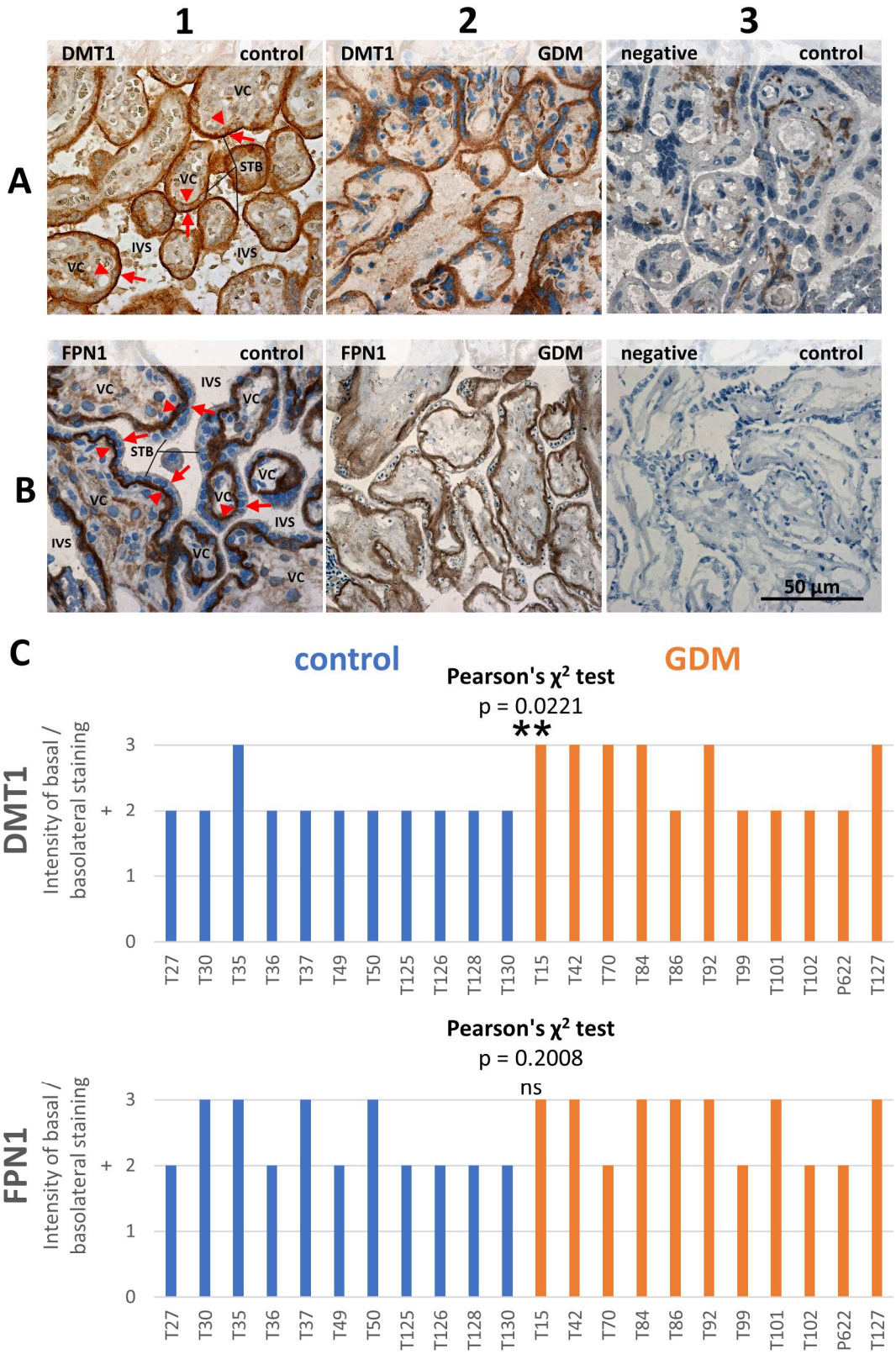

Figure 29: Effect of gestational diabetes mellitus (GDM) on the expression pattern of Divalent metal transporter 1 (DMT1, *SLC11A2*) and Ferroportin (FPN1, *SLC40A1*) in human term placenta detected by immunohistochemistry. A, In control tissues DMT1 was expressed exclusively in syncytiotrophoblasts (STB) and apically accentuated (**A1**), while GDM-tissue showed predominantly intracellular DMT1 expression (**A2**). FPN1 antibody-mediated staining was restricted to basal/basolateral structures of STB in both control (**B1**) and GDM tissues (**B2**). Negative controls are shown in the right panels (**A3**/**B3**). Arrows indicate the apical, i.e. maternal

blood-oriented side, arrowheads depict the basal membrane of the syncytiotrophoblasts. All images are displayed at 40 x magnification as indicated by the scale bar in B3. Abbreviations: IVS, intervillous space; STB, syncytiotrophoblast; VC, villous core. **C**, Results of the semi-quantitatively analysis of 22 placental tissues in a blinded trial performed by PD Dr. med. Meike Körner, an experienced external collaborator, and statistically assessed using Pearson's χ^2 test, $\alpha<0.05$.

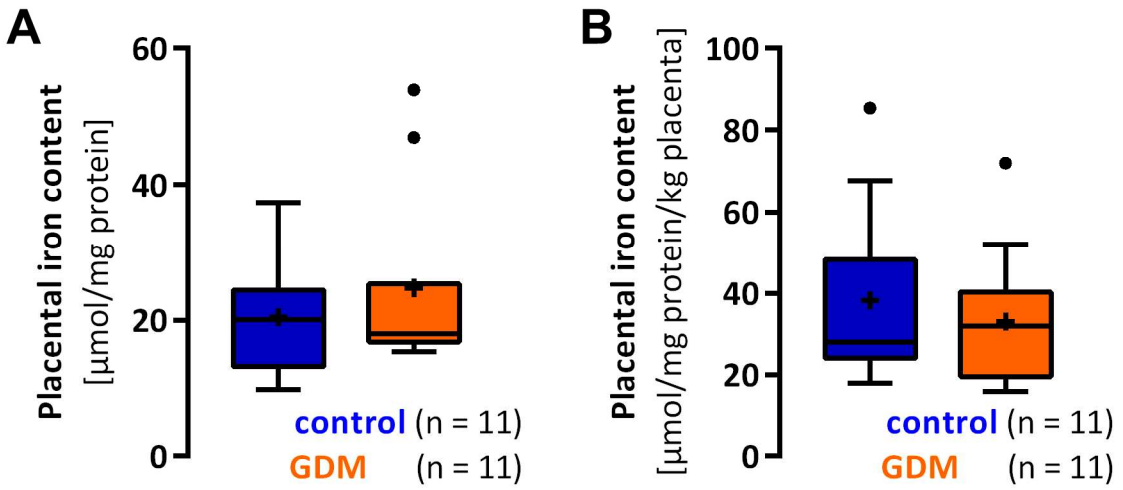

Figure 30: Placental iron content is not affected in gestational diabetes mellitus (GDM). Total iron contents in 22 placental tissue were measured by colorimetric ferrozine-based assay and normalized to the total protein concentration (**A**) and additionally to the placental weight (**B**). Iron content did not differ between control and GDM placentae. (**A/B**) Iron contents were compared using an unpaired T test, α = 0.05, and are presented as mean (+), median (-) and Tukey whiskers (1.5-times interquartile range).

3.2.2 Establishment of an *in vitro* trophoblast cell model to study hyperglycemic iron homeostasis

After adaption of conventionally cultured BeWo cells to physiological glucose concentration in the culture media for 28 passages as explained in 2.4, we investigated the effects of hyperglycemic and hyperlipidemic conditions mimicking the environment of trophoblasts during GDM with different grades of severity (as shown in **Figure 31**) during more than 30 days. Beside visualization of morphological changes, also the adaption of iron homeostasis gene expression was analyzed and compared to GDM-specific expression patterns.

3.2.2.1 BeWo cells alter cell morphology under hyperglycemic conditions

From the first week of culturing onwards the BeWo cells under hyperglycemic (**H**) and hyperglycemic/hyperlipidemic conditions (**HL**) divided faster than under normoglycemic control conditions (**N**). During 30 days of culturing the cells adapted their morphology to

the increased availability of glucose in **H** by increasing nuclei and vacuoles size respectively glucose and fatty acids in **HL** additionally extensive intracellular lipid store (**Figure 31**).

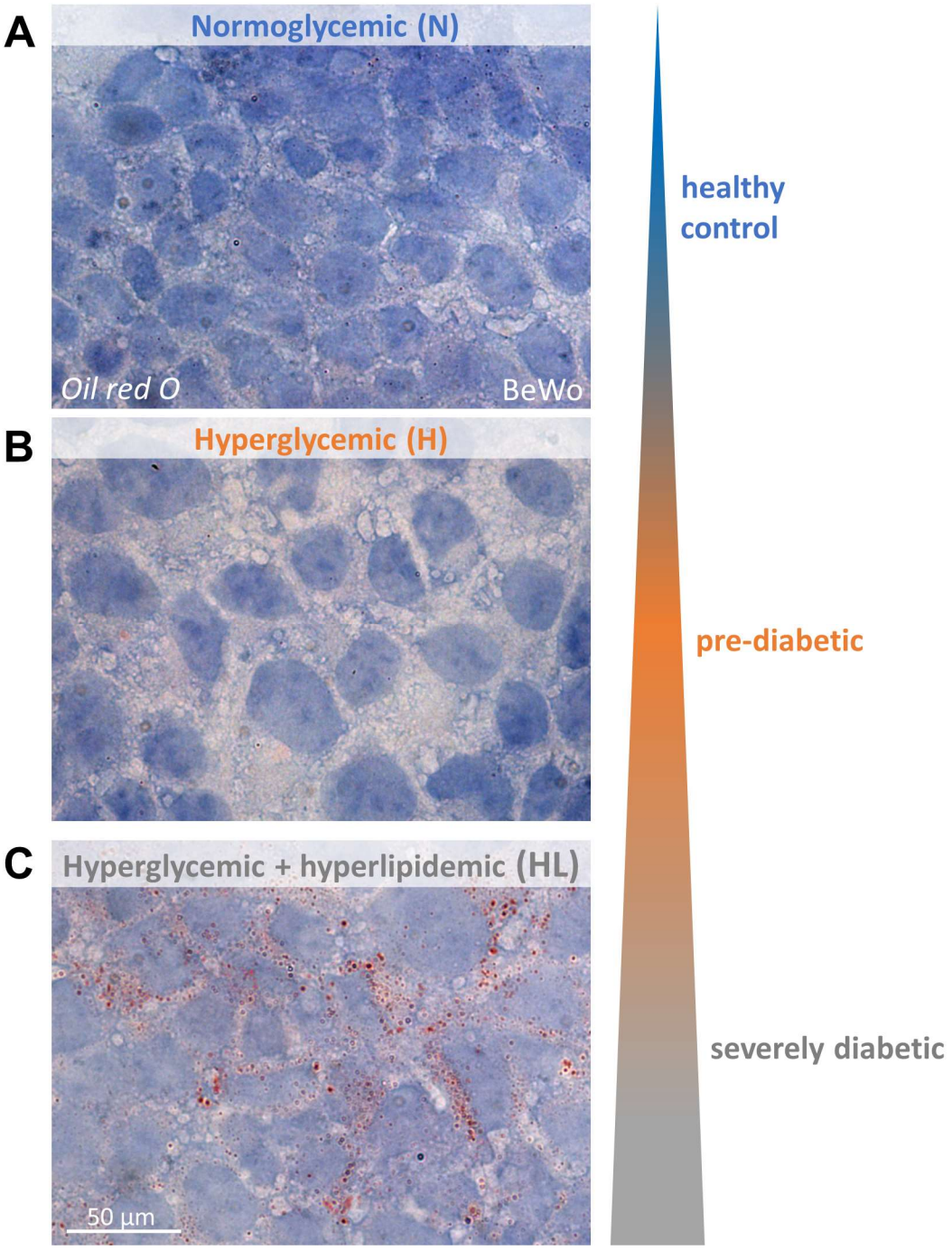

Figure 31: Cell biological visualization of time-dependent adaption of normoglycemic BeWo trophoblast cells to hyperglycemic and hyperglycemic/hyperlipidemic conditions. Representative images of Oil red O stained BeWo cells cultured on glass slides for 48 h after 30 days of culture in normoglycemic (N; Dulbecco's Modified Eagle's Medium (DMEM)- 5.5 mM glucose)(**A**), hyperlipidemic (H; DMEM- 25 mM glucose)(**B**), and hyperglycemic combined with hyperlipidemic (HL; DMEM-25 mM glucose + 100 µM palmitic acid) (**C**) conditions. Cells were counterstained with hematoxylin. The BeWo-derived cell models H (orange) and HL (grey) showed altered cell morphology, including increased nuclei and vacuole size. In HL extensive intracellular lipid stores (red staining) were detected. N represents the healthy control condition, H mimicks

pre-diabetic and HL severe diabetic condition with increasing severity as depicted to the right of the pictures according to the expected condition in GDM placentae. **A-C**, the pictures are captured as represents for each cell model.

3.2.2.2 Hyperglycemic adaptions in BeWo cell models reflect clinical observations in GDM

The effect of GDM on iron homeostasis in the clinical specimens was characterized *inter alia* by downregulation of the key iron-transporters DMT1, FPN1 and ZIP8 and the iron-uptake mediating TfR1 on either mRNA or protein level (3.2.1 on p. 89-96, **Figure 25** and **Figure 28**). When monitoring the expression levels of the genes regulated in GDM during 40 days of hyperglycemic/hyperlipidemic challenge in the BeWo cell models, there was an initial upregulation of *DMT1* and *ZIP8* after 3 days of stimulation and a stable downregulation of *FPN1* and *TfR1* after 20 days relative to normoglycemic conditions (**Figure 32 A1**). In the HL condition *DMT1* was downregulated after 28 days of stimulation (**Figure 32 B1**). Moreover, the upregulation of the ferroxidase *Zp* in H and HL during the entire stimulation time (**Figure 32 A2/B2**) also mimicked the clinical results found in GDM placentae (3.2.1 on p. 89-96), and strongly underlines the suitability of the applied cell models. Interestingly, the constant downregulation of *GLUT1* in H and HL confirmed the increased availability of glucose in H and HL (**Figure 32 A2/B2**).

3.2.3 BeWo trophoblasts reduce iron uptake under hyperglycemic and hyperglycemic-hyperlipidemic conditions

Based on the high comparability between the developed hyperglycemic BeWo cell models (H and HL) and the GDM-specific changes of placental iron homeostasis gene expression found in the clinical setup, we extended our studies to the functional level. We performed Tf-mediated $^{55}Fe^{3+}$ uptake assays to investigate the effect of hyperglycemia on placental iron transport function using the established BeWo cell models.

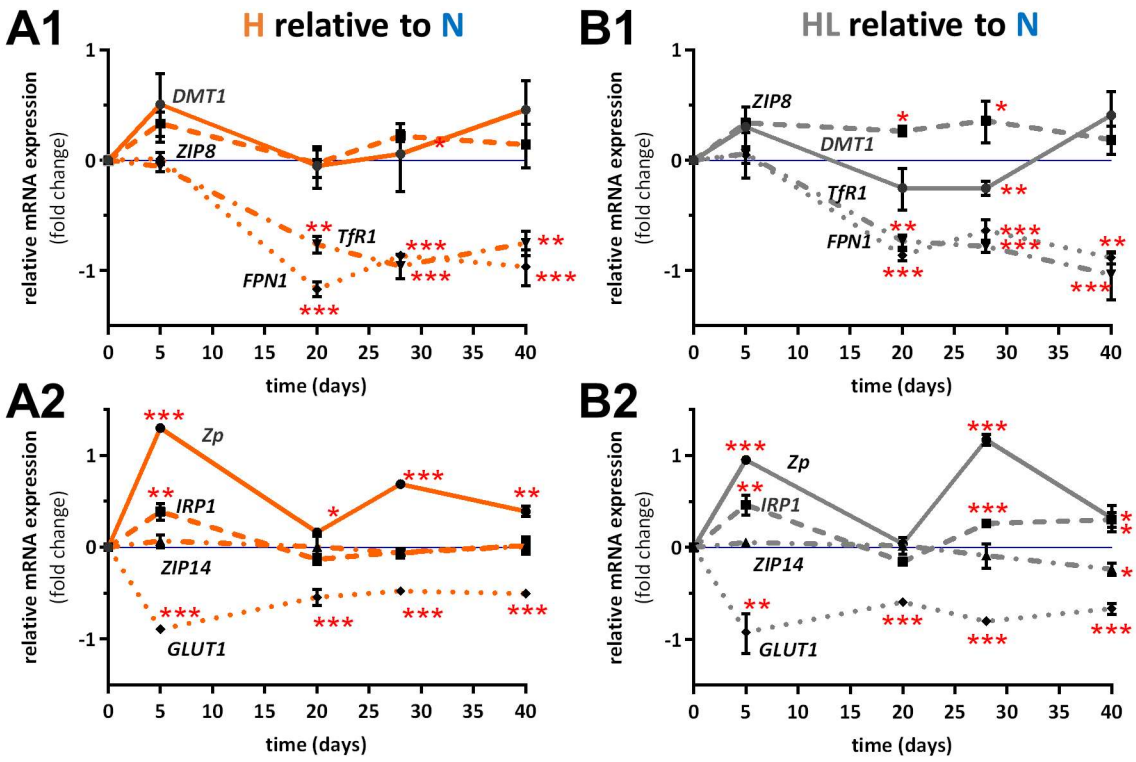

Figure 32: Expressional adaption of iron homeostasis genes during 40 days of hyperglycemic and hyperglycemic-hyperlipidemic stimulation on BeWo trophoblasts. Time-dependent adaption of mRNA levels of the iron transporters *DMT1* (solid line), *ZIP8* (dashed line), *FPN1* (dotted line) and *TfR1* (dash-dotted line) under hyperglycemic H (**A1**) and hyperglycemic-hyperlipidemic HL conditions (**B1**), but also of the iron transporter *ZIP14* (dash-dotted line), the ferroxidase *HEPHL* (solid line), iron sensor *IRP1* (dashed line) and of the glucose transporter *GLUT1* (dotted line) under hyperglycemic H (**A2**) and hyperglycemic-hyperlipidemic HL conditions (**B2**). Error bars represent standard deviation (SD) of triplicate measurements (n=3). Transcript data are presented as $2^{-\Delta\Delta Ct}$ values (ΔΔCt = Ct value of target gene – Ct value of the mean of YWHAZ, GAPDH and UBQ) and normalized to the mean of controls. Statistical significance was determined relative to normoglycemic conditions using two-tailed Mann-Whitney test, α=0.05, * p<0.05, ** p<0.01, *** p<0.001.

Already after several days of stimulation the Tf-dependent Fe^{3+}-uptake was significantly reduced in H and HL cell models independent of the cell differentiation stage (BeWo-CTB in **Figure 33A** / BeWo-STB in **Figure 33B**). Considering the total monitoring period of iron uptake, there was a consistent reduction of >40% in iron uptake in both H and HL (**Figure 33C**). While an initial increase of iron uptake was detected after 1 day of stimulation in H, the iron uptake was significantly reduced in H and HL already after 5 days of stimulation (**Figure 33C**). All iron uptake assays were performed in unstimulated BeWo and in BeWo cells stimulated for 48 h with 100 µM Forskolin. There was no significant difference between Forskolin stimulated, differentiated BeWo cells and unstimulated cells (**Figure 33A/B**).

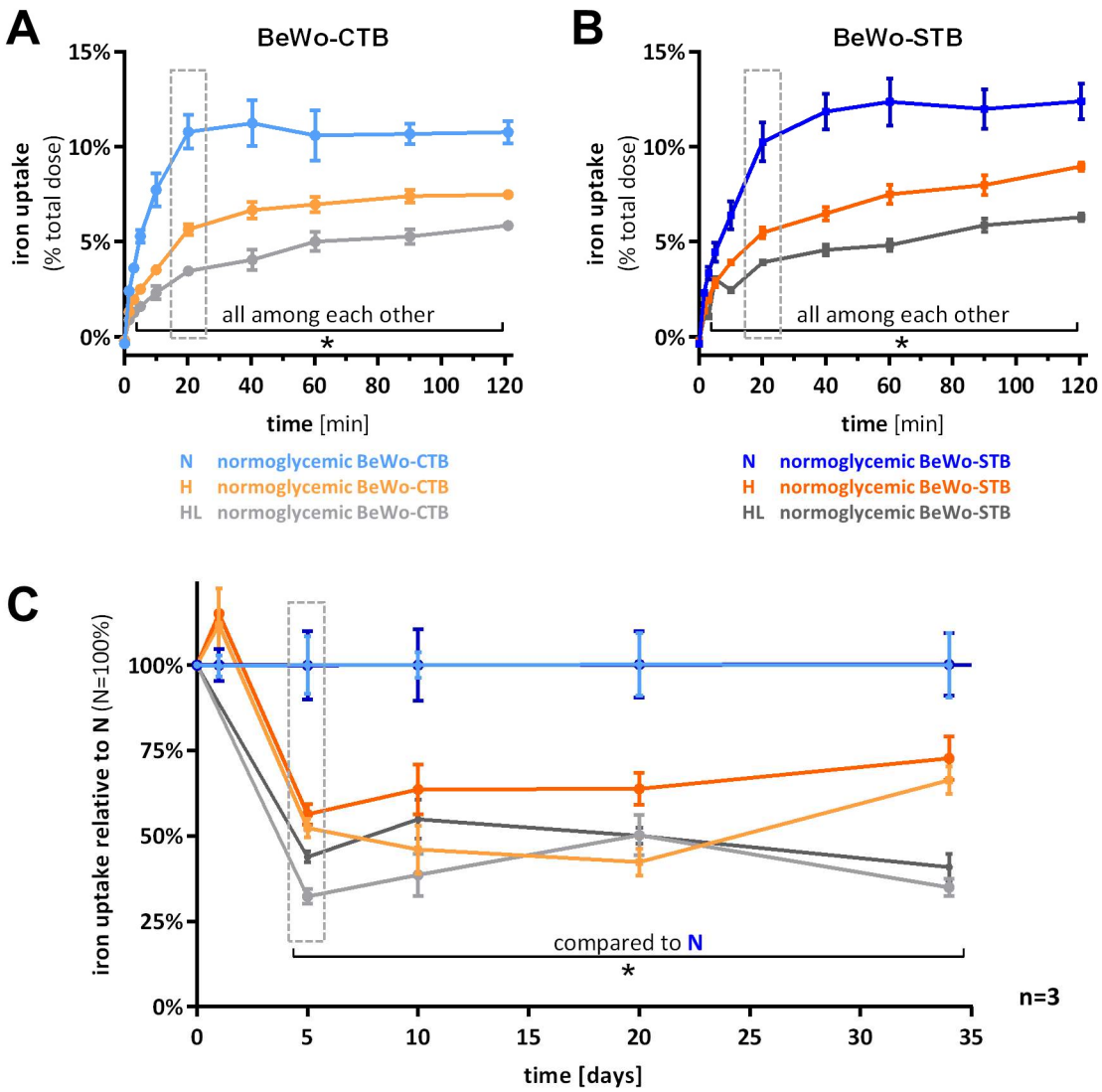

Figure 33: Assessment of functional changes in iron homeostasis by measuring transferrin-dependent radioactive $^{55}Fe^{3+}$-uptake during adaption of BeWo trophoblasts to hyperglycemic and hyperglycemic-hyperlipidemic conditions. Normoglycemic BeWo cells (N, blue) were cultured under hyperglycemic (H, orange) and hyperglycemic-hyperlipidemic (HL, grey) conditions for 34 days. In parallel, functional changes in iron-transport were serially assessed by measuring transferrin (Tf)-dependent Fe^{3+}-uptake in N, H and HL cell models. **A**/**B**, Representative iron uptake results of three independent experiments (n=3) after 5 days of adaption to hyperglycemic conditions. Alteration of iron-uptake was assessed in cytotrophoblast-stage (BeWo-CTB, 24 h after seeding) in A and in syncytiotrophoblast-stage (BeWo-STB, CTB with additional stimulation with 100 µM forskolin for 48 h) in **B**. Iron uptake values are displayed as percentage of the applied total dose. Concentration of Tf-Fe^{3+} total dose in all experiments was 16.14 pmol/100 µL (161.4 nM). Reduction of iron uptake measured at 20 min (dotted square in panel A and B) was monitored over 34 days normalized to N (N=100%) in panel **C**. Error bars represent SD of 7 replicates. Statistical significance was determined using two-way ANOVA with Sidak's multiple comparison post hoc analysis, α=0.05. The experiments were performed three times (n=3) with BeWo cells originating from the same normoglycemic BeWo line at different passage numbers.

3.2.4 Hyperglycemic conditions affect cellular death and oxidative stress pathways in trophoblasts

To characterize the cellular mechanisms underlying the alteration of placental iron homeostasis under diabetic conditions, we sampled BeWo cells during 30 days of H and HL challenge and assessed the protein expression of stress response markers by immunoblotting. From day 3 onwards the expression of the autophagy markers p62 and LC3-II were downregulated (**Figure 34**A). No differences in protein expression of the endoplasmic reticulum (ER) stress marker BiP (**Figure 34**B) were detected when comparing H and HL to N at the respective time points after starting the stimulation. Thus, trophoblasts under hyperglycemic conditions showed reduced autophagy, but no effect on the ER-stress pathway.

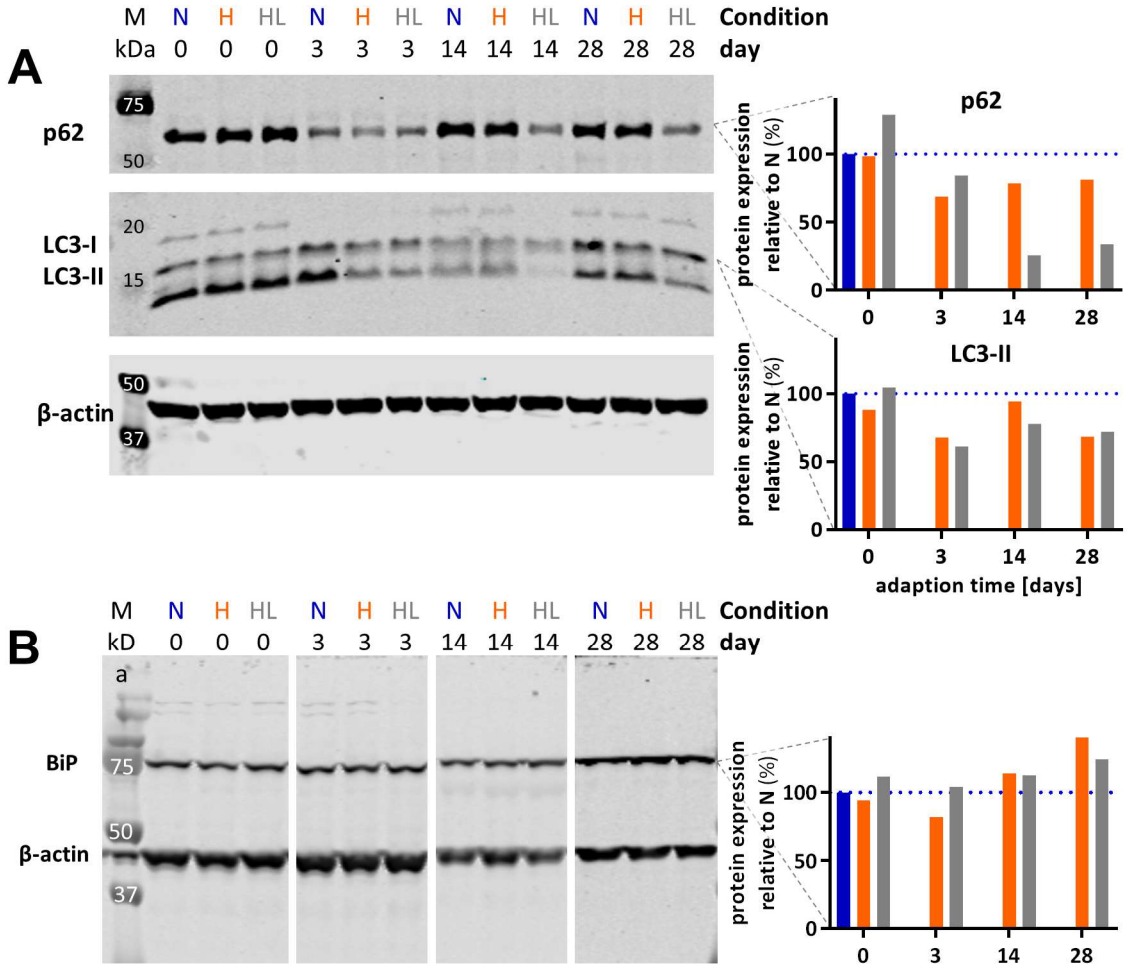

Figure 34: Trophoblasts under hyperglycemic conditions reduce autophagy but express no significant changes in the ER stress pathway. The expression of the autophagy markers p62 (62 kDa) and LC3-II (14 kDa) (**A**) and ER stress marker BiP (75 kDa) (**B**) during 28 days of adaption to hyperglycemic (H) and hyperglycemic combined with hyperlipidemic conditions (HL) by immunoblotting (left panels). p62 and LC3-II expression visualized by immunoblotting at day 0, 3, 14 and 28 was quantified by fluorescence detection analysis and presented relative to the

normoglycemic condition (N, blue bar) (right panels). Results of one representative experiment from three independent experimental setups are shown.

Beside autophagy and ER-stress we quantified cellular damage caused by oxidative stress by measuring the production of MDA equivalents and carbonyl formation. After 30 days of adaption to hyperglycemic conditions, there was still significantly increased lipid peroxidation detectable in the supernatant of BeWo under H (**Figure 35A**).

No change in protein carbonylation after 30 days of adaption to H and HL, respectively, was found (**Figure 35B**).

We furthermore determined oxidative stress damage in association with hyperglycemia and altered placental iron homeostasis by analyzing the antioxidative potential (total-GSH) in BeWo cell lysates cultured for 30 d in N, H and HL. The total-GSH levels were significantly reduced under HL (**Figure 35C**) reflecting increased GSH consumption for counteracting accelerated oxidative stress.

Taken together, increased oxidative stress seems to play a predominant role in BeWo trophoblasts adapting to hyperglycemic and hyperlipidemic conditions.

3.2.5 Antioxidant treatment - Rescue experiment

To investigate whether oxidative stress is indeed the main mediator of the disturbed iron homeostasis in the placenta, we determined the effect of an experimentally induced oxidative stress challenge on trophoblast cells. Additionally, we studied whether the effect of hyperglycemic conditions on iron homeostasis gene expression reproduced by just increasing the oxidative stress levels independent of glucose and fatty acid availability, could be rescued by increasing the antioxidative potential.

Therefore, we tested different chemicals such as Rotenone and tert-Butyl hydroperoxide. Rotenone is a mitochondrial toxin and a potent, reversible, and competitive inhibitor of complex I (NADH-CoQ reductase) of the respiratory chain leading to cellular ROS production. Oxidative stress induced by tert-BOOH was chosen because it was shown that tert-BOOH interferes with the placental transport of glucose in *in vitro* studies with BeWo cells (Araújo et al. 2013). Induced oxidative stress by tert-BOOH treatment led to clearly increased levels of MDA equivalents indicating increased lipid peroxidation, while the applied dose of rotenone just marginally induced lipid peroxidation compared to

untreated control (**Figure 35D**). Therefore, we choose tert-BOOH instead of Rotenone for oxidative stress induction. For antioxidative rescue, we tested additionally to NaSe, the flavonoid and dietary antioxidant quercetin (Bach et al. 2010) in our studies. Quercetin had a more pronounced rescue effect than NaSe (see **Figure 35D**). However, as quercetin has potential iron chelating properties (Morel et al. 1993) that would affect the interpretation of our results, we continued with NaSe instead of quercetin. In summary, the combination of the antioxidants NaSe with tert-BOOH as oxidative stress inducer showed suitable low dose rescue properties without iron chelation.

Thus, we treated BeWo cells under normoglycemic conditions with the oxidant tert-BOOH for 24 h and compared the effects with the phenotypes found in GDM tissues. In agreement with the results found in GDM placentae (**Figure 25**), the induction of oxidative stress significantly reduced the mRNA abundance of the iron transporters *DMT1* and *FPN1* (**Figure 35D**). The mRNA levels of *ZIP8* and *TfR1* were elevated whereas a profound decrease of *GLUT1* mRNA was detected (**Figure 35D**).

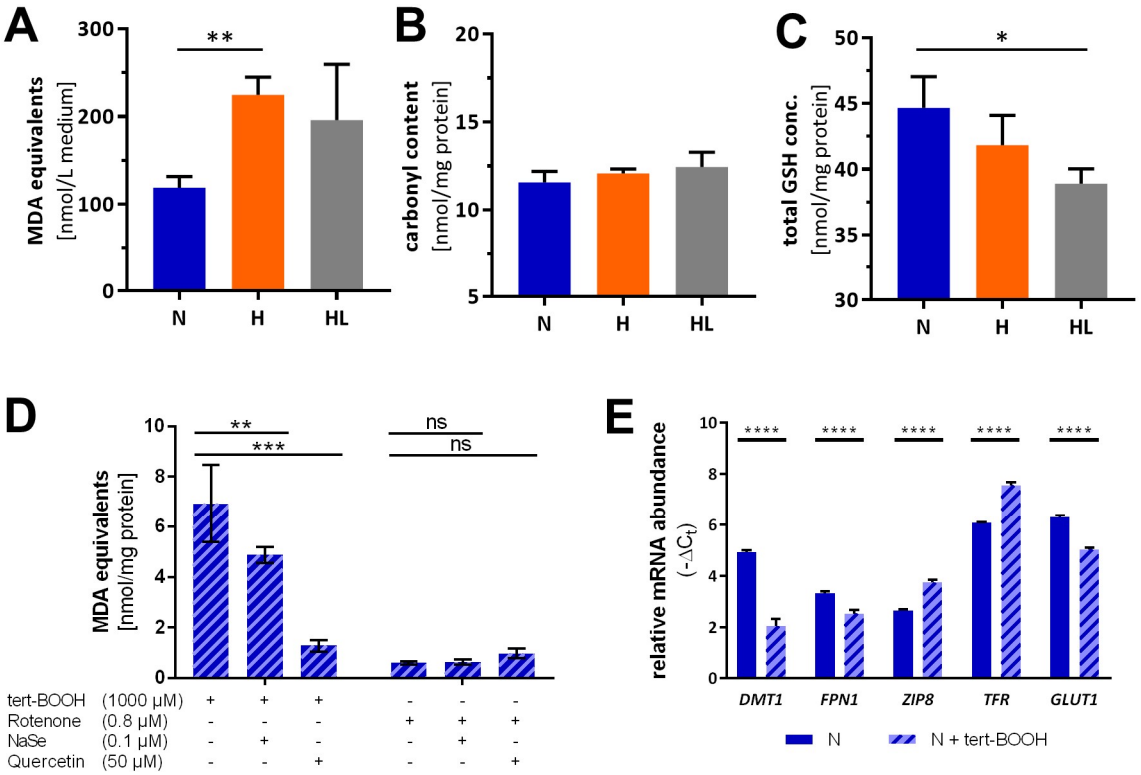

Figure 35: Trophoblasts under hyperglycemic conditions show increased oxidative stress damage and reduced antioxidative potential, while induced oxidative stress induce iron homeostasis gene alterations comparable to gestational diabetes mellitus (GDM). Increased oxidative stress in H and HL was detected in three independent experiments after 30 days of adaption time (n=3). **A**, Increased lipid peroxidation determined as the formation of malondialdehyde (MDA) equivalents in cell supernatants was found in H (orange) and HL (grey)

conditions. **B**, Protein carbonylation was measured by staining of cell lysates with 2,4-Dinitrophenylhydrazine (DNP). **C**, Decreased antioxidative potential was assessed by measuring total glutathione (GSH) levels. Statistical significance was determined using two-way ANOVA with Dunnett's multiple comparison test, α = 0.05, * p < 0.05, ** p < 0.01. **D**, Validation of effective agents to induce and reduce oxidative stress for the subsequent rescue experiments. BeWo cells were cultured in DMEM low glucose with 10% FBS, seeded in 6-well plates (350'000 cells/well resp. 36'500 cells/cm^2) overnight and treated with the antioxidants 0.1 µM NaSe or 50 µM Quercentin for 24 h at 37°C without FBS, followed by oxidative stress challenge by either 0.8 µM Rotenone or 1000 µM tert-BOOH for 4 h at 37°C. Oxidative stress was measured by lipid peroxidation assay and represented as bar diagram with mean and SD. Treatment conditions are represented in the matrix below the x-axis. The combination of the antioxidants NaSe with tert-BOOH as oxidative stress inducer showed low dose rescue properties without potential iron chelation. For statistical analysis parametric 2-way ANOVA test, α=0.05 was used; **p< 0.01, ***p<0.001. **E**, mRNA abundances of the Divalent metal transporter 1 (*DMT1*), Zrt- and Irt-like protein 8 (*ZIP8*), Ferroportin-1 (*FPN1*), Transferrin receptor protein 1 (*TfR1*) and Glucose transporter 1 (*GLUT1*) were determined in untreated normoglycemic BeWo cells (N, blue) and in normoglycemic BeWo cells treated with tert-Butyl hydroperoxide (tert-BOOH; 100 µM; blue striped bars). Cycle threshold (Ct) values were determined by qRT-PCR and normalized to the mean of the reference genes Tyrosine 3-monooxygenase/tryptophan 5-monooxygenase activation protein, zeta polypeptide (*YWHAZ*), Glyceraldehyde-3-phosphate dehydrogenase (*GAPDH*) and ubiquitin (*UBC*). Statistical significance was determined using two-way ANOVA with Sidak's multiple comparison post hoc analysis, α = 0.05, ****p < 0.0001.

3.2.6 Rescue of placental iron homeostasis by antioxidant supplementation

To further investigate the association between oxidative stress, hyperglycemia and placental iron homeostasis, we performed rescue experiments assuming that the negative effects of hyperglycemia on the regulation of placental iron homeostasis genes in BeWo cell models can be counteracted by supplementation with an antioxidant. Thus N, H and HL BeWo cells were treated with Se and challenged the with additional oxidative stress by adding tert-BOOH for 24 h as for **Figure 35D**. The exposure to tert-BOOH aggravated the hyperglycemic/hyperlipidemic effects in the BeWo models and reduced the inter replicate variability in all performed assays. Focusing on the iron transporter DMT1, FPN1 and ZIP8, we observed significant downregulation of *FPN1* under both hyperglycemic conditions and decreased *ZIP8* under H. *TfR1* was relative to N upregulated under H, but downregulated under HL. This typical pattern of gene regulation confirmed the results shown for GDM placentae in **Figure 25**, but also in the BeWo model treated with tert-BOOH in **Figure 35D**. Se supplementation reversed the hyperglycemic/hyperlipidemic effect at mRNA level almost completely (**Figure 36A**). Furthermore, Se supplementation reduced lipid peroxidation under HL (**Figure 36B**) and eliminated protein carbonylation

under both hyperglycemic conditions (**Figure 36C**). Importantly, Se supplementation increased the antioxidant potential and consequently rescued the hyperglycemic effect on gene expression by reducing oxidative damage in hyperglycemic trophoblasts.

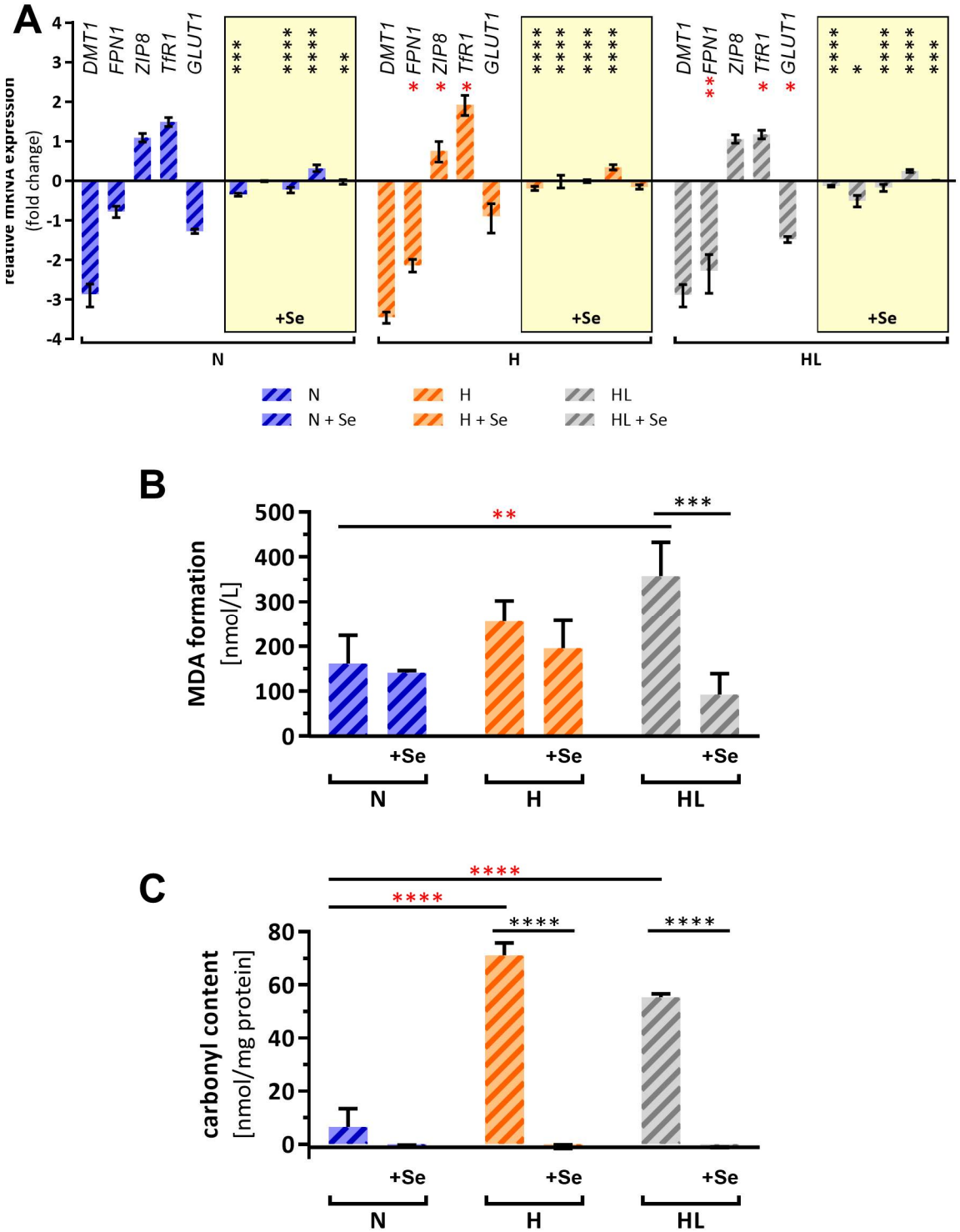

Figure 36: Effect of induced oxidative stress on mRNA abundances of iron homeostasis genes in trophoblasts and rescue of the hyperglycemic effects by selenium treatment. A, Oxidative stress was induced by tert-Butyl hydroperoxide (tert-BOOH; 100 µM) treatment in the three BeWo cell models (N, blue; H, orange; HL, grey) for 24 h (striped bars). In tert-BOOH treated cells supplementation with 400 nM sodium selenite (NaSe, +Se) significantly reduced the

hyperglycemic effect on iron homeostasis gene regulation. mRNA expression results were and normalized to the mean of the reference genes Tyrosine 3-monooxygenase/tryptophan 5-monooxygenase activation protein, zeta polypeptide (*YWHAZ*), Glyceraldehyde-3-phosphate dehydrogenase (*GAPDH*) and ubiquitin (*UBC*). Data are expressed as fold difference in relation to control cells for each condition, which were not treated with tert-BOOH. Samples treated with NaSe are displayed as striped bars in yellow boxes. Supplementation of 400 nM NaSe in the medium rescued the altered gene expression under hyperglycemic (H; orange) and hyperglycemic- and hyperlipidemic (HL; grey), conditions. **B**/**C**, In the three BeWo cell models (N, H, HL) oxidative stress was induced by tert-Butyl hydroperoxide (tert-BOOH; 100 µM) treatment for 24 h (striped bars). Supplementation with 400 nM sodium selenite significantly reduced the formation of malondialdehyde (MDA) equivalents (**B**) and protein carbonylation 2,4-Dinitrophenylhydrazine (DNP) staining (**C**). Both parameters serve as indicators for oxidative stress. Statistical significance was determined in (**A**-**C**) using two-way ANOVA with Sidak's multiple comparison post hoc analysis, $\alpha = 0.05$. * $p < 0.05$, ** $p < 0.01$, *** $p < 0.001$, **** $p < 0.0001$. Results are shown as mean ± SD of triplicate measurements (n=3). In all panels black asterisks display significant differences between Se-treated and untreated cells, while red asterisks indicate significant differences between conditions H or HL compared to N.

3.2.7 Effect of iron deficiency and iron overload on placental glucose transport

During the studies outlined above the effect of hyperglycemic conditions on placental iron homeostasis was investigated and we found that increased oxidative stress is one factor contributing to changes in iron homeostasis gene regulation and function. In collaboration with Thuvaraga Kalakaran, who performed her master project in the Albrecht laboratory, we further investigated, whether iron deficiency and iron overload could affect placental glucose homeostasis. This approach complements the previous results and helps to shed light on the association between placental glucose and iron homeostasis.

Initially, expressional changes of the glucose uniporter *GLUT1* as consequence of iron deficiency and overload was studied. Therefore, normoglycemic BeWo cells were cultured under iron deficiency by treating the cells with the iron chelator DFO and under iron overload by supplementation with holo-transferrin (Tf-2Fe^{3+}) during 24 h, 48 h and 72 h (**Figure 37A**). While *GLUT1* mRNA levels were unaffected in the iron overload condition, there were 2.3-times increased *GLUT1* transcript levels detected already after 24 h of stimulation with 30 µM DFO, followed by steady reduction of *GLUT1* to 1.5-fold overexpression. The *GLUT1* overexpression in the iron deficient condition was confirmed also on protein level (**Figure 37C**). In contrary to the reduction of *GLUT1* overexpression from 24 h to 48 h after stimulation on mRNA level, GLUT1 protein expression was even more pronounced after two days of DFO treatment.

Based on these results, we further investigated the effect of different DFO concentrations on *GLUT1* mRNA levels in a range of 3.75 – 30 µM DFO in normoglycemic BeWo cells for 48 h (**Figure 37B**). Interestingly, within this experiment significant GLUT1 upregulation was observed at 15 µM DFO only. To reveal, whether DFO-mediated changes of GLUT1 expression have a relevant effect for placental glucose uptake, we established a glucose uptake assay suitable to study GLUT1 function in BeWo cells. Hence, glucose uptake was measured using 2-DG that cannot undergo hexokinase-mediated glycolysis by trophoblasts (**Figure 37D**). Although there was rather high variation among the replicates in the glucose uptake assay, normoglycemic BeWo conveyed a significant glucose uptake increase after 80 min of 15 µM DFO treatment, while glucose uptake was reduced after 100 min of 30 µM DFO treatment. Within the glucose uptake time course of 1 h 40 min glucose levels increased within the first 45 min almost linearly independent of the treatment. BeWo cells reached a maximal glucose uptake level of approx. 2.5 mM/well with 15 µM DFO treatment. Due to time restrictions the glucose uptake experiments following DFO treatment were done only once.

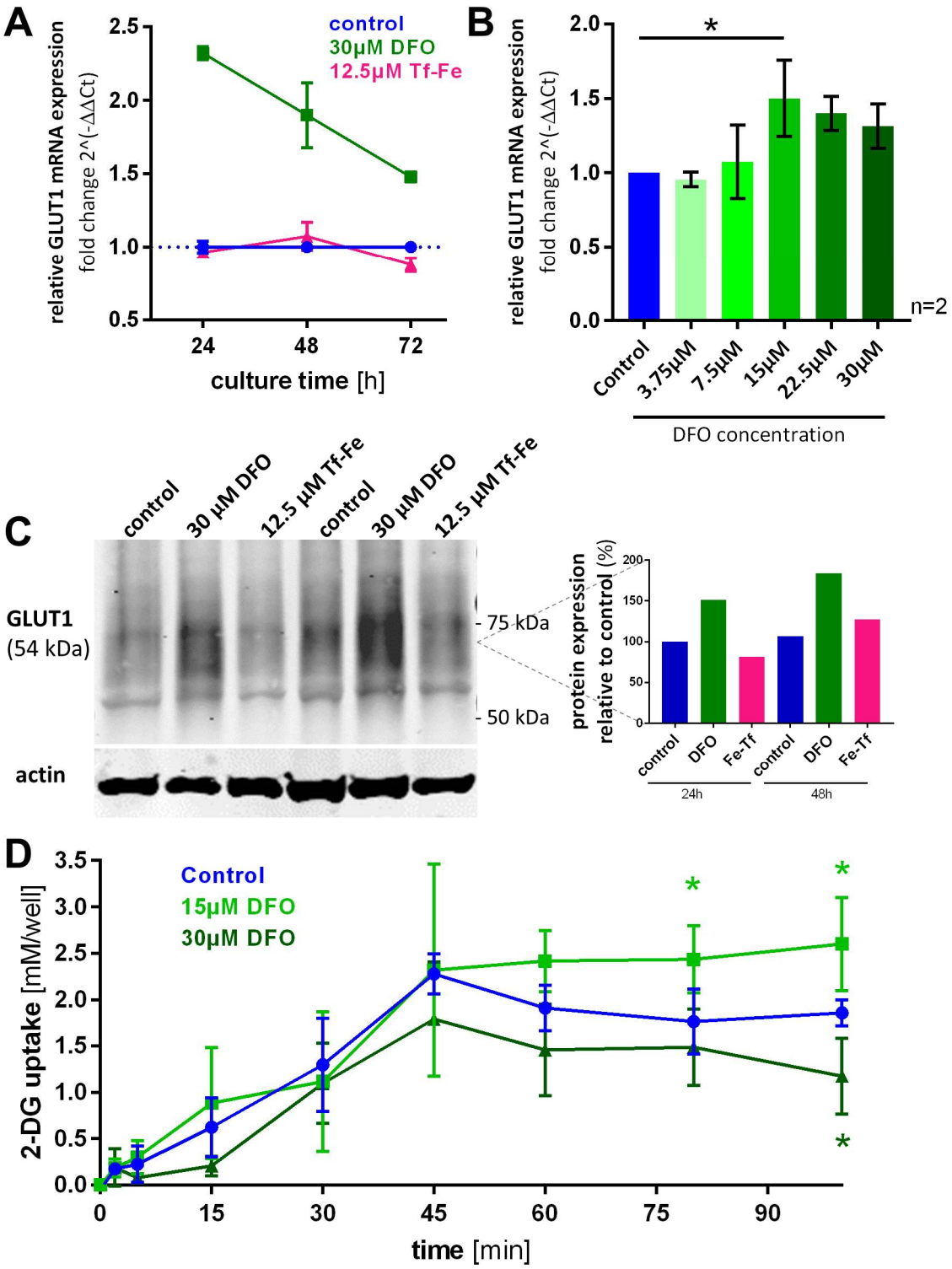

Figure 37: Iron deficiency leads to a temporal upregulation of the glucose transporter GLUT1 on mRNA and protein level, but partially reduced 2-Deoxy-D-glucose (2-DG) uptake function. A, Glucose transporter type 1 (GLUT1/*SLC2A1*) mRNA expression levels in normoglycemic BeWo cells were increased under iron deficiency induced by 30 µM deferoxamine (DFO) treatment (dark green) and unchanged with iron overload by 12.5 µM iron (Fe)-saturated holo-transferrin (Tf-Fe) supplementation (pink) during 72 h. **B**, *GLUT1* mRNA levels were determined after iron depletion with a DFO concentration range of 3.75 – 30 µM. *GLUT1* expression om mRNA level was significantly increased after application of 15 µM DFO for 48 h. *GLUT1* mRNA levels were tested using a paired one-way ANOVA with Tukey's multiple comparisons test, α=0.05, *p<0.05. mRNA levels are represented as mean ± standard deviation (SD) of two independent experiments (n=2)

and were normalized to the mean of the reference genes Tyrosine 3-monooxygenase/tryptophan 5-monooxygenase activation protein, zeta polypeptide (YWHAZ), Glyceraldehyde-3-phosphate dehydrogenase (GAPDH) and ubiquitin (UBC). Data are expressed as fold difference in relation to untreated control. **C**, GLUT1 protein levels were analyzed once (n=1) by immunoblotting after 30 µM DFP treatment or 12.5 µM Tf-Fe supplementation at 24 h and 48 h of stimulation. GLUT1 protein levels were increased after DFO treatment at both time points. **D**, Glucose uptake performance was measured using a total dose of 325 mM 2-Deoxy-D-glucose (2-DG) spiked with 0.5 µCi/well ^{3}H 2-DG during 100 min at 37°C. Glucose uptake was increased after 15 µM DFO treatment for 80 min, but reduced after 30 µM DFO treatment for 100 min. 2-DG uptake differences were determined in one experiment (n=1) and tested by 2 way ANOVA with Tukey's multiple comparisons test, α=0.05, *p<0.05.

3.2.8 Obesogenic diet in mice provoke similar effects in placental iron homeostasis as human GDM

In mice, a obesogenic high fat high sugar (HFHS) diet from the start of pregnancy compromised maternal glucose tolerance and insulin sensitivity in association with dysregulated lipid metabolism, thereby mimicking typical GDM symptoms (Sferruzzi-Perri et al. 2013; Musial et al. 2017). In collaboration with the Centre for Trophoblast Research, University of Cambridge, UK, we examined whether this mouse model of GDM shows similar changes in placental iron homeostasis as shown in human GDM before (3.2.1). At approx. 10 weeks of age, female C57Bl/6 mice without additional genetic modifications were time-mated to males and subsequently fed either standard (n=6) or HFHS (n=6) diet. Dams were sacrificed for tissue collection at day of pregnancy 16 or 19 (d16 or d19) and changes in the expression of iron homeostasis genes were determined in placental tissue by RT-qPCR (**Figure 38**).

At d16, when maximal placental size and maternal glucose intolerance is reached in mouse gestation, placental expression of the iron transporter, *Dmt1* was significantly upregulated in HFHS dams (**Figure 38A**). Such initial upregulation of *DMT1* was also found after exposing human trophoblasts to hyperglycemic conditions *in vitro* (**Figure 32A1**). At d19, when fetal growth is maximal in mice, placental expression of the iron receptor, *TfR1* and iron transporters, *Dmt1* and *Zip14* were downregulated and the iron uptake regulator, *Hepc* and ferroxidase, *Heph* upregulated in HFHS dams (**Figure 38B**). Together, changes in placental iron homeostasis genes observed in HFHS mice nicely reflected the alterations observed in human GDM placentae (**Figure 38C**).

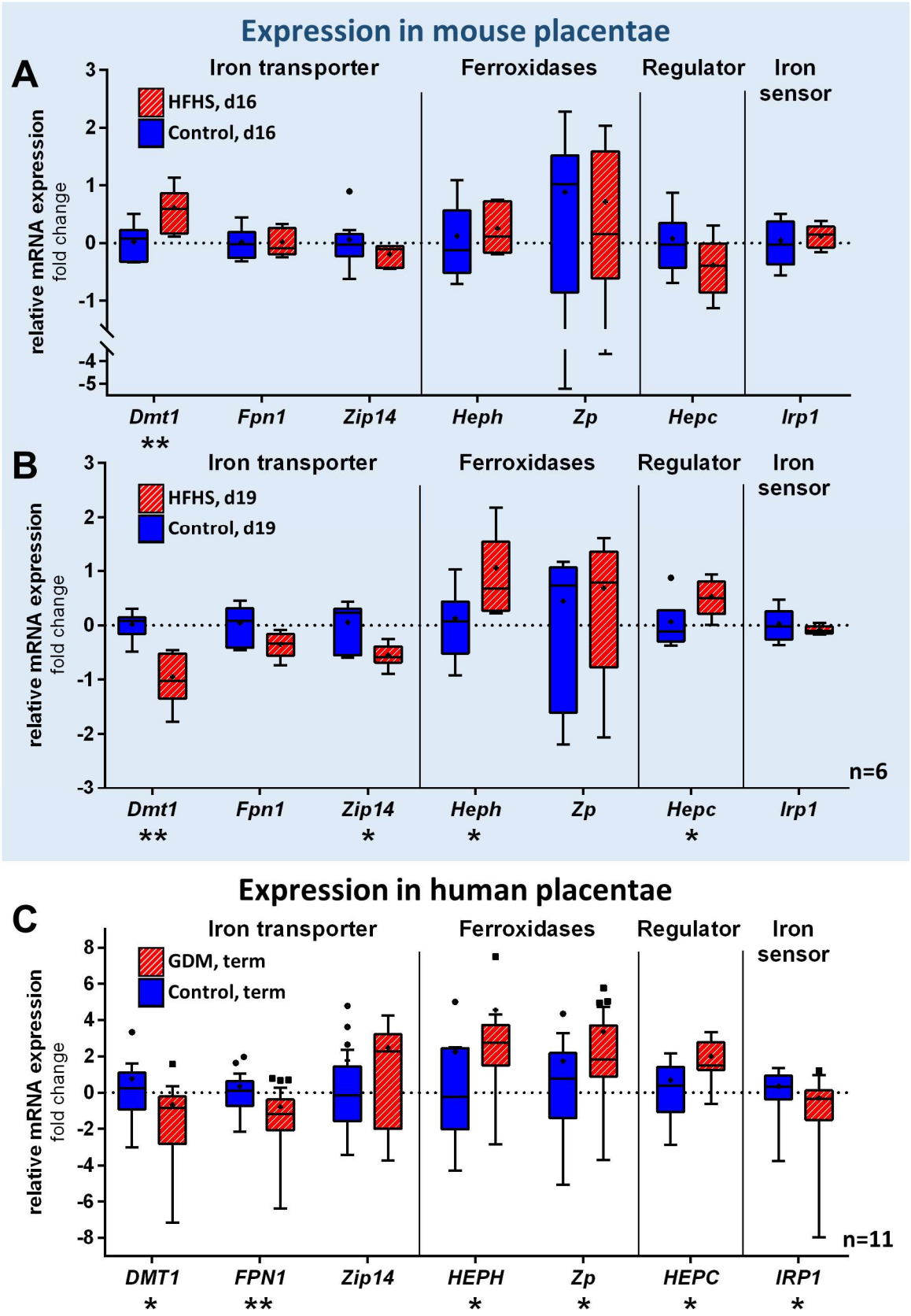

Figure 38: Expressional changes in mice with high fat and high sugar (HFHS) diet during pregnancy reflect regulation patterns found in human GDM placentae. RT-qPCR analyses revealed differential regulation of iron transporters Divalent metal transporter 1 (DMT1/*SLC11A2*), Ferroportin-1 (FPN1/*SLC40A1*), Zrt- and Irt-like protein 8 (ZIP8/*SLC39A8*), the

iron receptor Transferrin receptor protein 1 (TfR1/*TFRC*), the iron sensor Iron regulatory protein 1 (IRP1/*ACO1*), the iron homeostasis regulator Hepcidin (HEPC/*HAMP*) and the iron oxidoreductase Hephaestin (*HEPH*) and Zyklopen (Zp/*HEPHL1*) in mouse (**A**/**B**, blue background) and human (**C**, no background) placentae. **A**, mice were set on HFHS (n=6) or control (n=6) diet from day1 in pregnancy (d1) onwards. mRNA was isolated and quantified from mouse placentae at d16 (**A**) and d19 (**B**) and compared to human placentae affected by gestational diabetes mellitus (GDM, n=11) at term in panel **C**. **A**, There was upregulation of the iron transporter *Dmt1* in mice at d16 only, while significant downregulation of the iron transporters *Dmt1* and *Zip14* was detected at d19. Furthermore, there was significant upregulation of the ferroxidase *Heph* and the iron uptake regulator hepcidin (*Hepc*). The human data is the same as shown in **Figure 25**. Taken together, expressional changes in HFHS mice (**A**/**B**) reflect the GDM-mediated regulation of placental iron homeostasis genes in human placentae (**C**). mRNA levels were statistically compared using nonparametric Mann-Whitney test, α=0.5, *p<0.05, **p<0.01.

3.3 Establishment of knockout cell lines generated by CRISPR/Cas9 mutagenesis.

In the framework of two parallel MSc projects co-supervised by the PhD candidate, we were targeting transporter genes crucial for leucine and iron transfer across the placenta. Martyna Kazimierczak was targeting the System L transporters LAT1(*SLC7A5*) and LAT2 (*SLC7A8*), while Daniela Ramp was targeting DMT1 (*SLC11A2*) and ZIP8 (*SLC39A8*). Following the protocol explained in **Figure 39**, we first designed CRISPR/Cas9 target sites and validated them by sequencing the variant in the BeWo genome, optimized CRISPR/Cas9 transfection of either *sgRNA+Cas9-GFP plasmid* (Xfect) or *sgRNA-Cas9-GFP RNP* (jetCRISPR) into the trophoblast cell line BeWo using FACS for analysis of transfection rates, but also to collect GFP positive cells to grow knockout cell lines from single cells. The resulting CRISPR/Cas9-mutant candidates were characterized on expressional level using qPCR and immunoblotting and on functional level performing leucine and Tf-Fe uptake assays. Finally, we analyzed the target site for insertion or deletion (indel) mutation introduced by site-specific double strand break by sequencing. Although there were expressional and functional changes detected for several mutation candidates, final sequencing revealed unchanged target gene sequences for all of them. Despite the final negative outcome, the following chapter summarizes the procedures and results of our efforts to generate BeWo knockout cells for nutrient transporters.

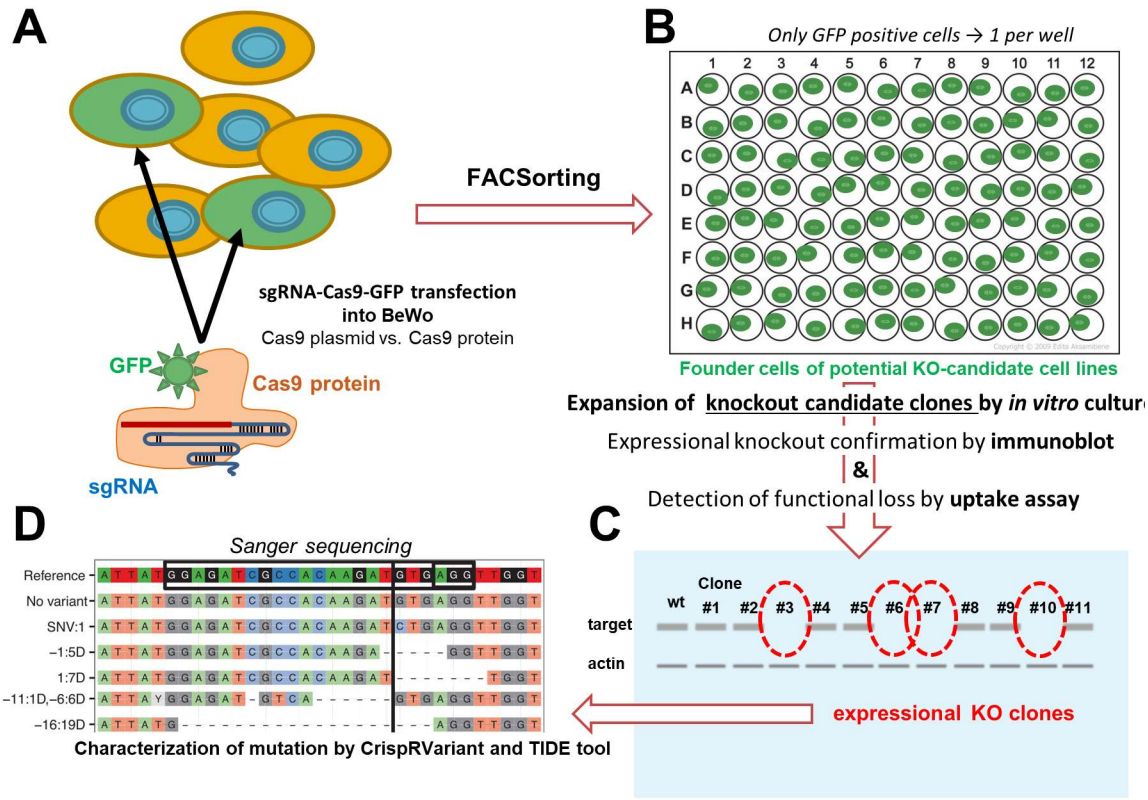

Figure 39: Workflow diagram of reporter gene (Cas9-GFP) assisted sorting of transfected mutant candidates and subsequent identification of knockout candidate clones. A, 24-48 h after transfection of BeWo trophoblasts with Cas9-GFP plasmid or protein, the transfected cells were GFP-positive, visually identified and distributed into 96-well plates by FACS-assisted cell sorting (**B**). The surviving cells become knockout candidates and founders of potentially novel knockout BeWo cell lines, respectively. Knockout candidate clones were expressionally characterized by immunoblot staining (**C**) and functionally assessed by leucine or iron uptake assays. Finally, the knockout candidates showing loss of the targeted protein expression and a loss of function were sequenced by Sanger sequencing to determine the mutation leading to gene loss. **D**, Systematic characterization of emerging mutant variants will be done using CrispRVariant (Lindsay et al. 2016) and TIDE tool (Brinkman et al. 2014).

3.3.1 Validation of genomic variants of the target sites in BeWo

The target sites were carefully designed and determined in the intention to create devastating double-strand-breaks on the one hand, but no off-target effects on the other hand (**Table 5** on p.45). To double check whether the sequences in BeWo genome were corresponding to the determined target site, we sequenced the region in proximity of the target site. Hence, single nucleotide polymorphism (SNP) were detected in the target sequence of *ZIP8* as shown in **Figure 40**. After successful validation of all target sites and exclusion of any SNP disturbing sgRNA-mediated sequence recognition in the BeWo target gene variants, we continued with sgRNA synthesis.

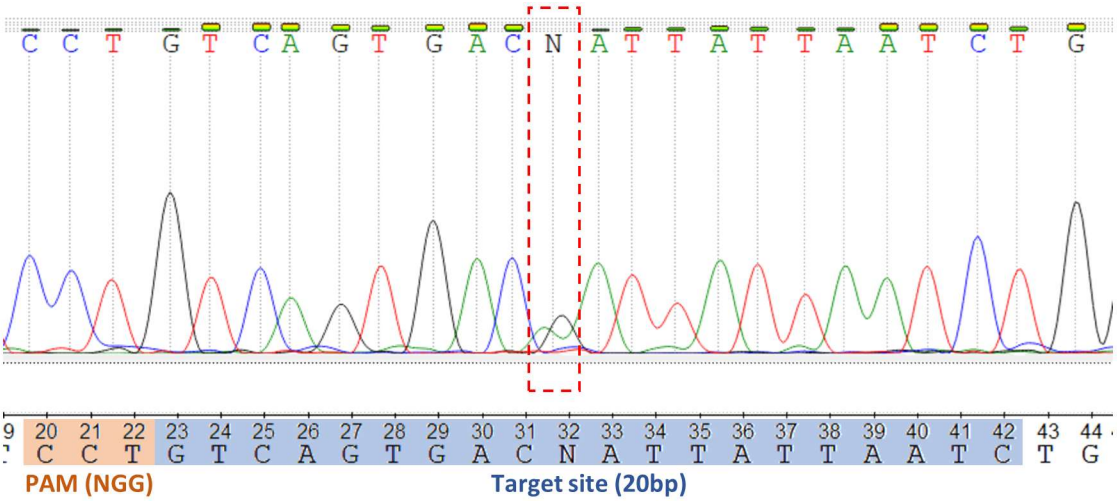

Figure 40: Detection of a single nucleotide polymorphism (SNP) by target site sequencing. Sequencing data as fluorescent peak trace chromatogram of the *ZIP8* target site "ZIP8_567_b", which was finally excluded. Sequence is represented on the reverse strand right (5') to left (3') with the target site on blue and the PAM (NGG) on orange background. N at position 11 in 5'-3' orientation indicates a G32A-mutation as indicated by two simultaneous upcoming peaks of A (Adenine, green) and G (Guanine, black). Such a SNP prevent gsRNA binding and therefore would lead to a reduction of knockout efficiency.

3.3.2 Optimization of CRISPR/Cas9 transfection and cell sorting

In a first step the transfection efficiency of BeWo cells with Cas9-GFP plasmid was tested and optimized before using 3 different transfection reagents: DharmafectDuo (Horizon), XtremeGENE 9 (Sigma) and Xfect plasmid (Takara Bio). Transfection efficiency and cell toxicity of these reagents were the main criteria for selecting the best reagent. HEK-293 which are known to be easy-to-transfect (Thomas and Smart 2005) were chosen as reference cells. The transfection of BeWo and HEK-293 cells with the Cas9-GFP labeled plasmid by using the DharmaFECT™ Duo transfection reagent (Horizon) was not successful. No GFP signal was detected in both cell lines after various experiments with varying amounts of the DharmaFECT reagent and plasmid as suggested in the manufacturer's protocol. At none of the different time points (24, 48 and 72 h post transfection) GFP was detectable by fluorescent microscopy. In contrast, by using the Xtreme Gene 9 (Roche) reagent the transfection procedure was more successful. The highest efficiency was obtained with 4:1 ratio of transfection reagent (in µL) to plasmid DNA (in µg), using 7.5 and 10 µL of the transfection complex and detected 48 and 72 h post transfection. As shown in **Figure 41A-B**, Xfect plasmid (TAKARA) transfection reagent led to the best transfection efficiencies and lowest toxicity, respectively (optimal

conditions see **Table 12**). Therefore, the Xfect plasmid (TAKARA) reagent was further used to transfect HEK-293 and BeWo cells with sgRNA targeting *DMT1*, *ZIP8* and *hCG* genes and the Cas9-GFP plasmid reaching approx. 30% transfection efficiency in BeWo, 70% in HEK-293 cells (**Figure 41A-C**).

Table 12 Optimized Xfect plasmid transfection conditions

Step	Condition
Preparation of target cells	40'000 cells/well overnight in complete growth medium
Preparation of transfection reagent	3.75 µg plasmid DNA with Xfect plasmid Reaction Buffer to a final volume of 10 µL Add 1.5 µL Xfect Polymer to the diluted plasmid DNA
Nanoparticle complexes to formation	Incubate for 10 min at room temperature
Transfection	Incubate the plate at 37°C for 8 h
Determination of transfection rate	Check for GFP expression after 48 h

Next, the above optimized Cas9 plasmid-based transfection method was compared to the direct transfection of sgRNA-Cas9 protein RNP complexes using the jetCRISPR reagent from Polyplus. For this optimization experiment sgRNA targeting the hCG gene was additionally used, as knockout of this gene is expected to be less problematic for cell survival compared to targeting putative essential nutrient transporter genes (Malhotra, Suman, and Gupta 2015). The transfection efficiency was measured for BeWo and HEK-293 by performing flow cytometry analysis 48 h after transfection (**Figure 41D**). Comparing the transfection efficiency between Cas9plasmid and the Cas9protein method (**Figure 41D**, left to right), Xfect sgRNA + Cas9plasmid - transfection reached in BeWo 13.8% and 62.9% higher efficiency rates in the easier-to-transfect HEK-293 cells. Therefore, the consecutive transfection experiments targeting the nutrient transporters *LAT1*, *LAT2*, *DMT1* and *ZIP8* were performed in BeWo using the optimized Xfect plasmid method, that usually reached an efficiency of approx. 50% in later experiments (data not shown).

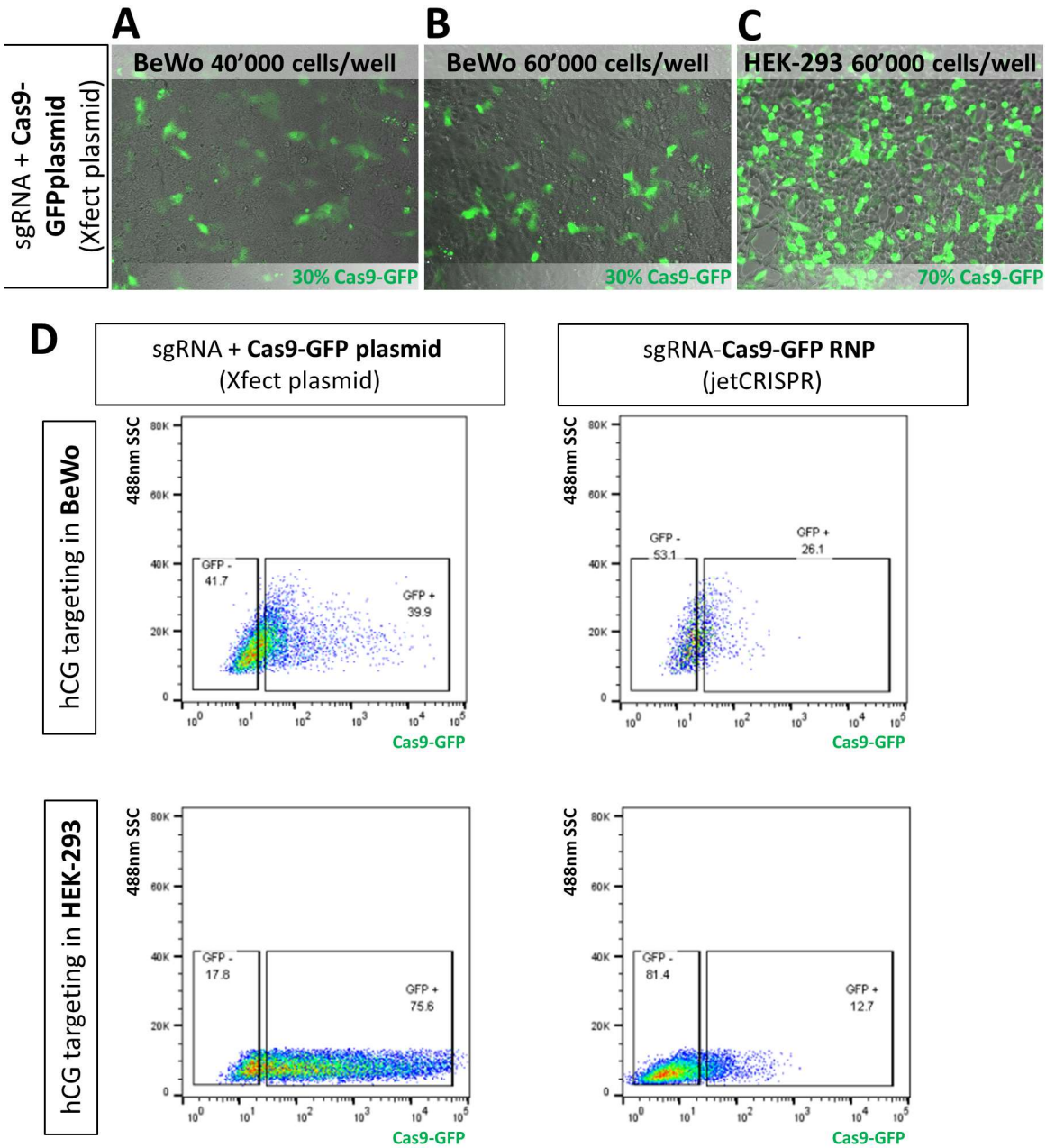

Figure 41: Optimization of transfection conditions for BeWo using Xfect plasmid (Takara Bio) *versus* jetCRISPR (Polyplus). A, Representative images of cells 48 h post transfection using the optimized sgRNA + Cas9-GFP plasmid transfection protocol in a 96-well plate scale. Transfection efficiency in BeWo cells was approx. 30% applied at different cell densities (**A-B**) and 70% in the easier-to-transfect HEK-293 cells (**C**). The transfection experiment was performed in DMEM low glucose (BeWo) resp. DMEM (HEK-293) + 10% FBS + 1 x antibiotics in duplicates. Images were acquired by phase contrast and fluorescence cell imaging using InCellis cell imager (Bertin, USA) with a 20 x magnification. **D**, Comparison of the two transfection reagents Xfect plasmid (**D**, panels on the left) for transferring sgRNA together with Cas9-plasmid and jetCRISPR protein (**D**, panels on the right) for transferring sgRNA-Cas9-GFP ribonucleoprotein (RNP) complexes into BeWo cells (**D**, upper panels) and HEK-293 cells (**D**, lower panels) by flow cytometry analysis. For these experiments sgRNA targeting the hCG gene was used. The transfection efficiency of Xfect plasmid compared to the Cas9protein method was 13.8% higher if applied on BeWo and 62.9% higher on HEK-293 cells. FACS data was analyzed using FlowJo® data analysis software and is presented as scatter plots with of the fluorescence emission intensity (λ_{em}=488 nm) as area under the peak on the x-axis and side scatter (SSC) on the y-axis.

3.3.3 Cell recovery and expressional effects of CRISPR/Cas9 mutagenesis

Following the optimization of sgRNA and Cas9 transfection, the newly established method was applied to target the nutrient transporters *LAT1*, *LAT2*, *DMT1* and *ZIP8* in BeWo cells. We intended to grow knockout candidate cell lines from a single founder cell as presented in **Figure 42A**, but most of the single sorted cells died within few days post transfection. Therefore, FACS was used to isolate successfully transfected, GFP-positive cells in 1, 100 or 200 cells/well format.

We further investigated the effect of *ZIP8*-knockout candidates in BeWo cells on the endogenous expression pattern of iron homeostasis genes such as the transporter *DMT1*, *ZIP8* itself, *ZIP14* and *FPN1*, but also the iron receptor *TfR1*, the iron sensor *IRP1*, the ferroxidase *Zp* and iron regulator *HEPC*. **Figure 42B** shows an overview on the expressional changes in the single-sorted C1 and 100/200-sorted D1, D2, D3, E1, E2, E3 and E4 *ZIP8*-knockout candidates after putative *ZIP8*-mutagenesis. The expression of iron homeostasis genes was normalized to the no-sgRNA, but Cas9 plasmid transfected control cell line I1 p8 (name l1; passage 8). Compared to I1 p8, the fold change of the non-transfected cell lines BeWo p28 and BeWo p29 were with +0.2 and -0.6 very low. Also 5 passages later only marginal changes in mRNA levels were observed as shown for l1 p13 as passage control. In general, all *ZIP8*-targeted BeWo cell lines showed a similar iron homeostasis gene expression pattern. The mRNA levels of *Zp*/*HEPHL1* showed the strongest upregulation, followed by *ZIP8* > *ZIP14* > *IRP1* > *TfR1* > *DMT1*, while the iron exporter *FPN1* and regulator *HEPC* were downregulated (**Figure 42B**). Interestingly *ZIP8* itself, which was targeted and expected to be knocked out, was in most of the samples even higher expressed than in controls.

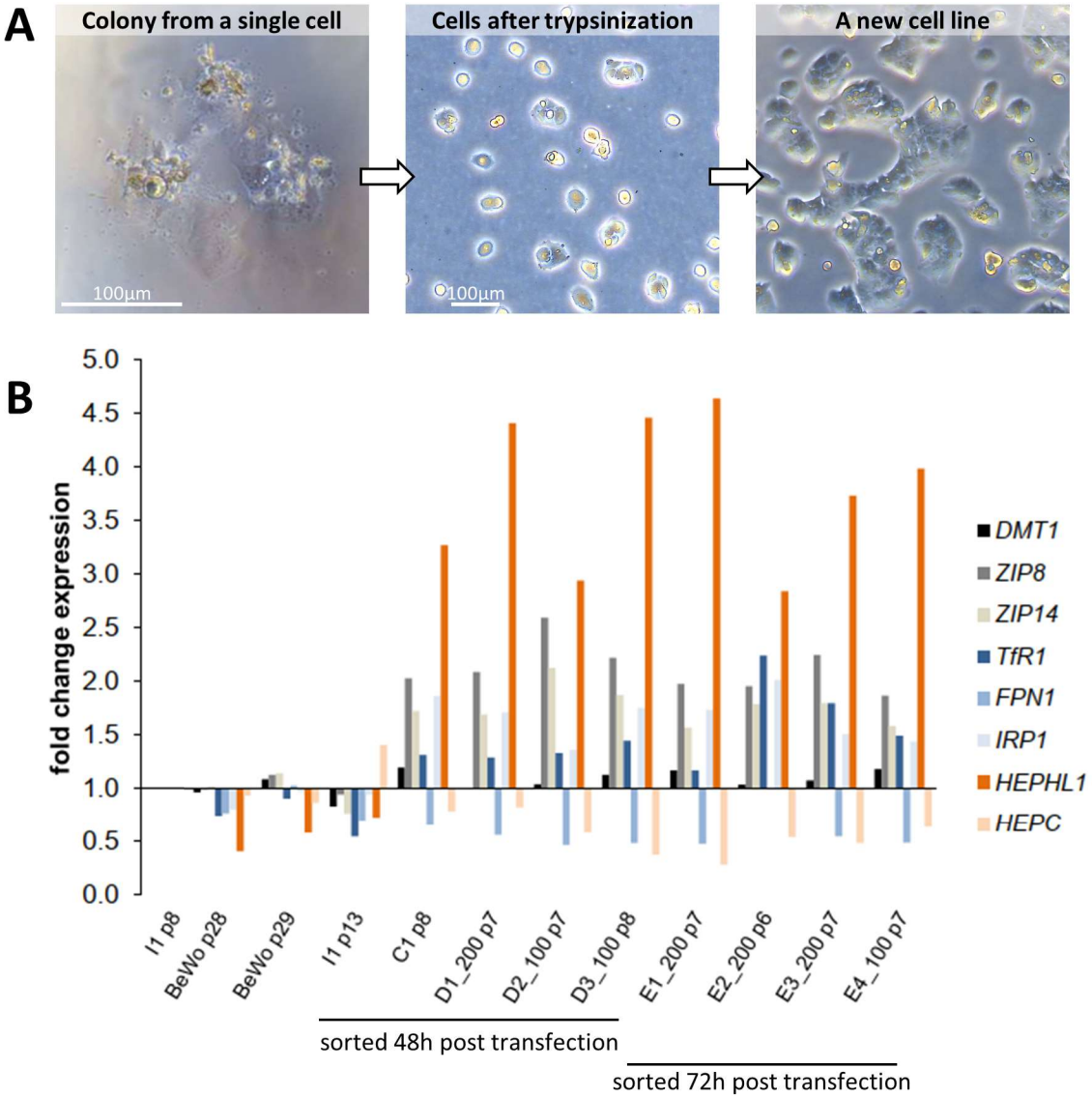

Figure 42: A single cell as founder of a new knockout cell line and expressional changes due to CRISPR/Cas9 mutagenesis. After growing a single cell for 14 days after Xfect plasmid transfection targeting *DMT1* and FACS-sorting, the cell has divided several times in a 96 well plate and formed a cell colony in culture (**A**, left panel). The cell knockout candidate clones in the founder colony were trypsinized and seeded again in a96-well plate to avoid spatial overgrowth and to expand the cell number (**A**, middle panel). 7 days later, the scattered cells adapted and became a slowly growing cell line (**A**, right panel). Magnification in left panel 50 x, in the middle and right panel 20 x. **B**, Composition of expressional changes of iron homeostasis genes on mRNA level after CRISPR/Cas9-mediated *ZIP8*-mutagenesis. BeWo cells were targeted using ZIP8_567 sgRNA (**Table 5**) and transfected using the optimized Xfect plasmid method (3.3.2). mRNA levels of candidate knockout cell lines were normalized to the no-sgRNA, Cas9plasmid transfected control cell line I1 p8. The transfected cells were sorted as single cells and 100 or 200 cells/well (_100 resp. _200) and lysed for expression analysis in different passages (p6-8 passages after transfection / p28-29 passages of original cell lines). L1, C1, D1, D2 and D3 were sorted 48 h post transfection and samples E1, E2, E3 and E4 were sorted 72 h post transfection. Expression levels were analyzed using the mean of reference genes YWHAZ and UBC. All mRNA levels are shown as the mean of duplicates from one experiment (n=1) and represented as fold change ($2^{-\Delta\Delta Ct}$).

In a next step, we analyzed the most promising knockout cell line candidates by immunoblotting. MVM and BM samples from membrane protein fractioning were loaded to confirm the transporter-specific expression ratio between apical MVM and basal BM expression. The exclusively MVM expression of LAT1 in **Figure 43A** and the MVM/BM expression of LAT2 **Figure 43B**, validate the immunoblot experiment. The untreated BeWo p27 in **Figure 43A** showed a very weak LAT1 band at 40 kDa. All clones transfected with anti-LAT1 sgRNA and Cas9 plasmid showed an increase in LAT1 expression by factor 3 or more compared to untreated BeWo p27 lysate (**Figure 43A**). The BeWo knockout candidate clones B1, B2 and B3 transfected with Xfect plasmid and anti-LAT2 sgRNA showed an increase in total LAT2 expression (50 kDa + 30 kDa band in **Figure 43B**) by a factor of 4-5, whereas for the clones B4, B5 and B8 there was only a slight increase of 10-20% compared to the BeWo p27 control. In the B1, B2 and B3 clones, the upper 50 kDa band was 2.5-times more prominent compared to the lower 30 kDa signal. The total LAT2 expression in deglycosylated BeWo wildtype cells p27 compared to untreated cells was slightly decreased but the intensity of the 30 kDa band did not get stronger after deglycosylation. For DMT1 quantification the bands between 150 and 75 kDa were selected according to (Tabuchi et al. 2000; Foot et al. 2016). All samples show increased DMT1 protein levels compared to the BeWo control (**Figure 43C**). In the immunoblots characterizing ZIP8-targeted knockout candidate clones sharp 65 kDa bands were quantified. Compared to the BeWo p25 control all samples have lower ZIP8 protein expression except sample C1 (**Figure 43D**).

Against our expectations, increased levels of target protein expression were detected for 7 LAT1-knockout candidates (**Figure 43A**), 6 LAT2-knockout candidates (**Figure 43B**) and 7 DMT1-knockout candidates (**Figure 43C**). Only CRISPR/Cas9-mediated ZIP8-mutagenesis resulted in decreased expression levels of the targeted *ZIP8* gene relative to the untransfected BeWo p25 control (**Figure 43D**). None of the candidates showed a complete loss of target gene expression on the immunoblots. As demonstrated in **Figure 42B** on mRNA level of iron homeostasis genes, the transfection itself led to various expressional changes.

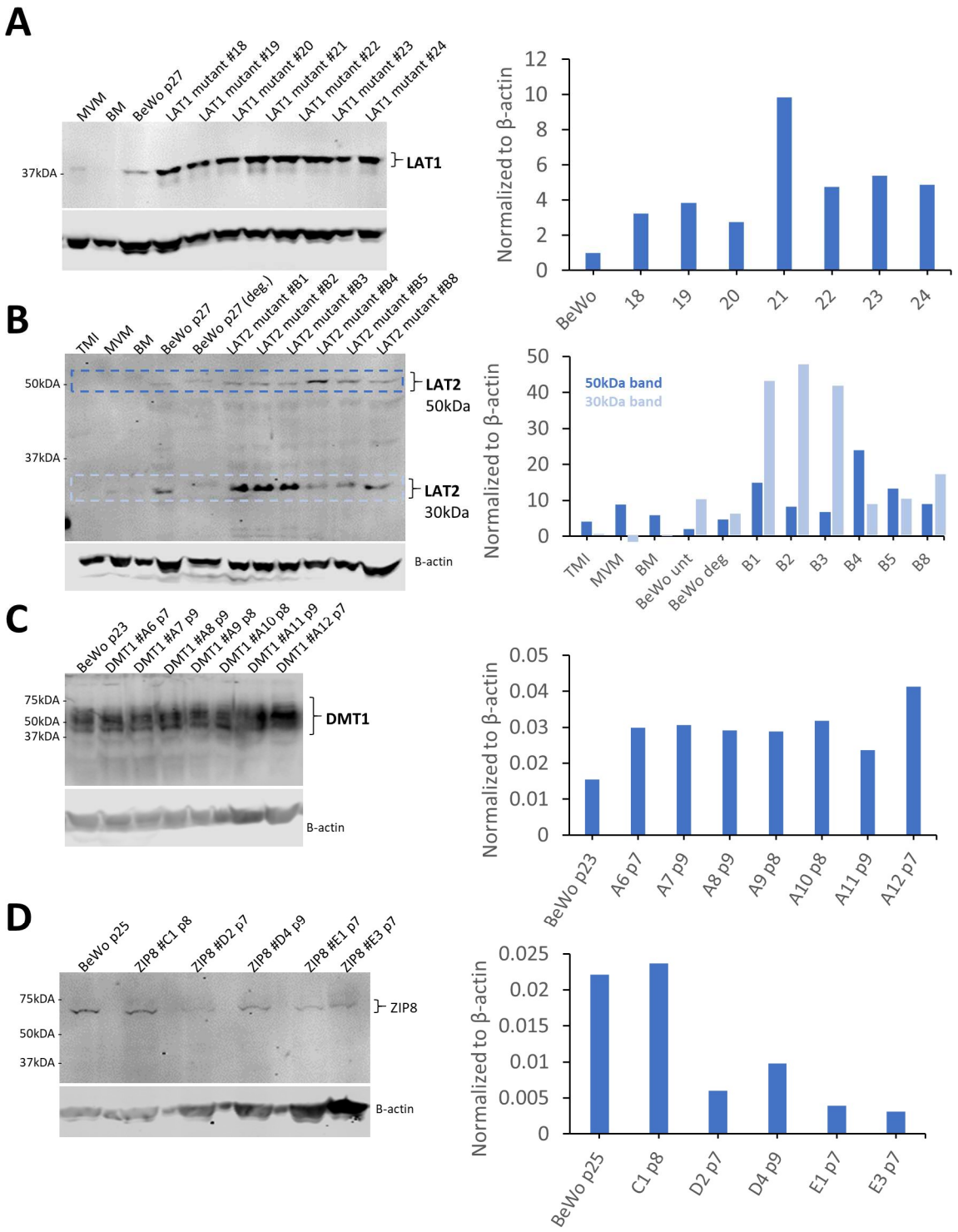

Figure 43: Target gene expression after CRISPR/Cas9 mutagenesis quantified by immunoblotting. The most promising knockout candidates where analyzed on protein level for target gene loss through site directed mutagenesis after Xfect plasmid assisted CRISPR/Cas9 transfection followed by the establishment of stable cell lines. The target gene expression was increased for all putative knockout candidates for LAT1 expression in LAT1 mutants #18-24 (**A**), LAT2 in LAT2 mutants #B1-8 and also DMT1 expression in DMT1 mutants #A6-12. In contrast, there was reduction of ZIP8 expression between 56% in clone D4 in passage (p) 9 to 86% in clone E3 p7. 30 µg protein of total cell lysates of 7 LAT1-targeted (LAT1 MK1 sgRNA) BeWo cell lines (#18-24) were plotted on nitrocellulose membrane after SDS-Page and stained with the primary antibody rabbit anti-LAT1 (1:1000) overnight at 4°C and with secondary anti-rabbit (1:20'000) for 2 hours

at room temperature. Detection of β-actin as loading control was performed using primary mouse anti-β-actin (1:5000) and secondary anti-mouse (1:20'000) for 2 hours at room temperature each. **B**, Immunoblot analysis of 6 LAT2-targeted (LAT2 142 sgRNA) BeWo cell lines (#B1-B8) according to the description for panel **A**, but using primary rabbit anti-LAT2 (1:1000). For LAT2 an upper 50 kDa and a lower 30 kDa band was quantified. **C**, Immunoblot analysis using 60µg total cell lysate from 7 DMT1-targeted BeWo cell lines (#A6-A12) with passage numbers between 7 and 9 using primary mouse anti-DMT1 (1:500) otherwise according to the description for panel **A**. **D**, Immunoblot analysis according to the description for panel **C**, but using rabbit anti-ZIP8 (1:1000). TMI: total membrane protein isolation sample; BM: basal membrane fraction; MVM: microvillous membrane fraction; BeWo p23-27 are non-transfected control samples with passage number (p); deg: deglycosylated sample after PNGase F treatment. All immunoblot experiments were repeated 2-times.

3.3.4 Effects of CRISPR/Cas9 mutagenesis on functional nutrient uptake

Despite of remaining expression of the targeted genes on protein level, we tested a selection of knockout candidate cell lines to investigate the CRISPR/Cas9 mutagenesis mediated effect on placental Leu and iron uptake. Furthermore, we established a strategy to characterize the knockout candidates by applying small molecule inhibitors bearing different specificities.

Amino acid uptake

In the case of targeting System L mediated leucine uptake, the LAT1-specific inhibitor JPH203 and the unspecific System L (mainly LAT1+LAT2) inhibitor JX009 was used. In LAT1 knockout trophoblasts JPH203 inhibition was expected to have no effect on leucine uptake, while other transporter such as LAT2 would compensate for the essential acquisition of leucine. Therefore, only JX009 but not JPH203 could mediate leucine uptake inhibition in LAT1-targeted BeWo cells. On the other hand, JPH203 inhibition on LAT2 knockout trophoblasts was expected to completely block leucine uptake, while inhibition trough JX009 would block leucine uptake similar as JPH203. Based on this expectations, the two LAT2-targeted BeWo cell lines B3 and B5 were investigated by leucine uptake assay in combination with JPH203 and JX009 inhibition (**Figure 44A-C**). The leucine uptake of untransfected control BeWo p27 cells was reduced by 10 µM JPH203 by about 50-60%, while leucine uptake inhibition by 10 µM JX009 reduced with approx. 85% almost completely. According to these expected JPH203 and JX009 inhibition pattern as characterized before in 3.1.4.1, the leucine uptake performance of B3 and B5 was experimentally assessed. There was 1.8-times increased leucine uptake efficiency of untreated B3 compared to control cells (**Figure 44A/B**). This increased leucine uptake was

unexpected but may be the result of adapted expression pattern of System L transporter in these CRISPR/Cas9-targeted cells. However, the expected similarity of JPH203 and JX009 inhibition in putative LAT2-knockout trophoblasts was observed for the B5, but not for the B3 clone.

Iron uptake

Through inhibition of Tf-mediated iron uptake by ferristatin II (also Chlorazol Black or NSC30611), which lead to the degradation of the TfR1, we expected to measure complete block of Tf-mediated and TfR1-dependent iron uptake. Hence, we expected to observe for the ZIP8-targeted candidate clones a reduction in Tf-Fe uptake during the iron uptake time course, e.g. a curve which is located between the untreated and ferristatin II treated cells. The iron uptake inhibition using ferristatin II in the Tf-dependent uptake setup has been measured with control BeWo p27 cells, C1 and D2 candidates (**Figure 44D-F**). Ferristatin II treatment led, as expected, to an almost complete inhibition of the iron uptake in all assay independent of testing transfected or control BeWo cells. Unfortunately, none of the tested ZIP8-knockout candidates conveyed a reduction of Tf-Fe uptake within the observed 2 h time course.

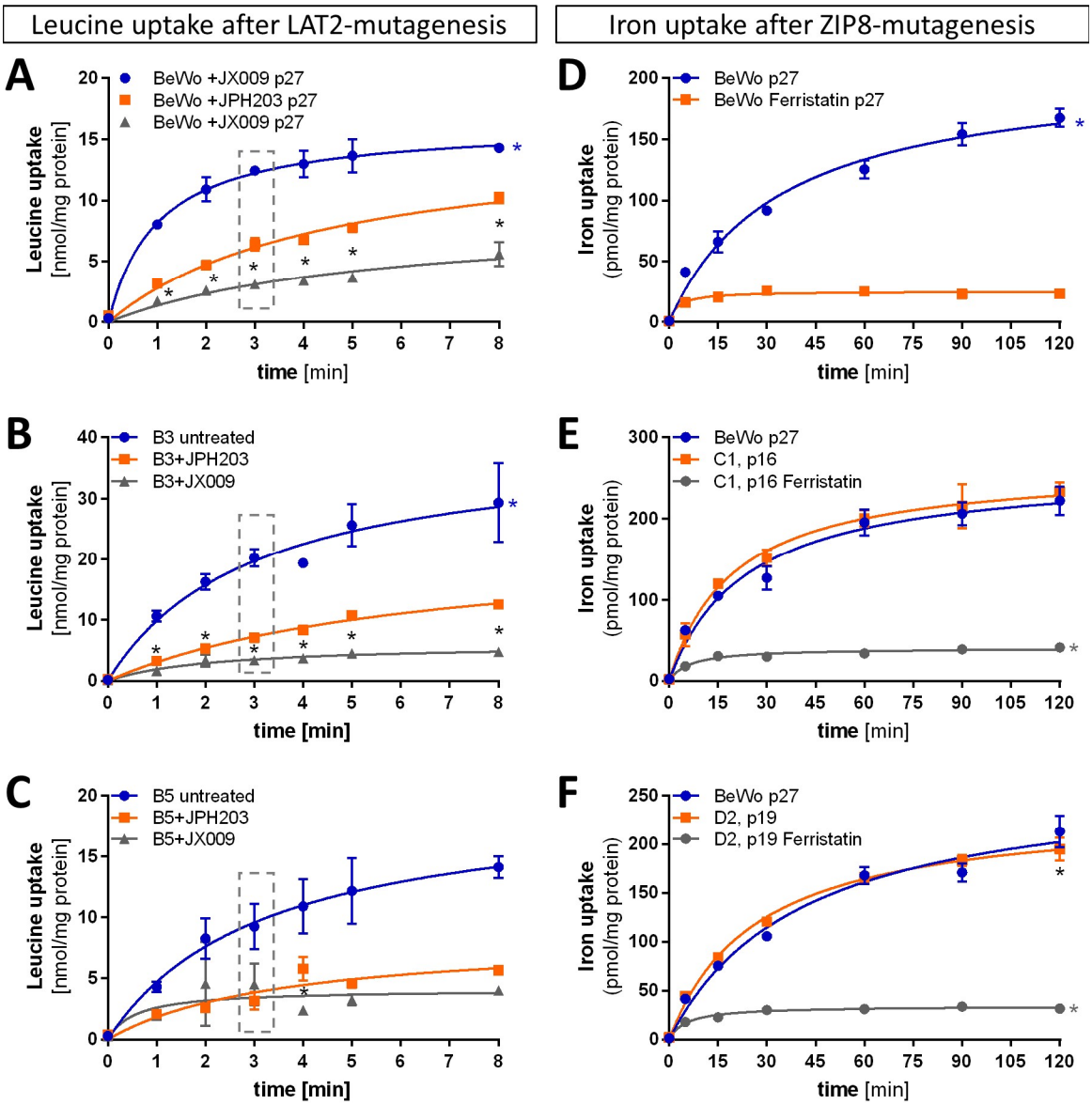

Figure 44: Functional characterization of CRISPR/Cas9-targeted BeWo cell lines by comparing leucine and iron uptake time courses of candidate knockout clones. In panel **A**, the inhibition of leucine (Leu) uptake of untransfected control BeWo passage number (p)27 cells by the LAT1-specific small molecule compound JPH203 led to a Leu uptake reduction after 3 min (dashed box) of 48% (**A**, orange). Additionally, the System L (mainly LAT1+LAT2) inhibitor JX009 blocked 76% Leu uptake within 3 min compared to control BeWo cells (**A**, grey). The Leu uptake kinetics of the two promising LAT2-knockout candidates B3 (**B**) and B5 (**C**) were compared to the "wildtype" respectively untargeted control BeWo cell line in **A**. B3 showed a 1.8-times increased Leu uptake efficiency within 3 min (**B**, dashed box) compared to control BeWo cells in **A**, while untreated B5 clones exhibited uptake levels similar to the control in **A** (**C**). Leu uptake of both B3 (**B**) and B5 (**C**) were reduced by JPH203 of 65% and 66% and by JX009 of 83% and 51%, respectively. There was clearly less difference between JX009 and JPH203 inhibition (difference between orange and grey curve) compared to control in **A**. **B&C**, A selection of LAT2_142 sgRNA and Cas9 plasmid transfected and FACS sorted cell lines, namely B2 and B5. The inhibitors JPH203 and JX009 were applied with a concentration of 10 µM during the 8 min of Leu uptake. Statistical significance between conditions was determined using the Holm-Sidak method, α=0.05, * $p<0.05$. In panel **D**, The inhibition of Transferrin-dependent iron uptake of untransfected control BeWo p27 cells by 50 µM ferristatin-II (NSC30611) inducing Transferrin receptor 1 (TfR1) degradation led to an iron uptake reduction of 82% within 60 min (**D**, orange). The two selected ZIP8-targeted (ZIP8_567)

knockout cell lines C1 (**E**, single sorted) and D2 (**F**, 100 sorted cells) showed without inhibition very similar iron uptake kinetics as the untransfected control BeWo p27 cell line. Furthermore, ferristatin-II inhibition conveyed for C1 85% (**E**) and for D2 a reduction of iron uptake of 80% within 60 min (**F**). There was no difference detectable between the two putative ZIP8-knockout candidate cell lines and the untransfected control BeWo p27. Ferristatin-II treatment was applied 4 h before and during the 120 min time course of the iron uptake assay. Statistical significance between conditions was determined using the Holm-Sidak method, $\alpha=0.05$, * $p<0.05$. In general, all uptake results were normalized to the protein concentration. Data are expressed as mean of 3 replicates for each time point.

3.3.5 Unsuccessful CRISPR/Cas9-mutagenesis in BeWo cells revealed by sequencing

CRISPR/Cas9 mutagenesis is depending on cellular double-strand-break repair. Since CRISPR/Cas9-mediated mutations result often in in-frame indel mutation with remaining function or partially function (Burger et al. 2016), we performed target site sequencing of mutant candidates to the end of the workflow. The four most promising knockout candidates were further analyzed by target site sequencing. The LAT2-targeted clones B3 and B5 were selected due to reduced difference comparing LAT1-specific inhibition by JPH203 and System L inhibition by JX009. ZIP8-targeted clones C1 and D2 were sent for sequencing due to characteristic regulation patterns in iron homeostasis gene expression on mRNA level (3.3.3) and promising changes on functional level (3.3.4). The sequences of all target sites perfectly matched the wildtype sequence (**Figure 45**) independent of which gene was targeted (B3/B5 compared to C1/D2) or whether the cells were single- or multi-sorted after transfection (C1 compared to D2).

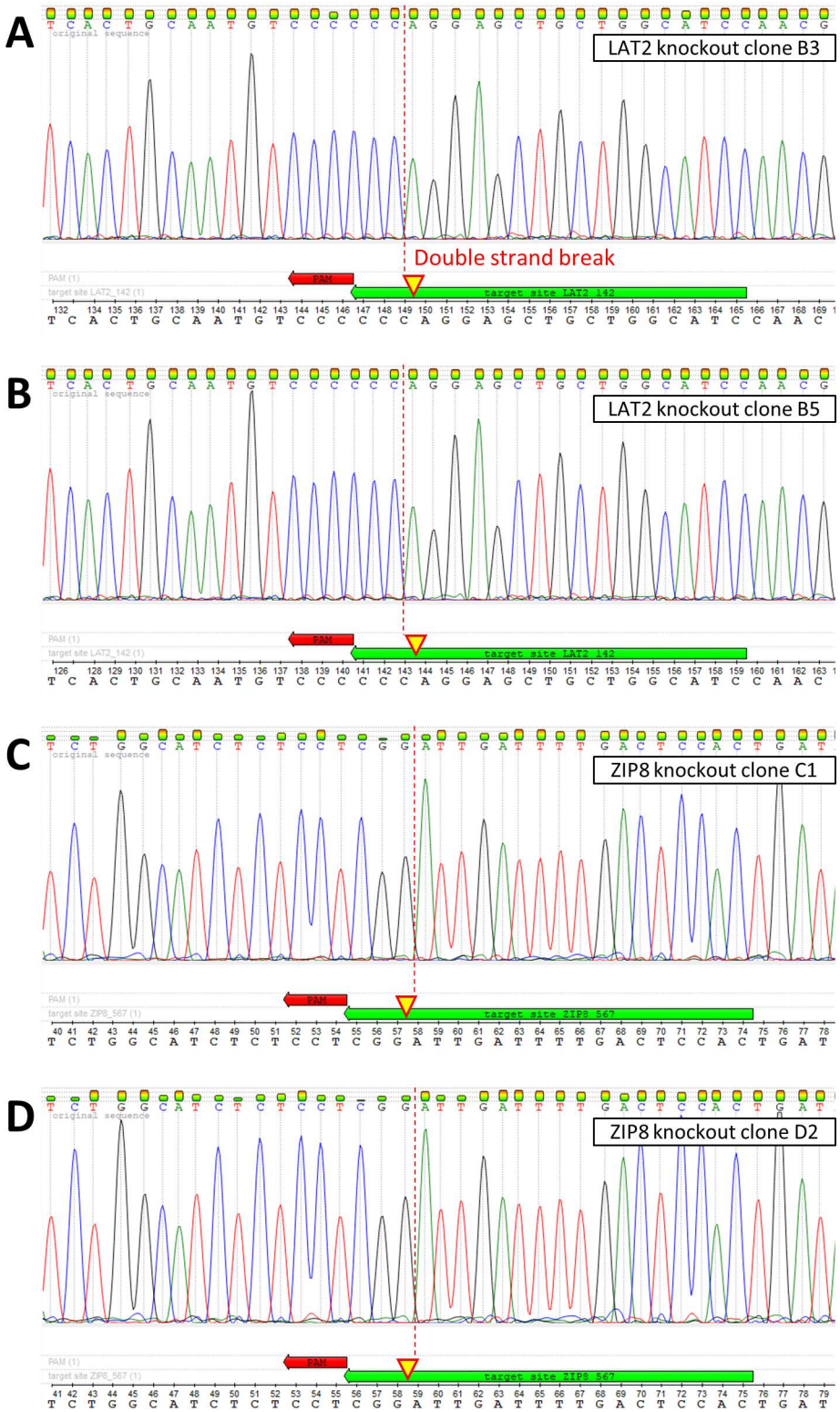

Figure 45: Sequence trace chromatogram analysis of the four most promising knockout candidates revealing unsuccessful CRISPR/Cas9-mutagenesis. None of the sequenced target sites of the *LAT2*-targeted knockout candidates B3 (**A**) and B5 (**B**), nor the sequenced target sites of *ZIP8*-targeted candidates C1 (**C**) and D2 (**D**) showed any sign of an insertion or deletion (indel) mutation. There were no indels detected close to the planned and Cas9-mediated double strand break (red dashed line) nor up- or downstream of the sequenced target site region. In parallel to the sequence trace chromatogram the previously designed target sites (green) and the corresponding PAM-sites (red) are annotated. In theory most indel mutations were expected close

to the site of Cas9-mediated double strand break 3 nucleotides upstream of the PAM sequence marked with a yellow triangle.

Nevertheless, to compare the mutagenesis efficiency between the two transfection methods based either on Cas9-plasmid (Xfect) or Cas9-protein (jetCRISPR) transfection and between different target sites, the CRISPR/Cas9-mutagenesis protocol used for BeWo targeting was applied on the easy-to-transfect HEK-293 cells. Unfortunately, no DNA shedding by T7-Endonuclease 1 and therefore no DNA mutagenesis was detected for any condition and target site analyzed (**Figure 46**). Of note, there was no difference in DNA shedding even when targeting a gene like *hCG* without expression in HEK-293.

Another straightforward method to quantitatively assess genome editing using chromatogram sequencing trace data is based on the tracking of indels by decomposition (TIDE) algorithm (Brinkman et al. 2014). Therefore, we uploaded sequence trace data of two standard capillary sequencing reactions in the ab1-format as provided by Microsynth to the https://tide.nki.nl/ online platform. The TIDE software quantifies the editing efficacy and identifies the predominant types of insertions and deletions (indels) in the DNA of a targeted clone pool. **Figure 46B** shows a representative example of the TIDE results from the *ZIP8* mutant candidate D2. The D2 was a clone pool that started originally with 100 sorted cells after transfection. In contrast to enzyme-based Cas9-editing detection method above, TIDE could detect a very low mutagenesis efficiency of 5.4%, which was below the detection limit of the T7-Endonuclease 1 assay.

In summary, we designed target sites, established methods and strategies to analyze CRISPR/Cas9-mutant candidates on expressional and functional level. However, within the framework of this thesis we were finally not able to generate BeWo knockout cell lines for our nutrient transporter genes of interest.

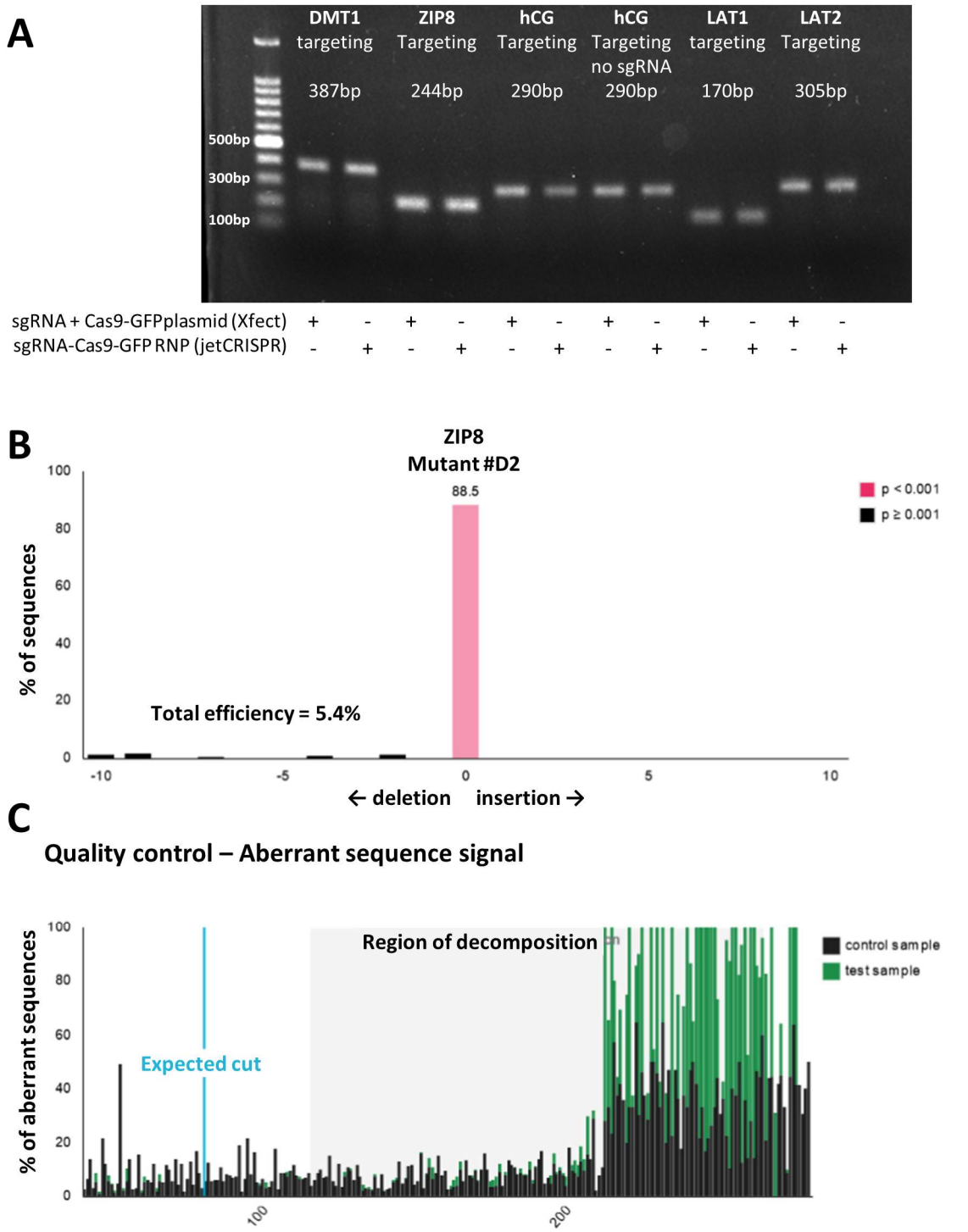

Figure 46: Undetectable Cas9-nuclease activity in transfected HEK-293 cells by T7-Endonuclease 1 assay, and low mutation efficiency detected by Tracking of insertion or deletion (indel) by Decomposition (TIDE) analysis. Easy-to-transfect HEK-293 cell were treated with different transfection reagents together with either target site-specific sgRNA and Cas9-GFP plasmid or with sgRNA-Cas9-GFP protein ribonucleotide complexes. **A**, After transfection, the genomic DNA of unsorted cells was isolated, the target site amplified in a conventional PCR, digested by T7-Endonuclease 1 and finally analyzed on a 1% agarose gel T7 Endonuclease 1 cleaves non-perfectly hybridized DNA. This would lead to a shedding of DNA, if there are different sequence variants after CRISPR/Cas9-mutagenesis. Different conditions were tested for efficient CRISPR/Cas9-mutagenesis. The two transfection protocols sgRNA+Cas9-GFPplasmid (Xfect) and sgRNA-Cas9-GFP RNP (jetCRISPR) were directly compared targeting different genes, such as *LAT1*, *LAT2*, *DMT1*,

ZIP8, but also *hCG* as silenced or unexpressed gene in HEK-293 cells. However, there was no DNA shedding detected independent of the transfection method or target gene (**A**). Expected amplicon sizes are given below the target gel labels: LAT1 MK1, 170 bp; LAT2 142, 305 bp; DMT1_1312, 387 bp; ZIP8 567, 244 bp; hCGB3, 290 bp. **B**-**C**, Tracking of indels s by Decomposition (TIDE) analysis of *ZIP8*-targeted and Xfect plasmid transfected BeWo cells. The sequence trace chromatogram data were uploaded on https://tide.deskgen.com. The program detects indel mutations based on the Sanger sequencing information and analyzes not only the highest peak, but also the noisy peaks behind. It is possible to detect mutations within a mixture of differently mutated cells compared to the wildtype control. The indel spectrum shows 88.5% consistency with the control and deletions of 2, 4, 9 or 10 nucleotides (**B**)The lower panel aberrant sequence signal panel does not show any frame shifts at the expected cutting site 3 nucleotides upstream of the PAM sequence, which would lead to a chromatogram data decomposition by various insertions or deletions (**C**) There was decomposition detected, due to poor sequencing data quality after 220 bp.

4 Discussion

This chapter includes the structured discussion of all key findings and results emerging from the experimental part of the PhD project. The previously defined specific aims (see 1.6.1 on p.29 and 1.6.2 on p.30) are discussed in corresponding sequence in the two sections amino acid and iron transport. Beside these two clinically oriented parts, there is an additional methodological part discussing the current state of CRISPR/Cas9-mediated trophoblast mutagenesis in our research group. The hypotheses are discussed in the conclusion part.

4.1 Amino acid transport

Since studies in the 1970s have shown that concentrations of most proteogenic amino acids are higher in the fetal compared to the maternal circulation, there is the central dogma that most amino acids are actively transported across the placenta against a counter-directed gradient (Philipps et al. 1978). We hypothesized that counter-directed materno-fetal amino acid gradients have an impact on the function of amino acid transporters such as LAT1 and thereby affect transplacental amino acid supply. Thus, the maintenance of amino acid gradients between the maternal and fetal circulation is essential for a normal pregnancy and for adequate fetal growth.

As only old and incomplete data on amino acid concentrations are found in literature, we first aimed to determine maternal and fetal concentrations of the 20 proteogenic amino acids in sera of healthy term pregnancies (aim A1). Subsequently, we performed correlation analyses between materno-fetal amino acid gradients as concentration differences of fetal and maternal compartments and parameters characterizing the maternal nutritional condition and fetal growth (A2). To test the resulting associations from a clinical and observational point of view with functional assays, we studied the effect of substrate concentrations on System L-mediated leucine uptake into trophoblasts and. Continuing, we determined the direct effect of a materno-fetal gradient on amino acid leucine transport across the placental barrier *in vitro* with BeWo cells using the Transwell® system (A3).

In a second step, we investigated the influence of extracellular amino acid concentrations on the functional level by assessing exchanger-mediated Leu uptake in conventional cell

culture of HT-29 and BeWo cells at two differentiation stages, to characterize the effect of trophoblast differentiation on placental leucine transport (A4).

In the third more transporter-oriented section of the amino acid part, we focused on the dissection of the single transporter by specific inhibition to elucidate the role of LAT1 and LAT2 in Na^+-independent leucine transport across the placenta using small molecule inhibitors as tool compounds (A5).

Each part of these three main sections of the amino acid project is separately discussed below (4.1.1-4.1.3).

4.1.1 Materno-fetal amino acid gradients are crucial for transplacental amino acid transport and correlate with selected maternal and fetal parameters

Variation of maternal and fetal amino acid concentrations

In agreement with literature (Pohlandt 1978; Malinow et al. 1998; McIntosh, Rodeck, and Heath 1984; Irene Cetin et al. 1988; Karsdorp et al. 1994; Irene Cetin et al. 2005; Bajoria et al. 2001; Cockburn et al. 1971) we detected higher amino acid concentrations in the fetal as compared to the maternal circulation. Within our cohort we found in materno-fetal paired analysis significant differences in the amino acid concentration especially for essential or conditionally essential amino acids such as Thr, Val, Trp, Lys, Gly and Tyr (**Table 8** on p.64). Although there are 15 different amino acid transport systems characterized in the human placenta and several amino acids are transported by different systems (Thomas Jansson 2001), half of the amino acids showing significant differences are preferentially substrates for system L transporters, particularly LAT1 (see concentrations of selected LAT1 substrates schematically depicted in **Figure 47C** on p.144).

The placenta is a metabolically active organ and interorgan exchange with fetal liver for non-essential amino acids like Gly to Ser and Gln to Glu was demonstrated in temporal amino acid interconversion characterization of sheep pregnancy using stable isotope methods (Marconi et al. 1989; Vaughn et al. 1995). Therefore, the comparison between maternal and fetal amino acid concentrations allows conclusions on materno-fetal transfer, but without including amino acid metabolism this can be misleading (I. Cetin 2001). It has been shown that the nutritional stage of the mother affects the use of amino

acids as fuels by the placenta during pregnancy (Lemons, Reyman, and Schreiner 1984). Due to standardization of sampling and selection of patients that delivered exclusively by cesarean section, we did not expect significant effects of fasting in this study. For Cys unexpectedly low concentrations were detected (**Figure 12** on p.63, **Table 8** on p.64), and the reason for this phenomenon is unclear. Increased preanalytical degradation of amino acids or analytical problems with amino acid detection can be largely excluded, due to stable measurements of other amino acids, measurement repetitions and validity of internal controls. On the other side, there could be metabolic reasons for low Cys levels in late pregnancy. Sulfur-containing amino acids can be interconverted by transsulfuration (Met→Cys) or transmethylation (Cys→Met). Due to the absence of transsulfuration activity in the fetal liver and high transmethylation activity for growth and cell proliferation, Cys consumption increases and becomes essential for the fetus in the 3rd trimester (Gaull, Sturman, and Räihä 1972; Sturman, Gaull, and Raiha 1970). Cys is also required for the synthesis of various proteins and glutathione. Therefore, high amounts of Cys are consumed and must be transported across the placenta particularly in the 3rd trimester, when fetal growth, amino acid metabolism and oxidative stress reach a maximum (Myatt and Cui 2004; Casasco et al. 1997). However, due to the discrepancies of our measured Cys concentrations with previously published data, Cys was excluded from the subsequent correlation studies.

Fetal veno-arterial differences reveal different phases of placental amino acid homeostasis

There is a high heterogeneity in the literature regarding the predominance of positive or negative veno-arterial differences in the fetal blood. Few studies showed positive FV-FA differences for most amino acids in healthy pregnancies (Irene Cetin et al. 1988), others larger or smaller proportions of negative FV-FA differences (Hayashi et al. 1978; Prenton and Young 1969; Velazquez et al. 1976; Steingrímsdóttir, Ronquist, and Ulmsten 1993; Irene Cetin et al. 2005; Tsuchiya et al. 2009). Cetin et al. found positive FV-FA amino acid concentration differences for most essential amino acids in normal fetuses, but less in intrauterine growth restriction (IUGR) (Irene Cetin et al. 1988). Furthermore, negative FV-FA differences were also interpreted as sign for fetal maturation by comparing amino acid concentrations in term and preterm (Hayashi et al. 1978). Due to the paired analysis mode, veno-arterial (FV-FA) differences of the 22 patients in our study cohort (**Table 7** on

p.62) were individually analyzed. Although the means of FV-FA differences for all amino acids were negative, 45% of analyzed cases showed a clearly positive FV-FA difference for most amino acids (**Figure 13** on p.65). Therefore, the negative mean FV-FA differences as listed in **Table 8** (p.64) is based on a highly heterogenic group of placentae being either in accumulative (positive FV-FA difference) or secretory (negative FV-FA difference) mode. 18 out of 22 placentae (82%) showed either accumulation or secretion of most amino acids into placenta towards the maternal circulation, while the remaining four placentae were showing a mixture of both modes (see ≈-marked placentae in **Figure 13** on p.65). Since fetal growth is dependent on amino acid supply throughout the pregnancy, the placenta likely alternates throughout pregnancy between amino acid accumulation and secretion modes. Total amino acid concentrations in cattle are following a circadian rhythm depending on growth hormone levels and food intake (Ndibualonji et al. 1995). A circadian effect on amino acid concentrations has also been found in human young males where the concentrations of 16 amino acids varied throughout the day (Wurtman et al. 1968). Another study reported that the circadian changes of amino acid concentrations in pregnant women were smaller than in non-pregnant women. Herein the authors observed changes of plasma glucose, free fatty acids and insulin levels suggesting a daily switching rhythm between anabolic and catabolic stages in pregnancy by (Phelps, Metzger, and Freinkel 1981). In summary, the different phases of placental amino acid homeostasis in individual pregnancies suggest a temporary switch between accumulation and secretion phases in placental amino acid transfer, which should be confirmed by *in vivo* determination of FV-FA differences. This could be achieved by using *in utero* cordocentesis allowing a relatively unstressed sampling unaffected by parturition and at different gestational ages (Irene Cetin et al. 1990; McIntosh, Rodeck, and Heath 1984).

Association between maternal/fetal amino acid concentrations and anthropometric data

To estimate the relevance of amino acid concentrations in different maternal and fetal compartments, and to investigate the importance of materno-fetal gradients, Spearman correlations with fetal and maternal anthropometric values were performed within our healthy study cohort. The results of our analyses complement data from a previous study that performed correlation analysis between amino acid concentrations among different maternal and fetal compartments (Holm et al. 2017).

Maternal amino acid concentrations correlate with maternal weight and BMI

Exchanger-mediated amino acid transport, including the transfer of large neutral amino acid by system L transporters, depends on the availability of their exchange partner (Jane K. Cleal et al. 2007). The transfer of essential amino acids can be affected, if amino acid concentration gradients across the placental barrier are changed (Hill and Young 1973). To investigate the potential impact of maternal, fetal and placental parameters, amino acid concentrations were tested for correlations with all available anthropometric values (**Table 7** on p.62). Remarkably, maternal (MV) and fetal (FA and FV) concentrations of essential amino acids such as the LAT1- substrates Val, Leu, Ile, Met, Phe, Tyr and His were positively correlated with maternal weights and BMI both before pregnancy and at *partum* (**Figure 14** on p.69 and **Table 9** on p.67). On the other side, the fetal amino acid levels of Val, Ile and Pro seem to be more dependent on the mother's preconceptional weight rather than on the maternal weight at the end of pregnancy. Similarly, fetal amino acid concentrations of Val, Leu Ile, and Pro were correlated more often with preconceptional BMI than with BMI at *partum*. It has been shown that preconceptional body weight has a lasting impact on gestational weight gain, fetal growth and contribute to develop obesity *postpartum* (Gunderson and Abrams 2000). Obese women are predisposed to get babies that are large for gestational age, even when they show the same gestational weight gain as non-obese women (Niswander et al. 1969; Melzer and Schutz 2010). Therefore, high amino acid levels before pregnancy tend to stay high throughout gestation and influence fetal amino acid levels at term. These results are in line with observations during temporal maternal infusions with increasing amino acid concentrations. These infusions resulted in a temporal fast increase of maternal amino acid concentrations and enhanced umbilical amino acid uptake in humans (Ronzoni et al. 1999) and sheep (Jozwik et al. 1999), but increased MV concentrations were ineffective after prolonged amino acid infusion in pregnant sheep (Jozwik et al. 1999). This inhibitory effect on fetal amino acid uptake were observed to a greater extent if large neutral amino acid were infused (Jóźwik et al. 2004). On the other hand, placental amino acid supply is highly vulnerable to maternal undernutrition. This was for instance detected as a consequence of the Dutch famine in the second world war, when newborns were growth restricted and showed an increased incidence of obesity and metabolic and cardiovascular disease in adulthood (Roseboom et al. 2011).

Amino acid gradients are associated with maternal and placental weight

Materno-fetal amino acid gradients of Ile, Pro, Phe, Tyr, and His correlated with anthropometric data characterizing the weight and the nutritional stage of subjects, respectively (**Table 9** on p.67). Of note, since amino acid levels are generally higher in the fetal as compared to the maternal circulation, those amino acid gradients are negative values and represent counter-directed materno-fetal gradients. The positive correlation between counter-directed materno-fetal gradients and anthropometric data indicates that increasing maternal amino acid levels lead to less-negative, smaller materno-fetal gradients. In other words, the heavier the mothers were before pregnancy or the more weight they gained, the smaller (more positive) the counter-directed gradients across the placental barrier were. Interestingly, the gradient of Gly was negatively correlated with gestational weight gain. Although there is a high Gly demand for fetal growth and consequently the Gly concentration in the fetal circulation is high, there is compared to Leu very low materno-fetal transport of Gly (Irene Cetin et al. 1995), probably due to Ser-Gly transformation through hydroxymethyltransferase activity in the fetus (Rohan M. Lewis et al. 2005). The association between Gly gradients and weight gain values suggest an increased materno-fetal Gly transport or fetal Ser-Gly transformation, if the weight gain is high. Excess or lack of gestational weight gain was related to various pregnancy complications and cardiovascular diseases and obesity in the offspring (Gaillard 2015; Mamun, Mannan, and Doi 2014). Although a recent multi-cohort meta-analysis associated gestational weight gain with an increased risk for preeclampsia, gestational diabetes, preterm birth and other disorders, weight gain remains a multifactorial parameter depending on maternal fat accumulation, fluid expansion, and the growth of fetus, placenta and uterus (Voerman et al. 2019). Of note, both gestational weight gain and maternal weight represent a modifiable risk factors that are considered in prenatal counseling. Therefore, reducing the risk by diet adjustment and gestational counseling could help to prevent adverse outcome including gestational diabetes (Hedderson, Gunderson, and Ferrara 2010; Abrams and Laros 1986).

Additionally, we found a relationship between placental weight and counter-directed amino acid gradients of the non-essential amino acids Gly, Ala, Asp and Glu (**Figure 12** on p.63, **Table 8** on p.64). While Gly and Ala are transported by different transport systems

such as system A, GLY or ASC, and are converted or metabolized by the placenta (F. C. Battaglia and Regnault 2001; Thomas Jansson 2001), the anionic amino acids Glu and Asp are synthesized by fetal tissue and have no net transfer across the perfused human placenta (H. Schneider et al. 1979; Moores et al. 1994). In a correlation study on small for gestational age babies, system A transporter activity was compared to a variety of anthropometric parameters. It was found that system A activity positively correlated with fetal proportions like skin-fold thicknesses and placental weight (Harrington et al. 1999). Therefore, the combination of system A transporter activity and smaller Gly and Ala gradients could represent a placental adaption to produce and supply more substrate towards the fetus (Harrington et al. 1999).

Fetal amino acid concentrations and materno-fetal gradients affect maternal blood pressure

Fetal concentrations of essential large neutral AA such as Met, Val, Leu and Phe, but also non-essential AA like Gly, Ala, Ser, Asn, Asp and Lys were negatively correlated with maternal blood pressure (**Table 9** on p.67). Furthermore, materno-fetal gradients were positively associated with maternal blood pressure. Interestingly, smaller materno-fetal gradients as a result of lower fetal and higher maternal AA concentrations were associated with preeclampsia before (Cockburn et al. 1971; Evans et al. 2003). Offspring from hypertensive or preeclamptic pregnancy are often born with low birth weight, even more pronounced the earlier they were born (Xiong et al. 2002). Beside placental insufficiency to transfer nutrients into the fetal circulation through impaired placentation and reduced placental perfusion (Rana and Karumanchi 2017), it could be speculated that the failure to establish appropriate materno-fetal AA gradient contributes to diminished nutrient supply and hence reduced intrauterine growth.

4.1.1.1 Counter-directed amino acid gradients in vivo affect leucine uptake into trophoblasts and transfer across the placental barrier

Extracellular amino acid levels affect leucine uptake into differentiated trophoblasts

In the placenta there are accumulative transporters, exchangers and facilitators forming a complex placental amino acid transport system, which is dependent of intracellular *versus* extracellular, maternal *versus* fetal, and fetal *versus* maternal substrate gradients.

The complex network of these transport systems enables an efficient materno-fetal transfer of essential amino acids against a counter-directed gradient (Jane K. Cleal and Lewis 2008; Thomas Jansson 2001). Extensive computational modeling suggests beside active transport also facilitated transport across the BM, which is highly dependent of amino acid gradients across the BM (Panitchob et al. 2015; Widdows et al. 2015; Rohan M Lewis, Cleal, and Sengers 2020). However, if and how counter-directed amino acid gradients affect the LAT1-dominated exchanger-mediated materno-fetal transfer of an essential amino acids like Leu, has not been investigated yet. In a first step, we examined whether the Leu uptake capacity in BeWo cells is sensitive to increased extracellular Leu levels. As expected, extracellular Leu levels in the upper clinical range (167 µM) increased Na^+-independent uptake of Leu into the trophoblasts and into colon carcinoma cells (HT-29). The choriocarcinoma cell line BeWo (clone b30) which differentiates upon cyclic adenosine monophosphate (cAMP) stimulation and further develops a polarized trophoblast monolayer (Orendi et al. 2010), has been validated with *ex vivo* placenta perfusion (Poulsen et al. 2009; H. Li et al. 2013) and selected to explore transport mechanisms *in vitro* before (Heaton et al. 2008).

Next, we investigated, whether the differentiation stage of trophoblasts affects the uptake capacity for Leu. Indeed, differentiated BeWo-STB showed two times higher Leu uptake than undifferentiated BeWo-CTB or HT-29 cells (**Figure 16A** on p.73). Since all uptake assays were performed within 3 min, the increase of Leu uptake cannot be explained by expressional changes of Leu transporters. Furthermore, the inhibition experiment with the LAT1-specific inhibitor JPH203 (Endou et al. 2008) demonstrated that Leu uptake in trophoblasts is predominantly LAT1-dependent (**Figure 16B** on p.73). Meier et al. showed a 1:1 exchange stoichiometry of heteromeric LAT1 and LAT2 transporter and substrate selectivity allowing the exchange of one extracellular large neutral amino acid against a non-essential intracellular amino acid using the Xenopus expression system (Meier et al. 2002). The underlying mechanisms of trophoblasts to further increase Leu uptake upon differentiation without changing the concentrations of exchange partners are not clear yet. In human pregnancies, maternal-fetal transfer rates have been investigated *in vivo* by stable isotope infusions into the maternal circulation followed by

fetal blood sampling. The materno-fetal transfer rate of nonessential amino acids like Gly was significantly lower than for essential amino acids like Leu (Irene Cetin et al. 1995).

Effect of counter-directed amino acid gradients on materno-fetal leucine transfer

To test whether different extracellular amino acid concentrations have an effect on Leu transfer across the materno-fetal barrier, we conducted Leu transport experiments using the Transwell® system. Hereby we compared Leu transfer under equimolar Leu concentrations in the maternal and in the fetal compartment against a counter-directed Leu gradient (**Figure 17** on p.75). To our knowledge this is the first time, that the effect of a physiological counter-directed amino acid gradient was functionally assessed *in vitro*. Although the applied gradient created a strong fetal to maternal directed transport pressure, we observed higher materno-fetal transfer rates in presence of the counter-directed Leu gradient as compared equimolar Leu concentrations (**Figure 47B** on p.144). Additionally, the significant reduction of Leu transfer by the LAT1-specific inhibitor JPH203 (Endou et al. 2008) underlines the importance of LAT1 in materno-fetal transport of Leu, but likely also affects placental transport of other LAT1 substrates like Ile, Phe, Met, Tyr, His, Trp, Val, Cys and Thr (Napolitano et al. 2017). At the end of the experiment no intracellular Leu retainment was detected, independent if the intracellular Leu content was calculated or measured, suggesting Leu uptake rather than efflux towards the fetal compartment as limiting step (**Figure 17D** on p.75). Intracellular Leu retainment would indicate fetal efflux as transfer limiting step, as shown in Leu uptake studies using LAT1/LAT2 small molecule inhibitors (Zaugg et al. in press). The asymmetry of the transplacental amino acid flux is favored by rapid uptake from the maternal circulation and transfer towards the fetus. It has been shown that amino acid transfer towards the fetal side is more rapid than in the reverse direction (H. Schneider et al. 1987). The importance of effective placental amino acid transport systems rather than maternal amino acid concentrations as crucial factor for fetal growth is supported by findings of Bajora and coworkers (Bajoria et al. 2001). They observed that in monochorionic twins from which one was growth retarded, the concentrations of Val, Leu, Ile, Phe, and Arg were only reduced in the growth restricted twin, but normal in the co-twin not suffering from IUGR (Bajoria et al. 2001). Furthermore, counter-directed amino acid gradients might play a crucial role after their establishment at the beginning of the second trimester

of human pregnancy and before starting the phase of biggest fetal growth (Jauniaux, Gulbis, and Gerloo 1999). Based on these results we suggest the incorporation of transplacental amino acid gradients relevant for fetal development in computational modeling based on placental perfusion studies (R. M. Lewis et al. 2013; Widdows et al. 2015).

4.1.2 Trophoblast differentiation affects placental amino acid uptake

Induced trophoblast differentiation leads to expressional reorganization of System L transport

The current understanding of transplacental leucine transport is based on the interplay between accumulative transporters such as members of the System A-family and exchangers such as System L-family members (Jane K. Cleal and Lewis 2008). System A-family transporters like SNAT1, 2, and 4 are expressed at the MVM and accumulate small neutral amino acids against a concentration gradient in the STB in a Na^+-dependent manner(Thomas Jansson 2001). The amino acids accumulated by System A-transporters can be used as substrates to exchange for essential large neutral amino acids such as leucine by the System L-exchangers LAT1 and LAT2 across the MVM into the STB. The principles of amino acid uptake at the MVM are largely characterized, but the contribution of single transporters in amino acid transfer across the BM to the fetus is less clear.

Therefore, we investigated the expression and localization of LAT1 in the human placenta by immunohistochemistry of term placental tissue and by immunoblotting of MVM- and BM-enriched membrane preparations. We found an exclusive apical expression of LAT1 at the MVM confirming previous reports (Gaccioli et al. 2015; Kudo and Boyd 2001).

BeWo cells represent a suitable model comparable to primary trophoblasts

So far most mechanistic studies are based on LAT1-overexpressing cell models like human colon cancer-derived HT-29 (Oda et al. 2010), mammary gland derived MCF-7 cells (Huttunen et al. 2016), Pichia pastoris(Costa et al. 2013) or reconstituted 4F2hc-LAT1 proteoliposomes (Napolitano et al. 2015). Acquiring further detailed knowledge on the complex mechanisms regulating materno-fetal amino acid transport at the placenta level could be beneficial to clarify the relevance of LAT1 and LAT2 in gestational diseases such as IUGR and LGA (Lager and Powell 2012). To choose an appropriate physiological

placental cell model, we compared the BeWo cell line with isolated primary human trophoblasts at different stages of differentiation by analyzing LAT1/LAT2 mRNA and protein expression and leucine uptake. Spontaneous differentiation in primary trophoblasts and forskolin-mediated differentiation in BeWo cells provoked expressional changes of LAT1, LAT2 and 4F2hc on mRNA and protein level (**Figure 20** on p.80). Our results demonstrated that the syncytialization process induced changes in the LAT1:LAT2 ratio as well as in 4F2hc expression in both trophoblast models (**Figure 20** on p.80) and resulted in an increased leucine uptake under Na^+-free conditions (**Figure 21** on p.82). These findings imply that differentiation induces a specialization process both in primary trophoblasts and BeWo cells, which results in an increased uptake, transport or transfer capacity as previously shown for the alanine-serine-cysteine-transporters and for alpha-aminoisobutyric acid transport (Furesz, Smith, and Moe 1993; P. I. Karl, Alpy, and Fisher 1992). This concept is in line with recent findings that differentiation processes such as syncytium formation resulted in an upregulation of MVM associated membrane proteins (Ohgaki et al. 2017).

Based on the validation of expression in the two trophoblast cell models (**Figure 20** on p.80) and comparable uptake behavior (**Figure 21** on p.82), the BeWo cell line was chosen to test the effect of different SLC7-specific inhibitors.

4.1.3 Specific inhibition of SLC7 transporters reveal the relevance of single solute carriers in placental nutrient acquisition

The response to LAT1- and System L-specific inhibition reveals the relevance of single transporter in transplacental leucine uptake and transfer

The low molecular weight inhibitors JPH203, JG336, JX009 and JX020 were assessed for their capacity to reduce leucine uptake into trophoblasts (**Figure 22** on p.85) and leucine transfer across the placental barrier (**Figure 24** on p.88). Due to the varying SLC7-specificity, different inhibition patterns were expected. JPH203 was previously reported as potent, LAT1-specific inhibitor (Oda et al. 2010; Enomoto et al. 2019; Cormerais et al. 2019; Muto et al. 2019; Häfliger et al. 2018; Yothaisong et al. 2017). JX009 has been described in the patent literature (Endo et al. 2008) to inhibit LAT1-mediated transport with similar efficacy as JPH203, albeit with significantly lower specificity, i.e. it is also a

potent LAT2 inhibitor. Beside the meta-tyrosine JX009 with a bulky side chain at the hydroxy group of the phenol, we additionally tested JX020 representing a bicyclic constrained meta-tyrosine (chemical structure is shown in **Figure 22** on p.85). Within the NCCR TransCure network in collaboration with the group of Prof. Karl-Heinz Altmann, we found phenyl or benzyl side chains on the tyrosine or meta-tyrosine as the minimum to generate an inhibitor that cannot be transported by LAT1. Due to the bicyclic structure of JX020, the flexibility is limited and the conformation is predetermined. Therefore, JX020 was more efficient inhibitor than JX009. Of note, similar bicyclic nitrogen mustards have already been described as system L inhibitors (Vistica 1983; Haines et al. 1987). As no other LAT2 inhibitors have been described in the literature, JX009 was considered the best available tool for the assessment of LAT2-related transport of leucine. JG336 was prepared based on a limited structure/activity relationship (SAR) study on JPH203 that investigated the effects of electron-donating (such as the methoxy group in JG336, see dashed red box in **Figure 22B** on p.85), electron-withdrawing and bulky substituents on the phenyl moiety at the 2-position of the benzoxazole ring on transport inhibition. The additional methoxy group in JG336 resulted in 3.8-times lower EC_{50} values in BeWo-CTB (**Figure 22B** on p.85) indicating that the inhibition efficiency of JPH203 was indeed increased by this modification.

Leucine uptake

Our results demonstrated that all four compounds are highly efficient LAT1 inhibitors, but JX009 and JX020 conveyed additionally LAT2 inhibition. Based on the complete leucine uptake inhibition of BeWo cells at the CTB stage, leucine uptake in undifferentiated trophoblasts seems to be completely dependent of LAT1 activity (**Figure 22** on p.85). Since the LAT1:LAT2 ratio in BeWo-CTB compared to BeWo-STB is lower as shown in the expression studies (**Figure 20** on p.80), JPH203 reduced leucine uptake in BeWo-STB by only 60%. This partial inhibition by JPH203 indicates that in BeWo-STB leucine uptake is mediated by alternative Na^+-independent leucine transporters such as LAT2, LAT3 or LAT4. JX009 and JX020 reduced leucine uptake near 100% regardless of the trophoblast differentiation stage with a low EC_{50} in the range of JPH203, suggesting that both JX009 and JX020 blocked most (if not all) Na^+-independent leucine uptake transporters. Thus, JX009 and JX020 are the first characterized System L-specific leucine uptake inhibitors in

the low µM-range (EC_{50}<4 µM; **Figure 22** on p.85) for use in placental cell models. To date, the most widely used SLC7-specific inhibitor is the non-metabolizable leucine analog BCH which has been also tested in this study (**Figure 23** on p.87) and other investigations (Otsuki et al. 2017; Kaji et al. 2010). In comparison to JX009 and JX020 this inhibitor is >100-times less effective and blocks System L-dependent amino acid transport with 709 µM in BeWo-CTB and 442 µM in BeWo-STB in the high µM-range (**Figure 23** on p.87). Nevertheless, further investigations of these small molecule compounds are needed to study viability, effects on amino acid metabolism and potential interactions with other transmembrane proteins such as System A-transporters.

Leucine transfer

To assess the functional importance of SLC7-transporters in leucine transfer across the placental barrier, the effect of the LAT1-specific inhibitors JPH203 and JG336 as well as the System L-inhibitor JX009 and JX020 were tested in the Transwell® system with polarized BeWo cells grown in a tight monolayer (**Figure 24** on p.88). Treatment with JPH203 during 6 h reduced leucine transfer across the placental barrier by 58%. Assuming 100% LAT1 inhibition after treatment with 10 µM JPH203 (approximately 5-times the EC_{50} of JPH203), these results suggest that more than half of the leucine transfer across the differentiated trophoblast monolayer was LAT1-dependent. The 3.8-times more efficient inhibitor JG336 (60% reduction), and the less specific System L-inhibitor JX009 (55% reduction) and JX020 (48% reduction) showed similar inhibition capacities as JPH203. These results demonstrate a predominantly LAT1-dependent leucine transfer across the polarized trophoblast layer which mimicks the physiological materno-fetal barrier (Xiao Huang et al. 2016). In these transfer studies we also measured the intracellular leucine content at the end of the experiment. In this context, the intracellular accumulation of leucine suggests that the efflux activity at the BM, i.e. the transport towards the fetus, represents the rate limiting process in materno-fetal transfer. In contrast, a reduced intracellular leucine content predicts leucine transport across the MVM into the trophoblast monolayer as the rate-limiting step (J. K. Cleal et al. 2011). In our experiments only the two LAT1-specific inhibitors JPH203 and JG336 caused a reduction of the intracellular leucine content (**Figure 24C** on p.88), indicating that LAT1-mediated leucine transfer occurs at the apical MVM. In contrast, the unchanged intracellular leucine

content after JX009 treatment suggests System L-transporter dependent leucine efflux across the BM. This is in agreement with the hypothesis that LAT1 is the major leucine transporter at the MVM, while other placental Na^+-independent System L-transporters such as LAT2, LAT3 or LAT4 mediate leucine efflux across the BM (see in introduction **Figure 5** on p.18) as has been previously proposed (J. K. Cleal et al. 2011; Thomas Jansson 2001; Kudo and Boyd 1990; Bodoy et al. 2005). Since the three tested inhibitors were applied at the maternal compartment, there is a certain membrane and cell layer permeability required to allow interactions with the transporters located at the BM. Permeability across the trophoblast barrier has not been investigated, but has been shown in Caco-2 cells for JPH203 (Wempe et al. 2012). Recently Lewis et al. demonstrated in a mathematical modelling approach of placental amino acid efflux based on placental perfusion data, that LAT2 allows the transport of a substrate across the BM without transport of another molecule in the other direction as normally expected from a classical exchanger (Rohan M Lewis, Cleal, and Sengers 2020).

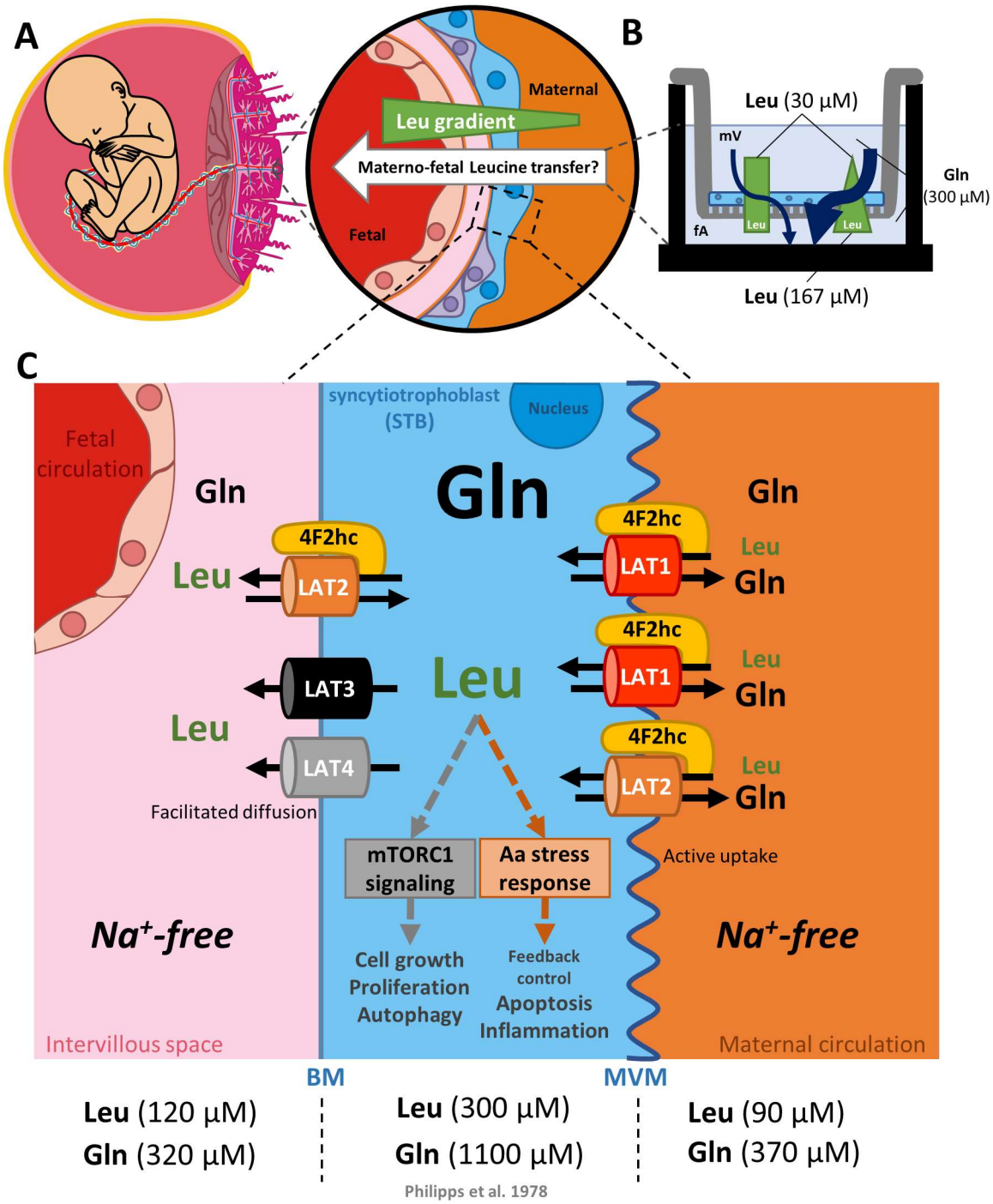

Figure 47: Schematic representation of leucine transport across the placental barrier induced through a counter-directed gradient and maintained by asymmetric LAT1/LAT2 expression. A, The placental barrier formed mainly by syncytiotrophoblast (STB) and located at the fetal border in direct contact with the maternal circulation. Since the fetal leucine (Leu) concentration is higher than in the maternal blood, the placenta needs to overcome a counter-directed Leu gradient by energy demanding active transport mechanism (panel **A** right). **B**, The comparison of Na^+-independent Leu transfer across the placental barrier in vitro using the Transwell® technique demonstrated for the first time an increased materno-fetal Leu transfer when a counter-directed Leu gradient is applied. **C**, The Na^+-independent uptake of the essential amino acid Leu from the maternal circulation (orange) across the microvillous membrane (MVM) into the STB (blue) represents the active step of placental Leu transport and is mediated by previously established intracellular co-substrate (e.g. glutamine, Gln) in the interplay with the amino acid exchangers

(LAT1/*SLC7A5* in red, LAT2/*SLC7A8* in yellow). LAT1 and LAT2, both expressed at the MVM, exchange one branched-chain amino acid amino acid (BCAA, like Leu) for another (in this case Gln), resulting in altered amino acid composition without changing the total intra-extracellular concentration. As indicated by the number of transporters (2 LAT1 versus 1 LAT2) LAT1 has been shown to be the major Leu uptake transporter at the maternal facing MVM. Under Na^+-free conditions there is no possibility for the STB to build up a Na^+-gradient driving System A amino acid uptake, hence only Na^+-independent System L transport is active. Furthermore, Leu is transferred across the BM by facilitators like LAT3-, LAT4-mediated diffusion driven by the extracellularly directed concentration gradient on the fetal side. The relevance of LAT1 compared to the other System L transporter was revealed by SLC7-specific inhibition studies (JPH203 and JG336 as LAT1-, and JX009 and JX020 as System L-specific small molecule inhibitors). This study demonstrated that the temporal application of transporter-specific inhibitors allows studying transporter interrelations in trophoblast models by avoiding an impact on cell fusion. The font size of the amino acid in the 3-letter code represent an estimation of their relative concentration in the fetal (left in pink and red), intracellular (middle in blue) and maternal (right in orange) compartment. Intracellular amino acid concentrations were taken from (Philipps et al. 1978).

4.2 Iron transport

In the second part of this PhD project, we compared two clinically well-characterized cohorts with balanced distribution of maternal and gestational age at *partum*. As expected, the GDM-specific clinical parameters showed not only increased periconceptional BMI, but also the clear LGA symptomatology of the GDM newborns (**Table 10** on p.90) verifying the suitability of our GDM cohort. Interestingly, also elevated maternal serum hemoglobin concentrations were detected which previously have been associated with increased risk for GDM (Afkhami-Ardekani and Rashidi 2009). However, the involved pathways linking iron homeostasis during pregnancy to disturbances in glucose handling and metabolism, as well as the role of the placenta in regulating materno-fetal iron transfer are largely unknown. To shed light on the involved pathways, we investigated the effects of hyperglycemic and hyperlipidemic conditions at distinct pathways controlling placental iron homeostasis *in vitro* using the BeWo cell model: at the level of uptake, transport, sensing and regulation of iron.

To investigate the relation between gestational hyperglycemia like in GDM and altered placental iron homeostasis, we successively discuss the five postulated specific aims (B1-5 on p.30). To challenge the hypothesis that the expression of placental iron-transporters and iron-regulatory proteins is altered in GDM, we characterized expressional changes of iron homeostasis genes in GDM-affected placental tissues (B1) and established and characterized trophoblast models mimicking human GDM conditions and investigated the effect of hyperglycemic and hyperlipidemic conditions on transplacental iron transfer

(B2). Furthermore, we used these hyperglycemic and hyperlipidemic models to identify cellular stress pathways responsible for altered placental iron homeostasis under hyperglycemic and hyperlipidemic conditions (B3) and to test whether increasing antioxidative potential rescues the hyperglycemic effect on placental iron homeostasis (B4). Finally, we discuss the suitability of an obesogenic mouse model developing GDM-like symptoms based on the altered expression of placental iron homeostasis genes (B5).

These five main sections of the iron transport project are separately discussed below (4.2.1-4.2.5).

4.2.1 Gestational diabetes alters placental iron homeostasis gene expression

To investigate if there is a functional relationship between GDM and disturbances in materno-fetal iron transport or placental iron homeostasis, we studied the expression of 24 genes, known to be involved in iron homeostasis, in control and GDM placentae. These included beside iron transporters and oxidoreductases also iron regulators and sensors. As no pathway for fetal iron excretion has been identified (Sangkhae and Nemeth 2018), nonheme iron transport across the placenta to the fetus was defined to be unidirectional. Consequently, fetal iron homeostasis depends exclusively on placental iron absorption and transport. Contrary to its vital importance in fetal development, the mechanism of materno-fetal iron transport is only incompletely understood (C. Cao and Fleming 2016).

In addition to *DMT1*, GDM placentae showed decreased mRNA levels of *FPN1*, and decreased protein levels for ZIP8 and TfR1. Despite downregulation of all these iron transport genes including *FPN1*, the only known transporter regulating iron export to the fetus, the total iron contents in GDM placental tissues were not increased in our cohort (**Figure 30** on p.98). In contrast to our study, recently published Fe concentrations in a bigger cohort of GDM and control pregnancies (n=38 each) showed reduced iron levels in GDM placental tissue (11%) and umbilical cord blood (12%), but not in maternal whole blood (Roverso et al. 2019). These findings suggest that reduced iron concentrations in the placenta and fetal serum could result from downregulated placental iron uptake under hyperglycemia. Therefore, a reduction of placental iron uptake could be a physiological mechanism to protect the placenta and the fetus from excessive, harmful iron concentrations. In this context also the observed upregulation of the ferroxidases HEPH and Zp in GDM placentae could play an important role as protective mechanism of

the placenta. Beside facilitating the export of ferric iron by FPN1, they oxidize the potential toxic ferrous iron and thereby reduce the oxidative levels at the placental barrier. In addition, these ferroxidases have a crucial role in oxidizing exported ferrous iron to ferric iron to enable loading onto fetal Tf, although some redundancy seems to exist (Fuqua et al. 2018).

Placental iron homeostasis depends on regulatory processes originating both from the mother, the fetus together with the placenta. Maternal, placental and fetal HEPC determine the rate of placental iron release to the fetal circulation through binding and degradation of placental FPN1 (Koenig et al. 2014). While HEPC is downregulated during normal pregnancy to ensure sufficient iron availability, we found increased placental HEPC levels in GDM. This indicates a placental mechanism to reduce systemic iron levels in the fetus by decreasing iron release towards the fetal circulation at the basolateral side of the STB by FPN1 degradation (**Figure 48A**). HEPC production is predominantly regulated at the transcriptional level, HEPC mRNA and protein levels show high correlation (Koenig et al. 2014). Therefore, the increased placental mRNA levels of *HEPC* found in GDM are in line with the concomitant downregulation of *FPN1*.

Beside the iron availability regulated by HEPC, the transfer of iron across the placental barrier depends mainly on the iron acquisition by activity of TfR1- and endosomal iron transport proteins like DMT1. Both, *TfR1* and *DMT1* are post-transcriptionally regulated by the iron-regulatory proteins IRP1 and IRP2. The IRPs bind at the stabilizing 3'-UTRs of *TfR1* and *DMT1* mRNA to the iron-responsive element (IRE) and further induce their translation (Wilkinson and Pantopoulos 2014). Thus, downregulation of *IRP1* could be responsible for the decreased TfR1 protein levels detected in GDM as compared to healthy controls, despite similar mRNA levels. Hence TfR1, DMT1, ZIP8 and FPN1 were significantly downregulated in GDM placentae though mRNA and protein expression did not always correlate. For example, DMT1 was downregulated on transcriptional but not on protein level (**Figure 28** on p.95). However, we observed a change in the intracellular localization of DMT1. This could be caused by altered subcellular trafficking, depending on the expression ratio between the two major splicing variants of *DMT1* (+/-IRE) in trophoblasts (Lam-Yuk-Tseung and Gros 2006; Chong et al. 2005), or altered ubiquitination (Foot et al. 2016). These cellular processes can result in reduced DMT1

transport activity without affecting the protein level. In brief, subcellular trafficking in trophoblasts may depend on the expression ratio between the two major isoforms *DMT1*-IRE and *DMT1*+IRE. *DMT1*-IRE undergoes clathrin-mediated endocytosis and is sorted to recycling endosomes, which allows Tf to release the two ferric iron molecules through acidification and creates the proton gradient required for DMT1-mediated iron transport (Lam-Yuk-Tseung and Gros 2006). As alternative to isoform-dependent trafficking, Foot et al. demonstrated a regulative interaction of NEDD4 family-interacting proteins (Ndfips) with both isoforms of DMT1 by acting as adaptors to recruit the ubiquitin ligase WWP2. Hence, ubiquitination of DMT1 and subsequent trafficking to the lysosome for degradation reduce the amount of DMT1 protein available to be transported to the cell membrane, reducing DMT1 activity and iron uptake (Foot et al. 2016).

As schematically summarized in **Figure 48A** (in yellow) GDM alters iron homeostasis in placental tissue through specific regulation of iron homeostasis genes involved in uptake (TfR1), transport (DMT1, ZIP8, FPN1), oxidation (zyklopen, Zp) and regulation (IRP1; HEPC) on mRNA and/or protein level. The major changes on expressional level comprise reduced DMT1, FPN1, ZIP8, and TfR1 abundance, and alterations in DMT1 localization. In analogy, trophoblasts under hyperglycemic conditions decrease iron acquisition by reducing TfR1 expression at the MVM, decrease transfer from the endosome into the cytoplasm through reduced expression of ZIP8 and mis-localization of DMT1 and diminish secretion of iron towards the fetal side through downregulation of FPN1.

4.2.2 The hyperglycemic and hyperlipidemic BeWo models allow to study functional effects by mimicking GDM-like expression patterns

To investigate the GDM-mediated effect on placental iron uptake on a functional level and to identify the underlying cellular mechanisms, we generated BeWo cell-derived hyperglycemic cell models. The BeWo cell line was chosen as primary trophoblasts freshly isolated from donated placentae do not proliferate and loose viability after a few days in culture (Xiao Huang et al. 2016). By examining BeWo cells cultured under N (normoglycemic), H (hyperglycemic) and HL (hyperglycemic and hyperlipidemic) conditions for 30 days, we were able to monitor and characterize the iron homeostasis-related expressional and functional adaptions occurring in trophoblasts over time. Hyperlipidemia was achieved by adding palmitic acid to the cell culture medium as free

palmitic acid has been associated with induced insulin resistance in different cell models (Sinha et al. 2004) and in GDM patients (Stirm et al. 2018). During the adaption process to hyperglycemic/hyperlipidemic culture conditions, the BeWo cells changed their morphology, due to increased energy availability, and showed extensive lipids storage as indicated by Oil red O staining. Interestingly, the hyperglycemic stimulation in BeWo cells resulted in very similar changes in the expression pattern of placental iron homeostasis genes as found before in GDM placentae. This strongly underlined that the established BeWo models are suitable for the identification of cellular pathways underlying the effect of hyperglycemia on placental iron homeostasis. Furthermore, we found that these trophoblasts cultured under H and HL reduced their Tf-mediated iron uptake already after 5 days of stimulation by more than 40% relative to N. The observed dramatic reduction of placental iron-uptake explains the inconspicuous iron-stores in placental tissue in combination with increased maternal hemoglobin levels. This is a clear indication for placental protection of fetal tissues from excessive iron-storage. Concomitantly, the observed alterations in placental iron-handling could promote increased iron-concentrations found in maternal serum (Roverso et al. 2019).

4.2.3 Autophagy and oxidative stress induce ferroptosis under hyperglycemic conditions and represent a potential target for treatment of altered iron homeostasis in GDM

To identify the cellular pathways mainly mediating the effects of GDM on placental iron homeostasis we focused on mechanisms that have been implicated in both GDM and cellular iron imbalance: ER-stress (Yung et al. 2016; Vecchi et al. 2009), autophagy (Avagliano et al. 2017; Dixon et al. 2012) and oxidative stress (Peuchant et al. 2004). Despite reports of increased ER-stress in GDM patients, we did not find marked changes in placental BiP-expression by immunoblotting. However, we detected reduced p62 protein and decreased LC3-II protein in H and HL compared to N. LC3-II is the lipidated, membrane-bound form of the widely used autophagic marker LC3 (Kabeya et al. 2000). Likewise, the downregulation of the p62 protein, also known as sequestosome or SQSTM1, indicates reduced autophagy, indicates reduced autophagy (Øvervatn et al. 2010). Further extensive analyses revealed increased oxidative damage and reduced antioxidative capacity in both hyperglycemic cell models. Both GSH depletion and accumulation of oxygen activated lipids as shown in **Figure 35A/C** on p.105 are two of the

main characteristics of the distinct regulated cell death process called ferroptosis. The non-apoptotic cell death pathway ferroptosis is induced by disruption of GSH synthesis, depends on high intracellular iron levels and accumulation of lipid peroxides (J. Y. Cao and Dixon 2016). Although our results have limited depths in the analysis of the cellular pathways like ER-stress and autophagy, they strongly suggest oxidative stress-mediated ferroptosis as a hallmark of the disturbed placental iron homeostasis which should be further investigated. So far hyperglycemia is not characterized as known promotor of ferroptosis, however our results including reduced GSH levels, disturbed transcellular iron transport and increased lipid peroxidation indicate ferroptosis as mediator between hyperglycemia and altered placental iron homeostasis.

To further confirm the concept that oxidative stress is a key pathway stimulated by hyperglycemia and a trigger for the placental regulation of iron-homeostasis, we performed rescue experiments by treating the cells with the antioxidant NaSe. Se-supplementation has been shown to protect trophoblasts from both endogenously and exogenously applied oxidative stress (A. Khera, Vanderlelie, and Perkins 2013; Alisha Khera et al. 2017). Reduced selenoenzyme activity during pregnancy results in oxidative stress within tissues was associated with premature birth, miscarriage, preeclampsia, and intrauterine growth retardation (Zachara 2018). NaSe supplementation has been shown to protect trophoblast cells from both endogenously and exogenously applied oxidative stress (A. Khera, Vanderlelie, and Perkins 2013) as selenium is essential for the expression and activity of the endogenous antioxidant systems dependent on the selenoenzymes glutathione peroxidases (GSH-Pxs), thioredoxin reductases (TrxRs), and selenoprotein P (SePP) (Alisha Khera et al. 2017; Zachara 2018). There are 3 different Se-dependent glutathione peroxidases present in humans, and these are known to add two electrons to reduce peroxides by forming selenole (Se-OH) and the antioxidant properties of these selenoenzymes allow them to eliminate peroxides as potential substrates for the Fenton reaction. Selenium-dependent glutathione peroxidase acts in association with GSH, which exists in high concentrations in cells and catalyzes the conversion of hydrogen peroxide or organic peroxide to water or alcohol while simultaneously oxidizing GSH (Kurutas 2016). Selenium supplementation strengthens the endogenous antioxidant potential of trophoblasts without disturbing the essential balance between oxidants and antioxidants

in living cells. Indeed, increasing the antioxidant potential in our experiments almost completely reverted the hyperglycemic effect on iron homeostasis genes. Additionally, Se supplementation protected BeWo cells under H and HL by reducing lipid peroxidation and eliminating protein carbonylation.

These results suggest that antioxidant supplementation is beneficial for pregnant women with increased risk of GDM, e.g. due to obesity, high fat diet, or excessive weight gain in pregnancy by protecting the placenta and the fetus against oxidative stress caused by hyperglycemia, high iron status or both. Furthermore, these findings support potential concerns regarding the recommendation of routine iron supplementation among iron-replete pregnant women (Rawal et al. 2017).

Figure 48B summarizes the findings associating GDM with altered placental iron homeostasis.

4.2.4 Iron deprivation affects glucose homeostasis in trophoblasts

José Manuel Fernandez-Real and colleges suggested a bidirectional relationship between iron metabolism and type 2 diabetes, i.e. iron affects glucose metabolism and glucose metabolism affects iron metabolic pathways (Fernández-Real, López-Bermejo, and Ricart 2002). As described before, oxidative stress seems to be a key factor in the effect of hyperglycemia and hyperlipidemia on placental iron homeostasis. However, there are contradictory publications about the relation between iron supplementation or maternal iron status and the increased the risk to develop GDM. While Afkhami-Ardekani et al. demonstrated in 34 women with diagnosed GDM and 34 non-GDM women an association between increased maternal iron status and GDM (Afkhami-Ardekani and Rashidi 2009), Chan et al. compared 565 women receiving 60 mg iron supplementation and 599 placebo controls and found that iron supplementation from early pregnancy onwards does not increase the risk of GDM (Chan et al. 2009). To our knowledge, there is no literature investigating whether different iron levels could have a direct effect on placental glucose uptake capability. Therefore, we challenged normoglycemic BeWo cells by inducing iron deficiency and iron overload and analyzed GLUT1 expression over time. GLUT1 expression and activity at the placental barrier and glucose concentration in the maternal blood are mainly responsible for the glucose transport during pregnancy (Baumann, Deborde, and Illsley 2002). Against our expectations iron deficiency, but not iron overload induced

GLUT1 expression and glucose uptake (**Figure 37** on p.110). Interestingly, in this experiment GLUT1 upregulation and stimulation of glucose uptake was pronounced especially after 15 µM DFO treatment. However, it is difficult to explain this phenomenon. Estimating an iron concentration in the iron deprivation experiment of approx. 3.3 µM (0.3 µM Ferric Nitrate $Fe(NO_3)_3$ + 3.0 µM Fe^{3+} from 10% FBS à 30 µM Fe^{3+} = <u>3.3 µM</u> Fe^{3+} in DMEM-lowG + 10% FBS) a DFO concentration of 15 µM is supposed to chelate 5-times more iron than theoretically available. Previously, GLUT1 expression at the BM has been shown to be rate-limiting in the materno-fetal transfer of glucose (Vardhana and Illsley 2002), hence alterations in GLUT1 expression at the BM would have significant consequences for fetal glucose supply. Whether the DFO-mediated increase in GLUT1 protein levels was affecting GLUT1 expression on BM or rather on MVM has not been investigated yet. Although GLUT1 expression at the BM was found elevated in GDM before, corresponding with a functional increase in glucose transfer (Gaither, Quraishi, and Illsley 1999), a better understanding and more experimental evidences are needed to estimate the presence and magnitude of a relationship between increased GLUT1 expression under iron deprivation and GDM. Of note, whether oxidative stress or other ferroptosis-related mechanisms are sufficient to affect placental glucose homeostasis via GLUT1 expression need further experimental approaches (as indicated in **Figure 48B** on p.154). However, at the present stage we were able to demonstrate that DFO-mediated iron deprivation does not only result in increased GLUT1 expression on mRNA and protein level, but also in enhanced glucose uptake into BeWo trophoblasts. These findings confirm a bidirectional relationship between iron levels and placental glucose homeostasis via oxidative stress as previously suggested (Fernández-Real, López-Bermejo, and Ricart 2002).

The schematic model in **Figure 48B** summarizes the effects of GDM and hyperglycemic conditions on placental iron homeostasis and materno-fetal iron transfer. Our data indicate that impaired autophagy and increased oxidative stress under hyperglycemic and hyperglycemic combined with hyperlipidemic conditions alter the expression and partly also the localization of transporters and thereby affect placental iron transfer. The observed adaptations could be part of a protective mechanism preventing oxidative damage for both the fetus and the placenta caused by hyperglycemia, highly oxidative

iron and excessive iron levels. Treatment with antioxidants such as selenium helps to balance placental oxidative stress levels by increasing GSH levels or DFO to reduce putative harmful iron levels and could thereby counteract impaired iron homeostasis found in GDM patients. These results indicate fundamental changes in the organization of transplacental iron transport under hyperglycemic conditions.

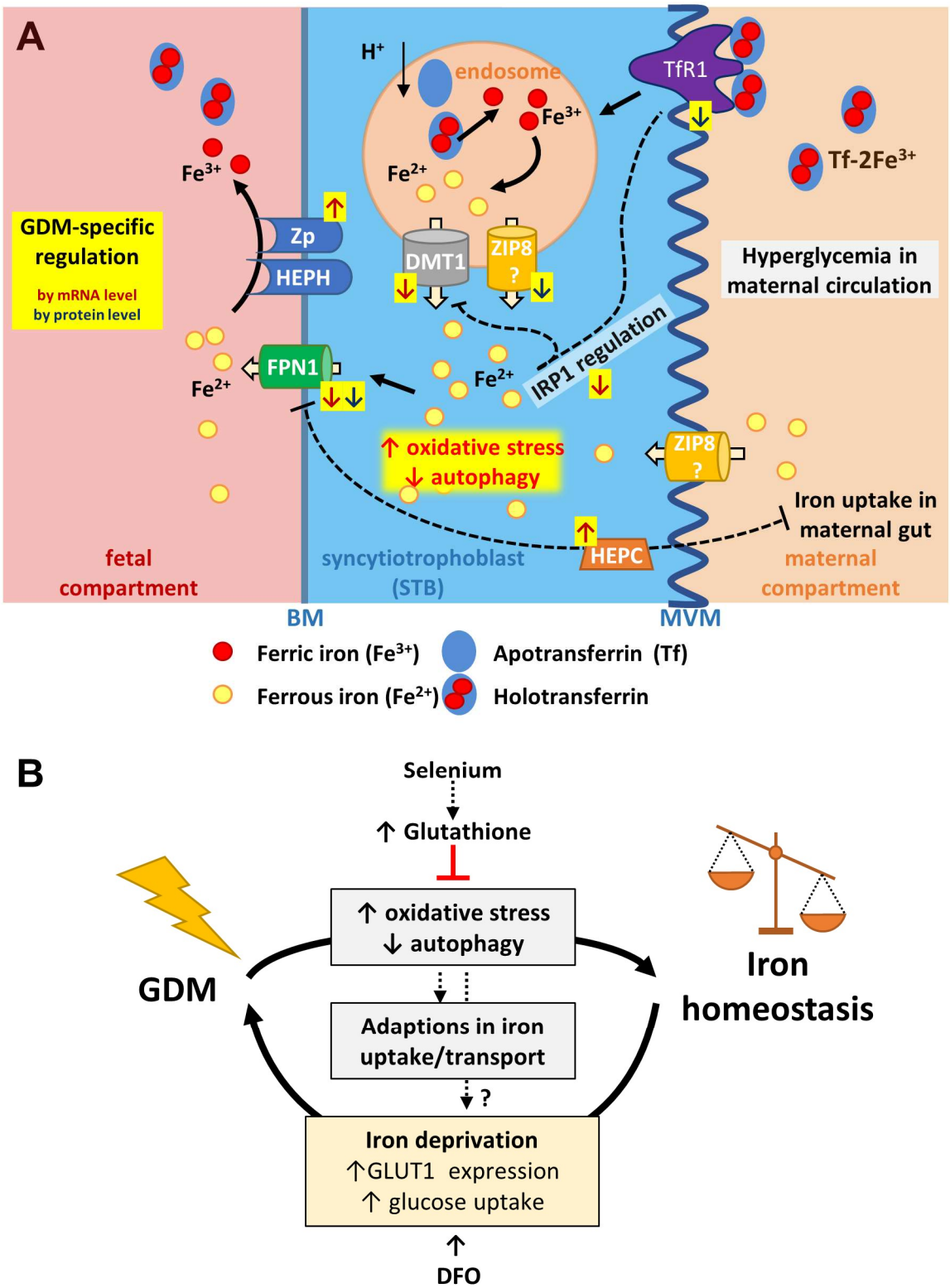

Figure 48: Schematic representation of the mechanisms and regulation of materno-fetal iron transfer across the placenta and dysregulation under hyperglycemic conditions. A, Iron (Fe) is transferred from the mother to the fetus across the blood-placenta barrier (right to left). The placenta is in direct contact with the maternal blood circulation via a monolayer of syncytialized trophoblast cells (blue). After transferrin receptor (TfR1)-mediated iron uptake by clathrin-dependent endocytosis at the maternal side of the syncytiotrophoblasts (villous membrane on the right side) into endosomes, divalent metal transporter 1 (DMT1) is supposed to release iron from endosomes into the cytosol. Cytosolic iron is transferred to the fetal circulation through the iron

exporter ferroportin (FPN1). The exact mechanisms as well as the role of other transporters such as the Zrt- and Irt-like proteins (ZIP) ZIP8 or ZIP14 in transplacental iron transfer are currently still unclear. (**A**, yellow) Gestational diabetes mellitus (GDM) alters iron homeostasis in placental tissue through specific regulation of iron homeostasis genes involved in uptake (*TfR1*), transport (*DMT1*, *ZIP8*, *FPN1*), oxidation (zyklopen, *Zp*) and regulation (iron regulatory protein 1, *IRP1*; Hepcidin, *HEPC*) on mRNA (highlighted dark red arrows) and/or protein level (highlighted blue arrows). The major changes on expressional level comprise reduced DMT1, FPN1, ZIP8, and TfR1 abundance, and alterations in DMT1 localization. The current study identified increased reactive oxygen species (ROS) and reduced autophagy as factors involved in altering iron homeostasis under hyperglycemic conditions. **B**, Schematic model summarizing the effects of GDM and hyperglycemic conditions on placental iron homeostasis and materno-fetal iron transfer. Our data indicate that impaired autophagy and increased oxidative stress under hyperglycemic and hyperglycemic combined with hyperlipidemic conditions alter the expression and partly also the localization of transporters and thereby affect placental iron transfer. Treatment with antioxidants such as selenium increasing glutathione levels or deferoxamine (DFO) reducing putative harmful iron levels could thereby counteract impaired iron homeostasis found in GDM patients.

4.2.5 Mice under HFHS diet represent a suitable GDM model to study iron homeostasis

Although the clinical parameters of our GDM cohort showed most of the typical characteristics described in literature (Rawal et al. 2017; Stirm et al. 2018), there are marked differences and variations concerning the time of diagnosis, optimal treatment and care during pregnancy and *postpartum*, making human GDM cohorts from clinical screenings highly heterogeneous (Nielsen et al. 2014). This was also found in our GDM cohort (**Table 10** on p.90). For example, we included in our the GDM group patients who were either treated with insulin (n=8) or received recommendations for a diabetes diet (n=3). Under these circumstances it is difficult to define the grade of placental exposure to hyperglycemia (Nielsen et al. 2014). Therefore, we aimed to find a suitable mouse model in which we could further explore the association between GDM and altered placental iron homeostasis. Indeed, it was reported in literature that wildtype mice receiving a western diet or HFHS diet from the first day in pregnancy onwards showed compromised maternal glucose tolerance and insulin sensitivity in association with dysregulated lipid metabolism, thereby mimicking typical GDM symptoms (Sferruzzi-Perri et al. 2013; Musial et al. 2017).

In collaboration with the University of Cambridge we made first steps in investigating this mouse model for the expression of iron related genes. Interestingly, analogous to human GDM, placentae from HFHS fed mice showed highly comparable expression patterns of iron homeostasis genes (**Figure 38** on p.112). Similar to human GDM, the placentae from

HFHS mice also seem to protect the fetus and themselves from excessive oxidative iron levels. Therefore, mice under HFHS diet could serve as suitable model to further investigate the molecular and physiological relationships between GDM and altered placental iron homeostasis and to study the therapeutic effects of antioxidants. The access to a mouse model mimicking human GDM would further allow to assess the impact of disturbed iron and glucose homeostasis on embryonic development. Furthermore, the high similarity between the expression pattern of iron homeostasis genes in human GDM and HFHS mice confirm and strengthen the observations discussed and characterized before, despite of the prevalent heterogeneity in the human GDM cohort.

4.3 Strategy for generation of SLC knockout trophoblast cell lines

Similar to other sequence specific genome editing tools such as TALENs (transcription activator-like effector nucleases) or ZFNs (Zinc-finger nucleases), CRISPR/Cas9 is also able to produce double strand breaks on a specific locus, but it has higher mutation efficiencies, is rather easy to use and can be used for multiplex genome editing (Ran et al. 2013). For example, it takes 3-4 days from the idea to target a certain gene until having the target site-specific sgRNA in hand (Bassett et al. 2013). This contrasts with the much more laborious re-engineering or selection of meganuclease, Zinc finger nuclease (ZFN) or Transcription activator-like effector nucleases (TALEN) proteins for each new genome target, which requires weeks or up to months (Robb 2019). This makes CRISPR/Cas9 mutagenesis a powerful tool for all kind of applications based on gene sequence manipulation including multiplex targeting and knock-in genome editing. CRISPR/Cas9 has been shown to be an efficient tool in genome engineering of primary cells, using adenoviral CRISPR/Cas9 vector human lung fibroblasts and human bronchial epithelial cells (Voets et al. 2017). Furthermore, human T-cells were efficiently targeted by electroporation-mediated transfection of RNP (Schumann et al. 2015). Recently, the progress for targeted gene therapy was published to engineer patient derived induced pluripotent stem cells with CRISPR/Cas9 (Dannenmann et al. 2020). However, CRISPR/Cas9 mutagenesis as technical tool has been rarely used in the field of placental nutrient transport research. It was reported that it is feasible to generate knockout BeWo cell lines using the CRISPR/Cas9 technology (Msheik et al. 2019; Kovács et al. 2019). Kovács et al. were able to knock out the gene of interest by electroporation of RNP complexes

into BeWo cells. Also embryonic stem cells were successfully knocked out for the ETS domain-containing transcription factor (*ERF)* gene, coding for a transcription factor involved in the differentiation of trophoblasts (Si et al. 2019). Forbes et al. compared the transfection efficiency of BeWo to primary trophoblasts transfected with different cationic lipid-based reagents and electroporation method (Forbes et al. 2009). They found that transfection efficiency in BeWo cells (40-70 %) is generally lower or similar to those of primary cells (40-95%).

Within this study, we aimed to generate stable knockout BeWo cell lines to study the relevance of single nutrient transporters in the complex placental amino acid and iron transfer across the human placenta.

Targeting single gene sequence by CRISPR/Cas9-mutagenesis allows the assessment of the role of a specific transporter in complex nutrient transport pathways such as materno-fetal amino acid or iron transport. Trophoblast cells lacking the function of single nutrient transporter by CRISPR/Cas9-mediated knockout, could help to reveal their role at the materno-fetal barrier in the human placenta. Novel findings in this context are important to unravel the causes and consequences associated with impaired transfer of nutrients in specific pregnancy diseases.

There are only few published articles about CRISPR/Cas9-mutagenesis in placental research. Recently, knockout BeWo cell lines were generated using the CRISPR/Cas9 technology for transcriptomic profiling to identify new target genes relevant for trophoblast fusion using BeWo and JEG-3 cells (Msheik et al. 2020). There were two major strategies to introduce sgRNA and functional Cas9 for mutagenesis via double-strand-break by non-homologous end joining (NHEJ). We tested the transfection of Cas9-plasmid and sgRNA (target-specific ribonucleic acid generated by IVT or transfection of preassembled complexes of sgRNA and Cas9, also called RNP. As mentioned above, Kovács and colleges were able to knock out the gene of interest by electroporation of the RNP complex into the cells (Kovács et al. 2019).

4.3.1 Design of potential CRISPR/Cas9 target sites, sgRNA synthesis and optimization of BeWo transfection

The design of the CRISPR/Cas9 target sites and corresponding primer pair for target site amplification and sequencing was performed with bioinformatic tools as previously described (Bassett et al. 2013; Gagnon et al. 2014; Burger et al. 2016). Target sites at the beginning of the gene and at positions essential for transcription are preferred because if an indel mutation happens, the frame shift would affect the whole gene and transcription would be blocked, respectively. We considered to choose one target site presumably inducing destructive effects in all isoforms of all target gene variants. In case of *DMT1* targeting, there are four human isoforms of *DMT1* to be considered having all the same metal-ion transport efficiencies (Mackenzie et al. 2007). Candidate target sites were tested for uniqueness in the online BLAST tool from NCBI to avoid off-target effects. Additionally, we sequenced selected target sites of all target genes to make sure that the target site has 100% identity with the endogenous gene sequence in the BeWo cell batch that we use.

To generate knockout BeWo cell lines by CRISPR/Cas9 mutagenesis for *LAT1*, *LAT2*, *DMT1* and *ZIP8,* two approaches based on either Cas9 plasmid or Cas9 protein delivery and 2-3 different transfection reagents per approach were tested. The transfection methods were optimized for Cas9 plasmid together with target-specific sgRNA using Xfect transfection reagent (TAKARA). For transfection of pre-assembled Cas9 protein sgRNA (RNP) the jetCRISPR (Polyplus) reagent reached the highest transfection rate and GFP-signal induction in BeWo cells, respectively.

Finally, the transfection of the Cas9 plasmid by Xfect transfection was optimized up to an efficiency of approx. 49% in BeWo cells. This result was almost comparable to the efficiency in the easy to transfect cell line HEK-293 with approx. 76% efficiency. The plasmid is with the size of 9271 bp quite big and might have a negative impact on the transfection efficiency. A comparable efficiency of 50% using Lipofectamin 2000 for siRNA transfection in BeWo has been reported (Forbes et al. 2009) and also the non-liposomal reagent FuGENE6 led to successful transfection in BeWo (Kudo et al. 2003). Of note, the Xfect transfection reagent has been designed to transfect plasmids only. In our approach we used it to transfect the plasmid together with the single-stranded sgRNA. There is no

protocol for this kind of application and no literature for successful CRISPR/Cas9 transfection with this reagent. Therefore, it is possible that the sgRNA has not been transfected or the 2:1 molar ratio of sgRNA : plasmid as described in other similar protocols was not appropriate.

However, the Cas9-sgRNA RNP approach was promising due to maximal mutagenesis efficiency of up to 100% by targeting GFP in ubiquitously GFP expressing zebrafish embryo (Burger et al. 2016). Also Kim et al. 2014 and Liang et al. 2015 showed that the delivery of RNP complexes have the advantage of fewer off-targets and higher editing rate. The transfection protocol using Xfect Protein was not designed for this kind of transfection, but it was adapted to the jetCRISPR protocol, which was optimized for RNP transfection. After unsuccessful transfection and sorting procedures additional assays with the Xfect Protein reagent, were omitted and instead the jetCRISPR reagent was further used for knockout generation. The sorting procedure turned out to be difficult because of the weak GFP signal after Cas9 protein transfection. It was not clear, if the Cas9-GFP was already degraded 48 h post transfection when FACS analyses were performed or whether the GFP signal on the Cas9 protein was not strong enough. Another reason for low transfection efficiencies could be the labeling of the Cas9 protein with GFP. This increases the cargo size of the RNP and therefore affect the delivery efficiency (Schubert et al. 2017).

Overall, the generation of *LAT1*, *LAT2*, *DMT1* and *ZIP8* transporter knockout in BeWo cell lines was despite different approaches not successful as demonstrated by the final target site sequencing analysis (see **Figure 45** on p.126 and in **Figure 46** on p.128). The reason for this could not be conclusively clarified. As the design of the target sites was performed as previously described in the literature and with the help of widely used online tools, sequence errors in the target site can be largely excluded. The chosen transfection reagents Xfect and Xfect Protein were originally not designed for combined Cas9 and sgRNA applications. Although GFP signal was detected after application of our optimized protocols (**Figure 41** on p.117), it was not clear whether also the sgRNA as well as the Cas9 plasmid and the Cas9 protein, respectively, was delivered into the cell. Furthermore, it has been demonstrated that CRISPR/Cas9 applications could be blocked for the access of repair enzymes by a persistent binding of the Cas9 protein to the DNA at the cutting site,

which occurred in 15% of CRISPR/Cas9 transfections before (Clarke et al. 2019). Hence, if the double strand break cannot be repaired, no mutations occur.

The sgRNA was produce by T7-MAXIscript® IVT according to previously optimized and published protocol (Burger et al. 2016). The bioanalyzer analysis revealed that there was no RNA shedding and further gave an estimation of the RNA concentration. There were two bands at 100 and 200 bp detected in the bioanalyzer analysis representing both sgRNA. It is a common phenomenon that the T7 polymerase can accept the former template and extend this RNA if the 3'end is not folded into a stable secondary structure (Triana-Alonso et al. 1995). Since the RNA concentration is calculated subsequentially to the bioanalyzer according to 28s/18s ribosomal RNA analysis, which was not present in the sgRNA after IVT, these concentration estimations were not reliable. Therefore, concentrations determined by Nanodrop were considered for further calculations for transfection.

4.3.2 Characterization of CRISPR/Cas9 mutant cell candidates

Immunoblotting of the obtained cell lines lysates with antibodies against LAT1, LAT2, ZIP8 and DMT1 protein after transfection and FACS sorting procedure was successful, but revealed, despite of CRISPR/Cas9 targeting, target gene expression. Most of the candidate clones generated from the transfection with Xfect plasmid and sgRNA showed even higher expression compared to untransfected BeWo cells. The mRNA upregulation of the transporter *ZIP14* and the slightly increased levels of *DMT1* mRNA could be the result of compensation, while the overexpression of *HEPHL1* could be interpreted as cellular protection mechanism against an excess of toxic ferrous iron. Furthermore, the downregulation of *FPN1* mRNA could be to keep iron levels in the cells by reduction of iron export. The down regulation of the iron regulator HEPC would lead increased iron acquisition *in vivo* via increasing FPN1 expression in maternal enterocytes. These expressional changes seemed to follow a certain pattern, that could suggest a molecular reorganization on transcriptional level to maintain iron homeostasis duet to a putative transporter loss. However, there were few clones showing a downregulation on protein level of approximately 50% (e.g. LAT2) compared to the no-sgRNA transfected control. However, eight out of eleven quantified *DMT1* knockout candidates showed increased protein levels compared to BeWo control cells as well (see **Figure 43** on p.121). ZIP8

knockout candidates were more promising in immunoblot analysis because most of them showed downregulation. Because 100 or 200 cells were sorted in one well, a knockdown phenotype was regarded due as possible. In this case, it is possible that not all alleles of every cell were mutated.

For future investigations, independent whether expressional of functional measurements are performed, a specific control undergoing the whole transfection and sorting procedure without being transfected with sgRNA should be included in every BeWo cell targeting series and in all follow-up analyses. However, we have measured so far only untransfected BeWo control cells and not an appropriate no-sgRNA control. The sorting procedure to single, 100 or 200 cells/well might be an additional stress factor for the cells and may disrupt the gene expression pattern directly after sorting (Richardson, Lannigan, and Macara 2015). However, in our experiment the protein lysates were taken several weeks after sorting, adaption and sufficient proliferation. Another factor is the transfection procedure which apparently resulted in increased protein expression of the cells.

While the functional characterization of CRISPR/Cas9-mediated DMT1, ZIP8 and LAT1 knockout candidates resulted in an iron and leucine uptake capacity comparable to the untransfected control cells, the LAT2 targeted clone B5 showed reduced leucine uptake during 8 min (**Figure 44** on p.124). Furthermore, the leucine uptake time course of clone B5 was reduced independent of JPH203-mediated LAT1 or JX009-mediated System L transport inhibition. Such characteristic inhibition patterns would be typical for successful LAT1 loss of function mutation, but clone B5 was LAT2-targeted and anyway not mutated as demonstrated later by target site sequencing (**Figure 45** on p.126). Desforges and Westwood showed that upon transfection with lipid-based reagents ligand-independent activation of insulin/IGF-1 receptor can be triggered (M Desforges and Westwood 2011). This leads to a stimulation of System A and ASC transporters like SNAT1/*SLC38A1* or ASCT2/*SLC1A5*. Both transporters are relevant for Na^+-dependent glutamine uptake enabling glutaminolysis within the cells, which is an important energy source for proliferation of cancer cells like BeWo (A. Bröer, Rahimi, and Bröer 2016). This effect could additionally influence leucine uptake behavior of targeted cells.

Sanger sequencing combined with TIDE analyses finally revealed that no genetic modification in the CRISPR/Cas9 targeted cell lines compared to BeWo control cells has occurred. Considering this result, we assume that the decreased protein levels detected in the immunoblot analyses and the altered leucine and iron uptake of the CRISPR/Cas9 targeted cells were side effects of the transfection and FACS sorting procedures. For these two analyses we have measured so far only untransfected BeWo control cells and not an appropriate no-sgRNA control which underwent the entire mutagenesis procedure.

We finally also considered the possibility, that CRISPR/Cas9-targeting of the nutrient transporters LAT1, LAT2, DMT1 and ZIP8 resulted in severe impairments and cellular lethality. If this hypothesis would be correct, we might have successfully targeted the respective transporters, but the cells died upon knockout. To test these concerns, we additionally targeted *hCG* with the same experimental approach. hCG is exclusively expressed by trophoblasts, but not in HEK-293 cells. Thus CRISPR/Cas9 mutagenesis in HEK-293 cells are expected to introduce indel mutations without causing a major phenotype or being lethal. Furthermore, hCG has already been successfully silenced in BeWo cells before and caused a phenotype at the STB-stage during and after differentiation (Malhotra, Suman, and Gupta 2015). For further analysis, the Cas9 plasmid and Cas9-RNP transfection and sorting procedure was performed according to our optimized protocol, followed by target site amplification of targeted and untargeted no-sgRNA control cells. Finally, the T7 endonuclease I assay demonstrated that also with this approach there were no mutations introduced neither with the Cas9 plasmid nor with the RNP transfection method. This finding strongly suggests a problem with the sgRNA availability in the cell leading to an unsuccessful transduction of CRISPR/Cas9 mutagenesis.

In summary, based on our obtained results, further optimization procedures are needed for the CRSPR/Cas9 approach. For our future CRISPR/Cas9 experiments with sgRNA we will also test specialized commercially available kits for their efficiency in CRSPR/Cas9 modulated knockout of nutrient transporters.

5 Conclusion

5.1 Amino acid transport

Accumulative transporters, exchangers and facilitators form complex placental amino acid transport systems, which are dependent of intra-extracellular and materno-fetal substrate gradients enabling an efficient materno-fetal transfer of essential amino acid such as leucine against a counter-directed gradient.

Based on prospectively analyzed amino acid concentrations in the serum of mothers and their newborns, we found associations with clinical and anthropometric values. First, there were significant relations between maternal amino acid concentrations of LAT1-specific substrates and maternal weights both before pregnancy and at term. These findings allow conclusions regarding the dependence of the maternal nutritional stage and the formation of transplacental gradients throughout gestation. Secondly, we could show for the first time that there is a relation between materno-fetal gradients of various LAT1 substrates and clinically relevant parameters such as maternal weight, gestational weight gain, BMI, blood pressure, but also placental growth. These statistical correlations confirm the hypothesis: “Materno-fetal amino acid gradients are crucial for transplacental amino acid transport and correlate with selected maternal and fetal parameters.” Moreover, these observations suggest that factors such as the maternal nutrition influence the formation of materno-fetal amino acid gradients and thereby might have an impact on reduced intrauterine growth in hypertensive gestational diseases like preeclampsia.

Beside these observational studies, we could also demonstrate in functional *in vitro* studies that leucine transfer across the materno-fetal barrier is increased against a counter-directed gradient. These results confirmed the second hypothesis: “Counter-directed amino acid gradients *in vivo* affect leucine uptake into trophoblasts and transfer across the placental barrier.” These findings also revealed a so far underestimated relevance of transplacental amino acid gradients in human pregnancy which could affect pregnancy outcome and may play a role in fetal development.

In a more cell biology-oriented approach, we confirmed that high and asymmetric expression of SLC7-family members makes the placental leucine uptake sensitive to LAT1-

and LAT2-inhibition. Based on this, we compared the choriocarcinoma cell line BeWo to primary trophoblasts and demonstrated that BeWo could serve as useful model system to test putative LAT1 inhibitors and characterize their effects at an active amino acid transporting and physiologically relevant cell barrier. Furthermore, we could show that the application of compounds like the LAT1-specific small molecule inhibitor JPH203 or the less specific System L transport inhibitor JX009, allows for distinguishing the contribution of single leucine transporters across the placental barrier. The combined application of the LAT1-specific inhibitor JPH203 and the System L-inhibitor JX009 in Transwell® studies identified LAT1 as major leucine transporter having an essential role in the materno-fetal supply of essential amino acids at the MVM and demonstrated the usefulness of applying small-compound inhibitors bearing different specificities. The identification of new lead structures or the further advancement of existing inhibitors targeting System L-facilitators such as LAT3 and LAT4 could be valuable tools for assessing the relevance of single transporters in materno-fetal amino acid transfer. From a pharmacological point of view, a better understanding of the SLC7 transporter-mediated supply of amino acids and its impact on pregnancy diseases including IUGR and GDM could be a first step towards the optimization of fetal growth and its effect on fetal programming in future. Due to the successful application of SLC7-specific small molecule inhibitors, we could partially confirm the third and last hypothesis in the amino acid transport part: "Specific inhibition of SLC7 transporters or knockout of single transporter genes can reveal the relevance of single solute carriers in placental nutrient acquisition." Of note, the short-term treatment with small molecule inhibitors exhibiting different specificities also reduces the risk of impacting trophoblast fusion and differentiation as for example with long-term gene silencing or constitutive knockout.

5.2 Iron transport

The findings outlined in this thesis explain clinical observations associating GDM with dysregulated placental iron homeostasis on a cellular and mechanistic level. Our study was based on a well-characterized clinical cohort, and combines clinical observations, analysis of clinical samples with complementary investigations using *in vitro* cell models. The newly established hyperglycemic cell models showed expressional changes which closely resembled the alterations observed in GDM tissues allowing novel mechanistic

insights. Due to the study design, we were not able to analyze additional iron-related blood parameters such as ferritin levels, Tf saturation or blood status of the newborns.

We found in GDM significant differences in the expression, trafficking and function of proteins involved in the uptake, transport, sensing, and regulation of iron, which clearly confirmed the first hypothesis of the iron transport part: “The expression of placental iron-transporters and iron-regulatory proteins is altered in GDM.” Newly established trophoblast cell models exposed to hyperglycemic culture conditions, but also obesogenic HFHS diet in wildtype mice, mimicked to a great extent the expression patterns found in the clinical specimens of GDM patients at term. This strengthens the validity of our results and demonstrates the significance of our findings. Cellular adaption to GDM-like conditions reduced placental iron uptake by mechanisms involving alterations in autophagy and oxidative stress pathways. These adaptations could be part of a protective mechanism preventing oxidative damage for both the fetus and the placenta caused by hyperglycemia and highly oxidative iron. Hence, a putative and clinically relevant relation between hyperglycemia and altered iron transport in trophoblast was functionally characterized, confirming the second iron transport hypothesis; “Simulation of hyperglycemic and hyperlipidemic conditions in trophoblasts induces cellular stress and affects iron uptake.” The almost complete reversion of hyperglycemic effects on placental iron homeostasis gene expression in trophoblasts after antioxidant treatment suggests beneficial effects of antioxidant supplementation in pregnant women with increased risk to develop GDM. Taken together these results confirm the last hypothesis: “The reduction of cellular stress levels recues placental iron homeostasis.” Such antioxidant treatment could and should be further investigated using the HFHS mouse model spontaneously developing GDM-like changes in iron homeostasis gene expression patterns.

The herein identified adaptive processes of the placenta in GDM are presumably part of a protective mechanism preventing oxidative damage for both the fetus and the placenta caused by hyperglycemia and highly oxidative iron. On the other side, these findings also raise potential concerns regarding the recommendation of routine iron-supplementation among iron-replete pregnant women. Importantly, our results suggest that antioxidant supplementation could be beneficial for pregnant women with increased risk to develop

GDM by protecting the placenta and fetus against oxidative stress caused by hyperglycemia, high iron status or both.

5.3 CRISPR/Cas9-mutagenesis of placental SLC transporter

Within this smaller and more methodologically oriented part of the PhD thesis, we aimed to target single genes relevant for leucine and iron transport across the placenta by CRISPR/Cas9-mutagenesis. Trophoblast cells lacking the function of single nutrient transporter by specifically and CRISPR/Cas9-mediated knockout, would reveal their role at the materno-fetal barrier in the placenta. The generation of such SLC-knockout trophoblast cell lines could have helped to unravel the causes and consequences associated with impaired transfer of nutrients in specific pregnancy diseases. Probably due to failed introduction of functionally active sgRNA into BeWo cells, we were unfortunately not yet able to generate knockout cell lines. However, extensive optimization of target site validation, the establishment of transfection and characterization procedures of potential CRISPR/Cas9-mutant candidates on expressional and functional level set the stage for successful future studies in this context. In fact, we have created an advanced toolbox for a successful continuation of nutrient transporter characterization by CRISPR/Cas9-mediated mutagenesis in human trophoblasts. This may help to delineate the role of single placental nutrient transporters in a cell biological context.

6 Perspectives

The work presented in this thesis has shed light on specific molecular mechanisms related to transplacental transfer of amino acids and iron, but it has also raised several questions which should be addressed in future investigations. In the first part of this thesis, amino acid concentrations in fetal and maternal blood from uncomplicated pregnancies were measured and investigated by correlation analysis. To complement the amino acid concentrations measurement, LC-MS/MS-based quantification of cysteine and its metabolic products in serum should be intensified to provide additional information about the unexpectedly low cysteine concentrations in all analyzed samples. Moreover, LC-MS/MS-based amino acid quantification would further allow the assessment of the full amino acid spectra in the fetal and maternal compartments of a Transwell® experiment without depending on radio-labeled amino acid derivates as detectable substrate after placental transfer. With this analytical advancement the monitoring of amino acid fluxes and their metabolism would be feasible. In this system the clinically relevant System L-mediated transport across the placenta could be investigated under physiological or even pathophysiological conditions. Additionally, it could be tested whether an *in vitro* placental barrier is able to create amino acid gradients which has never been demonstrated before.

In our amino acid studies we identified two states into which healthy human term placentae could be categorized, namely either an accumulative (positive FV-FA difference) or a secretory (negative FV-FA difference) mode suggesting a temporary switch between accumulation and secretion phases in placental amino acid transfer. This should be confirmed by *in vivo* determination of FV-FA differences during pregnancy which could be achieved by using *in utero* cordocentesis at different gestational stages (Irene Cetin et al. 1990; McIntosh, Rodeck, and Heath 1984). Within the correlation studies, we found, beside associations between materno-fetal gradients and maternal pregnancy weights, also strong positive correlations with maternal systolic blood pressure at term. Based on this finding, it would be interesting to compare materno-fetal amino acid gradients between preeclampsia patients and a healthy control group within a prospective study. This would allow to assess at an early stage of pregnancy, whether materno-fetal amino

acid gradients are altered in pregnancies that subsequently develop hypertension and become preeclamptic later in pregnancy (Sibai 2012).

In the last chapter of the amino acid part, we demonstrated the benefit of applying small molecule inhibitors bearing different nutrient transporter specificities. Of note, there are currently new inhibitor lead compounds, and, interestingly, also new SLC7 transport activators in the pipeline of the SLC7 project of NCCR TransCure (https://www.nccr-transcure.ch/research/projects/slc7-family-amino-acid-transporters/). These compounds are currently being studied by other investigators in the context of cancer therapy strategies. These newly developed compounds could be valuable tools for the transporter-specific investigation of placental amino acid transfer as shown for inhibitors within this project. Moreover, potent and safe activators of System L transporters should be investigated in the context of placental biology since such compounds could be interesting future drug candidates for the treatment of reduced fetal growth in IUGR.

In the second part of this PhD thesis, we investigated the relation between GDM and dysregulated placental iron homeostasis by analyzing human placentae. Due to the retrospective study design, we were not able to measure additional iron-related blood parameters such as ferritin levels, Tf saturation or blood status of the newborns. These parameters, however, would give valuable important additional information and could support the current findings of altered placental iron homeostasis suggested in this study. In this context, it would be beneficial to organize a prospective clinical study in collaboration with the collaborating hospitals in Bern. Herein glucose tolerance tests and the collection of maternal / fetal blood for the determination of systemic iron status should be performed. These parameters should be combined with the expressional and functional assessment of the corresponding placentae and isolated primary trophoblasts cells as well as iron transport studies in villous explants and placental dual-perfusion. The combination of all these *ex vivo* methods, that are already established in the Albrecht laboratory, could shed more light on the molecular pathways disturbed in GDM. Moreover, these *in vitro* and *ex vivo* model systems would allow to investigate iron transporter expressional changes and/or functional transport time courses in combination with the application of exogenous stress such as oxidative stress, hypoxia, hyperglycemia or hyperlipidemia. Additionally, the effects of iron depletion by DFO

treatment or increased antioxidative potential by NaSe supplementation could be further elaborated. Another approach which should be followed-up is to design experiments with mice developing GDM during pregnancy. The further establishment of diets, such as HFHS to induce GDM in wildtype mice or to test antioxidative treatments in these mice would allow to characterize effects on fetal growth and could provide deeper insights into the relationship between placental glucose and iron homeostasis. Within future studies to investigate the association between placental glucose and iron homeostasis, there should be a special focus on the ferroptosis pathway. To date hyperglycemia is not characterized as known promotor of ferroptosis, but our results strongly suggest disturbed transplacental iron transport, GSH depletion and increased lipid peroxidation as mediator between hyperglycemia and altered placental iron homeostasis.

There are also open questions concerning the placental iron transfer on a cellular level. As emphasized in the introduction section of this thesis, a systematic approach to localize all proteins potentially involved in placental iron uptake and transfer across the placental barrier including alternative heme- and non-heme-iron transporter, receptors, chaperones, storage proteins, reductases and oxidases, would inspire the whole field of placental nutrient transport research. Isolation of different plasma and endosomal membranes for expressional studies, confocal microscopy on placental tissue and trophoblasts in the Transwell® system, preferentially with experts for correlative light and electron microscopy such as Prof. Wanda Kukulski, who recently joined our institute, would be a promising strategy of to achieve these goals.

Different technical approaches or the refinement and optimization of the current methodology is also needed for the generation of knockout cell lines for nutrient transporters by CRISPR/Cas9 mutagenesis. Although we adapted and optimized the strategy and corresponding protocols to generate SLC transporter-specific trophoblast knockout cell lines by CRISPR/Cas9 mutagenesis, we were not able to produce stable BeWo cells bearing loss-of-function mutations. Our results in this context suggest a problem with the transfection and/or the activity of the *in vitro* synthesized sgRNA. To overcome this problem, we need to guarantee the introduction of functional sgRNA into the cell. As a first approach, we recommend to further optimize the transfection by using plasmids expressing both guide RNA and Cas9-GFP. Alternatively, commercially available

kits should be carefully selected and tested for successful CRISPR/Cas9 mutagenesis of nutrient transporters.

In parallel to the CRISPR/Cas9 approach in this PhD project, the Albrecht laboratory started to establish placenta specific knockout mouse models targeting DMT1 and ZIP8 with support from Prof. Willy Hofstetter, University of Bern, and Prof. Mitchell D. Knutson, University of Florida. To generate placenta specific *DMT1*$^{-/-}$ and *Zip8*$^{-/-}$ mice, we utilize mice expressing cre recombinase under the control of the mouse glial cells missing homolog 1 promoter (Tg(Gcm1-cre)1Chrn/J), which specifically expresses the Cre recombinase in syncytiotrophoblast layer II cells of the labyrinth in mouse placenta (V. Nadeau et al. 2009; Valérie Nadeau and Charron 2014). Gcm1-cre mice (*Zip8*$^{+/+}$; *Gcm1Cre*$^{tg/+}$) will be crossed with *Zip8*$^{flox/flox}$ (*Zip8*$^{flox/flox}$;Gcm1Cre$^{+/+}$) to finally generate female mice that produce *Zip8*$^{flox/flox}$;Cre$^{tg/+}$ embryos under time controlled mating. Using this approach, we lose Dmt1 or Zip8 expression only in trophoblasts, that are responsible for nutrient transfer in mice. Importantly, this time-controlled mating approach allows the investigation of mouse embryos at defined developmental stages. The fetuses will be thoroughly characterized for changes in glucose and iron homeostasis. This will complement our data generated in humans and will eventually provide new insights into the role of the placenta in materno-fetal iron transfer.

7 References

Abrams, Barbara F., and Russell K. Laros. 1986. “Prepregnancy Weight, Weight Gain, and Birth Weight.” *American Journal of Obstetrics and Gynecology* 154 (3): 503–9. https://doi.org/10.1016/0002-9378(86)90591-0.

Afkhami-Ardekani, Mohammad, and Maryam Rashidi. 2009. “Iron Status in Women with and without Gestational Diabetes Mellitus.” *Journal of Diabetes and Its Complications* 23 (3): 194–98. https://doi.org/10.1016/j.jdiacomp.2007.11.006.

Akker, Chris H.P. Van Den, Henk Schierbeek, Gardi Minderman, Andras Vermes, Ernst M. Schoonderwaldt, Johannes J. Duvekot, Eric A.P. Steegers, and Johannes B. Van Goudoever. 2011. “Amino Acid Metabolism in the Human Fetus at Term: Leucine, Valine, and Methionine Kinetics.” *Pediatric Research* 70 (6): 566–71. https://doi.org/10.1203/PDR.0b013e31823214d1.

American Diabetes Association. 2007. “Standards of Medical Care in Diabetes - 2007.” *Diabetes Care* 30 (Suppl 1): S4–41. https://doi.org/10.2337/dc07-S004.

Araújo, João R., Ana C. Pereira, Ana Correia-Branco, Elisa Keating, and Fátima Martel. 2013. “Oxidative Stress Induced by Tert-Butylhydroperoxide Interferes with the Placental Transport of Glucose: In Vitro Studies with BeWo Cells.” *European Journal of Pharmacology* 720 (1–3): 218–26. https://doi.org/10.1016/j.ejphar.2013.10.023.

Augustyn, Evan, Karissa Finke, Arik A. Zur, Logan Hansen, Nathan Heeren, Huan Chieh Chien, Lawrence Lin, et al. 2016. “LAT-1 Activity of Meta-Substituted Phenylalanine and Tyrosine Analogs.” *Bioorganic and Medicinal Chemistry Letters* 26 (11): 2616–21. https://doi.org/10.1016/j.bmcl.2016.04.023.

Avagliano, Laura, Valentina Massa, Laura Terraneo, Michele Samaja, Patrizia Doi, Gaetano Pietro Bulfamante, and Anna Maria Marconi. 2017. “Gestational Diabetes Affects Fetal Autophagy.” *Placenta* 55: 90–93. https://doi.org/10.1016/j.placenta.2017.05.002.

Ayuk, P T, C P Sibley, P Donnai, S D’Souza, and J D Glazier. 2000. “Development and Polarization of Cationic Amino Acid Transporters and Regulators in the Human Placenta.” *American Journal of Physiology. Cell Physiology* 278 (6): C1162–71.

Azar, Christopher, Mark Valentine, Julie Trausch-Azar, Todd Druley, D. Michael Nelson, and Alan L. Schwartz. 2018. “RNA-Seq Identifies Genes Whose Proteins Are Transformative in the Differentiation of Cytotrophoblast to Syncytiotrophoblast, in Human Primary Villous and BeWo Trophoblasts.” *Scientific Reports* 8 (1): 1–12. https://doi.org/10.1038/s41598-018-23379-2.

Bach, Aline, Julia Bender Sigel, Dieter Schrenk, Daniela Flügel, and Thomas Kietzmann. 2010. “The Antioxidant Quercetin Inhibits Cellular Proliferation via HIF-1-Dependent Induction of P21WAF.” *Antioxidants & Redox Signaling* 13 (4).

Baergen, Rebecca N. 2005. *Manual of Benirschke and Kaufmann’s Pathology of the Human Placenta. Springer Science & Business Media*. http://dx.doi.org/10.1016/j.jsames.2011.03.003%0Ahttps://doi.org/10.1016/j.gr.2017.08.001%0Ahttp://dx.doi.org/10.1016/j.precamres.2014.12.018%0Ahttp://dx.doi.org/10.1016/j.precamres.2011.08.005%0Ahttp://dx.doi.org/10.1080/00206814.2014.902757%0Ahttp://dx.

Bajoria, Rekha, Suren R. Sooranna, Stuart Ward, Stephen D’Souza, and Maggie Hancock. 2001. “Placental Transport Rather than Maternal Concentration of Amino Acids Regulates Fetal

Growth in Monochorionic Twins: Implications for Fetal Origin Hypothesis." *American Journal of Obstetrics and Gynecology* 185 (5): 1239–46. https://doi.org/10.1067/mob.2001.118269.

Balthasar, Christina, Herbert Stangl, Raimund Widhalm, Sebastian Granitzer, Markus Hengstschläger, and Claudia Gundacker. 2017. "Methylmercury Uptake into Bewo Cells Depends on LAT2-4F2hc, a System l Amino Acid Transporter." *International Journal of Molecular Sciences* 18 (8). https://doi.org/10.3390/ijms18081730.

Basevi, V., S. Di Mario, C. Morciano, F. Nonino, and N. Magrini. 2011. "Comment on: American Diabetes Association. Standards of Medical Care in Diabetes--2011. Diabetes Care 2011;34(Suppl. 1):S11-S61." *Diabetes Care* 34 (5): e53–e53. https://doi.org/10.2337/dc11-0174.

Bassett, Andrew R., Charlotte Tibbit, Chris P. Ponting, and Ji-Long Liu. 2013. "Highly Efficient Targeted Mutagenesis of Drosophila with the CRISPR/Cas9 System." *Cell Reports* 4 (1): 220–28. https://doi.org/10.1016/J.CELREP.2013.06.020.

Bastin, Judy, Hal Drakesmith, Margaret Rees, Ian Sargent, and Alain Townsend. 2006. "Localisation of Proteins of Iron Metabolism in the Human Placenta and Liver." *British Journal of Haematology* 134 (5): 532–43. https://doi.org/10.1111/j.1365-2141.2006.06216.x.

Battaglia, F. C., and T. R. H. Regnault. 2001. "Placental Transport and Metabolism of Amino Acids." *Placenta* 22: 145–61.

Battaglia, Frederick C., and Giacomo Meschia. 1988. "Fetal Nutrition." *Annual Review of Nutrition* 8: 43–61. https://doi.org/10.1016/S0271-5317(05)80493-2.

Baumann, Marc U., Sylvie Deborde, and Nicholas P. Illsley. 2002. "Placental Glucose Transfer and Fetal Growth." *Endocrine* 19 (1): 13–22. https://doi.org/10.1385/ENDO:19:1:13.

Bo, Simona, Guido Menato, Paola Villois, Roberto Gambino, Maurizio Cassader, Ilenia Cotrino, and Paolo Cavallo-Perin. 2009. "Iron Supplementation and Gestational Diabetes in Midpregnancy." *American Journal of Obstetrics and Gynecology* 201 (2): 158.e1-158.e6. https://doi.org/10.1016/j.ajog.2009.04.049.

Bodoy, Susanna, Dimitrios Fotiadis, Claudia Stoeger, Yoshikatsu Kanai, and Manuel Palacín. 2013. "The Small SLC43 Family: Facilitator System l Amino Acid Transporters and the Orphan EEG1." *Molecular Aspects of Medicine* 34 (2–3): 638–45. https://doi.org/10.1016/j.mam.2012.12.006.

Bodoy, Susanna, Lorena Martín, Antonio Zorzano, Manuel Palacín, Raúl Estévez, and Joan Bertran. 2005. "Identification of LAT4, a Novel Amino Acid Transporter with System L Activity." *Journal of Biological Chemistry* 280 (12): 12002–11. https://doi.org/10.1074/jbc.M408638200.

Boney, Charlotte M., Anila Verma, Richard Tucker, and Betty R Vohr. 2005. "Metabolic Syndrome in Childhood: Association With Birth Weight, Maternal Obesity, and Gestational Diabetes Mellitus." *Pediatrics* 115 (3): e290–96. https://doi.org/10.1542/peds.2004-1808.

Booth, A. G., and M. J. Wilson. 1981. "Human Placental Coated Vesicles Contain Receptor-Bound Transferrin." *Biochemical Journal* 196 (1): 355–62. https://doi.org/10.1042/bj1960355.

Bothwell, T H, R W Charlton, J D Cook, and C A Finch. 1979. *Iron Metabolism in Man.* Oxford: Blackwell Scientific Publications. https://www.cabdirect.org/cabdirect/abstract/19801408535.

Bothwell, Thomas H. 2000. "Iron Requirements in Pregnancy and Strategies to Meet Them."

American Journal of Clinical Nutrition 72 (1 SUPPL.). https://doi.org/10.3389/fphar.2014.00155.

Bradley, Jenni, Elizabeth A. Leibold, Z. Leah Harris, Jane D. Wobken, Stephen Clarke, Kimberly B. Zumbrennen, Richard S. Eisenstein, and Michael K. Georgieff. 2004. "Influence of Gestational Age and Fetal Iron Status on IRP Activity and Iron Transporter Protein Expression in Third-Trimester Human Placenta." *American Journal of Physiology - Regulatory Integrative and Comparative Physiology* 287 (4 56-4): 894–901. https://doi.org/10.1152/ajpregu.00525.2003.

Brinkman, Eva K, Tao Chen, Mario Amendola, and Bas Van Steensel. 2014. "Easy Quantitative Assessment of Genome Editing by Sequence Trace Decomposition," no. 10: 1–8. https://doi.org/10.1093/nar/gku936.

Bröer, Angelika, Farid Rahimi, and X Stefan Bröer. 2016. "Deletion of Amino Acid Transporter ASCT2 (SLC1A5) Reveals an Essential Role for Transporters SNAT1 (SLC38A1) and SNAT2 (SLC38A2) to Sustain Glutaminolysis in Cancer Cells *." *The Journal of Biological Chemistry* 291 (25): 13194–205. https://doi.org/10.1074/jbc.M115.700534.

Bröer, Stefan. 2002. "Adaptation of Plasma Membrane Amino Acid Transport Mechanisms to Physiological Demands." *Pflugers Archiv European Journal of Physiology* 444 (4): 457–66. https://doi.org/10.1007/s00424-002-0840-y.

Brown, P. J., P. M. Johnson, A. O. Ogbimi, and J. A. Tappine. 1979. "Characterization and Localization of Human Placental Ferritin." *Biochemical Journal* 182 (3): 763–69. https://doi.org/10.1042/bj1820763.

Brownbill, Paul, Diane Edwards, Carolyn Jones, Dhushy Mahendran, David Owen, Colin Sibley, Roger Johnson, Paul Swanson, and D. Michael Nelson. 1995. "Mechanisms of Alphafetoprotein Transfer in the Perfused Human Placental Cotyledon from Uncomplicated Pregnancy." *Journal of Clinical Investigation* 96 (5): 2220–26. https://doi.org/10.1172/JCI118277.

Brownlee, Michael. 2001. "Biochemistry and Molecular Cell Biology of Diabetic Complications." *Nature* 414: 813–20. https://doi.org/10.1038/414813a.

Burger, Alexa, Helen Lindsay, Anastasia Felker, Christopher Hess, Carolin Anders, Elena Chiavacci, Jonas Zaugg, et al. 2016. "Maximizing Mutagenesis with Solubilized CRISPR-Cas9 Ribonucleoprotein Complexes." *Development*, 2025–37. https://doi.org/10.1242/dev.127993.

Burton, Graham J., Abigail L. Fowden, and Kent L. Thornburg. 2016. "Placental Origins of Chronic Disease." *Physiological Reviews* 96 (4): 1509–65. https://doi.org/10.1152/physrev.00029.2015.

Burton, Graham J., Adrian L. Watson, Joanne Hempstock, Jeremy N. Skepper, and Eric Jauniaux. 2002. "Uterine Glands Provide Histiotrophic Nutrition for the Human Fetus during the First Trimester of Pregnancy." *Journal of Clinical Endocrinology and Metabolism* 87 (6): 2954–59. https://doi.org/10.1210/jcem.87.6.8563.

Cao, Chang, and Mark D. Fleming. 2016. "The Placenta: The Forgotten Essential Organ of Iron Transport." *Nutrition Reviews* 74 (7): 421–31. https://doi.org/10.1093/nutrit/nuw009.

Cao, Jennifer Yinuo, and Scott J. Dixon. 2016. "Mechanisms of Ferroptosis." *Cellular and Molecular Life Sciences* 73 (11–12): 2195–2209. https://doi.org/10.1007/s00018-016-2194-1.

Carter, Anthony M. 2012. "Evolution of Placental Function in Mammals: The Molecular Basis of

Gas and Nutrient Transfer, Hormone Secretion, and Immune Responses." *Physiological Reviews* 92 (4): 1543–76. https://doi.org/10.1152/physrev.00040.2011.

Casasco, A., A. Calligaro, M. Casasco, S. Tateo, A. I. Cornaglia, M. Reguzzoni, and A. Farina. 1997. "Immunohistochemical Localization of Lipoperoxidation Products in Normal Human Placenta." *Placenta* 18 (4): 249–53. https://doi.org/10.1016/S0143-4004(97)80058-6.

Cetin, I. 2001. "Amino Acid Interconversions in the Fetal-Placental Unit: The Animal Model and Human Studies in Vivo." *Pediatric Research* 49 (2): 148–54. https://doi.org/10.1203/00006450-200102000-00004.

Cetin, Irene, Carlo Corbetta, Lucia P. Sereni, Anna Maria Marconi, Patrizia Bozzetti, Giorgio Pardi, and Frederick C. Battaglia. 1990. "Umbilical Amino Acid Concentrations in Normal and Growth-Retarded Fetuses Sampled in Utero by Cordocentesis." *American Journal of Obstetrics and Gynecology* 162 (1): 253–61. https://doi.org/10.1016/0002-9378(90)90860-A.

Cetin, Irene, Anna M. Marconi, Patrizia Bozzetti, Lucia P. Sereni, Carlo Corbetta, Giorgio Pardi, and Frederick C. Battaglia. 1988. "Imbilical Amino Acid Concentrations in Appropriate and Small for Gestational Age Infants: A Biochemical Difference Present in Utero." *American Journal of Obstetrics and Gynecology* 158 (1): 120–26. https://doi.org/10.1016/0002-9378(88)90792-2.

Cetin, Irene, Anna Maria Marconi, Anna Maria Baggiani, Mauro Buscaglia, Giorgio Pardi, Paul V. Fennessey, and Frederick C. Battaglia. 1995. "In Vivo Placental Transport of Glycine and Leucine in Human Pregnancies." *Pediatric Research* 37 (5): 571–75. https://doi.org/10.1203/00006450-199505000-00002.

Cetin, Irene, Maria S. Nobile De Santis, Emanuela Taricco, Tatjana Radaelli, Cecilia Teng, Stefania Ronzoni, Elena Spada, Silvano Milani, and Giorgio Pardi. 2005. "Maternal and Fetal Amino Acid Concentrations in Normal Pregnancies and in Pregnancies with Gestational Diabetes Mellitus." *American Journal of Obstetrics and Gynecology* 192 (2): 610–17. https://doi.org/10.1016/j.ajog.2004.08.011.

Cha, Jeeyeon, Sudhansu K. Dey, and Hyunjung Lim. 2015. *Embryo Implantation*. *Knobil and Neill's Physiology of Reproduction: Two-Volume Set*. Fourth Edi. Vol. 2. Elsevier. https://doi.org/10.1016/B978-0-12-397175-3.00038-7.

Chan, K. K L, B. C P Chan, K. F. Lam, S. Tam, and T. T. Lao. 2009. "Iron Supplement in Pregnancy and Development of Gestational Diabetes - A Randomised Placebo-Controlled Trial." *BJOG: An International Journal of Obstetrics and Gynaecology* 116 (6): 789–97. https://doi.org/10.1111/j.1471-0528.2008.02014.x.

Chen, Huijun, Zouhair K Attieh, Basharut a Syed, Yien-Ming Kuo, Valerie Stevens, Brie K Fuqua, Henriette S Andersen, et al. 2010. "Identification of Zyklopen, a New Member of the Vertebrate Multicopper Ferroxidase Family, and Characterization in Rodents and Human Cells." *The Journal of Nutrition* 140 (10): 1728–35. https://doi.org/10.3945/jn.109.117531.

Chien, P. F.W., K. Smith, P. W. Watt, C. M. Scrimgeour, D. J. Taylor, and M. J. Rennie. 1993. "Protein Turnover in the Human Fetus Studied at Term Using Stable Isotope Tracer Amino Acids." *American Journal of Physiology - Endocrinology and Metabolism* 265 (1 28-1): 31–35. https://doi.org/10.1152/ajpendo.1993.265.1.e31.

Chomczynski, Piotr, and Nicoletta Sacchi. 2006. "The Single-Step Method of RNA Isolation by Acid Guanidinium Thiocyanate-Phenol-Chloroform Extraction: Twenty-Something Years On." *Nature Protocols* 1 (2): 581–85. https://doi.org/10.1038/nprot.2006.83.

Chong, W. S., P. C. Kwan, L. Y. Chan, P. Y. Chiu, T. K. Cheung, and T. K. Lau. 2005. "Expression of Divalent Metal Transporter 1 (DMT1) Isoforms in First Trimester Human Placenta and Embryonic Tissues." *Human Reproduction* 20 (12): 3532–38. https://doi.org/10.1093/humrep/dei246.

Clarke, Ryan, Robert Heler, Matthew MacDougall, Nan Cher Yeo, Alejandro Chavez, Maureen Regan, Leslyn Hanakahi, George M. Church, Luciano A. Marraffini, and Bradley J. Merrill. 2019. "Enhanced Bacterial Immunity and Mammalian Genome Editing via RNA Polymerase-Mediated Dislodging of Cas9 from Double Strand DNA Breaks." *Molecular Cell*. https://doi.org/10.1016/j.physbeh.2017.03.040.

Cleal, J. K., J. D. Glazier, G. Ntani, S. R. Crozier, P. E. Day, N. C. Harvey, S. M. Robinson, et al. 2011. "Facilitated Transporters Mediate Net Efflux of Amino Acids to the Fetus across the Basal Membrane of the Placental Syncytiotrophoblast." *Journal of Physiology* 589 (4): 987–97. https://doi.org/10.1113/jphysiol.2010.198549.

Cleal, Jane K., Paul Brownbill, Keith M. Godfrey, John M. Jackson, Alan A. Jackson, Colin P. Sibley, Mark A. Hanson, and Rohan M. Lewis. 2007. "Modification of Fetal Plasma Amino Acid Composition by Placental Amino Acid Exchangers in Vitro." *Journal of Physiology* 582 (2): 871–82. https://doi.org/10.1113/jphysiol.2007.130690.

Cleal, Jane K., and R. M. Lewis. 2008. "The Mechanisms and Regulation of Placental Amino Acid Transport to the Human Foetus." *Journal of Neuroendocrinology* 20 (4): 419–26. https://doi.org/10.1111/j.1365-2826.2008.01662.x.

Cockburn, F., A. Blagden, E. A. Michie, and J. O. Forfar. 1971. "The Influence of Pre-Eclampsia and Diabetes Mellitus on Plasma Free Amino Acids in Maternal, Umbilical Vein and Infant Blood." *BJOG: An International Journal of Obstetrics & Gynaecology* 78 (3): 215–31. https://doi.org/10.1111/j.1471-0528.1971.tb00260.x.

Contractor, S F, and B M Eaton. 1986. "Role of Transferrin in Iron Transport between Maternal and Fetal Circulations of a Perfused Lobule of Human Placenta." *Cell Biochemistry and Function* 4 (1): 69–74. https://doi.org/10.1002/cbf.290040111.

Cormerais, Yann, Marina Pagnuzzi-Boncompagni, Sandra Schrötter, Sandy Giuliano, Eric Tambutté, Hitoshi Endou, Michael F. Wempe, Gilles Pagès, Jacques Pouysségur, and Vincent Picco. 2019. "Inhibition of the Amino-Acid Transporter LAT1 Demonstrates Anti-Neoplastic Activity in Medulloblastoma." *Journal of Cellular and Molecular Medicine* 23 (4): 2711–18. https://doi.org/10.1111/jcmm.14176.

Costa, Meritxell, Albert Rosell, Elena Álvarez-Marimon, Antonio Zorzano, Dimitrios Fotiadis, and Manuel Palacín. 2013. "Expression of Human Heteromeric Amino Acid Transporters in the Yeast Pichia Pastoris." *Protein Expression and Purification* 87 (1): 35–40. https://doi.org/10.1016/j.pep.2012.10.003.

Cox, Jürgen, and Matthias Mann. 2008. "MaxQuant Enables High Peptide Identification Rates, Individualized p.p.b.-Range Mass Accuracies and Proteome-Wide Protein Quantification." *Nature Biotechnology* 26 (12): 1367–72. https://doi.org/10.1038/nbt.1511.

Crowther, Caroline A., Janet E. Hiller, John R. Moss, Andrew J. McPhee, William S. Jeffries, and Jeffrey S. Robinson. 2005. "Effect of Treatment of Gestational Diabetes Mellitus on Pregnancy Outcomes." *The New England Journal of Medicine* 352: 2477–86. https://doi.org/10.1056/NEJMoa030781.

Dannenmann, Benjamin, Masoud Nasri, Karl Welte, and Julia Skokowa. 2020. "CRISPR/Cas9 Genome Editing of Human-Induced Pluripotent Stem Cells Followed by Granulocytic

Differentiation." In , 471–83. https://doi.org/10.1007/978-1-0716-0290-4_27.

Demir, R., P. Kaufmann, M. Castelluce, T. Erbeng, and A. Kotowsk. 1989. "Fetal Vasculogenesis and Angiogenesis in Human Placental Villi." *Cells Tissues Organs* 136 (3): 190–203. https://doi.org/10.1159/000146886.

Desforges, M, and M Westwood. 2011. "A Limitation of the Method for SiRNA Delivery into Primary Human Cytotrophoblast Cells." *Placenta* 32 (2): 192–94. https://doi.org/10.1016/j.placenta.2010.11.013.

Desforges, Michelle, K. J. Mynett, R. L. Jones, S. L. Greenwood, M. Westwood, C. P. Sibley, and J. D. Glazier. 2009. "The SNAT4 Isoform of the System A Amino Acid Transporter Is Functional in Human Placental Microvillous Plasma Membrane." *Journal of Physiology* 587 (1): 61–72. https://doi.org/10.1113/jphysiol.2008.161331.

DeSisto, Carla L., Shin Y. Kim, and Andrea J. Sharma. 2014. "Prevalence Estimates of Gestational Diabetes Mellitus in the United States, Pregnancy Risk Assessment Monitoring System (PRAMS), 2007–2010." *Preventing Chronic Disease*. https://doi.org/10.5888/pcd11.130415.

Desoye, Gernot, Martin Gauster, and Christian Wadsack. 2011. "Placental Transport in Pregnancy Pathologies." *American Journal of Clinical Nutrition* 94 (6): 1896–1902. https://doi.org/10.3945/ajcn.110.000851.

Dicke, Jeffrey M., Deborah Verges, Lucky K. Kelley, and Carl H. Smith. 1993. "Glycine Uptake by Microvillous and Basal Plasma Membrane Vesicles from Term Human Placentae." *Placenta* 14 (1): 85–92. https://doi.org/10.1016/S0143-4004(05)80251-6.

Dixon, Scott J., Kathryn M. Lemberg, Michael R. Lamprecht, Rachid Skouta, Eleina M. Zaitsev, Caroline E. Gleason, Darpan N. Patel, et al. 2012. "Ferroptosis: An Iron-Dependent Form of Nonapoptotic Cell Death." *Cell* 149 (5): 1060–72. https://doi.org/10.1016/j.cell.2012.03.042.

Edwards, D, C J Jones, C P Sibley, and D M Nelson. 1993. "Paracellular Permeability Pathways in the Human Placenta: A Quantitative and Morphological Study of Maternal-Fetal Transfer of Horseradish Peroxidase." *Placenta* 14 (1): 63–73.

Endo, Hitoshi, Yoshikatsu Kanai, Saito Kunio, and Oda Koji. 2008. Aromatic amino acid derivative with LAT1 inhibitory activity, LAT1 inhibitor containing the same and method for producing the same. WO 2008/081537 A1, issued 2008.

Endou, Hitoshi, Yoshikatsu Kanai, Kenji Tsujihara, and Kunio Saito. 2008. Amino acid derivatives and medicinal compositions. US 7,345,068 B2, issued 2008.

Enomoto, Keisuke, Fuyuki Sato, Shunji Tamagawa, Mehmet Gunduz, and Naoyoshi Onoda. 2019. "A Novel Therapeutic Approach for Anaplastic Thyroid Cancer through Inhibition of LAT1." *Scientific Reports*, 1–11. https://doi.org/10.1038/s41598-019-51144-6.

Eriksson, J, T Forsen, C Osmond, and D Barker. 2003. "Obesity from Cradle to Grave." *International Journal of Obesity and Related Metabolic Disorders : Journal of the International Association for the Study of Obesity* 27 (6): 722–27. https://doi.org/10.1038/sj.ijo.0802278.

Escher, Claudia, Lukas Reiter, Brendan Maclean, Reto Ossola, Franz Herzog, John Chilton, Michael J. Maccoss, and Oliver Rinner. 2012. "Using IRT, a Normalized Retention Time for More Targeted Measurement of Peptides." *Proteomics* 12 (8): 1111–21. https://doi.org/10.1002/pmic.201100463.

Evans, R. W., R. W. Powers, R. B. Ness, L. J. Cropcho, A. R. Daftary, G. F. Harger, R. Vergona, and D. N. Finegold. 2003. "Maternal and Fetal Amino Acid Concentrations and Fetal Outcomes

during Pre-Eclampsia." *Reproduction* 125 (6): 785–90. https://doi.org/10.1530/rep.0.1250785.

Faichney, G. J., and G. A. White. 1987. "Effects of Maternal Nutritional Status on Fetal and Placental Growth and on Fetal Urea Synthesis in Sheep." *Australian Journal of Biological Sciences* 40 (4): 365–77. https://doi.org/10.1071/BI9870365.

Farcich, E a, and E H Morgan. 1992. "Diminished Iron Acquisition by Cells and Tissues of Belgrade Laboratory Rats." *The American Journal of Physiology* 262 (2 Pt 2): R220-4.

Fernández-Real, José Manuel, Abel López-Bermejo, and Wifredo Ricart. 2002. "Cross-Talk Between Iron Metabolism and Diabetes." *Diabetes* 51 (8): 2348–54. https://doi.org/10.2337/diabetes.52.1.1.

Filant, Justyna, and Thomas E. Spencer. 2014. "Uterine Glands: Biological Roles in Conceptus Implantation, Uterine Receptivity, and Decidualization." *Int J Dev Biol.* 58 (0): 107–16. https://doi.org/10.1038/jid.2014.371.

Foot, Natalie J, Hazel E Dalton, Linda M Shearwin-whyatt, Loretta Dorstyn, Seong-seng Tan, Baoli Yang, and Sharad Kumar. 2016. "Regulation of the Divalent Metal Ion Transporter DMT1 and Iron Homeostasis by a Ubiquitin-Dependent Mechanism Involving Ndfips and WWP2." *Blood* 112 (10): 4268–76. https://doi.org/10.1182/blood-2008-04-150953.

Forbes, K., M. Desforges, R. Garside, J. D. Aplin, and M. Westwood. 2009. "Methods for SiRNA-Mediated Reduction of MRNA and Protein Expression in Human Placental Explants, Isolated Primary Cells and Cell Lines." *Placenta* 30 (2): 124–29. https://doi.org/10.1016/j.placenta.2008.10.003.

Fotiadis, Dimitrios, Yoshikatsu Kanai, and Manuel Palacín. 2013. "The SLC3 and SLC7 Families of Amino Acid Transporters." *Molecular Aspects of Medicine* 34 (2–3): 139–58. https://doi.org/10.1016/j.mam.2012.10.007.

Frewen, Barbara, and Michael J. MacCoss. 2007. "Using BiblioSpec for Creating and Searching Tandem MS Peptide Libraries." *Current Protocols in Bioinformatics*, 1–12. https://doi.org/10.1002/0471250953.bi1307s20.

Fu, Shimin, Feifei Li, Jianguo Zhou, and Zhiping Liu. 2016. "The Relationship between Body Iron Status, Iron Intake and Gestational Diabetes: A Systematic Review and Meta-Analysis." *Medicine (United States)* 95 (2): e2383. https://doi.org/10.1097/MD.0000000000002383.

Fuchs, Bryan C., and Barrie P. Bode. 2005. "Amino Acid Transporters ASCT2 and LAT1 in Cancer: Partners in Crime?" *Seminars in Cancer Biology* 15 (4): 254–66. https://doi.org/10.1016/j.semcancer.2005.04.005.

Fuchs, Renate, and Isabella Ellinger. 2004. "Endocytic and Transcytotic Processes in Villous Syncytiotrophoblast: Role in Nutrient Transport to the Human Fetus." *Traffic* 5 (10): 725–38. https://doi.org/10.1111/j.1600-0854.2004.00221.x.

Fuqua, Brie K, Yan Lu, David M Frazer, Deepak Darshan, Sarah J Wilkins, Linda Dunn, Alex V Loguinov, et al. 2018. "Severe Iron Metabolism Defects In Mice With Double Knockout Of." *Cellular and Molecular Gastroenterology and Hepatology*, no. July. https://doi.org/10.1016/j.jcmgh.2018.06.006.

Furesz, T. C., C. H. Smith, and A. J. Moe. 1993. "ASC System Activity Is Altered by Development of Cell Polarity in Trophoblast from Human Placenta." *American Journal of Physiology - Cell Physiology* 265 (1 34-1). https://doi.org/10.1152/ajpcell.1993.265.1.c212.

Furesz, T C, A J Moe, and C H Smith. 1995. “Lysine Uptake by Human Placental Microvillous Membrane: Comparison of System Y+ with Basal Membrane.” *The American Journal of Physiology* 268 (3 Pt 1): C755-61. http://www.ncbi.nlm.nih.gov/pubmed/7534987.

Gaccioli, Francesca, Irving L. M. H. Aye, Sara Roos, Susanne Lager, Vanessa I. Ramirez, Yoshikatsu Kanai, Theresa L. Powell, and Thomas Jansson. 2015. “Expression and Functional Characterisation of System L Amino Acid Transporters in the Human Term Placenta.” *Reproductive Biology and Endocrinology* 13 (1): 57. https://doi.org/10.1186/s12958-015-0054-8.

Gagnon, James A., Eivind Valen, Summer B. Thyme, Peng Huang, Laila Ahkmetova, Andrea Pauli, Tessa G. Montague, Steven Zimmerman, Constance Richter, and Alexander F. Schier. 2014. “Efficient Mutagenesis by Cas9 Protein-Mediated Oligonucleotide Insertion and Large-Scale Assessment of Single-Guide RNAs.” *PLoS ONE* 9 (5): e98186. https://doi.org/10.1371/journal.pone.0098186.

Gaillard, Romy. 2015. “Maternal Obesity during Pregnancy and Cardiovascular Development and Disease in the Offspring.” *European Journal of Epidemiology* 30 (11): 1141–52. https://doi.org/10.1007/s10654-015-0085-7.

Gaither, Kecia, Abid N. Quraishi, and Nicholas P. Illsley. 1999. “Diabetes Alters the Expression and Activity of the Human Placental GLUT1 Glucose Transporter.” *Journal of Clinical Endocrinology and Metabolism* 84 (2): 695–701. https://doi.org/10.1210/jc.84.2.695.

Gallo, L. A., H. L. Barrett, and M. Dekker Nitert. 2017. “Review: Placental Transport and Metabolism of Energy Substrates in Maternal Obesity and Diabetes.” *Placenta* 54: 59–67. https://doi.org/10.1016/j.placenta.2016.12.006.

Gambling, Lorraine, Ruth Danzeisen, Susan Gair, Richard G Lea, Zehane Charania, Nita Solanky, Kavita D Joory, S Kaila S Srai, Harry J M C Ardle, and H J McArdle. 2001. “Effect of Iron Deficiency on Placental Transfer of Iron and Expression of Iron Transport Proteins in Vivo and in Vitro.” *Biochem J* 889 (Pt 3): 883–89. https://doi.org/10.1042/0264-6021:3560883.

Gaull, Gerald, John A. Sturman, and Niels C.R. Räihä. 1972. “Development of Mammalian Sulfur Metabolism: Absence of Cystathionase in Human Fetal Tissues.” *Pediatric Research* 6 (6): 538–47. https://doi.org/10.1203/00006450-197206000-00002.

Geier, Ethan G., Avner Schlessinger, Hao Fan, Jonathan E. Gable, John J. Irwin, Andrej Sali, and Kathleen M. Giacomini. 2013. “Structure-Based Ligand Discovery for the Large-Neutral Amino Acid Transporter 1, LAT-1.” *Proceedings of the National Academy of Sciences of the United States of America* 110 (14): 5480–85. https://doi.org/10.1073/pnas.1218165110.

Georgieff, M. K., S. A. Berry, J. D. Wobken, and E. A. Leibold. 1999. “Increased Placental Iron Regulatory Protein-1 Expression in Diabetic Pregnancies Complicated by Fetal Iron Deficiency.” *Placenta* 20 (1): 87–93. https://doi.org/10.1053/plac.1998.0339.

Georgieff, M. K., J. K. Wobken, J. Welle, J. R. Burdo, and J. R. Connor. 2000. “Identification and Localization of Divalent Metal Transporter-1 (DMT-1) in Term Human Placenta.” *Placenta* 21 (8): 799–804. https://doi.org/10.1053/plac.2000.0566.

Gruper, Yaron, Jacob Bar, Eran Bacharach, and Rachel Ehrlich. 2005. “Transferrin Receptor Co-Localizes and Interacts with the Hemochromatosis Factor (HFE) and the Divalent Metal Transporter-1 (DMT1) in Trophoblast Cells.” *Journal of Cellular Physiology* 204 (3): 901–12. https://doi.org/10.1002/jcp.20349.

Guller, Seth, Catalin S. Buhimschi, Yula Y. Ma, Se Te J. Huang, Liubin Yang, Edward Kuczynski,

Eduardo Zambrano, Charles J. Lockwood, and Irina A. Buhimschi. 2008. “Placental Expression of Ceruloplasmin in Pregnancies Complicated by Severe Preeclampsia.” *Laboratory Investigation* 88 (10): 1057–67. https://doi.org/10.1038/labinvest.2008.74.

Gunderson, Erica P., and Barbara Abrams. 2000. “Epidemiology of Gestational Weight Gain and Body Weight Changes after Pregnancy.” *Epidemiologic Reviews* 22 (2): 261–74. https://doi.org/10.1093/oxfordjournals.epirev.a018038.

Gunshin, Hiromi, Yuko Fujiwara, Angel O. Custodio, Cristina DiRenzo, Sylvie Robine, and Nancy C. Andrews. 2005. “Slc11a2 Is Required for Intestinal Iron Absorption and Erythropoiesis but Dispensable in Placenta and Liver.” *Journal of Clinical Investigation* 115 (5): 1258–66. https://doi.org/10.1172/JCI200524356.

Häfliger, Pascal, and Roch Philippe Charles. 2019. “The L-Type Amino Acid Transporter LAT1—an Emerging Target in Cancer.” *International Journal of Molecular Sciences* 20 (10): 1–14. https://doi.org/10.3390/ijms20102428.

Häfliger, Pascal, Julien Graff, Matthias Rubin, Amandine Stooss, Matthias S. Dettmer, Karl Heinz Altmann, Jürg Gertsch, and Roch Philippe Charles. 2018. “The LAT1 Inhibitor JPH203 Reduces Growth of Thyroid Carcinoma in a Fully Immunocompetent Mouse Model.” *Journal of Experimental and Clinical Cancer Research* 37 (1). https://doi.org/10.1186/s13046-018-0907-z.

Haines, David R., Richard W. Fuller, Shakeel Ahmad, David T. Vistica, and Victor E. Marquez. 1987. “Selective Cytotoxicity of a System L Specific Amino Acid Nitrogen Mustard.” *Journal of Medicinal Chemistry* 30 (3): 542–47. https://doi.org/10.1021/jm00386a017.

Handel, Ben Van, Sacha L. Prashad, Nargess Hassanzadeh-Kiabi, Andy Huang, Mattias Magnusson, Boriana Atanassova, Angela Chen, Eija I. Hamalainen, and Hanna K.A. Mikkola. 2010. “The First Trimester Human Placenta Is a Site for Terminal Maturation of Primitive Erythroid Cells.” *Blood* 116 (17): 3321–30. https://doi.org/10.1182/blood-2010-04-279489.

Harder, Thomas, Elke Rodekamp, Karen Schellong, Joachim W. Dudenhausen, and Andreas Plagemann. 2007. “Birth Weight and Subsequent Risk of Type 2 Diabetes: A Meta-Analysis.” *American Journal of Epidemiology* 165 (8): 849–57. https://doi.org/10.1093/aje/kwk071.

Harrington, Brendan, Jocelyn Glazier, Stephen D’Souza, and Colin Sibley. 1999. “System A Amino Acid Transporter Activity in Human Placental Microvillous Membrane Vesicles in Relation to Various Anthropometric Measurements in Appropriate and Small for Gestational Age Babies.” *Pediatric Research* 45 (6): 810–14. https://doi.org/10.1203/00006450-199906000-00005.

Harris, Z. Leah, Alison P. Durley, Tsz Kwong Man, and Jonathan D. Gitlin. 1999. “Targeted Gene Disruption Reveals an Essential Role for Ceruloplasmin in Cellular Iron Efflux.” *Proceedings of the National Academy of Sciences of the United States of America* 96 (19): 10812–17. https://doi.org/10.1073/pnas.96.19.10812.

Hayashi, S., K. Sanada, N. Sagawa, N. Yamada, and K. Kido. 1978. “Umbilical Vein-Artery Differences of Plasma Amino Acids in the Last Trimester of Human Pregnancy.” *Biology of the Neonate* 34 (1–2): 11–18. https://doi.org/10.1159/000241099.

Heaton, Sarah J., John J. Eady, Mary L. Parker, Kathryn L. Gotts, Jack R. Dainty, Susan J. Fairweather-Tait, Harry J. McArdle, Kaila S. Srai, and Ruan M. Elliott. 2008. “The Use of BeWo Cells as an in Vitro Model for Placental Iron Transport.” *American Journal of Physiology - Cell Physiology* 295 (5): 1445–53. https://doi.org/10.1152/ajpcell.00286.2008.

Hedderson, Monique M., Erica P. Gunderson, and Assiamira Ferrara. 2010. "Gestational Weight Gain and Risk of Gestational Diabetes Mellitus." *Obstetrics & Gynecology* 115 (3): 597–604. https://doi.org/10.3760/cma.j.issn.0366-6999.20132772.

Hess, S. Y., M. B. Zimmermann, S. Brogli, and R. F. Hurrell. 2001. "A National Survey of Iron and Folate Status in Pregnant Women in Switzerland." *International Journal for Vitamin and Nutrition Research* 71 (5): 268–73. https://doi.org/10.1024/0300-9831.71.5.268.

Hill, Penny M M, and Maureen Young. 1973. "Net Placental Transfer of Free Amino Acids against Varying Concentrations." *Journal of Physiology* 235: 409–22.

Hoeltzli, S. D., L. K. Kelley, A. J. Moe, and C. H. Smith. 1990. "Anionic Amino Acid Transport Systems in Isolated Basal Plasma Membrane of Human Placenta." *American Journal of Physiology - Cell Physiology* 259 (1 28-1). https://doi.org/10.1152/ajpcell.1990.259.1.c47.

Hoeltzli, S. D., and C. H. Smith. 1989. "Alanine Transport Systems in Isolated Basal Plasma Membrane of Human Placenta." *American Journal of Physiology - Cell Physiology* 256 (3). https://doi.org/10.1152/ajpcell.1989.256.3.c630.

Hojyo, Shintaro, Toshiyuki Fukada, Shinji Shimoda, Wakana Ohashi, Bum Ho Bin, Haruhiko Koseki, and Toshio Hirano. 2011. "The Zinc Transporter SLC39A14/ZIP14 Controls G-Protein Coupled Receptor-Mediated Signaling Required for Systemic Growth." *PLoS ONE* 6 (3). https://doi.org/10.1371/journal.pone.0018059.

Holm, Maia Blomhoff, Nasser Ezzatkhah Bastani, Ane Moe Holme, Manuela Zucknick, Thomas Jansson, Helga Refsum, Lars Mørkrid, Rune Blomhoff, Tore Henriksen, and Trond Melbye Michelsen. 2017. "Uptake and Release of Amino Acids in the Fetal-Placental Unit in Human Pregnancies." *PLoS ONE* 12 (10): 1–15. https://doi.org/10.1371/journal.pone.0185760.

Huang, X., M. Baumann, L. Nikitina, F. Wenger, D. Surbek, M. Körner, and C. Albrecht. 2013. "RNA Degradation Differentially Affects Quantitative MRNA Measurements of Endogenous Reference Genes in Human Placenta." *Placenta* 34 (7): 544–47. https://doi.org/10.1016/j.placenta.2013.03.011.

Huang, Xiao, Michael Lüthi, Edgar C. Ontsouka, Sampada Kallol, Marc U. Baumann, Daniel V. Surbek, and Christiane Albrecht. 2016. "Establishment of a Confluent Monolayer Model with Human Primary Trophoblast Cells: Novel Insights into Placental Glucose Transport." *Molecular Human Reproduction* 0 (0): gaw018. https://doi.org/10.1093/molehr/gaw018.

Huppertz, B. 2008. "The Anatomy of the Normal Placenta." *Journal of Clinical Pathology*. https://doi.org/10.1136/jcp.2008.055277.

Huttunen, Kristiina M., Mikko Gynther, Johanna Huttunen, Elena Puris, Julie A. Spicer, and William A. Denny. 2016. "A Selective and Slowly Reversible Inhibitor of l -Type Amino Acid Transporter 1 (LAT1) Potentiates Antiproliferative Drug Efficacy in Cancer Cells." *Journal of Medicinal Chemistry* 59 (12): 5740–51. https://doi.org/10.1021/acs.jmedchem.6b00190.

Illsley, N.P. 2000. "Glucose Transporters in the Human Placenta." *Placenta* 21 (1): 14–22. https://doi.org/10.1053/plac.1999.0448.

Illsley, Nicholas P., Zhi Qiong Wang, Andrea Gray, Mary C. Sellers, and Mark M. Jacobs. 1990. "Simultaneous Preparation of Paired, Syncytial, Microvillous and Basal Membranes from Human Placenta." *BBA - Biomembranes* 1029 (2): 218–26. https://doi.org/10.1016/0005-2736(90)90157-J.

Jansson, T., K. Ylvén, M. Wennergren, and T. L. Powell. 2002. "Glucose Transport and System A Activity in Syncytiotrophoblast Microvillous and Basal Plasma Membranes in Intrauterine

Growth Restriction." *Placenta* 23 (5): 392–99. https://doi.org/10.1053/plac.2002.0826.

Jansson, Thomas. 2001. "Amino Acid Transporters in the Human Placenta." *Pediatric Research* 49 (2): 141–47. https://doi.org/10.1203/00006450-200102000-00003.

Jansson, Thomas, Ylva Ekstrand, Caroline Björn, Margareta Wennergren, and Theresa L. Powell. 2002. "Alterations in the Activity of Placental Amino Acid Transporters in Pregnancies Complicated by Diabetes." *Diabetes* 51 (7): 2214–19. https://doi.org/10.2337/diabetes.51.7.2214.

Jansson, Thomas, and Theresa L. Powell. 2007. "Role of the Placenta in Fetal Programming: Underlying Mechanisms and Potential Interventional Approaches." *Clinical Science* 113 (1): 1–13. https://doi.org/10.1042/CS20060339.

Jauniaux, Eric, Beatrice Gulbis, and Erik Gerloo. 1999. "Free Amino Acids in Human Fetal Liver and Fluids at 12-17 Weeks of Gestation." *Human Reproduction* 14 (6): 1638–41. https://doi.org/10.1093/humrep/14.6.1638.

Jauniaux, Eric, Adrian L. Watson, Joanne Hempstock, Yi Ping Bao, Jeremy N. Skepper, and Graham J. Burton. 2000. "Onset of Maternal Arterial Blood Flow and Placental Oxidative Stress: A Possible Factor in Human Early Pregnancy Failure." *American Journal of Pathology* 157 (6): 2111–22. https://doi.org/10.1016/S0002-9440(10)64849-3.

Jenkitkasemwong, Supak, Chia Yu Wang, Bryan MacKenzie, and Mitchell D. Knutson. 2012. "Physiologic Implications of Metal-Ion Transport by ZIP14 and ZIP8." *BioMetals* 25 (4): 643–55. https://doi.org/10.1007/s10534-012-9526-x.

Jinek, Martin, Krzysztof Chylinski, Ines Fonfara, Michael Hauer, Jennifer A. Doudna, and Emmanuelle Charpentier. 2012. "A Programmable Dual-RNA-Guided DNA Endonuclease in Adaptive Bacterial Immunity." *Science* 337 (6096): 816–21. https://doi.org/10.1126/science.1225829.

Johansson, M., T. Jansson, and T. L. Powell. 2000. "Na+-K+-ATPase Is Distributed to Microvillous and Basal Membrane of the Syncytiotrophoblast in Human Placenta." *American Journal of Physiology - Regulatory Integrative and Comparative Physiology* 279 (1 48-1): 287–94. https://doi.org/10.1152/ajpregu.2000.279.1.r287.

Johnson, L. W., and C. H. Smith. 1988. "Neutral Amino Acid Transport Systems of Microvillous Membrane of Human Placenta." *American Journal of Physiology - Cell Physiology* 254 (6). https://doi.org/10.1152/ajpcell.1988.254.6.c773.

Johnson, Larry W., and Carl H. Smith. 1985. "Glucose Transport across the Basal Plasma Membrane of Human Placental Syncytiotrophoblast." *BBA - Biomembranes* 815 (1): 44–50. https://doi.org/10.1016/0005-2736(85)90472-9.

Jozwik, M., C. Teng, F. C. Battaglia, and G. Meschia. 1999. "Fetal Supply of Amino Acids and Amino Nitrogen after Maternal Infusion of Amino Acids in Pregnant Sheep." *American Journal of Obstetrics and Gynecology* 180 (2 I): 447–53. https://doi.org/10.1016/S0002-9378(99)70230-9.

Jóźwik, Maciej, Cecilia Teng, Randall B. Wilkening, Giacomo Meschia, and Frederick C. Battaglia. 2004. "Reciprocal Inhibition of Umbilical Uptake within Groups of Amino Acids." *American Journal of Physiology - Endocrinology and Metabolism* 286 (3 49-3): 376–83. https://doi.org/10.1152/ajpendo.00428.2003.

Kabeya, Yukiko, Noboru Mizushima, Takashi Ueno, Akitsugu Yamamoto, Takayoshi Kirisako, Takeshi Noda, Eiki Kominami, Yoshinori Ohsumi, and Tamotsu Yoshimori. 2000. "LC3 , a

Mammalian Homologue of Yeast Apg8p , Is Localized in Autophagosome Membranes after Processing" 19 (21).

Kaira, Kyoichi, Noboru Oriuchi, Hisao Imai, Kimihiro Shimizu, Noriko Yanagitani, Noriaki Sunaga, Takeshi Hisada, et al. 2008. "L-Type Amino Acid Transporter 1 and CD98 Expression in Primary and Metastatic Sites of Human Neoplasms." *Cancer Science* 99 (12): 2380–86. https://doi.org/10.1111/j.1349-7006.2008.00969.x.

Kaji, Masahiko, Maryam Kabir-Salmani, Naohiko Anzai, Chun Ji Jin, Yoshihiro Akimoto, Ayako Horita, Atsuhiko Sakamoto, Yoshikatsu Kanai, Hiroyuki Sakurai, and Mitsutoshi Iwashita. 2010. "Properties of L-Type Amino Acid Transporter 1 in Epidermal Ovarian Cancer." *International Journal of Gynecological Cancer : Official Journal of the International Gynecological Cancer Society* 20 (3): 329–36. https://doi.org/10.1111/IGC.0b013e3181d28e13.

Kallol, Sampada, Xiao Huang, Stefan Müller, Corneille Ontsouka, and Christiane Albrecht. 2018. "Novel Insights into Concepts and Directionality of Maternal–Fetal Cholesterol Transfer across the Human Placenta." *International Journal of Molecular Sciences* 19 (8): 2334. https://doi.org/10.3390/ijms19082334.

Kallol, Sampada, Ruedi Moser-Haessig, Corneille Edgar Ontsouka, and Christiane Albrecht. 2018. "Comparative Expression Patterns of Selected Membrane Transporters in Differentiated BeWo and Human Primary Trophoblast Cells." *Placenta* 72–73 (October): 48–52. https://doi.org/10.1016/j.placenta.2018.10.008.

Karl, P. I., K. L. Alpy, and S. E. Fisher. 1992. "Amino Acid Transport by the Cultured Human Placental Trophoblast: Effect of Insulin on AIB Transport." *American Journal of Physiology - Cell Physiology* 262 (4 31-4). https://doi.org/10.1152/ajpcell.1992.262.4.c834.

Karl, Peter I., Helen Tkaczevski, and Stanley E. Fisher. 1989. "Characteristics of Histidine Uptake by Human Placental Microvillous Membrane Vesicles." *Pediatric Research* 25 (1): 19–26. https://doi.org/10.1203/00006450-198901000-00005.

Karsdorp, Veronique H.M., John M.G. van Vugt, Cornells Jakobs, Guus A. Dekker, and Herman P. van Geijn. 1994. "Amino Acids, Glucose and Lactate Concentrations in Umbilical Cord Blood in Relation to Umbilical Artery Flow Patterns." *European Journal of Obstetrics and Gynecology and Reproductive Biology* 57 (2): 117–22. https://doi.org/10.1016/0028-2243(94)90053-1.

Kertschanska, Sonya, Georg Kosanke, and Peter Kaufmann. 1997. "Pressure Dependence of So-Called Transtrophoblastic Channels during Fetal Perfusion of Human Placental Villi." *Microscopy Research and Technique* 38 (1–2): 52–62. https://doi.org/10.1002/(SICI)1097-0029(19970701/15)38:1/2<52::AID-JEMT7>3.0.CO;2-W.

Khera, A., J. J. Vanderlelie, and A. V. Perkins. 2013. "Selenium Supplementation Protects Trophoblast Cells from Mitochondrial Oxidative Stress." *Placenta* 34 (7): 594–98. https://doi.org/10.1016/j.placenta.2013.04.010.

Khera, Alisha, Jessica J. Vanderlelie, Olivia Holland, and Anthony V. Perkins. 2017. "Overexpression of Endogenous Anti-Oxidants with Selenium Supplementation Protects Trophoblast Cells from Reactive Oxygen Species-Induced Apoptosis in a Bcl-2-Dependent Manner." *Biological Trace Element Research* 177 (2): 394–403. https://doi.org/10.1007/s12011-016-0870-5.

Kim, Sojung, Daesik Kim, Seung Woo Cho, Jungeun Kim, and Jin Soo Kim. 2014. "Highly Efficient RNA-Guided Genome Editing in Human Cells via Delivery of Purified Cas9 Ribonucleoproteins." *Genome Research* 24 (6): 1012–19.

https://doi.org/10.1101/gr.171322.113.

Koenig, Mary Dawn, Lisa Tussing-humphreys, Jessica Day, Brooke Cadwell, and Elizabeta Nemeth. 2014. "Hepcidin and Iron Homeostasis during Pregnancy," 3062–83. https://doi.org/10.3390/nu6083062.

Kongpracha, Pornparn, Shushi Nagamori, Pattama Wiriyasermkul, Yoko Tanaka, Kazuko Kaneda, Suguru Okuda, Ryuichi Ohgaki, and Yoshikatsu Kanai. 2017. "Structure-Activity Relationship of a Novel Series of Inhibitors for Cancer Type Transporter L-Type Amino Acid Transporter 1 (LAT1)." *Journal of Pharmacological Sciences* 133 (2): 96–102. https://doi.org/10.1016/j.jphs.2017.01.006.

Kovács, Árpád Ferenc, Nóra Fekete, Lilla Turiák, András Ács, László Kőhidai, Edit I. Buzás, and Éva Pállinger. 2019. "Unravelling the Role of Trophoblastic-Derived Extracellular Vesicles in Regulatory T Cell Di Ff Erentiation." *Int. J. Mol. Sci.2* 20 (14): 3457. https://doi.org/10.3390/ijms20143457.

Kudo, Yoshiki, and C. A.R. Boyd. 1990. "Characterization of Amino Acid Transport Systems in Human Placental Basal Membrane Vesicles." *BBA - Biomembranes* 1021 (2): 169–74. https://doi.org/10.1016/0005-2736(90)90030-R.

Kudo, Yoshiki, C. A.R. Boyd, Hiroshi Kimura, P. R. Cook, C. W.G. Redman, and I. L. Sargent. 2003. "Quantifying the Syncytialisation of Human Placental Trophoblast BeWo Cells Grown in Vitro." *Biochimica et Biophysica Acta - Molecular Cell Research* 1640 (1): 25–31. https://doi.org/10.1016/S0167-4889(03)00004-1.

Kudo, Yoshiki, and C. A R Boyd. 2001. "Characterisation of L-Tryptophan Transporters in Human Placenta: A Comparison of Brush Border and Basal Membrane Vesicles." *Journal of Physiology* 531 (2): 405–16. https://doi.org/10.1111/j.1469-7793.2001.0405i.x.

Kurutas, Ergul Belge. 2016. "The Importance of Antioxidants Which Play the Role in Cellular Response against Oxidative/Nitrosative Stress: Current State." *Nutrition Journal* 15 (1): 1–22. https://doi.org/10.1186/s12937-016-0186-5.

Lager, Susanne, and Theresa L. Powell. 2012. "Regulation of Nutrient Transport across the Placenta." *Journal of Pregnancy* 2012: 179827. https://doi.org/10.1155/2012/179827.

Lam-Yuk-Tseung, Steven, and Philippe Gros. 2006. "Distinct Targeting and Recycling Properties of Two Isoforms of the Iron." *Biochemistry* 45: 2294–2301.

Lambot, N., P. Lybaert, A. Boom, J. Delogne-Desnoeck, A.M. Vanbellinghen, G. Graff, P. Lebrun, and S. Meuris. 2006. "Evidence for a Clathrin-Mediated Recycling of Albumin in Human Term Placenta1." *Biology of Reproduction* 75 (1): 90–97. https://doi.org/10.1095/biolreprod.105.050021.

Lamparelli, R. D.V., B. M. Friedman, A. P. Macphail, T. H. Bothwell, J. I. Phillips, and R. D. Baynes. 1989. "The Fate of Intravenously Injected Tissue Ferritin in Pregnant Guinea-pigs." *British Journal of Haematology* 72 (1): 100–105. https://doi.org/10.1111/j.1365-2141.1989.tb07659.x.

Lappas, Martha, Ursula Hiden, Gernot Desoye, Julia Froehlich, Sylvie Hauguel-de Mouzon, and Alicia Jawerbaum. 2011. "The Role of Oxidative Stress in the Pathophysiology of Gestational Diabetes Mellitus." *Antioxidants & Redox Signaling* 15 (12): 3061–3100. https://doi.org/10.1089/ars.2010.3765.

Lassance, Luciana, Maricela Haghiac, Patrick Leahy, Subhabrata Basu, Judi Minium, Joanna Zhou, Mitchell Reider, Patrick M. Catalano, and Sylvie Hauguel-De Mouzon. 2015. "Identification

of Early Transcriptome Signatures in Placenta Exposed to Insulin and Obesity." *American Journal of Obstetrics and Gynecology* 212 (5): 647.e1-647.e11. https://doi.org/10.1016/j.ajog.2015.02.026.

Lee, Lydia K., Masaya Ueno, Ben Van Handel, and Hanna K.A. Mikkola. 2010. "Placenta as a Newly Identified Source of Hematopoietic Stem Cells." *Current Opinion in Hematology* 17 (4): 313–18. https://doi.org/10.1097/MOH.0b013e328339f295.

Lemons, James A., Debra Reyman, and Richard L. Schreiner. 1984. "Fetal and Maternal Amino Acid Concentrations During Fasting in the Ewe." *Journal of Pediatric Gastroenterology and Nutrition* 3: 249–55.

Leon, D a, H O Lithell, D Vâgerö, I Koupilová, R Mohsen, L Berglund, U B Lithell, and P M McKeigue. 1998. "Reduced Fetal Growth Rate and Increased Risk of Death from Ischaemic Heart Disease: Cohort Study of 15 000 Swedish Men and Women Born 1915-29." *BMJ (Clinical Research Ed.)* 317 (7153): 241–45. https://doi.org/10.1136/bmj.317.7153.241.

Levine, Rodney L., Donita Garland, Cynthia N. Oliver, Adolfo Amici, Isabel Climent, Anke-G. Lenz, Bong-Whan Ahn, Shmuel Shaltiel, and Earl R. Stadtman. 2009. "Determination of Carbonyl Content in Oxidatively Modified Proteins." *Methods in Enzymology* 186 (1983): 1–8.

Levy, Joanne E., Ou Jin, Yuko Fujiwara, Frank Kuo, and Nancy C. Andrews. 1999. "Transferrin Receptor Is Necessary for Development of Erythrocytes and the Nervous System." *Nature Genetics* 21 (4): 396–99. https://doi.org/10.1038/7727.

Lewis, R. M., S. Brooks, I. P. Crocker, J. Glazier, M. A. Hanson, E. D. Johnstone, N. Panitchob, et al. 2013. "Review: Modelling Placental Amino Acid Transfer - From Transporters to Placental Function." *Placenta* 34 (SUPPL): S46–51. https://doi.org/10.1016/j.placenta.2012.10.010.

Lewis, R. M., J. Glazier, S. L. Greenwood, E. J. Bennett, K. M. Godfrey, a. a. Jackson, C. P. Sibley, I. T. Cameron, and M. a. Hanson. 2007. "L-Serine Uptake by Human Placental Microvillous Membrane Vesicles." *Placenta* 28 (5–6): 445–52. https://doi.org/10.1016/j.placenta.2006.06.014.

Lewis, Rohan M., Keith M. Godfrey, Alan A. Jackson, Iain T. Cameron, and Mark A. Hanson. 2005. "Low Serine Hydroxymethyltransferase Activity in the Human Placenta Has Important Implications for Fetal Glycine Supply." *Journal of Clinical Endocrinology and Metabolism* 90 (3): 1594–98. https://doi.org/10.1210/jc.2004-0317.

Lewis, Rohan M, Jane K Cleal, and Bram G Sengers. 2020. "Placental Perfusion and Mathematical Modelling." *Placenta*. https://doi.org/10.1016/j.placenta.2020.02.015.

Li, Hequn, Bennard Van Ravenzwaay, Ivonne M.C.M. Rietjens, and Jochem Louisse. 2013. "Assessment of an in Vitro Transport Model Using BeWo B30 Cells to Predict Placental Transfer of Compounds." *Archives of Toxicology* 87 (9): 1661–69. https://doi.org/10.1007/s00204-013-1074-9.

Li, Jau Yi, Neal Paragas, Renee M. Ned, Andong Qiu, Melanie Viltard, Thomas Leete, Ian R. Drexler, et al. 2009. "Scara5 Is a Ferritin Receptor Mediating Non-Transferrin Iron Delivery." *Developmental Cell* 16 (1): 35–46. https://doi.org/10.1016/j.devcel.2008.12.002.

Li, Jiali, Mingzhu Yin, Wanjing Song, Fengyun Cui, Wei Wang, Shuyang Wang, and Hongguang Zhu. 2018. "B Subunit of Human Chorionic Gonadotropin Promotes Tumor Invasion and Predicts Poor Prognosis of Early-Stage Colorectal Cancer." *Cellular Physiology and Biochemistry* 45 (1): 237–49. https://doi.org/10.1159/000486770.

Li, Yan Qin, Bin Bai, Xiao Xiao Cao, Hong Yan, and Gui Hua Zhuang. 2012. "Ferroportin 1 and

Hephaestin Expression in BeWo Cell Line with Different Iron Treatment." *Cell Biochemistry and Function* 30 (3): 249–55. https://doi.org/10.1002/cbf.1843.

Liang, Xiquan, Jason Potter, Shantanu Kumar, Yanfei Zou, Rene Quintanilla, Mahalakshmi Sridharan, Jason Carte, et al. 2015. "Rapid and Highly Efficient Mammalian Cell Engineering via Cas9 Protein Transfection." *Journal of Biotechnology* 208: 44–53. https://doi.org/10.1016/j.jbiotec.2015.04.024.

Lindsay, H., A. Burger, B. Biyong, A. Felker, C. Hess, J. Zaugg, E. Chiavacci, et al. 2016. "CrispRVariants Charts the Mutation Spectrum of Genome Engineering Experiments." *Nature Biotechnology* 34 (7). https://doi.org/10.1038/nbt.3628.

Liuzzi, Juan P, Fikret Aydemir, Hyeyoung Nam, Mitchell D Knutson, and Robert J Cousins. 2006. "Zip14 (Slc39a14) Mediates Non-Transferrin-Bound Iron Uptake into Cells." *Proceedings of the National Academy of Sciences of the United States of America* 103 (37): 13612–17. https://doi.org/10.1073/pnas.0606424103.

Mackenzie, Bryan, Hitomi Takanaga, Nadia Hubert, Andreas Rolfs, and Matthias A. Hediger. 2007. "Functional Properties of Multiple Isoforms of Human Divalent Metal-Ion Transporter 1 (DMT1)." *Biochemical Journal* 403 (1): 59–69. https://doi.org/10.1042/BJ20061290.

MacLean, Brendan, Daniela M. Tomazela, Nicholas Shulman, Matthew Chambers, Gregory L. Finney, Barbara Frewen, Randall Kern, David L. Tabb, Daniel C. Liebler, and Michael J. MacCoss. 2010. "Skyline: An Open Source Document Editor for Creating and Analyzing Targeted Proteomics Experiments." *Bioinformatics* 26 (7): 966–68. https://doi.org/10.1093/bioinformatics/btq054.

Malhotra, Sudha Saryu, Pankaj Suman, and Satish Kumar Gupta. 2015. "Alpha or Beta Human Chorionic Gonadotropin Knockdown Decrease BeWo Cell Fusion by Down-Regulating PKA and CREB Activation." *Scientific Reports* 5 (May): 1–15. https://doi.org/10.1038/srep11210.

Malinow, M. R., A. Rajkovic, P. B. Duell, D. L. Hess, and B. M. Upson. 1998. "The Relationship between Maternal and Neonatal Umbilical Cord Plasma Homocyst(e)Ine Suggests a Potential Role for Maternal Homocyst(e)Ine in Fetal Metabolism." *American Journal of Obstetrics and Gynecology* 178 (2): 228–33. https://doi.org/10.1016/S0002-9378(98)80005-7.

Maltepe, Emin, and Susan J. Fisher. 2014. "PLACENTA: The Forgotten Organ." *Annual Review of Cell and Developmental Biology* 31 (1): annurev-cellbio-100814-125620. https://doi.org/10.1146/annurev-cellbio-100814-125620.

Mamun, A. A., M. Mannan, and S. A.R. Doi. 2014. "Gestational Weight Gain in Relation to Offspring Obesity over the Life Course: A Systematic Review and Bias-Adjusted Meta-Analysis." *Obesity Reviews* 15 (4): 338–47. https://doi.org/10.1111/obr.12132.

Mao, Jinzhe, David M McKean, Sunita Warrier, Joshua G Corbin, Lee Niswander, and Irene E Zohn. 2010. "The Iron Exporter Ferroportin 1 Is Essential for Development of the Mouse Embryo, Forebrain Patterning and Neural Tube Closure." *Development Cambridge England* 137 (18): 3079–88. https://doi.org/10.1242/dev.048744.

Marconi, Anna Maria, Giacomo Meschia, John W Sparks, and Anna Maria. 1989. "A Comparison of Amino Acid Arteriovenous Differences across the Liver and Placenta of the Fetal Lamb." *American Journal of Physiology - Endocrinology and Metabolism* 257 (6): 909–15.

Maymon, Ron, Eric Jauniaux, Nathalie Greenwold, and Chaya Moroz. 2000. "Localization of P43 Placental Isoferritin in Human Maternal-Fetal Tissue Interface." *American Journal of Obstetrics and Gynecology* 182 (3): 670–74. https://doi.org/10.1067/mob.2000.104145.

McIntosh, N., C. H. Rodeck, and R. Heath. 1984. “Plasma Amino Acids of the Mid-Trimester Human Fetus.” *Biology of the Neonate* 45 (5): 218–24. https://doi.org/10.1159/000242007.

Meier, Christian, Zorica Ristic, Stefan Klauser, and Francois Verrey. 2002. “Activation of System L Heterodimeric Amino Acid Exchangers by Intracellular Substrates.” *The EMBO Journal* 21 (4): 580–89. https://doi.org/10.1093/emboj/21.4.580.

Melzer, K., and Y. Schutz. 2010. “Pre-Pregnancy and Pregnancy Predictors of Obesity.” *International Journal of Obesity* 34: S44–52. https://doi.org/10.1038/ijo.2010.239.

Miyamoto, Yusei, Daniel F. Balkovetz, Frederick H. Leibach, Virendra B. Mahesh, and Vadivel Ganapathy. 1988. “Na+ + Cl--Gradient-Driven, High-Affinity, Uphill Transport of Taurine in Human Placental Brush-Border Membrane Vesicles.” *FEBS Letters* 231 (1): 263–67. https://doi.org/10.1016/0014-5793(88)80744-0.

Moe, A. J., and C. H. Smith. 1989. “Anionic Amino Acid Uptake by Microvillous Membrane Vesicles from Human Placenta.” *The American Journal of Physiology* 257 (5 Pt 1). https://doi.org/10.1152/ajpcell.1989.257.5.c1005.

Mok, Henry, Miriam Mendoza, Josef T. Prchal, Péter Balogh, and Armin Schumacher. 2004. “Dysregulation of Ferroportin 1 Interferes with Spleen Organogenesis in Polycythaemia Mice.” *Development* 131 (19): 4871–81. https://doi.org/10.1242/dev.01342.

Moores, R. R., P. R. Vaughn, F. C. Battaglia, P. V. Fennessey, R. B. Wilkening, and G. Meschia. 1994. “Glutamate Metabolism in Fetus and Placenta of Late-Gestation Sheep.” *American Journal of Physiology - Regulatory Integrative and Comparative Physiology* 267 (1 36-1): 89–96. https://doi.org/10.1152/ajpregu.1994.267.1.r89.

Morel, Isabelle, Gérard Lescoat, Pascale Cogrel, Odile Sergent, Nicole Pasdeloup, Pierre Brissot, Pierre Cillard, and Josiane Cillard. 1993. “Antioxidant and Iron-Chelating Activities of the Flavonoids Catechin, Quercetin and Diosmetin on Iron-Loaded Rat Hepatocyte Cultures.” *Biochemical Pharmacology* 45 (1): 13–19. https://doi.org/10.1016/0006-2952(93)90371-3.

Msheik, H, S El Hayek, M Furqan Bari, J Azar, F Kobeissy, M Vatish, and G Daoud. 2020. “Transcriptomic Profiling of Trophoblast Fusion Using BeWo and JEG-3 Cell Lines” 25 (12): 811–24. https://doi.org/10.1093/molehr/gaz061.

Musial, Barbara, Owen R. Vaughan, Denise S. Fernandez-Twinn, Peter Voshol, Susan E. Ozanne, Abigail L. Fowden, and Amanda N. Sferruzzi-Perri. 2017. “A Western-Style Obesogenic Diet Alters Maternal Metabolic Physiology with Consequences for Fetal Nutrient Acquisition in Mice.” *Journal of Physiology* 595 (14): 4875–92. https://doi.org/10.1113/JP273684.

Muto, Yasuhide, Tomomi Furihata, Meika Kaneko, Kosuke Higuchi, Kentaro Okunushi, Hanae Morio, Yoshie Reien, Masaya Uesato, Hisahiro Matsubara, and Naohiko Anzai. 2019. “Different Response Profiles of Gastrointestinal Cancer Cells to an L-Type Amino Acid Transporter Inhibitor, JPH203.” *Anticancer Research* 39 (1): 159–65. https://doi.org/10.21873/anticanres.13092.

Myatt, Leslie, and Xiaolan Cui. 2004. “Oxidative Stress in the Placenta.” *Histochemistry and Cell Biology* 122 (4): 369–82. https://doi.org/10.1007/s00418-004-0677-x.

Nadeau, V., S. Guillemette, L.-F. Belanger, O. Jacob, S. Roy, and J. Charron. 2009. “Map2k1 and Map2k2 Genes Contribute to the Normal Development of Syncytiotrophoblasts during Placentation.” *Development* 136 (8): 1363–74. https://doi.org/10.1242/dev.031872.

Nadeau, Valérie, and Jean Charron. 2014. “Essential Role of the ERK/MAPK Pathway in Blood-Placental Barrier Formation.” *Development* 141 (14): 2825–37.

https://doi.org/10.1242/dev.107409.

Napolitano, Lara, Michele Galluccio, Mariafrancesca Scalise, Chiara Parravicini, Luca Palazzolo, Ivano Eberini, and Cesare Indiveri. 2017. "Novel Insights into the Transport Mechanism of the Human Amino Acid Transporter LAT1 (SLC7A5). Probing Critical Residues for Substrate Translocation." *Biochimica et Biophysica Acta (BBA) - General Subjects* 1861 (4): 727–36. https://doi.org/10.1016/j.bbagen.2017.01.013.

Napolitano, Lara, Mariafrancesca Scalise, Michele Galluccio, Lorena Pochini, Leticia Maria Albanese, and Cesare Indiveri. 2015. "LAT1 Is the Transport Competent Unit of the LAT1/CD98 Heterodimeric Amino Acid Transporter." *International Journal of Biochemistry and Cell Biology* 67: 25–33. https://doi.org/10.1016/j.biocel.2015.08.004.

Ndibualonji, B. B., D. Dehareng, F. Beckers, C. Van Eenaeme, and J.-M. Godeau. 1995. "Continuous Profiles and Within-Day Variations of Metabolites and Hormones in Cows Fed Diets Varying in Alimentary Supplies before Short-Term Feed Deprivation." *Journal of Animal Science* 75: 3262–77.

Nicolas, Gaël, Myriam Bennoun, Arlette Porteu, Sandrine Mativet, Carole Beaumont, Bernard Grandchamp, Mario Sirito, Michèle Sawadogo, Axel Kahn, and Sophie Vaulont. 2002. "Severe Iron Deficiency Anemia in Transgenic Mice Expressing Liver Hepcidin." *Proceedings of the National Academy of Sciences of the United States of America* 99 (7): 4596–4601. https://doi.org/10.1073/pnas.072632499.

Nielsen, Karoline Kragelund, Anil Kapur, Peter Damm, Maximilian De Courten, and Ib Christian Bygbjerg. 2014. "From Screening to Postpartum Follow-up – the Determinants and Barriers for Gestational Diabetes Mellitus (GDM) Services , a Systematic Review."

Nikitina, L., F. Wenger, M. Baumann, D. Surbek, M. Körner, and C. Albrecht. 2011. "Expression and Localization Pattern of ABCA1 in Diverse Human Placental Primary Cells and Tissues." *Placenta* 32 (6): 420–30. https://doi.org/10.1016/j.placenta.2011.03.003.

Niswander, Kenneth R., Judith Singer, Milton Westphal, and William Weiss. 1969. "Weight Gain During Pregnancy and Prepregnancy Weight Association with Birth Weight of Term Gestation." *Obstetrics and Gynecology* 33 (4): 482–91.

Norberg, Staffan, Theresa L Powell, and Thomas Jansson. 1998. "Intrauterine Growth Restriction Is Associated with a Reduced Activity of Placental Taurine Transporters." *Pediatric Research* 44 (2): 233–38. https://doi.org/10.1203/00006450-199808000-00016.

Novak, D. A., and M. J. Beveridge. 1997. "Glutamine Transport in Human and Rat Placenta." *Placenta* 18: 379–86.

O'Brien, Kimberly O., Nelly Zavaleta, Steven A. Abrams, and Laura E. Caulfield. 2003. "Maternal Iron Status Influences Iron Transfer to the Fetus during the Third Trimester of Pregnancy." *The American Journal of Clinical Nutrition* 77 (4): 924–30. https://doi.org/10.1093/ajcn/77.4.924.

Oda, Koji, Noriko Hosoda, Hiroshi Endo, Kunio Saito, Kenji Tsujihara, Michio Yamamura, Takeshi Sakata, et al. 2010. "L-Type Amino Acid Transporter 1 Inhibitors Inhibit Tumor Cell Growth." *Cancer Science* 101 (1): 173–79. https://doi.org/10.1111/j.1349-7006.2009.01386.x.

Ohgaki, Ryuichi, Takahiro Ohmori, Saori Hara, Saya Nakagomi, Masami Kanai-Azuma, Kazuko Kaneda-Nakashima, Suguru Okuda, Shushi Nagamori, and Yoshikatsu Kanai. 2017. "Essential Roles of L-Type Amino Acid Transporter 1 in Syncytiotrophoblast Development by Presenting Fusogenic 4F2hc." *Molecular and Cellular Biology* 37 (March): e00427-16.

https://doi.org/10.1128/MCB.00427-16.

Ohgami, Robert S., Dean R. Campagna, Alice McDonald, and Mark D. Fleming. 2006. "The Steap Proteins Are Metalloreductases." *Blood* 108 (4): 1388–94. https://doi.org/10.1182/blood-2006-02-003681.

Okamoto, Yoko, Masahiro Sakata, Kazuhiro Ogura, Toshiya Yamamoto, Masaaki Yamaguchi, Keiichi Tasaka, Hirohisa Kurachi, Masato Tsurudome, and Yuji Murata. 2002. "Expression and Regulation of 4F2hc and HLAT1 in Human Trophoblasts." *American Journal of Physiology. Cell Physiology* 282 (1): C196–204.

Orecchio, Andrea, Daniel Periard, Amged Kashef, Jean Luc Magnin, Daniel Hayoz, and Enzo Fontana. 2014. "Incidence of Gestational Diabetes and Birth Complications in Switzerland: Screening in 1042 Pregnancies." *Gynecological Endocrinology* 30 (8): 561–64. https://doi.org/10.3109/09513590.2013.879853.

Orendi, Kristina, Martin Gauster, Gerit Moser, Hamutal Meiri, and Berthold Huppertz. 2010. "The Choriocarcinoma Cell Line BeWo: Syncytial Fusion and Expression of Syncytium-Specific Proteins." *Reproduction* 140 (5): 759–66. https://doi.org/10.1530/REP-10-0221.

Otsuki, Hideo, Toru Kimura, Takashi Yamaga, Takeo Kosaka, Jun Ichi Suehiro, and Hiroyuki Sakurai. 2017. "Prostate Cancer Cells in Different Androgen Receptor Status Employ Different Leucine Transporters." *Prostate* 77 (2): 222–33. https://doi.org/10.1002/pros.23263.

Øvervatn, Aud, John D. Hayes, Ashish Jain, Terje Johansen, Trond Lamark, Kenneth Bowitz Larsen, Michael McMahon, et al. 2010. "P62/SQSTM1 Is a Target Gene for Transcription Factor NRF2 and Creates a Positive Feedback Loop by Inducing Antioxidant Response Element-Driven Gene Transcription ." *Journal of Biological Chemistry* 285 (29): 22576–91. https://doi.org/10.1074/jbc.m110.118976.

Panitchob, N., K. L. Widdows, I. P. Crocker, M. A. Hanson, E. D. Johnstone, C. P. Please, C. P. Sibley, J. D. Glazier, R. M. Lewis, and B. G. Sengers. 2015. "Computational Modelling of Amino Acid Exchange and Facilitated Transport in Placental Membrane Vesicles." *Journal of Theoretical Biology* 365: 352–64. https://doi.org/10.1016/j.jtbi.2014.10.042.

Paolini, Cinzia L, Anna Maria Marconi, Stefania Ronzoni, Michela D I Noio, Paul V Fennessey, Giorgio Pardi, Frederick C Battaglia, C L P Gynecology, and San Paolo. 2001. "Placental Transport of Leucine , Phenylalanine ," 86 (11): 5427–32.

Papanikolaou, G., and K. Pantopoulos. 2005. "Iron Metabolism and Toxicity." *Toxicology and Applied Pharmacology* 202 (2): 199–211. https://doi.org/10.1016/j.taap.2004.06.021.

Peuchant, Evelyne, Jean Luc Brun, Vincent Rigalleau, Liliane Dubourg, Marie Josée Thomas, Jean Yves Daniel, Jean Joël Leng, and Henri Gin. 2004. "Oxidative and Antioxidative Status in Pregnant Women with Either Gestational or Type 1 Diabetes." *Clinical Biochemistry* 37 (4): 293–98. https://doi.org/10.1016/j.clinbiochem.2003.12.005.

Peura, Lauri, Kalle Malmioja, Krista Laine, Jukka Leppänen, Mikko Gynther, Antti Isotalo, and Jarkko Rautio. 2011. "Large Amino Acid Transporter 1 (LAT1) Prodrugs of Valproic Acid: New Prodrug Design Ideas for Central Nervous System Delivery." *Molecular Pharmaceutics* 8 (5): 1857–66. https://doi.org/10.1021/mp2001878.

Phelps, Richard L., Boyd E. Metzger, and Norbert Freinkel. 1981. "Carbohydrate Metabolism in Pregnancy. XVII. Diurnal Profiles of Plasma Glucose, Insulin, Free Fatty Acids, Triglycerides, Cholesterol, and Individual Amino Acids in Late Normal Pregnancy." *American Journal of Obstetrics and Gynecology* 140 (7): 730–36. https://doi.org/10.1016/0002-9378(81)90731-

6.

Philipps, A. F., I. R. Holzman, C. Teng, and F. C. Battaglia. 1978. "Tissue Concentrations of Free Amino Acids in Term Human Placentas." *American Journal of Obstetrics and Gynecology* 131 (8): 881–87. https://doi.org/10.1016/S0002-9378(16)33136-2.

Pohlandt, Frank. 1978. "Plasma Amino Acid Concentrations in Umbilical Cord Vein and Artery of Newborn Infants after Elective Cesarean Section or Spontaneous Delivery" 92 (4): 617–23.

Potter, Timothy M., Barry W. Neun, and Stephan T. Stern. 2011. "Assay to Detect Lipid Peroxidation upon Exposure to Nanoparticles." *Methods in Molecular Biology (Clifton, N.J.)* 697: 181–89. https://doi.org/10.3797/scipharm.br-11-01.

Poulsen, Marie Sønnegaard, Erik Rytting, Tina Mose, and Lisbeth E. Knudsen. 2009. "Modeling Placental Transport: Correlation of in Vitro BeWo Cell Permeability and Ex Vivo Human Placental Perfusion." *Toxicology in Vitro* 23 (7): 1380–86. https://doi.org/10.1016/j.tiv.2009.07.028.

Pramod, Akula Bala, James Foster, Lucia Carvelli, and L. Keith Henry. 2013. "SLC6 Transporters: Structure, Function, Regulation, Disease Association and Therapeutics." *Molecular Aspects of Medicine* 34 (2–3): 197–219. https://doi.org/10.1016/j.mam.2012.07.002.

Prenton, M. A., and Maureen Young. 1969. "Umbilical Vein-artery and Uterine Arterio-venous Plasma Amino Acid Differences DIFFERENCES: In the Human Subject." *BJOG: An International Journal of Obstetrics & Gynaecology* 76 (5): 404–11. https://doi.org/10.1111/j.1471-0528.1969.tb05855.x.

Preziosi, Paul, Alain Prual, Pilar Galan, Hamani Daouda, Hamidov Boureima, and Serge Hercberg. 1997. "Effectof Ironsupplementation on the Ironstatusof Pregnantwomen : Consequencesfor Newborns13." *American Society for Clinical Nutrition* 66: 1178–82.

Qiao, Bo, Priscilla Sugianto, Eileen Fung, Alejandro Del-Castillo-Rueda, Maria Josefa Moran-Jimenez, Tomas Ganz, and Elizabeta Nemeth. 2012. "Hepcidin-Induced Endocytosis of Ferroportin Is Dependent on Ferroportin Ubiquitination." *Cell Metabolism* 15 (6): 918–24. https://doi.org/10.1016/j.cmet.2012.03.018.

Rahman, Irfan, Aruna Kode, and Saibal K. Biswas. 2007. "Assay for Quantitative Determination of Glutathione and Glutathione Disulfide Levels Using Enzymatic Recycling Method." *Nature Protocols* 1 (6): 3159–65. https://doi.org/10.1038/nprot.2006.378.

Ran, F. Ann, Patrick D. Hsu, Jason Wright, Vineeta Agarwala, David A. Scott, and Feng Zhang. 2013. "Genome Engineering Using the CRISPR-Cas9 System." *Nature Protocols* 8 (11): 2281–2308. https://doi.org/10.1038/nprot.2013.143.

Rana, Sarosh, and S Ananth Karumanchi. 2017. *172 - Pathophysiology of Preeclampsia*. *Fetal and Neonatal Physiology, 2-Volume Set*. Fifth Edit. Elsevier Inc. https://doi.org/10.1016/B978-0-323-35214-7.00172-4.

Rawal, Shristi, Stefanie N. Hinkle, Wei Bao, Yeyi Zhu, Jagteshwar Grewal, Paul S. Albert, Natalie L. Weir, Michael Y. Tsai, and Cuilin Zhang. 2017. "A Longitudinal Study of Iron Status during Pregnancy and the Risk of Gestational Diabetes: Findings from a Prospective, Multiracial Cohort." *Diabetologia* 60 (2): 249–57. https://doi.org/10.1007/s00125-016-4149-3.

Richardson, Graham M., Joanne Lannigan, and Ian G. Macara. 2015. "Does FACS Perturb Gene Expression?" *Cytometry Part A* 87 (2): 166–75. https://doi.org/10.1002/cyto.a.22608.

Robb, G Brett. 2019. "Genome Editing with CRISPR-Cas: An Overview." *Current Protocols Essential*

Laboratory Techniques 19 (1): 1–20. https://doi.org/10.1002/cpet.36.

Ronzoni, Stefania, Anna Maria Marconi, Irene Cetin, Cinzia L. Paolini, Cecilia Teng, Giorgio Pardi, and Frederick C. Battaglia. 1999. "Umbilical Amino Acid Uptake at Increasing Maternal Amino Acid Concentrations: Effect of a Maternal Amino Acid Infusate." *American Journal of Obstetrics and Gynecology* 181 (2): 477–83. https://doi.org/10.1016/S0002-9378(99)70581-8.

Roos, Sara, Theresa L Powell, and Thomas Jansson. 2009. "Placental MTOR Links Maternal Nutrient Availability to Fetal Growth." *Biochemical Society Transactions* 37: 295–98. https://doi.org/10.1042/BST0370295.

Rosario, Fredrick J, Yoshikatsu Kanai, Theresa L Powell, and Thomas Jansson. 2013. "Mammalian Target of Rapamycin Signalling Modulates Amino Acid Uptake by Regulating Transporter Cell Surface Abundance in Primary Human Trophoblast Cells." *The Journal of Physiology* 591 (Pt 3): 609–25. https://doi.org/10.1113/jphysiol.2012.238014.

Roseboom, Tessa J., Rebecca C. Painter, Annet F.M. Van Abeelen, Marjolein V.E. Veenendaal, and Susanne R. De Rooij. 2011. "Hungry in the Womb: What Are the Consequences? Lessons from the Dutch Famine." *Maturitas* 70 (2): 141–45. https://doi.org/10.1016/j.maturitas.2011.06.017.

Roverso, Marco, Valerio Di Marco, Denis Badocco, Paolo Pastore, Marilia Calanducci, Erich Cosmi, and Silvia Visentin. 2019. "Maternal, Placental and Cordonal Metallomic Profiles in Gestational Diabetes Mellitus." *Metallomics*. https://doi.org/10.1039/C8MT00331A.

Sadovsky, Yoel, and Thomas Jansson. 2015. *Placenta and Placental Transport Function*. *Knobil and Neill's Physiology of Reproduction: Two-Volume Set*. Vol. 2. https://doi.org/10.1016/B978-0-12-397175-3.00039-9.

Sangkhae, Veena, and Elizabeta Nemeth. 2018. "Placental Iron Transport: The Mechanism and Regulatory Circuits." *Free Radical Biology and Medicine*, no. June: 1–8. https://doi.org/10.1016/j.freeradbiomed.2018.07.001.

Scalise, Mariafrancesca, Michele Galluccio, Lara Console, Lorena Pochini, and Cesare Indiveri. 2018. "The Human SLC7A5 (LAT1): The Intriguing Histidine/Large Neutral Amino Acid Transporter and Its Relevance to Human Health." *Frontiers in Chemistry* 6 (June): 1–12. https://doi.org/10.3389/fchem.2018.00243.

Schiöth, Helgi B., Sahar Roshanbin, Maria G.A. Hägglund, and Robert Fredriksson. 2013. "Evolutionary Origin of Amino Acid Transporter Families SLC32, SLC36 and SLC38 and Physiological, Pathological and Therapeutic Aspects." *Molecular Aspects of Medicine* 34 (2–3): 571–85. https://doi.org/10.1016/j.mam.2012.07.012.

Schmidt, André, Diana M. Morales-Prieto, Jana Pastuschek, Karolin Fröhlich, and Udo R. Markert. 2015. "Only Humans Have Human Placentas: Molecular Differences between Mice and Humans." *Journal of Reproductive Immunology* 108: 65–71. https://doi.org/10.1016/j.jri.2015.03.001.

Schneider, H., K. -H Möhlen, J. -C Challier, and J. Dancis. 1979. "Transfer of Glutamic Acid Across the Human Placenta Perfused in Vitro." *BJOG: An International Journal of Obstetrics & Gynaecology* 86 (4): 299–306. https://doi.org/10.1111/j.1471-0528.1979.tb11260.x.

Schneider, H., M. Proegler, R. Sodha, and J. Dancis. 1987. "Asymmetrical Transfer of α-Aminoisobutyric Acid (AIB), Leucine and Lysine across the in Vitro Perfused Human Placenta." *Placenta* 8 (2): 141–51. https://doi.org/10.1016/0143-4004(87)90017-8.

Schneider, Henning, and Richard K. Miller. 2010. "Receptor-Mediated Uptake and Transport of Macromolecules in the Human Placenta." *International Journal of Developmental Biology* 54 (2–3): 367–75. https://doi.org/10.1387/ijdb.082773hs.

Schroeder, Andreas, Odilo Mueller, Susanne Stocker, Ruediger Salowsky, Michael Leiber, Marcus Gassmann, Samar Lightfoot, Wolfram Menzel, Martin Granzow, and Thomas Ragg. 2006. "The RIN: An RNA Integrity Number for Assigning Integrity Values to RNA Measurements." *BMC Molecular Biology* 7: 1–14. https://doi.org/10.1186/1471-2199-7-3.

Schubert, Mollie, Rolf Turk, Ashley Jacobi, Nolan Speicher, Justin Barr, and Mark Behlke. 2017. "Fluorescently Labeled TracrRNA Provides Efficient Genome Editing While Allowing Cellular Microscopy and FACS Analysis," 1–4.

Schumann, Kathrin, Steven Lin, Eric Boyer, Dimitre R. Simeonov, Meena Subramaniam, Rachel E. Gate, Genevieve E. Haliburton, et al. 2015. "Generation of Knock-in Primary Human T Cells Using Cas9 Ribonucleoproteins." *Proceedings of the National Academy of Sciences of the United States of America* 112 (33): 10437–42. https://doi.org/10.1073/pnas.1512503112.

Seligman, Paul A., Rhoda B. Schleicher, and Allen H. Robert. 1979. "Isolation and Characterization of the Transferrin Receptor from Human Placenta." *The Journal of Biological Chemistry* 254 (20): 9943–46.

Sengers, B G, C P Please, and R M Lewis. 2010. "Computational Modelling of Amino Acid Transfer Interactions in the Placenta." *Experimental Physiology* 95 (7): 829–40. https://doi.org/10.1113/expphysiol.2010.052902.

Sferruzzi-Perri, Amanda N., Owen R. Vaughan, Maria Haro, Wendy N. Cooper, Barbara Musial, Marika Charalambous, Diogo Pestana, et al. 2013. "An Obesogenic Diet during Mouse Pregnancy Modifies Maternal Nutrient Partitioning and the Fetal Growth Trajectory." *FASEB Journal* 27 (10): 3928–37. https://doi.org/10.1096/fj.13-234823.

Shao, Jie, Jingan Lou, Raghavendra Rao, Michael K. Georgieff, Niko Kaciroti, Barbara T. Felt, Zheng-Yan Zhao, and Betsy Lozoff. 2012. "Maternal Serum Ferritin Concentration Is Positively Associated with Newborn Iron Stores in Women with Low Ferritin Status in Late Pregnancy." *The Journal of Nutrition* 142 (11): 2004–9. https://doi.org/10.3945/jn.112.162362.

Shi, Q J, Z M Lei, C V Rao, and J Lin. 1993. "Novel Role of Human Chorionic Gonadotropin in Differentiation of Human Cytotrophoblasts." *Endocrinology* 132 (3): 1387–95.

Si, Lihui, Ruiqi Yang, Jian Liu, Yubo Dong, Hongtao Zhang, and Xiaohong Xu. 2019. "Generation of Two ERF Gene Knockout Human Embryonic Stem Cell Lines Using CRISPR/Cas9 System." *Stem Cell Research* 41 (October): 101644. https://doi.org/10.1016/j.scr.2019.101644.

Sibai, Baha M. 2012. "Etiology and Management of Postpartum Hypertension-Preeclampsia." *American Journal of Obstetrics and Gynecology* 206 (6): 470–75. https://doi.org/10.1016/j.ajog.2011.09.002.

Singh, Natesh, Mariafrancesca Scalise, Michele Galluccio, Marcus Wieder, Thomas Seidel, Thierry Langer, Cesare Indiveri, and Gerhard F. Ecker. 2019. "Discovery of Potent Inhibitors for the Large Neutral Amino Acid Transporter 1 (LAT1) by Structure-Based Methods." *International Journal of Molecular Sciences* 20 (1). https://doi.org/10.3390/ijms20010027.

Sinha, Sandeep, German Perdomo, Nicholas F. Brown, Robert M. O'Doherty, Robert M O Doherty, and Robert M. O'Doherty. 2004. "Fatty Acid-Induced Insulin Resistance in L6 Myotubes Is Prevented by Inhibition of Activation and Nuclear Localization of Nuclear Factor KB." *Journal of Biological Chemistry* 279 (40): 41294–301. https://doi.org/10.1074/jbc.M406514200.

Steingrímsdóttir, Thóra, Gunnar Ronquist, and Ulf Ulmsten. 1993. "Balance of Amino Acids in the Pregnant Human Uterus at Term." *European Journal of Obstetrics and Gynecology and Reproductive Biology* 50 (3): 197–202. https://doi.org/10.1016/0028-2243(93)90201-M.

Stirm, Laura, Markéta Kovářová, Sarah Perschbacher, Renate Michlmaier, Louise Fritsche, Dorothea Siegel-Axel, Erwin Schleicher, et al. 2018. "BMI-Independent Effects of Gestational Diabetes on Human Placenta." *Journal of Clinical Endocrinology and Metabolism* 103 (9): 3299–3309. https://doi.org/10.1210/jc.2018-00397.

Sturman, John A., Gerald Gaull, and Neils C.R. Raiha. 1970. "Absence of Cystathionase in Human Fetal Liver: Is Cystine Essential?" *Science* 169 (3940): 74–76. https://doi.org/10.1126/science.169.3940.74.

Tabuchi, Mitsuaki, Tamotsu Yoshimori, Kazuhito Yamaguchi, Tsutomu Yoshida, and Fumio Kishi. 2000. "Human NRAMP2/DMT1, Which Mediates Iron Transport across Endosomal Membranes, Is Localized to Late Endosomes and Lysosomes in HEp-2 Cells." *Journal of Biological Chemistry* 275 (29): 22220–28. https://doi.org/10.1074/jbc.M001478200.

Tang, Zhonghua, Vikki M. Abrahams, Gil Mor, and Seth Guller. 2011. "Placental Hofbauer Cells and Complications of Pregnancy." *Annals of the New York Academy of Sciences* 1221: 103–8. https://doi.org/10.1038/jid.2014.371.

Thomas, Philip, and Trevor G. Smart. 2005. "HEK293 Cell Line: A Vehicle for the Expression of Recombinant Proteins." *Journal of Pharmacological and Toxicological Methods* 51 (3 SPEC. ISS.): 187–200. https://doi.org/10.1016/j.vascn.2004.08.014.

Thornburg, K. L., and J. J. Faber. 1976. "The Steady State Concentration Gradients of an Electron Dense Marker (Ferritin) in the 3 Layered Hemochorial Placenta of the Rabbit." *Journal of Clinical Investigation* 58 (4): 912–25. https://doi.org/10.1172/JCI108544.

Triana-Alonso, F. J., M. Dabrowski, J. Wadzack, and K. H. Nierhaus. 1995. "Self-Coded 3'-Extension of Run-off Transcripts Produces Aberrant Products during in Vitro Transcription with T7 RNA Polymerase." *Journal of Biological Chemistry* 270 (11): 6298–6307. https://doi.org/10.1074/jbc.270.11.6298.

Tsuchiya, H., K. Matsui, T. Muramatsu, T. Ando, and F. Endo. 2009. "Differences between the Amino Acid Concentrations of Umbilical Venous and Arterial Blood." *Archives of Disease in Childhood: Fetal and Neonatal Edition* 94 (2): 155–57. https://doi.org/10.1136/adc.2008.147256.

Turco, Margherita Y., and Ashley Moffett. 2019. "Development of the Human Placenta." *Development (Cambridge)* 146 (22): 1–14. https://doi.org/10.1242/dev.163428.

Türker, C, F Akal, D Joho, and C Panse. 2010. "B-Fabric: The Swiss Army Knife for Life Sciences." *Proceedings of the 13th*, no. March: 717–20. https://doi.org/10.1145/1739041.1739135.

Vardhana, Pratibhasri A., and Nicholas P. Illsley. 2002. "Transepithelial Glucose Transport and Metabolism in BeWo Choriocarcinoma Cells." *Placenta* 23 (8): 653–60. https://doi.org/10.1053/plac.2002.0857.

Vaughan, O. R., F. J. Rosario, T. L. Powell, and T. Jansson. 2017. *Regulation of Placental Amino Acid Transport and Fetal Growth*. *Progress in Molecular Biology and Translational Science*. 1st ed. Vol. 145. Elsevier Inc. https://doi.org/10.1016/bs.pmbts.2016.12.008.

Vaughn, Philip R, Claudia Lobo, C Battaglia, Paul V Fennessey, Paul V Fennessey, and B Wilkening. 1995. "Glutamine-Glutamate and Fetal Liver Exchange between Placenta." *American Journal of Physiology - Endocrinology and Metabolism* 268 (4): 705–11.

Vecchi, Chiara, Giuliana Montosi, Kezhong Zhang, Igor Lamberti, Stephen A. Duncan, Randal J. Kaufman, and Antonello Pietrangelo. 2009. "ER Stress Controls Iron Metabolism Through Induction of Hepcidin." *Science* 325 (5942): 877–880. https://doi.org/10.1038/jid.2014.371.

Velazquez, Anselmo, Adolfo Rosado, Alfonso Bernal, Luis Noriega, and Noel Arévalo. 1976. "Amino Acid Pools in the Feto-Maternal System." *Neonatology* 29 (1–2): 28–40. https://doi.org/10.1159/000240845.

Veuthey, Tania, and Marianne Wessling-Resnick. 2014. "Pathophysiology of the Belgrade Rat." *Frontiers in Pharmacology* 5 (April): 1–13. https://doi.org/10.3389/fphar.2014.00082.

Vistica, David T. 1983. "Cellular Pharmacokinetics of the Phenylalanine Mustards." *Pharmacology & Therapeutics* 22 (3): 379–405.

Voerman, Ellis, Susana Santos, Hazel Inskip, Pilar Amiano, Henrique Barros, Marie Aline Charles, Leda Chatzi, et al. 2019. "Association of Gestational Weight Gain With Adverse Maternal and Infant Outcomes." *Jama* 321 (17): 1702–15. https://doi.org/10.1001/jama.2019.3820.

Voets, Olaf, Frans Tielen, Edo Elstak, Julian Benschop, Max Grimbergen, Jan Stallen, Richard Janssen, Andre Van Marle, and Christian Essrich. 2017. "Highly Efficient Gene Inactivation by Adenoviral CRISPR/Cas9 in Human Primary Cells." *PLoS ONE* 12 (8): 1–20. https://doi.org/10.1371/journal.pone.0182974.

Wang, Bin, Lei He, Hongbin Dong, Timothy P. Dalton, and Daniel W. Nebert. 2011. "Generation of a Slc39a8 Hypomorph Mouse: Markedly Decreased ZIP8 Zn 2+/(HCO 3 -) 2 Transporter Expression." *Biochemical and Biophysical Research Communications* 410 (2): 289–94. https://doi.org/10.1016/j.bbrc.2011.05.134.

Wempe, Michael F., Peter J. Rice, Janet W. Lightner, Promsuk Jutabha, Michinari Hayashi, Naohiko Anzai, Shin Wakui, Hiroyuki Kusuhara, Yuichi Sugiyama, and Hitoshi Endou. 2012. "Metabolism and Pharmacokinetic Studies of JPH203, an L-Amino Acid Transporter 1 (LAT1) Selective Compound." *Drug Metabolism and Pharmacokinetics* 27 (1): 155–61. https://doi.org/10.2133/dmpk.DMPK-11-RG-091.

Widdows, Kate L., Nuttanont Panitchob, Ian P. Crocker, Colin P. Please, Mark A. Hanson, Colin P. Sibley, Edward D. Johnstone, Bram G. Sengers, Rohan M. Lewis, and Jocelyn D. Glazier. 2015. "Integration of Computational Modeling with Membrane Transport Studies Reveals New Insights into Amino Acid Exchange Transport Mechanisms." *FASEB Journal* 29 (6): 2583–94. https://doi.org/10.1096/fj.14-267773.

Wilkening, R. B., and G. Meschia. 1992. "Comparative Physiology of Placental Oxygen Transport." *Placenta* 13 (1): 1–15. https://doi.org/10.1016/0143-4004(92)90002-B.

Wilkinson, Nicole, and Kostas Pantopoulos. 2014. "The IRP/IRE System in Vivo: Insights from Mouse Models." *Frontiers in Pharmacology* 5 JUL. https://doi.org/10.3389/fphar.2014.00176.

Winterhager, Elke, and Alexandra Gellhaus. 2017. "Transplacental Nutrient Transport Mechanisms of Intrauterine Growth Restriction in Rodent Models and Humans." *Frontiers in Physiology* 8 (NOV): 1–13. https://doi.org/10.3389/fphys.2017.00951.

Wiśniewski, Jacek R., Alexandre Zougman, Nagarjuna Nagaraj, and Matthias Mann. 2009. "Universal Sample Preparation Method for Proteome Analysis." *Nature Methods* 6 (5): 359–62. https://doi.org/10.1038/nmeth.1322.

Wu, Di, Yu Liu, Xiaoxia Liu, Weifang Liu, Haoran Shi, Yang Zhang, Li Zou, and Yin Zhao. 2020. "Heme Oxygenase-1 Gene Modified Human Placental Mesenchymal Stem Cells Promote Placental

Angiogenesis and Spiral Artery Remodeling by Improving the Balance of Angiogenic Factors in Vitro." *Placenta* In Press,. https://doi.org/10.1016/j.jmii.2020.03.034.

Wurtman, Richard J., Christopher M. Rose, Chuan Chou, and Frances F. Larin. 1968. "Daily Rhythms in the Concentrations of Various Amino Acids in Human Plasma." *The New England Journal of Medicine* 279 (4): 171–75.

Xiong, Xu, Nestor N. Demianczuk, L. Duncan Saunders, Fu Lin Wang, and William D. Fraser. 2002. "Impact of Preeclampsia and Gestational Hypertension on Birth Weight by Gestational Age." *American Journal of Epidemiology* 155 (3): 203–9. https://doi.org/10.1093/aje/155.3.203.

Yanatori, Izumi, Des R. Richardson, Kiyoshi Imada, and Fumio Kishi. 2016. "Iron Export through the Transporter Ferroportin 1 Is Modulated by the Iron Chaperone PCBP2." *Journal of Biological Chemistry* 291 (33): 17303–18. https://doi.org/10.1074/jbc.M116.721936.

Yasemin, Nasir, Nergiz Yusuf, Aktaş Ayfer, and Akdeniz Nurten. 2011. "Immunohistochemical Evaluation of Iron Accumulation in Term Placenta of Preeclamptic Patients." *African Journal of Biotechnology* 10 (54): 11273–79. https://doi.org/10.5897/ajb11.1161.

Yoon, Donghoon, Yves D. Pastore, Vladimir Divoky, Enli Liu, Agnieszka E. Mlodnicka, Karin Rainey, Premysl Ponka, Gregg L. Semenza, Armin Schumacher, and Josef T. Prchal. 2006. "Hypoxia-Inducible Factor-1 Deficiency Results in Dysregulated Erythropoiesis Signaling and Iron Homeostasis in Mouse Development." *Journal of Biological Chemistry* 281 (35): 25703–11. https://doi.org/10.1074/jbc.M602329200.

Yothaisong, Supak, Hasaya Dokduang, Naohiko Anzai, Keitaro Hayashi, Nisana Namwat, Puangrat Yongvanit, Sakkarn Sangkhamanon, Promsuk Jutabha, Hitoshi Endou, and Watcharin Loilome. 2017. "Inhibition of L-Type Amino Acid Transporter 1 Activity as a New Therapeutic Target for Cholangiocarcinoma Treatment." *Tumor Biology* 39 (3). https://doi.org/10.1177/1010428317694545.

Young, M. F., E. Pressman, M. L. Foehr, T. McNanley, E. Cooper, R. Guillet, M. Orlando, A. W. McIntyre, J. Lafond, and K. O. O'Brien. 2010. "Impact of Maternal and Neonatal Iron Status on Placental Transferrin Receptor Expression in Pregnant Adolescents." *Placenta* 31 (11). https://doi.org/10.1016/j.placenta.2010.08.009.

Yung, Hong-wa, Patji Alnæs-katjavivi, Carolyn J P Jones, Tatiana El-bacha, Michaela Golic, Anne-cathrine Staff, Graham J Burton, and Graham J Burton. 2016. "Placental Endoplasmic Reticulum Stress in Gestational Diabetes : The Potential for Therapeutic Intervention with Chemical Chaperones and Antioxidants." *Diabetologia*, 2240–50. https://doi.org/10.1007/s00125-016-4040-2.

Zachara, Bronislaw A. 2018. "Selenium in Complicated Pregnancy. A Review." *Advances in Clinical Chemistry* 86: 157–78. https://doi.org/10.1016/bs.acc.2018.05.004.

Zein, Salam, Samar Rachidi, Sanaa Awada, Mireille Osman, Amal Al-Hajje, Nadine Shami, Iman Sharara, Khawla Cheikh-Ali, Pascale Salameh, and Isabelle Hininger-Favier. 2015. "High Iron Level in Early Pregnancy Increased Glucose Intolerance." *Journal of Trace Elements in Medicine and Biology* 30: 220–25. https://doi.org/10.1016/j.jtemb.2014.09.004.

Zhao, Ningning, Junwei Gao, Caroline A. Enns, and Mitchell D. Knutson. 2010. "ZRT/IRT-like Protein 14 (ZIP14) Promotes the Cellular Assimilation of Iron from Transferrin." *Journal of Biological Chemistry* 285 (42): 32141–50. https://doi.org/10.1074/jbc.M110.143248.

Ziaei, S., M. Norrozi, S. Faghihzadeh, and E. Jafarbegloo. 2007. "A Randomised Placebo-Controlled Trial to Determine the Effect of Iron Supplementation on Pregnancy Outcome in Pregnant

Women with Haemoglobin ≥ 13.2 g/Dl." *BJOG: An International Journal of Obstetrics and Gynaecology* 114 (6): 684–88. https://doi.org/10.1111/j.1471-0528.2007.01325.x.

8 Curriculum vitae and list of publications

Jonas Zaugg

	Particulars
Address:	Rathausgasse 29 5000 Aarau
Contact:	Cell: +41 (0) 76 465 56 54 jonas0zaugg@gmail.com
Date of birth:	22. December 1987
Nationality:	Swiss
ORCID ID:	https://orcid.org/0000-0002-3153-2806

	Education
since 2015	PhD GCB for Cellular and Biomedical Sciences med. University of Bern (UniBe)
2012 - 2014	Master of Science UZH in Biology, molecular and cellular biology Faculty of Science of the University of Zurich (UZH) Thesis: CRISPR-mutagenesis by injection of RNA/Cas9 protein complexes
2009 - 2012	Bachelor of molecular life sciences (MLS), bioanalytics at the University of Applied Sciences (FHNW) in Muttenz BL Thesis: Genetic and metabolic potential of Microbacterium sp.
2005 - 2008	Apprenticeship in biology laboratory technician, with the higher education entrance qualification, RCC Ltd, Itingen BL

	Employment history
Since 16.03.20	Volunteer as biomedical technician to fight against COVID19 pandemic, Aarau Cantonal Hospital, Aarau AG
Since 21.10.19	Member of the NCCR TransCure student and fellow committee. The student committee oversees organizing some of the scientific events of the network, such as seminars and symposia. The committee helps coordinating the communication between the fellows, the admin team and the directorate.

01.05.09 - 30.11.15	Side job as medical laboratory assistant in pathology institute Bern, dual function in histology and in immunohistochemistry
31.03.09 - 25.04.09	temporarily job as an assistant civil engineering and tunneling, Rothpletz, Lienhard + Cie AG in Aarau
27.10.08 - 14.03.09	Recruit school, paramedic tank driver in Chamblon, Airolo and Bure
18.08.08 - 24.10.08	Aquatic and terristric ecotoxicology, Ulrich Memmert, RCC Ltd, Itingen BL. Support of sub chronic fishtoxicology tests; validate a new flow method for fish egg studies (Danio rerio). Quantify and identity of earthworms in an agricultural toxicology study and support of many bee and ladybugs studies for neurotoxin or insecticide clarification.

Technical skills

Membrane protein and functional vesicle isolation from human tissue; histological analysis of mammalian tissue;
Mammalian cell culture; development of cell based nutrient transport assay including Transwell technique; flow cytometry analysis and sorting;
Target site design, application and analysis of CRISPR/Cas9 edited cells / organisms;
Bright-field microscopy, fluorescence microscopy and confocal microscopy;
RNA quantification by RT-qPCR; immunoblot and MS/MS-based protein quantification;
Isolation and analysis of genomic DNA; cloning and microinjection / transfection of molecular constructs into Danio rerio embryos and into human cell lines;
Biochemical analysis of cellular stress response pathways;
Statistical correlation studies including experimental and clinical data

Other Skills

IT	good experience with office (Word, Excel and PowerPoint), various statistics programs (GraphPad Prism, JMP, basics in R) and UGENE, Image J, FlowJo
Language skills	German; English and basics in French
Hobbies	Diving, sailing, hiking, scouting: I was scout group leader for seven years and department head of a scout group in the great Swiss federal camp 2008.

Aims

	PostDoc abroad, Science lecturer and/or leading task in research

List of publications

Zaugg J, Melhem H, Huang X, Wegner M, Baumann M, Surbek D, Körner M, Albrecht C. Gestational diabetes mellitus affects placental iron homeostasis: Mechanism and clinical implications. The Federation of American Societies for Experimental Biology (FASEB) Journal. First published: 14 April 2020; 34: 7311– 7329. https://doi.org/10.1096/fj.201903054R

Zaugg J, Huang X., Ziegler F., Rubin M., Graff J., Müller J., Moser-Hässig R., Powell T., Gertsch J., Altmann K.H., Albrecht C. Small molecule inhibitors provide insights into the relevance of LAT1 and LAT2 in materno-fetal amino acid transport. Journal of Cellular and Molecular Medicine (JCMM). First published: 01 October 2020; Early View. https://doi.org/10.1111/jcmm.15840

Zaugg J, Ziegler F., Nuoffer J.M., Moser-Hässig R., Albrecht C. Counter-directed leucine gradient promotes amino acid transfer across the human placenta. In revision Journal of Nutritional Biochemistry (JNB), Sept 2020. Manuscript Number: JNB-D-20-00465.

Coauthor articles

Karahoda R., Abad C., Horackova H., Kastner P., **Zaugg J.**, Cerveny L., Kucera R., Albrecht C., Staud F. Dynamics of Tryptophan Metabolic Pathways in Human Placenta and Placental-Derived Cells; Effect of Gestation Age and Trophoblast Differentiation. 2020. Frontiers in Cell and Developmental Biology. 8. September: 1–15. https://doi.org/10.3389/fcell.2020.574034.

Drożdżyk K., Sawicka M., Bahamonde-Santos M.I., **Zaugg J,** Deneka D., Albrecht C., Dutzler R. Cryo-EM Structures and Functional Properties of Calhm Channels of the Human Placenta. 2020. *ELife* 9: 1–27. https://doi.org/10.7554/eLife.55853.

Schroeder, M., Jakovcevski, M., Polacheck, T., Drori, Y., Luoni, A., Röh, S., **Zaugg, J.,** Bendor, S., Albrecht, C., Chen, A., 2018. Placental miR-340 mediates vulnerability to activity-based anorexia in mice. Nature Communications. 2018; 9 (1). https://doi.org/10.1038/s41467-018-03836-2.

Burger, A., Lindsay, H., Felker, A., Hess, C., Anders, C., Chiavacci, E., **Zaugg, J.,** Weber, L.M., Catena, R., Jinek, M., Robinson, M.D., Mosimann, C., 2016. Maximizing mutagenesis with solubilized CRISPR-Cas9 ribonucleoprotein complexes. Development. 2016 143: 2025-2037; https://doi: 10.1242/dev.134809

Lindsay, H., Burger, A., Biyong, B., Felker, A., Hess, C., **Zaugg, J.,** Chiavacci, E., Anders, C., Jinek, M., Mosimann, C., Robinson, M.D., 2015. CrispRVariants: precisely charting the mutation spectrum in genome engineering experiments. bioRxiv 034140; doi: https://doi.org/10.1101/034140; Nature Biotechnology doi: 10.1038/nbt.3628

Conference abstracts

Kallol, S.A., **Zaugg, J.**, Lüthi, M.P., Moser, R., Mistry, H.D., Schneider, H., Albrecht, C., 2018. A pre-eclampsia cell model: Effect of hypoxia and hypoxia-reoxygenation in the primary cytotrophoblast. Placenta 69, e12-93.

Zaugg, J., Huang, X., Burri, F., Ziegler, F., Körner, M., Rubin, M., Graff, J., Keller, C., Gertsch, J., Altmann, K.-H., Albrecht, C., 2017. SLC7-mediated amino acid transport across the materno-fetal barrier. Placenta 57, 294.

Zaugg, J., Wegner, M., Huang, X., Ontsouka, E., Baumann, M., Surbek, D., Körner, M., Hediger, M.A., Albrecht, C., 2016. Influence of gestational diabetes mellitus on transplacental iron transport. Placenta 45, 110.

Zaugg, J., Melhem, H., Kalakaran, T., Wegner, M., Huang, X., Baumann, M., Surbek, D., Körner, M., Albrecht, C., 2018. Impact of gestational diabetes mellitus on transplacental iron transport. Placenta 69, e12—e93.

Zaugg, J., Nuoffer, J.-M., Moser-Hässig, R., Albrecht, C., 2018. Determination of physiological amino acid gradients across the materno-fetal barrier. Placenta 69, e12—e93.

Huang, X., **Zaugg, J.**, Körner, M., Rubin, M., Graff, J., Baumann, M., Surbek, D., Altmann, K.-H., Albrecht, C., 2016. The role of the L-type amino acid transporter 1 (LAT1) in placenta pathologies. Placenta 45, 128–129.

Zaugg, J., Wegner, M., Huang, X., Baumann, M., Surbek, D., Körner, M., Albrecht, C., 2017. Gestational diabetes mellitus affects placental iron homeostasis. Placenta 57, 265.

Kallol, S., Huang, X., **Zaugg, J.**, Lüthi, M., Baumann, M., Surbek, D., Albrecht, C., 2017. Effect of placental cell differentiation on materno-fetal nutrient transport. Placenta 57, 298.

Awards & Prizes

12.5.2017: NCCR TransCure retreat in Baden, CH; NCCR TransCure Poster Award

30.8.2017; International Federation of Placenta Associations (IFPA) conference in Manchester, UK; Elsevier Travel Awards

21.9.2018; International Federation of Placenta Associations (IFPA) conference in Tokyo, JPN; Y.W.Loke New Investigator Travel Award

10.9.2019; International Federation of Placenta Associations (IFPA) conference in Buenos Aires, RA; Y.W.Loke New Investigator Travel Award

References

PhD thesis	**Prof. Dr. Christiane Albrecht** Institute of Biochemistry and Molecular Medicine Faculty of Medicine University of Bern Bühlstrasse 28 CH-3012 Bern Phone: +41 31 631 41 08 christiane.albrecht@ibmm.unibe.ch
Master thesis	**Prof. Dr. Christian Mosimann** Department of Pediatrics, Section of Developmental Biology University of Colorado Anschutz Medical Campus RC1 South, 12400 12801 E. 17th Avenue Aurora, CO 80045, USA christian.mosimann@cuanschutz.edu
Bachelor thesis	**Dr. Armin Zenker** Lecturer in Microbiology and Ecotoxicology University of Applied Sciences in Muttenz Institute for Ecopreneurship Hofackerstrasse 30 CH-4132 Muttenz T +41 61 228 54 47 armin.zenker@fhnw.ch

9 Appendix

9.1 Publications resulting from this thesis

9.1.1 Published in the FASEB Journal (14 April 2020)

Received: 4 December 2019 | Revised: 7 February 2020 | Accepted: 2 March 2020

DOI: 10.1096/fj.201903054R

RESEARCH ARTICLE

THE FASEB JOURNAL

Gestational diabetes mellitus affects placental iron homeostasis: Mechanism and clinical implications

Jonas Zaugg[1,2] | **Hassan Melhem**[1,2] | **Xiao Huang**[1,2] | **Malgorzata Wegner**[1,2] | **Marc Baumann**[3] | **Daniel Surbek**[3] | **Meike Körner**[4] | **Christiane Albrecht**[1,2]

[1]Institute of Biochemistry and Molecular Medicine, University of Bern, Bern, Switzerland

[2]Swiss National Centre of Competence in Research (NCCR) TransCure, University of Bern, Bern, Switzerland

[3]Department of Obstetrics and Gynaecology, University Hospital, Bern, Switzerland

[4]Pathology Laenggasse, Bern, Switzerland

Correspondence
Christiane Albrecht, Institute of Biochemistry and Molecular Medicine, University of Bern, Bühlstrasse 28, CH-3012 Bern, Switzerland.
Email: christiane.albrecht@ibmm.unibe.ch

Funding information
This study was supported by the Swiss National Centre of Competence in Research, NCCR TransCure, University of Bern, Switzerland, and the Swiss National Science Foundation (SNSF) (Grant No. 310030_149958). JZ was supported by the Graduate School for Cellular and Biomedical Sciences (GCB), University of Bern, Switzerland.

Abstract

Clinical studies suggest that pregnant women with elevated iron levels are more vulnerable to develop gestational diabetes mellitus (GDM), but the causes and underlying mechanisms are unknown. We hypothesized that hyperglycemia induces cellular stress responses leading to dysregulated placental iron homeostasis. Hence, we compared the expression of genes/proteins involved in iron homeostasis in placentae from GDM and healthy pregnancies (n = 11 each). RT-qPCR and LC-MS/MS analyses revealed differential regulation of iron transporters/receptors (*DMT1*/*FPN1*/*ZIP8*/*TfR1*), iron sensors (*IRP1*), iron regulators (*HEPC*), and iron oxidoreductases (*HEPH*/*Zp*). To identify the underlying mechanisms, we adapted BeWo trophoblast cells to normoglycemic (N), hyperglycemic (H), and hyperglycemic-hyperlipidemic (HL) conditions and assessed Fe^{3+}-uptake, expression patterns, and cellular pathways involving oxidative stress (OS), ER-stress, and autophagy. H and HL induced alterations in cellular morphology, differential iron transporter expression, and reduced Fe^{3+}-uptake confirming the impact of hyperglycemia on iron transport observed in GDM patients. Pathway analysis and rescue experiments indicated that dysregulated OS and disturbed autophagy processes contribute to the reduced placental iron transport under hyperglycemic conditions. These adaptations could represent a protective mechanism preventing the oxidative damage for both fetus and placenta caused by highly oxidative iron. In pregnancies with risk for

Abbreviations: AGC, automatic gain control; BeWo, choriocarcinoma cell line (subclone b30); BiP, binding-immunoglobulin protein; BSA, bovine serum albumin; BSS, balanced salt solution; cpm, counts per minute; DC, dose control; DMEM, Dulbecco's modified Eagle's medium; DMT1, divalent metal transporter 1 (SLC11A2); ER, endoplasmic reticulum; Fe, ferrum (iron); FPN1, ferroportin-1 (SLC40A1); GAPDH, glyceraldehyde-3-phosphate dehydrogenase; GDM, gestational diabetes mellitus; GRP78, 78 kDa glucose-regulated protein; GSH, glutathione; H, *hyperglycemic condition*; HEPC, hepcidin; HEPH, hephaestin; HL, *hyperglycemic-hyperlipidemic condition*; HRP, horseradish peroxidase; IRP1, iron regulatory protein 1; LC3-II, phosphatidylethanolamine conjugated microtubule-associated protein 1A/1B-light chain 3; MDA, malondialdehyde; MS, mass spectrometry; MS/MS, liquid chromatography–tandem MS; N, *Normoglycemic condition*; NaSe, sodium selenite; NCE, normalized collision energy; OD, optical density; oGTT, oral glucose tolerance test; OS, oxidative stress; PBS, phosphate-buffered saline; PRM, parallel reaction monitoring; p62, ubiquitin-binding protein p62/Sequestosome-1; ROS, reactive oxygen species; rpm, revolutions per minute; RT, room temperature; RT-qPCR, reverse transcription-quantitative polymerase chain reaction; SD, standard deviation; SRM, selected reaction monitoring; TBARS, thiobarbituric acid reactive substances; TBST, Tris-buffered saline with Tween20; tert-BOOH, tert-Butylhydroperoxide; Tf, transferrin; TfR1, transferrin receptor protein 1; TMI, total membrane isolation; UBQ, ubiquitin C; YWHAZ, 14-3-3 protein zeta/delta; ZIP8, Zrt- and Irt-like protein 8 (SLC39A8); Zp, zyklopen (Hephaestin-like protein 1).

GDM, antioxidant treatment, and controlled iron supplementation could help to balance placental OS levels protecting mother and fetus from impaired iron homeostasis.

KEYWORDS

antioxidant treatment, autophagy, *DMT1*, ferroportin, immunohistochemistry, iron uptake, oxidative stress, placenta, transferrin receptor, trophoblast cells, *ZIP8*

1 | INTRODUCTION

Gestational diabetes mellitus (GDM), defined as any degree of glucose intolerance with onset or first recognition during pregnancy, is among the most common pregnancy complications and has in western countries a prevalence of approximately 5%[1] and 9% in the United States,[2] respectively. The etiology of GDM is multifactorial. Well-known modifiable risk factors for GDM include obesity, high-fat diet, high blood pressure, excess weight gain in pregnancy, and endocrine dysfunction.[3] Several clinical studies ascertain a positive association between GDM and elevated serum iron levels. Thus it has been reported that glucose levels in oral glucose tolerance tests (oGTTs) correlate positively with the ferritin levels at early pregnancy.[4] Moreover, Rawal et al found in a longitudinal prospective study a relationship between GDM and increased ferritin levels already in gestational week 10-14.[5] These results suggest that GDM-mediated hyperglycemic conditions can affect the placental iron homeostasis, but the pathophysiological association of GDM and elevated maternal iron-plasma levels as well as the underlying mechanism are still unclear. Moreover, these findings raise potential concerns for the recommendation of routine iron supplementation among iron-replete pregnant women.

Both the hyperglycemic environment and increased iron levels may play a role in the generation of oxidative stress (OS) during pregnancy. OS occurs when the delicate balance between the generation of reactive oxygen species (ROS) and production of antioxidant neutralizing species, such as NADPH and glutathione (GSH), is disturbed. Hyperglycemia increases the OS levels through different metabolic pathways: it induces an overrepresentation of ROS by antioxidant depletion[6] while concomitantly excessive iron supplementation can expose women to increased lipid peroxidation and protein carbonylation by intracellular generation of ROS.[7,8] Notably, whether hyperglycemia could alter iron homeostasis in the placenta has not been explored yet. To unravel the underlying mechanism associating GDM with disturbed placental iron homeostasis, we studied whether GDM-mediated hyperglycemia (1) affects the expression of placental iron transporters and iron regulatory proteins, (2) influences transplacental iron transport function in vitro and (3) causes disturbances in OS or autophagy pathways affecting iron homeostasis in placental cells. Moreover, this study discusses the putative involvement of ferroptosis, an alternative regulated form of cell death, which is characterized by disturbed GSH synthesis and imbalanced cellular iron homeostasis that leads to the generation and accumulation of lipid peroxides.[9]

By establishing novel hyperglycemic trophoblast cell models which overall mimicked the pathological changes found in clinical GDM specimens, we demonstrated that OS is majorly involved in the disturbed placental iron homeostasis. Application of the antioxidant sodium selenite (NaSe) rescued the cellular phenotypes suggesting beneficial effects of antioxidant treatment in patients with GDM.

2 | MATERIALS AND METHODS

All chemicals and reagents were purchased from Sigma-Aldrich distributor in Switzerland unless otherwise stated.

2.1 | Patient selection and tissue collection

In this study 22 women with elective Caesarean section at the Department of Obstetrics and Gynecology, University Hospital Bern, Switzerland were enrolled. Placental tissues were collected as previously described.[10] GDM was diagnosed in 11 pregnancies according to the criteria of the American Diabetes Association.[11] The control group (n = 11) consisted of term pregnancies without pathologies. This study was approved by the cantonal ethical committee (KEK_178/03), Bern, Switzerland, and written informed consent was obtained from all participants.

2.2 | RNA isolation, reverse transcription, and quantitative RT-PCR

RNA isolation, first-strand cDNA synthesis, and qPCR analysis was performed as previously described.[10,12] Primer nucleotide sequences are listed in Table 1.

TABLE 1 Primer sequences used to quantify iron homeostasis and reference genes by RT-qPCR

Gene	Forward sequence, 5'-3'	Reverse sequence, 5'-3'	fragment length [bp]
β-actin	AACTCCATCATGAAGTGTGACG	GATCCACATCTGCTGGAAGG	234
GAPDH	ACCACAGTCCATGCCATCAC	TCCACCACCCTGTTGCTGTA	452
UBC	TCGCAGCCGGGATTTG	GCATTGTCAAGTGACGATCACA	64
YWHAZ	CCGTTACTTGGCTGAGGTTG	AGTTAAGGGCCAGACCCAGT	143
DMT1	TGCTATCAATCTTCTGTCT	ACTGTAACATACTCATATCCA	177
ZIP8	GACAGTTATGTTGAGAAGG	TGACCATTCTGACCATAT	107
CP	CACTTACACCGTTCTACA	GTATGCTTCCAGTCTTCT	170
HEPH	GCTGAGATGGTGCCCTGGGAAC	AGGAGGGGCCATGGAGCAAGAC	117
HEPHL1	AAGATTCAGAAGGAGCCCTATACCCAG	CGTCGATGTGCGAATGGTACACCC	171
TfR1	GTAGATGGCGATAACAGT	CCAATCATAAATCCAATCAAGA	167
FPN1	AGATCACAACCGCCAGAGAG	CACATCCGATCTCCCCAAGT	111
Zip14	CTGCTGCTCTACTTCATA	CAGACTTGGAGACATAATAATC	118
Mitoferrin	AACACTCAGGAGAACGTGGC	AAGCAATTTCTCGCTCCCCT	467
FTH	TTGAGACACATTACCTGAA	AAGAGATATTCCGCCAAG	112
HAMP	TCCCACAACAGACGGGACAACTTG	GCAGATGGGGAAGTGGGTGTCTC	119
IREB1	ACAAGCAGGCACCACAGACTATCC	GCACCGTACTCTTTGCCAGCCAG	124
IREB2	GGTGGATTTTGCTGCTATGAGGGAG	CACCTCCAGGATTTGGTGCATTCTG	155
HIF-1α	TCCATGTGACCATGAGGAAA	CCAAGCAGGTCATAGGTGGT	251
SLC2A1	GAACTCTTCAGCCAGGGTCC	ACCACACAGTTGCTCCACAT	114
Tf	AGCCTGCACTTTCCGTAGAC	AACCACTTGGGCCAGTGAAA	112
Hfe	ATTGGAGAGCAGCAGAACCC	TGGTAGGTCCCATCCCCATT	334
TfR2	CAATCACAGGACCTCCACCC	GTTGTCCAGGCTCACGTACA	322
Steap3	GAAAACCACACTGGCTCCAAC	CACAGGGGAAGTAAGCTAGAGTC	207
HCP1	AACTAAGCACACCCCTCTGC	AGGCTATTCACACAGGCCAC	244
HCP1	CGCTCACCACGCAGTATCTG	GTGGGAGGTAAGGGTCTCCAC	131
HRG1	TTCTCAGAGTGCCCTTGCTG	GCTGATACAAATGGCCGCTG	327
FLVCR1	CTCGCGAAAGGATACCTCCC	CTGGATCCACTGAAAGGCGT	330
FLVCR2	CCCAACATTGAAGACCGGGA	AGCATTCACTTCTTCCCCCG	327
LRP1	CAGCAAACGAGGCCTAAGTC	CATGGGTTGGTCACTTCGGG	201
SCARA5	TCTGAGGGGACAAGGCTCTA	CTTGCCCGCCGTTTGTGAC	195
HMOX1	ATGACACCAAGGACCAGAGC	GTCGCCACCAGAAAGCTGAG	172
HMOX2	GGAAACCTCAGAGGGGGTAG	TGTGAAGTAAAGTGCCGTGG	317

Note: Gene names and accession numbers are listed in Table 3.

2.3 | Protein quantification of placental membrane proteins by mass spectrometry (MS)

2.3.1 | Total membrane isolation

Prior to proteomic analysis total membrane isolation (TMI) was performed for the depletion of high abundant proteins (eg, albumin, IgG). Approx. 50 mg of placental tissue from snap-frozen samples was thawed in 1.3 mL lysis buffer (250 mM Sucrose; 10 mM Hepes; protease inhibitor cocktail; adjusted pH to 6.95) and homogenized with a Polytron homogenizer (Kinematica AG, Switzerland) in iced water. Large cellular debris was removed by a first centrifugation step at 1000 *g* (5 minutes, 4°C). The supernatants were subjected to two differential ultracentrifugation steps at 10 000 *g* (15 minutes, 4°C). After the 1st centrifugation the supernatants were collected, the pellets were resuspended in lysis buffer, homogenized for 2 minutes, and subjected to the 2nd centrifugation (same as before). The remaining pellet was discarded. Membrane proteins were obtained after a final ultracentrifugation step of the two combined supernatants at 125 000 *g* (30 minutes, 4°C). For quantitative LC-MS/MS analysis the pellets were washed with 1 M KCl and 100 mM

Na_2CO_3. The final TMI pellets were resuspended in 200 µL 50 mM Tris-HCl buffer (pH 8) using a glass-teflon homogenizer. The TMI homogenates were aliquoted and stored at −80°C until proteomics analysis. Protein concentrations of the TMIs were measured using Pierce BCA Protein Assay Kit (Thermo Fisher Scientific, USA).

2.3.2 | Development of Parallel Reaction Monitoring (PRM) assay

For the development of the quantification assay for a target set of proteins, a preliminary set of experiments was performed to optimize the sample preparation and to select the proteotypic peptides of each target protein. About 30 µg protein of TMI samples were subjected to filter-assisted sample preparation and tryptic digestion[13] with a subsequent desalting step by C18 solid phase extraction columns (Sep-Pak Fenisterre; Waters Corporation, USA). The dried samples were re-solubilized in 3% acetonitrile, 0.1% formic acid, and spiked with iRT peptides (Biognosys, Switzerland) for MS analysis which was performed on a QExactive mass spectrometer coupled to a nano EasyLC 1000 (Thermo Fisher Scientific). Solvent composition at the two channels was 0.1% formic acid for channel A and 0.1% formic acid, 99.9% acetonitrile for channel B. For each sample 1 µL of peptides were loaded on a commercial Acclaim PepMap Trap Column (75 µm × 20 mm, Thermo Fisher Scientific) followed by a PepMap RSLC C18 Snail Column (75 µm × 500 mm, Thermo Fisher Scientific). The peptides were eluted at a flow rate of 300 nL/min by a gradient from 2% to 30% B in 115 minutes, 47% B in 4 minutes, and 95% B in 4 minutes. The mass spectrometer was operated in data-dependent mode, acquiring a full-scan MS spectrum (300-1700 m/z) at a resolution of 70 000 at 200 m/z after accumulation to a target value of 3 000 000, followed by higher energy collision dissociation fragmentation on the 12 most intense signals per cycle. These spectra were acquired at a resolution of 35 000 using a normalized collision energy of 25 and a maximum injection time of 120 ms The automatic gain control was set to 50 000 ions. Charge state screening was enabled and singly and unassigned charge states were rejected. Precursor masses previously selected for MS/MS measurement were excluded from further selection for 30 seconds, and the exclusion window was set at 10 ppm. The samples were acquired using internal lock mass calibration on m/z 371.1010 and 445.1200.

The acquired raw MS data were processed by MaxQuant (version 1.4.2.1),[14] followed by protein identification using the integrated Andromeda search engine. Spectra were searched against a uniprot Homo Sapiens (taxonomy 9606) reference proteome (canonical version from 2016-12-09), concatenated to its reversed decoyed fasta database and common protein contaminants. Carbamidomethylation of cysteine was set as fixed, while methionine oxidation and N-terminal protein acetylation were set as variable modifications. MaxQuant Orbitrap default search settings were used. Enzyme specificity was set to trypsin/P. The MS proteomics data were handled using the local laboratory information management system.[15]

2.3.3 | Optimization of sample preparation protocol

Protein digestion for the 22 TMI samples was further improved using a commercial iST Kit (PreOmics, Germany) with an adapted version of the protocol. Briefly, 30 µg of protein were solubilized in lysis buffer, boiled at 95°C for 10 minutes, and processed with High Intensity Focused Ultrasound for 30 seconds setting the ultrasonic amplitude to 85%. Then the samples were transferred to the cartridge and digested by adding 50 µL of the digestion solution (provided in the kit). After 60 minutes of incubation at 37°C the digestion was stopped with 100 µL of stop solution (provided in the kit). The solutions in the cartridge were removed by centrifugation at 3800 *g*, while the peptides were retained by the iST-filter. Finally, the peptides were washed, eluted, dried, and re-solubilized in LC-Load buffer for MS analysis.

2.3.4 | Settings for label free and MS/MS-based protein quantification

Solvent composition at the two channels was 0.1% formic acid for channel A and 0.1% formic acid, 99.9% acetonitrile for channel B. For each sample 1 µL of peptides were loaded on a commercial MZ Symmetry C18 Trap Column (100 Å, 5 µm, 180 µm × 20 mm, Waters, Switzerland) followed by nanoEase MZ C18 HSS T3 Column (100 Å, 1.8 µm, 75 µm × 250 mm, Waters, Switzerland). The peptides were eluted at a flow rate of 300 nL/min by a gradient from 5% to 35% B in 50 minutes and 98% B in 5 minutes. The Q Exactive HF performed MS scans (350-1250m/z) followed by 16 MS/MS acquisitions in PRM mode. The full scan event was collected at a resolution of 15 000 (at m/z 200) and an automatic gain control (AGC) value of 3e6 and a maximum injection time of 15 ms. The PRM scan events used an Orbitrap resolution of 120 000, maximum fill time of 200 ms with an isolation width of 1.4m/z, an isolation offset of 0.5 m/z and an AGC value of 2e5. Higher-energy collisional dissociation fragmentation was performed at a normalized collision energy (NCE) of 27. The whole method included 74 L/H peptide precursors and 11 Biognosys iRT standard peptides. Based on the spiked iRTs, the retention time of the target peptides was normalized and transformed into iRT values[16] allowing to set the scan windows to

4 minutes for each peptide in the final PRM method (Table S1). This ensured the measurement of 6-10 points per LC peak per transition.

2.3.5 | LC-MS/MS assay

Based on preceding development of the PRM assay as outlined above, a set of proteotypic peptides was selected for nine protein targets and three housekeeping proteins. For proteins with no or less than three proteotypic peptides, additional peptides were selected from the selected reaction monitoring Atlas (www.srmatlas.org) as listed in Table S1. Stable isotope-labeled standard peptides corresponding to the proteotypic peptides and containing either a C-terminal (13C(6) 15N(4)) arginine or a (13C(6) 15N(2)) lysine residue were chemically synthesized via SPOT synthesis (JPT Peptide Technologies, Germany) and used in unpurified form for PRM analysis. In total, the scheduled PRM assay targeted 85 peptides (12 proteins, 37 peptides in Light/Heavy (L/H) form and 11 iRT peptides). The MS/MS spectra of these peptides were used for the generation of spectral libraries using Mascot (Matrixscience) according to the parameters previously described for MaxQuant. Finally, both the MaxQuant and the Mascot search results were imported into the Skyline software v3.7[17] and spectral libraries were built using the BiblioSpec algorithm.[18] Based on the spiked iRTs, the retention time of the target peptides was normalized and transformed into iRT values[16] allowing to set the scan windows to 4 minutes for each peptide in the final PRM method (Table S1). This ensured the measurement of 6-10 points per LC peak per transition.

A summary and graphical overview of the MS/MS-based protein quantification approach from tissue collection, placental membrane protein preparation to membrane protein quantification as performed in this study is shown in Figure S3.

2.4 | Semi-quantitative analysis of placental iron transporters by immunohistochemistry

Tissues from GDM and control placentae were embedded in Neg50-Frozen Section Medium (Histocom AG, Switzerland), cut at 5 µm thickness and mounted on Superfrost plus slides (Menzel, Germany). The frozen tissue blocks were stored at −80°C upon sectioning. The tissue sections were fixed in precooled acetone (−20°C) for 10 minutes and washed twice for 5 minutes in 10 mM phosphate buffered saline (PBS, pH 7.4). Fixed sections were incubated in H_2O_2-Block (Dako) at room temperature (RT) for 10 minutes to block endogenous peroxidase activity and again washed twice in PBS. The same placental tissues as used for RT-PCR and proteomic analysis were stained on cryosections with antibodies against DMT1 (anti-SLC11A2 antibody clone 4C6 WH0004891M1) and FPN1 (anti-Ferroportin antibody PA5-22993, Thermo Fisher Scientific). The primary antibodies were diluted in PBS with 0.5% bovine serum albumin (BSA) (DMT1, 1:1000; FPN1, 1:1000). Diluted primary antibodies (100 µL per slide) were added to cover the tissue on the slides and incubated in a humidified chamber (DMT1 for 2 hours; FPN1 for 1.5 hours) at 4°C. For the visualization of the antigens on the next day UltraVision LP Detection System (Thermo Fisher Scientific) was used according to the manufacturer's instructions. Slides were washed with PBS and incubated with Antibody Enhancer solution for 20 minutes. After an additional washing step with PBS, the HRP polymer was added for 30 minutes, the slides were washed again, and AEC chromogen was applied for 5 minutes in the dark. Sections were washed in distilled water, counterstained with hematoxylin and mounted with Aquatex (EMD Millipore 1.08562). Negative controls were stained without prior incubation with the primary antibody. Immunohistochemical images were prepared with a DM6000 B microscope (Leica Microsystems, Germany). The staining intensity of *DMT1* and *FPN1* expression in all specimens was semi-quantitatively scored by a blinded external expert for pathological histology. Staining intensity was rated on a scale of 0-3, with 0 = negative, 1 = weak, 2 = moderate, and 3 = strong.

2.5 | Colorimetric ferrozine-based assay for iron quantification

Total iron content in placental tissues was determined using a colorimetric ferrozine-based assay.[19] Approximately 50 mg placental tissue, taken from the same localization as for mRNA and protein quantification, were lysed in 0.9% cold NaCl and homogenized with a Polytron homogenizer in iced water. $FeCl_3$ standard dilutions with concentrations ranging from 1.562 to 300 µM were prepared in 10 mM HCl diluent. NaOH solution was added with equal volume to the samples to reach the same NaOH and HCl concentration as in standard dilutions. Aliquots of these lysates were used for iron quantification and protein measurements (Pierce BCA Protein Assay, Thermo Fisher Scientific). Freshly prepared iron releasing reagent (solution of equal volumes of 1.4 M HCl and 4.5% weight/volume (w/v) $KMnO_4$, in distilled water) was added 1:1 v/v. Samples were incubated for 2 hours at 60°C. After cooling the samples to RT, iron detection reagent (6.5 mM ferrozine; 6.5 mM neocuproine; 2.5 M ammonium acetate; 1 M ascorbic acid; all dissolved in distilled water) was added in a 1:10 ratio v/v. Samples were further incubated at RT for 30 minutes. The absorbance was measured in duplicates at 550 nm using the microplate reader (VMax Kinetic ELISA Microplate Reader with Softmax Pro Software, Molecular Devices LLC, USA). Absorbance of samples was compared to the absorbance of equally treated

$FeCl_3$ standards. The iron content was normalized to the protein concentration of the sample.

2.6 | BeWo-based cell models for hyperglycemia

The choriocarcinoma-derived BeWo cell line (clone b30) was used as trophoblast cell model. BeWo cells were adapted under normoxic (approx. 21% pO_2) conditions and 5% pCO_2 atmosphere to physiological glucose concentrations by growing them for approximately 30 passages in medium containing 5.5 mM glucose (DMEM-low glucose, Gibco). Beside the normoglycemic condition (N; DMEM 5.5 mM glucose) two hyperglycemic BeWo batches were created by exposing the cells either to a hyperglycemic (H; DMEM 25 mM glucose) or hyperglycemic/hyperlipidemic condition (HL; H + 100 µM palmitic acid). The palmitic acid was prepared by conjugation BSA adapted from Sinha et al.[20] In brief, palmitic acid was dissolved in pre-heated 0.1 M NaOH and diluted 1:10 in pre-warmed 12% w/v BSA solution to obtain a final concentration of 10 mM. N and H media contained same amounts of 0.1 M NaOH and BSA without lipid.

2.7 | Transferrin-mediated iron uptake assay

The different BeWo cell lines N, H, and HL were seeded 24 hours before starting the experiment into 96-well plates at a density of 60 000 cells/well and incubated with the respective medium. The preparation of iron-binding transferrin (Tf), the experimental procedure and calculation of the iron uptake assay were adapted from.[21] In brief, to prepare $^{55}FeCl_3$ (PerkinElmer, Germany)-labelled uptake solution, human apo-Tf was dissolved in balanced salt solution (BSS; 136 mM NaCl, 5 mM KCl, 1 mM $CaCl_2$, 1 mM $MgCl_2$, and 18 mM HEPES, pH 7.4) and added to 7.5% w/v $NaHCO_3$. After brief mixing, the previously mixed hot and cold iron was added for Tf binding at 37°C for 2 hours. The concentrated Fe-Tf solution with the concentration of 45 nmol/mL Tf, 90 nmol/mL $^{55}FeCl_3$, and 243 µmol/mL $NaHCO_3$ was diluted in BSS buffer to final iron concentration of 179.8 pmol/mL. Binding of Fe^{3+} to Tf was confirmed by measuring E_{470nm}/E_{280nm} absorption ratio (data not shown). The cells were washed 3x with BSS and incubated 30 minutes at 37°C for equilibration before 100 µL of the diluted uptake solution was added. Iron uptake was stopped at defined time points (1.5 minutes-2 hours) by washing 3x with BSS. 10% of uptake solution volume was measured separately to obtain dosage control (DC) values. For cell lysis and ^{55}Fe detection 100 µL scintillation solution (MicroScint-20, PerkinElmer) was added and the wells were shaken for 1.5 hours at RT. Radioactivity was acquired by TopCount Microplate Scintillation and Luminescence Counter (PerkinElmer, Germany). Counts per minute (cpm) were determined for each timepoint and then transformed into iron uptake in % of total dose using the following equation:

$$\text{Iron uptake (\%)} = \frac{\text{count/well (cpm) of S} - \text{count/well (cpm) of BG}}{\text{mean of DC} \times 10} \times 100$$

where S = Sample; BG = background; DC = dosage control.

To monitor the time-dependent adaptation processes on a functional level, iron uptake time courses in BeWo cells were performed for 30 days under N, H, and HL conditions.

2.8 | Assessment of autophagy and ER stress by immunoblotting

Protein expression changes of biomarkers for endoplasmic reticulum (ER) stress (BiP/GRP78) and autophagy pathways (p62, LC3-II) were determined by immunoblotting. BeWo cells were lysed by adding hypotonic lysis buffer (10 mM Tris-HCl; 10 mM NaCl; 1.5 mM $MgCl_2$, 1% Triton X-100; protease inhibitor cocktail; pH 7.4). The samples were vortexed in hypotonic lysis buffer every 5 minutes during 30 minutes on ice for thorough lysis of the cells. Subsequently, the cell lysates were centrifuged at 1000 *g* for 10 minutes at 4°C to remove cellular debris and stored upon analysis at −20°C. Protein content was measured using a commercial Pierce BCA Protein Assay Kit. 20 µg cell lysates were loaded on 10% acrylamide gels and separated by SDS-PAGE. The immobilized bands were then semi-dry transferred to nitrocellulose membranes (GE Healthcare). Blots were blocked with 5% w/v nonfat milk in Tris Buffered Saline with 0.1% Tween-20 (TBST). The following primary antibodies were used: Purified Mouse Anti-BiP/GRP78 (BD Transduction Lab. 610978), SQSTM1/p62 Antibody (Cell Signaling Technology 5114S), Anti-LC3-I/II Antibody (Millipore ABC929), and for the reference signal (loading control) mouse anti-β-actin antibody (Sigma A2228). Primary antibody incubations were performed at 4°C by shaking overnight, followed by four times washing with TBST, and incubation with DyLight 680 or 800 fluorescence conjugated secondary antibodies (Thermo Fisher Scientific). The specific bands for BiP/GRP78, p62 and LC3-II were densitometrically analyzed (OdysseyW Sa Infrared Imaging System; LI-COR) and related to β-actin as loading control.

2.9 | Oxidative damage and antioxidative potential of trophoblasts

To measure OS levels in the BeWo cell models (N, H, and HL), we determined products of the lipid peroxidation cycle

and protein carbonylation. Furthermore we assessed the antioxidant potential of BeWo cells by quantifying GSH levels according to.[22]

2.9.1 | Measurement of lipid peroxidation products (TBARS)

The products of lipid peroxidation, such as malondialdehyde (MDA), were measured using a thiobarbituric acid reactive substances (TBARS) assay in cell culture media. MDA combines with thiobarbituric acid (TBA) in a 1:2 stoichiometry to form a fluorescent adduct. TBARS are expressed as MDA equivalents and normalized to total cellular protein concentration.[23] Cell media were collected after 30 days of treatment and stored upon analysis at −20°C. For the other OS assays the cells were trypsinized, washed in cold PBS, and stored at −20°C. 15% w/v trichloroacetic acid (TCA, Merck, Germany), sample or MDA standard (1,1,3,3 Tetraethoxypropane) and 0.67% w/v TBA (VWR, Switzerland) in 2.5 M HCl were mixed in a 4:5:8 ratio, vortexed,and boiled for 20 minutes at 95°C. The MDA standard curve was prepared as a 1:2 dilution series from 2 to 0.007 nmol/mL. After cooling the samples to RT, 2 mL 1-butanol was added and gently mixed. Spinning the samples for 1 minute at 1000 *g* speeded up the phase separation. For the measurement the butanol phase (top) was transferred to a black-wall 96-well plate and measured using Flex Station II fluorescence microplate reader (Thermo Fisher Scientific) at an excitation/emission wavelength of 530/550 nm, respectively. MDA equivalents were calculated by interpolation to the MDA standard curve.

2.9.2 | Measurement of protein carbonylation

Carbonyl groups (aldehydes and ketones) are produced on protein side chains when they are oxidized. The detection of protein carbonyl groups involves their reaction with 2,4-dinitrophenylhydrazine (DNP), which leads to the formation of a stable 2,4-dinitrophenylhydrazone product, followed by its spectrophotometric quantification.[24] The cell pellets were resuspended with 2.5% w/v TCA and centrifuged at 11 000 *g* for 3 minutes. 500 µL of 10 mM DNP in 2 M HCl was added to the precipitates, and allowed to stand for 1 hour at RT, with vortexing every 10-15 minutes. Thereafter, 20% w/v TCA was added for precipitation, followed by three washing steps with ethanol-ethylacetate (1:1) to remove free reagent. The precipitated proteins were dissolved in 600 µL of 6 M guanidine solution. The carbonyl content was calculated from the OD_{405nm} measured by V_{max} Kinetic ELISA Microplate Reader (VWR) using a molar absorption coefficient of 22 000 M^{-1} cm^{-1}. Carbonyl contents were normalized to the protein concentration.

2.9.3 | Measurement of total glutathione levels

The assay to estimate the antioxidant potential of cultured trophoblasts is based on the reaction of GSH with 5,5′-dithiobis-2-nitrobenzoic acid (DTNB) forming the chromophore 5-thio-2-nitrobenzoic acid (TNB). The rate of TNB formation was measured at 405 nm using V_{max} Kinetic ELISA Microplate Reader and is proportional to the concentration of GSH in the sample. The determination of total-GSH concentration detects both forms of GSH, the reduced sulfhydryl form (GSH) and the oxidized glutathione disulfide (GSSG). The assay was performed according to the protocol from Rahman et al 2007.[22] The total-GSH concentration was calculated from the linear standard curve based on a 1:2 dilution series ranging from 125-1.96 nmol/mL. GSH contents were normalized to the protein concentration.

2.10 | Selenium supplementation of trophoblasts

To assess whether an increased antioxidative potential could protect the trophoblast cells from endogenous and exogenous OS, the N, H, and HL cell models were treated for 42 days under standard culture conditions with the antioxidant NaSe (400 nM). To enhance the stress-mediated cellular response, the six cell models (N; H; HL; N+Se; H+Se; HL+Se) were subjected to additional treatment with 100 µM tert-Butylhydroperoxide (tert-BOOH) for 24 hours. To investigate whether increased antioxidative activity can rescue the effect of hyperglycemia/hyperlipidemia on placental iron homeostasis, mRNA levels, oxidative damage, and antioxidative potential were assessed as described above.

2.11 | Statistical analysis

Anthropometric and clinical data were compared between GDM and controls by Student's *t* test and placental protein levels by multiple *t* test. Mann-Whitney test was performed to detect differences in placental mRNA levels of all genes involved in iron homeostasis between GDM patients and controls. For statistical analysis of mRNA levels determined in the in vitro experiments, the two-way ANOVA test with Sidak's multiple comparison post hoc analysis was applied. For immunohistochemistry the nonparametric chi-square (χ^2) test was used to compare semi-quantitative protein expression

between control and GDM placentae. A P value < .05 was considered as statistically significant. Statistical comparisons were performed using GraphPad Prism (GraphPad).

3 | RESULTS

3.1 | GDM affects clinical parameters of newborns and iron homeostasis genes

As shown in Table 2 mothers with GDM exhibited significantly increased pre-conceptional BMI and increased hemoglobin concentrations. The corresponding newborns of GDM pregnancies were born large for gestational age as demonstrated by increased weight and body length (Table 2). Increased hemoglobin levels were detected in maternal sera, but no changes in the fetal iron status was documented. The RT-qPCR screening of 24 iron homeostasis genes (Table 1) in GDM and control placentae revealed significant downregulation of the iron transporters *DMT1* and *FPN1*, upregulation of the ferroxidases *HEPH* and *Zp*, and of the iron entry regulator *HEPC* in GDM (Table 3; Figure 1A). For further quantification on protein level, *TfR1*, as sensitive indicator of changes in iron homeostasis, and the iron transporters *DMT1*, *ZIP8*, and *FPN1* were selected. Since it was not possible to quantify the three iron-transporters by LC-MS/MS analysis in placental tissue lysates, TMI from all placentae was performed. The subsequent MS-based quantification and the comparison of protein levels between GDM and healthy control revealed a GDM-specific downregulation of the iron transporter *ZIP8* and the holo-Tf binding receptor TfR1 (Figure 1B). There were no significant gender differences for any of the 24 measured iron homeostasis genes as analyzed by nonparametric Mann-Whitney test.

3.2 | GDM-specific changes in placental DMT1 localization

To investigate potential GDM-mediated effects on the cellular distribution of the iron transporters, semi-quantitative immunohistochemical analysis for DMT1 and FPN1 was performed in placental tissues. STB-specific staining of FPN1 was restricted to basal/basolateral structures (data not shown) and did not differ between GDM and controls (χ^2 (2) = 3.21, P = .201, α < 0.05). In contrast, the apically accentuated expression pattern of *DMT1* in controls was significantly shifted towards the cytoplasm of the syncytiotrophoblasts (χ^2 (2) = 7.62, P = .022, α < 0.05) in GDM (Figure 1C).

TABLE 2 Anthropometric and clinical characteristics of gestational diabetes mellitus (GDM) patients and controls including their offspring

Characteristics	Control	GDM	*P* value
Number of individuals	11	11	
Delivery mode	Cesarean section	Cesarean section	
Maternal age (years)	30.91 ± 5.43	31.91 ± 7.66	.7276
BMI (pre-conceptional)	23.14 ± 3.92	29.53 ± 5.16	.0038**
Parity	2.36 ± 0.67	2.09 ± 0.83	.4080
Gestational age at partum	39.00 ± 0.60	39.06 ± 1.29	.8814
Glucose (mmol/l)	4.92 ± 0.74	5.25 ± 1.51	.5190
Treatment	none	8 insulin/3 diabetes diet	
Creatinine (μmol/L)	46.82 ± 7.90	51.09 ± 10.67	.2985
RBC (T/l)	3.86 ± 0.35	4.10 ± 0.34	.1201
Hemoglobin (g/L)	115.27 ± 6.96	124.82 ± 10.90	.0237*
MCV (fl)	88.64 ± 5.61	88.36 ± 3.96	.8965
MCH (pg)	30.00 ± 2.14	30.55 ± 2.07	.5505
MCHC (g/L)	337.82 ± 3.76	344.18 ± 9.45	.0512
Hematocrit (%)	0.34 ± 0.02	0.36 ± 0.03	.0640
Weight of baby (g)	3182 ± 242	3787 ± 419	.0005***
Length (cm)	48.4 ± 1.8	50.6 ± 2.0	.0095**
Sex of baby	5♂, 6♀	5♂, 6♀	

Note: Data are represented as mean ± standard deviation (SD). Differences between GDM and the control group were analyzed by two-way Student's t test; α = 0.05, *P < .05, **P < .01, ***P < .001.

Abbreviations: BMI, body mass index; MCH, mean corpuscular hemoglobin; MCHC, mean corpuscular hemoglobin concentration; MCV, mean corpuscular volume; PCV, packed cell volume; RBC, red blood cells.

TABLE 3 Expression analysis of iron homeostasis genes in placentae from GDM patients and controls

Unique gene identifier	Gene name	Protein name	*P* value
		Iron endocytosis	
P02787	*Tf*	Serotransferrin	.6047
P02786	*TfR1*	Transferrin receptor protein 1	.9725
Q07954	*LRP1*	Lipoprotein receptor-related protein 1	.3494
Q6ZMJ2	*SCARA5*	Scavenger receptor class A member 5	.6539
		Iron transporters	
P49281	*DMT1*	Divalent metal transporter 1	.0139* ↓
Q9C0K1	*ZIP8*	Zrt- and Irt-like protein 8	.7564
Q15043	*ZIP14*	Zrt- and Irt-like protein 14	.1545
Q9NP59	*FPN1*	Ferroportin-1	.0032** ↓
Q9NYZ2	*MFRN1*	Mitoferrin-1	.8633
Q9Y5Y0	*FLVCR1*	Feline leuk. virus subg. C receptor 1	.5516
Q9UPI3	*FLVCR2*	Feline leuk. virus subg. C receptor 2	.8238
Q96NT5	*HCP1*	Heme carrier protein 1	.2230
Q6P1K1	*HRG1*	Heme transporter HRG1	.1971
		Iron storage	
P02794	*FHC*	Ferritin heavy chain	.2816
		Oxidoreductases	
P00450	*CP*	Ceruloplasmin	.3144
Q9BQS7	*HEPH*	Hephaestin	.0242* ↑
Q6MZM0	*Zp*	Zyklopen	.0201* ↑
P09601	*HO1*	Heme oxygenase 1	.6539
P30519	*HO2*	Heme oxygenase 2	.1517
Q658P3	*STEAP3*	Metalloreductase STEAP3	.4679
		Regulators	
P81172	*HEPC*	Hepcidin	.0242* ↑
Q30201	*HFE*	Hereditary hemochromatosis protein	.2512
		Iron sensing, mRNA binding	
P21399	*IRP1*	Iron regulatory protein 1	.0251* ↓
P48200	*IRP2*	Iron regulatory protein 2	.5116

Note: Quantitative RT-PCR analysis of placental tissues from gestational diabetes mellitus (GDM) patients (n = 11) and controls (n = 10) was performed in two independent experiments and normalized to the mean of the reference genes 14-3-3 protein zeta/delta (*YWHAZ*), Glyceraldehyde-3-phosphate dehydrogenase (*GAPDH*) and ubiquitin (*UBC*). The results of the comparison between GDM and controls are represented by target-specific *P* values and arrows displaying up- (↑) or downregulation (↓) in GDM. Statistical significance was determined using two-tailed Mann-Whitney test; $\alpha = 0.05$, $^{*}P < .05$, $^{**}P < .01$, $^{***}P < .001$. Genes were selected upon proven placental expression in literature or according to data from protein atlas (www.proteinatlas.org).

3.3 | Unchanged iron content in placental tissue from GDM pregnancies

Based on our findings showing GDM-specific regulation of iron transporters and TfR1, we compared the iron contents between GDM and control placentae. The total iron contents measured by colorimetric ferrozine-based assay were similar between control and GDM placentae (Figure 1D).

3.4 | BeWo cells alter cell morphology under hyperglycemic conditions

During 30 days of culturing the cells adapted their morphology to the enhanced availability of glucose in H and HL by increasing nuclei and vacuoles size. The increased provision of fatty acids in HL additionally resulted in extensive intracellular lipid stores (Figure 2A).

3.5 | Hyperglycemic adaptions in BeWo cell models reflect clinical observations in GDM

The effect of GDM on iron homeostasis in the clinical specimens was characterized by downregulation of the key iron transporters *DMT1*, *FPN1*, and *ZIP8* and the iron uptake mediating *TfR1* on either mRNA or protein level (Figure 1A/B). When monitoring the expression levels of the same genes during 30 days of hyperglycemic/hyperlipidemic challenge in the BeWo cell models, there was an initial upregulation of *DMT1* and ZIP8 after 3 days of stimulation and a stable downregulation of *FPN1* and *TfR1* after 20 days relative to normoglycemic conditions (Figure 2B, upper left panel). In the HL condition *DMT1* was downregulated from 28 days of stimulation (Figure 2B, upper right panel). Moreover, the upregulation of the ferroxidase *Zp* in H and HL during the entire stimulation time (Figure S1) also mimicked the clinical results found in GDM placentae, and strongly underlines the suitability of the applied cell models. Interestingly, the constant downregulation of *GLUT1* confirmed the increased availability of glucose in H and HL (Figure S1).

3.6 | Hyperglycemia reduces iron uptake in trophoblasts

We then extended our studies to the functional level and performed Tf-$^{55}Fe^{3+}$-mediated uptake assays. Considering the total monitoring period of iron uptake, there was a consistent reduction of >40% in iron uptake during 2 hours in both H and HL (Figure 2C, left panel). While an initial increase

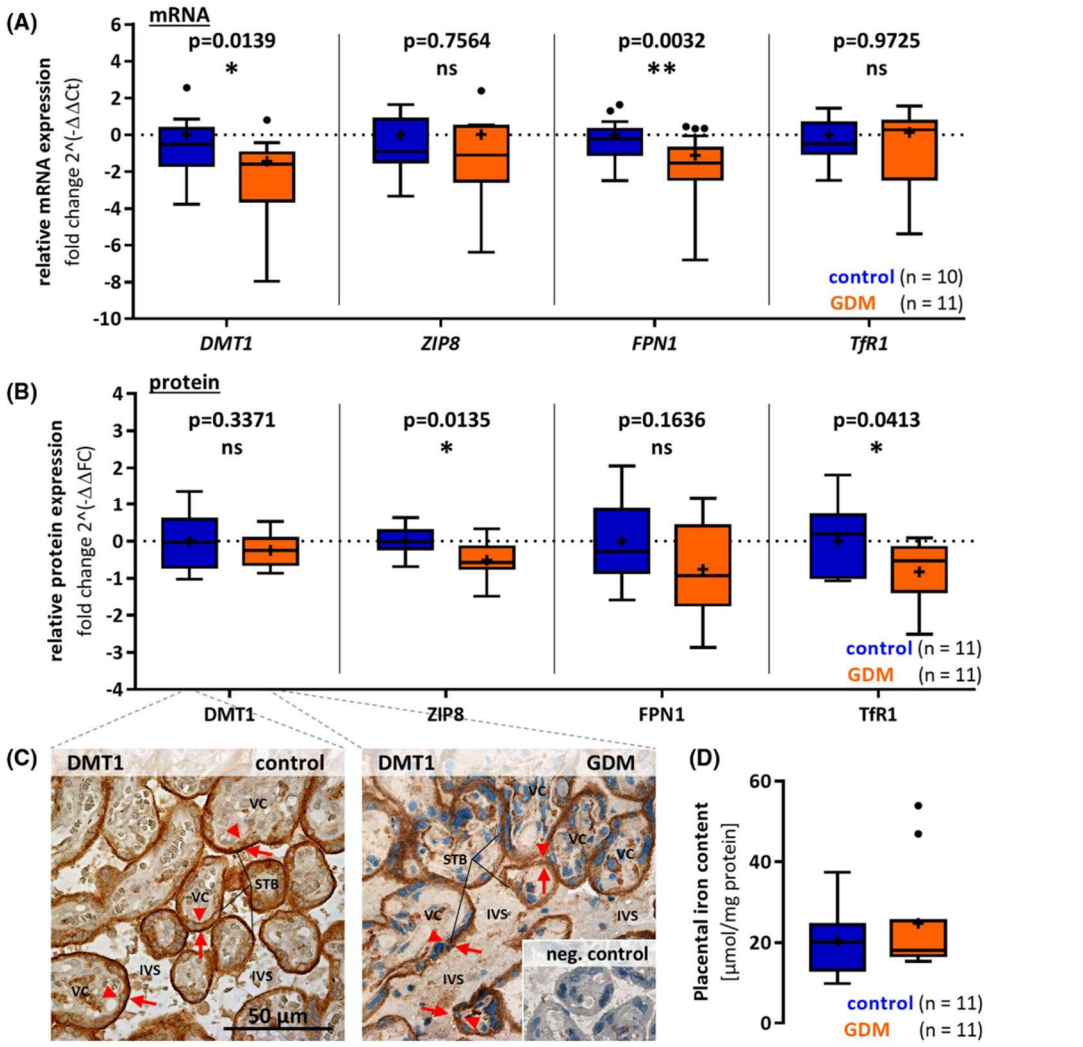

FIGURE 1 Expression changes of selected iron homeostasis genes in placental tissue from GDM patients and controls on transcript and protein level. Normalized expression of iron homeostasis genes critical for transplacental iron transport, which were regulated in GDM either on mRNA (A) or protein (B) level. A, Transcript levels of divalent metal transporter 1 (*DMT1*), Zrt- and Irt-like protein 8 (*ZIP8*), Ferroportin-1 (*FPN1,*) and Transferrin receptor protein 1 (*TfR1*) were analyzed in placental tissues of GDM patients (orange) and term controls (blue). Expression results were determined in two independent experiments and normalized to the mean of the reference genes 14-3-3 protein zeta/delta (*YWHAZ*), Glyceraldehyde-3-phosphate dehydrogenase (*GAPDH*), and ubiquitin (*UBC*). Transcript data are presented as $2^{-\Delta\Delta Ct}$ values (ΔΔCt = Ct value of target gene—Ct value of the mean of *YWHAZ*, *GAPDH* and *UBQ*) and normalized to the mean of controls. Statistical significance was determined as described in Table 3 using two-tailed Mann-Whitney test, $\alpha = 0.05$, $^{*}P < .05$, $^{**}P < .01$, $^{***}P < .001$. B, Results of LC-MS/MS-based protein quantification in total membrane isolations of placental tissues from the same patient cohort and for the same targets as presented in A. Protein levels were calculated as fold changes relative to spiked peptides and subsequently normalized to the reference gene *GAPDH*. Protein data are presented as delta-delta FC values (ΔΔFC = fold changes (FC) relative to spiked peptides of target gene—FC relative to spiked peptides of *GAPDH*) and normalized to the mean of controls. Statistical significance was determined by two-tailed Student's *t* test, $\alpha = 0.05$. C, Expression pattern of *DMT1* in human term placenta detected by immunohistochemistry. *DMT1* was expressed exclusively in syncytiotrophoblasts. DMT1 in control tissue was apically accentuated (C, left panel), while GDM tissue showed predominantly intracellular *DMT1* expression (C, right panel). The negative control is shown as insert in the right panel. Arrows indicate the apical, maternal blood-oriented side, arrowheads depict the fetal-oriented basal membrane of the syncytiotrophoblasts. All images are displayed at 40x magnification. Abbreviations: IVS, intervillous space; STB, syncytiotrophoblast; VC, villous core. D, Total iron contents in placental tissue were measured by a colorimetric ferrozine-based assay and normalized to the total protein concentration. Iron content did not differ between control and GDM placentae. A, B, D, Data are presented as mean (x), median (-), and Tukey whiskers (1.5-times interquartile range), $\alpha = 0.05$, $^{*}P < .05$, $^{**}P < .01$

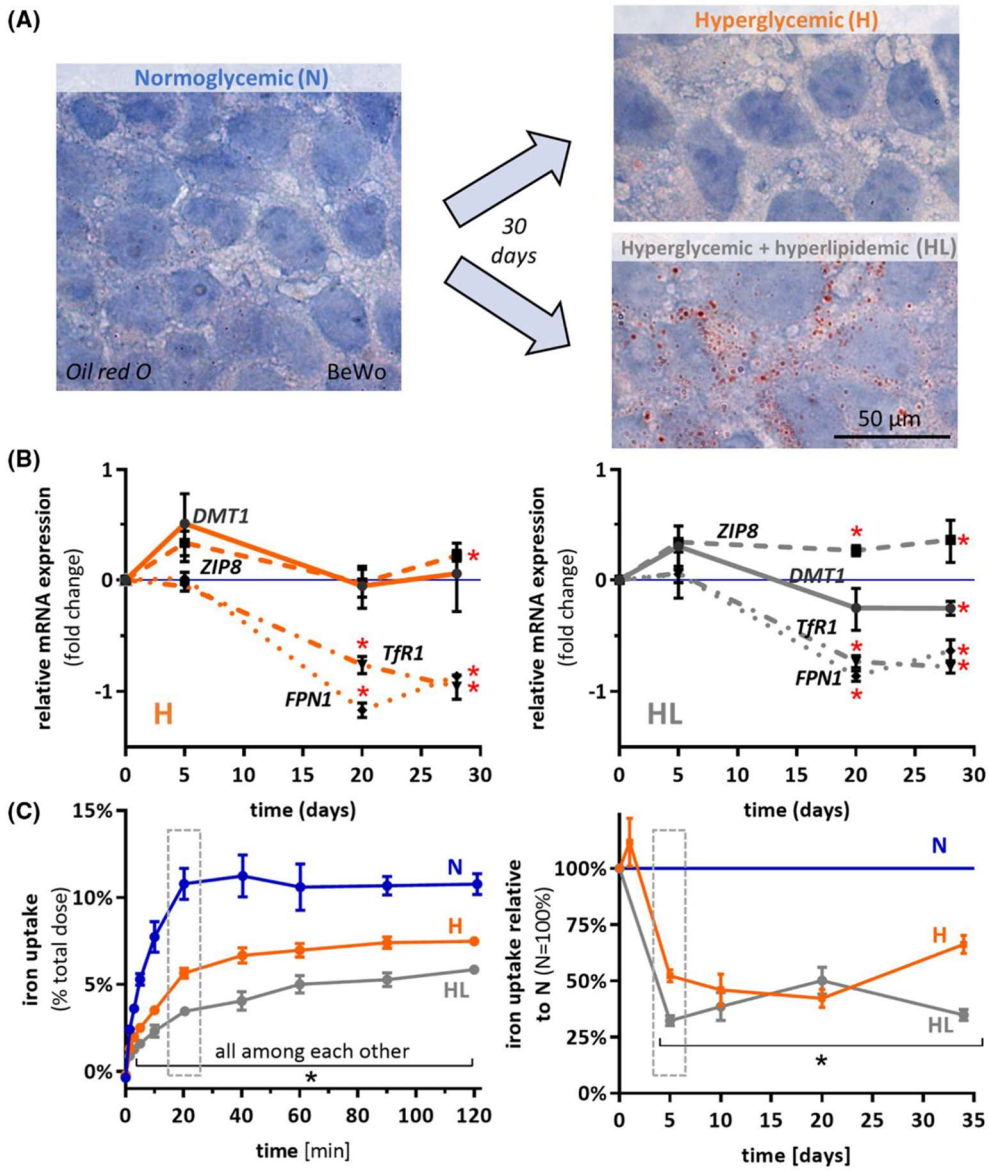

FIGURE 2 Assessment of time-dependent adaption of trophoblasts to hyperglycemic and hyperglycemic-hyperlipidemic conditions. A, Representative images of Oil red O stained BeWo cells cultured on glass slides for 48 hours after 30 days of culture in normoglycemic (N; Dulbecco's Modified Eagle's Medium (DMEM)-5.5 mM glucose), hyperlipidemic (H; DMEM-25 mM glucose), and hyperglycemic combined with hyperlipidemic (HL; DMEM-25 mM glucose + 100 µM palmitic acid) conditions. Cells were counterstained with hematoxylin. The BeWo-derived cell models H (orange) and HL (gray) showed altered cell morphology, including increased nuclei and vacuole size. In HL extensive intracellular lipid stores were detected. B, Time-dependent adaption of mRNA levels of the iron transporters *DMT1* (solid line), *ZIP8* (dashed line), *FPN1* (dotted line) and *TfR1* (dash-dotted line) under H (left panel) and HL (right panel) conditions. Error bars represent standard deviation (SD) of triplicate measurements. mRNA expression was calculated as described in Figure 1A. The figure shows representative results of two independent experiments (n = 2). C, Assessment of functional changes in iron homeostasis by measuring radioactive transferrin ^{55}Fe- uptake in the N (blue), H (orange), and HL (gray) cell models. Left panel: Representative iron uptake results of three independent experiments (n = 3) after 5 days of adaption to hyperglycemic conditions (left panel). Iron uptake values are displayed as percentage of the applied total dose. Concentration of Tf-Fe^{3+} total dose in all experiments was 16.14 pmol/100 µL (161.4 nM). Right panel: Reduction of iron uptake measured at 20 minutes (dotted square in panel C and D) over 30 days normalized to N (N = 100%). Error bars represent SD of seven replicates. The experiments were performed three times with BeWo cells originating from the same normoglycemic BeWo line at different passage numbers

was detected after 1 day of stimulation in H, iron uptake was significantly reduced in H and HL already after 5 days of stimulation (Figure 2C, right panel).

3.7 | Hyperglycemia induces cellular stress responses and impairs placental iron homeostasis

To characterize the cellular mechanisms underlying the alteration of placental iron homeostasis under diabetic conditions, we sampled BeWo cells during 30 days of H and HL challenge and assessed the protein expression of stress response markers by immunoblotting. From day 3 onwards the expression of the autophagy markers *p62* and *LC3-II* were downregulated (Figure 3A). No differences in *BiP* protein expression (Figure S2) were detected at the respective time points. Thus, trophoblasts under hyperglycemic conditions showed reduced autophagy, but no effect on the ER stress pathway.

In addition, we quantified the cellular damage caused by OS by measuring the production of MDA equivalents and carbonyl formation. After 30 days of adaption to hyperglycemic conditions, there was still significantly increased lipid peroxidation detectable in the supernatant of BeWo cells grown in H (Figure 3B, left panel). For HL a marked variation between the experiments prevented clear conclusions. There was no change in protein carbonylation after 30 days of adaption to H and HL, respectively (Figure 3B, middle panel).

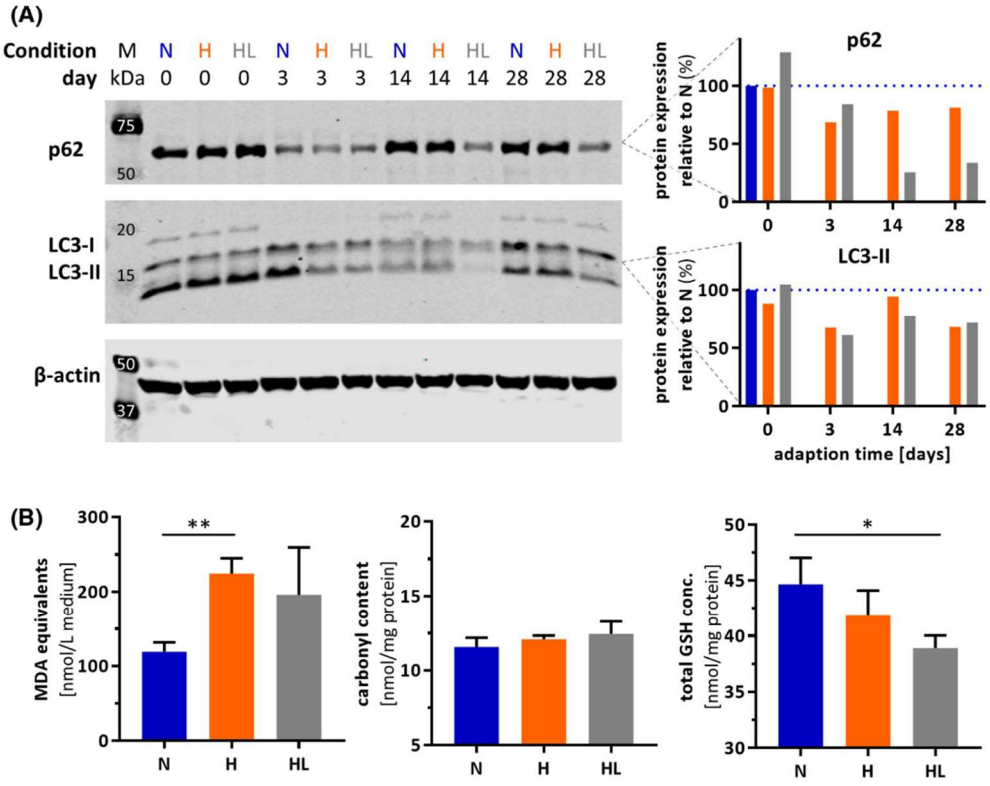

FIGURE 3 Trophoblasts under hyperglycemic conditions reduce autophagy and increase oxidative stress pathways. A, Reduction of the autophagy marker p62 (62 kDa) and LC3-II (14 kDa) during 28 days of adaption to hyperglycemic (H) and hyperglycemic combined with hyperlipidemic conditions (HL) as shown by immunoblotting (left panel). *p62* and *LC3-II* expression visualized by immunoblotting at day 0, 3, 14, and 28 was quantified by fluorescence detection analysis and presented relative to the normoglycemic condition (N, blue bar) (right panels). Samples were obtained from the same experiment as shown in Figure 2. Results of one representative experiment from three independent experimental setups are shown. B, Increased oxidative stress in H and HL was detected in three independent experiments after 30 days of adaption time (n = 3). The three different assays for measurement of oxidative stress are explained in the section Materials and Methods. Left panel: Increased lipid peroxidation determined as the formation of malondialdehyde (MDA) equivalents in cell supernatants was found in H (orange) and HL (gray) conditions. Middle panel: Protein carbonylation was measured by staining of cell lysates with 2,4-Dinitrophenylhydrazine (DNP). Right panel: Decreased antioxidative potential was assessed by measuring total glutathione (GSH) levels. Statistical significance was determined using two-way ANOVA with Dunnett's multiple comparison test, $\alpha = 0.05$, $^*P < .05$, $^{**}P < .01$

We furthermore determined OS associated with hyperglycemia and altered iron-homeostasis by analyzing the antioxidative potential (total-GSH) in BeWo cell lysates cultured for 30 days in N, H, and HL. Total GSH levels were significantly reduced under HL (Figure 3B, right panel) reflecting increased GSH consumption for counteracting accelerated OS.

3.8 | Rescue of placental iron homeostasis by antioxidant supplementation

To investigate whether OS is indeed the main mediator of the disturbed iron homeostasis in the placenta, we determined the effect of an experimentally induced OS challenge on trophoblast cells. Thus we treated BeWo cells under normoglycemic conditions with the oxidant tert-BOOH for 24 hours and compared the effects with the phenotypes found in GDM tissues. In agreement with the results found in GDM placentae (Figure 1A), the induction of OS significantly reduced the mRNA abundance of the iron transporters *DMT1* and *FPN1* (Figure 4A). The mRNA levels of *ZIP8* and *TfR1* were elevated, whereas a profound decrease of *GLUT1* mRNA was detected (Figure 4A).

We further studied the effects of OS in trophoblasts under hyperglycemic conditions and performed rescue experiments by applying an antioxidant. Thus N, H and HL BeWo cells were treated with the antioxidant NaSe and additionally challenged with OS by adding tert-BOOH for 24 hours. The

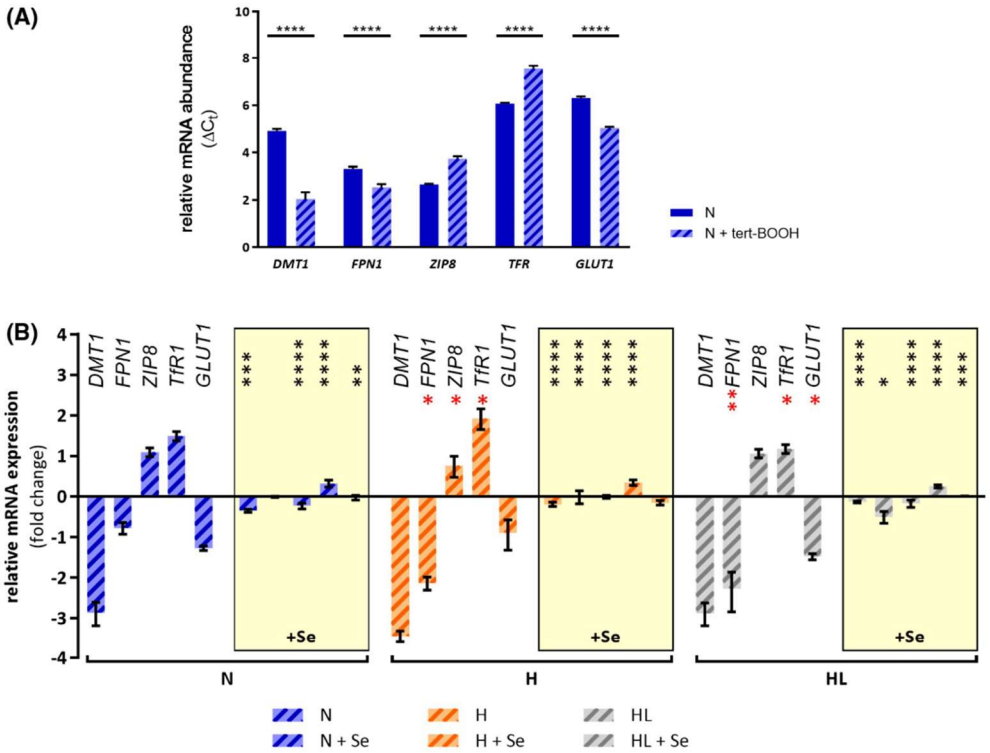

FIGURE 4 Effect of induced oxidative stress on mRNA abundances of iron homeostasis genes in trophoblast cells and rescue by selenium treatment. A, The mRNA abundances of the divalent metal transporter 1 (*DMT1*), Zrt- and Irt-like protein 8 (*ZIP8*), Ferroportin-1 (*FPN1*), Transferrin receptor protein 1 (*TfR1*), and Glucose transporter 1 (*GLUT1*) were determined in untreated normoglycemic BeWo cells (N, blue) and in normoglycemic BeWo cells treated with tert-Butylhydroperoxide (tert-BOOH; 100 μM; blue striped). Cycle threshold (Ct) values were determined by RT-qPCR and normalized to the arithmetic mean of same reference genes as described in Figure 1A to obtain ΔCt values. Data are presented as mean ± SD of three independent experiments (n = 3). B, In the three BeWo cell models (N, H, HL) oxidative stress was induced by tert-BOOH (100 μM) treatment for 24 hours (striped bars). In tert-BOOH treated cells supplementation with 400 nM sodium selenite (NaSe, + Se) significantly reduced the hyperglycemic effect on iron homeostasis gene regulation. mRNA expression results were normalized to the same reference genes and calculated as described in Figure 1A. Data are expressed as fold difference in relation to control cells which were not treated with tert-BOOH. Samples treated with NaSe are displayed in yellow boxes. Supplementation of 400 nM NaSe in the medium rescued the altered gene expression under hyperglycemic (H; orange) and hyperglycemic- and hyperlipidemic (HL; gray), conditions. Statistical analysis for the data sets presented in A and B was performed using two-way ANOVA with Sidak's multiple comparison post hoc analysis, $\alpha = 0.05$. $^{*}P < .05$, $^{**}P < .01$, $^{***}P < .001$, $^{****}P < .0001$

exposure to tert-BOOH aggravated the hyperglycemic/hyperlipidemic effects in the BeWo models. Significant downregulation of *FPN1* under both hyperglycemic conditions and decreased *ZIP8* under H was observed (Figure 4B). Relative to N, *TfR1* was upregulated under H, but downregulated under HL. This typical pattern of gene regulation confirmed the results shown in Figure 2. Se supplementation reversed the hyperglycemic/hyperlipidemic effect at mRNA level almost completely (Figure 4B).

Importantly, Se supplementation also reduced lipid peroxidation under HL (Figure 5A) and eliminated protein carbonylation under both hyperglycemic conditions (Figure 5B).

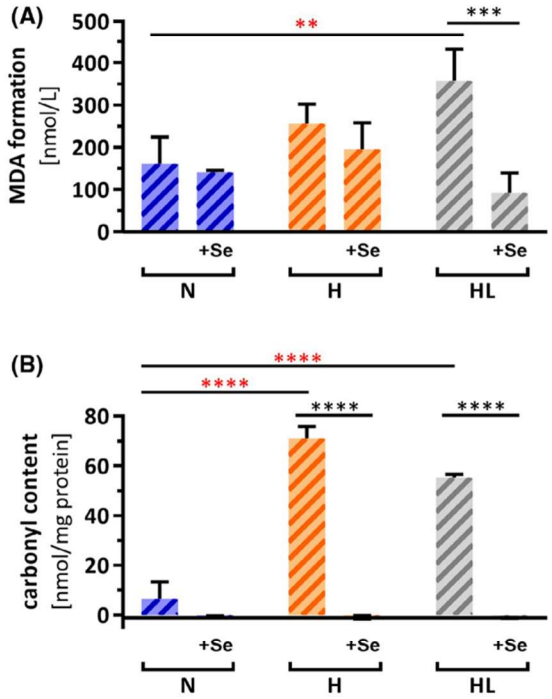

FIGURE 5 Rescue of hyperglycemic effects during induced oxidative stress in trophoblast cells by selenium treatment. In the three BeWo cell models (N, H, HL) oxidative stress was induced by tert-Butylhydroperoxide (tert-BOOH; 100 μM) treatment for 24 hours (striped bars). Supplementation with 400 nM sodium selenite (NaSe, + Se) significantly reduced the formation of malondialdehyde (MDA) equivalents (A) and protein carbonylation 2,4-Dinitrophenylhydrazine (DNP) staining (B). Both parameters serve as indicators for oxidative stress. The experimental setup was as described in Figure 3B. Results are shown as mean ± SD of triplicate measurements. Statistical significance was determined using two-way ANOVA with Sidak's multiple comparison *post hoc* analysis, $\alpha = 0.05$. In all panels black asterisks display significant differences between Se-treated and untreated cells, while red asterisks indicate significant differences between conditions H or HL compared to N

4 | DISCUSSION

In this study we compared two clinically well-characterized cohorts of GDM patients and controls with balanced distribution of fetal sex, maternal, and gestational age with respect to placental iron homeostasis. Recently elevated maternal serum hemoglobin concentrations, as found in our GDM cohort, have been associated with increased risk for GDM.[3-5,25-27] However, the involved pathways linking iron homeostasis during pregnancy to disturbances in glucose handling and metabolism, as well as the role of the placenta in regulating materno-fetal iron transfer are largely unknown. To clarify these aspects, we investigated the effects of hyperglycemic conditions at distinct pathways controlling placental iron homeostasis: at the level of uptake, transport, sensing, and regulation of iron.

Analyzing the expression of 24 genes involved in iron uptake, regulation, transport and sensing in control and GDM placentae revealed that all these pathways were affected. A key player in the *regulation* of iron concentrations is *HEPC*, which originates from the mother, the fetus, and the placenta. *HEPC* determines the rate of placental iron release to the fetal circulation through degradation of placental FPN1.[28] While *HEPC* is normally downregulated during healthy pregnancy to ensure sufficient iron availability,[28,29] we detected increased placental *HEPC* levels in GDM. This indicates a placental mechanism to reduce materno-fetal iron transfer by decreasing iron release towards the fetal circulation via FPN1 (see below). HEPC production is predominantly regulated at the transcriptional level, thus mRNA and protein levels show high correlation.[28]

Moreover, at the level of iron uptake and transport marked GDM-mediated alterations were found. Hence *TfR1*, *DMT1*, *ZIP8*, and *FPN1* were significantly downregulated in GDM placentae, though mRNA and protein expression did not always correlate. The latter is probably due to posttranscriptional regulation by IRP1.[30] Indeed, the detected upregulation of *IRP1* could be responsible for the decreased *TfR1* protein levels found in GDM despite similar mRNA levels. *DMT1* was downregulated on transcriptional but not on protein level, but we observed a change in the intracellular localization of DMT1. This could be caused by altered subcellular trafficking, depending on the expression ratio between the two major isoforms of *DMT1* in trophoblasts,[31,32] or altered ubiquitination.[33] These cellular processes can result in reduced DMT1 transport activity without affecting the protein level. To exclude that the sex of the fetus could affect the mRNA expression data, we analyzed potential differences between male and female placentae for all 24 iron homeostasis genes. There were no significant gender-based differences between male and female tissues that could explain the detected differences between control and GDM placentae for any of the 24 genes.

Coherent with our studies, these findings suggest that reduced iron concentrations in the placenta and fetal serum could result from downregulated placental iron uptake under hyperglycemia. The observed reduction of placental iron uptake and transport processes could be a physiological mechanism to protect the placenta and fetus from excessive, harmful iron acquisition. Also the observed upregulation of the ferroxidases *HEPH* and *Zp* in GDM placentae could be interpreted in this context: Beside facilitating the export of Fe^{3+} by FPN1, they oxidize the potentially toxic Fe^{2+} and thereby reduce the oxidative levels at the placental barrier.[34]

Next, we aimed to identify the underlying mechanisms leading to placental adaptations in iron handling at high glucose concentrations. Therefore, we established trophoblast cell lines which were exposed to either hyperglycemic (H) or hyperglycemic/hyperlipidemic (HL) culture conditions. The latter was achieved by adding palmitic acid to the cell culture medium. Free palmitic acid has been associated with induced insulin resistance in different cell models[20] and in GDM patients.[35] In the H and HL models, BeWo cells changed their morphology and showed extensive intracellular lipid storage under HL. Interestingly, HL stimulation in BeWo cells resulted in similar expressional changes of iron homeostasis genes as found in GDM placentae underlining that the established cell models are suitable for the identification of underlying cellular pathways.

Furthermore, trophoblasts cultured under H and HL reduced their iron uptake already after 5 days of stimulation by more than 40% relative to N. The observed dramatic reduction of placental iron uptake explains the inconspicuous iron stores in placental tissue in combination with increased maternal hemoglobin levels. This is a clear indication for placental protection of fetal tissues from excessive iron storage. Concomitantly, the observed alterations in placental iron handling could promote the increased iron concentrations found in maternal serum.

Despite the downregulation of *FPN1*, the only known transporter regulating iron export to the fetus, the total iron contents in GDM placentae were not increased in our cohort. In contrast to our study, recently published iron concentrations in a bigger cohort of GDM and control pregnancies showed reduced iron levels in GDM placental tissue and umbilical cord blood, but not in maternal whole blood.[36] In agreement with our studies, these findings suggest that reduced iron concentrations in the placenta and fetal serum could result from downregulated placental iron uptake under hyperglycemia. Therefore, a reduction of placental iron uptake could be a physiological mechanism to protect the placenta and fetus from excessive, harmful iron concentrations.

To identify the cellular pathways mainly mediating the effects of GDM on placental iron homeostasis we focused on mechanisms that have been implicated in both GDM and cellular iron imbalance: ER-stress,[37,38] autophagy[9,39] and OS.[40] Despite reports of increased ER-stress in GDM patients,[37] we did not find marked changes in placental *BiP*-expression by immunoblotting. Due to the negative result for *BiP*, which is normally strongly regulated when ER stress occurs,[41] we omitted analyses of further ER stress markers. Of note, based on the limited data set, our results on ER stress have to be carefully interpreted and consequently a potential involvement of ER stress in the investigated phenomena cannot be fully excluded. In the context of our autophagy studies, we detected reduced *p62* protein and decreased *LC3-II* protein in H and HL compared to N. LC3-II is the lipidated, membrane-bound form of the widely used autophagic marker *LC3*.[42] Likewise, the downregulation of the p62 protein indicates reduced autophagy.[43] Further extensive analyses of OS damage products and antioxidant consumption revealed increased oxidative damage and reduced antioxidative capacity in both hyperglycemic cell models.

Both GSH depletion and accumulation of oxygen activated lipids as shown in Figure 3B are two of the main characteristics of ferroptosis, an iron-mediated cell death process. This non-apoptotic cell death pathway is induced by disruption of GSH synthesis, depends on high intracellular iron levels and accumulation of lipid peroxides.[44] Although hyperglycemia has not been reported as promotor of ferroptosis so far, our results on reduced GSH levels, disturbed transcellular iron transport and increased lipid peroxidation strongly suggest the involvement of this pathway. Indeed, the relevance and underlying mechanisms of ferroptosis in GDM should be subject of future detailed investigations.

To further confirm the concept that OS is a key pathway stimulated by hyperglycemia and a trigger for the placental regulation of iron homeostasis, we challenged our cell models with the prooxidant tert-BOOH and performed rescue experiments by treating the cells with the antioxidant NaSe. Challenging normoglycemic trophoblasts with tert-BOOH resulted in decreased *DMT1* and *FPN1* mRNA levels (Figure 4A) similarly as previously shown in the placental tissues from GDM patients (Figure 1A). The upregulation of *ZIP8* mRNA was not observed in GDM placentae (Figure 4A), but was a characteristic early response when BeWo cells were cultured under hyperglycemic (H and HL) conditions (Figure 2B). These results further support the link between high glucose levels, OS and altered iron homeostasis. In a next step we studied the effects of induced OS in trophoblasts under hyperglycemic conditions and performed rescue experiments by applying NaSe as antioxidant. The exposure to tert-BOOH aggravated the hyperglycemic/hyperlipidemic effects in the BeWo models. Interestingly, the observed pattern of gene regulation after tert-BOOH treatment (Figure 4A) largely confirmed the results obtained after long-term exposure to hyperglycemic conditions (Figure 2). Finally, as expected, Se supplementation reversed the hyperglycemic/hyperlipidemic effect at mRNA level almost completely (Figure 4B).

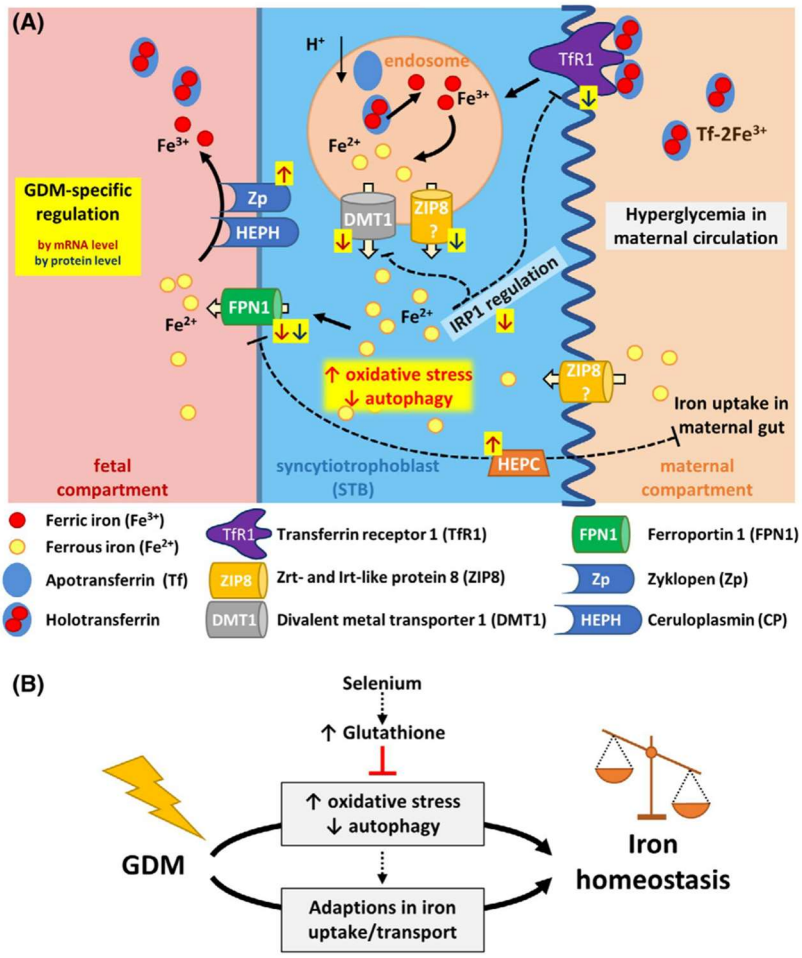

FIGURE 6 Schematic representation of the mechanisms and regulation of materno-fetal iron transfer across the placenta and dysregulation under hyperglycemic conditions. A, Iron (Fe) is transferred from the mother to the fetus across the blood-placenta barrier (right to left). The placenta is in direct contact with the maternal blood circulation via a monolayer of syncytialized trophoblast cells (blue). After transferrin receptor (TfR1)-mediated iron uptake by clathrin-dependent endocytosis at the maternal side of the syncytiotrophoblasts (villous membrane on right side) into endosomes, divalent metal transporter 1 (DMT1) is supposed to release divalent iron from endosomes into the cytosol. Cytosolic iron is transferred to the fetal circulation through the iron exporter ferroportin (FPN1). The exact mechanisms as well as the role of other transporters such as the Zrt- and Irt-like proteins (ZIP) ZIP8 or ZIP14 in transplacental iron transfer are currently still unclear. (A, yellow) Gestational diabetes mellitus (GDM) alters iron homeostasis in placental tissue through specific regulation of iron homeostasis genes involved in uptake (*TfR1*), transport (*DMT1*, *ZIP8*, *FPN1*), oxidation (zyklopen, *Zp*) and regulation (iron regulatory protein 1, *IRP1*; Hepcidin, *HEPC*) on mRNA (highlighted dark red arrows) and/or protein level (highlighted blue arrows). The major changes on expressional level comprise reduced *DMT1*, *FPN1*, *ZIP8,* and *TfR1* abundance, and alterations in DMT1 localization. In analogy, trophoblasts under hyperglycemic conditions decrease iron acquisition by reducing *TfR1* expression at the apical membrane, decrease transfer from the endosome into the cytoplasm through reduced expression of *ZIP8* and mis-localization of DMT1 and diminish secretion of iron towards the fetal side through downregulation of *FPN1*. The current study identified increased reactive oxygen species (ROS) and reduced autophagy as factors involved in altering iron homeostasis under hyperglycemic conditions. B, Schematic model summarizing the effects of GDM and hyperglycemic conditions on placental iron homeostasis and materno-fetal iron transfer: Our data indicate that impaired autophagy and increased oxidative stress under hyperglycemic and hyperglycemic combined with hyperlipidemic conditions alter the expression and partly also the localization of transporters and thereby affect placental iron transfer. The observed adaptations could be part of a protective mechanism preventing oxidative damage for both the fetus and the placenta caused by hyperglycemia and highly oxidative iron. Treatment with antioxidants such as selenium helps to balance placental oxidative stress levels by increasing glutathione levels and could thereby counteract impaired iron homeostasis found in GDM patients. These results indicate fundamental changes in the organization of transplacental iron transport under hyperglycemic conditions

NaSe as antioxidant was chosen as Se supplementation has been previously shown to protect trophoblast cells from OS.[45,46] Se is essential for the expression and activity of endogenous antioxidant systems such as the selenoenzymes glutathione peroxidases (GSH-Pxs), thioredoxin reductases (TrxRs), and selenoprotein P (SePP).[46] Interestingly, reduced selenoenzyme activity during pregnancy was shown to result in OS within tissues and was previously associated with premature birth, miscarriage, preeclampsia, and intrauterine growth retardation.[47] Se-dependent GSH-Pxs act in association with GSH, which exists in high concentrations in cells and catalyzes the conversion of hydrogen peroxide or organic peroxide to water or alcohol while simultaneously oxidizing GSH.[48] Thus, Se supplementation strengthens the endogenous antioxidant potential of trophoblasts without disturbing the delicate balance between oxidants and antioxidants in living cells. Of note, the choice of Se as antioxidant treatment was also based on our finding that total GSH levels were reduced in hyperglycemic BeWo cells (Figure 3B). Indeed, in our experiments the application of NaSe and the concomitant increase of the antioxidant potential almost completely reverted the hyperglycemic effect on iron homeostasis genes. In addition, Se supplementation protected BeWo cells under H and HL by reducing the lipid peroxidation (Figure 5A) and eliminating the protein carbonylation (Figure 5B).

Our findings explain clinical observations associating GDM with dysregulated iron homeostasis on a cellular and mechanistic level. The herein identified adaptive processes of the placenta in GDM are presumably part of a protective mechanism preventing oxidative damage for both the fetus and placenta caused by hyperglycemia and highly oxidative iron. These findings raise potential concerns regarding the recommendation of routine iron supplementation among iron-replete pregnant women.[5] Furthermore, our results suggest that antioxidant supplementation could be beneficial for pregnant women with increased risk of GDM by protecting the placenta and fetus against OS caused by hyperglycemia, high iron status, or both.

The study is based on a well-characterized clinical cohort, and combines clinical observations, analysis of clinical samples with complementary investigations using in vitro cell models. Due to the study design, we were not able to analyze additional iron-related blood parameters such as ferritin levels, transferrin saturation, or blood status of the newborns. The newly established hyperglycemic cell models, however, showed expressional changes which closely resembled the alterations observed in GDM tissues allowing novel mechanistic insights.

As graphically summarized in Figure 6, we found in GDM significant differences in the expression, trafficking and function of proteins involved in the uptake, transport, sensing, and regulation of iron. The major changes on the expressional level comprise reduced *DMT1*, *FPN1*, *ZIP8,* and *TfR1* abundance (Figure 6A), and alterations in DMT1 localization. Hence, trophoblasts under hyperglycemic conditions decrease iron acquisition by reducing the *TfR1* expression at the apical membrane, decrease transfer from the endosome into the cytoplasm through the reduced expression of *ZIP8* and mis-localization of DMT1, and diminish secretion of iron towards the fetal side through downregulation of *FPN1* (Figure 6A). The newly established trophoblast cell models exposed to hyperglycemic culture conditions mimicked to a great extent the expression results found in the clinical specimens of GDM patients. Thus, the cellular adaption to GDM-like conditions reduced placental iron uptake by mechanisms involving alterations in autophagy and OS pathways (Figure 6A,B). These results indicate fundamental changes in the organization of transplacental iron transport under hyperglycemic conditions. The observed adaptations could be part of a protective mechanism preventing oxidative damage for both the fetus and placenta caused by hyperglycemia and highly oxidative iron. The almost complete reversion of hyperglycemic effects in trophoblasts after antioxidant treatment (Figure 6B) suggests beneficial effects of antioxidant supplementation in pregnant women with increased risk to develop GDM.

ACKNOWLEDGMENTS

The authors thank Claudia Fortes, Dr Paolo Nanni, Dr Christian Trachsel, and Dr Witold Wolski, Functional Genomics Center Zurich, ETH Zurich, for very supportive and customized help in HPLC-MS instrumentation, quantification by MS and computational analysis of MS data. We are grateful to Dr Alan L. Schwartz, Washington University School of Medicine, USA for the donation of the BeWo cells (b30 clone). Prof. Matthias Hediger and Dr Jonai Pujol-Giménez, Institute of Biochemistry and Molecular Medicine, University of Bern, are kindly acknowledged for introducing and helping with the adaptation of in vitro iron quantification protocols. We also thank Michael Lüthi, Nithya Venkateswaran, Regina Berchtold, and Thuvaraga Kalakaran, Institute of Biochemistry and Molecular Medicine, University of Bern, for their help and support in the lab.

CONFLICT OF INTEREST

The authors declare no conflicts of interest.

AUTHOR CONTRIBUTIONS

J. Zaugg designed the experiments, performed cell culture, in vitro experiments and data analysis, wrote the manuscript, reviewed and approved the article. MW initially started the experiments and performed qPCR analysis. X. Huang developed the study concept and experimental design. H. Melhem performed immunoblotting and qPCR experiments. M. Baumann and D. Surbek were responsible for the clinical recruitment and characterization of patient cohorts. M. Körner performed semi-quantitative analysis of

immunohistochemically stained sections. C. Albrecht developed the study concept, discussed the data, reviewed and approved the article and is the guarantor of this work taking responsibility for the integrity of the data and the accuracy of the data analysis.

REFERENCES

1. Orecchio A, Periard D, Kashef A, Magnin JL, Hayoz D, Fontana E. Incidence of gestational diabetes and birth complications in Switzerland: screening in 1042 pregnancies. *Gynecol Endocrinol*. 2014;30(8):561-564. https://doi.org/10.3109/09513590.2013.879853
2. DeSisto CL, Kim SY, Sharma AJ. Prevalence estimates of gestational diabetes mellitus in the United States, pregnancy risk assessment monitoring system (PRAMS), 2007–2010. *Prev Chronic Dis*. 2014;11:130415. https://doi.org/10.5888/pcd11.130415
3. Lappas M, Hiden U, Desoye G, Froehlich J, Mouzon SH, Jawerbaum A. The role of oxidative stress in the pathophysiology of gestational diabetes mellitus. *Antioxid Redox Signal*. 2011;15(12):3061-3100. https://doi.org/10.1089/ars.2010.3765
4. Zein S, Rachidi S, Awada S, et al. High iron level in early pregnancy increased glucose intolerance. *J Trace Elem Med Biol*. 2015;30:220-225. https://doi.org/10.1016/j.jtemb.2014.09.004
5. Rawal S, Hinkle SN, Bao W, et al. A longitudinal study of iron status during pregnancy and the risk of gestational diabetes: findings from a prospective, multiracial cohort. *Diabetologia*. 2017;60(2):249-257. https://doi.org/10.1007/s00125-016-4149-3
6. Brownlee M. Biochemistry and molecular cell biology of diabetic complications. *Nature*. 2001;414:813-820. https://doi.org/10.1038/414813a
7. Papanikolaou G, Pantopoulos K. Iron metabolism and toxicity. *Toxicol Appl Pharmacol*. 2005;202(2):199-211. https://doi.org/10.1016/j.taap.2004.06.021
8. Ziaei S, Norrozi M, Faghihzadeh S, Jafarbegloo E. A randomised placebo-controlled trial to determine the effect of iron supplementation on pregnancy outcome in pregnant women with haemoglobin ≥ 13.2 g/dl. *BJOG*. 2007;114(6):684-688. https://doi.org/10.1111/j.1471-0528.2007.01325.x
9. Dixon S, Lemberg K, Lamprecht M, et al. Ferroptosis: an iron-dependent form of nonapoptotic cell death. *Cell*. 2012;149(5):1060-1072. https://doi.org/10.1016/j.cell.2012.03.042
10. Huang X, Baumann M, Nikitina L, et al. RNA degradation differentially affects quantitative mRNA measurements of endogenous reference genes in human placenta. *Placenta*. 2013;34(7):544-547. https://doi.org/10.1016/j.placenta.2013.03.011
11. Basevi V, Di Mario S, Morciano C, Nonino F, Magrini N. Comment on: American Diabetes Association. Standards of Medical Care in Diabetes–2011. Diabetes Care 2011;34(Suppl. 1):S11–S61. *Diabetes Care*. 2011;34(5): e53. https://doi.org/10.2337/dc11-0174
12. Huang X, Anderle P, Hostettler L, et al. Identification of placental nutrient transporters associated with intrauterine growth restriction and pre-eclampsia. *BMC Genomics*. 2018;19(1):1-17. https://doi.org/10.1186/s12864-018-4518-z
13. Wiśniewski JR, Zougman A, Nagaraj N, Mann M. Universal sample preparation method for proteome analysis. *Nat Methods*. 2009;6(5):359-362. https://doi.org/10.1038/nmeth.1322
14. Cox J, Mann M. MaxQuant enables high peptide identification rates, individualized p.p.b.-range mass accuracies and proteome-wide protein quantification. *Nat Biotechnol*. 2008;26(12):1367-1372. https://doi.org/10.1038/nbt.1511
15. Türker C, Akal F, Joho D, Panse C. B-Fabric: the Swiss Army Knife for life sciences. EDBT '10: Proceedings of the 13th International Conference on Extending Database Technology. 2010(March):717-720. https://doi.org/10.1145/1739041.1739135
16. Escher C, Reiter L, Maclean B, et al. Using iRT, a normalized retention time for more targeted measurement of peptides. *Proteomics*. 2012;12(8):1111-1121. https://doi.org/10.1002/pmic.201100463
17. MacLean B, Tomazela DM, Shulman N, et al. Skyline: an open source document editor for creating and analyzing targeted proteomics experiments. *Bioinformatics*. 2010;26(7):966-968. https://doi.org/10.1093/bioinformatics/btq054
18. Frewen B, MacCoss MJ. Using BiblioSpec for creating and searching tandem MS peptide libraries. *Curr Protoc Bioinformatics*. 2007;1-12. https://doi.org/10.1002/0471250953.bi1307s20
19. Riemer J, Hoepken HH, Czerwinska H, Robinson SR, Dringen R. Colorimetric ferrozine-based assay for the quantitation of iron in cultured cells. *Anal Biochem*. 2004;331(2):370-375. https://doi.org/10.1016/j.ab.2004.03.049
20. Sinha S, Perdomo G, Brown NF, O'Doherty RM, Doherty RMO, O'Doherty RM. Fatty acid-induced insulin resistance in L6 myotubes is prevented by inhibition of activation and nuclear localization of nuclear factor κB. *J Biol Chem*. 2004;279(40):41294-41301. https://doi.org/10.1074/jbc.M406514200
21. Gambling L, Danzeisen R, Gair S, et al. Effect of iron deficiency on placental transfer of iron and expression of iron transport proteins in vivo and in vitro. *Biochem J*. 2001;889(Pt 3):883-889. https://doi.org/10.1042/0264-6021:3560883
22. Rahman I, Kode A, Biswas SK. Assay for quantitative determination of glutathione and glutathione disulfide levels using enzymatic recycling method. *Nat Protocols*. 2007;1(6):3159-3165. https://doi.org/10.1038/nprot.2006.378
23. Potter TM, Neun BW, Stern ST. Assay to detect lipid peroxidation upon exposure to nanoparticles. *Methods Mol Biol*. 2011:697;181-189. https://doi.org/10.3797/scipharm.br-11-01
24. Levine RL, Garland D, Oliver CN, et al. Determination of carbonyl content in oxidatively modified proteins. *Methods Enzymol*. 1983;2009(186):1-8.
25. Afkhami-Ardekani M, Rashidi M. Iron status in women with and without gestational diabetes mellitus. *J Diabetes Complications*. 2009;23(3):194-198. https://doi.org/10.1016/j.jdiacomp.2007.11.006
26. Bo S, Menato G, Villois P, et al. Iron supplementation and gestational diabetes in midpregnancy. *Am J Obstet Gynecol*. 2009;201(2):158.e1-158.e6. https://doi.org/10.1016/j.ajog.2009.04.049
27. Xiaoqiu Xiao PS. Iron biomarker in gestational diabetes pathogenesis. *J Mol Biomark Diagn*. 2014;5(6):13-15. https://doi.org/10.4172/2155-9929.1000205
28. Koenig MD, Tussing-humphreys L, Day J, Cadwell B, Nemeth E. Hepcidin and iron homeostasis during pregnancy. *Nutrients*. 2014;3062-3083. https://doi.org/10.3390/nu6083062
29. Van Santen S, Kroot JJC, Zijderveld G, Wiegerinck ET, Spaanderman MEA, Swinkels DW. The iron regulatory hormone hepcidin is decreased in pregnancy: a prospective longitudinal study. *Clin Chem Lab Med*. 2013;51(7):1395-1401. https://doi.org/10.1515/cclm-2012-0576
30. Wilkinson N, Pantopoulos K. The IRP/IRE system in vivo: insights from mouse models. *Front Pharmacol*. 2014;5:176. https://doi.org/10.3389/fphar.2014.00176

31. Lam-Yuk-Tseung S, Gros P. Distinct targeting and recycling properties of two isoforms of the iron. *Biochemistry*. 2006;45:2294-2301.
32. Chong WS, Kwan PC, Chan LY, Chiu PY, Cheung TK, Lau TK. Expression of divalent metal transporter 1 (DMT1) isoforms in first trimester human placenta and embryonic tissues. *Hum Reprod*. 2005;20(12):3532-3538. https://doi.org/10.1093/humrep/dei246
33. Foot NJ, Dalton HE, Shearwin-whyatt LM, et al. Regulation of the divalent metal ion transporter DMT1 and iron homeostasis by a ubiquitin-dependent mechanism involving Ndfips and WWP2. *Blood*. 2016;112(10):4268-4276. https://doi.org/10.1182/blood-2008-04-150953
34. Fuqua BK, Lu Y, Frazer DM, et al. Severe iron metabolism defects in mice with double knockout of the multicopper ferroxidases hephaestin and ceruloplasmin. *Cell Mol Gastroenterol Hepatol*. 2018;6(4):405-427. https://doi.org/10.1016/j.jcmgh.2018.06.006
35. Stirm L, Kovářová M, Perschbacher S, et al. BMI-independent effects of gestational diabetes on human placenta. *J Clin Endocrinol Metab*. 2018;103(9):3299-3309. https://doi.org/10.1210/jc.2018-00397
36. Roverso M, Di Marco V, Badocco D, et al. Maternal, placental and cordonal metallomic profiles in gestational diabetes mellitus. *Metallomics*. 2019;11(3):676-685. https://doi.org/10.1039/C8MT00331A
37. Yung H, Alnæs-katjavivi P, Jones CJP, et al. Placental endoplasmic reticulum stress in gestational diabetes: the potential for therapeutic intervention with chemical chaperones and antioxidants. *Diabetologia*. 2016;59:2240-2250. https://doi.org/10.1007/s00125-016-4040-2
38. Vecchi C, Montosi G, Zhang K, et al. ER stress controls iron metabolism through induction of hepcidin. *Science*. 2009;325(5942):877-880. https://doi.org/10.1038/jid.2014.371
39. Avagliano L, Massa V, Terraneo L, et al. Gestational diabetes affects fetal autophagy. *Placenta*. 2017;55:90-93. https://doi.org/10.1016/j.placenta.2017.05.002
40. Peuchant E, Brun JL, Rigalleau V, et al. Oxidative and antioxidative status in pregnant women with either gestational or type 1 diabetes. *Clin Biochem*. 2004;37(4):293-298. https://doi.org/10.1016/j.clinbiochem.2003.12.005
41. Kopp MC, Nowak PR, Larburu N, Adams CJ, Ali MMU. In vitro FRET analysis of IRE1 and BiP association and dissociation upon endoplasmic reticulum stress. *eLife*. 2018;7:1-13. https://doi.org/10.7554/eLife.30257
42. Kabeya Y, Mizushima N, Ueno T, et al. LC3, a mammalian homologue of yeast Apg8p, is localized in autophagosome membranes after processing. *EMBO J*. 2000;19(21):5720-5728.
43. Øvervatn A, Hayes JD, Jain A, et al. p62/SQSTM1 is a target gene for transcription factor NRF2 and creates a positive feedback loop by inducing antioxidant response element-driven gene transcription. *J Biol Chem*. 2010;285(29):22576-22591. https://doi.org/10.1074/jbc.m110.118976
44. Cao JY, Dixon SJ. Mechanisms of ferroptosis. *Cell Mol Life Sci*. 2016;73(11-12):2195-2209. https://doi.org/10.1007/s00018-016-2194-1
45. Khera A, Vanderlelie JJ, Perkins AV. Selenium supplementation protects trophoblast cells from mitochondrial oxidative stress. *Placenta*. 2013;34(7):594-598. https://doi.org/10.1016/j.placenta.2013.04.010
46. Khera A, Vanderlelie JJ, Holland O, Perkins AV. Overexpression of endogenous anti-oxidants with selenium supplementation protects trophoblast cells from reactive oxygen species-induced apoptosis in a Bcl-2-dependent manner. *Biol Trace Elem Res*. 2017;177(2):394-403. https://doi.org/10.1007/s12011-016-0870-5
47. Zachara BA. Selenium in complicated pregnancy. A review. *Adv Clin Chem*. 2018;86:157-178. https://doi.org/10.1016/bs.acc.2018.05.004
48. Kurutas EB. The importance of antioxidants which play the role in cellular response against oxidative/nitrosative stress: current state. *Nutr J*. 2016;15(1):1-22. https://doi.org/10.1186/s12937-016-0186-5

SUPPORTING INFORMATION

Additional Supporting Information may be found online in the Supporting Information section.

How to cite this article: Zaugg J, Melhem H, Huang X, et al. Gestational diabetes mellitus affects placental iron homeostasis: Mechanism and clinical implications. *The FASEB Journal*. 2020;00:1–19. https://doi.org/10.1096/fj.201903054R

9.1.2 Published in Journal of Cellular and Molecular Medicine (1 October 2020)

Received: 6 June 2020 | Revised: 20 July 2020 | Accepted: 10 August 2020

DOI: 10.1111/jcmm.15840

Check for updates

ORIGINAL ARTICLE

WILEY

Small molecule inhibitors provide insights into the relevance of LAT1 and LAT2 in materno-foetal amino acid transport

Jonas Zaugg[1,2] | Xiao Huang[1,2] | Fabian Ziegler[1,2] | Matthias Rubin[1,2] | Julien Graff[2,3] | Jennifer Müller[2,3] | Ruedi Moser-Hässig[4] | Theresa Powell[5] | Jürg Gertsch[1,2] | Karl-Heinz Altmann[2,3] | Christiane Albrecht[1,2]

[1]Institute of Biochemistry and Molecular Medicine, Faculty of Medicine, University of Bern, Bern, Switzerland

[2]Swiss National Centre of Competence in Research (NCCR) TransCure, University of Bern, Bern, Switzerland

[3]Institute of Pharmaceutical Sciences, Department of Chemistry and Applied Biosciences, ETH Zurich, Zurich, Switzerland

[4]Division of Gynecology and Obstetrics, Lindenhofgruppe, Bern, Switzerland

[5]Department of Pediatrics, Neonatology Section, University of Colorado, Denver, CO, USA

Correspondence
Christiane Albrecht, Institute of Biochemistry and Molecular Medicine, University of Bern, Bühlstrasse 28, CH-3012 Bern, Switzerland.
Email: christiane.albrecht@ibmm.unibe.ch

Funding information
Swiss National Centre of Comptence in Research TransCure; Stiftung Lindenhof Bern

Abstract

The placenta supplies the foetus with critical nutrients such as essential amino acids (AA, eg leucine) for development and growth. It also represents a cellular barrier which is formed by a polarized, differentiated syncytiotrophoblast (STB) monolayer. Active Na^+-independent leucine transport across the placenta is mainly attributed to the System L transporters LAT1/SLC7A5 and LAT2/SLC7A8. This study explored the influence of trophoblast differentiation on the activity of LAT1/LAT2 and the relevance of LAT1/LAT2 in leucine uptake and transfer in trophoblasts by applying specific small molecule inhibitors (JPH203/JG336/JX009). L-leucine uptake (total dose = 167 μmol/L) was sensitive to LAT1-specific inhibition by JPH203 (EC_{50} = 2.55 μmol/L). The inhibition efficiency of JPH203 was increased by an additional methoxy group in the JPH203-derivate JG336 (EC_{50} = 1.99 μmol/L). Interestingly, JX009 showed efficient System L inhibition (EC_{50} = 2.35 μmol/L) and was the most potent inhibitor of leucine uptake in trophoblasts. The application of JPH203 and JX009 in Transwell®-based leucine transfer revealed LAT1 as the major accumulative transporter at the apical membrane, but other System L transporters such as LAT2 as rate-limiting for leucine efflux across the basal membrane. Therefore, differential specificity of the applied inhibitors allowed for estimation of the contribution of LAT1 and LAT2 in materno-foetal AA transfer and their potential impact in pregnancy diseases associated with impaired foetal growth.

KEYWORDS

BeWo, LAT1 (SLC7A5), LAT2 (SLC7A8), leucine uptake, monolayer, placenta, transplacental amino acid transport, Transwell, trophoblast, trophoblast differentiation

1 | INTRODUCTION

Adequate amino acid (AA) supply is vital especially for highly proliferative tissues like the placenta. Other tissues which are critical for nutrient absorption and transport, such as the intestine and liver, mainly use the efficient sodium (Na^+)-dependent uptake maintained by System A transporters,[1] such as the SNAT family.[2] The heteromeric SLC7 AA transporters, a subgroup of the System L-exchanger

family, are driven by System A-dependent AA gradients. Both AA transporter families are highly expressed in polarized epithelial tissues such as blood-brain and placental barriers.[3,4] There are two important cell layers in the placental villi coordinating the nutrient transfer across the placental barrier, namely syncytiotrophoblasts (STB) and foetal capillary endothelial cells. Endothelial cells lining the foetal vessels allow relatively unrestricted paracellular diffusion of small molecules like glucose and AA through endothelial junctions.[5] In contrast, STB represent the limiting barrier for AA due to the formation of an epithelial syncytium composed of two polarized monolayers, the microvillous plasma membrane (MVM) facing the maternal blood supply and the basal membrane (BM) directed towards the foetal capillary (Figure 1A).

The Na^+-independent System L transporters expressed in the human placenta are heterodimeric exchangers consisting of the light chain L-type AA transporter LAT1 (SLC7A5) or LAT2 (SLC7A8) covalently attached to the heavy chain 4F2hc (SLC3A2). Moreover, the SLC43 family members LAT3 (SLC43A1) and LAT4 (SLC43A2), known to be involved in facilitated AA diffusion,[6,7] are expressed at the BM (Figure 1A). Both LAT1 and LAT2 are predominantly localized to the MVM of human term placenta, LAT2 as well as LAT3 and LAT4 are also present at the BM and in endothelial cells lining the foetal capillaries.[7,8] In the last decade, increasing evidence suggests a tight link between the reduced activity of placental System L transporters and intrauterine growth restriction (IUGR),[9,10] and their up-regulation in placentae of large for gestational age (LGA) infants.[11] Such altered foetal development has a fundamental impact on lifelong health and wellbeing, and may contribute by foetal programming to an increased prevalence for cardiovascular disease and diabetes/adiposity later in life.[12-15] Notably, it has been reported that LAT1 or its associated glycoprotein 4F2hc is involved in placenta decidualization and fusogenic trophoblast differentiation.[16] This could imply that the diminished leucine uptake found in knock-down cell models[17] results rather from failure in trophoblast differentiation than from reduced SLC7 transport activity. Hence, small molecules which induce only short-term inhibition of transporter activity are a valuable experimental tool to study placental transfer mechanisms as they will not affect trophoblast differentiation and associated processes like trophoblast fusion. Therefore, studying placental AA transfer by using specific small molecule inhibitors of AA transporters instead of silencing or knock-out could help to reveal the relevance of LAT1 or LAT2 in materno-foetal leucine transfer without affecting cell differentiation.

Since LAT1 was found to be selectively expressed and up-regulated in various rapidly proliferative cancer types[18-20] and has a putative role in drug delivery across the blood-brain barrier,[21] efforts have been made to pharmaceutically target this transporter using substrate-mimicking or virtual screening approaches.[22-26] The substrate-mimicking tyrosine analog JPH203 (also known as KYT-0353) was tested in several in vitro and in vivo cancer cell proliferation experiments and described as potent LAT1-specific inhibitor.[27-31] To delineate the contribution of LAT1 from LAT2 in materno-foetal leucine transport, we synthesized the LAT1-specific inhibitor JPH203, the structurally closely related inhibitor (JG336), as well as a third small molecule inhibitor (JX009) with comparable leucine uptake inhibition efficiency but lower LAT1-specificity (structures see Figure 4).

In this study, we assessed the contribution of LAT1-mediated Na^+-independent leucine uptake into trophoblasts and investigated the transfer of this essential AA across the placental barrier by transient inhibition. To achieve these goals, we (a) tested primary human trophoblast and BeWo (clone b30) cell models for LAT1, LAT2 and 4F2hc expression and leucine uptake capacity under Na^+-free conditions, (b) investigated whether the differentiation status of primary trophoblasts and BeWo cells has an impact on leucine uptake and (c) assessed the contribution of LAT1 for the uptake and transfer of leucine by application of small molecule inhibitors.

2 | MATERIALS AND METHODS

All chemicals and reagents were purchased from Sigma-Aldrich in Switzerland unless otherwise stated.

2.1 | Isolation of primary human trophoblast cells

Placentae from normal healthy pregnancies were collected after elective Caesarean section at the Division of Gynecology and Obstetrics, Lindenhofgruppe, Bern, Switzerland. Details on the study subjects are found in Table 1. The study was conducted in accordance with the Declaration of Helsinki, and the protocol was approved by the Ethics Committee of the Canton of Bern (Basec Nr2016-00250). The collected tissue was used to isolate primary cytotrophoblasts as previously described.[32] Isolated cells were cultured on Cell-BIND plates in Dulbecco's modified Eagle's medium containing 4.5 g/L glucose (DMEM-highGlucose; Gibco, Paisley, UK) and characterized by analysing the expression of cytokeratin-7 and vimentin as previously described.[33] Primary trophoblasts were evaluated for leucine uptake at the cytotrophoblast (CTB) and syncytiotrophoblast (STB) stage (ie after 12 and 48 hours of culture, respectively) when spontaneous differentiation and fusion has occurred.

2.2 | BeWo cell culture

BeWo cells (clone b30) were cultured in DMEM containing 1.0 g/L glucose (DMEM-lowGlucose; Gibco). BeWo cells require stimulation by forskolin to induce STB formation.[34] Unstimulated BeWo cells representing the CTB stage were studied after 24 hours of culture; differentiated, syncytialized BeWo cells were analysed after stimulation with 100 μmol/L forskolin for 48 hours when markers for syncytialization are significantly increased.[32] For leucine transfer experiments, BeWo cells were seeded at a density of 100 000 cells/cm^2 onto permeable membranes (0.4 μm pore size) mounted in

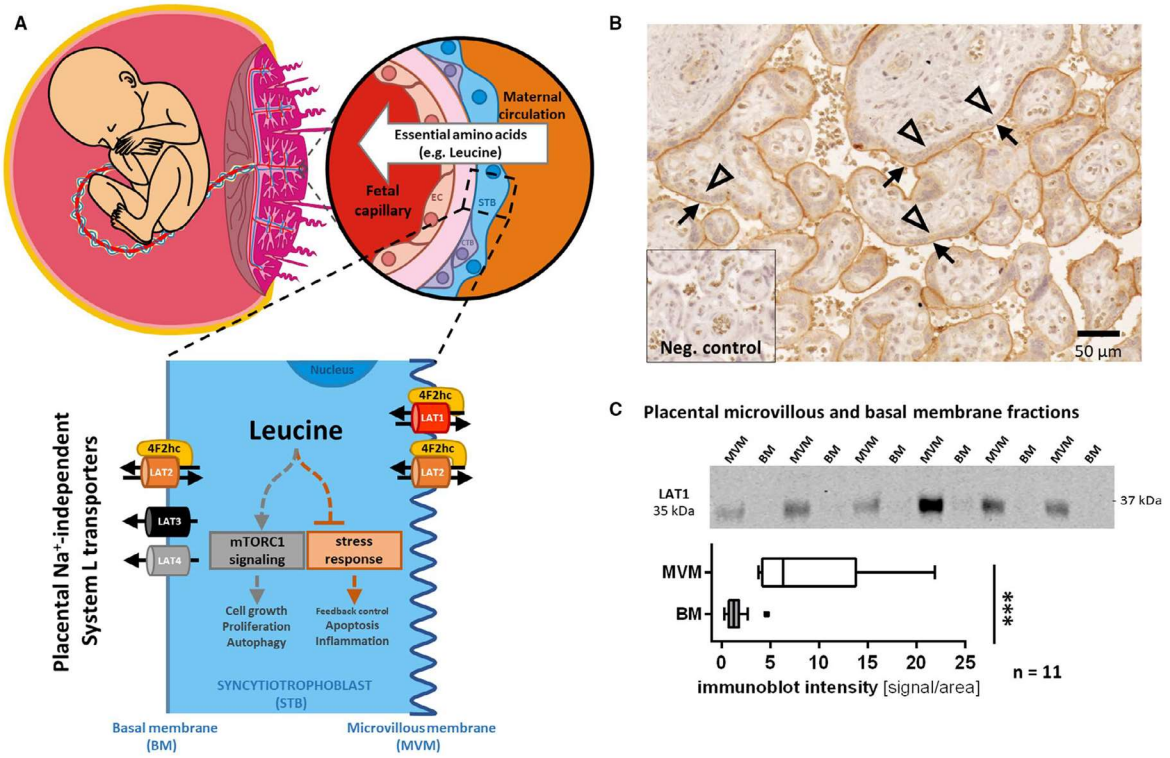

FIGURE 1 Schematic representation of Na^+-independent leucine transfer across the placental barrier with asymmetric LAT1 expression. Scheme of the placental villous structures as interface between the foetal capillaries and the maternal circulation (A, upper left panel) and the human placental barrier (A, upper right panel) involving three different cell types: endothelial cells lining the foetal capillaries (EC), varying intercellular space (pink), single-nucleated cytotrophoblasts (CTB) and syncytiotrophoblasts (STB) forming a multi-nucleated monolayer, which is in direct contact with maternal blood and mainly responsible for materno-foetal nutrient transport. In (A) lower panel, Na^+-independent System L exchanger and System L-like facilitators known to be expressed in the human placenta are shown. They are present either at the apical microvillous membrane (MVM) or at the basal membrane (BM) of STB. LAT1 (SLC7A5), expressed at the MVM, and LAT2 (SLC7A8), present at both the MVM and BM, are SLC7 family members and colocalize with their heavy chain partner 4F2hc (SLC3A2, CD98). LAT3 (SLC43A1) and LAT4 (SLC43A2) were described as System L-like facilitators and are most likely expressed at the BM. Increased intracellular leucine concentrations stimulate mTORC1-mediated cell proliferation and survival, and repress the ATF4-mediated amino acid balance sensing system, which reduces global translation and increases biosynthesis. (B) Representative picture showing apical LAT1 localization in immunohistochemistry of human term placenta. Arrows indicate the apical MVM, that is, maternal blood orientated side; arrowheads depict the BM of the STB. There was no signal in negative control. (C) upper panel, representative immunoblot of 6 purified membrane protein samples isolated from term placental tissues. (C) lower panel, LAT1 was highly expressed in MVM, but negligible in BM protein fractions isolated from a total of 11 human term placentae. The data is normalized to the respective tissue homogenate before membrane separation and shown as boxplots with Tukey whiskers (Mann-Whitney test, $\alpha = 0.05$; $^{***}P < 0.0001$)

12-well format from the Transwell® system (Corning Inc., Corning, NY, USA). Cells were cultured in DMEM-lowGlucose at 37°C with 5% CO_2 atmosphere for 7-14 days.

2.3 | Placental membrane protein isolation

Placental tissues from healthy pregnancies were used to simultaneously isolate microvillous membranes (MVM) and basal membranes (BM) by Mg^{2+} precipitation based on a published method[35] and described in the Supporting Information. Expression levels in MVM and BM were normalized to the total membrane isolation (TMI) fraction collected prior to Mg^{2+} precipitation for MVM/BM separation. Further details regarding the enrichment and characterization of the MVM/BM fractions are found in Supporting Information and Figure S1.

2.4 | LAT1 localization by immunohistochemistry and immunoblotting

LAT1 protein was localized in two experimental approaches. LAT1 expression in MVM and BM fractions was determined by immunoblotting using rabbit polyclonal anti-LAT1 antibody (Anti-human LAT1, KE026/TG170215 Transgenic Inc., Kobe, Japan; 1:1000).

TABLE 1 Anthropometric characteristics of healthy patients donating placental tissue and their offspring

	Characteristics	Healthy controls
Mother	Number of individuals	11
	Maternal age (y)	33.9 ± 3.48
	Parity	1.8 ± 0.60
	Gestational age at partum	39 3/7 ± 6/7
Newborn	Weight of placenta (g)	569.3 ± 86.1
	Weight of baby (g)	3367.3 ± 284.0
	Sex of baby	3♂/6♀

For the reference signal (loading control) a mouse anti-beta-actin antibody (A2228, Sigma Aldrich, Buchs SG, Switzerland) was used. Details regarding the immunoblotting procedures are described in Supporting Information. Densitometrical analysis of immunoblots was performed using the LI-COR OdysseyW Imaging System. LAT1 expression in placental tissue was visualized by immunohistochemistry using the same LAT1-specific antibody (10 μg/mL). The preparation of cryosections and the staining procedure including visualization are described in Supporting Information.

2.5 | Expression changes of LAT1, LAT2 and 4F2hc during trophoblast differentiation

To compare changes in expression of LAT1, LAT2 and 4F2hc during cell differentiation, mRNA and protein levels were determined by RT-qPCR and immunoblotting, respectively. RNA isolation, first-strand cDNA synthesis and RT-qPCR analysis were performed as previously described.[36] Expression results were normalized to the mean of the reference genes YWHAZ, GAPDH and β-actin. Primer nucleotide sequences are listed in Table S1. For protein quantification 40 μg cell lysates were loaded on 10% acrylamide gels and separated by SDS–PAGE. The immobilized bands were semi-dry transferred to nitrocellulose membranes (GE Healthcare, Glattbrugg, Switzerland). Blots were blocked with 5% w/v non-fat milk in Tris Buffered Saline with 0.1% Tween-20 (TBST). Proteins were detected by antibodies against LAT1 (see above), LAT2 (Anti-SLC7A8, AV43930, Sigma-Aldrich) and 4F2hc (CD98 (E-5), sc-376815, Santa Cruz, Biotechnology Inc., Heidelberg, Germany). Protein content was measured using a commercial Pierce™ BCA Protein Assay Kit.

2.6 | Leucine uptake assay

The leucine uptake protocol was based on a recently published method[30] and adapted to physiological leucine concentrations. In brief, BeWo cells were seeded at a density of 60 000 cells/well into white-walled 96-well plates (Corning). The isolated primary trophoblasts were seeded at a density of 100 000 cells/well on 96-well plates which were coated with Matrigel (BD, New Jersey, USA) according to the suppliers' instructions. Primary trophoblasts and BeWo cells were cultured until they reached their assigned differentiation stage and then washed 3-times with pre-warmed Na^+-free Hank's buffer (125 mmol/L choline chloride, 25 mmol/L HEPES, 4.8 mmol/L KCl, 1.2 mmol/L $MgSO_4$, 1.2 mmol/L KH_2PO_4, 1.3 mmol/L $CaCl_2$, 5.6 mmol/L glucose, adjusted pH to 7.4). After equilibration in the same buffer (37°C, 7 minutes), cells were incubated for 3 minutes with pre-warmed Na^+-free Hank's buffer containing 167 μmol/L L-leucine and 20 nmol/L radioactive L-[3,4,5-^{3}H(N)]-leucine (PerkinElmer, Waltham, MA, USA). Leucine uptake was stopped by three washing steps with ice-cold Na^+-free Hank's buffer. The use of Na^+-free buffer prevents leucine uptake by other Na^+-dependent transporters such as System A-family members. Cells were lysed by intense shaking for 1.5 hours in MicroScint™-20 scintillation liquid (PerkinElmer). ^{3}[H]-leucine was quantified using TopCount® NXT™ Scintillation and Luminescence Counter (PerkinElmer).

2.7 | Specific inhibition of LAT1/2 mediated placental leucine uptake

JPH203, JG336 and JX009 were synthesized following the routes described in the European Patent Application EP 2-959-918-A1, 2014. Compounds were obtained as hydrochlorides, dissolved in dimethyl sulfoxide (DMSO, Merck, Darmstadt, Germany) and applied in the concentration range from 0.001 to 31.6 μmol/L. JPH203 has been characterized as highly LAT1-specific; JX009 is described as LAT1 and LAT2-specific inhibitor.[37] JG336 is a derivate of JPH203 with an additional methoxy group at the peripheral phenyl moiety residue. Compound structures are depicted in Figure 4. The ^{1}H-NNMR and ^{13}C-NMR spectra data of the compounds were in agreement with the expected structures and are included in the Supporting Information.

2.8 | Leucine transfer across a polarized trophoblast monolayer

Before starting the transfer experiment, the formation of a tight trophoblast monolayer in BeWo cells was monitored by measuring transepithelial electrical resistance (TEER, [Ω*cm^2]) and passive diffusion as reported previously.[38] TEER and cellular capacitance (C_{cl}, [μF/cm^2]) were measured every 30 minutes and analysed using the cellZscope system (nanoAnalytics, Münster, Germany) according to the manufacturer's instructions. The apparent permeability coefficient (Papp, [cm/s]) was calculated by measuring the rates of passive transfer of the paracellular pathway marker Lucifer yellow (LY) as previously described.[39] BeWo monolayers with verified tightness were selected after 7 days of culturing on Transwell® membranes and randomly assigned to leucine transfer time courses and inhibition experiments. The inserts with cultured BeWo cells and an insert without cells (no cell control) were placed in 12-well plates and washed 3-times with pre-warmed Na^+-free Hank's buffer. Prior to starting the time course,

the cells were equilibrated in Hank's buffer for 30 minutes at 37°C. Leucine transfer from the upper (maternal) towards the lower (foetal) compartment was started by simultaneously replacing the buffer in both compartments. The buffer in the lower chamber was replaced with Na^+-free Hank's containing 300 µmol/L glutamine and 167 µmol/L unlabelled L-leucine to obtain a physiological counter-directed leucine gradient. Consecutively the buffer in the upper compartment was replaced with Hank's containing 30 µmol/L leucine (labelled with 3.7 nmol/L L-[3,4,5-^{3}H(N)]-leucine), 300 µmol/L glutamine and either vehicle (DMSO) or a constant 10 µmol/L-dose of JPH203, JG336 or JX009, respectively. Inhibitors were applied in the upper compartment which is comparable to previous in vivo experiments.[40] At defined time points between 5 minutes and 6 hours, 50 µL samples were taken from the maternal and foetal compartment. At the end of the experiment, all membranes were washed twice with DPBS and sampled to determine intracellular leucine levels. The medium and membrane samples including no cell controls were collected in 3 mL of scintillation cocktail (Zinsser Analytic, Frankfurt, Germany). Radioactivity was quantified using Tri-carb 2100TR Liquid Scintillation Counter (PerkinElmer).

2.9 | Statistical analysis

Anthropometric and clinical data are expressed as mean ± standard deviation (SD) for normal distribution or median with interquartile range for not normal distribution. Student t tests were performed to detect differences in mRNA levels between CTBs and STBs. MVM and BM membrane protein fractions were compared by using Mann-Whitney test. A *P*-value <0.05 was considered as statistically significant. Statistical comparisons were performed using GraphPad Prism software, La Jolla, USA.

3 | RESULTS

3.1 | LAT1, LAT2 and 4F2hc are asymmetrically expressed in the human placenta

Histological investigation of healthy placental tissue demonstrated strong expression of LAT1 at the apical membrane of STB (arrows in Figure 1B) which was confirmed by the strong signal found in the MVM fraction (Figure 1C). The asymmetric expression of LAT1 in syncytialized trophoblasts was further confirmed by immunoblot analysis in paired MVM/BM isolated from term control placentae. LAT1 was predominantly expressed at the MVM as reflected in a mean MVM to BM ratio of 6.9 (range 3.5-14.9; Figure 1C). Western blot analysis of 12 MVM and BM pairs revealed a significantly higher expression of LAT1 in MVM compared to BM ($P = 0.0015$; Figure 1C). The results of these two independent experimental approaches suggest almost exclusive LAT1 expression at the apical membrane which is in direct contact with maternal blood. In contrast, LAT2 was found to be expressed in both MVM and BM (Figure S2), with an apparent predominance of the two LAT2 variants (30 and 50 kDa) in BM as reported before.[4] Expression of 4F2hc, the heavy chain partner protein of LAT1 and LAT2, was higher in MVM as compared to BM (Figure S2).

3.2 | Trophoblast differentiation induces up-regulation of LAT1 and 4F2hc expression

To study the role of LAT1 at the placental barrier on the cellular level, LAT1 expression during trophoblast differentiation was analysed in both primary human trophoblast cells and in the BeWo cell line model on mRNA and protein level. Forskolin-stimulated differentiation in BeWo cells resulted in a significant up-regulation of LAT1 and 4F2hc, but no significant changes for LAT2 were observed (Figure 2A). Spontaneously occurring trophoblast differentiation in primary trophoblasts tended to increase LAT1 and 4F2hc mRNA levels, but due to the high variation between the individual placental cell isolations this effect did not reach statistical significance (Figure 2B). Interestingly, protein analysis by immunoblotting revealed a clear difference in the protein expression pattern between LAT1 and LAT2 depending on the differentiation state: while both 50 kDa and 30 kDa LAT2 variants were predominantly found in undifferentiated primary CTB and BeWo-CTB, LAT1 protein levels were clearly increased in differentiated primary STB and BeWo-STB (Figure 2C). Furthermore, increased 4F2hc expression was detected after differentiation in both primary and BeWo cells. 4F2hc protein expression was identified in the form of multiple bands ranging from 70 to 120 kDa under reducing conditions. The expression pattern of 4F2hc was found previously and is presumably due to formation of 4F2hc/4F2hc homodimers, 4F2hc/LAT2 heterodimers and 4F2hc monomers.[16,41,42] BeWo cells exhibited higher expression levels, but comparable expression changes during differentiation as primary trophoblasts.

3.3 | Leucine uptake increases with trophoblast differentiation

We further investigated whether the expression changes caused by trophoblast differentiation resulted also in an increased leucine uptake efficiency in both primary (n = 3; Figure 3A) and BeWo cells (n = 3; Figure 3B). Indeed, both spontaneously differentiated primary trophoblasts (pCTB-V_{max} = 1.05 nmol/mg protein vs pSTB-V_{max} = 2.34 nmol/mg protein = 2.2-fold) and forskolin-stimulated BeWo cells (BeWo-CTB-V_{max} = 4.96 nmol/mg protein vs BeWo-STB-V_{max} = 13.41 nmol/mg protein = 2.7-fold) reached more than 2-times higher maximal uptake levels after 6 minutes compared to the undifferentiated stage. By comparing maximal leucine uptake levels between BeWo and primary cells, a 4.7-fold greater uptake capacity for the BeWo-CTB and 5.7-fold difference for the BeWo-STB stage was observed. However, the half-maximal leucine uptake time, calculated as K_d from the time course curve fit, for primary cells (pCTB-Kd = 1.45 nmol/min; pSTB-hillslope = 1.36 nmol/min) and BeWo cells (BeWo-CTB-Kd = 1.19 nmol/min; BeWo-STB-Kd = 1.42 nmol/min) was similar between the differentiation stages. Thus, in accordance to expressional changes, also

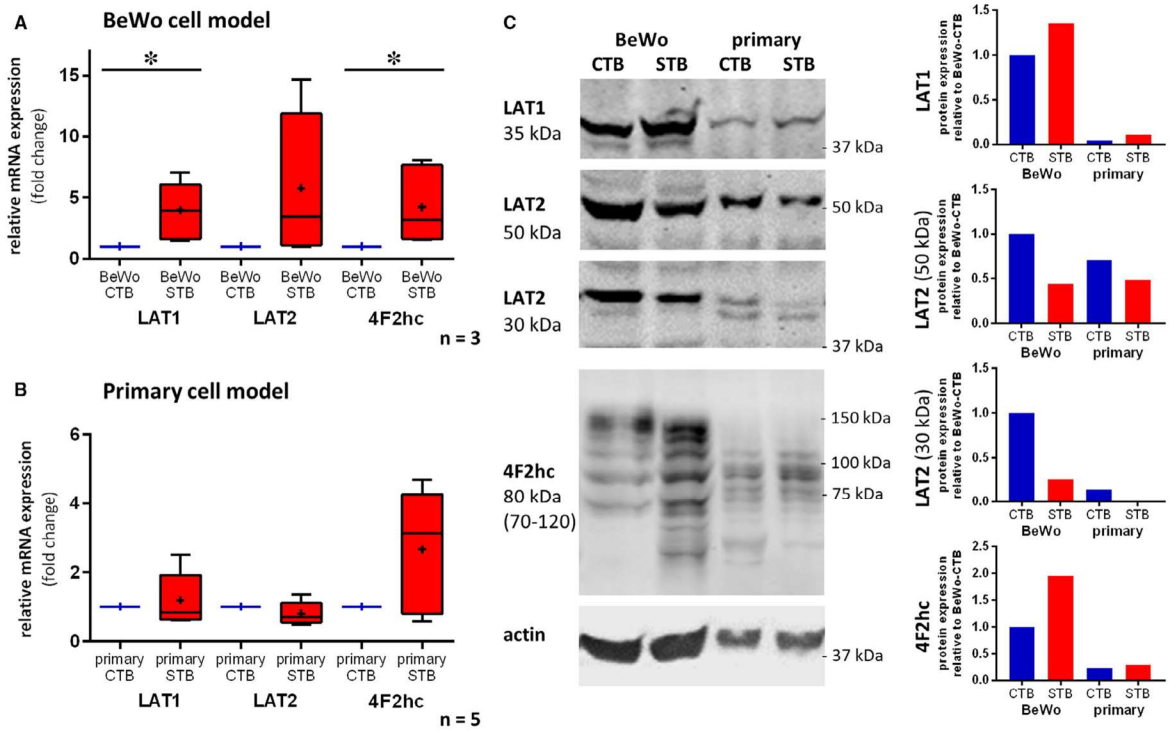

FIGURE 2 Expression patterns of the placental System L transporters in primary trophoblasts and BeWo cells depend on their differentiation stage. Comparison of the choriocarcinoma derived BeWo cell line (A) and primary trophoblasts (B) with respect to LAT1 (SLC7A5), LAT2 (SLV7A8) and 4F2hc (SLC3A2, CD98) mRNA levels at the undifferentiated cytotrophoblast (CTB) and differentiated syncytiotrophoblast (STB) stage. (A) LAT1 and 4F2hc were up-regulated, while LAT2 expression in BeWo-STB cells was not significantly increased relative to their BeWo-CTB counterpart (paired t test of 3 independent experiments). BeWo-CTB were sampled after 24 h of culturing and BeWo-STB were analysed after stimulation with 100 μmol/L forskolin for 48 h. (B) LAT1, LAT2 and 4F2hc transcript levels of primary trophoblasts were not significantly increased in STB as compared to the CTB counterpart (paired t test). Primary trophoblasts were harvested from 5 individual trophoblast isolations (n = 5). They were lysed for mRNA isolation and quantitative RT-qPCR after 12 h at the CTB stage and after 72 h of culturing at the STB stage. (A)/(B) Expression results were normalized to the mean of the reference genes YWHAZ, GAPDH and β-actin. Transcript data are presented as fold-change ($2^{-\Delta\Delta Ct}$). Data are shown as mean (+), median (–) and Tukey whiskers (1.5-times IQR), $\alpha = 0.05$, $^*P < 0.05$. (C) Representative immunoblot (left panel) and densitometric analysis of both cell types revealed increased LAT1 protein expression after cell differentiation (CTB < STB). Generally higher LAT1 protein expression levels were found in the BeWo cell line compared to primary cells (BeWo-CTB/STB > pCTB/STB). The expression of the two LAT2 variants (50 kD; 30 kD) decreased after trophoblast differentiation in both cell types (primary trophoblasts and BeWo cells). 4F2hc was increased in both primary trophoblasts and BeWo-STB as compared to the corresponding CTB stage. Densitometric analysis in the right panel was corrected for the β-actin signal

on functional level leucine uptake capacity was higher in BeWo cells compared to primary trophoblasts, but the kinetic changes due to cell differentiation were similar in both cell models (Figure 3).

3.4 | Leucine uptake is modulated by System L-specific small molecule inhibitors

Based on the high leucine uptake capacity and the high expression levels of functional LAT1, the BeWo cell model was selected to test different LAT1 or LAT1/LAT2-specific small molecular inhibitors in dose-response experiments. Two new alternative compounds, JX009 and JG336 (Figure 4B,C), were investigated and compared in two separate experiments to the already established potent LAT1-specific inhibitor JPH203 (Figure 4A). In BeWo-CTB all three inhibitors reached a maximal inhibition of less than 0.8 nmol/mg protein at a concentration of 10 μmol/L (corresponding to the bottom value of a four-parameter nonlinear fit with variable slope; kinetic parameters are listed in the panels on the right). The leucine analog 2-amino-2-norbornane-carboxylic acid (BCH) maximally inhibited leucine uptake at a concentration of approx. 1 mmol/L regardless of the differentiation stage (Figure 4D). This observation further verifies the relevance of SLC7-mediated leucine uptake in BeWo cells. Although there was profound leucine uptake inhibition in BeWo-CTB, 10 μmol/L of JPH203 and JG336 showed a residual uptake of 3.8 (56.3% inhibition) and 3.2 nmol/mg protein (62.4% inhibition), respectively. JX009

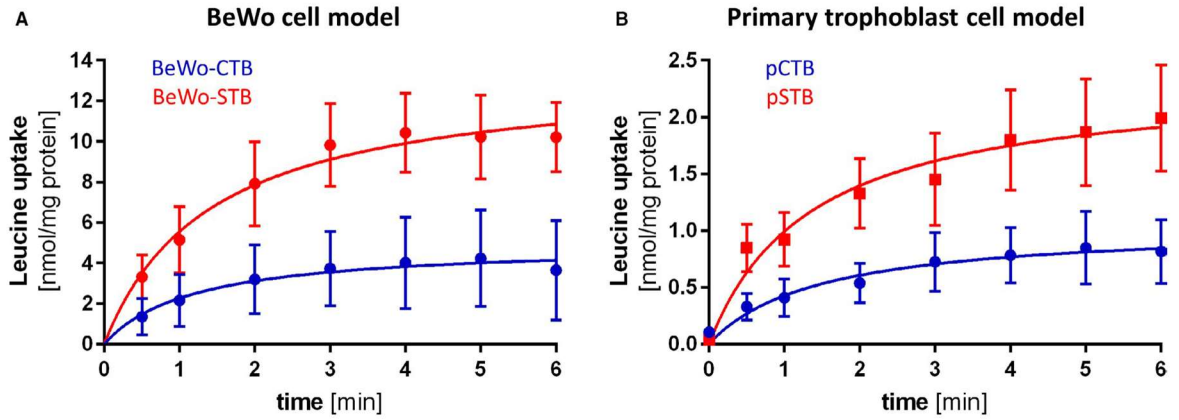

FIGURE 3 Similar leucine uptake kinetics in primary and BeWo trophoblast cells. A, In the BeWo cell model, Na^+-independent maximal uptake capacity (V_{max}) for leucine was significantly increased in 3 independent experiments (n = 3). Leucine uptake increased from 4.96 nmol/mg protein in BeWo CTBs to 13.41 nmol/mg protein in BeWo STBs (2 way ANOVA, $\alpha = 0.05$; $P = 0.018$). Leucine uptake for BeWo-CTB was performed after 24 h of culturing and for BeWo-STB after stimulation with 100 µmol/L forskolin for 48 h. B, Primary trophoblasts isolated from 3 individual control placentae (n = 3) significantly increased their V_{max} over 6 min from 1.046 nmol/mg protein in pCTB to 2.345 nmol/mg protein in the pSTB stage (2 way-ANOVA, $\alpha = 0.05$; $P < 0.0001$). The maximal leucine uptake capacity (V_{max}) and half-maximal uptake time (K_d) was calculated using a saturation model curve fitting ($y = V_{max}{}^*X/(K_d + x)$). The final concentration of leucine in all experiments was 167 nmol/mL including 1 µCi/mL ^{3}[H]-L-leucine for detection. Error bars represent standard deviation (SD) of 3 individual experiments with 6 replicates each

(10 µmol/L) blocked leucine uptake regardless of the trophoblast differentiation stage. In BeWo-STB leucine uptake was inhibited by 87% suggesting inhibition of most Na^+-independent SLC7 transporters. While the dose-response experiments with the less specific inhibitor JX009 revealed an EC_{50} of 3.9 µmol/L for BeWo-CTB and 2.3 µmol/L for BeWo-STB, which is comparable with JPH203 (EC_{50} = 3.1 µmol/L for BeWo-CTB and 2.6 µmol/L for BeWo-STB), JG336 was identified as the most efficient inhibitor (EC_{50} = 0.8 µmol/L for BeWo-CTB and 2.0 µmol/L for BeWo-STB) in both differentiation stages of BeWo cells. Compared to the dose-response curve of BCH, JX009 shows comparable efficiency but >180-times higher potency (Figure 4C,D). The new inhibitors JG336 and JX009 as well as JPH203 reached maximal inhibition (first concentration without significant difference to the bottom value) at a concentration of 10 µmol/L, JG336 required 1 µmol/L for maximal inhibition in BeWo-CTB. Of note, comparable inhibition patterns were also found in the colorectal adenocarcinoma cell line HT-29 where lower substrate concentrations (30 µmol/L instead of 167 µmol/L leucine) lead to lower EC_{50} values (Figure S3). In summary, the dose-response analysis of the three inhibitors suggested that JG336 inhibits LAT1-specific placental leucine transport similar as JPH203, but exhibits an almost 4-times higher efficiency. JX009, represents an inhibitor of System L transporters which in trophoblast is 180-times more potent than BCH.

3.5 | Transfer of leucine across the placental barrier is reduced by inhibitors of System L transporters

The small molecule inhibitors JPH203, JG336 and JX009 were also used to assess the relevance of LAT1 and LAT2 in leucine transport across the placental barrier using the Transwell® system (Figure 5). Leucine transfer experiments were performed in the presence or absence of the individual inhibitors with a fixed concentration of 10 µmol/L applied at the upper compartment. This concentration was chosen as it showed in dose-response experiments maximal inhibition for all three compounds (see above). Figure 5B shows the experimental setup and the applied leucine concentrations in the upper compartment (corresponding to the maternal side of the placental barrier) and the lower chamber (corresponding to the foetal side) of the Transwell® system. Gradually diminishing radioactive signal ^{3}[H]-leucine on the maternal side and increasing radioactivity on the foetal side was considered to represent leucine transfer across the BeWo monolayer. Treatment with JPH203, JG336 and JX009 at the apical (maternal) side caused significant reduction of leucine transfer by 58%, 60% and 55%, respectively. All inhibitors significantly decreased leucine transfer from the apical towards the basal compartment from 60 minutes onwards. Measurement of intracellular ^{3}[H]-leucine content in the BeWo monolayer at the end of the transfer experiment (6 hours) indicated significantly decreased intracellular leucine concentrations of 24% for JPH203 and 41% for JG336, respectively (Figure 5C). In contrast, JX009 had no effect on the intracellular ^{3}[H]-leucine concentration within the tested time course. The higher retention of leucine in JX009 treated cells suggests inhibition of leucine secretion towards the lower foetal compartment.

4 | DISCUSSION

The placenta plays a crucial role in the distribution of essential nutrients from the mother to the growing foetus. In this context,

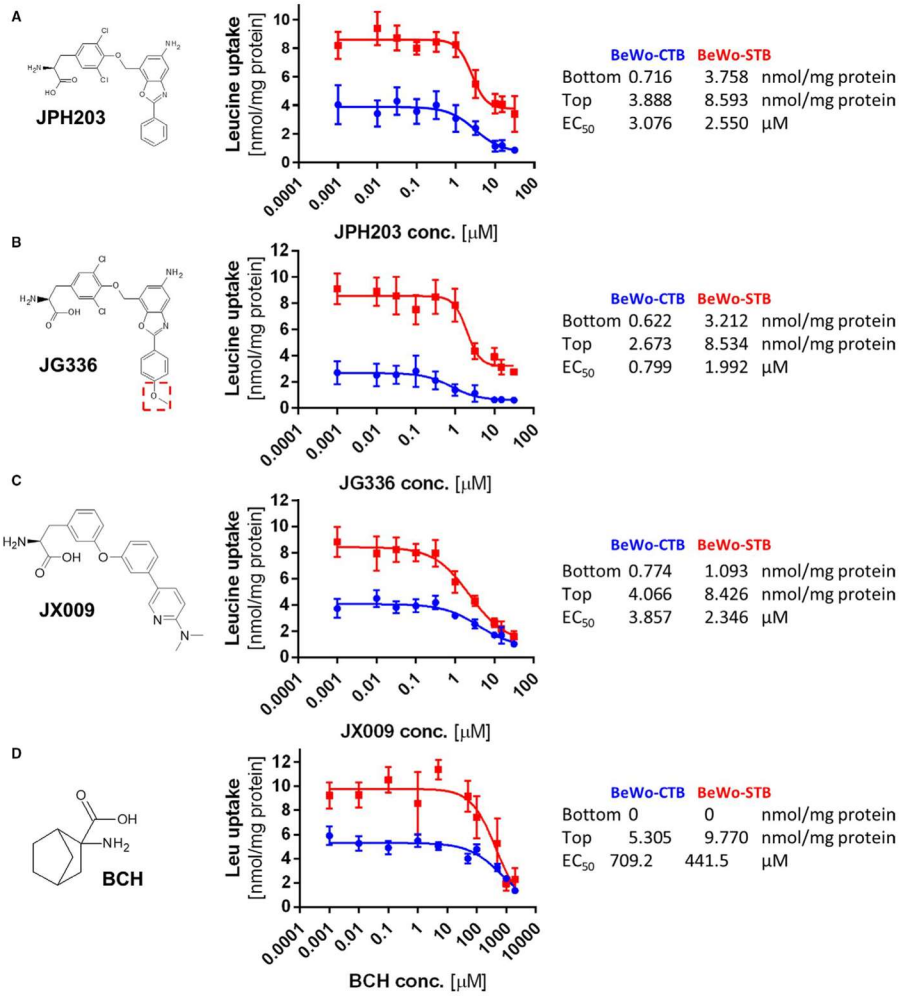

FIGURE 4 Inhibition of leucine uptake in BeWo cells using small molecule inhibitors with different specificities. Dose-response experiments in BeWo-cytotrophoblasts (BeWo-CTB) and forskolin-stimulated BeWo-syncytiotrophoblasts (BeWo-STB) for the established LAT1-specific inhibitor JPH203 (A) and for the alternative compound JG336 which carries an additional methoxy group as marked in the dashed red box (B). The results showed that both compounds conveyed a significant inhibition (JPH203 = 56%, JG336 = 62%), but also suggest that approximately 40% of Na^+-independent leucine uptake is LAT1 independent. (C) Application of JX009, an inhibitor of both LAT1 and LAT2, resulted in maximal leucine uptake inhibition in BeWo-CTB and BeWo-STB. Compared to the dose-response curve of the leucine analog 2-amino-2-norbornane-carboxylic acid (BCH, D), JX009 shows comparable efficiency but >180-times higher potency. BCH is a widely accepted inhibitor blocking all System L mediated transport. BCH completely blocked leucine uptake in BeWo-CTB with an EC_{50} of 709 µmol/L and BeWo-STB with an EC_{50} of 442 µmol/L (D). (A-C) The new inhibitors JG336 and JX009 as well as JPH203 reached maximal inhibition (first concentration without significant difference to the bottom value) at a concentration of 10 µmol/L, JG336 required 1 µmol/L for maximal inhibition in BeWo-CTB. BCH reached maximal inhibition at 1 mmol/L in both differentiation stages. A-D, All uptake assays were performed in two individual experimental setups (n = 2) for 3 min, under the same conditions in Na^+-free Hanks buffer with 167.2 µmol/L leucine (1 µCi/mL ^{3}H-L-leucine). Dose-response kinetics were calculated using the nonlinear four-parameter model [Y = Bottom + (Top − Bottom)/(1 + 10^((LogEC50-X)*HillSlope))] and ordinary fit with GraphPad Prism software. Best-fit values of the including EC_{50} values are shown to the right of the dose-response curves. Error bars represent standard deviation (SD) of 2 experiments with 6 replicates

fine-tuned regulatory mechanisms are needed to control the materno-foetal transfer of essential AA to support the rapidly developing foetus during pregnancy.[43] The current understanding of transplacental AA transport is based on the interplay between accumulative transporters such as members of the System A family and exchangers such as System L family members.[44] System A family transporters like SNAT1, 2 and 4 are expressed at the MVM and accumulate small neutral AA against a concentration gradient in the

STB in a Na^+-dependent manner.[43] The AA accumulated by System A transporters can be used as substrates to exchange for essential large neutral AA such as leucine by the System L exchangers LAT1 and LAT2 across the MVM into the STB. The principles of AA uptake at the MVM are largely characterized, but the contribution of single transporters in AA transfer across the BM to the foetus is less clear.

In a first step, we investigated the expression and localization of LAT1 in the human placenta by immunohistochemistry of term placental tissue and by immunoblotting of MVM- and BM-enriched membrane preparations. We found an exclusive apical expression of LAT1 at the MVM confirming previous reports.[8,45]

So far most mechanistic studies are based on LAT1-overexpressing cell models like human colon cancer-derived HT-29,[46] mammary gland derived MCF-7 cells,[47] Pichia pastoris[42] or reconstituted 4F2hc-LAT1 proteoliposomes.[48] Acquiring further detailed knowledge on the complex mechanisms regulating materno-foetal AA transport at the placenta level could be beneficial to clarify the relevance of LAT1 and LAT2 in gestational diseases such as IUGR and LGA.[10] To choose an appropriate physiological placental cell model, we compared the BeWo cell line with isolated primary human trophoblasts at different stages of differentiation by analysing LAT1/LAT2 mRNA and protein expression and leucine uptake. Spontaneous differentiation in primary trophoblasts and forskolin-mediated differentiation in BeWo cells provoked expressional changes of LAT1, LAT2 and 4F2hc on mRNA and protein level (Figure 2). Our results demonstrated that the syncytialization process induced changes in the LAT1:LAT2 ratio as well as in 4F2hc expression in both trophoblast models (Figure 2) and resulted in an increased leucine uptake under Na^+-free conditions (Figure 3). These findings imply that differentiation induces a specialization process both in primary trophoblasts and BeWo cells, which results in an increased uptake, transport or transfer capacity as previously shown for the alanine-serine-cysteine transporters and for alpha-aminoisobutyric acid transport.[49,50] This concept is in line with recent findings that differentiation processes such as syncytium formation resulted in an up-regulation of MVM associated membrane proteins.[16]

Based on the validation of expression in the two trophoblast cell models (Figure 2) and comparable uptake behaviour (Figure 3), the BeWo cell line was chosen to test the effect of different SLC7-specific inhibitors. However, to our knowledge LAT1 and LAT2 localization in MVM or BM of BeWo cells after forskolin-induced differentiation has not been reported yet. Thus localization differences between primary trophoblasts and BeWo cells cannot be completely excluded and therefore the Transwell® data using polarized BeWo cells should be interpreted with caution.

The low molecular weight inhibitors JPH203, JG336 and JX009 were assessed for their capacity to reduce leucine uptake into BeWo cells (Figure 4) and leucine transfer across the placental barrier (Figure 5). Due to the varying SLC7 specificity, different inhibition patterns were expected. JPH203 was previously reported as potent, LAT1-specific inhibitor.[27-31,46] JX009 had been described in the patent literature[37] to inhibit LAT1-mediated transport with similar efficacy as JPH203, albeit with significantly lower specificity, that is, it is also a potent LAT2 inhibitor. As no other LAT2 inhibitors have been described in the literature, JX009 was considered the best available tool for the assessment of LAT2-related transport of leucine. JG336 was prepared based on a limited structure activity relationships (SAR) study on JPH203 that investigated the effects of electron-donating (such as the methoxy group in JG336, see dashed red box in Figure 4B), electron-withdrawing and bulky substituents on the phenyl moiety at the 2-position of the benzoxazole ring on transport inhibition. The additional methoxy group in JG336 resulted in 3.8-times lower EC_{50} values in BeWo-CTB (Figure 4B) indicating that the inhibition efficiency of JPH203 was indeed increased by this modification. Further results of this SAR study on JPH203 will be published separately.

Our results demonstrated that all three compounds are highly efficient LAT1 inhibitors, but only JX009 conveyed additionally LAT2 inhibition. Based on the complete leucine uptake inhibition of BeWo cells at the CTB stage, leucine uptake in undifferentiated trophoblasts seems to be highly dependent of LAT1 activity (Figure 4). Although we demonstrated in the expression studies (Figure 2) that the LAT1:LAT2 ratio in BeWo-STB is higher compared to BeWo-CTB, JPH203 reduced leucine uptake in BeWo-STB by only 60%. This partial inhibition by JPH203 indicates that in BeWo-STB leucine uptake is mediated by alternative Na^+-independent System L or System L-like facilitators such as LAT2, LAT3 or LAT4. JX009 reduced leucine uptake by 87% regardless of the trophoblast differentiation stage with a low EC_{50} in the range of JPH203, suggesting that JX009 blocked most (if not all) Na^+-independent leucine uptake transporters. Thus, JX009 is the first characterized System L-specific leucine uptake inhibitor in the low μM-range (EC_{50} < 4 μmol/L; Figure 4) for use in placental cell models. To date, the most widely used SLC7-specific inhibitor is the non-metabolizable leucine analog BCH which has been also tested in this study (Figure 4D) and other investigations.[51,52] In comparison to JX009 this inhibitor is >100-times less effective and blocks System L-dependent AA transport with 709 μmol/L in BeWo-CTB and 442 μmol/L in BeWo-STB in the high μM-range (Figure 4D). Nevertheless, further investigations of these small molecule compounds are needed to study viability, effects on AA metabolism and potential interactions with other transmembrane proteins such as System A transporters.

To assess the functional importance of SLC7 transporters in leucine transfer across the placental barrier, the effect of the LAT1-specific inhibitors JPH203 and JG336 as well as the System L inhibitor JX009 was tested in the Transwell® system with polarized BeWo cells grown in a tight monolayer (Figure 5). Treatment with JPH203 during 6 hours reduced leucine transfer across the placental barrier by 58%. Assuming 100% LAT1 inhibition after treatment with 10 μmol/L JPH203 (approximately 5-times the EC_{50} of JPH203), these results suggest that more than half of the leucine transfer across the differentiated BeWo monolayer was LAT1-dependent. The 3.8-times more efficient inhibitor JG336 (60% reduction), and the less specific System L inhibitor JX009 (55% reduction) showed similar inhibition

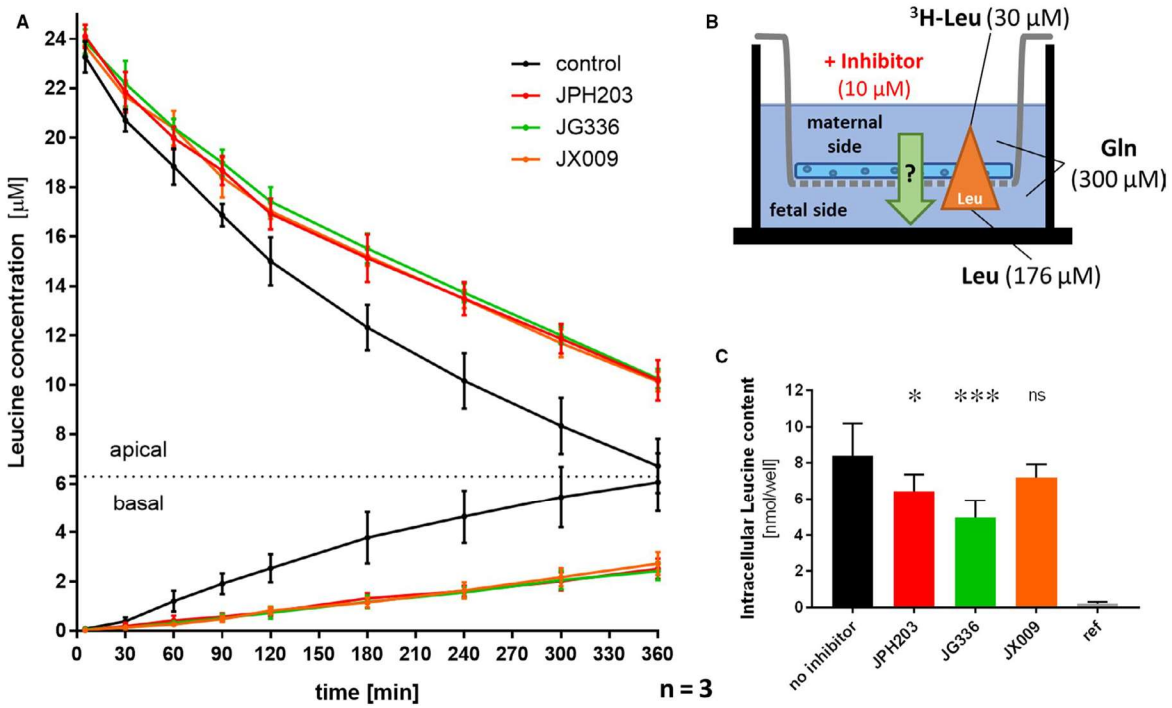

FIGURE 5 Relevance of LAT1 and System L inhibition in leucine transfer across the placental barrier in vitro. A, Leucine transfer across a tight BeWo monolayer was measured from the apical (ie upper compartment) towards the basal (ie lower compartment) side during 6 h using the Transwell® system. Leucine transfer was significantly reduced by the System L inhibitor JX009 (orange) and the LAT1-specific inhibitors JPH203 (red) and JG336 (green) compared to the DMSO-control (black) already after 1 h. Equal concentrations (10 µmol/L) of each inhibitor and DMSO as vehicle control were applied in three experiments with two replicates per condition. B, Illustration of the experimental setup. All leucine transfer assays were performed against a counter-directed gradient of 137 µmol/L (30 → 167 µmol/L) leucine, in the presence of 300 µmol/L glutamine (Gln) in both compartments. The leucine in the upper compartment was spiked with 1 µCi/mL ^{3}H-L-leucine for transfer quantification. C, The intracellular leucine content was measured after washing the cell layers with DPBS at the end of the experiment (after 6 h). A significant reduction of intracellular leucine contents was detected for the LAT1-specific inhibitors JPH203 ($P = 0.020$) and JG336 ($P = 0.0001$), but not for the System L inhibitor JX009- ($P = 0.215$). The detected intracellular leucine retention caused through LAT1 and LAT2 inhibition by JX009 suggests a System L-dependent leucine efflux across the BM as rate-limiting step. Statistical analyses were performed using a parametric one-way ANOVA analysis ($\alpha = 0.05$)

capacities as JPH203. These results demonstrated a predominantly LAT1-dependent leucine transfer across the polarized BeWo monolayer which mimicks the physiological materno-foetal barrier.[39] In these transfer studies, we also measured the intracellular leucine content at the end of the experiment. In this context, the intracellular accumulation of leucine suggests that the efflux activity at the BM; that is, the transport towards the foetus, represents the rate-limiting process in materno-foetal transfer. In contrast, a reduced intracellular leucine content predicts leucine transport across the MVM into the BeWo monolayer as the rate-limiting step.[7] In our experiments only the two LAT1-specific inhibitors JPH203 and JG336 caused a reduction of the intracellular leucine content (Figure 5C), indicating that LAT1-mediated leucine transfer occurs at the apical MVM. In contrast, the unchanged intracellular leucine content after JX009 treatment suggests System L transporter-dependent leucine efflux across the BM. This is in agreement with the hypothesis that LAT1 is the major leucine transporter at the MVM, while other placental Na^+-independent System L or System L-like facilitated AA transporters such as LAT2, LAT3 or LAT4 mediate leucine efflux across the BM (Figure 1) as previously proposed.[7,43,53,54] LAT1 and LAT2 localization in BeWo cell before and after differentiation has not been demonstrated yet; hence the interpretation of our results is based on the assumption that System L-transporter expression in differentiated BeWo is similar to primary trophoblasts and placental tissue. Since the three tested inhibitors were applied at the maternal compartment, there is a certain membrane and cell layer permeability required to allow interactions with the transporters located at the BM. Permeability across the trophoblast barrier has not been investigated, but has been shown in Caco-2 cells for JPH203.[40] Recently Lewis et al demonstrated in a mathematical modelling approach of placental AA efflux based on placental perfusion data, that LAT2 allows the transport of a substrate across the BM without transport of another molecule in the other direction as normally expected from a classical exchanger.[55]

The selective expression and overexpression in various cancer types with poor survival expectancy[20,56-60] made LAT1 an interesting pharmaceutical target.[27] This study demonstrates that the choriocarcinoma cell line BeWo could serve as useful model system to test putative LAT1 inhibitors and characterize their effect at an active AA transporting and physiologically relevant cell barrier. It was shown that high and asymmetric expression of SLC7 family members makes the placental leucine uptake sensitive to LAT1- and LAT2 inhibition.[8,41] Furthermore, the application of compounds like the LAT1-specific inhibitor JPH203 or the less specific SLC7-transporter inhibitor JX009, allows for distinguishing the contribution of single leucine transporters across the placental barrier. The short-term treatment with small molecule inhibitors also reduces the risk of affecting trophoblast fusion and differentiation which could occur after long-term gene silencing or constitutive knockout.[16] If further efforts are made to identify new lead structures or to further develop existing inhibitors targeting System L-like transporters such as the AA facilitators LAT3 and LAT4, these new compounds could be valuable tools for assessing the relevance of single transporter in materno-foetal AA transfer.

In summary, the combined application of the LAT1-specific inhibitor JPH203 and the System L inhibitor JX009 in Transwell® studies helped to identify LAT1 as major leucine transporter playing an important role in the materno-foetal supply of essential AA at the MVM. In this context, the present study demonstrates the usefulness of applying small-compound inhibitors bearing different specificities. A better understanding of the SLC7 transporter-mediated supply of AA and its impact on mTORC1-mediated placental function in pregnancy diseases including IUGR and gestational diabetes mellitus could be a first step towards the optimization of foetal growth and its effect on foetal programming in the future.[61]

ACKNOWLEDGEMENTS

This study was supported by the Swiss National Centre of Competence in Research, NCCR TransCure, University of Bern, Switzerland, and the Lindenhof Stiftung Bern. The authors thank Dr Alan L. Schwartz, Washington University School of Medicine, USA for donating the BeWo cells (b30 clone). The authors are grateful to Dr Meike Körner, Pathologie Länggasse, for help with the immunohistochemical work. Michael Lüthi, Regina Berchtold and Martyna Kazimierczak are greatly acknowledged for their help and support in the lab. Further, the authors express their gratitude to the patients, physicians and midwives from the Lindenhofgruppe, Bern, for participating in this study. JZ was supported by the Graduate School for Cellular and Biomedical Sciences (GCB), University of Bern, Switzerland.

CONFLICT OF INTEREST

The authors declare no conflict of interest.

AUTHOR CONTRIBUTION

Jonas Zaugg: Conceptualization (equal); data curation (lead); formal analysis (lead); investigation (lead); methodology (lead); validation (lead); writing – original draft (lead); writing – review and editing (equal). **Xiao Huang:** Conceptualization (equal); data curation (equal); investigation (equal); writing – review and editing (equal). **Fabian Ziegler:** Data curation (equal); formal analysis (equal); validation (equal). **Matthias Rubin:** Data curation (equal); formal analysis (supporting). **Julien Graff:** Data curation (equal); formal analysis (supporting). **Jennifer Müller:** Data curation (equal); formal analysis (supporting). **Ruedi Moser – Hässig:** Conceptualization (equal); methodology (equal); writing – review and editing (equal). **Theresa Powell:** Methodology (equal); writing – review and editing (equal). **Jürg Gertsch:** Supervision (equal); writing – review and editing (equal). **Karl-Heinz Altmann:** Resources (equal); validation (equal); writing – review and editing (equal). **Christiane Albrecht:** Conceptualization (lead); formal analysis (supporting); funding acquisition (lead); investigation (supporting); project administration (lead); resources (equal); supervision (lead); writing – original draft (equal); writing – review and editing (lead).

DATA AVAILABILITY STATEMENT

The data that support the findings of this study are available from the corresponding author upon reasonable request.

ORCID

Jonas Zaugg https://orcid.org/0000-0002-3153-2806
Theresa Powell https://orcid.org/0000-0001-7410-1080
Jürg Gertsch https://orcid.org/0000-0003-0978-1555
Karl-Heinz Altmann https://orcid.org/0000-0002-0747-9734
Christiane Albrecht https://orcid.org/0000-0002-7846-6930

REFERENCES

1. Palacín M, Estévez R, Bertran J, Zorzano A. Molecular biology of mammalian plasma membrane amino acid transporters. *Physiol Rev*. 1998;78(4):969-1054.
2. Desforges M, Greenwood SL, Glazier JD, Westwood M, Sibley CP. The contribution of SNAT1 to system A amino acid transporter activity in human placental trophoblast. *Biochem Biophys Res Commun*. 2010;398(1):130-134.
3. Fotiadis D, Kanai Y, Palacín M. The SLC3 and SLC7 families of amino acid transporters. *Mol Aspects Med*. 2013;34(2-3):139-158.
4. Rosario FJ, Kanai Y, Powell TL, Jansson T. Mammalian target of rapamycin signalling modulates amino acid uptake by regulating transporter cell surface abundance in primary human trophoblast cells. *J Physiol*. 2013;591(Pt 3):609-625.
5. Edwards D, Jones CJ, Sibley CP, Nelson DM. Paracellular permeability pathways in the human placenta: a quantitative and morphological study of maternal-fetal transfer of horseradish peroxidase. *Placenta*. 1993;14(1):63-73.
6. Bodoy S, Fotiadis D, Stoeger C, Kanai Y, Palacín M. The small SLC43 family: facilitator system l amino acid transporters and the orphan EEG1. *Mol Aspects Med*. 2013;34(2-3):638-645.
7. Cleal JK, Glazier JD, Ntani G, et al. Facilitated transporters mediate net efflux of amino acids to the fetus across the basal membrane of the placental syncytiotrophoblast. *J Physiol*. 2011;589(Pt 4):987-997.
8. Gaccioli F, Aye ILMH, Roos S, et al. Expression and functional characterisation of System L amino acid transporters in the human term placenta. *Reprod Biol Endocrinol*. 2015;13(1):57.
9. Paolini CL, Marconi AM, Ronzoni S, et al. Placental transport of leucine. *Phenylalanine*. 2001;86(11):5427-5432.

10. Lager S, Powell TL. Regulation of nutrient transport across the placenta. *J Pregnancy*. 2012;2012:179827.
11. Jansson T, Ekstrand Y, Björn C, Wennergren M, Powell TL. Alterations in the activity of placental amino acid transporters in pregnancies complicated by diabetes. *Diabetes*. 2002;51(7):2214-2219.
12. Harder T, Rodekamp E, Schellong K, Dudenhausen JW, Plagemann A. Birth weight and subsequent risk of type 2 diabetes: a meta-analysis. *Am J Epidemiol*. 2007;165(8):849-857.
13. Eriksson J, Forsen T, Osmond C, Barker D. Obesity from cradle to grave. *Int J Obesity*. 2003;27(6):722-727.
14. Boney CM, Verma A, Tucker R, Vohr BR. Metabolic syndrome in childhood: association with birth weight, maternal obesity, and gestational diabetes mellitus. *Pediatrics*. 2005;115(3):e290-e296.
15. Leon DA, Lithell HO, Vâgerö D, et al. Reduced fetal growth rate and increased risk of death from ischaemic heart disease: cohort study of 15 000 Swedish men and women born 1915-29. *BMJ*. 1998;317(7153):241-245.
16. Ohgaki R, Ohmori T, Hara S, et al. Essential roles of L-type amino acid transporter 1 in syncytiotrophoblast development by presenting fusogenic 4F2hc. *Mol Cell Biol*. 2017;37(11):e00427–16.
17. Balthasar C, Stangl H, Widhalm R, Granitzer S, Hengstschläger M, Gundacker C. Methylmercury uptake into bewo cells depends on LAT2-4F2hc, a system l amino acid transporter. *Int J Mol Sci*. 2017;18(8):2-4.
18. Häfliger P, Charles RP. The l-type amino acid transporter LAT1 – an emerging target in cancer. *Int J Mol Sci*. 2019;20(10):1-14.
19. Fuchs BC, Bode BP. Amino acid transporters ASCT2 and LAT1 in cancer: partners in crime? *Semin Cancer Biol*. 2005;15(4):254-266.
20. Kaira K, Oriuchi N, Imai H, et al. L-type amino acid transporter 1 and CD98 expression in primary and metastatic sites of human neoplasms. *Cancer Sci*. 2008;99(12):2380-2386.
21. Peura L, Malmioja K, Laine K, et al. Large amino acid transporter 1 (LAT1) prodrugs of valproic acid: new prodrug design ideas for central nervous system delivery. *Mol Pharm*. 2011;8(5):1857-1866.
22. Singh N, Scalise M, Galluccio M, et al. Discovery of potent inhibitors for the large neutral amino acid transporter 1 (LAT1) by structure-based methods. *Int J Mol Sci*. 2019;20(1):27.
23. Augustyn E, Finke K, Zur AA, et al. LAT-1 activity of meta-substituted phenylalanine and tyrosine analogs. *Bioorg Med Chem Lett*. 2016;26(11):2616-2621.
24. Geier EG, Schlessinger A, Fan H, et al. Structure-based ligand discovery for the large-neutral amino acid transporter 1, LAT-1. *Proc Natl Acad Sci USA*. 2013;110(14):5480-5485.
25. Kongpracha P, Nagamori S, Wiriyasermkul P, et al. Structure-activity relationship of a novel series of inhibitors for cancer type transporter L-type amino acid transporter 1 (LAT1). *J Pharmacol Sci*. 2017;133(2):96-102.
26. Scalise M, Galluccio M, Console L, Pochini L, Indiveri C. The human SLC7A5 (LAT1): the intriguing histidine/large neutral amino acid transporter and its relevance to human health. *Front Chem*. 2018;6(June):1-12.
27. Enomoto K, Sato F, Tamagawa S, et al. A novel therapeutic approach for anaplastic thyroid cancer through inhibition of LAT1. *Sci Rep*. 2019;9(1):1-11.
28. Cormerais Y, Pagnuzzi-Boncompagni M, Schrötter S, et al. Inhibition of the amino-acid transporter LAT1 demonstrates anti-neoplastic activity in medulloblastoma. *J Cell Mol Med*. 2019;23(4):2711-2718.
29. Muto Y, Furihata T, Kaneko M, et al. Different response profiles of gastrointestinal cancer cells to an L-type amino acid transporter inhibitor, JPH203. *Anticancer Res*. 2019;39(1):159-165.
30. Häfliger P, Graff J, Rubin M, et al. The LAT1 inhibitor JPH203 reduces growth of thyroid carcinoma in a fully immunocompetent mouse model. *J Exp Clin Cancer Res*. 2018;37(1):2428–2442.
31. Yothaisong S, Dokduang H, Anzai N, et al. Inhibition of l-type amino acid transporter 1 activity as a new therapeutic target for cholangiocarcinoma treatment. *Tumor Biol*. 2017;39(3):1–14.
32. Kallol S, Moser-Haessig R, Ontsouka CE, Albrecht C. Comparative expression patterns of selected membrane transporters in differentiated BeWo and human primary trophoblast cells. *Placenta*. 2018;72-73(October):48-52.
33. Kallol S, Huang X, Müller S, Ontsouka C, Albrecht C. Novel insights into concepts and directionality of maternal-fetal cholesterol transfer across the human placenta. *Int J Mol Sci*. 2018;19(8):2334.
34. Azar C, Valentine M, Trausch-Azar J, Druley T, Nelson DM, Schwartz AL. RNA-Seq identifies genes whose proteins are transformative in the differentiation of cytotrophoblast to syncytiotrophoblast, in human primary villous and BeWo trophoblasts. *Sci Rep*. 2018;8(1):1-12.
35. Illsley NP, Wang ZQ, Gray A, Sellers MC, Jacobs MM. Simultaneous preparation of paired, syncytial, microvillous and basal membranes from human placenta. *BBA – Biomembranes*. 1990;1029(2):218-226.
36. Huang X, Anderle P, Hostettler L, et al. Identification of placental nutrient transporters associated with intrauterine growth restriction and pre-eclampsia. *BMC Genom*. 2018;19(1):1-17.
37. Endo H, Kanai Y, Kunio S, Koji O. Aromatic amino acid derivative with LAT1 inhibitory activity, LAT1 inhibitor containing the same and method for producing the same. 2008. http://www.freepatentsonline.com/WO2008081537.html
38. Liu F, Soares MJ, Audus KL, et al. Permeability properties of monolayers of the human trophoblast cell line BeWo. *Am J Physiol Cell Physiol*. 1997;273(5):1596-1604.
39. Huang X, Lüthi M, Ontsouka EC, et al. Establishment of a confluent monolayer model with human primary trophoblast cells: novel insights into placental glucose transport. *Mol Hum Reprod*. 2016;22(6):442-456.
40. Wempe MF, Rice PJ, Lightner JW, et al. Metabolism and pharmacokinetic studies of JPH203, an L-Amino acid transporter 1 (LAT1) selective compound. *Drug Metab Pharmacokinet*. 2012;27(1):155-161.
41. Okamoto Y, Sakata M, Ogura K, et al. Expression and regulation of 4F2hc and hLAT1 in human trophoblasts. *Am J Physiol Cell Physiol*. 2002;282(1):C196-C204.
42. Costa M, Rosell A, Álvarez-Marimon E, Zorzano A, Fotiadis D, Palacín M. Expression of human heteromeric amino acid transporters in the yeast Pichia pastoris. *Protein Expr Purif*. 2013;87(1):35-40.
43. Jansson T. Amino acid transporters in the human placenta. *Pediatr Res*. 2001;49(2):141-147.
44. Cleal JK, Lewis RM. The mechanisms and regulation of placental amino acid transport to the human foetus. *J Neuroendocrinol*. 2008;20(4):419-426.
45. Kudo Y, Boyd CAR. Characterisation of L-tryptophan transporters in human placenta: a comparison of brush border and basal membrane vesicles. *J Physiol*. 2001;531(2):405-416.
46. Oda K, Hosoda N, Endo H, et al. L-Type amino acid transporter 1 inhibitors inhibit tumor cell growth. *Cancer Sci*. 2010;101(1):173-179.
47. Huttunen KM, Gynther M, Huttunen J, Puris E, Spicer JA, Denny WA. A Selective and slowly reversible inhibitor of l -type amino acid transporter 1 (LAT1) potentiates antiproliferative drug efficacy in cancer cells. *J Med Chem*. 2016;59(12):5740-5751.
48. Napolitano L, Scalise M, Galluccio M, Pochini L, Albanese LM, Indiveri C. LAT1 is the transport competent unit of the LAT1/CD98 heterodimeric amino acid transporter. *Int J Biochem Cell Biol*. 2015;67:25-33.
49. Furesz TC, Smith CH, Moe AJ. ASC system activity is altered by development of cell polarity in trophoblast from human placenta. *Am J Physiol-Cell Physiol*. 1993;265(1):C212-C217.
50. Karl PI, Alpy KL, Fisher SE. Amino acid transport by the cultured human placental trophoblast: effect of insulin on AIB transport. *Am J Physiol-Cell Physiol*. 1992;262(4):C834-C839.

51. Otsuki H, Kimura T, Yamaga T, Kosaka T, Suehiro JI, Sakurai H. Prostate cancer cells in different androgen receptor status employ different leucine transporters. *Prostate*. 2017;77(2):222-233.
52. Kaji M, Kabir-Salmani M, Anzai N, et al. Properties of L-type amino acid transporter 1 in epidermal ovarian cancer. *Int J Gynecol Cancer*. 2010;20(3):329-336.
53. Kudo Y, Boyd CAR. Characterization of amino acid transport systems in human placental basal membrane vesicles. *BBA – Biomembranes*. 1990;1021(2):169-174.
54. Bodoy S, Martín L, Zorzano A, Palacín M, Estévez R, Bertran J. Identification of LAT4, a novel amino acid transporter with system L activity. *J Biol Chem*. 2005;280(12):12002-12011.
55. Lewis RM, Cleal JK, Sengers BG. Placental perfusion and mathematical modelling. *Placenta*. 2020;93:43-48.
56. Kaira K, Oriuchi N, Imai H, et al. Prognostic significance of l-type amino acid transporter 1 (LAT1) and 4F2 heavy chain (CD98) expression in stage I pulmonary adenocarcinoma. *Lung Cancer*. 2009;66(1):120-126.
57. Kaira K, Oriuchi N, Imai H, et al. Prognostic significance of L-type amino acid transporter 1 expression in resectable stage I-III nonsmall cell lung cancer. *Br J Cancer*. 2008;98(4):742-748.
58. Kaira K, Nakamura K, Hirakawa T, et al. Prognostic significance of l-type amino acid transporter 1 (Lat1) expression in patients with ovarian tumors. *Am J Transl Res*. 2015;7(6):1161-1171.
59. Namikawa M, Kakizaki S, Kaira K, et al. Expression of amino acid transporters (LAT1, ASCT2 and xCT) as clinical significance in hepatocellular carcinoma. *Hepatol Res*. 2015;45(9):1014-1022.
60. Furuya M, Horiguchi J, Nakajima H, Kanai Y, Oyama T. Correlation of L-type amino acid transporter 1 and CD98 expression with triple negative breast cancer prognosis. *Cancer Sci*. 2012;103(2):382-389.
61. Roos S, Powell TL, Jansson T. Placental mTOR links maternal nutrient availability to fetal growth. *Biochem Soc Trans*. 2009;37:295-298.

SUPPORTING INFORMATION

Additional supporting information may be found online in the Supporting Information section.

How to cite this article: Zaugg J, Huang X, Ziegler F, et al. Small molecule inhibitors provide insights into the relevance of LAT1 and LAT2 in materno-foetal amino acid transport. *J Cell Mol Med*. 2020;00:1–13. https://doi.org/10.1111/jcmm.15840

9.1.3 Submitted to the Journal of Nutritional Biochemistry (21 July 2020)

Journal of Nutritional Biochemistry

Counter-directed leucine gradient promotes amino acid transfer across the human placenta

Manuscript Number: JNB-D-20-00465

Jonas Zaugg [a,b], Fabian Ziegler [a,b], Jean-Marc Nuoffer [c], Ruedi Moser-Hässig [d] & Christiane Albrecht [* a,b]

Affiliations

[a] Institute of Biochemistry and Molecular Medicine, Faculty of Medicine, University of Bern, Switzerland

[b] Swiss National Centre of Competence in Research (NCCR) TransCure, University of Bern, Switzerland

[c] Center for Metabolic Analysis, University Hospital, Bern, Switzerland

[d] Lindenhofspitalgruppe Bern, Switzerland

* Corresponding author:
Prof. Christiane Albrecht
University of Bern
Institute of Biochemistry and Molecular Medicine
Bühlstrasse 28
CH-3012 Bern, Switzerland
Phone: +41-31-631 41 08
Fax: +41-31-631 37 37
E-mail: christiane.albrecht@ibmm.unibe.ch

A running title of up to 50 characters:

Materno-fetal amino acid transfer across gradient

Materno-fetal amino acid transfer across gradient

Abstract
The developing fetus is highly vulnerable to imbalances in the supply of essential amino acids (AA). Transplacental AA transfer depends on complex interactions between accumulative transporters, exchangers and facilitators, which maintain both intra-extracellular and materno-fetal substrate gradients. We determined physiological AA gradients between maternal and fetal blood and assessed their importance by studying maternal-fetal leucine transfer in human trophoblasts. Maternal-venous and corresponding fetal-arterial/fetal-venous sera were collected from 22 healthy patients at *partum*. The acquisition of the full AA spectra in serum was performed by ion exchange chromatography. Physiological materno-fetal AA levels were evaluated using paired two-way ANOVA with Tukey's correction. AA concentrations and gradients were tested for associations with anthropometric data by Spearman correlation analysis. Functional effects of a physiological leucine gradient versus equimolar concentrations were tested in BeWo cells using ^{3}[H]-L-leucine in conventional and Transwell®-based uptake and transfer experiments. The LAT1/SLC7A5-specific inhibitor JPH203 was used to evaluate LAT1-transporter-mediated leucine transport. Maternal AA concentrations correlated with preconceptional and maternal weights at *partum*. Interestingly, low materno-fetal AA gradients were associated with maternal weight, BMI and gestational weight gain. Leucine uptake was promoted by increased extracellular substrate concentrations. Materno-fetal leucine transfer was significantly increased against a 137µM leucine gradient demonstrating that transplacental leucine transport is stimulated by a counter-directed gradient. Moreover, leucine transfer was inhibited by 10µM JPH203 confirming that Leu transport across the placental barrier is LAT1-dependent. This study demonstrates a currently underestimated effect of transplacental AA gradients on efficient leucine transfer which could severely affect fetal development.

Keywords
Amino acid gradients, materno-fetal amino acid concentrations, gestational weight gain, preconceptional weight, Transwell, LAT1

Highlights

- Selected maternal amino acid concentrations are associated with maternal weight.
- Selected materno-fetal amino acid gradients correlate with gestational weight gain.
- Fetal veno-arterial differences reveal varying states of amino acid homeostasis.
- Materno-fetal leucine transfer is induced against a counter-directed gradient.

Funding
This study was supported by the Swiss National Centre of Competence in Research, NCCR TransCure, University of Bern, Switzerland, and the Stiftung Lindenhof. J.Z. was supported by the Graduate School for Cellular and Biomedical Sciences (GCB), University of Bern, Switzerland.

Graphical abstract

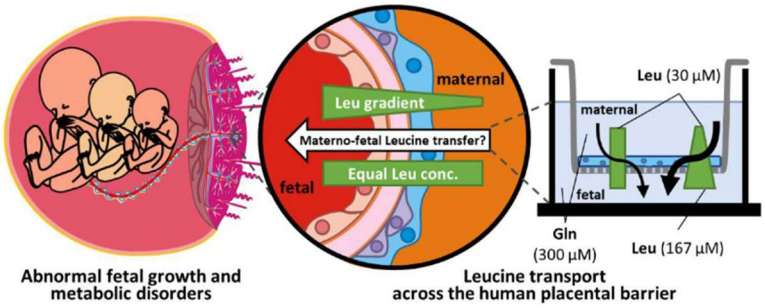

1 Introduction

Appropriate *in utero* fetal growth is largely dictated by the availability of amino acids (AA) in the maternal circulation, which is ensured during pregnancy by the capacity of the placenta to transfer AA from the maternal into the fetal circulation [1,2]. Since all proteogenic AA are higher concentrated in the fetal circulation [3,4], they have to be actively transferred from the maternal to the fetal blood against counter-directed feto-maternal gradients. Already in 1973 Hill et al. demonstrated in placenta perfusion experiments in guinea pigs that materno-fetal leucine (Leu) transfer was two-times increased after application of feto-maternal gradients [5]. However, extrapolation of results from animal experiments to humans must be done with caution, specifically as the structure and anatomy of the human placenta is quite unique among mammals [6]. There are few studies that investigated materno-fetal AA transfer under different physiological and pathological conditions *in vivo*. This was performed by measuring AA concentration differences between fetal arterial and fetal venous sera obtained from umbilical cord blood and/or from the uteroplacental unit in the maternal circulation [7–14]. Such observational correlation studies revealed interesting associations by comparing paired AA concentrations in maternal radial artery and uterine vein with fetal umbilical vein and artery sides with each other [15]. However, potential relationships between AA gradients and demographic data such as maternal constitution or fetal growth have not been reported yet. Computational modelling of AA transfer demonstrated the importance and interrelation of AA gradients by considering separate maternal and fetal compartments and specific kinetic properties of accumulative and exchanging AA transporter systems [16]. However, to our knowledge, no human trophoblast studies have assessed the functional effect of counter-directed AA gradients on transplacental AA transfer *in vitro*. To validate system L transporter dependent Leu uptake and particularly to determine the role of LAT1 in this context, the LAT1-specific inhibitor JPH203 was previously synthesized and applied [17,18]. This compound as well as other small molecule inhibitors targeting SLC7 transporters proved also useful in the context of placental physiology. Hence, using these inhibitors we recently determined the fraction of Leu that is taken up by human trophoblasts under Na^+-free conditions [19].

In this study we hypothesized that the maternal body condition is associated with the formation of materno-fetal AA gradients and that this affects the placental uptake and transplacental transfer of AA. To investigate these hypotheses, we aimed i) to determine the concentrations of all proteogenic AA in maternal vein, fetal artery and fetal vein samples in healthy human pregnancies, ii) to investigate correlations between the obtained corresponding AA concentrations, their gradients and anthropometric data and iii) to determine the effect of

extracellular substrate concentrations and physiological AA gradients on Leu uptake and materno-fetal Leu transfer in different trophoblast cell models. These studies allow to assess the variation and relevance of transplacental AA gradients for a normal pregnancy outcome. Moreover, the obtained *in vitro* results enable conclusions on the functional relevance of materno-fetal AA gradients for transplacental AA transfer which has a major impact on fetal growth.

2 Materials and Methods

All chemicals and reagents were purchased from Sigma-Aldrich in Switzerland unless otherwise stated.

2.1 Serum collection of mother-baby pairs at birth

Placentae from normal healthy pregnancies (n=22) were collected after elective Caesarean section at the Division of Gynecology and Obstetrics, Lindenhofgruppe, Bern, Switzerland. The study was conducted in accordance with the Declaration of Helsinki, and the protocol was approved by the Ethics Committee of the Canton of Bern (Basec Nr. 2016-00250). Anthropometric characteristics of healthy patients donating placenta are shown in Table 1. Maternal venous (MV) and corresponding fetal venous (FV) and fetal arterial (FA) serum samples were prospectively sampled before administration of the spinal anesthesia approx. 5min prior to parturition by caesarean section. The corresponding fetal blood was sampled from placental arteries and veins within 20min after delivery. Contamination with maternal blood was impossible. After collection of the whole blood sample in a S-Monovette with clotting activator (Sarstedt Group, Nümbrecht, DE), the blood was allowed to clot for 15-30min at room temperature (RT). The clot was removed by centrifugation with 1000rcf for 10min at 4°C. The supernatants (=sera) were aliquoted and stored at -20°C upon analysis.

2.2 Profiling of free amino acids in mother-baby paired sera

The acquisition of the full amino acid spectra was carried out in serum by ion exchange chromatography. The concentrations of 20 AA were determined in the Centre of Laboratory Medicine (ISO 17025 accredited) at the University Hospital of Bern by ion exchange chromatography with post column derivatization with Ninhydrin on an automated Biochrom 30+ Series amino acid analyser (Biochrom, Cambridge, UK). Norleucin (5.24mg/100mL sulfosalicylic acid) was used as internal standard and calibration was obtained using amino acid standards from Laborservice Onken (Art. Nr. 5.403.151) and Sigma (Art. Nr. A-9906). The inter-assay coefficient of variation of the analysis was 7%.

2.3 Leucine uptake assay

BeWo cells were cultured in complete growth medium (DMEM-lowGlucose, Gibco, Paisley, UK) containing 10% fetal bovine serum (Seraglob, Schaffhausen, Switzerland) and 1x antibiotic-antimycotic (Gibco, Grand Island, NY, USA). Cells were seeded at a density of 60'000 cells/well into white-walled 96-well plate flat clear bottom (Corning® #3610) to obtain a confluent cell culture overnight. Unstimulated BeWo cells (BeWo-CTB) were investigated after overnight culturing. To obtain the syncytiotrophoblast (BeWo-STB) stage, BeWo cells were cultured overnight followed by stimulation with 100µM forskolin for 48h as described in [20].

The recently published Leu uptake method [18] was adapted to test the effect of different substrate concentrations on Leu uptake kinetics. In brief, cultured BeWo cells were washed 3-times after culturing according to their assigned differentiation stage with pre-warmed Na^+-free Hank's buffer (125mM choline chloride, 25mM HEPES, 4.8mM KCl, 1.2mM $MgSO_4$, 1.2mM KH_2PO_4, 1.3mM $CaCl_2$, 5.6mM glucose, adjusted pH to 7.4). After equilibration by incubation in the same buffer at 37°C for 7min in a humidified incubator under 5% CO_2 atmosphere, the

cells were incubated for 3min with pre-warmed Na^+-free Hank's buffer containing different L-Leu concentrations ranging from 0.7-350µM including 1µCi/mL radioactive L-[3,4,5-^{3}H(N)]-leucine (PerkinElmer, Waltham, MA, USA). Leu uptake was stopped by three washing steps with ice-cold Na^+-free Hank's buffer to remove the substrate. Cells were lysed by intense shaking for 1.5h in MicroScint™-20 (PerkinElmer, Waltham, MA, USA). Finally, Leu uptake was quantified by a TopCount® NXT™ Scintillation and Luminescence Counter (PerkinElmer, Waltham, MA, USA).

2.4 Cellular leucine uptake

To verify the cellular Leu uptake in the assay described in 2.3 and to identify the involved AA transporter(s), the LAT1-specific inhibitor JPH203 was applied in a concentration range of 0.0316-31.6 µM. JPH203 was synthesized according to a previously published protocol [17] and dissolved in dimethyl sulfoxide (DMSO, Merck). The analytical data for JPH203 were recently published [18].

2.5 Leucine transfer across trophoblasts

2.5.1 Seeding and experiment preparation

For Leu transfer experiments BeWo cells were seeded at a density of 100'000 cells/cm^2 onto permeable membranes with 0.4µm pore size kept in 12-well inserts from the Transwell® system (Corning Inc., Corning, NY, USA). Cells were cultured in DMEM-lowGlucose at 37°C with 5% CO_2 atmosphere for 7 to 14 days.

2.5.2 Monitoring trophoblast cell layer formation

Before starting the transfer experiment the gradually increasing tightness of the trophoblast cell layer and the corresponding reduction of permeability was monitored by measuring transepithelial electrical resistance (TEER) and passive diffusion, respectively, as reported before [21]. TEER and the cellular capacitance (C_{cl}) were measured and analyzed using the cellZscope system (nanoAnalytics, Münster, Germany) according to manufacturer's instructions. The apparent permeability coefficient (Papp) was calculated by measuring the rates of passive transfer of the paracellular pathway marker Lucifer yellow (LY) as previously described [22].

2.5.3 Materno-fetal leucine transfer assay

Trophoblast cell layers with verified tightness were selected after 7 days of culturing on Transwell® membranes and randomly assigned for Leu transfer time courses and substrate gradient experiments. The cultured inserts and an insert without cells (non-cell control) were placed in 12-well plates and 3-times washed with pre-warmed Na^+-free Hank's buffer. The cells were equilibrated in Hank's buffer for 30min at 37°C before use. Leu transfer from the upper (maternal) toward the lower (fetal) compartment was started by simultaneously replacing the buffer in both compartments. The buffer in the lower chamber was replaced with Na^+-free Hank's containing either 30 or 167µM unlabeled L-Leu and 300µM glutamine. Then the buffer in the maternal compartment was replaced with Hank's containing 30µM Leu including 1µCi/mL ^{3}H-labeled Leu and 300µM glutamine. Time points from 5min to 6h hours were selected for sampling 50µL medium from the donating (maternal) and receiving (fetal) compartment. At the end of the transfer experiment, all membranes were washed twice with DPBS and sampled as well. The medium and membrane samples including negative controls (non-cell controls) were collected in 3mL of scintillation cocktail (Zinsser Analytic, Frankfurt,

Germany) and radioactivity was quantified using a Tri-carb 2100TR Liquid Scintillation Counter (PerkinElmer, Waltham, US).

2.6 Statistical Analysis

Anthropometric data were statistically characterized by mean and standard deviation (SD). Statistical analyses comparing maternal-vein, fetal-artery and fetal-vein AA profiles were performed using paired two-way ANOVA with Tukey's correction. Spearman correlation was performed to test associations between physiological AA levels and anthropometric values (Table 1). Differences between various uptake and transfer conditions were tested by Sidak's multiple comparisons test. A difference with a probability value $p<0.05$ was considered as statistically significant.

3 Results

3.1 Determination of maternal and fetal amino acid spectra

Transplacental AA gradients were determined for all proteogenic AA and defined as difference between AA concentrations in mother-baby paired serum samples. MV serum and the corresponding FV and FA serum samples were prospectively collected from 22 clinically unsuspicious patients by Caesarian section at term (Table 1). There was no significant difference between female and male babies. The concentrations of the 20 standard proteinogenic AA are shown in Figure 1 and Table 2. Brackets represent expected physiological ranges of AA concentrations in adults (>15 years) and newborns (0-1 month), respectively, based on internally measured standard values at the University Hospital Bern. Particularly essential AA like Thr, Val, Trp and Lys and some conditionally essential AA such as Gly and Tyr were significantly higher concentrated in both fetal FA and FV compartments compared to MV. There was no difference between maternal and-fetal concentrations for Cys and Asn. Ser and Gln showed significant greater concentrations in FA compared to MV. For Cys all quantitative measurements (4µM in FV and 5µM in MV) were clearly below the expected range of 25-80µM for FV and 20-85µM for MV. Due to the discrepancy with published data [10,23,24], Cys concentrations and Cys-related gradients were excluded from the following correlation analysis.

3.2 Individual and amino acid-specific differences in materno-fetal gradients

The difference between FA and MV was defined as AA gradient relevant for materno-fetal transfer. We found significant FA-MV differences for the small AA Gly, the nucleophilic AA Ser and Thr, the hydrophobic AA Val, and the aromatic AA Tyr and Trp. Similar differences were also found when comparing the FA-MV against FV-MV gradients. Of note, large differences were found for essential AA. The non-essential AA Ser, Asp and Gln additionally showed highly negative veno-arterial (FV-FA) differences (Table 2), i.e. they disappear from the fetal circulation and are transported across the placenta into the maternal blood [15]. Although there were negative means of FV-FA differences for all AA except Trp (Table 2), 10 out of 22 individuals showed predominantly positive FV-FA differences (Figure 2). Thus, the placentae included in our studies can be classified into either accumulative (positive FV-FA difference; 45.5%) or secretive (negative FV-FA difference; 54.5%) tissues.

3.3 Amino acid concentrations and materno-fetal gradients correlate with anthropometric data

Within our cohort of healthy placenta donors we performed correlation analysis between AA concentrations/ AA gradients and anthropometric parameters characterizing the body condition of either the mother or the newborn (Table 1). The summary of all significant Spearman correlations is shown in Table 3, negative correlations are marked with (↓). In summary, 95% of all significant Spearman correlations between the sera from different compartments and

clinical parameters concerning maternal body condition or fetal growth were positively associated. Interestingly, 34 out of 62 (55%) significant positive Spearman correlations were associated with AA concentrations in the MV, which generally are affected by the diet and fasting time of the mother. In contrast, all negative correlations were associated with fetal AA concentrations. 56% of all and 59% of MV correlations, respectively, were associations between LAT1 substrates and anthropometric parameters. Based on the latter results, we focused in this study specially on LAT1 substrates (highlighted green in Table 3).

3.3.1 Associations between serum amino acid concentrations and maternal weight

The correlations between clinical data with AA concentrations in maternal and fetal sera, but also with materno-fetal gradients are listed in Table 3. There were positive correlations between preconceptional weights and the MV concentrations of Ala, Val, Leu, Ile, Pro, Asp and Glu (Table 3). Moreover, preconceptional weights correlated with FA concentrations for Val and Pro, and with FV concentrations of Ile. All MV concentrations correlating with preconceptional weights correlated also with maternal weight at *partum*. In addition, Met, Phe, Tyr, Gln and His were associated with maternal weight at *partum* (Table 3). Figure 3 shows Spearman correlations with maternal weights and BMI as scatter plot for Leu, which seem to persist throughout pregnancy. The group of hydrophobic AA and LAT1 substrates Val, Leu and Ile showed very similar correlation patterns as Leu. Maternal weight gain, which combines the parameters preconceptional weight and weight *at partum*, showed significant correlations exclusively with fetal concentrations of Gly Ala and Trp (Table 3). The similar trend between preconceptional weights and weights *at partum* was also found between preconceptional BMI and BMI *at partum*.

3.3.2 Associations of AA gradients with maternal and placental weight

AA gradients across the materno-fetal barrier were calculated as difference between MV and FV or FA. Positive correlations were detected between materno-fetal AA gradients and maternal weights for Pro, Phe and Tyr before conception and Tyr *at partum* (Table 3). Furthermore, Glu MV-FV correlated with BMI at *partum*. A negative correlation was found between the MV-FV gradient for Gly and maternal weight gain (Table 3). The MV-FV gradients of the three essential aromatic AA Phe, Tyr and Trp were correlated with different maternal weight parameters like preconceptional weight, weight at *partum* and weight gain (see Figure 4A,B,C for Tyr and Trp).

MV-FV gradients of the non-essential small AA Gly and Ala, but also of the two acidic AA Asp and Glu were positively associated with placental weight (Figure 4D, Table 3). Interestingly, fetal birth weight was largely independent of the AA concentrations and gradients with few exceptions (Table 3).

3.4 Increased extracellular leucine levels facilitate leucine uptake into trophoblast cells

The effect of different extracellular AA concentrations on system L mediated uptake was characterized using Na^+-free Leu uptake assay on the BeWo trophoblast model. Two different extracellular Leu concentrations were applied to test the effect of AA gradients on Leu uptake efficiency into the choriocarcinoma cell line BeWo and the colon carcinoma cell line HT-29. A Leu concentration in the upper clinical range (167µM) was selected and compared to a lower concentration of 30µM Leu. 30µM Leu corresponds to approx. 1/3 of the mean Leu-MV concentration. As shown in Figure 5A, increased extracellular Leu levels facilitated uptake of Leu into undifferentiated BeWo-CTB from 15.9 to 47.3nmol/mg protein (mean difference and standard error = 31.4 ± 3.5nmol/mg protein), and into differentiated BeWo-STB from 30.7 to 103.4nmol/mg protein (mean difference and standard error = 72.8 ± 8.5nmol/mg protein). In comparison, the uptake into HT-29 cells increased from 32.7 to 66.2nmol/mg protein (mean

difference and standard error = 33.5 ± 5.0nmol/mg protein). Therefore, for trophoblasts a 2-times higher basic Leu uptake rate was found in BeWo-STB compared to BeWo-CTB. While comparable Leu uptake capacity was observed in BeWo-STB and HT-29 cells under low substrate conditions, a clearly enhanced uptake capacity of trophoblasts was detected under high extracellular Leu concentrations (Figure 5A). The LAT1-specific inhibitor JPH203 was applied to assure that Leu uptake in Na^+-free conditions was mediated by LAT1. LAT1-specific inhibition in a dose-response experiment resulted in a dramatic reduction of Leu uptake into both BeWo-CTB with 85% and into BeWo-STB 76% reduction with IC_{50} values in the nanomolar range (Figure 5B), suggesting an only minor involvement of other system L transporters like LAT2 at exceeding Leu concentrations. These results indicate a primarily LAT1-mediated Leu uptake process in trophoblasts with high dependency on extracellular substrate availability.

3.5 Counter-directed gradient promotes leucine transfer across the materno-fetal barrier

The functional effect of physiological counter-directed AA gradients was tested on an *in vitro* Transwell system mimicking the placental cellular barrier. Herein we compared materno-fetal Leu transfer in a setup of equimolar Leu concentrations on both sides with physiological materno-fetal AA gradients derived from the analyses of mother-baby paired serum samples. Thus, the materno-fetal Leu transfer was measured by applying either 30µM Leu in the upper (maternal) and lower (fetal) compartment (materno-fetal Leu gradient = 0µM) or by applying a counter-directed gradient with 30µM Leu in the maternal and 167µM Leu in the fetal compartment (materno-fetal Leu gradient = 137µM). Figure 6A shows the experimental setup and the concentration changes of radio-labeled Leu measured in the upper (Maternal venous (Mv)) compartment and in the receiving lower (Fetal arterial (Fa)) compartment from a representative Transwell® experiment over 6 h. The application of a counter-directed Leu gradient of 137µM significantly stimulated the materno-fetal transfer of Leu by on average 47.2% within the last three time points (4 – 6h). Moreover, Leu transfer was significantly reduced by adding the LAT-specific inhibitor JPH203 (10µM; Figure 6A, dashed lines), indicating that mainly LAT1-mediated Leu transfer across the materno-fetal barrier occurs. Within three successively and independently performed Transwell® experiments (n=3), there were significant differences detected from 120min transfer time onwards (Suppl. Figure 1). To investigate whether Leu uptake at the apical side or efflux at the basal side is the limiting step in Leu transfer, we calculated (Figure 6B) and measured (Figure 6C) the intracellular retainment of Leu within the barrier-forming trophoblasts. Figure 6B shows the calculated intracellular Leu content (difference between the applied total dose and the sum of the two Leu concentrations measured in the Mv and Fa compartment), while Figure 6C depicts the results from the intracellular Leu content measured at the end of the experiment. Independent of the type of analysis, no significant difference in intracellular Leu retainment was found between equimolar Leu concentrations and a counter-directed Leu gradient suggesting that Leu uptake rather than efflux towards the fetal compartment is the limiting step in Leu transfer.

4 Discussion

Since studies in the 1970s have shown that concentrations of most proteogenic AA are higher in the fetal compared to the maternal circulation, there is the central dogma that most AA are actively transported across the placenta against a counter-directed gradient [3]. We hypothesized that counter-directed materno-fetal AA gradients have an impact on the function of AA transporters such as LAT1 and thereby affect transplacental AA supply. Thus, the maintenance of AA gradients between the maternal and fetal circulation is essential for a normal course of pregnancy and for adequate fetal growth. To test this hypothesis, we measured the concentrations of the 20 proteogenic AA in sera from maternal vein, fetal artery and fetal vein

at *partum* and analyzed the correlation between AA concentrations and calculated materno-fetal gradients with anthropometric data in healthy pregnancies. Moreover, we investigated the influence of extracellular AA concentrations on the functional level by assessing exchanger-mediated Leu uptake in conventional cell culture of HT-29 and BeWo cells at two differentiation stages. Finally, we determined the direct effect of a materno-fetal gradient on functional AA transfer in BeWo cells using the Transwell® system.

4.1 Variation of maternal and fetal AA concentrations

In agreement with literature [7–14] we detected higher AA concentrations in the fetal as compared to the maternal circulation. Within our cohort we found in materno-fetal paired analysis significant differences in the AA concentration especially for essential or conditionally essential AA such as Thr, Val, Trp, Lys, Gly and Tyr (Table.2). Although there are 15 different AA transport systems characterized in the human placenta and several AA are transported by different systems [25], half of the AA showing significant differences are preferentially substrates for system L transporters, particularly LAT1.

The placenta is a metabolically active organ and interorgan exchange with fetal liver for non-essential AA like Gly to Ser and Gln to Glu was demonstrated in temporal AA interconversion characterization of sheep pregnancy using stable isotope methods [26,27]. Therefore, the comparison between maternal and fetal AA concentrations allows conclusions on materno-fetal transfer, but without including AA metabolism this can be misleading [28]. It has been shown that the nutritional stage of the mother affects the use of AA as fuels by the placenta during pregnancy [29]. Due to standardization of sampling and selection of patients that delivered exclusively by cesarean section, we do not expect significant effects of fasting in this study. For Cys unexpectedly low concentrations were detected (Figure 1, Table 2), and the reason for this phenomenon is unclear. Increased preanalytical degradation of AA or analytical problems with AA detection can be largely excluded, due to stable measurements of other AA, measurement repetitions and validity of internal controls. On the other side, there could be metabolic reasons for low Cys levels in late pregnancy. Sulfur-containing AA can be interconverted by transsulfuration (Met→Cys) or transmethylation (Cys→Met). Due to the absence of transsulfuration activity in the fetal liver and high transmethylation activity for growth and cell proliferation, Cys consumption increases and becomes essential for the fetus in the 3rd trimester [30,31]. Cys is also required for the synthesis of various proteins and glutathione. Therefore, high amounts of Cys are consumed and must be transported across the placenta particularly in the 3rd trimester, when fetal growth, AA metabolism and oxidative stress reach a maximum [32,33]. However, due to the discrepancies of our measured Cys concentrations with previously published data, Cys was excluded from the subsequent correlation studies.

4.2 Fetal veno-arterial differences reveal different phases of placental amino acid homeostasis

There is a high heterogeneity in the literature regarding the predominance of positive or negative veno-arterial differences in the fetal blood. Few studies showed positive FV-FA differences for most AA in healthy pregnancies [10], others larger or smaller proportions of negative FV-FA differences [12,23,24,34–36]. Cetin et al. found positive FV-FA AA concentration differences for most essential AA in normal fetuses, but less in intrauterine growth restriction (IUGR) [10]. Furthermore, negative FV-FA differences were also interpreted as sign for fetal maturation by comparing AA concentrations in term and preterm [23]. Due to the paired analysis mode, veno-arterial (FV-FA) differences of the 22 patients in this study cohort (Table 1) were individually analyzed. Although the means of FV-FA differences for all AA were negative, 45% of analyzed cases showed a clearly positive FV-FA difference for most AA (Figure 2). Therefore, the negative mean FV-FA differences as listed in Table 2 is based on a highly heterogenic group of placentae being either in accumulative (positive FV-FA difference) or secretory (negative FV-FA difference) mode. 16 out of 22 placentae (73%)

showed either accumulation or secretion of most AA into placenta towards the maternal circulation. Since fetal growth is dependent on AA supply throughout the pregnancy, the placenta likely alternates throughout pregnancy between AA accumulation and secretion modes. Total AA concentrations in cattle are following a circadian rhythm depending on growth hormone levels and food intake [37]. A circadian effect on AA concentrations has also been found in human young males where the concentrations of 16 AA varied throughout the day [38]. Another study reported that the circadian changes of AA concentrations in pregnant women were smaller than in non-pregnant women. Herein the authors observed changes of plasma glucose, free fatty acids and insulin levels suggesting a daily switching rhythm between anabolic and catabolic stages in pregnancy by [39]. In summary, the different phases of placental AA homeostasis in individual pregnancies suggest a temporary switch between accumulation and secretion phases in placental AA transfer, which should be confirmed by *in vivo* determination of FV-FA differences. This could be achieved by using *in utero* cordocentesis allowing a relatively unstressed sampling unaffected by parturition and at different gestational ages [4,9].

4.3 Association between maternal/fetal amino acid concentrations and anthropometric data

To estimate the relevance of AA concentrations in different maternal and fetal compartments, and to investigate the importance of materno-fetal gradients, Spearman correlations with fetal and maternal anthropometric values were performed within our healthy study cohort. The results of our analyses complement data from a previous study that performed correlation analysis between AA concentrations among different maternal and fetal compartments [15].

4.3.1 Maternal amino acid concentrations correlate with maternal weight and BMI

Exchanger-mediated AA transport, including the transfer of large neutral AA by system L transporters, depends on the availability of their exchange partner [40]. The transfer of essential AA can be affected, if AA concentration gradients across the placental barrier are changed [5]. To investigate the potential impact of maternal, fetal and placental parameters, AA concentrations were tested for correlations with all available anthropometric values (Table 1). Remarkably, maternal (MV) and fetal (FA and FV) concentrations of essential AA such as the LAT1- substrates Val, Leu, Ile, Met, Phe, Tyr and His were positively correlated with maternal weights and BMI both before pregnancy and at *partum* (Figure 3 and Table 3). On the other side, the fetal AA levels of Val, Ile and Pro seem to be more dependent on the mother's preconceptional weight rather than on the maternal weight at the end of pregnancy. Similarly, fetal AA concentrations of Val, Leu Ile, and Pro were correlated more often with preconceptional BMI than with BMI at *partum*. It has been shown that preconceptional body weight has a lasting impact on gestational weight gain, fetal growth and contribute to develop obesity postpartum [41]. Obese women are predisposed to get babies that are large for gestational age, even when they show the same gestational weight gain as non-obese women [42,43]. Therefore, high AA levels before pregnancy tend to stay high throughout gestation and influence fetal AA levels at term. These results are in line with observations during temporal maternal infusions with increasing AA concentrations. These infusions resulted in a temporal fast increase of maternal AA concentrations and enhanced umbilical AA uptake in humans [44] and sheep [45], but increased MV concentrations were ineffective after prolonged AA infusion in pregnant sheep [45]. This inhibitory effect on fetal AA uptake were observed to a greater extent if large neutral AA were infused [46]. On the other hand, placental AA supply is highly vulnerable to maternal undernutrition. This was for instance detected as a consequence of the Dutch famine in the second world war, when newborns were growth restricted and showed an increased incidence of obesity and metabolic and cardiovascular disease in adulthood [47].

4.3.2 Amino acid gradients are associated with maternal and placental weight

Materno-fetal AA gradients of Ile, Pro, Phe, Tyr, and His correlated with anthropometric data characterizing the weight and the nutritional stage of subjects, respectively. Of note, since AA levels are generally higher in the fetal as compared to the maternal circulation, those AA gradients are negative values and represent counter-directed materno-fetal gradients. The positive correlation between counter-directed materno-fetal gradients and anthropometric data indicates that increasing maternal AA levels lead to less-negative, smaller materno-fetal gradients. In other words, the heavier the mothers were before pregnancy or the more weight they gained, the smaller (more positive) the counter-directed gradients across the placental barrier were. Interestingly, the gradient of Gly was negatively correlated with gestational weight gain. Although there is a high Gly demand for fetal growth and consequently the Gly concentration in the fetal circulation is high, there is compared to Leu very low materno-fetal transport of Gly [48], probably due to Ser-Gly transformation through hydroxymethyltransferase activity in the fetus [49]. The association between Gly gradients and weight gain values suggest an increased materno-fetal Gly transport or fetal Ser-Gly transformation, if the weight gain is high. Excess or lack of gestational weight gain was related to various pregnancy complications and cardiovascular diseases and obesity in the offspring [50,51]. Although a recent multi-cohort meta-analysis associated gestational weight gain with the increased risk for preeclampsia, gestational diabetes, preterm birth and others, weight gain remains a multifactorial parameter depending on maternal fat accumulation, fluid expansion, and the growth of fetus, placenta and uterus [52]. Of note, both gestational weight gain and maternal weight represent a modifiable risk factor that is considered in prenatal counseling and could help to prevent adverse outcome including gestational diabetes [53,54].

Additionally, a relationship was found between placental weight and counter-directed AA gradients of the non-essential AA Gly, Ala, Asp and Glu (Figure 4D, Table 3). While Gly and Ala are transported by different transport systems such as system A, GLY or ASC, and are converted or metabolized by the placenta [25,55], the anionic AA Glu and Asp are synthesized by fetal tissue and have no net transfer across the perfused human placenta [56,57]. In a correlation study on small for gestational age babies, system A transporter activity was compared to a variety of anthropometric parameters. It was found that system A activity positively correlated with fetal proportions like skin-fold thicknesses and placental weight [58]. Therefore, the combination of system A transporter activity and smaller Gly and Ala gradients could represent a placental adaption to produce and supply more substrate towards the fetus [58].

4.4 Extracellular amino acid levels affect leucine uptake into differentiated trophoblasts

In the placenta there are accumulative transporters, exchangers and facilitators forming a complex placental amino acid transport system, which is dependent of intracellular versus extracellular, maternal versus fetal, and fetal versus maternal substrate gradients. The complex network of these transport systems enables an efficient materno-fetal transfer of essential AA against a counter-directed gradient [25,59]. Extensive computational modeling suggests beside active transport also facilitated transport across the BM, which is highly dependent of AA gradients across the BM [60–62]. However, if and how counter-directed AA gradients affect the LAT1-dominated exchanger-mediated materno-fetal transfer of an essential AA like Leu, has not been investigated yet. In a first step, we examined whether the Leu uptake capacity in BeWo cells is sensitive to increased extracellular Leu levels. As expected, extracellular Leu levels in the upper clinical range (167µM) increased Na^+-independent uptake of Leu into the trophoblasts and into colon carcinoma cells (HT-29). The choriocarcinoma cell line BeWo (clone b30) which differentiates upon cyclic adenosine monophosphate (cAMP) stimulation

and further develops a polarized trophoblast monolayer [63], has been validated with *ex vivo* placenta perfusion [64,65] and selected to explore transport mechanisms *in vitro* before [66].

Next, we investigated, whether the differentiation stage of trophoblasts affects the uptake capacity for Leu. Indeed, differentiated BeWo-STB showed two times higher Leu uptake than undifferentiated BeWo-CTB or HT-29 cells (Figure 5A). Since all uptake assays were performed within 3 min, the increase of Leu uptake cannot be explained by expressional changes of Leu transporters. Furthermore, the inhibition experiment with the LAT1-specific inhibitor JPH203 [17] demonstrated that Leu uptake in trophoblasts is predominantly LAT1-dependent. Meier et al. showed a 1:1 exchange stoichiometry of heteromeric LAT1 and LAT2 transporter and substrate selectivity allowing the exchange of one extracellular large neutral AA against a non-essential intracellular AA using the Xenopus expression system [67]. The underlying mechanisms of trophoblasts to further increase Leu uptake upon differentiation without changing the concentrations of exchange partners are not clear yet. In human pregnancies, maternal-fetal transfer rates have been investigated *in vivo* by stable isotope infusions into the maternal circulation followed by fetal blood sampling. The materno-fetal transfer rate of nonessential AA like Gly was significantly lower than for essential amino acids like Leu [48].

4.5 Effect of counter-directed amino acid gradients on materno-fetal leucine transfer

To test whether different extracellular AA concentrations have an effect on Leu transfer across the materno-fetal barrier, we conducted Leu transport experiments using the Transwell® system. Hereby we compared Leu transfer under equimolar Leu concentrations in the maternal and in the fetal compartment against a counter-directed Leu gradient (Figure 6). To our knowledge this is the first time, that the effect of a physiological counter-directed AA gradient was functionally assessed *in vitro*. Although the applied gradient created a strong fetal to maternal directed transport pressure, we observed higher materno-fetal transfer rates in presence of the counter-directed Leu gradient as compared equimolar Leu concentrations. Additionally, the significant reduction of Leu transfer by the LAT1-specific inhibitor JPH203 [17] underlines the importance of LAT1 in materno-fetal transport of Leu, but likely also affects placental transport of other LAT1 substrates like Ile, Phe, Met, Tyr, His, Trp, Val, Cys and Thr [68]. At the end of the experiment no intracellular Leu retainment was detected, independent if the intracellular Leu content was calculated or measured, suggesting Leu uptake rather than efflux towards the fetal compartment as limiting step (Figure 6B/C). Intracellular Leu retainment would indicate fetal efflux as transfer limiting step, as shown in Leu uptake studies using LAT1/LAT2 small molecule inhibitors (Zaugg et al. unpublished). The asymmetry of the transplacental AA flux is favored by rapid uptake from the maternal circulation and transfer towards the fetus. It has been shown that AA transfer towards the fetal side is more rapid than in the reverse direction [69]. The importance of effective placental AA transport systems rather than maternal AA concentrations as crucial factor for fetal growth is supported by findings of Bajora and coworkers [13]. They observed that in monochorionic twins from which one was growth retarded, the concentrations of Val, Leu, Ile, Phe, and Arg were only reduced in the growth restricted twin, but normal in the co-twin not suffering from IUGR [13]. Furthermore, counter-directed AA gradients might play a crucial role after their establishment at the beginning of the second trimester of human pregnancy and before starting the phase of biggest fetal growth [70]. Based on these results we suggest the incorporation of transplacental AA gradients relevant for fetal development in computational modeling based on placental perfusion studies [61,71].

4.6 Conclusion

Accumulative transporters, exchangers and facilitators form a complex placental AA transport system, which is dependent of intra-extracellular and materno-fetal substrate gradients enabling an efficient materno-fetal transfer of essential AA against a counter-directed gradient [25]. Particularly maternal AA concentrations of LAT1-specific substrates were correlating with

maternal weights and BMI both before pregnancy and at term, suggesting that the preconceptional nutritional stage affects maternal AA levels and the formation of transplacental gradients throughout gestation. We could show the first time that there is a relation between materno-fetal gradients of various LAT1 substrates and important clinical parameters such as preconceptional and at *partum* weight or gestational weight gain. Furthermore, the obtained results suggest an association between placental growth and the presence or maintenance of counter-directed AA gradients. Finally, the relevance of appropriate AA gradients was demonstrated in Leu transfer experiments across the materno-fetal barrier in the Transwell® system, which showed increased Leu transfer against a counter-directed gradient. This study demonstrates a so far underestimated impact of transplacental AA gradients in human pregnancy which could affect pregnancy outcome and may play a role in fetal development.

Acknowledgments

This study was supported by the Swiss National Centre of Competence in Research, NCCR TransCure, University of Bern, Switzerland, the Swiss National Science Foundation (SNSF) and the Lindenhof Foundation. J.Z. was supported by the Graduate School for Cellular and Biomedical Sciences (GCB), University of Bern, Switzerland. We are grateful to the mothers who participated in these studies, and to the midwives at the Lindenhof Hospital in Bern, for their skillful help and patient care. The authors thank Karl-Heinz Altmann and Julien Graff for synthesizing and providing JHP203. Dr. Alan L. Schwartz, Washington University School of Medicine, USA is acknowledged for donating the BeWo cells (b30 clone). The authors are grateful to Michael Lüthi, Regina Berchtold, Fabian Ziegler and Martyna Kazimierczak, for their help and support in the lab.

Author Contributions

J.Z. designed the experiments, performed cell culture, *in vitro* experiments and data analysis, wrote the manuscript, and reviewed and approved the article. F.Z. performed the Leu uptake studies and contributed significantly to monitoring and execution of the Transwell® experiments. J-M.N. was organizing the amino acid quantification and discussed the data. R.M-H. was responsible for the clinical recruitment of patients and placenta donations. C.A. developed the study concept, discussed the data, reviewed and approved the article and is the guarantor of this work taking responsibility for the integrity of the data and the accuracy of the data analysis.

References

[1] Battaglia FC, Meschia G. Fetal nutrition. Annu Rev Nutr 1988;8:43–61. doi:10.1016/S0271-5317(05)80493-2.

[2] Vaughan OR, Rosario FJ, Powell TL, Jansson T. Regulation of Placental Amino Acid Transport and Fetal Growth. vol. 145. 1st ed. Elsevier Inc.; 2017. doi:10.1016/bs.pmbts.2016.12.008.

[3] Philipps AF, Holzman IR, Teng C, Battaglia FC. Tissue concentrations of free amino acids in term human placentas. Am J Obstet Gynecol 1978;131:881–7. doi:10.1016/S0002-9378(16)33136-2.

[4] Cetin I, Corbetta C, Sereni LP, Marconi AM, Bozzetti P, Pardi G, et al. Umbilical amino acid concentrations in normal and growth-retarded fetuses sampled in utero by cordocentesis. Am J Obstet Gynecol 1990;162:253–61. doi:10.1016/0002-9378(90)90860-A.

[5] Hill PMM, Young M. Net placental transfer of free amino acids against varying concentrations. J Physiol 1973;235:409–22.

[6] Schmidt A, Morales-Prieto DM, Pastuschek J, Fröhlich K, Markert UR. Only humans have human placentas: Molecular differences between mice and humans. J Reprod Immunol 2015;108:65–71. doi:10.1016/j.jri.2015.03.001.

[7] Pohlandt F. Plasma amino acid concentrations in umbilical cord vein and artery of newborn infants after elective cesarean section or spontaneous delivery 1978;92:617–23.

[8] Malinow MR, Rajkovic A, Duell PB, Hess DL, Upson BM. The relationship between maternal and neonatal umbilical cord plasma homocyst(e)ine suggests a potential role for maternal homocyst(e)ine in fetal metabolism. Am J Obstet Gynecol 1998;178:228–33. doi:10.1016/S0002-9378(98)80005-7.

[9] McIntosh N, Rodeck CH, Heath R. Plasma amino acids of the mid-trimester human fetus. Biol Neonate 1984;45:218–24. doi:10.1159/000242007.

[10] Cetin I, Marconi AM, Bozzetti P, Sereni LP, Corbetta C, Pardi G, et al. Imbilical amino acid concentrations in appropriate and small for gestational age infants: a biochemical difference present in utero. Am J Obstet Gynecol 1988;158:120–6. doi:10.1016/0002-9378(88)90792-2.

[11] Karsdorp VHM, van Vugt JMG, Jakobs C, Dekker GA, van Geijn HP. Amino acids, glucose and lactate concentrations in umbilical cord blood in relation to umbilical artery flow patterns. Eur J Obstet Gynecol Reprod Biol 1994;57:117–22. doi:10.1016/0028-2243(94)90053-1.

[12] Cetin I, Nobile De Santis MS, Taricco E, Radaelli T, Teng C, Ronzoni S, et al. Maternal and fetal amino acid concentrations in normal pregnancies and in pregnancies with gestational diabetes mellitus. Am J Obstet Gynecol 2005;192:610–7. doi:10.1016/j.ajog.2004.08.011.

[13] Bajoria R, Sooranna SR, Ward S, D'Souza S, Hancock M. Placental transport rather than maternal concentration of amino acids regulates fetal growth in monochorionic twins: Implications for fetal origin hypothesis. Am J Obstet Gynecol 2001;185:1239–46. doi:10.1067/mob.2001.118269.

[14] Cockburn F, Blagden A, Michie EA, Forfar JO. the Influence of Pre-Eclampsia and Diabetes Mellitus on Plasma Free Amino Acids in Maternal, Umbilical Vein and Infant Blood. BJOG An Int J Obstet Gynaecol 1971;78:215–31. doi:10.1111/j.1471-0528.1971.tb00260.x.

[15] Holm MB, Bastani NE, Holme AM, Zucknick M, Jansson T, Refsum H, et al. Uptake and release of amino acids in the fetal-placental unit in human pregnancies. PLoS One 2017;12:1–15. doi:10.1371/journal.pone.0185760.

[16] Sengers BG, Please CP, Lewis RM. Computational modelling of amino acid transfer interactions in the placenta. Exp Physiol 2010;95:829–40. doi:10.1113/expphysiol.2010.052902.

[17] Endou H, Kanai Y, Tsujihara K, Saito K. Amino acid derivatives and medicinal compositions. US 7,345,068 B2, 2008.

[18] Häfliger P, Graff J, Rubin M, Stooss A, Dettmer MS, Altmann KH, et al. The LAT1 inhibitor JPH203 reduces growth of thyroid carcinoma in a fully immunocompetent mouse model. J Exp Clin Cancer Res 2018;37. doi:10.1186/s13046-018-0907-z.

[19] Zaugg J, Huang X, Burri F, Ziegler F, Körner M, Rubin M, et al. SLC7-mediated amino acid transport across the materno-fetal barrier. Placenta 2017;57:294. doi:10.1016/j.placenta.2017.07.222.

[20] Azar C, Valentine M, Trausch-Azar J, Druley T, Nelson DM, Schwartz AL. RNA-Seq identifies genes whose proteins are transformative in the differentiation of cytotrophoblast to syncytiotrophoblast, in human primary villous and BeWo trophoblasts. Sci Rep 2018;8:1–12. doi:10.1038/s41598-018-23379-2.

[21] Liu F, Soares MJ, Audus KL, Srai KS, Elliott RM, Physiol AJ, et al. Permeability properties of monolayers of the human trophoblast cell line BeWo. Am J Physiol Cell Physiol 1997;273:1596–604. doi:10.1152/ajpcell.1997.273.5.C1596.

[22] Huang X, Lüthi M, Ontsouka EC, Kallol S, Baumann MU, Surbek D V., et al. Establishment of a confluent monolayer model with human primary trophoblast cells: novel insights into placental glucose transport. Mol Hum Reprod 2016;0:gaw018. doi:10.1093/molehr/gaw018.

[23] Hayashi S, Sanada K, Sagawa N, Yamada N, Kido K. Umbilical vein-artery differences of plasma amino acids in the last trimester of human pregnancy. Biol Neonate 1978;34:11–8. doi:10.1159/000241099.

[24] Velazquez A, Rosado A, Bernal A, Noriega L, Arévalo N. Amino acid pools in the feto-maternal system. Neonatology 1976;29:28–40. doi:10.1159/000240845.

[25] Jansson T. Amino Acid Transporters in the Human Placenta. Pediatr Res 2001;49:141–7. doi:10.1203/00006450-200102000-00003.

[26] Marconi AM, Meschia G, Sparks JW, Maria A. A comparison of amino acid arteriovenous differences across the liver and placenta of the fetal lamb. Am J Physiol - Endocrinol Metab 1989;257:909–15.

[27] Vaughn PR, Lobo C, Battaglia C, Fennessey P V, Fennessey P V, Wilkening B. Glutamine-glutamate and fetal liver exchange between placenta. Am J Physiol - Endocrinol Metab 1995;268:705–11.

[28] Cetin I. Amino acid interconversions in the fetal-placental unit: The animal model and human studies in vivo. Pediatr Res 2001;49:148–54. doi:10.1203/00006450-200102000-00004.

[29] Lemons JA, Reyman D, Schreiner RL. Fetal and Maternal Amino Acid Concentrations During Fasting in the Ewe. J Pediatr Gastroenterol Nutr 1984;3:249–55.

[30] Gaull G, Sturman JA, Räihä NCR. Development of mammalian sulfur metabolism: Absence of cystathionase in human fetal tissues. Pediatr Res 1972;6:538–47. doi:10.1203/00006450-197206000-00002.

[31] Sturman JA, Gaull G, Raiha NCR. Absence of cystathionase in human fetal liver: Is cystine essential? Science (80-) 1970;169:74–6. doi:10.1126/science.169.3940.74.

[32] Myatt L, Cui X. Oxidative stress in the placenta. Histochem Cell Biol 2004;122:369–82. doi:10.1007/s00418-004-0677-x.

[33] Casasco A, Calligaro A, Casasco M, Tateo S, Cornaglia AI, Reguzzoni M, et al. Immunohistochemical localization of lipoperoxidation products in normal human placenta. Placenta 1997;18:249–53. doi:10.1016/S0143-4004(97)80058-6.

[34] Prenton MA, Young M. Umbilical vein-artery and uterine arterio-venous plasma amino acid differences DIFFERENCES: in the human subject. BJOG An Int J Obstet Gynaecol 1969;76:404–11. doi:10.1111/j.1471-0528.1969.tb05855.x.

[35] Steingrímsdóttir T, Ronquist G, Ulmsten U. Balance of amino acids in the pregnant human uterus at term. Eur J Obstet Gynecol Reprod Biol 1993;50:197–202. doi:10.1016/0028-2243(93)90201-M.

[36] Tsuchiya H, Matsui K, Muramatsu T, Ando T, Endo F. Differences between the amino acid concentrations of umbilical venous and arterial blood. Arch Dis Child Fetal Neonatal Ed 2009;94:155–7. doi:10.1136/adc.2008.147256.

[37] Ndibualonji BB, Dehareng D, Beckers F, Eenaeme C Van, Godeau J-M. Continuous profiles and within-day variations of metabolites and hormones in cows fed diets varying in alimentary supplies before short-term feed deprivation. J Anim Sci 1995;75:3262–77.

[38] Wurtman RJ, Rose CM, Chou C, Larin FF. Daily rhythms in the concentrations of various amino acids in human plasma. N Engl J Med 1968;279:171–5.

[39] D RLPM, D BEMM, D NFM. Carbohydrate metabolism in pregnancy acids , triglycerides , cholesterol , and individual amino acids in late normal pregnancy. Am J Obstet Gynecol 1981;140:730–6. doi:10.1016/0002-9378(81)90731-6.

[40] Cleal JK, Brownbill P, Godfrey KM, Jackson JM, Jackson AA, Sibley CP, et al. Modification of

fetal plasma amino acid composition by placental amino acid exchangers in vitro. J Physiol 2007;582:871–82. doi:10.1113/jphysiol.2007.130690.

[41] Gunderson EP, Abrams B. Epidemiology of gestational weight gain and body weight changes after pregnancy. Epidemiol Rev 2000;22:261–74. doi:10.1093/oxfordjournals.epirev.a018038.

[42] Niswander KR, Singer J, Westphal M, Weiss W. Weight Gain During Pregnancy and Prepregnancy Weight Association with Birth Weight of Term Gestation. Obstet Gynecol 1969;33:482–91.

[43] Melzer K, Schutz Y. Pre-pregnancy and pregnancy predictors of obesity. Int J Obes 2010;34:S44–52. doi:10.1038/ijo.2010.239.

[44] Ronzoni S, Marconi AM, Cetin I, Paolini CL, Teng C, Pardi G, et al. Umbilical amino acid uptake at increasing maternal amino acid concentrations: Effect of a maternal amino acid infusate. Am J Obstet Gynecol 1999;181:477–83. doi:10.1016/S0002-9378(99)70581-8.

[45] Jozwik M, Teng C, Battaglia FC, Meschia G. Fetal supply of amino acids and amino nitrogen after maternal infusion of amino acids in pregnant sheep. Am J Obstet Gynecol 1999;180:447–53. doi:10.1016/S0002-9378(99)70230-9.

[46] Jóźwik M, Teng C, Wilkening RB, Meschia G, Battaglia FC. Reciprocal inhibition of umbilical uptake within groups of amino acids. Am J Physiol - Endocrinol Metab 2004;286:376–83. doi:10.1152/ajpendo.00428.2003.

[47] Roseboom TJ, Painter RC, Van Abeelen AFM, Veenendaal MVE, De Rooij SR. Hungry in the womb: What are the consequences? Lessons from the Dutch famine. Maturitas 2011;70:141–5. doi:10.1016/j.maturitas.2011.06.017.

[48] Cetin I, Marconi AM, Baggiani AM, Buscaglia M, Pardi G, Fennessey P V., et al. In vivo placental transport of glycine and leucine in human pregnancies. Pediatr Res 1995;37:571–5. doi:10.1203/00006450-199505000-00002.

[49] Lewis RM, Godfrey KM, Jackson AA, Cameron IT, Hanson MA. Low serine hydroxymethyltransferase activity in the human placenta has important implications for fetal glycine supply. J Clin Endocrinol Metab 2005;90:1594–8. doi:10.1210/jc.2004-0317.

[50] Gaillard R. Maternal obesity during pregnancy and cardiovascular development and disease in the offspring. Eur J Epidemiol 2015;30:1141–52. doi:10.1007/s10654-015-0085-7.

[51] Mamun AA, Mannan M, Doi SAR. Gestational weight gain in relation to offspring obesity over the life course: A systematic review and bias-adjusted meta-analysis. Obes Rev 2014;15:338–47. doi:10.1111/obr.12132.

[52] Voerman E, Santos S, Inskip H, Amiano P, Barros H, Charles MA, et al. Association of Gestational Weight Gain With Adverse Maternal and Infant Outcomes. Jama 2019;321:1702–15. doi:10.1001/jama.2019.3820.

[53] Hedderson MM, Gunderson EP, Ferrara A. Gestational Weight Gain and Risk of Gestational Diabetes Mellitus. Obstet Gynecol 2010;115:597–604. doi:10.3760/cma.j.issn.0366-6999.20132772.

[54] Abrams BF, Laros RK. Prepregnancy weight, weight gain, and birth weight. Am J Obstet Gynecol 1986;154:503–9. doi:10.1016/0002-9378(86)90591-0.

[55] Battaglia FC, Regnault TRH. Placental Transport and Metabolism of Amino Acids. Placenta 2001;22:145–61.

[56] Schneider H, Möhlen K -H, Challier J -C, Dancis J. Transfer of Glutamic Acid Across the Human Placenta Perfused in Vitro. BJOG An Int J Obstet Gynaecol 1979;86:299–306. doi:10.1111/j.1471-0528.1979.tb11260.x.

[57] Moores RR, Vaughn PR, Battaglia FC, Fennessey P V., Wilkening RB, Meschia G. Glutamate

metabolism in fetus and placenta of late-gestation sheep. Am J Physiol - Regul Integr Comp Physiol 1994;267:89–96. doi:10.1152/ajpregu.1994.267.1.r89.

[58] Harrington B, Glazier J, D'Souza S, Sibley C. System A Amino Acid Transporter Activity in Human Placental Microvillous Membrane Vesicles in Relation to Various Anthropometric Measurements in Appropriate and Small for Gestational Age Babies. Pediatr Res 1999;45:810–4. doi:10.1203/00006450-199906000-00005.

[59] Cleal JK, Lewis RM. The mechanisms and regulation of placental amino acid transport to the human foetus. J Neuroendocrinol 2008;20:419–26. doi:10.1111/j.1365-2826.2008.01662.x.

[60] Panitchob N, Widdows KL, Crocker IP, Hanson MA, Johnstone ED, Please CP, et al. Computational modelling of amino acid exchange and facilitated transport in placental membrane vesicles. J Theor Biol 2015;365:352–64. doi:10.1016/j.jtbi.2014.10.042.

[61] Widdows KL, Panitchob N, Crocker IP, Please CP, Hanson MA, Sibley CP, et al. Integration of computational modeling with membrane transport studies reveals new insights into amino acid exchange transport mechanisms. FASEB J 2015;29:2583–94. doi:10.1096/fj.14-267773.

[62] Lewis RM, Cleal JK, Sengers BG. Placental perfusion and mathematical modelling. Placenta 2020. doi:10.1016/j.placenta.2020.02.015.

[63] Orendi K, Gauster M, Moser G, Meiri H, Huppertz B. The choriocarcinoma cell line BeWo: Syncytial fusion and expression of syncytium-specific proteins. Reproduction 2010;140:759–66. doi:10.1530/REP-10-0221.

[64] Poulsen MS, Rytting E, Mose T, Knudsen LE. Modeling placental transport: Correlation of in vitro BeWo cell permeability and ex vivo human placental perfusion. Toxicol Vitr 2009;23:1380–6. doi:10.1016/j.tiv.2009.07.028.

[65] Li H, Van Ravenzwaay B, Rietjens IMCM, Louisse J. Assessment of an in vitro transport model using BeWo b30 cells to predict placental transfer of compounds. Arch Toxicol 2013;87:1661–9. doi:10.1007/s00204-013-1074-9.

[66] Heaton SJ, Eady JJ, Parker ML, Gotts KL, Dainty JR, Fairweather-Tait SJ, et al. The use of BeWo cells as an in vitro model for placental iron transport. Am J Physiol - Cell Physiol 2008;295:1445–53. doi:10.1152/ajpcell.00286.2008.

[67] Meier C, Ristic Z, Klauser S, Verrey F. Activation of system L heterodimeric amino acid exchangers by intracellular substrates. EMBO J 2002;21:580–9. doi:10.1093/emboj/21.4.580.

[68] Napolitano L, Galluccio M, Scalise M, Parravicini C, Palazzolo L, Eberini I, et al. Novel Insights into the Transport Mechanism of the human amino acid transporter LAT1 (SLC7A5). Probing critical residues for substrate translocation. Biochim Biophys Acta - Gen Subj 2017;1861:727–36. doi:10.1016/j.bbagen.2017.01.013.

[69] Schneider H, Proegler M, Sodha R, Dancis J. Asymmetrical transfer of α-aminoisobutyric acid (AIB), leucine and lysine across the in vitro perfused human placenta. Placenta 1987;8:141–51. doi:10.1016/0143-4004(87)90017-8.

[70] Jauniaux E, Gulbis B, Gerloo E. Free amino acids in human fetal liver and fluids at 12-17 weeks of gestation. Hum Reprod 1999;14:1638–41. doi:10.1093/humrep/14.6.1638.

[71] Lewis RM, Brooks S, Crocker IP, Glazier J, Hanson MA, Johnstone ED, et al. Review: Modelling placental amino acid transfer - From transporters to placental function. Placenta 2013;34:S46–51. doi:10.1016/j.placenta.2012.10.010.

Tables

Table 1: Anthropometric characteristics of healthy patients and their offspring.

	Characteristics	Control
Mother	Number (n)	22
	Delivery mode	cesarean sections
	Maternal age (years)	34.36 ± 3.74
	Preconceptional weight (kg)	67.52 ± 11.47
	Weight at *partum* (kg)	82.05 ± 14.30
	Height (cm)	163.95 ± 7.50
	Preconceptional BMI (kg/m^2)	25.04 ± 4.76
	BMI at *partum* (kg/m^2)	30.53 ± 5.06
	Weight gain (kg)	15.86 ± 5.83
	Gravidity	2.55 ± 1.34
	Parity	1.82 ± 0.85
	Gestational age at *partum*	38 3/4 ± 1
	Systolic blood pressure	117.36 ± 9.33
	Diastolic blood pressure	69.91 ± 10.05
	Placental weight (g)	644.18 ± 112.80
Newborn	Gender	9 ♂ / 13 ♀
	Weight (g)	3410.23 ± 456.95
	Percentile[#] (%)	47.45 ± 28.56

Data are presented as mean ± standard deviation (SD). Abbreviations: BMI, body mass index.
[#] Percentile were calculated by using child growth standards published by WHO (www.who.int/childgrowth/standards/weight_for_age/; March 2020).

Table 2: Maternal and fetal amino acid concentrations and materno-fetal gradients.

Amino acid / classification		Fetal arterial (FA) [µM]	Fetal venous (FV) [µM]	Maternal venous (MV) [µM]	FA-MV Gradients [µM]	FV-MV Gradients [µM]	FV-FA Difference [µM]
		mean ± SD	mean ± SD	mean ± SD	mean ± SD	mean ± SD	mean ± SD
Small	Gly(!)	324 ± 67	290 ± 68	195 ± 38	129 ± 73 ***	95 ± 64 ***	-34 ± 56 ***
	Ala	429 ± 88	425 ± 77	421 ± 65	8 ± 87	5 ± 86	-4 ± 52
Nucleophilic	Ser	141 ± 26	124 ± 35	118 ± 18	23 ± 26 *	6 ± 32	-17 ± 32
	Thr!	260 ± 41	252 ± 39	194 ± 35	66 ± 27 ***	58 ± 30 ***	-8 ± 23
	Cys(!)	5 ± 5	4 ± 4	5 ± 6	0 ± 3	-1 ± 3	-1 ± 2
Hydrophobic	Val!	216 ± 38	212 ± 33	170 ± 39	46 ± 30 ***	42 ± 34 ***	-4 ± 22
	Leu!	116 ± 21	113 ± 19	94 ± 13	22 ± 21	18 ± 20	-4 ± 17
	Ile!	60 ± 13	59 ± 10	46 ± 8	14 ± 11	13 ± 10	-1 ± 8
	Met!	28 ± 5	27 ± 4	21 ± 4	7 ± 5	6 ± 5	-1 ± 3
	Pro(!)	189 ± 45	184 ± 42	173 ± 52	16 ± 25	11 ± 33	-5 ± 19
Aromatic	Phe!	79 ± 12	76 ± 10	64 ± 11	15 ± 13	12 ± 12	-3 ± 9
	Tyr(!)	77 ± 15	75 ± 13	50 ± 21	27 ± 25 *	25 ± 24 *	-2 ± 7
	Trp!	70 ± 10	71 ± 8	39 ± 7	31 ± 11 **	32 ± 10 **	1 ± 8
Amide	Asn	55 ± 13	54 ± 11	55 ± 10	0 ± 13	-2 ± 11	-1 ± 11
	Gln(!)	391 ± 145	376 ± 144	362 ± 62	29 ± 171 **	14 ± 167	-16 ± 55
Acidic	Asp	98 ± 81	74 ± 51	41 ± 13	57 ± 82 ***	33 ± 56 **	-24 ± 75 *
	Glu	279 ± 116	218 ± 99	111 ± 34	168 ± 115 ***	107 ± 104 ***	-61 ± 100 ***
Basic	His!	122 ± 45	120 ± 46	104 ± 39	18 ± 16	15 ± 16	-2 ± 11
	Lys!	320 ± 48	311 ± 48	152 ± 23	168 ± 35 ***	159 ± 38 ***	-9 ± 29
	Arg(!)	79 ± 23	72 ± 14	74 ± 17	5 ± 24	-2 ± 19	-7 ± 14

Legend: Statistical comparison between different blood compartments, e.g. FA vs. MV, FV vs. MV and FV vs. FA were performed using 2way ANOVA and multiple comparison with Tukey testing; α=0.05, * p<0.05, ** p<0.01, *** p<0.001. Amino acids are abbreviated according to 3-letter amino acid code. Fetal arterial (FA); Fetal venous (FV); Maternal venous (MV); !, essential amino acids; (!), Conditionally essential amino acids.

Table 3: Correlations between amino acid concentrations, materno-fetal gradients and corresponding anthropometric data

		Gly(!)	Ala	Ser	Thr!	Val!	Leu!	Ile!	Met!	Pro(!)	Phe!	Tyr(!)	Trp!	Asn	Gln(!)	Asp	Glu	His!	Lys!	Arg(!)
Mother	**Preconceptional weight**		MV			FA MV	MV	FV MV		FA MV MV-FV	MV-FV	MV-FV				MV	MV			
Mother	**Weight at partum**		MV			MV	MV	MV	MV	FA MV	MV	MV MV-FV			MV		MV	MV		
Mother	**Weight gain**	FA FV ↓MV-FV	FV										↓FV MV-FA MV-FV							
Mother	**BMI at *partum***		MV			MV	MV	FA FV MV	MV	FA MV							MV MV-FV	MV		
Mother	**Preconceptional BMI**					FA MV	FV MV	FA FV MV		FA MV							MV	MV		
Fetus	**Weight placenta**	MV-FV	MV-FV	MV												MV-FV	MV			
Fetus	**Weight newborn**	FV										↓FA					MV-FV			

Legend: The table shows significant associations according to Spearman correlation analysis. Amino acids are abbreviated according to 3-letter amino acid code. Fetal arterial (FA); Fetal venous (FV); Maternal venous (MV); !, essential amino acids; (!), conditionally essential amino acids; green highlights depict amino acids that are substrates for LAT1; orange highlight marks Glutamine (Gln), the co-substrate for LAT1; ↓, negative correlations; BP, blood pressure.

Figure Legends

Figure 1: Full proteinogenic amino acid profile of maternal-fetal matched blood samples. The concentrations of the 20 standard proteinogenic amino acids (AA) were measured in prospectively collected blood sera from clinically unsuspicious woman (n=22) and the corresponding placentae within 20min after elective Caesarian section. The AA concentrations were measured by ion exchange chromatography in blood sera from maternal vein (grey), fetal artery (red) and fetal vein (blue). Data are depicted as boxplots with Tukey whiskers. The various AA are classified according to their chemical structure and properties (see colored backgrounds). Brackets represent expected physiological ranges of AA concentrations of adults (>15years) and newborns (0-1month), respectively. The maternal-fetal matched blood samples were compared using paired two-way ANOVA with Tukey's correction; * $p<0.05$, ** $p<0.01$, *** $p<0.001$. AA concentrations in sera from healthy mother-baby pairs at birth were significantly different by comparing maternal vein vs. fetal artery for Gly, Ser, Thr, Val, Tyr, Trp, Gln, Asp, Glu and Lys. An overview on all results is presented in Table 2.

Figure 2: Individual differences in fetal net amino acid accumulation and secretion. The means of veno-arterial (FV-FA) differences of 20 amino acids (AA) are presented in a stacked bar diagram. The analyzed individuals are depicted on the x axis in ascending order. 12/22 individuals showed a negative, while 10/22 individuals exhibited a positive sum of veno-arterial differences. In general, the 22 individuals can be classified based on their veno-arterial differences in either accumulative placentae, performing fetal AA uptake, or in secretory placentae, performing fetal AA efflux. Since in our cohort there were more secretory placentae present at the time of delivery, the total FV-FA difference as listed in Table 2 is negative.

Figure 3: Correlation between leucine concentrations and maternal anthropometric data. The relation between measured leucine (Leu) concentrations in maternal venous sera (MV) and **(A)** maternal preconceptional weights, **(B)** maternal weights at *partum* **(C)** preconceptional body mass index (BMI) and **(D)** BMI at *partum* was analyzed by Spearman correlation for 22 healthy controls (n=22). Data are presented as scatter plots with the anthropometric parameters on the x-axis and AA concentrations in the maternal vein (MV) on the y-axis. Preconceptional weights, maternal weights at *partum* and BMI were mainly correlating with MV concentrations of AA which are LAT1 substrates. The results of all significant correlations are listed in Table 3. Statistical values describing the linear relationship between two parameters are denoted to the right of the scatter plots: r_s , Spearman correlation coefficient; CI, confidence interval; p, two-tailed p value.

Figure 4: Correlations between selected amino acid gradients and anthropometric data. Amino acid (AA) gradients across the materno-fetal barrier were calculated as difference between concentrations in maternal vein (MV) and fetal artery (FA) or fetal vein (FV) for 22 mother-fetus paired serum samples (n=22). Since AA levels are generally higher in the fetal as compared to the maternal circulation, AA gradients are negative values and therefore represent counter-directed materno-fetal gradients. Significant Spearman correlations were found between **(A)** tyrosine (Tyr) gradients and maternal preconceptional weights, **(B)** Tyr gradients and maternal weights at *partum*, **(C)** Trp gradients and maternal weight gain (defined as maternal weight at *partum* minus preconceptional weight) and **(D)** Alanine (Ala) gradients and placental weight. Results are presented as scatter plots with anthropometric data on the x-axis and AA gradients on the y-axis. Additional significant correlations for AA gradients are presented in Table 3. Statistical parameters describing the linear relationship are denoted below

the scatter plots: r_s , Spearman correlation coefficient; CI, confidence interval; p, two-tailed p value.

Figure 5: LAT1-mediated leucine uptake in trophoblasts is influenced by extracellular amino acid concentrations.
(**A**) The effect of extracellular Leucine (Leu) concentrations on the Leu uptake capacity into BeWo trophoblasts was assessed and compared to the frequently used colon cancer cell model HT-29. Leu uptake assays were performed with Leu concentrations of 167µM, reflecting an upper clinical range, and a lower concentration of 30µM. The uptake capacity between syncytiotrophoblasts (STB) and cytotrophoblasts (CTB) was compared by stimulating undifferentiated BeWo cells (BeWo-CTB) with 100µM forskolin for 48h (BeWo-STB). For all cell types Leu uptake was measured at 3min and normalized to the total protein concentration. BeWo-CTB are depicted in blue, BeWo STB in red and HT-29 in grey. Of note, the stimulation of Leu uptake through increased extracellular Leu concentrations was more then 2-times higher in BeWo-STB, as compared to the other undifferentiated cell types. (**B**) To verify the presence of LAT1/SLC7A5-mediated Leu uptake and its susceptibility to different substrate concentrations, a dose-response experiment with the LAT1-specific inhibitor JPH203 was performed. Leu uptake under high Leu concentration (167µM Leu) are depicted as solid lines and lower (30µM Leu) as dashed lines. BeWo-STB with high Leu levels showed significantly higher Leu uptake rates, but also a much higher susceptibility to inhibition by JPH203 compared to BeWo-CTB. (**A-B**) Differences were tested by Sidak's multiple comparisons test; * $p<0.05$, ** $p<0.01$, *** $p<0.001$.

Figure 6: Counter-directed leucine gradient increases amino acid transfer across the placental barrier.
(A) Materno-fetal Leu transfer across a tight trophoblast monolayer was studied using the Transwell® system. BeWo cells were cultured on a semi-permeable membrane and differentiated by stimulation with 100µM forskolin 24h after seeding. Leu transfer was measured over 360min by simultaneous sampling and measurement of the diminishing radiolabeled Leu (L-[3,4,5-^{3}H(N)]-leucine) in the upper, maternal vein (Mv)-corresponding compartment and the appearance of radiolabeled Leu in the lower, fetal artery (Fa)-corresponding compartment. Two different conditions were compared: materno-fetal Leu transfer with 30µM Leu both in the Mv and the Fa compartment (no gradient, blue) or against a counter-directed Leu gradient with 30µM Leu in Mv and 167µM Leu in the Fa compartment (orange). In all conditions there was 300µM Gln as exchange partner in both compartments. The schematic representation of the experimental setup is shown in the insert of panel A. Leu transfer across the placental barrier was increased against a counter-directed 137µM Leu-gradient. Data show the results of one representative dataset from a total of 3 independent experiments. The combination of the 3 independent Transwell® experiments is shown in Suppl. Figure 1. **(B)** Calculated accumulation of intracellular Leu (total dose of labeled Leu minus sum of Mv and Fa) during the experiment. **(C)** Measured accumulation of intracellular Leu at the end of the experiment. No significant differences in the intracellular Leu contents were found between application of equimolar Leu concentrations or of a counter-directed Leu gradient (**B,C**) Differences were tested by 2way ANOVA with Tukey's multiple comparisons test; * $p<0.05$, ** $p<0.01$, *** $p<0.001$.

Figures

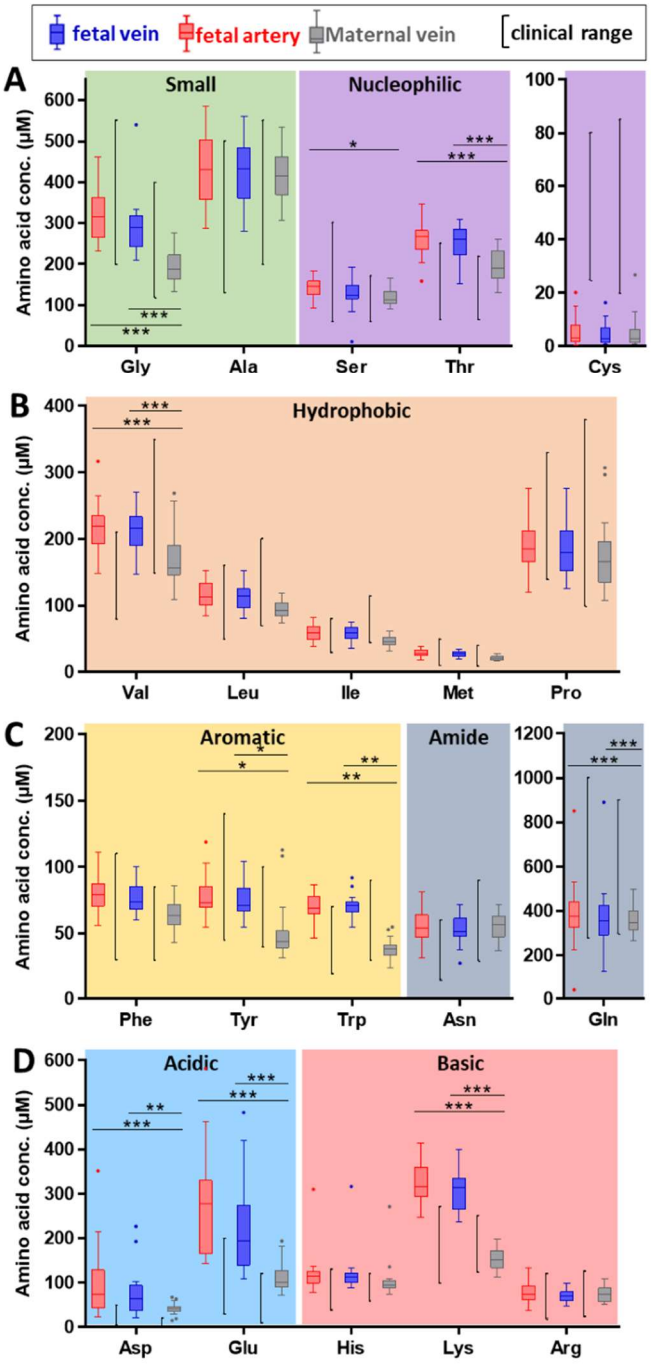

Figure 1

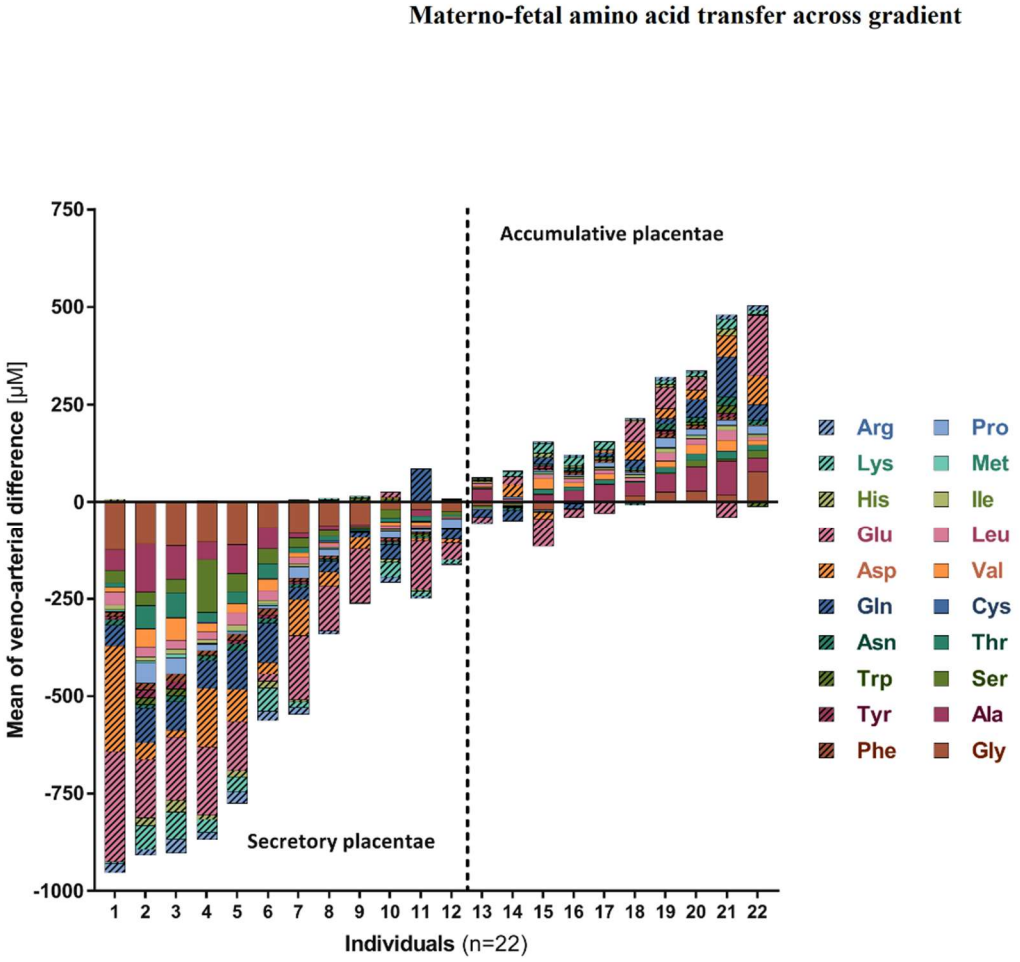
Materno-fetal amino acid transfer across gradient
Accumulative placentae
Secretory placentae
Mean of veno-arterial difference [µM]
750
500
250
0
-250
-500
-750
-1000
1 2 3 4 5 6 7 8 9 10 11 12 13 14 15 16 17 18 19 20 21 22
Individuals (n=22)
Arg
Lys
His
Glu
Asp
Gln
Asn
Trp
Tyr
Phe
Pro
Met
Ile
Leu
Val
Cys
Thr
Ser
Ala
Gly

Figure 2

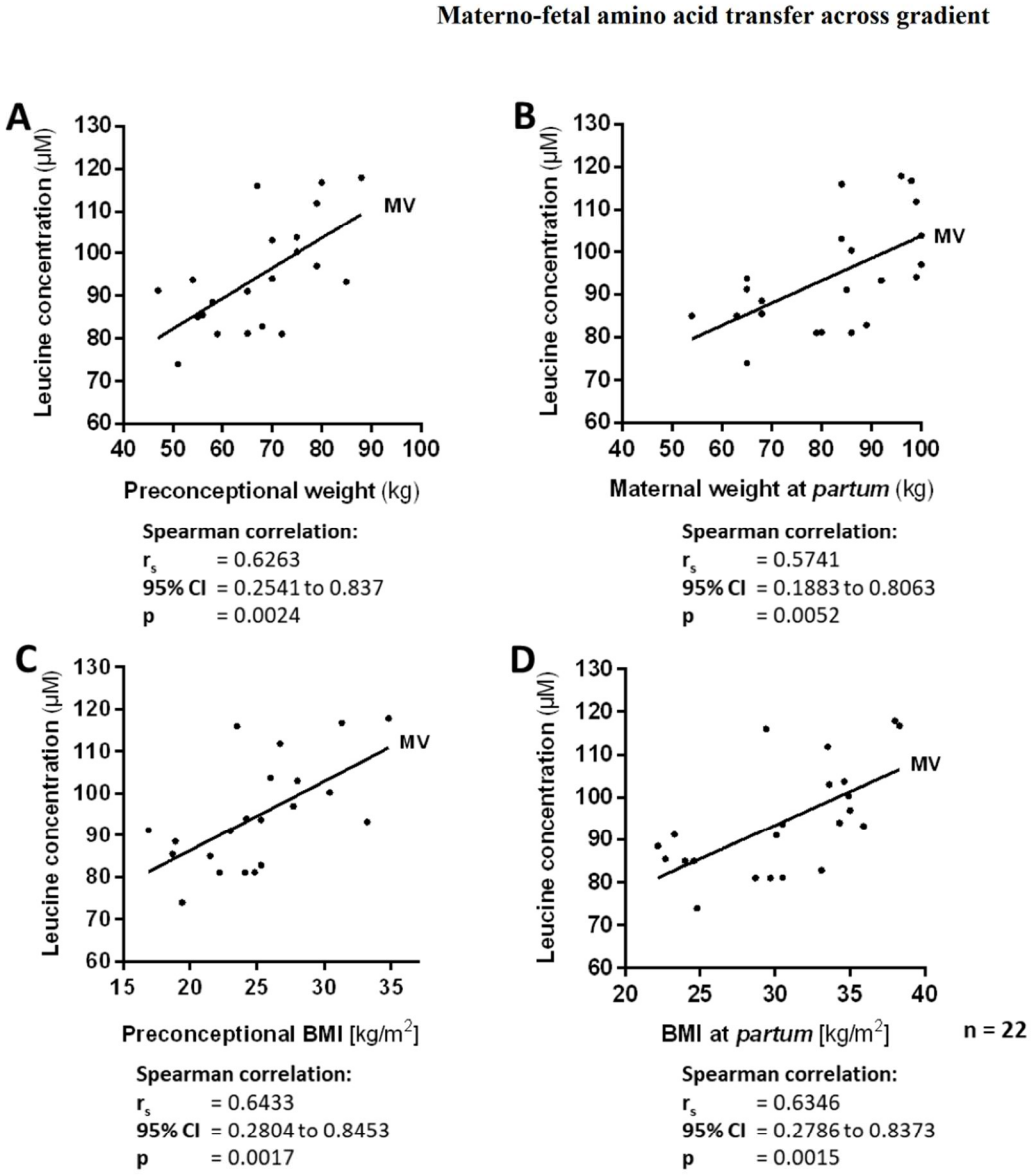
Materno-fetal amino acid transfer across gradient
A
Leucine concentration (µM)
MV
Preconceptional weight (kg)
Spearman correlation:
r_s = 0.6263
95% CI = 0.2541 to 0.837
p = 0.0024
B
Leucine concentration (µM)
MV
Maternal weight at *partum* (kg)
Spearman correlation:
r_s = 0.5741
95% CI = 0.1883 to 0.8063
p = 0.0052
C
Leucine concentration (µM)
MV
Preconceptional BMI [kg/m^2]
Spearman correlation:
r_s = 0.6433
95% CI = 0.2804 to 0.8453
p = 0.0017
D
Leucine concentration (µM)
MV
BMI at *partum* [kg/m^2]
Spearman correlation:
r_s = 0.6346
95% CI = 0.2786 to 0.8373
p = 0.0015
n = 22

Figure 3

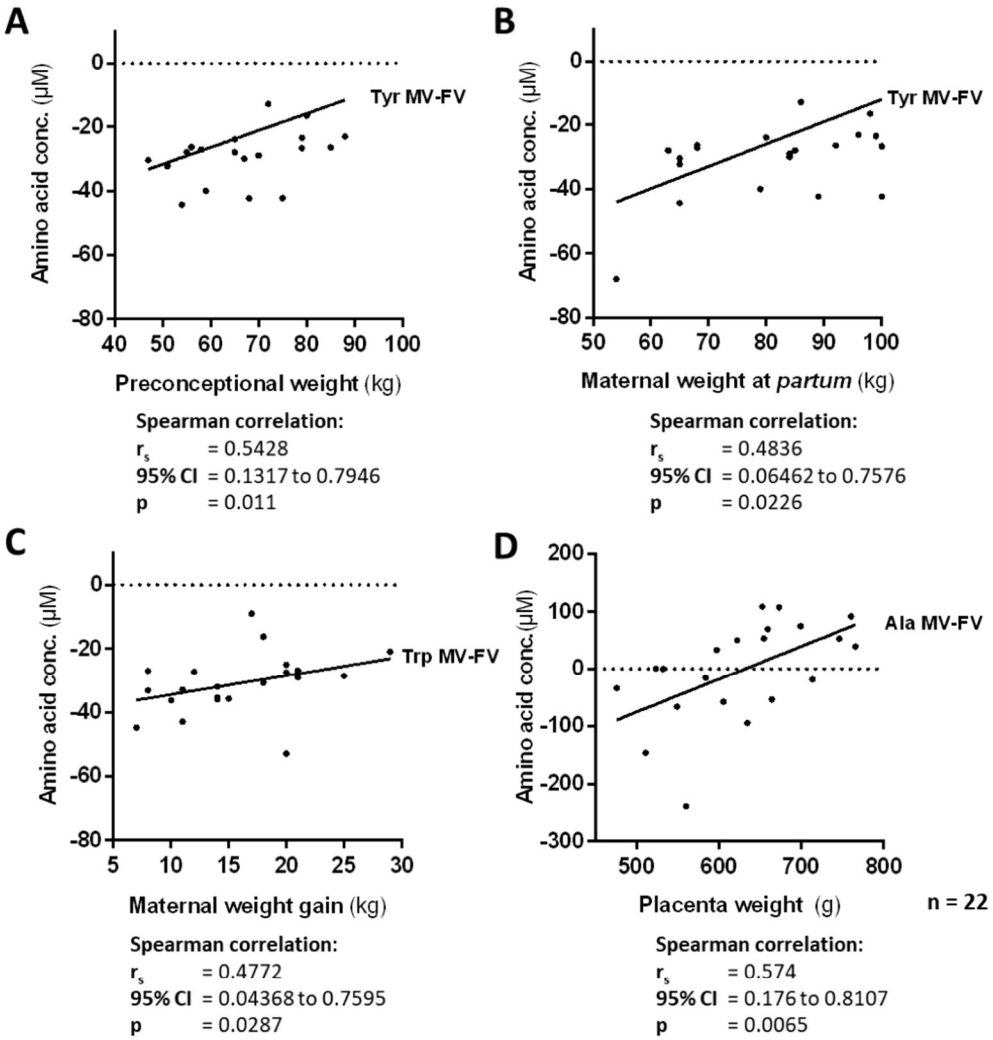
A
Amino acid conc. (µM)
Tyr MV-FV
Preconceptional weight (kg)
Spearman correlation:
r_s = 0.5428
95% CI = 0.1317 to 0.7946
p = 0.011
B
Amino acid conc. (µM)
Tyr MV-FV
Maternal weight at *partum* (kg)
Spearman correlation:
r_s = 0.4836
95% CI = 0.06462 to 0.7576
p = 0.0226
C
Amino acid conc. (µM)
Trp MV-FV
Maternal weight gain (kg)
Spearman correlation:
r_s = 0.4772
95% CI = 0.04368 to 0.7595
p = 0.0287
D
Amino acid conc.(µM)
Ala MV-FV
Placenta weight (g)
Spearman correlation:
r_s = 0.574
95% CI = 0.176 to 0.8107
p = 0.0065
n = 22

Figure 4

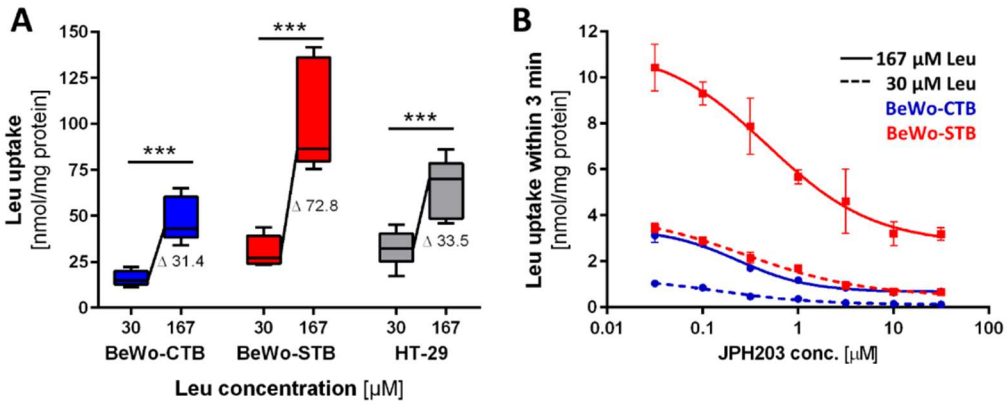
A
Leu uptake
[nmol/mg protein]
150
125
100
75
50
25
0
***
***
***
Δ 31.4
Δ 72.8
Δ 33.5
30
167
30
167
30
167
BeWo-CTB
BeWo-STB
HT-29
Leu concentration [µM]
B
Leu uptake within 3 min
[nmol/mg protein]
12
10
8
6
4
2
0
167 µM Leu
30 µM Leu
BeWo-CTB
BeWo-STB
0.01
0.1
1
10
100
JPH203 conc. [µM]

Figure 5

Materno-fetal amino acid transfer across gradient

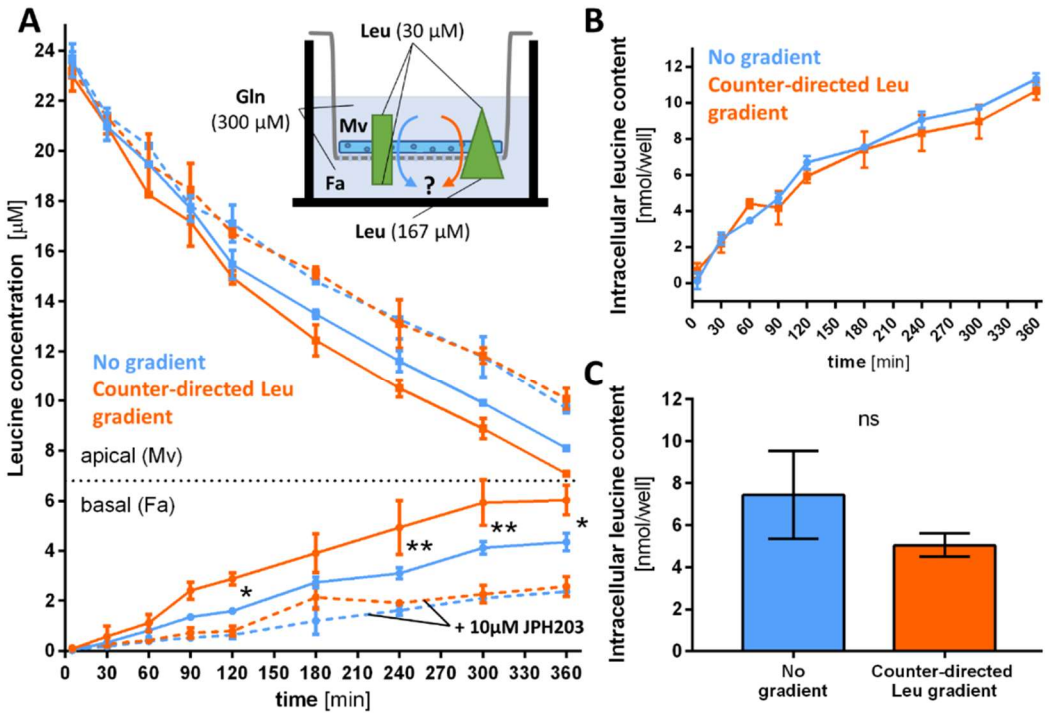

Figure 6

28

Supplementary Information

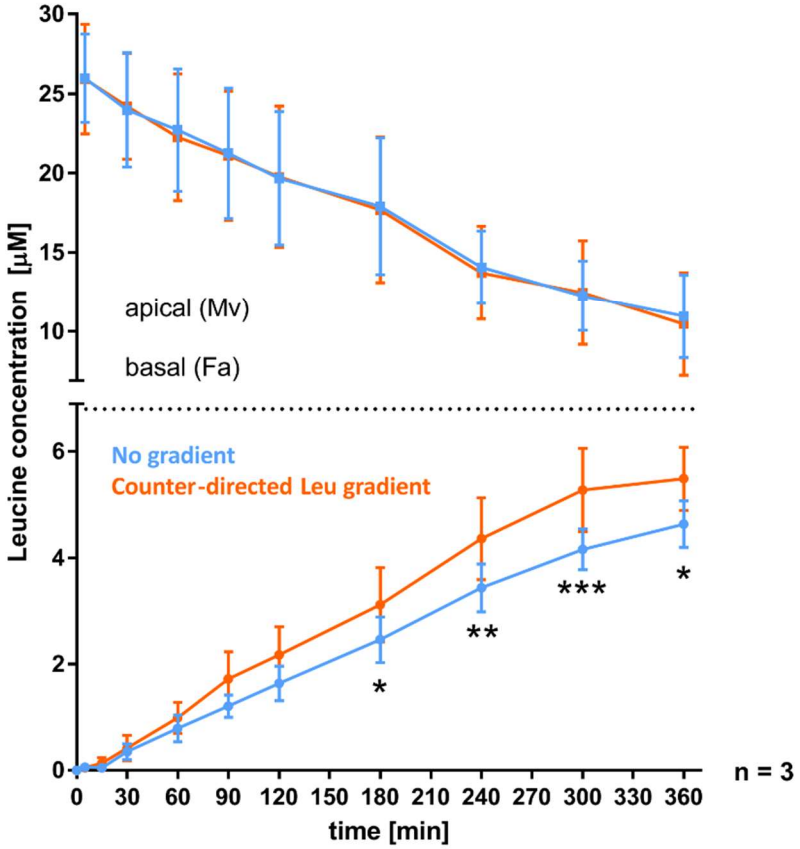

Suppl. Figure 1: Combination of Transwell experiments showing increased Leu transfer against a Leu gradient.
Materno-fetal Leu transfer across an *in vitro* placental barrier was performed using the Transwell® system. The results represent data from 3 independent Transwell experiments (n=3). BeWo cells were cultured on a semi-permeable membrane and differentiated by stimulation with 100µM forskolin 24h after seeding. Leu transfer was measured by simultaneous sampling and measurement of diminishing radiolabeled Leu (L-[3,4,5-^{3}H(N)]-leucine) in the upper maternal vein (Mv) compartment and appearing radiolabeled Leu in the lower compartment representing the fetal artery (Fa) over 360min. As shown in Figure 6, two different conditions were compared: materno-fetal Leu transfer in the condition with 30µM Leu both in the Mv and the Fa compartment (no gradient, blue) or against a counter-directed Leu gradient with 30µM Leu in Mv and 167µM Leu in the Fa compartment (orange). In all conditions there was 300µM Gln as exchange partner in both compartments. Differences were tested by 2way ANOVA with Tukey's multiple comparisons test; * $p<0.05$, ** $p<0.01$, *** $p<0.001$.

9.1.4 Published in ELife (6 May 2020)

eLife RESEARCH ARTICLE

Cryo-EM structures and functional properties of CALHM channels of the human placenta

Katarzyna Drożdżyk[1†], Marta Sawicka[1†*], Maria-Isabel Bahamonde-Santos[1], Zaugg Jonas[2], Dawid Deneka[1], Christiane Albrecht[2], Raimund Dutzler[1*]

[1]Department of Biochemistry, University of Zurich, Zurich, Switzerland; [2]Institute of Biochemistry and Molecular Medicine, University of Bern, Bern, Switzerland

Abstract The transport of substances across the placenta is essential for the development of the fetus. Here, we were interested in the role of channels of the calcium homeostasis modulator (CALHM) family in the human placenta. By transcript analysis, we found the paralogs CALHM2, 4, and 6 to be highly expressed in this organ and upregulated during trophoblast differentiation. Based on electrophysiology, we observed that activation of these paralogs differs from the voltage- and calcium-gated channel CALHM1. Cryo-EM structures of CALHM4 display decameric and undecameric assemblies with large cylindrical pore, while in CALHM6 a conformational change has converted the pore shape into a conus that narrows at the intracellular side, thus describing distinct functional states of the channel. The pore geometry alters the distribution of lipids, which occupy the cylindrical pore of CALHM4 in a bilayer-like arrangement whereas they have redistributed in the conical pore of CALHM6 with potential functional consequences.

***For correspondence:**
m.sawicka@bioc.uzh.ch (MS);
dutzler@bioc.uzh.ch (RD)

[†]These authors contributed equally to this work

Competing interests: The authors declare that no competing interests exist.

Funding: See page 23

Received: 07 February 2020
Accepted: 05 May 2020
Published: 06 May 2020

Reviewing editor: Kenton J Swartz, National Institute of Neurological Disorders and Stroke, National Institutes of Health, United States

Introduction

The placenta, a complex organ that develops during pregnancy, serves as a hub for the exchange of nutrients and waste products between the mother and the fetus. The flow of substances across the placenta is controlled by two distinct cell-layers, namely fetal capillary endothelial cells and syncytiotrophoblasts (STB). While endothelial cells lining the fetal vessels allow to a certain extent diffusion of (small) molecules through paracellular pathways (***Edwards et al., 1993***; ***Lewis et al., 2013***), the STB layer constitutes a tight diffusion barrier. STB are polarized multinucleated cells presenting their apical side towards the maternal blood and their basal side towards the fetal capillaries. Hence, the targeted expression of receptors, channels or transport proteins of the STB determines the directionality of transport across the placenta, which is essential for the adequate development of the fetus (***Lager and Powell, 2012***). Among the transport proteins in the placenta, the role of the calcium homeostasis modulator (CALHM) family is currently unknown. In humans, the CALHM family encompasses six paralogs, some of which function as non-selective channels that are permeable to large substances such as ATP (***Ma et al., 2016***). CALHM1, the currently best characterized paralog, forms ion channels that are activated by depolarization and a decrease in the extracellular Ca^{2+}-concentration (***Ma et al., 2012***; ***Taruno et al., 2013b***) with mutations being associated with an increased risk for late-onset Alzheimer's disease (***Dreses-Werringloer et al., 2008***). Although functional on its own (***Ma et al., 2012***), in a physiological context CALHM1 probably forms heteromers with the subunit CALHM3 (***Ma et al., 2018b***). These heteromeric channels play an important role as secondary receptors for sweet, bitter and umami taste reception in type II taste bud cells by catalyzing the non-vesicular release of ATP (***Ma et al., 2018b***; ***Taruno et al., 2013a***; ***Taruno et al., 2013b***). A second paralog with an assigned physiological role is CALHM2, which is ubiquitously expressed and was proposed to mediate ATP release in astrocytes (***Ma et al., 2018a***). The role of other

paralogs has thus far remained elusive. Insight into the structural properties of the family was recently provided from studies on CALHM1 and 2 by cryo-electron microscopy (***Choi et al., 2019***; ***Demura et al., 2020***; ***Syrjanen et al., 2020***). CALHM2 was found to assemble into undecameric channels, which in certain cases dimerize via contacts on the extracellular side in an assembly that resembles gap-junctions. Based on this architecture, a potential role of CALHM2 as intercellular channels was proposed. Although predicted to be related to connexins and volume-regulated anion channels (VRACs) of the LRRC8 family (***Siebert et al., 2013***), the four membrane-spanning helices of the CALHM subunit exhibit a distinct arrangement, which refutes a common structural ancestry between these protein families (***Choi et al., 2019***). In contrast to CALHM2 channels, the structure of CALHM1 shows a smaller octameric organization (***Demura et al., 2020***; ***Syrjanen et al., 2020***), thus suggesting that the functional properties of activation and conduction might not be conserved within the family.

In the present study we were investigating the structural and functional properties of CALHM channels in the context of the placenta. We identified the three paralogs, CALHM2, 4 and 6, to be highly expressed in this organ. A systematic comparative functional characterization by electrophysiology did not reveal pronounced activity of either of these paralogs under conditions where CALHM1 channels are open, thus suggesting that the former might be regulated by different and currently unknown mechanisms. The structural characterization of the three paralogs reveals insight into their organization and into potential gating transitions which, although related to previously described properties of CALHM2, show distinct features with respect to subunit organization, conformational changes and the distribution of lipids residing inside the wide pore of CALHM channels.

Results

Expression of CALHM channels in the human placenta

To investigate the role of CALHM channels in the placenta, we have characterized the expression of family members in healthy human placental tissues obtained from term pregnancies. Quantification of transcripts by reverse transcription (RT) PCR revealed high levels of CALHM2, 4, and 6, but comparably low expression of other paralogs (***Figure 1A***). We also analyzed the expression patterns of CALHM paralogs in primary trophoblast cells isolated from healthy term placentae and examined

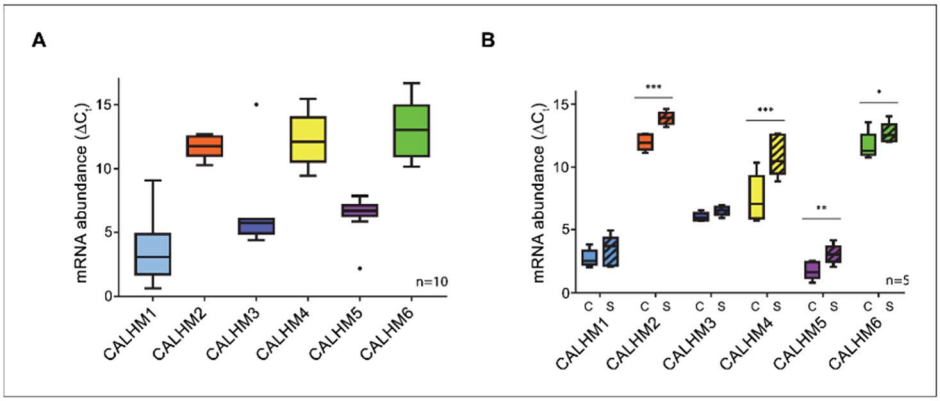

Figure 1. Expression analysis of CALHM genes in the human placenta. mRNA abundances of different CALMH paralogs in (**A**), human placental tissues (n = 10) and (**B**), human trophoblasts isolated from healthy term placentae (n = 5) was assessed by quantitative RT PCR and normalized to the reference gene YWHAZ. The relative amounts of the different CALHM genes are shown as ΔC_t values (ΔC_t = C_t value of YWHAZ – C_t value of CALHM gene). Comparative transcript data are presented as mRNA abundance ($\Delta Ct = Ct_{reference\ gene} - Ct_{traget\ gene}$) between undifferentiated cytotrophoblasts (C) and differentiated syncytiotrophoblast (S) cells. Data analysis and statistical evaluations were performed using paired 2-way ANOVA with Sidak's multiple comparisons test; *p<0.05; **p<0.01; ***p<0.001.

The online version of this article includes the following figure supplement(s) for figure 1:

Figure supplement 1. Comparative mRNA expression data for other physiologically relevant transporters/receptors in the human placenta.

changes during the differentiation process of trophoblast precursor cells into mature STB. We found marked upregulation of CALHM2, 4 and 6 during differentiation, which was most pronounced for CALHM4 (***Figure 1B***) and which might indicate a differentiation-dependent role of these proteins in the human placenta. In all cases, the concentrations of the respective CALHM mRNAs are high in comparison to other transport proteins (***Figure 1—figure supplement 1***) suggesting their involvement in important placenta-related membrane transport processes.

Functional characterization of CALHM paralogs

Due to the abundance of CALHM2, 4, and 6 in the placenta, we have focused our subsequent investigations on these three paralogs. Apart from CALHM2, which was described to form ATP-conducting channels in astrocytes (***Ma et al., 2018a***), they have so far not been characterized. For a functional comparison of channels composed of the three placental subunits with the well-studied protein CALHM1, we have expressed the homomeric proteins in *X. laevis* oocytes and recorded currents by two-electrode voltage-clamp electrophysiology. This method has previously allowed a detailed characterization of CALHM1, which is activated by depolarization and the removal of Ca^{2+} from the extracellular side (***Ma et al., 2012***). To detect proteins in the plasma membrane, we have used a surface-biotinylation approach and found all placental paralogs to be expressed and targeted at high levels to the surface of oocytes at the time of the measurement (*i.e.* 40–60 hr after injection of mRNA) (***Figure 2A***). Assuming that CALHM proteins form channels of large conductance, we thus can directly compare the average magnitude of recorded currents between populations of oocytes expressing the respective constructs and relate their activation properties in response to voltage change and the depletion of extracellular Ca^{2+} to the well-characterized CALHM1. In our studies, we were able to reproduce the functional hallmarks of CALHM1, which are manifested in the absence of currents at negative voltage and slowly activating currents at positive voltage at millimolar concentrations of extracellular Ca^{2+} and a strong increase of currents upon Ca^{2+} removal in the entire voltage range (***Figure 2***, ***Figure 2—figure supplement 1A and B***). In contrast to CALHM1, the current response of homomeric CALHM2, 4, and 6 channels was generally small and within the range of endogenous currents of *X. laevis* oocytes not expressing any of the proteins (***Figure 2A***, ***Figure 2—figure supplement 1C-F***). These currents neither showed pronounced voltage-dependence nor were they altered by Ca^{2+}-removal in a statistically significant manner (***Figure 2B–D***). We thus conclude that the CALHM channels expressed in the placenta are not regulated in a similar manner as CALHM1-subunit containing channels and that their activation instead proceeds by distinct, currently unknown mechanisms.

Biochemical characterization and structure determination of CALHM2, 4, and 6

For a biochemical and structural characterization of placental CALHM channels, we have expressed constructs coding for human CALHM2, 4 and 6 in HEK293 cells. In contrast to the poor yields obtained for human CALHM1, all three placental paralogs expressed high levels of protein. The elution properties of fusions to green fluorescent protein (GFP) extracted in the detergent glycol-diosgenin (GDN) and analyzed by fluorescent size-exclusion chromatography (FSEC) (***Kawate and Gouaux, 2006***) indicate assemblies of high molecular weight (***Figure 3—figure supplement 1A***). We next proceeded with a scale-up of homomeric CALHM2, 4 and 6 channels in HEK293 cells and purified each protein in the detergent GDN. Consistent with FSEC studies, all purified constructs eluted as large oligomers during gel-filtration chromatography, although at different volumes. The highest elution volume was observed for CALHM6, a similar but slightly lower volume for CALHM2 and the smallest volume for CALHM4, thus hinting towards distinct oligomeric organizations of the three proteins with CALHM4 forming larger complexes than CALHM6 (***Figure 3—figure supplement 1B***). The peak fractions were concentrated, vitrified on cryo-EM grids and used for data collection by cryo-electron microscopy (***Figure 3—figure supplements 2–6***, ***Tables 1–2***). As expected from the size-exclusion profiles, all paralogs form large and heterogenic multimeric assemblies containing between 10 and 12 subunits. Whereas in the CALHM6 sample a vast majority of these oligomeric channels do not interact (***Figure 3B***, ***Figure 3—figure supplement 4***), we have found almost complete dimerization for CALHM4 (***Figure 3A***, ***Figure 3—figure supplements 2–3***) and a significant fraction of particles to dimerize in case of CALHM2 (***Figure 3C***, ***Figure 3—figure supplement***

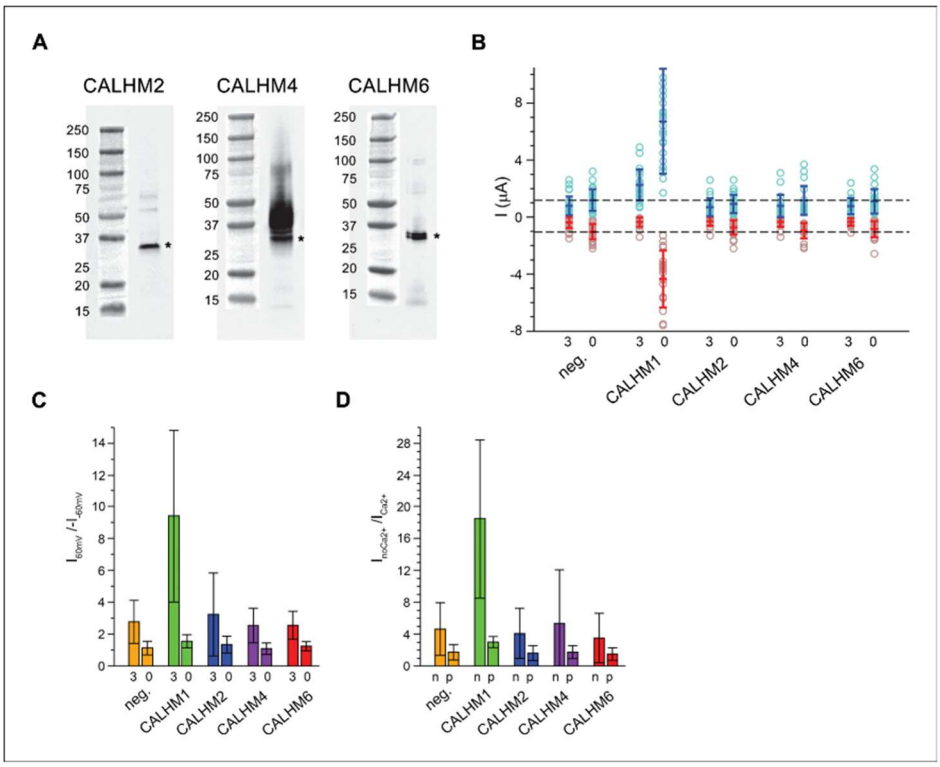

Figure 2. Functional characterization of CALHM channels expressed in *X. laevis* oocytes. (**A**) Western blot of proteins located in the plasma membrane of *X. laevis* oocytes heterologously expressing the indicated CALHM channels. Protein was isolated after surface-biotinylation by binding to avidin-resin. The proteins are detected with specific antibodies recognizing the respective CALHM paralog. Left, CALHM2, center CALHM4, right CALHM6. The blot demonstrates the targeting of all three paralogs to the plasma membrane. Bands corresponding to the respective CALHM paralogs are indicated by asterisk. (**B**) Electrophysiological characterization of *X. laevis* oocytes heterologously expressing the paralogs CALHM1, CALHM2, CALHM4 and CALHM6 in comparison to control oocytes (neg.) recorded at extracellular solutions either containing 3 mM Ca^{2+} (3) or 0.5 mM EDTA and 0.5 mM EGTA (Ca^{2+}-free, 0). Data show currents of individual oocytes (circle) recorded by two-electrode voltage-clamp (TEVC) at 60 (light blue) and −60 mV (light red). In each case, currents were tabulated at the end of a 5 s voltage step. Averages are shown as bars in red (−60 mV) and blue (60 mV), respectively. Dashed lines indicate mean current levels of control oocytes (neg.) recorded in Ca^{2+}-free extracellular solutions at 60 and −60 mV. Currents measured for all investigated channels, except CALHM1, are not significantly different from control oocytes (as judged by a Student t-test). (**C**), Rectification of steady-state currents of oocytes displayed in (**B**) expressed as I_{60mV}/I_{-60mV} calculated for individual oocytes at 3 mM Ca^{2+} (3) and in Ca^{2+}-free solutions (0) and averaged. The large value of CALHM1 reflects the activation of the protein at positive voltage in presence of Ca^{2+}. (**D**) Ca^{2+}-dependence of activation. Change of steady-state currents of oocytes displayed in (**B**) after Ca^{2+}-removal expressed as I_{noCa2+}/I_{Ca2+} calculated from individual oocytes at −60 mV (n) and 60 mV (p) and averaged. The large value of CALHM1 at −60 mV reflects the strong activation of currents at negative voltages upon Ca^{2+}-depletion. C, D, The difference between the corresponding values of the CALHM paralogs 2, 4, and 6 and neg. are statistically insignificant (as judged by a Student t-test). B-D, Data show averages of 27 (neg.), 21 (CALHM1), 26 (CALHM2), 19 (CALHM4) and 21 (CALHM6) oocytes respectively. Errors are standard deviations.
The online version of this article includes the following figure supplement(s) for figure 2:

Figure supplement 1. Electrophysiology traces.

Table 1. Cryo-EM data collection, refinement and validation statistics of CALHM4.

	Dataset 1				Dataset 2		
	CALHM4_Ca^{2+}				CALHM4_Ca^{2+}_free		
	10-mer		11-mer		10-mer	11-mer	
Data collection and processing							
Microscope	FEI Tecnai G^2 Polara				FEI Tecnai G^2 Polara		
Camera	Gatan K2 Summit + GIF				Gatan K2 Summit + GIF		
Magnification	37,313				37,313		
Voltage (kV)	300				300		
Electron exposure (e–/Å^2)	40				32		
Defocus range (μm)	-0.8 to -3.0				-0.8 to -3.0		
Pixel size (Å)	1.34				1.34		
Initial particle images (no.)	422,281				576,841		
Final particle images (no.)	35,229	70,4581*	27,094	54,1881*	21,264	25,703	51,4061*
Reconstruction strategy2†	Std	Loc	Std	Loc	Std	Std	Loc
Symmetry imposed	D10	C10	D11	C11	D10	D11	C11
Global map resolution (Å) FSC threshold 0.143	4.24	4.07	4.02	3.92	4.07	3.82	3.69
Map resolution range (Å)	4.0-5.1	3.8-5.0	3.8-5.0	3.8-5.0	3.8-5.0	3.6-4.4	3.5-4.3
Map sharpening *B* factor (Å^2)	-200	-200	-185	-177	-169	-145	-126
EMDB identifier	10920	10920*‡	10921	10921*‡	10917	10919	10919*‡
Refinement		N/A		N/A			N/A
Model resolution (Å) FSC threshold 0.5	4.2		4.0		4.0	3.7	
Model composition Non-hydrogen atoms Protein residues	 41,620 5,340		 45,782 5,874		 41,620 5,340	 45,782 5,874	
B factors (Å^2) Protein	 62		 61		 34	 51	
R.m.s. deviations Bond lengths (Å) Bond angles (°)	 0.005 0.694		 0.005 0.672		 0.003 0.550	 0.005 0.754	
Validation MolProbity score Clash score Poor rotamers (%)	 1.53 10.19 0		 1.57 6.50 0		 1.48 7.59 0	 1.73 9.79 0	
Ramachandran plot Favored (%) Allowed (%) Disallowed (%)	 98.10 1.90 0		 96.66 3.34 0		 97.72 2.28 0	 96.65 3.35 0	
PDB identifier	6YTO		6YTQ		6YTK	6YTL	

*Subparticles from localized reconstruction.

†Std – standard reconstruction; Loc – localized reconstruction.

‡Higher-resolution map from localized reconstruction submitted as an additional map under the same entry as the main map.

6). Unlike to previous reports of CALHM2 structures, where interactions between channels were mediated by extracellular loops (***Choi et al., 2019***; ***Syrjanen et al., 2020***), the pairing in the CALHM4 sample proceeds via contacts at the intracellular side (***Figure 3A***). We also observed two distinct protein conformations in our data with CALHM4 and CALHM6 channels forming cylindrical and conical pores, respectively (***Figure 3D***). Although 2D class averages of CALHM2 appear of high quality, 3D classification of this dataset did not yield high-resolution structures. We believe that the strong preferential orientation of CALHM2 particles resulting in a predominance of views along the

Table 2. Cryo-EM data collection, refinement and validation statistics of CALHM6 and CALHM2.

	Dataset 3 CALHM6_Ca^{2+}		Dataset 4 CALHM2_Ca^{2+}
	10-mer	11-mer	
Data collection and processing			
Microscope	FEI Tecnai G^2 Polara		FEI Tecnai G^2 Polara
Camera	Gatan K2 Summit + GIF		Gatan K2 Summit + GIF
Magnification	37,313		37,313
Voltage (kV)	300		300
Electron exposure (e–/Å^2)	40		55
Defocus range (μm)	-0.8 to -3.0		-0.8 to -3.0
Pixel size (Å)	1.34		1.34
Initial particle images (no.)	216,859		417,612
Final particle images (no.)	98,104	63,310	N/A
Reconstruction strategy1*	Std	Std	Std
Symmetry imposed	C10	C11	C1
Global map resolution (Å) FSC threshold 0.143	4.39	6.23	N/A
Map resolution range (Å)	4.3-5.1	5.0-7.0	N/A
Map sharpening *B* factor (Å^2)	-259	-435	N/A
EMDB identifier	10924	10925	N/A
Refinement			N/A
Model resolution (Å) FSC threshold 0.5	4.4	6.6	
Model composition			
Non-hydrogen atoms	19,560	21,516	
Protein residues	2,520	2,772	
B factors (Å^2)			
Protein	85	86	
R.m.s. deviations			
Bond lengths (Å)	0.004	0.004	
Bond angles (°)	0.773	0.822	
Validation			
MolProbity score	2.14	2.15	
Clash score	16.18	17.75	
Poor rotamers (%)	0	0	
Ramachandran plot			
Favored (%)	93.55	93.95	
Allowed (%)	6.05	5.65	
Disallowed (%)	0.40	0.40	
PDB identifier	6YTV	6YTX	

*Std – standard reconstruction; Loc – localized reconstruction.

pore axis combined with sample heterogeneity has limited our data processing workflow to 2D classification (***Figure 3—figure supplement 6***). In general, we found an oligomeric distribution of CALHM2 channels that corresponds to previously determined structure with a majority of channels being organized as undecamers and a smaller population showing dodecameric assemblies (***Figure 3C***, ***Figure 3—figure supplement 6***). Due to the higher quality of the CALHM4 and 6 samples, we continued to use structures derived from these proteins for a detailed characterization of both pore conformations.

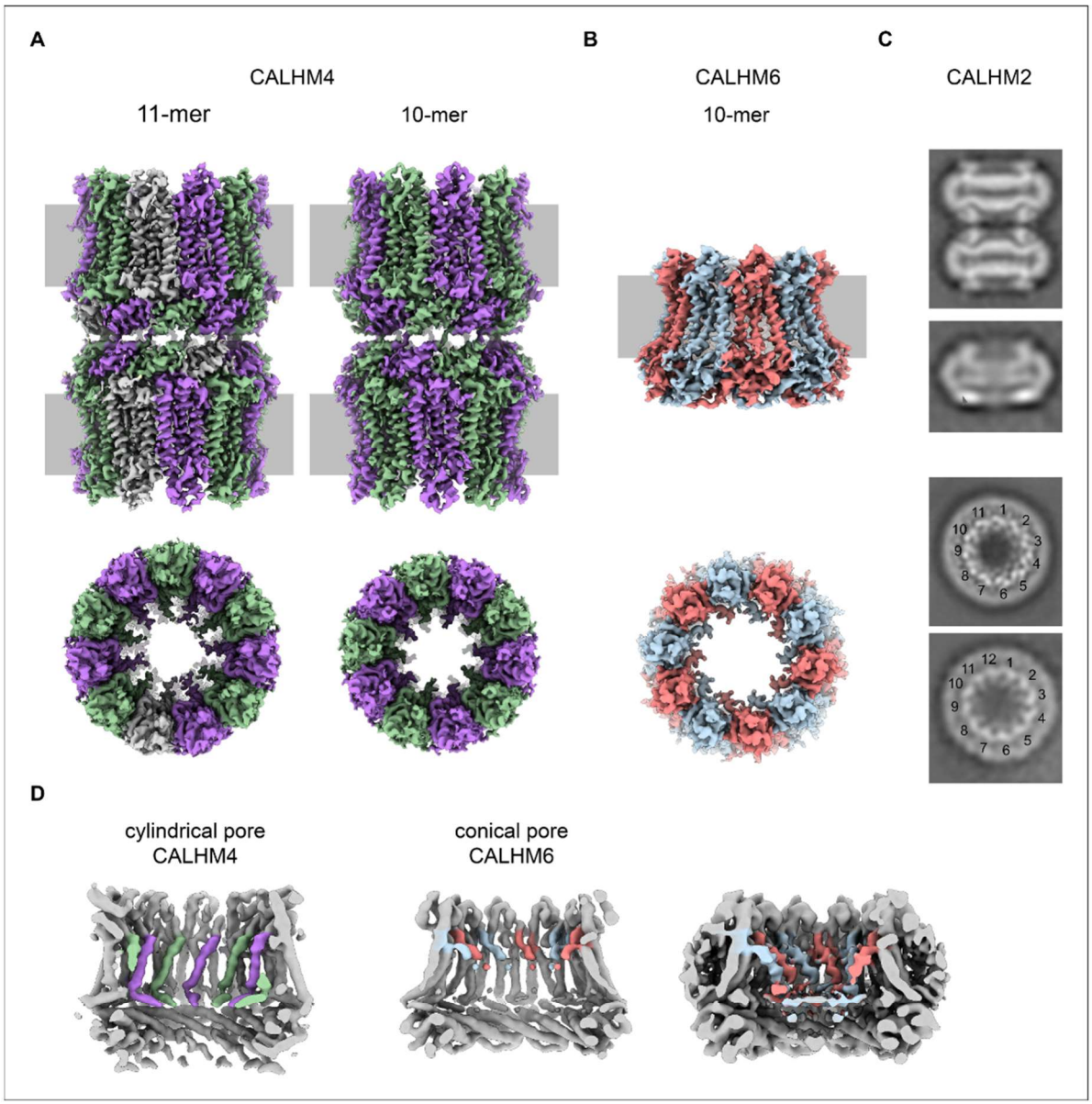

Figure 3. Cryo-EM analysis. (**A**) Cryo-EM density of undecameric (11-mer) and decameric (10-mer) pairs of CALHM4 channels at 3.8 and 4.1 Å respectively. Data were recorded from a Ca^{2+}-free sample. Subunits are colored in lilac and green, respectively. (**B**) Cryo-EM density of decameric CALHM6 channels at 4.4 Å. Subunits are colored in red and light-blue, respectively. A, B, Views are from within the membrane with membrane indicated as grey rectangle (top) and from the outside (bottom). (**C**) Selected 2D classes of the CALHM2 data showing interacting channel pairs and single channels viewed from within the membrane (top) and views of undecameric and dodecameric channels with subunits numbered (bottom). (**D**) Slices through the CALHM4 (left) and the CALHM6 (right) channels illustrating the distinct features of the cylindrical and conical pore conformations. View of CALHM6 at lower contour (right) shows extended density for the mobile TM1. Maps are low-pass filtered at 6 Å. Colored features refer to density corresponding to TM1 and NH.

The online version of this article includes the following figure supplement(s) for figure 3:

Figure supplement 1. Biochemical characterization.

Figure supplement 2. Cryo-EM reconstruction of CALHM4 in presence of Ca^{2+}.

Figure 3 continued on next page

Figure 3 continued

Figure supplement 3. Cryo-EM reconstruction of CALHM4 in absence of Ca^{2+}.
Figure supplement 4. Cryo-EM reconstruction of CALHM6 in presence of Ca^{2+}.
Figure supplement 5. Cryo-EM density of CALHM4 and CALHM6.
Figure supplement 6. Cryo-EM reconstruction of CALHM2 in presence of Ca^{2+}.

Cylindrical pore conformation of the CALHM4 structure

For the determination of the CALHM4 structure, we have recorded cryo-EM data in the presence and absence of Ca^{2+} and observed similar structural properties in both samples, which are not affected by divalent cations (***Figure 3—figure supplements 2*** and ***3***). In each case, we found a heterogeneous, about equal distribution of particles with two distinct oligomeric states. The smaller particles are composed of decameric and the larger of undecameric assemblies, both of which we refer to as CALHM4 channels (***Figure 4***). Due to the slightly higher quality of the Ca^{2+}-free sample, we continued to use this data for our further analysis unless specifically indicated. The cryo-EM density of the decamers extends to a resolution of 4.1 Å and undecamers to 3.7 Å, which in both cases permitted the unambiguous interpretation by an atomic model (***Figure 3—figure supplements 2***, ***3*** and ***5A***, ***Video 1***, ***Table 1***). In each structure, the subunits are arranged around a central axis of symmetry that defines the ion-conduction path. As described before, both assemblies contain pairs of CALHM4 channels of the same size related by two-fold symmetry that interact via their cytoplasmic parts (***Figure 4—figure supplement 1A–C***). The CALHM4 channels form approximately 90 Å high cylindrical proteins that span the lipid bilayer with regions at their respective periphery

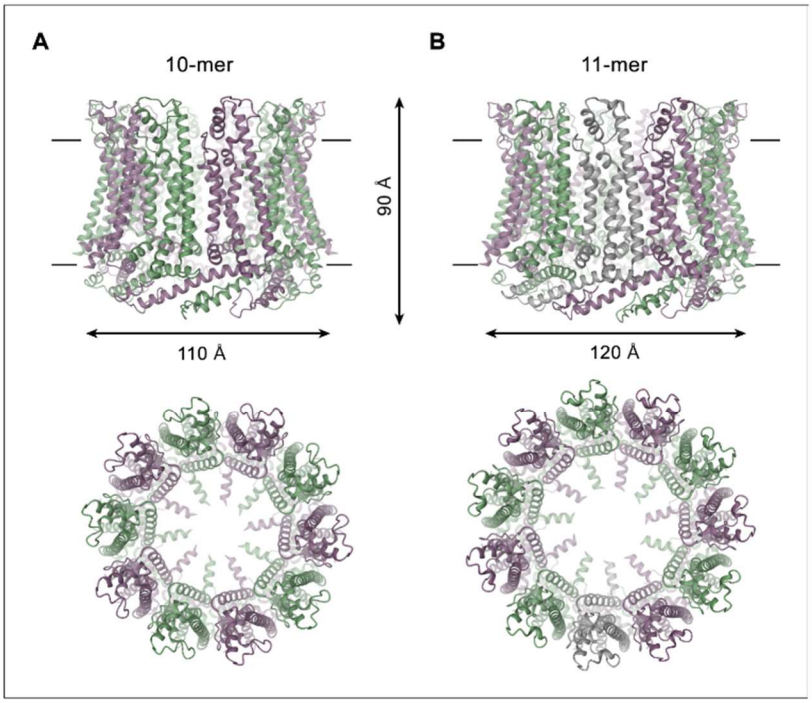

Figure 4. CALHM4 structure. Ribbon representation of (**A**), decameric and (**B**), undecameric CALHM4 channels. Top views are from within the membrane with membrane boundaries indicated, bottom views are from the extracellular side. The approximate dimensions are indicated. Subunits are colored in lilac and green.
The online version of this article includes the following figure supplement(s) for figure 4:

Figure supplement 1. Features of the CALHM4 structure.

Video 1. Cryo-EM density map of a single subunit of CALHM4 obtained in absence of Ca^{2+}. Shown is the cryo-EM map of the protein in detergent with the atomic model superimposed.
https://elifesciences.org/articles/55853#video1

extending into the aqueous environment on either side of the membrane (***Figure 4***). In the plane of the membrane, the dimensions of decameric and undecameric CALHM4 channels amount to 110 Å and 120 Å respectively (***Figure 4***, ***Figure 4—figure supplement 1D–E***). Irrespective of their distinct oligomerization, the individual subunits in both assemblies show equivalent conformations, which resemble the recently described structures of CALHM1 and 2 (***Choi et al., 2019***; ***Demura et al., 2020***; ***Syrjanen et al., 2020***) and thus define an organization that is likely general for the CALHM family (***Figure 5A***, ***Figure 5—figure supplement 1***). Although the members of this family were predicted to share their architecture with connexins and related innexin and LRRC8 channels (***Siebert et al., 2013***), this turns out not to be

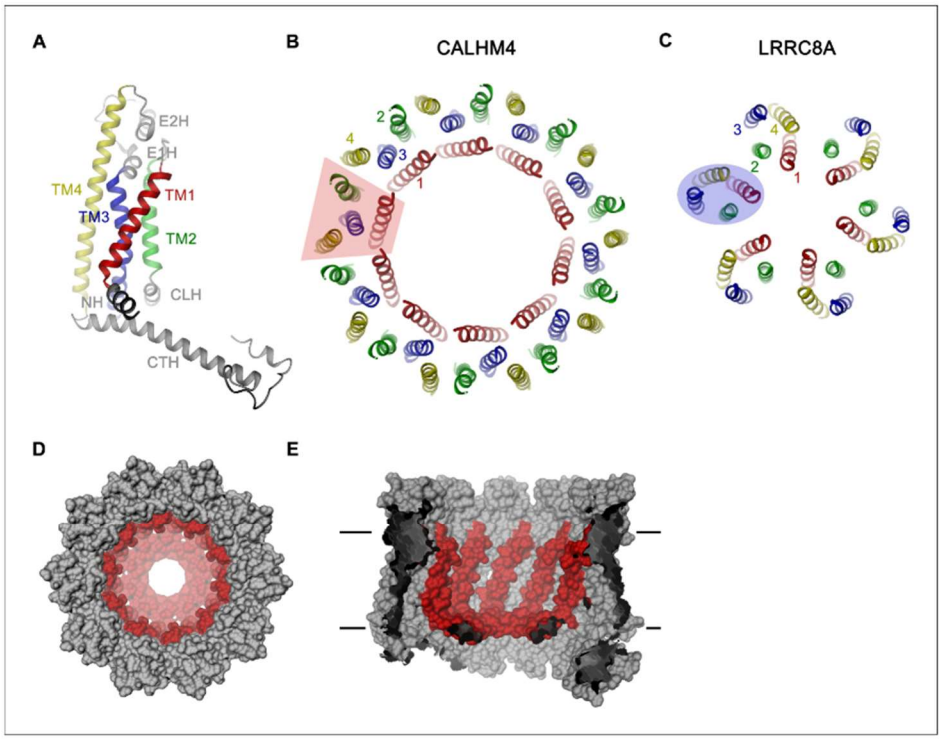

Figure 5. CALHM4 subunit and oligomeric arrangement. (**A**) Ribbon representation of the CALHM4 subunit. Secondary structure elements are labeled and transmembrane α-helices are shown in unique colors. View of the transmembrane α-helices of (**B**), the CALHM4 decamer and (**C**), the volume regulated anion channel LRRC8A from the extracellular side. B-C, color code is as in A, transmembrane segments of one subunit are numbered. The general shape of a single subunit is indicated (B, trapezoid, C, oval). (**D**) Surface representation of the CALHM4 decamer. The view is from the outside. (**E**), Slice through the CALHM4 pore viewed from within the membrane. D, E, TM1 and the N-terminal α-helix NH are colored in red.
The online version of this article includes the following figure supplement(s) for figure 5:

Figure supplement 1. Sequence and topology.
Figure supplement 2. Features of the CALHM4 structure.

the case. Whereas subunits in all families contain four transmembrane helices, which run perpendicular to the membrane, the mutual arrangement of these α-helices differs between CALHM channels and their connexin-like counterparts. When viewed from the extracellular side, the transmembrane helices in connexin, innexin and VRAC channels (***Deneka et al., 2018***; ***Kasuya et al., 2018***; ***Kefauver et al., 2018***; ***Maeda et al., 2009***; ***Oshima et al., 2016***) are arranged in a clockwise manner, whereas the arrangement in CALHM channels is anticlockwise (***Figure 5B,C***). Moreover, in connexins and related channels, the four helices form a tightly interacting left-handed bundle with a common core, resulting in a structure with an oval cross-section (***Figure 5C***). Conversely, the helices of the CALHM subunit are organized as two layers conferring an overall trapezoid cross-section (***Figure 5B***). Finally, whereas connexins and LRRC8 channels form hexamers, and innexins form octamers, an oligomeric arrangement that has also been observed for CALHM1, the larger CALHM4 channels contain either 10 or 11 subunits (***Figure 4A,B***). The outer layer of the CALHM subunit is composed of the interacting α-helices TM2-4, which are arranged in one row sharing mutual interactions only with their respective neighbor. The inner layer consists of TM1, which on its entire length exclusively interacts with TM3, the central helix of the outer layer (***Figure 5A,B***). When assembled into oligomers, the helices of the outer layer form a ring, which defines the boundaries of the channel (***Figure 5B***). In this outer ring, the peripheral helices TM2 and 4 are involved in extended interactions with neighboring subunits resulting in a tightly packed interface. Apart from a small fenestration between TM3 and 4 in the center of each subunit, this structural unit shields the interior of the pore from the surrounding membrane (***Figure 5—figure supplement 2A***). In contrast, the respective TM1 helices forming the inner layer are distant from each other and thus not involved in mutual inter-subunit interactions (***Figure 5D,E***). In the region preceding TM1, the residues of the N-terminus form a helix (NH) that is oriented perpendicular to the first transmembrane segment parallel to the plane of the lipid bilayer (***Figure 4***, ***Figure 5D***, ***Figure 3—figure supplement 5A*** and ***Figure 5—figure supplement 2B***). Among the family members of known structures, the conformations of NH and TM1 are best defined in CALHM4 (***Figure 3—figure supplement 5A***), whereas weaker density of these fragments in the equivalent state of CALHM1 and 2 points towards a higher mobility of this region in latter proteins (***Choi et al., 2019***; ***Syrjanen et al., 2020***). On the extracellular side, a short loop bridges α-helices TM1 and 2 and an extended region containing two short α-helices (E1H and E2H), connects TM3 with the long TM4, which extends beyond the membrane plane (***Figure 5A***). Both segments of the extracellular domain are stabilized by two conserved disulfide bridges (***Figure 5—figure supplement 2C***). On the intracellular side, TM2 precedes a short helix (CLH) that projects away from the pore axis with TM3 being bent in the same direction (***Figure 5—figure supplement 2D***). Both α-helices are connected by a 12-residue long loop that is probably mobile and thus not defined in the density. Downstream of TM4, we find an extended intracellular region. The first halve of this region consists of a long α-helix (CTH), which is tilted by 70˚ towards the membrane plane. By mutual interaction with neighboring subunits, the CTH-helices form a 30 Å-high intracellular ring that extends from the membrane into the cytoplasm (***Figures 4*** and ***5A***, ***Figure 4—figure supplement 1C***). Distal to CTH, a weakly defined 62-residue long extended loop, which contains interspersed secondary structure elements, folds back towards the intracellular ring and extends to the juxtaposed CALHM4 channel (***Figure 4—figure supplement 1B,C***). In this way the C-terminal loops mediate the bulk of the interaction relating CALHM4 channel pairs in an arrangement whose relevance in a cellular context is still ambiguous.

Pore architecture

Decameric and undecameric CALHM4 channels contain wide pores, which are cylindrical throughout except for a constriction at the intracellular membrane boundary. The diameter at both entrances of the pore measures about 52 Å and 60 Å for decameric and undecameric assemblies respectively, thus defining the properties of an unusually large channel, which could be permeable to molecular substrates (***Figure 6A***, ***Figure 4—figure supplement 1D,E***). Even at the constriction located at the intracellular membrane leaflet where the respective N-terminal helices NH project towards the pore axis, the decameric channels are about 20 Å and undecameric channels 30 Å wide (***Figure 6A***). In both cases the pore would thus be sufficiently large to accommodate an ATP molecule, consistent with the notion of CALHM proteins forming ATP-permeable channels (***Figure 4—figure supplement 1D,E***). Remarkably, this large pore size is in sharp contrast to our functional characterization by electrophysiology where we did not observe appreciable currents for CALHM4 (***Figure 2A***, ***Figure 2—***

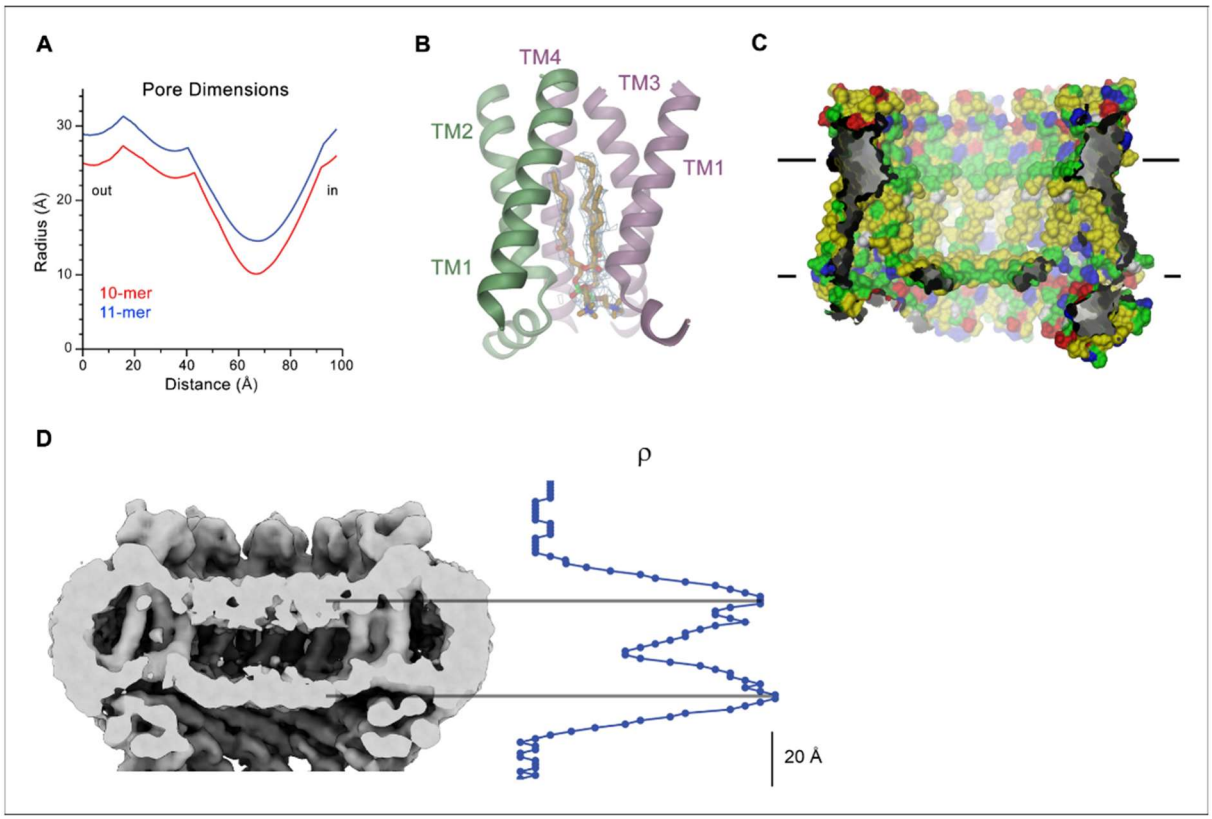

Figure 6. CALHM4 pore properties and lipid interactions. (**A**), Pore radius of the CALHM4 decamer (red) and undecamer (blue) as calculated in HOLE (***Smart et al., 1996***). (**B**) Two phosphatidylcholine molecules modeled into residual cryo-EM density (blue mesh) in a cavity at the interface between neighboring α-helices TM1. Secondary structure elements are indicated. (**C**) Chemical properties of residues lining the pore of the CALHM4 channel. Shown is a slice through the pore viewed from within the membrane. The protein is displayed as molecular surface. Hydrophobic residues are colored in yellow, polar residues in green, acidic residues in red and basic residues in blue. (**D**) Slice through the pore region of the CALHM4 undecamer viewed from within the membrane. Shown is non-averaged density in a single copy of the undecameric CALHM4 channel pair at low contour to highlight the location of increased density within the pore corresponding to a bilayer of either phospholipids or detergents. A plot of the density along the pore axis showing two maxima that are separated by the expected distance between the headgroup regions of a lipid bilayer is shown right. B, D, Displayed cryo-EM density refers to data from the undecameric channel in presence of Ca^{2+}.
The online version of this article includes the following figure supplement(s) for figure 6:

Figure supplement 1. Lipid interactions in the pore of CALHM4.
Figure supplement 2. LC-MS analysis of co-purified lipids.

figure supplement 1E), which suggests that either the absence of activating or presence of inhibiting components might impede ion conduction.

Within the membrane, the pore diameter of CALHM4 is confined by the ring of non-interacting TM1 helices, which is placed inside an outer ring of the channel formed by helices TM2-4 (***Figure 5B,D***). This arrangement creates clefts between neighboring helices of the inner ring which are delimited by helices TM2 and 4 at the respective subunit interfaces (***Figure 5B,E***). In our sample, this cleft appears to be filled with lipids as indicated by the residual density observed in the cryo-EM maps (***Figure 6B***, ***Figure 6—figure supplement 1A,B***). Due to the prevalence of aliphatic residues lining the pore at the assumed location of the membrane core, the pore is highly hydrophobic, whereas the regions extending into the aqueous environment contain polar and charged residues (***Figure 6C***). Similarly, the side of the helical N-terminus, which faces the membrane at its intracellular boundary, is hydrophobic (***Figure 5—figure supplement 2B***). In light of its large cross-section

and high hydrophobicity, it is conceivable that the interior of the pore would accommodate lipids, which potentially could form bilayers that would restrict ion permeation as recently suggested for CALHM2 based on molecular dynamics simulations (***Syrjanen et al., 2020***). In our data, we find strong evidence for a layered distribution of density inside the pore within the presumed membrane region in non-symmetrized maps and after application of symmetry. This density is observed with similar properties in decameric and undecameric proteins in both datasets of CALHM4 obtained in either absence or presence of Ca^{2+} (***Figure 6D***, ***Figure 6—figure supplement 1C***). Its distribution displays features that quantitatively match the corresponding properties of lipid membranes obtained from a comparison to cryo-EM density of liposomes and computer simulations (***Figure 6—figure supplement 1D,E***) and could thus either reflect the presence of lipids or detergent molecules arranging in a bilayer-like structure facilitated by the confined pore geometry. We thus analyzed the composition of small molecules that are co-purified with CALHM4 by mass spectrometry and were able to detect phospholipids that are commonly found in the membranes of HEK cells (***Figure 6—figure supplement 2***). Collectively, our data are compatible with the presence of a lipid bilayer located within the pore region of CALHM4 channels, which could interfere with the diffusion of charged substances. Thus, despite of its large pore diameter, it is at this point unclear whether the CALHM4 structure defines a conductive conformation of CALHM channel or alternatively a conformation that harbors a membrane-like assembly residing inside the pore that would impede ion conduction.

Conical pore conformation of the CALHM6 structure

As in case of CALHM4, data of CALHM6 shows a heterogeneous distribution of decameric and undecameric channels, but in this case with a prevalence of the former amounting to 60% of the classified particles (***Figure 3—figure supplement 4***). Both assemblies of CALHM6 contain subunits with equivalent conformations, which are better defined in the smaller oligomers (***Figure 3B***, ***Figure 3—figure supplement 4***). We have thus chosen the decameric CALHM6 structure for a description of the conical pore of a CALHM channel (***Figures 3D*** and ***7A–C***). Unlike CALHM4, the lower resolution of the CALHM6 density of 4.4 Å, precludes a detailed interpretation of the structure for all parts of the protein. Still, the high homology between the two paralogs and density attributable to large side chains constrains the placement of helices and conserved loop regions and thus allows the credible analysis of major conformational differences (***Figure 3—figure supplement 5B***, ***Video 2***, ***Table 2***). Unlike CALHM4, there is no dimerization of CALHM6 channels and the C-terminal region following the cytoplasmic helix CTH instead appears to engage in intramolecular interactions with the outside of the cytoplasmic rim for most of its length (***Figure 7A***). This observation further supports the notion that the dimerization of CALHM4 might be a consequence of interactions formed between solubilized proteins where the mobile C-terminus could equally well engage in intra- and intermolecular interactions, of which the latter would be multiplied in the highly symmetric arrangement. Although the general organization of the CALHM6 channel closely resembles CALHM4, it shows a distinctly different state of the pore (***Figure 3D***). Upon comparison of decameric channels of both paralogs, in CALHM6 we find a slight expansion of the protein parallel to the membrane and an accompanying moderate contraction in perpendicular direction (***Figure 7—figure supplement 1A***, ***Video 3***). In a superposition of the subunits, similar conformations are observed for α-helices TM2 and 4 and the C-terminal helix CTH and larger differences in the interacting helices TM1 and 3 (***Figure 7D***, ***Figure 7—figure supplement 1B,C***). These differences are most pronounced for TM1, which in CALHM6 has detached from TM3 and moved by 60˚ towards the pore axis around a hinge located upstream of a conserved phenylalanine at the end of TM1 (***Figure 7B–E***). In both structures, the conformation of the proximal loop connecting TM1 and 2 is stabilized by two conserved cysteines, which are involved in disulfide bridges with the region connecting TM3 and TM4 (***Figure 7F–G***, ***Figure 5—figure supplement 2C***, ***Video 4***). As a consequence of the disruption of its interaction with TM1, the intracellular halve of TM3 tilts away from the pore axis by 30˚ around a pivot located close to a conserved proline residue (P115 in CALHM4), which probably destabilizes the helix (***Figure 7—figure supplement 1B,D***). The transition from a conformation observed in CALHM4 to a conformation defined by CALHM6 is accompanied by the dissociation of interactions between TM1 and 3, which are mediated by conserved residues involving a cluster of hydrophobic interactions at the extracellular side and additional interactions on the entire length of both α-helices (***Figure 7F–G***, ***Figure 7—figure supplement 1C,D***, ***Video 4***). The iris-like movement of TM1 in the

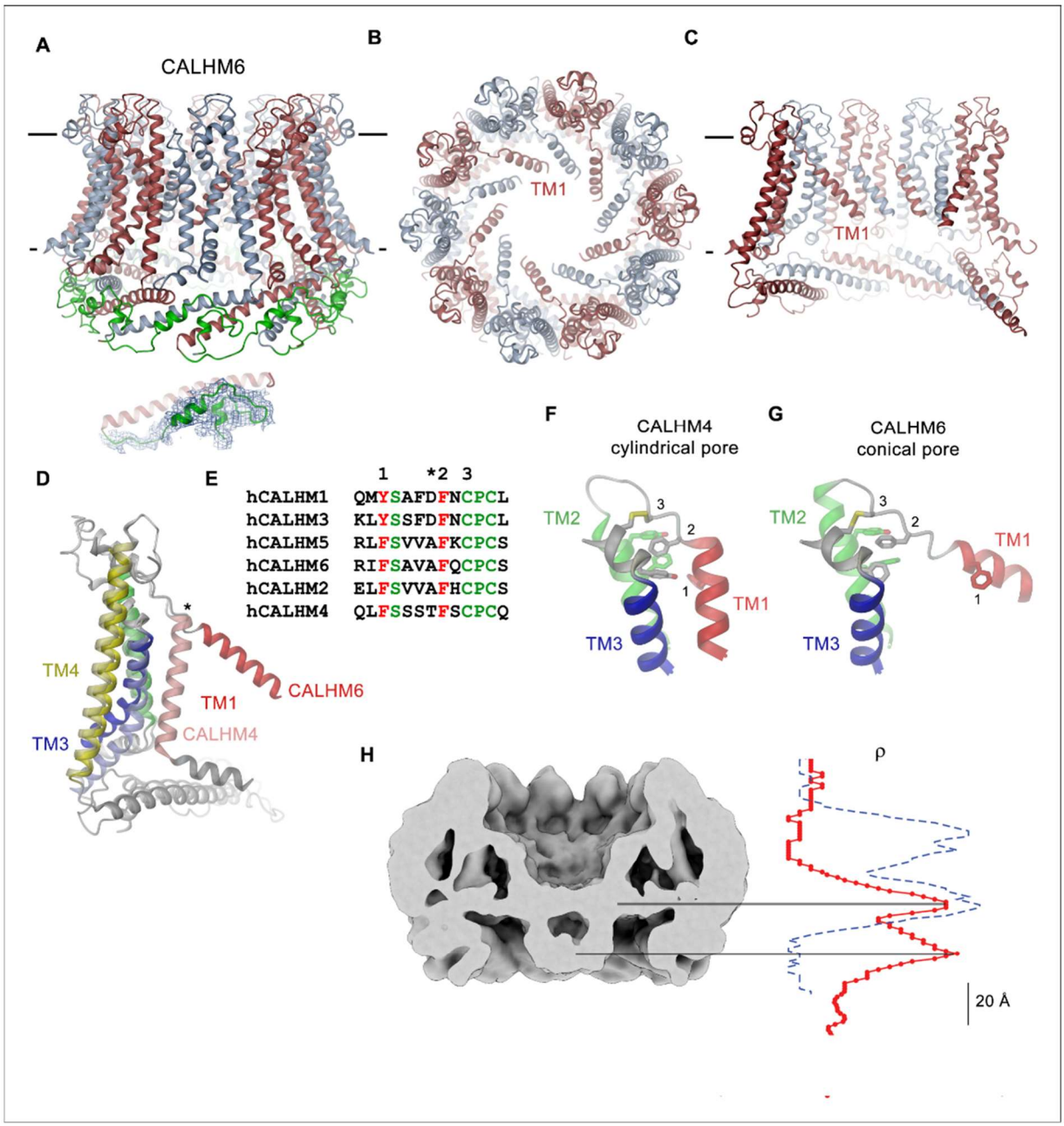

Figure 7. CALHM6 structure. (**A**) Ribbon representation of the decameric CALHM6 structure viewed from within the membrane. Subunits are colored in red and light blue. The C-terminus following CTH is colored in green. Inset (below) shows a close-up of this region with cryo-EM density superimposed. (**B**) View of the CALHM structure from the extracellular side. (**C**) Slice through the pore of the CALHM6 structure. B, C, TM1, which has moved towards the pore axis is labeled. A, C, the membrane boundary is indicated. (**D**) Superposition of single subunits of the CALHM4 and CALHM6 structures illustrating conformational changes. Coloring is as in ***Figure 5A*** with CALHM4 shown in brighter shades of the same color. Secondary structure elements are labeled and the hinge for the movement of TM1 is indicated by an asterisk. (**E**) Sequence alignment of the end of TM1 and the following loop of CALHM paralogs. Selected conserved residues are colored in green and red. Numbering corresponds to residues indicated in panels F and G. Asterisk marks the hinge region displayed in D. Close-up of the extracellular region involved in conformational changes in (**F**), the cylindrical

Figure 7 continued on next page

Figure 7 continued

conformation displayed in CALHM4 and (**G**), the conical conformation displayed in CALHM6. Residues contributing to a cluster of aromatic residues on TM1-3 and a conserved disulfide bridge are shown as sticks. Selected positions highlighted in E are labeled. F, G, Coloring is as in ***Figure 5A***. (**H**) Slice through the pore region of the CALHM6 decamer viewed from within the membrane. Shown is non-averaged density at low contour to highlight the location of diffuse density within the pore. A plot of the density along the pore axis of CALHM6 is shown in red, the corresponding density in CALHM4 is shown as a dashed blue line for comparison. The two maxima in the CALHM6 density are shifted towards the intracellular side. The density corresponding to the headgroups of the outer leaflet of the bilayer in CALHM4 is absent. Density at the location of the headgroup region at the inner leaflet of the bilayer and further towards the intracellular side could correspond to either lipids or to the poorly ordered N-terminus.
The online version of this article includes the following figure supplement(s) for figure 7:

Figure supplement 1. Features of the CALHM6 structure.

oligomeric channel in its transition between conformations probably requires concerted rearrangements to avoid steric clashes in the crowded environment of the pore. When viewed from the outside this transition thus resembles the closing of an aperture and it converts a cylindrical pore to a funnel which narrows towards the intracellular side while creating a large cavity between TM1 and TM3 that becomes accessible from the cytoplasm (***Figure 7C***, ***Video 3***). In the cryo-EM density, TM1 is less well defined compared to the rest of the protein reflecting its increased flexibility in the observed structure (***Figure 3—figure supplement 5B***). Since the conformation of NH, which has moved towards the pore axis, is not defined in the density, the size of the CALHM6 channel at its constriction remains ambiguous. It could range from an occluded pore if NH helices make contacts in the center of the channel (modeled as clogged conformation) to a pore with similar diameter as found at the CALHM4 constriction. The latter could be obtained in case the mutual relationship between TM1 and NH remains unchanged compared to the CALHM4 structure (defined as kinked conformation) or if NH straightens in continuation of TM1 (in an extended conformation) (***Figure 7—figure supplement 1E***). In any case, the large conformational changes would affect the location of lipids within the pore, which in case of an internal bilayer would have to rearrange in response to the severely altered pore geometry. Such rearrangement is reflected in the changed distribution of the residual electron density inside the pore (***Figure 7H***). Whereas, compared to CALHM4, we find density at the location of the intracellular layer of lipids and further towards the cytoplasm, part of which might be attributable to the mobile N-terminal α-helix NH, the outer layer of density corresponding to the putative extracellular leaflet of a bilayer has disappeared. A comparable distribution of pore density is found in the structure of CALHM2 in complex with ruthenium red, which resides in a similar conical pore conformation (***Choi et al., 2019***). Thus, despite the pronounced conformational differences to CALHM4 and the fact that the CALHM6 structure appears to contain features of a closed pore, a definitive functional assignment remains also in this case ambiguous.

Discussion

In the presented study, we have addressed the structural and functional properties of CALHM channels in the human placenta. To identify relevant CALHM paralogs in this organ, we have quantified their expression in samples of the whole placenta and in isolated trophoblast cells and found CALHM2, 4 and 6 to be abundant on a transcript level (***Figure 1***). Their high expression compared to other membrane proteins (***Figure 1—figure supplement 1***) suggests an important functional relevance of these membrane channels in mediating transport processes during the development of the fetus, although their detailed role still awaits to be explored.

The structural characterization of the three placental paralogs by cryo-electron microscopy has provided insight into fundamental features

Video 2. Cryo-EM density map of a single subunit of CALHM6. Shown is the cryo-EM map of the protein in detergent with the atomic model superimposed.
https://elifesciences.org/articles/55853#video2

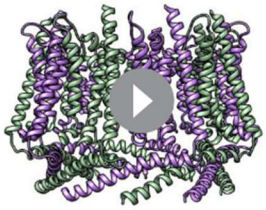

Video 3. Morph between the cylindrical pore conformation of CALHM4 and the conical pore conformation displayed in the 'extended' model of CALHM6. In the latter the N-terminal α-helix NH is modeled in continuation of TM1 resulting in a constricting pore diameter similar to CALHM4.
https://elifesciences.org/articles/55853#video3

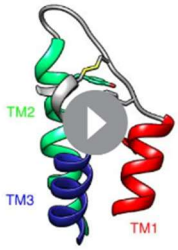

Video 4. Morph of the extracellular region of a single CALHM subunit involved in conformational changes between the cylindrical conformation displayed in CALHM4 and the conical conformation displayed in CALHM6. Residues contributing to a cluster of aromatic residues on TM1-2 and a conserved disulfide bridge are shown as sticks. Coloring is as in ***Figure 5A***.
https://elifesciences.org/articles/55853#video4

of the family which largely conform with properties that have recently been described for CALHM1 and 2 (***Choi et al., 2019***; ***Demura et al., 2020***; ***Syrjanen et al., 2020***) but which also show substantial differences. Similar to previous studies, our structures have defined the architecture of the CALHM subunit which, although containing the same number of membrane-spanning helices as VRACs and gap-junctions forming connexins, innexins and pannexins, is distinct from these proteins (***Figure 5B,C***). The CALHM subunits thus constitute unique modular building blocks that assemble with different stoichiometries into large membrane channels. In contrast to previously described CALHM structures, where the oligomeric state of individual channels was described as uniform, our data show heterogeneous populations with CALHM4 and CALHM6 assembling as decameric and undecameric channels with similar abundance and CALHM2 as predominantly undecameric proteins with a smaller population of dodecamers (***Figure 3***, ***Figure 3—figure supplements 2–4*** and ***6***). The diverse oligomerization of different paralogs is generally consistent with the assemblies observed for the previously described CALHM1 and CALHM2 structures, which were reported to form octamers and undecamers, respectively (***Choi et al., 2019***; ***Demura et al., 2020***; ***Syrjanen et al., 2020***), and it underlines the ability of CALHM proteins to constitute membrane channels of different sizes. Although the physiological role of these different oligomeric states is currently unclear, the observed heterogeneity might reflect the low energetic penalty for the incorporation of additional subunits into large oligomeric channels of the CALHM family. In this respect, the smaller size of CALHM1 channels could be responsible for its functional properties, which are manifested in electrophysiological recordings. Whereas CALHM1 in our hands showed the previously described functional hallmarks of a channel that is activated by depolarization and removal of extracellular calcium, we have not observed pronounced activity of CALHM2, 4 and 6 under the same conditions, despite their efficient targeting to the plasma membrane (***Figure 2***, ***Figure 2—figure supplement 1***). The low current response contrasts with the larger oligomeric organization of these proteins, which should lead to channels of even higher conductance than observed for CALHM1, and thus likely reflects their low open probability. Together our findings suggest that CALHM2, 4, and 6 are regulated by distinct, still unknown mechanisms. In that respect it remains puzzling how the large pores observed for the investigated structures (with diameters of CALHM4 decamers exceeding 40 Å within the membrane and 20 Å at the respective constriction, ***Figure 6A***) can be regulated to prevent leakage of substances under resting conditions, which would be deleterious to the cell. Despite the unknown activating stimuli, our study has provided insight into gating transitions of CALHM channels by showing two conformations with either a cylindrical pore of uniform large dimeter within the membrane that is constricted at the intracellular side as in case of CALHM4 and a conical pore that continuously

narrows from its extracellular entry towards the cytoplasm as in case of CALHM6 (***Figures 4*** and ***7***). The main difference in the pore geometry results from a large rearrangement of the pore-lining α-helix TM1 which is accompanied by a smaller change in TM3 (***Figure 7D***). Whereas in the cylindrical pore conformation of CALHM4, TM1 tightly interacts with TM3, which is a part of a densely packed outer rim of the pore consisting of TM2-4, the helix has dissociated from its interaction site and instead moved towards the symmetry axis to alter the pore geometry in the conical conformation of CALHM6. Similar conformational properties have previously been described for CALHM2 channels, although with a different orientation of TM1 in the conical pore conformation (***Choi et al., 2019***; ***Figure 8—figure supplement 1A–C***). In this previous study, the cylindrical conformation was assigned to an open state and the conical conformation to a closed state of the pore, a proposal that is further supported by a structure of the bound blocker rubidium red which appears to stabilize the conical conformation (***Choi et al., 2019***; ***Figure 8***). While, at first glance, the relationship between observed pore conformations and their corresponding functional states appears evident, there are still puzzling questions which prevent a definitive assignment at this stage. For example in light of the large diameter of the CALHM4 pore, the poor conductance properties in functional recordings remain mysterious. In that respect, the presence of lipids within the pore of large CALHM channels is noteworthy as it offers a potential alternative mechanism for regulation. In our structure of CALHM4, we find bound lipids inside the pore to stabilize the gap between non-interacting TM1 helices from different subunits (***Figure 6B***). Additionally, the bimodal diffuse residual cryo-EM density within the hydrophobic interior of CALHM4, which either originates form detergents or co-purified lipids that assemble as bilayers in the constrained environment of the pore are remarkable (***Figure 6D***). This distribution of density has changed markedly in the conical structure of CALHM6 (***Figure 7H***) and hints at a potential role of lipids in shaping the activation and permeation properties

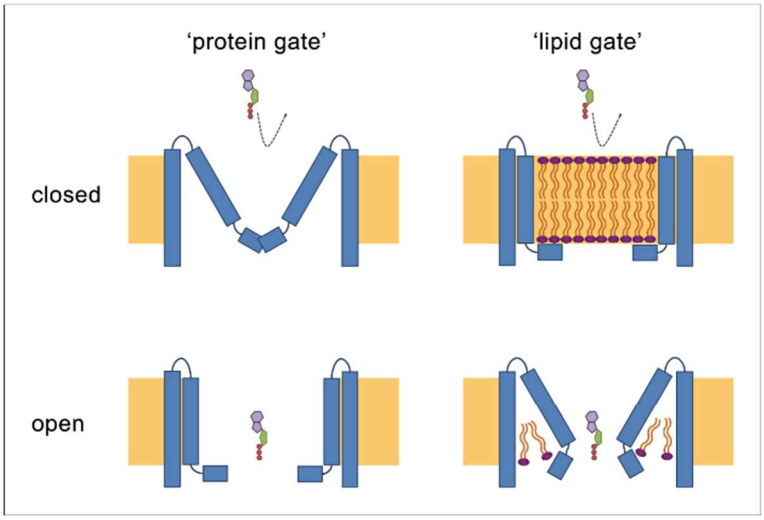

Figure 8. Hypothetical gating mechanisms. Schematic illustration of hypothetical gating mechanisms of large CALHM channels. Left, 'protein gate'. The gate impeding ion conduction of large CALHM channels (i.e. CALHM2, 4, 6) in the closed state is formed by the N-terminus of the protein, which closes the pore as observed in the modeled 'clogged' conformation of CALHM6 (top). In this case the conical conformation of CALHM6 would display a closed pore and the cylindrical conformation (bottom) an open pore. Right, 'lipid gate'. The gate impeding ion conduction of large CALHM channels in the closed state is formed by lipids assembling as a bilayer within the protein, which impedes ion conduction. Since bilayer formation is facilitated in the cylindrical conformation of CALHM4, this structure represents a closed pore (top) whereas the structure of the bilayer would be disturbed in the conical conformation of CALHM6 (bottom). Since both the 'kinked' and 'extended' pore conformations of CALHM6 show a large opening, these conformations could represent open pores.
The online version of this article includes the following figure supplement(s) for figure 8:

Figure supplement 1. Comparison of pore conformations.

of large CALHM channels, which is currently still not understood (***Figure 8***). We thus could envision two alternative scenarios which might underly regulation in large CALHM channels where the gate in the closed state could either be formed by part of the protein or by lipids (***Figure 8***, ***Figure 8—figure supplement 1D***). Both models are at this stage hypothetical and it is still unclear how lipids in the pore would rearrange during activation. Another remarkable feature of large CALHM channels concerns their tendency to form pairwise assemblies upon extraction from the membranes (***Figure 3A,C***, ***Figure 3—figure supplements 2***, ***3*** and ***6***). This property has previously been observed for undecameric CALHM2 channels, which were described to dimerize on the extracellular side thus forming structures that resemble gap-junctions, and in the present study, where dimerization was found to some degree in all samples. In our data, the described behavior is most pronounced in case of CALHM4 where dimerization proceeds on the intracellular side mediated by interactions with the partly mobile C-terminus. Although intriguing, it is currently unclear whether any of the observed pairwise interactions is of relevance in a physiological context.

Thus, although our data have provided a large step forward towards the comprehension of CALHM channels, it has also opened many questions. An important area of future investigations relates to the characterization of the localization of CALHM channels in different placental cell types and the identification of their subcellular distribution. Knowledge of their localization would provide a first glimpse into potential roles of these large channels for transport processes in this organ and should provide answers on the potential relevance of intra- and extracellular interactions of channel pairs. Another question concerns the ability of the three paralogs to heteromerize and the potential relevance of such heteromeric channels in a physiological environment. Finally, it will be important to study the activation mechanism of the described channels and whether they are embedded in larger interaction networks, which shape their activation properties. These topics will be addressed in future studies for which our current data provide an important foundation.

Materials and methods

Placenta collection

Human placental tissues were collected from the Division of Obstetrics and Gynecology, Lindenhofgruppe Bern, Switzerland, under approval by the ethical commission of the Canton of Bern (approval No. Basec 2016–00250). Written informed consent was obtained from all participants. Placentas were collected from uncomplicated pregnancies following elective cesarean section beyond 37 weeks of gestation without prior labor upon patients request or due to breech presentation. All experiments were carried out in accordance with the relevant guidelines and regulations.

Expression analysis in placental tissue

RNA isolation, reverse transcription and quantitative RT-PCR

Approximately 50 mg of frozen placental tissue was subjected to RNA isolation as previously described (***Huang et al., 2018***; ***Huang et al., 2013***). All RNA samples included in the study had an OD260/280 ratio >1.8. First-strand cDNA was synthesized from 2 µg of total RNA with oligo $(dT)_{15}$ primers and GoScript Reverse Transcriptase (Promega, Switzerland) according to the manufacturer's instructions. The qPCR reaction in SYBR Green reagent (10 µl) contained 0.5 µM primers, 2 x GoTaqqPCR Master Mix (Promega, Switzerland) and 1 µl cDNA. Primer nucleotide sequences and PCR efficiencies are shown in ***Figure 1—figure supplement 1C and D***. Amplification reactions were performed in duplicates in 384-well plates with the ViiA7 system (Applied Biosystems, USA). To evaluate mRNA quantities, data were obtained as C_t values (describing the cycle number at which logarithmic plots cross calculated threshold lines). C_t values were used to determine ΔC_t values (ΔC_t = C_t value of the reference gene minus the C_t value of the target gene). The applied reference gene was Tyrosine 3-monooxygenase/tryptophan 5-monooxygenase activation protein, zeta polypeptide (YWHAZ). Comparative transcript data between undifferentiated (CTB) and differentiated (STB) cells were calculated as $2^{-\Delta\Delta Ct}$ values ($\Delta\Delta C_t$ = C_t value of CALHM gene – C_t value of YWHAZ) and are presented as x-fold difference. Data analysis and statistical evaluations were performed using paired 2-way ANOVA with Sidak's multiple comparisons test with GraphPad Prism software.

Primary trophoblast isolation and characterization

Villous trophoblast cells were isolated from healthy human term placentas by enzymatic digestion and gravitational separation as previously described (***Nikitina et al., 2011***; ***Huang et al., 2013***) with minor modifications. Briefly, villi-rich tissues were digested three times with 0.25% trypsin (Sigma, USA) and 300 IU/ml Deoxyribonuclease I (Sigma, USA), and then subjected to Percoll (Sigma, USA) density gradient centrifugation to isolate villous cytotrophoblast cells. In order to assure the purity of the cells, flow cytometry analysis was performed by using the trophoblast-specific epithelial cell marker cytokeratin 7 (***Maldonado-Estrada et al., 2004***) (anti-cytokeratin 7, Dako, Switzerland). Vimentin (anti-vimentin, Sigma, USA), which is only expressed in potentially contaminating cells (e.g. mesenchymal cells, fibroblasts, smooth muscle cells, stromal cells) served as a negative marker (***Soares and Hunt, 2006***).

Primary trophoblast cell culture

Isolated human trophoblast cells were cultured in Dulbecco's modified Eagle's medium containing 4.5 g/l glucose (DMEM-HG, Gibco, UK) supplemented with 10% fetal bovine serum (FBS, Seraglob, Switzerland) and Antibiotic-Antimycotic (Gibco, USA) in a humidified incubator under a 5% CO_2 atmosphere at 37˚C. Cells were seeded at a density of 0.2 10^6 cells/cm^2 in costar CellBIND six well plates (Corning, USA) and harvested after 24 hr (cytotrophoblast stage) or 48 hr (STB stage). The syncytialization process was confirmed by visualization under the microscope.

Expression cell lines

Adherent HEK293T cells used for protein expression and screening experiments were cultured in DMEM medium supplemented with 10% FBS and penicillin/streptomycin in a humidified incubator under a 5% CO_2 atmosphere at 37˚C. Suspension-adapted HEK293S GnTI$^-$ cells used for protein expression and purification were grown in HyClone TransFx-H media, supplemented with 2% fetal bovine serum (FBS), 4 mM L-glutamine, 1.5% Poloxamer 188 and penicillin/streptomycin in a humidified incubator under 5% CO_2 atmosphere at 37˚C. Both cell lines were tested negative for mycoplasma contamination.

For construct generation, cDNAs of human CALHM proteins, with SapI restriction sites removed, were obtained from GenScript. For expression in *X. laevis* oocytes, cDNAs of CALHM1, CALHM2, CALHM4 and CALHM6 were cloned into a pTLNX vector. For expression in mammalian cells, cDNAs of all human CALHM homologs were cloned into a pcDNA 3.1 vector which was modified to be compatible with FX cloning technology (***Geertsma and Dutzler, 2011***) and to encode a C-terminal 3C protease cleavage site followed by Venus-Myc-SBP tag.

Homolog screening

For overexpression studies of CALHM paralogs, adherent HEK293T cells were seeded on 10 cm dishes and grown to a density of 7 10^6 cells/well. Subsequently, cells were transiently transfected with mixtures of respective *CALHM* cDNA constructs and polyethylenimine with an average molecular weight of 25 kDa (PEI 25K, branched). As a preparative step, 12 µg of DNA and 48 µg of PEI were separately incubated in 0.5 ml of DMEM medium. After 5 min, both solutions were mixed, incubated for 15 min and added to respective cell cultures. 36 hr post transfection cells were washed with PBS, harvested by centrifugation at 400 g for 5 min, flash-frozen in liquid nitrogen and stored at −20˚C. For protein extraction, cells were thawed on ice, lysed with lysis buffer (25 mM HEPES, 150 mM NaCl, 0.5 mM $CaCl_2$, 2 mM $MgCl_2$, 2% GDN, protease inhibitors, RNase, DNase, pH 7.6) for 1 hr and clarified by centrifugation at 16,000 g for 10 min. The obtained supernatants were filtered through 0.22 µm centrifugal filters and injected onto a Superose 6 5/150 column equilibrated with elution buffer (10 mM HEPES, 150 mM NaCl, 50 µM GDN pH 7.6) and eluted in the same buffer. Proteins were identified by recording of the fluorescence of the attached Venus YFP.

Protein expression and purification

Suspension HEK293S GnTI$^-$ cells were grown in Bioreactor 600 vessels (TPP) and seeded to a density of 0.6 10^6 cells/ml a day prior to transfection. For protein expression, cells were transiently transfected with mixtures of *CALHM* cDNA constructs and PEI MAX 40K. For 300 ml of cell culture, 0.5 mg of DNA and 1.2 mg of PEI MAX were suspended in 20 ml volume of DMEM medium. After 5

min the DNA solutions were mixed with the PEI MAX solutions, incubated for 15 min and supplemented with 4 mM valproic acid. Transfection mixtures were subsequently added to cell cultures and expression proceeded for 36 hr. Afterwards, cells were harvested by centrifugation at 500 g for 15 min, washed with PBS and stored at −20˚C for further use. All following purification steps were carried out at 4˚C. For protein extraction, cells were suspended in lysis buffer (25 mM HEPES, 150 mM NaCl, 1% Lauryl Maltose Neopentyl Glycol (LMNG), 0.5 mM $CaCl_2$, 2 mM $MgCl_2$, protease inhibitors, RNase, DNase, pH 7.6) and incubated for 1 hr under constant stirring. For CALHM4 purification in Ca^{2+}-free conditions, Ca^{2+} was replaced by 5 mM EGTA after extraction. To clarify the extracts, lysates were centrifugated at 16,000 g for 15 min. Supernatants filtered through a 0.5 µm filter were applied to the StrepTactin Superflow affinity resin and incubated with the slurry for 2.5 hr under gentle agitation. Unbound proteins were removed and bound proteins were eluted with elution buffer (10 mM HEPES, 150 mM NaCl, 50 µM GDN, 2 mM $CaCl_2$ and 10 mM d-Desthiobiotin, pH 7.6). For purification in Ca^{2+}-free conditions, Ca^{2+} was replaced by 2 mM EGTA. For cleavage of fusion tags, eluates were incubated for 30 min with 3C protease. Subsequently, samples were concentrated, filtered through 0.22 µm filters and subjected to size exclusion chromatography on a Superose 6 10/300 GL column equilibrated with SEC buffer (10 mM HEPES, 150 mM NaCl, 50 µM GDN, 2 mM $CaCl_2$/2 mM EGTA, pH 7.6). Peak fractions were pooled and concentrated with 100 kDa MWCO centrifugal filters.

LC-MS analysis of co-purified lipids

For the analysis of lipids co-purified with CALHM4, the protein was prepared in the presence of Ca^{2+} in the same manner as described for structure determination. For lipid extraction, chloroform was added in a 1:1 ratio (v/v) to 200 µl of a CALHM4 sample with a protein concentration of 3.75 mg ml^{-1} or to 200 µl of SEC buffer as a control (blank). The samples were briefly vortexed and incubated for 5 min at ambient temperature until phases have separated. The lower organic phase was collected and used for liquid chromatography and mass spectrometry (LC-MS) analysis. Prior to analysis, 25 µl of chloroform extract was mixed with 475 µl of a 50% aqueous methanol solution. The suspension was vortexed and centrifuged at 20˚C for 10 min at 16,000 g. 100 µl of the supernatant were transferred to a glass vial with narrowed bottom (Total Recovery Vials, Waters) and subjected to LC-MS. Lipids were separated on a nanoAcquity UPLC (Waters) equipped with a HSS T3 capillary column (150 µm x 30 mm, 1.8 µm particle size, Waters), applying a gradient of 5 mM ammonium acetate in water/acetonitrile 95:5 (A) and 5 mM ammonium acetate in isopropanol/acetonitrile 90:10 (B) from 5% B to 100% B over 10 min. The following 5 min conditions were kept at 100% B, followed by 5 min re-equilibration to 5% B. The injection volume was 1 µl. The flow rate was constant at 2.5 µl/min. The UPLC was coupled to a QExactive mass spectrometer (Thermo) by a nano-ESI source. MS data were acquired using positive polarization and data-dependent acquisition (DDA). Full scan MS spectra were acquired in profile mode from 80 to 1,200 m/z with an automatic gain control target of 1 10^6, an Orbitrap resolution of 70,000, and a maximum injection time of 200 ms. The five most intense charged (z = +1 or +2) precursor ions from each full scan were selected for collision induced dissociation fragmentation. Precursor was accumulated with an isolation window of 0.4 Da, an automatic gain control value of 5 10^4, a resolution of 17,500, a maximum injection time of 50 ms and fragmented with a normalized collision energy of 20 and 30 (arbitrary unit). Generated fragment ions were scanned in the linear trap. Minimal signal intensity for MS2 selection was set to 500. Lipid datasets were evaluated with Progenesis QI software (Nonlinear Dynamics), which aligns the ion intensity maps based on a reference data set, followed by a peak picking on an aggregated ion intensity map. Detected ions were identified based on accurate mass, detected adduct patterns and isotope patterns by comparing with entries in the LipidMaps Data Base (LM). A mass accuracy tolerance of 5 mDa was set for the searches. Fragmentation patterns were considered for the identifications of metabolites. Matches were ranked based on mass error (observed mass – exact mass), isotope similarity (observed versus theoretical) and relative differences between sample and blank.

Cryo-EM sample preparation and data collection

For structure determination of human CALHM2, 4 and 6 in the presence of Ca^{2+} and of human CALHM4 in the absence of Ca^{2+} by cryo-EM, 2.5 µl samples of GDN-purified proteins at a concentration of 1.5–3 mg ml^{-1} were applied to glow-discharged holey carbon grids (Quantifoil R1.2/1.3 or

R0.6/1 Au 200 mesh). Excess liquid was removed in a controlled environment (4˚C and 100% relative humidity) by blotting grids for 4–6 s. Grids were subsequently flash frozen in a liquid propane-ethane mix using a Vitrobot Mark IV (Thermo Fisher Scientific). All samples were imaged in a 300 kV Tecnai G^2 Polara (FEI) with a 100 µm objective aperture. All data were collected using a post-column quantum energy filter (Gatan) with a 20 eV slit and a K2 Summit direct detector (Gatan) operating in counting mode. Dose-fractionated micrographs were recorded in an automated manner using SerialEM (***Mastronarde, 2005***) with a defocus range of –0.8 to –3.0 µm. All datasets were recorded at a nominal magnification of 37,313 corresponding to a pixel size of 1.34 Å/pixel with a total exposure time of 12 s (30 individual frames) and a dose of approximately 1.3 $e^-/Å^2$/frame. The total electron dose on the specimen level for all datasets was approximately between 32 $e^-/Å^2$ and 55 $e^-/Å^2$.

Cryo-EM image processing

Micrographs from all four datasets were pre-processed in the same manner. Briefly, all individual frames were used for correction of the beam-induced movement using a dose-weighting scheme in RELION's own implementation of the MotionCor2 algorithm available in version 3.0 (***Zivanov et al., 2018***). The CTF parameters were estimated on summed movie frames using CTFFIND4.1 (***Rohou and Grigorieff, 2015***). Low-quality micrographs showing a significant drift, ice contamination or poor CTF estimates were discarded resulting in datasets of 1,125 images of CALHM4 in the presence of Ca^{2+} (dataset 1), 717 images of Ca^{2+}-free CALHM4 (dataset 2), 1,059 images of CALHM6 (dataset 3) and 2,065 images of CALHM2 (dataset 4), which were subjected to further data processing in RELION (***Scheres, 2012***). Particles of CALHM4 and CALHM6 were initially picked using the Laplacian-of-Gaussian method and subjected to 2D classification. 2D class averages showing protein features were subsequently used as templates for more accurate auto-picking as well as input for generating an initial 3D model. From dataset one, 422,281 particles were extracted with a box size of 234 pixels, down-scaled three times and subjected to 2D classification. Having discarded false positives and particles of poor quality, the dataset was reduced to 201,782 particles. Two rounds of non-symmetrized 3D classification using the 60 Å low-pass filtered initial 3D model as a reference allowed to isolate two populations of homogenous particles representing dihedrally-related decameric and undecameric assemblies. These two subsets were refined separately with either D10 or D11 symmetry imposed followed by unbinning to an original pixel size and iterative rounds of 3D refinement, per-particle CTF correction and Bayesian polishing (***Zivanov et al., 2018***; ***Zivanov et al., 2019***). Extra 3D classification without angular alignment showed increased flexibility within the dimerization interface of interacting intracellular regions in the decameric assembly while no such flexibility was observed for the undecameric population. In order to improve the resolution of the reconstructions, localized reconstruction was performed. For this purpose, the signal corresponding to the detergent belt and to one dihedrally-related monomer was subtracted from each particle followed by auto-refinement of merged in silico modified particles in the presence of a soft mask around the protein density with either C10 or C11 symmetry imposed. The final map of the decameric and undecameric assembly was improved to 4.07 Å and 3.92 Å, respectively. The maps were sharpened using isotropic b-factors of –200 $Å^2$ and –177 $Å^2$, respectively. Datasets of Ca^{2+}-free CALHM4 and Ca^{2+}-CALHM6 were processed in a similar manner. Briefly, from dataset two, 576,841 particles were extracted and cleaned by 2D classification. The pool, reduced to 97,978 particles, was subjected to non-symmetrized 3D classification that also yielded two populations of dihedrally-related decameric and undecameric assemblies. The final map of the decameric assembly at 4.07 Å and of the undecameric assembly at 3.69 Å was sharpened using isotropic b-factors of –169 $Å^2$ and –126 $Å^2$, respectively. From dataset three, 216,859 particles were extracted with a box size of 200 pixels and reduced to 201,761 particles after 2D classification. Non-symmetrized 3D classification also revealed decameric and undecameric populations, although no dihedrally-symmetrized dimers, as in case of CALHM4 in the presence and absence of Ca^{2+}, were observed. The final auto-refined map of the decameric assembly at 4.39 Å and of the undecameric assembly at 6.23 Å was sharpened using isotropic b-factors of –259 $Å^2$ and –435 $Å^2$, respectively. In all cases, resolution was estimated in the presence of a soft solvent mask and based on the gold standard Fourier Shell Correlation (FSC) 0.143 criterion (***Chen et al., 2013***; ***Rosenthal and Henderson, 2003***; ***Scheres, 2012***; ***Scheres and Chen, 2012***). High-resolution noise substitution was applied to correct FSC curves for the effect of soft masking in real space (***Chen et al., 2013***). The local resolution was estimated using RELION (***Zivanov et al., 2018***).

Visual inspection of micrographs in dataset 4 (CALHM2) during pre-processing hinted at preferential orientation of particles. 2D class averages generated from the particles picked with the Laplacian-of-Gaussian method showed primarily views from the extracellular side with a small percentage of side or tilted views, similar to those found in CALHM4 datasets (dihedrally-related dimers) and the CALHM6 dataset (monomers). In order to recover projections at orientations other than from the extracellular side, representative 2D class averages of CALHM4 and 6 were combined and used as 2D templates for auto-picking. The pool of 417,612 particles was subjected to two rounds of 2D classification, after which the dataset was reduced to 71,555 particles. 2D class averages showed that the majority of the remaining particles comprised a view from the extracellular side with only a small fraction representing other orientations. As a consequence of this preferential orientation, projections from other angles were underpopulated and did not show high-resolution features. In other to separate monomeric and dimeric populations, non-symmetrized 3D classification was performed using low-pass filtered reconstructions of CALHM4 and CALHM6. However, both monomeric and dimeric 3D reconstructions of CALHM2 suffered from missing views and therefore were not able to converge to a reliable model during 3D auto-refinement. Additional 2D classification on particles classified either as CALHM2 monomers or dimers showed significant amount of remaining heterogeneity in form of undecameric and dodecameric assemblies, which together with the preferential orientation impeded obtaining a high-resolution reconstruction from this dataset.

Model building and refinement

The models of CALHM4 and CALHM6 were built in Coot (***Emsley and Cowtan, 2004***). CALHM4 was built de novo into the cryo-EM density of the dimer of undecameric channels at 3.82 Å. The slightly better resolved cryo-EM density of the unpaired undecameric channel at 3.69 Å obtained by localized reconstruction and a map blurred in Coot with a *b*-factor of 50 aided map interpretation. CALHM6 was built using the CALHM4 structure as a reference with the aid of modified cryo-EM maps of CALHM6 which were either low-pass filtered to 6 Å, blurred in Coot with a *b*-factor of 200 or sharpened in Coot with a *b*-factor of −50. The cryo-EM density of CALHM4 was of sufficiently high resolution to unambiguously assign residues 4–83 and 94–280. The cryo-EM density of CALHM6 allowed us to assign residues 20–82 and 94–282. The atomic models were improved iteratively by cycles of real-space refinement in PHENIX (***Adams et al., 2002***) with secondary structure and 22-fold (for CALHM4) and 10-fold (for CALHM6) NCS constraints applied followed by manual corrections in Coot. Validation of the models was performed in PHENIX. Surfaces were calculated with MSMS (***Sanner et al., 1996***). Figures and videos containing molecular structures and densities were prepared with DINO (http://www.dino3d.org), PyMOL (***DeLano, 2002***), Chimera (***Pettersen et al., 2004***) and ChimeraX (***Goddard et al., 2018***).

Analysis of the density inside the pore

For analysis of the density inside the pore, non-symmetrized final 3D reconstructions of CALHM4 and CALHM6 were opened as a stack in Fiji (***Schindelin et al., 2012***), where the mean density of the area inside the pore was quantified along the slices of each 3D reconstruction. The size of the measured area was chosen based on the 3D mask generated from the atomic models of CALHM4 and 6. In both cases, the area of 6 × 6 pixels centered around the pore axis was located outside the 3D mask ensuring that the procedure did not include density of CALHM4 or 6.

The 'experimental' reference profile was generated based on the electron density map of the MPEG-1 protein bound to a lipidic vesicle (EMD-20622) (***Pang et al., 2019***). The electron density corresponding to the protein was selected and subtracted in Chimera using the structure of MPEG-1 (PDBID 6U2W). Due to the membrane deformation, the central region of the bilayer was excluded from the measurement. The 'simulation' reference profile was generated using the atomistic model of a membrane obtained from the MemProtMD database (PDBID 2N5S) (***Mineev et al., 2015***; ***Newport et al., 2019***). All atoms corresponding to protein, ions and water molecules were removed from the model and the remaining lipids were used to generate an electron density map with 1.34 Å pixel spacing at 6 Å resolution using Chimera (***Pettersen et al., 2004***). Electron density profiles were generated by measuring a mean pixel intensity of selected regions on map slices along the Z-axis using the Fiji software (***Schindelin et al., 2012***).

Two-electrode voltage-clamp recording

For preparation of cRNA coding for CALHM paralogs, *CALHM*-pTLNX DNA constructs were linearized with the FastDigest MluI restriction enzyme (ThermoFisher) purified, transcribed in vitro with the mMessage mMachine kit (Ambion) and purified with the RNeasy kit (Qiagen). The obtained cRNAs were either used immediately or aliquoted and stored at -20˚C. Defolliculated *X. laevis* oocytes obtained from Ecocyte Bioscience, were injected with mixtures containing either 1 ng of *CALHM1* cRNA or 5 ng of *CALHM 2, 4 and 6* cRNA and 10 ng of *X. laevis* connexin-38 antisense oligonucleotide (Cx38 ASO) to inhibit endogenous Cx38 currents (**Bahima et al., 2006**). Oocytes used as negative control (neg.) were injected with 10 ng of Cx38 ASO only. For protein expression, oocytes were kept in ND69 solution (96 mM NaCl, 2 mM KCl, 1.8 mM $CaCl_2$, 1 mM $MgCl_2$, 2.5 mM Na-pyruvate, 5 mM HEPES and 50 µg/ml gentamicin, pH 7.5) at 16˚C. Two-electrode voltage-clamp (TEVC) measurements were performed 48–60 hr after RNA injections at 20˚C. TEVC data were recorded on an OC-725B amplifier (Warner Instrument Corp.) Data recorded at 5 kHz and filtered at 1 kHz were and digitized using a Digidata interface board (1322A or 1440A, Axon Instruments) and analyzed with pCLAMP 10.3 software (Molecular Devices, Sunnyvale, CA). Microelectrodes with a resistance of 1–4 MΩ were filled with 3 M KCl. A VC-8 valve controller (Warner Instruments) was used for perfusion of different Ca^{2+} concentrations. Prior to recording, oocytes were additionally injected with a 50 nl of a mixture containing 20 mM BAPTA and 10 mM Ca^{2+} solution to minimize activation of Ca^{2+}-activated Cl^- currents. High Ca^{2+} bath solutions contained,100 mM Na^+, 5.4 mM K^+, 95 mM Cl^-, 1 mM Mg^{2+}, 3 mM Ca^{2+} and 10 mM HEPES, pH 7.2. Divalent cation-free solutions contained 0.5 mM EGTA and 0.5 mM EDTA instead of divalent cations. Intermediate Ca^{2+} concentrations were prepared from both stocks by mixing solution according to the volume calculated with WEBMAXC calculator.

Cell surface biotinylation

Surface biotinylation of proteins expressed in *X. laevis* oocytes was performed using the Pierce Cell Surface Protein Isolation kit. Oocytes (20-50), injected with *CALHM* cRNAs and incubated for 40–60 hr, were washed three times with ND96 solution, transferred to a white 6-well plate (NUNC) and biotinylated by 30 min incubation in 4 ml ND96 solution supplemented with 0.5 mg ml^{-1} EZ-link sulfo-NHS-SS biotin. After incubation, the biotinylation reaction was stopped by addition of quenching solution and oocytes were washed several times with ND96 solution to remove residual reagents. For protein extraction, oocytes were incubated in lysis buffer (25 mM HEPES, 150 mM NaCl, 0.5 mM $CaCl_2$, 1% LMNG, 2 mM $MgCl_2$, protease inhibitors, RNase, DNase, pH 7.6) for 1 hr at 4˚C and centrifuged at 10,000 g for 15 min. The supernatants were collected and incubated with NeutrAvidin agarose slurry for 1 hr at room temperature under constant mixing. After this step, agarose beads binding the biotinylated proteins were washed with wash solution (10 mM HEPES, 150 mM NaCl, 0.0058% GDN, 2 mM $CaCl_2$, protease inhibitors, RNase, DNase). Subsequently, the unbound material was discarded and biotinylated proteins were incubated with SDS-Page sample buffer containing 50 mM DTT for 1 hr at RT. Eluted protein fraction was obtained by centrifugation at 1,000 g for 2 min at RT. Membrane protein samples were stored at −20˚C. For western blot analysis, samples were loaded on a 4–20% SDS-polyacrylamide gel. After electrophoretic separation, the proteins were transferred to a polyvinylidene fluoride membrane by a semi-dry blotting procedure. The membranes were first blocked at room temperature for 2 hr with 5% non-fat milk in TBS-T buffer (50 mM Tris, 150 mM NaCl, 0.075% Tween20, pH 7.5) and then incubated with respective anti-CALHM primary antibodies overnight at 4˚C. To remove unbound primary antibodies, the membranes were washed with TBS-T buffer and subsequently blotted with goat anti-rabbit-HRP conjugated secondary antibody for 2 hr at 4˚C. The membranes were washed again with TBS-T buffer and chemiluminescent signals were developed with the Amersham ECL Prime Western Blotting Detection kit.

Statistics and reproducibility

Paired 2-way ANOVA with Sidak's multiple comparisons test was applied to detect differences in placental mRNA levels of CALHM isoforms between undifferentiated cytotrophoblast and differentiated syncytiotrophoblast cells. A p-value<0.05 was considered as statistically significant. Statistical comparisons were performed using GraphPad Prism (GraphPad). Electrophysiology data were repeated multiple times with different batches of cRNA and *X. laevis* oocytes with very similar

results. Conclusions of experiments were not changed upon inclusion of further data. In all cases, leaky oocytes were discarded. For Ca^{2+} concentration-response analysis using TEVC methods, statistical significance was determined by analysis of variance and by Student's t test. A p-value<0.05 was considered statistically significant. The number of independent experimental repetitions is represented by n.

Accession codes

The cryo-EM density maps of CALHM4 in absence of Ca^{2+} and CALHM4 and CALHM6 in presence of Ca^{2+} have been deposited in the Electron Microscopy Data Bank under following ID codes: EMD-10917, EMD-10919, EMD-10920, EMD-10921, EMD-10924 and EMD-10925. The coordinates of the corresponding atomic models of CALHM4 and CALHM6 have been deposited in the Protein Data Bank under ID codes 6YTK, 6YTL, 6YTO, 6YTQ, 6YTV and 6YTX.

Acknowledgements

This research was supported by a grant from the Swiss National Science Foundation (No. 31003A_163421) to RD. CA acknowledges support from the Swiss National Science Foundation through the National Centre of Competence in Research TransCure and from the Stiftung Lindenhof Bern. We thank O Medalia and M Eibauer, the Center for Microscopy and Image Analysis (ZMB) of the University of Zurich, and the Mäxi foundation for the access to electron microscopes, S Klauser and S Rast for their help in establishing the computer infrastructure. We are grateful to R Karahoda and S Shahnawaz for their expert help with qPCR and immunoblotting. The authors want to express their gratitude to the patients, physicians and midwives of the Lindenhofgruppe Bern, who participated in this study. Special thanks also to R Moser, Lindenhofgruppe Bern, for coordinating the placenta sampling process. Lipid analysis was performed with the help of the FGCZ of UZH/ETH Zurich. The support of Sebastian Streb and Endre Lacko is acknowledged. All members of the Dutzler lab are acknowledged for their help at various stages of the project.

Additional information

Funding

Funder	Grant reference number	Author
Schweizerischer Nationalfonds zur Förderung der Wissenschaftlichen Forschung	31003A_163421	Raimund Dutzler
Stiftung Lindenhof Bern		Christiane Albrecht
Schweizerischer Nationalfonds zur Förderung der Wissenschaftlichen Forschung	NCCR TransCure	Christiane Albrecht

The funders had no role in study design, data collection and interpretation, or the decision to submit the work for publication.

Author contributions

Katarzyna Drożdżyk, Conceptualization, Data curation, Formal analysis, Validation, Investigation, Visualization, Methodology, Writing - original draft, Writing - review and editing, Generated expression constructs, purified proteins and assisted with structure determination and functional experiments; Marta Sawicka, Conceptualization, Data curation, Formal analysis, Validation, Investigation, Visualization, Methodology, Writing - original draft, Writing - review and editing, Prepared the samples for cryo-EM, collected EM data and proceeded with structure determination; Maria-Isabel Bahamonde-Santos, Conceptualization, Data curation, Formal analysis, Validation, Investigation, Visualization, Methodology, Writing - original draft, Writing - review and editing, Recorded and analyzed electrophysiology data; Zaugg Jonas, Conceptualization, Data curation, Formal analysis, Validation, Investigation, Visualization, Methodology, Writing - original draft, Writing - review and editing, Carried out expression analysis in the placenta; Dawid Deneka, Investigation, Methodology,

Writing - review and editing, Generated and characterized initial constructs; Christiane Albrecht, Conceptualization, Data curation, Formal analysis, Supervision, Funding acquisition, Validation, Visualization, Writing - original draft, Project administration, Writing - review and editing, Carried out expression analysis in the placenta; Raimund Dutzler, Conceptualization, Data curation, Formal analysis, Supervision, Funding acquisition, Validation, Visualization, Writing - original draft, Project administration, Writing - review and editing

Author ORCIDs
Katarzyna Drożdżyk https://orcid.org/0000-0001-6288-4735
Marta Sawicka https://orcid.org/0000-0003-4589-4290
Raimund Dutzler https://orcid.org/0000-0002-2193-6129

Ethics
Human subjects: Human placental tissues were collected from the Division of Obstetrics and Gynecology, Lindenhofgruppe Bern, Switzerland, under approval by the ethical commission of the Canton of Bern (approval No Basec 2016-00250). Written informed consent was obtained from all participants.

Decision letter and Author response
Decision letter https://doi.org/10.7554/eLife.55853.sa1
Author response https://doi.org/10.7554/eLife.55853.sa2

Additional files
Supplementary files
- Supplementary file 1. Key resources table.

- Transparent reporting form

Data availability
Coordinates of the atomic models were deposited with the PDB and cryo-EM densities were deposited with the Electron Microscopy databank.

The following datasets were generated:

Author(s)	Year	Dataset title	Dataset URL	Database and Identifier
Sawicka M, Drozdzyk K, Dutzler R	2020	Cryo-EM structure of a dimer of decameric human CALHM4 in the absence of Ca2+	https://www.rcsb.org/structure/6YTK	RCSB Protein Data Bank, 6YTK
Sawicka M, Drozdzyk K, Dutzler R	2020	Cryo-EM structure of a dimer of undecameric human CALHM4 in the absence of Ca2+	https://www.rcsb.org/structure/6YTL	RCSB Protein Data Bank, 6YTL
Sawicka M, Drozdzyk K, Dutzler R	2020	Cryo-EM structure of a dimer of decameric human CALHM4 in the presence of Ca2+	https://www.rcsb.org/structure/6YTO	RCSB Protein Data Bank, 6YTO
Sawicka M, Drozdzyk K, Dutzler R	2020	Cryo-EM structure of a dimer of undecameric human CALHM4 in the presence of Ca2+	https://www.rcsb.org/structure/6YTQ	RCSB Protein Data Bank, 6YTQ
Sawicka M, Drozdzyk K, Dutzler R	2020	Cryo-EM structure of decameric human CALHM6 in the presence of Ca2+	https://www.rcsb.org/structure/6YTV	RCSB Protein Data Bank, 6YTV
Sawicka M, Drozdzyk K, Dutzler R	2020	Cryo-EM structure of undecameric human CALHM6 in the presence of Ca2+	https://www.rcsb.org/structure/6YTX	RCSB Protein Data Bank, 6YTX
Sawicka M, Drozdzyk K, Dutzler R	2020	Cryo-EM structure of a dimer of decameric human CALHM4 in the	https://www.ebi.ac.uk/pdbe/entry/emdb/EMD-	Electron Microscopy Data Bank, 10917

		absence of Ca2+	10917	
Sawicka M, Drozdzyk K, Dutzler R	2020	Cryo-EM structure of a dimer of undecameric human CALHM4 in the absence of Ca2+	https://www.ebi.ac.uk/pdbe/entry/emdb/EMD-10919	Electron Microscopy Data Bank, 10919
Sawicka M, Drozdzyk K, Dutzler R	2020	Cryo-EM structure of a dimer of decameric human CALHM4 in the presence of Ca2+	https://www.ebi.ac.uk/pdbe/entry/emdb/EMD-10920	Electron Microscopy Data Bank, 10920
Sawicka M, Drozdzyk K, Dutzler R	2020	Cryo-EM structure of a dimer of undecameric human CALHM4 in the presence of Ca2+	https://www.ebi.ac.uk/pdbe/entry/emdb/EMD-10921	Electron Microscopy Data Bank, 10921
Sawicka M, Drozdzyk K, Dutzler R	2020	Cryo-EM structure of decameric human CALHM6 in the presence of Ca2+	https://www.ebi.ac.uk/pdbe/entry/emdb/EMD-10924	Electron Microscopy Data Bank, 10924
Sawicka M, Drozdzyk K, Dutzler R	2020	Cryo-EM structure of undecameric human CALHM6 in the presence of Ca2+	https://www.ebi.ac.uk/pdbe/entry/emdb/EMD-10925	Electron Microscopy Data Bank, 10925

References

Adams PD, Grosse-Kunstleve RW, Hung LW, Ioerger TR, McCoy AJ, Moriarty NW, Read RJ, Sacchettini JC, Sauter NK, Terwilliger TC. 2002. *PHENIX*: building new software for automated crystallographic structure determination. *Acta Crystallographica Section D Biological Crystallography* **58**:1948–1954. DOI: https://doi.org/10.1107/S0907444902016657, PMID: 12393927

Bahima L, Aleu J, Elias M, Martín-Satué M, Muhaisen A, Blasi J, Marsal J, Solsona C. 2006. Endogenous hemichannels play a role in the release of ATP from *Xenopus* oocytes. *Journal of Cellular Physiology* **206**:95–102. DOI: https://doi.org/10.1002/jcp.20440, PMID: 15965959

Chen S, McMullan G, Faruqi AR, Murshudov GN, Short JM, Scheres SH, Henderson R. 2013. High-resolution noise substitution to measure overfitting and validate resolution in 3D structure determination by single particle electron cryomicroscopy. *Ultramicroscopy* **135**:24–35. DOI: https://doi.org/10.1016/j.ultramic.2013.06.004, PMID: 23872039

Choi W, Clemente N, Sun W, Du J, Lu W. 2019. The structures and gating mechanism of human calcium homeostasis modulator 2. *Nature* **576**:163–167. DOI: https://doi.org/10.1038/s41586-019-1781-3, PMID: 31776515

DeLano WL. 2002. Pymol: an open-source molecular graphics tool. *CCP4 Newsletter on Protein Crystallography* **40**:82–92.

Demura K, Kusakizako T, Shihoya W, Hiraizumi M, Nomura K, Shimada H, Yamashita K, Nishizawa T, Taruno A, Nureki O. 2020. Cryo-EM structures of calcium homeostasis modulator channels in diverse oligomeric assemblies. *bioRxiv*. DOI: https://doi.org/10.1101/2020.01.31.928093

Deneka D, Sawicka M, Lam AKM, Paulino C, Dutzler R. 2018. Structure of a volume-regulated anion channel of the LRRC8 family. *Nature* **558**:254–259. DOI: https://doi.org/10.1038/s41586-018-0134-y, PMID: 29769723

Dreses-Werringloer U, Lambert JC, Vingtdeux V, Zhao H, Vais H, Siebert A, Jain A, Koppel J, Rovelet-Lecrux A, Hannequin D, Pasquier F, Galimberti D, Scarpini E, Mann D, Lendon C, Campion D, Amouyel P, Davies P, Foskett JK, Campagne F, et al. 2008. A polymorphism in CALHM1 influences Ca2+ homeostasis, Abeta levels, and Alzheimer's disease risk. *Cell* **133**:1149–1161. DOI: https://doi.org/10.1016/j.cell.2008.05.048, PMID: 18585350

Edwards D, Jones CJ, Sibley CP, Nelson DM. 1993. Paracellular permeability pathways in the human placenta: a quantitative and morphological study of maternal-fetal transfer of horseradish peroxidase. *Placenta* **14**:63–73. DOI: https://doi.org/10.1016/S0143-4004(05)80249-8, PMID: 8456090

Emsley P, Cowtan K. 2004. *Coot*: model-building tools for molecular graphics. *Acta Crystallographica. Section D, Biological Crystallography* **60**:2126–2132. DOI: https://doi.org/10.1107/S0907444904019158, PMID: 15572765

Geertsma ER, Dutzler R. 2011. A versatile and efficient high-throughput cloning tool for structural biology. *Biochemistry* **50**:3272–3278. DOI: https://doi.org/10.1021/bi200178z, PMID: 21410291

Goddard TD, Huang CC, Meng EC, Pettersen EF, Couch GS, Morris JH, Ferrin TE. 2018. UCSF ChimeraX: meeting modern challenges in visualization and analysis. *Protein Science* **27**:14–25. DOI: https://doi.org/10.1002/pro.3235, PMID: 28710774

Huang X, Baumann M, Nikitina L, Wenger F, Surbek D, Körner M, Albrecht C. 2013. RNA degradation differentially affects quantitative mRNA measurements of endogenous reference genes in human placenta. *Placenta* **34**:544–547. DOI: https://doi.org/10.1016/j.placenta.2013.03.011, PMID: 23623484

Huang X, Anderle P, Hostettler L, Baumann MU, Surbek DV, Ontsouka EC, Albrecht C. 2018. Identification of placental nutrient transporters associated with intrauterine growth restriction and pre-eclampsia. *BMC Genomics* **19**:173. DOI: https://doi.org/10.1186/s12864-018-4518-z, PMID: 29499643

Kasuya G, Nakane T, Yokoyama T, Jia Y, Inoue M, Watanabe K, Nakamura R, Nishizawa T, Kusakizako T, Tsutsumi A, Yanagisawa H, Dohmae N, Hattori M, Ichijo H, Yan Z, Kikkawa M, Shirouzu M, Ishitani R, Nureki O. 2018. Cryo-EM structures of the human volume-regulated anion channel LRRC8. *Nature Structural & Molecular Biology* **25**:797–804. DOI: https://doi.org/10.1038/s41594-018-0109-6, PMID: 30127360

Kawate T, Gouaux E. 2006. Fluorescence-detection size-exclusion chromatography for precrystallization screening of integral membrane proteins. *Structure* **14**:673–681. DOI: https://doi.org/10.1016/j.str.2006.01.013, PMID: 16615909

Kefauver JM, Saotome K, Dubin AE, Pallesen J, Cottrell CA, Cahalan SM, Qiu Z, Hong G, Crowley CS, Whitwam T, Lee WH, Ward AB, Patapoutian A. 2018. Structure of the human volume regulated anion channel. *eLife* **7**: e38461. DOI: https://doi.org/10.7554/eLife.38461, PMID: 30095067

Lager S, Powell TL. 2012. Regulation of nutrient transport across the placenta. *Journal of Pregnancy* **2012**:1–14. DOI: https://doi.org/10.1155/2012/179827

Lewis RM, Brooks S, Crocker IP, Glazier J, Hanson MA, Johnstone ED, Panitchob N, Please CP, Sibley CP, Widdows KL, Sengers BG. 2013. Review: modelling placental amino acid transfer–from transporters to placental function. *Placenta* **34 Suppl**:S46–S51. DOI: https://doi.org/10.1016/j.placenta.2012.10.010, PMID: 23187090

Ma Z, Siebert AP, Cheung KH, Lee RJ, Johnson B, Cohen AS, Vingtdeux V, Marambaud P, Foskett JK. 2012. Calcium homeostasis modulator 1 (CALHM1) is the pore-forming subunit of an ion channel that mediates extracellular Ca2+ regulation of neuronal excitability. *PNAS* **109**:E1963–E1971. DOI: https://doi.org/10.1073/pnas.1204023109, PMID: 22711817

Ma Z, Tanis JE, Taruno A, Foskett JK. 2016. Calcium homeostasis modulator (CALHM) ion channels. *Pflügers Archiv - European Journal of Physiology* **468**:395–403. DOI: https://doi.org/10.1007/s00424-015-1757-6

Ma J, Qi X, Yang C, Pan R, Wang S, Wu J, Huang L, Chen H, Cheng J, Wu R, Liao Y, Mao L, Wang FC, Wu Z, An JX, Wang Y, Zhang X, Zhang C, Yuan Z. 2018a. Calhm2 governs astrocytic ATP releasing in the development of depression-like behaviors. *Molecular Psychiatry* **23**:883–891. DOI: https://doi.org/10.1038/mp.2017.229, PMID: 29180673

Ma Z, Taruno A, Ohmoto M, Jyotaki M, Lim JC, Miyazaki H, Niisato N, Marunaka Y, Lee RJ, Hoff H, Payne R, Demuro A, Parker I, Mitchell CH, Henao-Mejia J, Tanis JE, Matsumoto I, Tordoff MG, Foskett JK. 2018b. CALHM3 is essential for rapid ion Channel-Mediated purinergic neurotransmission of GPCR-Mediated tastes. *Neuron* **98**:547–561. DOI: https://doi.org/10.1016/j.neuron.2018.03.043, PMID: 29681531

Maeda S, Nakagawa S, Suga M, Yamashita E, Oshima A, Fujiyoshi Y, Tsukihara T. 2009. Structure of the connexin 26 gap junction channel at 3.5 A resolution. *Nature* **458**:597–602. DOI: https://doi.org/10.1038/nature07869, PMID: 19340074

Maldonado-Estrada J, Menu E, Roques P, Barré-Sinoussi F, Chaouat G. 2004. Evaluation of cytokeratin 7 as an accurate intracellular marker with which to assess the purity of human placental villous trophoblast cells by flow cytometry. *Journal of Immunological Methods* **286**:21–34. DOI: https://doi.org/10.1016/j.jim.2003.03.001, PMID: 15087219

Mastronarde DN. 2005. Automated electron microscope tomography using robust prediction of specimen movements. *Journal of Structural Biology* **152**:36–51. DOI: https://doi.org/10.1016/j.jsb.2005.07.007, PMID: 16182563

Mineev KS, Panova SV, Bocharova OV, Bocharov EV, Arseniev AS. 2015. The membrane mimetic affects the spatial structure and mobility of EGFR transmembrane and juxtamembrane domains. *Biochemistry* **54**:6295–6298. DOI: https://doi.org/10.1021/acs.biochem.5b00851, PMID: 26440883

Newport TD, Sansom MSP, Stansfeld PJ. 2019. The MemProtMD database: a resource for membrane-embedded protein structures and their lipid interactions. *Nucleic Acids Research* **47**:D390–D397. DOI: https://doi.org/10.1093/nar/gky1047

Nikitina L, Wenger F, Baumann M, Surbek D, Körner M, Albrecht C. 2011. Expression and localization pattern of ABCA1 in diverse human placental primary cells and tissues. *Placenta* **32**:420–430. DOI: https://doi.org/10.1016/j.placenta.2011.03.003

Oshima A, Tani K, Fujiyoshi Y. 2016. Atomic structure of the innexin-6 gap junction channel determined by cryo-EM. *Nature Communications* **7**:13681. DOI: https://doi.org/10.1038/ncomms13681, PMID: 27905396

Pang SS, Bayly-Jones C, Radjainia M, Spicer BA, Law RHP, Hodel AW, Parsons ES, Ekkel SM, Conroy PJ, Ramm G, Venugopal H, Bird PI, Hoogenboom BW, Voskoboinik I, Gambin Y, Sierecki E, Dunstone MA, Whisstock JC. 2019. The cryo-EM structure of the acid activatable pore-forming immune effector Macrophage-expressed gene 1. *Nature Communications* **10**:4288. DOI: https://doi.org/10.1038/s41467-019-12279-2, PMID: 31537793

Pettersen EF, Goddard TD, Huang CC, Couch GS, Greenblatt DM, Meng EC, Ferrin TE. 2004. UCSF chimera–a visualization system for exploratory research and analysis. *Journal of Computational Chemistry* **25**:1605–1612. DOI: https://doi.org/10.1002/jcc.20084, PMID: 15264254

Rohou A, Grigorieff N. 2015. CTFFIND4: fast and accurate defocus estimation from electron micrographs. *Journal of Structural Biology* **192**:216–221. DOI: https://doi.org/10.1016/j.jsb.2015.08.008, PMID: 26278980

Rosenthal PB, Henderson R. 2003. Optimal determination of particle orientation, absolute hand, and contrast loss in single-particle electron cryomicroscopy. *Journal of Molecular Biology* **333**:721–745. DOI: https://doi.org/10.1016/j.jmb.2003.07.013, PMID: 14568533

Sanner MF, Olson AJ, Spehner JC. 1996. Reduced surface: an efficient way to compute molecular surfaces. *Biopolymers* **38**:305–320. DOI: https://doi.org/10.1002/(SICI)1097-0282(199603)38:3<305::AID-BIP4>3.0.CO;2-Y, PMID: 8906967

Scheres SH. 2012. RELION: implementation of a bayesian approach to cryo-EM structure determination. *Journal of Structural Biology* **180**:519–530. DOI: https://doi.org/10.1016/j.jsb.2012.09.006, PMID: 23000701

Scheres SHW, Chen S. 2012. Prevention of overfitting in cryo-EM structure determination. *Nature Methods* **9**: 853–854. DOI: https://doi.org/10.1038/nmeth.2115

Schindelin J, Arganda-Carreras I, Frise E, Kaynig V, Longair M, Pietzsch T, Preibisch S, Rueden C, Saalfeld S, Schmid B, Tinevez JY, White DJ, Hartenstein V, Eliceiri K, Tomancak P, Cardona A. 2012. Fiji: an open-source platform for biological-image analysis. *Nature Methods* **9**:676–682. DOI: https://doi.org/10.1038/nmeth.2019, PMID: 22743772

Siebert AP, Ma Z, Grevet JD, Demuro A, Parker I, Foskett JK. 2013. Structural and functional similarities of calcium homeostasis modulator 1 (CALHM1) ion channel with connexins, pannexins, and innexins. *Journal of Biological Chemistry* **288**:6140–6153. DOI: https://doi.org/10.1074/jbc.M112.409789, PMID: 23300080

Smart OS, Neduvelil JG, Wang X, Wallace BA, Sansom MS. 1996. HOLE: a program for the analysis of the pore dimensions of ion channel structural models. *Journal of Molecular Graphics* **14**:354–360. DOI: https://doi.org/10.1016/S0263-7855(97)00009-X, PMID: 9195488

Soares MJ, Hunt JS. 2006. Placenta and trophoblast: methods and protocols: overview II. *Methods in Molecular Medicine* **122**:3–7. DOI: https://doi.org/10.1385/1-59259-989-3:1, PMID: 16511972

Syrjanen JL, Michalski K, Chou TH, Grant T, Rao S, Simorowski N, Tucker SJ, Grigorieff N, Furukawa H. 2020. Structure and assembly of calcium homeostasis modulator proteins. *Nature Structural & Molecular Biology* **27**:150–159. DOI: https://doi.org/10.1038/s41594-019-0369-9, PMID: 31988524

Taruno A, Matsumoto I, Ma Z, Marambaud P, Foskett JK. 2013a. How do taste cells lacking synapses mediate neurotransmission? CALHM1, a voltage-gated ATP channel. *BioEssays* **35**:1111–1118. DOI: https://doi.org/10.1002/bies.201300077, PMID: 24105910

Taruno A, Vingtdeux V, Ohmoto M, Ma Z, Dvoryanchikov G, Li A, Adrien L, Zhao H, Leung S, Abernethy M, Koppel J, Davies P, Civan MM, Chaudhari N, Matsumoto I, Hellekant G, Tordoff MG, Marambaud P, Foskett JK. 2013b. CALHM1 ion channel mediates purinergic neurotransmission of sweet, bitter and umami tastes. *Nature* **495**:223–226. DOI: https://doi.org/10.1038/nature11906, PMID: 23467090

Zivanov J, Nakane T, Forsberg BO, Kimanius D, Hagen WJ, Lindahl E, Scheres SH. 2018. New tools for automated high-resolution cryo-EM structure determination in RELION-3. *eLife* **7**:e42166. DOI: https://doi.org/10.7554/eLife.42166, PMID: 30412051

Zivanov J, Nakane T, Scheres SHW. 2019. A bayesian approach to beam-induced motion correction in cryo-EM single-particle analysis. *IUCrJ* **6**:5–17. DOI: https://doi.org/10.1107/S205225251801463X, PMID: 30713699

9.1.5 Published in Nature Communications (23 April 2018)

nature COMMUNICATIONS

ARTICLE

DOI: 10.1038/s41467-018-03836-2 OPEN

Placental miR-340 mediates vulnerability to activity based anorexia in mice

Mariana Schroeder[1,2], Mira Jakovcevski[2], Tamar Polacheck[1,2], Yonat Drori[1,2], Alessia Luoni[2], Simone Röh[3], Jonas Zaugg[4,5], Shifra Ben-Dor[6], Christiane Albrecht[4,5] & Alon Chen[1,2]

Anorexia nervosa (AN) is a devastating eating disorder characterized by self-starvation that mainly affects women. Its etiology is unknown, which impedes successful treatment options leading to a limited chance of full recovery. Here, we show that gestation is a vulnerable window that can influence the predisposition to AN. By screening placental microRNA expression of naive and prenatally stressed (PNS) fetuses and assessing vulnerability to activity-based anorexia (ABA), we identify miR-340 as a sexually dimorphic regulator involved in prenatal programming of ABA. PNS caused gene-body hypermethylation of placental miR-340, which is associated with reduced miR-340 expression and increased protein levels of several target transcripts, GR, Cry2 and H3F3b. MiR-340 is linked to the expression of several nutrient transporters both in mice and human placentas. Using placenta-specific lentiviral transgenes and embryo transfer, we demonstrate the key role miR-340 plays in the mechanism involved in early life programming of ABA.

[1] Department of Neurobiology, Weizmann Institute of Science, 7610001 Rehovot, Israel. [2] Department of Stress Neurobiology and Neurogenetics, Max Planck Institute of Psychiatry, 80804 Munich, Germany. [3] Department of Translational Research in Psychiatry, Max Planck Institute of Psychiatry, 80804 Munich, Germany. [4] Institute of Biochemistry and Molecular Medicine, University of Bern, 3012 Bern Switzerland. [5] Swiss National Center of Competence in Research, NCCR TransCure, University of Bern, 3012 Bern, Switzerland. [6] Bioinformatics and Biological Computing Unit, Biological Services, Weizmann Institute of Science, 7610001 Rehovot Israel. Correspondence and requests for materials should be addressed to M.S. (email: mariana_schroeder@psych.mpg.de) or to A.C. (email: alon_chen@psych.mpg.de)

Eating disorders (ED) are destructive mental disorders that dramatically decrease quality of life and have life-threatening consequences. They are ten times more common in women than in men and represent one of the most common psychiatric disorders, affecting up to 4.5% of women at some point in their lives[1]. Anorexia nervosa (AN), the most severe ED, accounts for the highest mortality rate of all mental illnesses (about 10%)[2]. Despite being so immensely destructive to health and affecting such a significant number of young women, the understanding of AN remains poor due to its multi-factorial and complex origins. As a consequence, treatment is sparse, unspecific and unlikely to lead to full recovery[3].

Due to the significantly greater prevalence of AN in women, most of the clinical literature and preclinical models have aimed at providing a rationale for specific factors precipitating AN disproportionately in females at the time of puberty[4]. Susceptibility to EDs is often associated with early life stress or trauma[5,6]. However, it is important to make a distinction between the different types of "early life trauma" and how they may affect subsequent predisposition to disease. Trauma during childhood may serve as a trigger for an existing predisposition, while gestational or even pre-gestational trauma may be more involved in programming the predisposition or protecting from it, depending on the severity, timing, and extent of the insult[7]. As such, increased risk of bulimia nervosa and mixed eating disorders was reported among girls who were exposed to either prenatal stress (PNS) or early postnatal life stress. In contrast, this was not true for AN[8]. Yet, early postnatal and childhood trauma are both frequently referred to as "early life", but they are in fact taking place at different developmental windows, exerting potentially very different effects on the susceptibility for the different eating disorders in the offspring.

In any case, stress alone does not necessarily prompt EDs but rather a combination of an innate predisposition pooled with the additive effect of early life trauma is more likely to lead to disease[5,9]. This concept coincides with the developmental origin of health and disease hypothesis, and has received compelling epidemiological support from animal studies. Early life stress, particularly in the form of intrauterine maternal emotional stress or nutrition-related (high fat diet/deprivation), may ultimately predispose male and female offspring to different diseases[10–12]. The fetal perception of the intrauterine environment is mediated by the placenta, a feto-maternal organ that connects the developing fetus to the uterine wall to allow nutrient uptake, waste elimination, and gas exchange via the mother's blood supply. Although the placenta has long been considered a "sexless" organ, in fact given its predominantly fetal origin, it carries the same genetic information as the fetus and is therefore differentially sensitive to environmental stimuli[13] and fetal hormones[14]. The placenta of one sex may also possess a greater ability to respond and buffer against selective environmental insults[15], as is the case for the sex-specific placental contribution to nutritional programming in the offspring[16]. It is broadly recognized that compromised placental function can have both short- and long-lasting consequences for the developing fetus, e.g., with maternal hypoxia, pre-eclampsia, or placental insufficiency[17], which are closely related to a specific stage of development and fetal sex. Finally, distinct sex-dependent structural and functional placental factors have been repeatedly reported in normal pregnancies (reviewed in ref. [15]). This further suggests that the physiological and molecular basis for the sex-specific developmental trajectory toward susceptibility to disease may originate in utero, through placental disparities between the sexes despite exposure to a similar maternal environment.

Recently, microRNAs (miRs) have received major attention in the context of placenta-associated abnormalities[18]. Specific placental miRs were found to be associated with several pregnancy disorders and therefore are strong candidates for the mediation of gestational programming[19]. In the present study, we explored this possibility by comparing placental differences in miR expression between opposite sex siblings of undisturbed and PNS pregnancies in parallel to adolescent susceptibility to activity-based anorexia (ABA). The ABA model successfully mimics the choice of exercise above eating, relying on limited food intake while allowing unlimited access to running wheels (RW)[20]. While first modeled in rats, the ABA model has also been widely examined in mice[21] with varying criteria[22]. It is characterized by dramatic weight loss as a consequence of decreased food intake[21], hyperactivity and circadian disruption in the running pattern[23].

To test our hypothesis that susceptibility to AN may originate in utero, we examined placental miR expression in control and PNS mice and exposed a parallel cohort to the ABA protocol during adolescence. We demonstrate that susceptibility to ABA is associated with endogenous levels of placental miR-340 and overexpression dramatically increased the susceptibility to ABA. We propose that programming of ABA vulnerability originates in utero, and renders specifically female offspring vulnerable to metabolic challenges during adolescence.

Results

ABA affects mainly adolescent females and is abolished by PNS. To examine the vulnerability of female mice to ABA, we exposed them to a modified version of the ABA protocol[24] when they reached adolescence. We allowed the animals to habituate to voluntary wheel running for 1 week with free access to food, followed by 5 days of free access to wheels combined with gradual food restriction (FR) in the form of 3–4 h of food access a day, during the dark cycle (Fig. 1a). An undisturbed control group with no wheels and free access to food as well as a further FR group with no access to wheels was added to control for the impact of FR on body weight (BW). The results revealed similar BW in all control female groups with free access to food. FR alone did not induce perdurable weight loss despite the reduction in food consumption, suggesting that the number of calories consumed was enough to maintain their BW if the necessary adjustments were made (such as reduction in general activity). In contrast, when exposed to the ABA protocol (FR + RW), the animals split into two sub-groups, denominated either "Resistant" (Res) or "Anorexic" (ABA). Overall, 40% of the control females developed ABA and 60% were resistant (Fig. 1b). Classification of the animals into each category was performed retrospectively by cluster analysis, based on the following parameters during the FR phase of the protocol: (1) BW loss; (2) Food intake in kcal; (3) Food intake recovery (% from the first FR day); (4) Circadian disruption (running distance in km during the light phase); (5) Total distance ran with FR (total activity) and (6) Time until collapse (in days). ABA females displayed dramatic weight loss compared to all other groups (Fig. 1c). Weight loss resulted from a gradual reduction in voluntary food intake (Fig. 1d). The FR group and Res females adapted and increased their kcal intake during the FR period, but ABA females did not (Fig. 1d). While Res females showed an intact circadian running pattern (Fig. 1e), ABA females showed disrupted running with high activity levels during the light phase (Fig. 1f) and running up to 12 km/day during the FR phase (Fig. 1g). In the long term (about 6 weeks after the end of the intervention), all females exposed to food restriction during adolescence weighed more than undisturbed controls, but did not differ according to predisposition to ABA (Fig. 1h). In order to better characterize each female mouse in this experiment, we assigned them an "ABA score" composed by the

sum of the *Z* scores of the ABA parameters. Accordingly, ABA females (as revealed by the previous cluster analysis) scored significantly higher on this new scale than Res females (Fig. 1i). Finally, we examined gene expression in the hypothalamus, focusing on genes that have been specifically linked to anorexia in women and in various animal models as potential candidates. Hypothalamic dysregulation in anorexia has been reported for the melanocortin, the neurotrophic and the serotonin systems and the HPA axis. We chose representative genes of these systems that repeatedly emerged as potential mediators of the anorexic phenotype: Agouti-related peptide (AgRP)[25], Melanocortin receptor 4 (Mc4R)[26], Serotonin receptor (Htr)1a[27], Bdnf[28], Arginine vasopressin (Avp)[29] and Hypocretin/Orexin (Hcrt)[30]. We found that, as expected, *AgRP*, *Htr1a*, *Avp* and *Hcrt* were dysregulated in recovered ABA animals (Fig. 1j).

In order to test the potential mechanistic link between early life stress and later predisposition to ABA, we performed PNS on a further set of females starting 1 day after the detection of the copulation plug and until GD.16.5, that induced the expected stress-related responses in the mother and the fetuses (Supplementary Fig. 1A). The resulting offspring, including males, were then exposed to the ABA protocol upon reaching adolescence (Fig. 1k). We next calculated the *Z* scores for each ABA parameter according to their strength of prediction as determined by a two-step cluster analysis in the original female group (Fig. 1l, raw data in Supplementary Fig. 2). We found that 30-day-old adolescent males and PNS offspring of both sexes scored similarly to Res females in intake recovery (Fig. 1m), days until collapse (Fig. 1n), BW change (Fig. 1o), circadian disruption (Fig. 1p), food intake (Fig. 1q), and total activity with FR (Fig. 1r). Thus, all males and PNS females were largely resistant to ABA, scoring similarly to Res control females in the ABA score (Fig. 1s). When examining basal metabolic parameters in this group, the PNS females appear to be programmed to become overweight, rather than underweight, and this may be at least one of the reasons underlying their resistance to ABA (Supplementary Fig. 1B).

PNS placentas show downregulation of miR-340 by gene-body DNA methylation. To elucidate the early origins of vulnerability/resistance to ABA, we next focused on gestational aspects and placental adaptations in control vs. PNS male and female offspring. BW gain in dams subjected to stress when pregnant (PNS dams) was significantly lower than in controls, despite similar food intake (Fig. 2a, b) and they also showed increased corticosterone levels (Fig. 2c). PNS did not affect fetal weight, but did reduce placental weight in female offspring only, suggesting an increase in placental efficiency in this group (Fig. 2d–f). Accordingly, placental 11βhsd$_2$, the enzyme that converts active corticosterone into inactive cortisone, was decreased and fetal corticosterone levels were increased exclusively in female PNS fetuses (Fig. 2g, h). This suggests that females were exposed to higher levels of endocrine stress signals compared to their male siblings, an effect reported previously[31].

To gain better insight into the mechanisms that mediate the differences between controls and PNS, we next compared the placental miRs expression profile using miR arrays. We identified several miRs differentially expressed in PNS placentas with miR-340 being most severely affected by the manipulation (Fig. 2i and Supplementary data 1). We then validated the array findings by qPCR and detected a clear sexually dimorphic expression pattern, since miR-340 was expressed in very low levels in control and PNS male placentas (Fig. 2j). Importantly, expression of miR-340, as shown by in situ hybridization, appears to be restricted to the junctional zone of the placenta in particular on the labyrinth side, a major site of feto-maternal exchange and hormone production respectively (Fig. 2k).

To elucidate the regulating mechanism of miR-340 by PNS, we performed a bioinformatic analysis on the *Rnf130* gene, which hosts miR-340 in its second intron. Like miR-340, *Rnf130* was downregulated by PNS (Supplementary Fig. 3A). Intronic miRs are frequently found in a sense orientation and thus are frequently transcribed together with their host gene[32]. The analysis revealed that *Rnf130* has a CpG island about 800 bp long around its promoter region and the first exon (Fig. 2l). Furthermore, miR-340 was previously suggested to be regulated by DNA methylation in different types of cancer[33]. To examine this possibility, we used the DNA methyltransferase inhibitor 5-aza in an in vitro assay and showed that increasing concentrations of the inhibitor led to increasingly higher levels of miR-340, implying DNA methylation in its regulation (Fig. 2m). We next examined the methylation levels in the CpG Island of the *Rnf130* promoter and on the miR-340 sequence through bisulfite conversion and pyrosequencing in control and PNS female placentas. While DNA methylation at promoters is widely accepted to be associated with transcriptional repression, recent studies suggested that gene body methylation also plays a critical role in gene regulation[34]. Interestingly, the CpG Island in the *Rnf130* promoter region displayed very low levels of methylation, both in female control and PNS placentas (Supplementary Fig. 3B). In contrast, the two CpGs located on the sequence of miR-340 revealed high methylation in both groups, with CpG_2 significantly more methylated in PNS than in control female placentas (Fig. 2n), which also show global hypermethylation compared both to control females and males (Fig. 2o). Taken together, these findings suggest that placental miR-340 is a sexually dimorphic miRNA robustly affected by PNS and regulated through gene body DNA methylation.

MiR-340 targets Nr3c1/GR, Cry2, and H3f3b in the placenta. In order to explore the mechanism through which placental miR-340 exerts its effects on ABA predisposition, we next performed bioinformatic predictions on potential targets focusing on genes involved in placental functioning and structure. The conservation of the miR-340 seed matches on the 3′UTR of these targets are shown in Supplementary Fig. 4. Based on those predictions, we performed a Taqman custom gene expression array comparing placentas of control and PNS females. Among the potential targets, *Sirt7, Nr3c1* (which encodes the *GR*), *Hdac9*, Histone 3 mammalian isoform, family 3b (*H3f3b*) and *Ythdf3* were upregulated in placentas of PNS females (Supplementary Table 1). We expanded the analysis using RT-PCR, adding additional samples and performing correlations between the expression of miR-340 and the putative targets (Fig. 3a–f). *GR* (Fig. 3b), *Hdac9* (Fig. 3c), *Cry2* (Fig. 3d), and *H3f3b* (Fig. 3e) showed a significant inverse correlation with the expression of miR-340 in these samples, while *Sirt7* (Fig. 3a) and *Ythdf3* did not (Fig. 3f). When examining the PNS group alone, the strongest correlations were evident for *GR*/GR, *Cry2*/CRY2, and *H3f3b*/H3F3b (Supplementary Fig. 5a), which also showed increased placental protein levels (Fig. 3g–i). In contrast, *Hdac9*/HDAC9 did not show a similar effect (Supplementary Fig. 5b). To explore the link between the miR-340 and the relevant targets further, we next infected BeWo placental cells with a lentivirus designed to knockdown (KD) miR-340 and thus mimic the effects of PNS. As expected, the KD virus significantly reduced the expression of miR-340 in the cells (Fig. 3j). In addition, while mRNA levels did not change significantly in any of the putative targets (Fig. 3k), we found an increase in protein levels of GR, CRY2, and H3F3b (Fig. 3l), but again not in HDAC9 (Supplementary Fig. 5B).

Given the variability within the control female group in vulnerability to ABA, we next focused on this group in an

additional experiment where we analyzed the relative expression of miR-340 in 28 female samples from an additional six control pregnant females. Nine out of the 28 placentas (32%) showed miR-340 levels 25% above the average (Fig. 3m), which resembles the number of ABA-prone females in our first group (40%). Remarkably, the levels of miR-340 were affected by the sex of the adjacent fetus. Females located between two males showed the lowest levels of miR-340 (Fig. 3n), suggesting prenatal androgen exposure may be linked to miR-340 expression levels and the subsequent resistance to ABA. Furthermore, we found an inverse correlation with the expression of miR-340 for *GR*, *Cry2*, and *H3f3b* in this group (Fig. 3o–q). Finally, we examined the

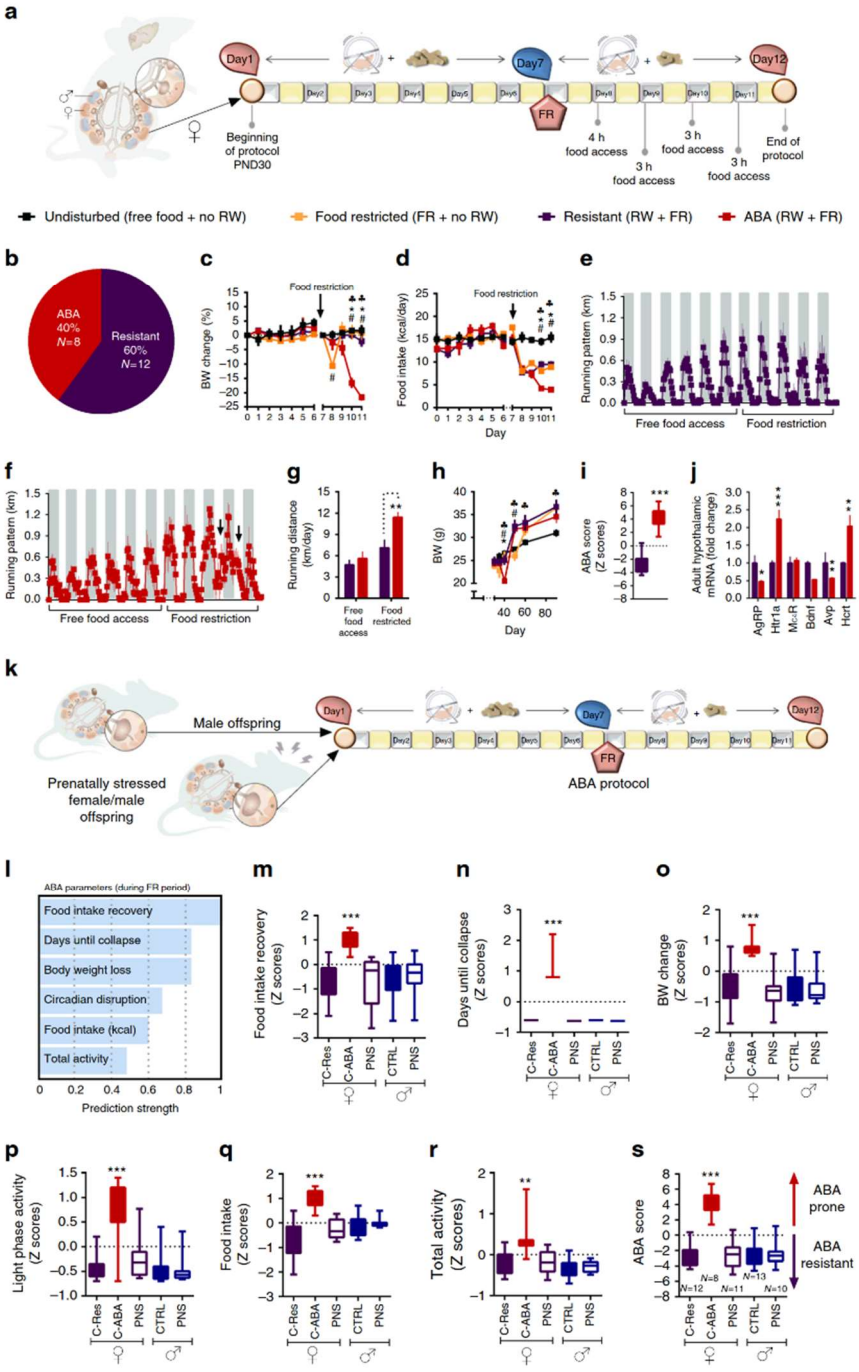

expression of the AN candidate genes in the hypothalamus of the fetuses according to placental miR-340 levels. We found that *AgRP* and *Hcrt* were highly expressed in control fetuses with high levels of miR-340 compared to fetuses with low levels of miR-340. In contrast, *Htr1a* and *Bdnf* were decreased (Fig. 3r).

MiR-340 inversely correlates with placental amino acid transporters. To gain insight into the potential effects of miR-340 levels on placental function and the uterinal environment that the fetuses were exposed to, we performed RNAseq in placentas with high and low endogenous miR-340 levels (Fig. 3m). Sleuth gene expression analysis revealed 881 upregulated and 779 downregulated genes in the high miR-340 group. Of these, we chose to focus on the solute carrier (SLC) group of membrane transport proteins, as well as on cholesterol transporters and the insulin-like growth factor (IGF) family given their crucial involvement in placental structure and function[35]. The two groups' profiles appear remarkably different in their capacity to allocate nutrients, as reflected by the different global expression in selected nutrient transporters (Fig. 4a). In particular, the levels of miR-340 inversely correlate with the expression of the amino acid transporters *Slc7a5c*, *Slc7a11*, and *Slc38a1*; the main lactate transporter *Slc16a3* and *Igf2* and *Igf2bp1* in mice (Fig. 4b). The Igf2 and the Igf family are heavily involved in nutrient transport and can further regulate thickness of the interhemel membrane connecting the maternal and fetal circulation[36]. Therefore, we examined the thickness of the junction in the two groups and found a thicker junctional area in the high miR-340 group, which was in accordance with reduced Igf2 levels[36] (Fig. 4c). When we explored the potential link between miR-340 levels and these transporters and growth factor, we found a potential pathway through the targets Nr3c1, Cry2, and H3f3b (Fig. 4d, based on STRING database https://string-db.org[37]). These findings suggest that the particular location of miR-340 in the junction may be linked to the regulation of nutrient transport to the fetuses, both by reducing fetal access to nutrients and amino acids and potentially through structural changes via Igf2. To examine the translational potential of our findings, we collected central, medial, and lateral human placental samples from healthy, full-term male and female pregnancies (see Supplementary Table 3 for the mothers' demographics and clinical characteristics). Analysis of the expression of miR-340 showed similar levels among boys and in the medial and lateral areas, but girls presented dramatically higher levels in the central area, which is closest to the umbilical cord (Fig. 4e). Similarly to mice, human female placentas showed a higher variability in the expression of miR-340 and when correlated with the expression of the relevant transporters identified in mice, we found an inverse correlation between miR-340 and *SLC7A5*, *SLC7A11*, *SLC38A1*, *SLC16A3*, *IGF2*, and *IGF2BP1* (Fig. 4f, further transporters examined are presented in Supplementary Table 3). Thus, the results suggest that miR-340 may be involved in mediating the fetal acquisition of selective nutrients, thus affecting developmental programming of the offspring, both in humans and in mice.

MiR-340 overexpression increases susceptibility to ABA. With the aim of exploring whether high levels of placental miR-340 are directly related to increased vulnerability to ABA, we next generated placenta-specific transgenes[38,39]. Blastocysts were then infected with lentiviruses designed to overexpress (OE) miR-340 or with a control virus (CV) and were then transferred into pseudo-pregnant females for further development (Fig. 5a). As expected, infection of the blastocysts' trophoblast cells with lentiviruses led to placenta-specific infection (Fig. 5b) predominantly in the junctional area of the placenta (Supplementary Fig. 6). Validation of miR-340 expression in placentas infected with the miR-340 OE virus confirmed a threefold increase in miR-340 levels in both sexes. A similar increase was found in infected BeWo cells (Fig. 5c). Examination of fetal hypothalamic expression of AN candidate genes revealed a similar profile to wild-type females with high endogenous expression of placental miR-340, including upregulation of *AgRP* and downregulation of *Htr1a* (Fig. 5c and Fig. 3r).

We next explored the mRNA expression and protein levels of the targets both in the transgene placentas and in infected BeWo cells respectively. As expected, miR-340 OE generally inversely correlated with mRNA and protein of the targets in placental samples (Fig. 5d, f, h) and in BeWo cells (Fig. 5e, g, i). In a separate set of pregnancies, the transferred embryos were allowed to reach term. They remained untouched until 30 days old, when they underwent the ABA protocol (Fig. 6a). To determine susceptibility to ABA, we next calculated the Z scores of the ABA parameters according to the prediction strength of the original experiment (Fig. 1k). All raw data are presented in Supplementary Fig. 7. Accordingly, we found that the pattern of food intake recovery during FR was inefficient in miR-340 OE animals

Fig. 1 Adolescent females show high susceptibility to activity-based anorexia (ABA), which is absent in males and is abolished by prenatal stress (PNS) in females. **a** ABA protocol experimental design. **b** Hierarchical cluster analysis split the females into ABA-prone and resistant to ABA. **c**, **d** The ABA protocol induced a dramatic decrease in body weight (BW) (repeated measures ANOVA $F(27,60) = 4.17$, $p = 0.000$ for time × treatment interaction) and food intake ($F_{(33,54)} = 3.71$, $p = 0.000$ for time × treatment interaction) in ABA females compared to all other groups ($N = 6$ for undisturbed, $N = 6$ for FR, $N = 8$ for ABA and $N = 12$ for resistant). **e**, **f** Running pattern was normal in resistant females (**e**) and disrupted in the ABA group, which displayed high activity in the light phase (**f**). **g** Total running distance was significantly increased during food restriction (FR) in the ABA group ($F_{int(1,14)} = 7.33$, $p = 0.017$). **h** Long-term BW differed between the groups (repeated measures ANOVA $F_{int(15,100)} = 6.67$, $p < 0.0001$). All FR females weighed significantly more than undisturbed females. $^{*}p < 0.05$ ABA vs. Resistant, $\#p < 0.05$ ABA vs. FR and (black club) $p < 0.05$ ABA vs. undisturbed based on Tukey's multiple comparisons test. Data are presented as mean and s.e.m. **i** ABA animals scored significantly higher in the global ABA score compared to resistant females (Student's t test $t_{(18)} = 10.49$, $p < 0.0001$), which is composed of the sum of the Z scores of the six ABA parameters. Data presented in min. to max with median. **j** Hypothalamic gene expression of AN candidate genes differed between resistant and ABA females (MANOVA $F_{(6,5)} = 24.60$, $p = 0.001$). **k** To test the sex specificity and the contribution of PNS to ABA predisposition, we tested PNS offspring of both sexes together with control males on the ABA protocol using one-way ANOVA for each parameter with Tukey's multiple comparisons test. **l** ABA individual parameters for the males and PNS animals were calculated in Z scores according to each parameter's strength of prediction. **m**–**r** Control males and PNS males and females scored similarly low in food intake recovery ($F_{(4,49)} = 7.26$, $p < 0.0001$) (**m**), days until collapse ($F_{(4,49)} = 82.89$, $p < 0.001$) (**n**), BW change ($F_{(4,49)} = 9.81$, $p < 0.0001$) (**o**), circadian disruption (light phase activity)($F_{(4,49)} = 13.06$, $p < 0.0001$) (**p**), food intake ($F_{(4,49)} = 7.06$, $p < 0.0001$) (**q**) and total activity ($F_{(4,49)} = 8.34$, $p < 0.001$) (**r**) compared to resistant control (C-Res) females. **s** While control females split into resistant and ABA-prone subgroups, PNS females and all males were largely resistant to ABA ($F_{(4,49)} = 32.30$, $p < 0.0001$). RW running wheel, CTRL control. Data presented as min. to max with median

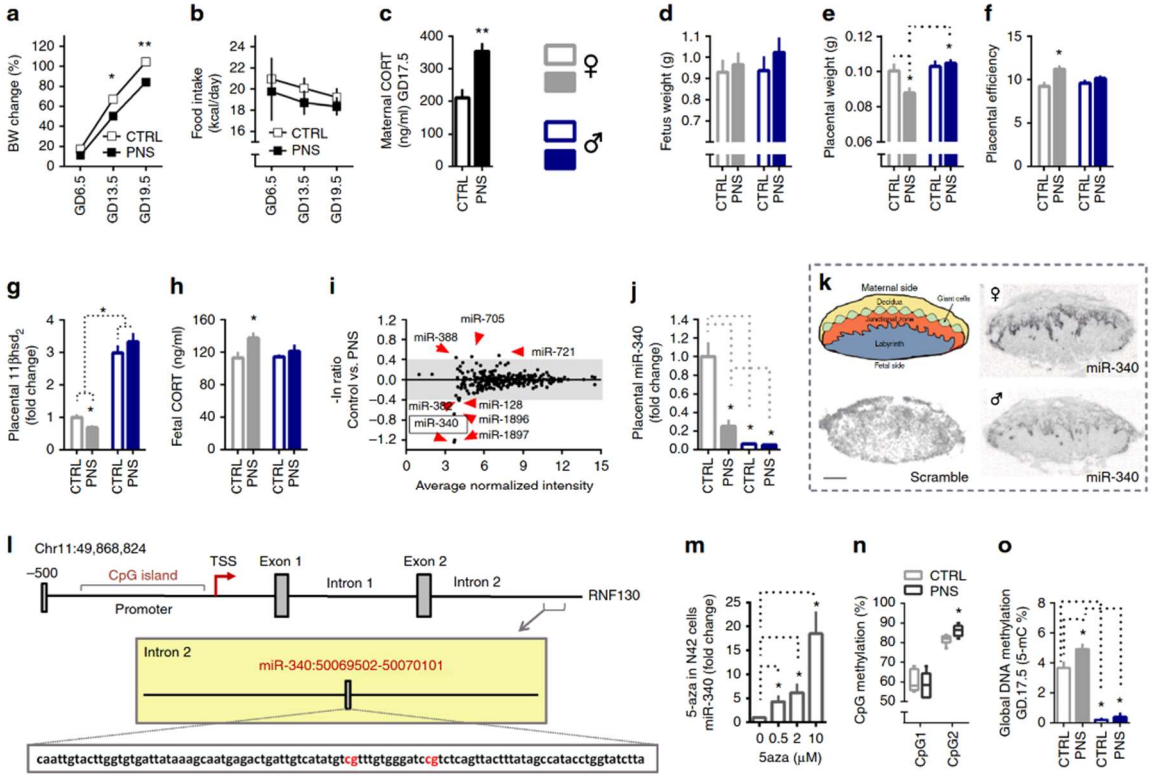

Fig. 2 Prenatal stress (PNS) downregulates placental miR-340 through gene body DNA methylation. **a**, **b** PNS affected the pregnant dams' body weight (BW) (repeated measures ANOVA $F_{(1,9)} = 21.56$, $p < 0.0001$) without affecting food intake ($N = 5$–6). **c** PNS increased maternal corticosterone (CORT) ($t_{(10)} = 3.88$, $p = 0.003$). **d**–**f** Fetus weight was similar in control and PNS offspring (**d**), but placental weight was reduced by PNS only in females (two-way ANOVA $F_{int(1,18)} = 4.54$, $p = 0.047$) (**e**), resulting in increased placental efficiency (Kruskal–Wallis $H = 11.82$, $p = 0.008$, specific groups comparisons based on Mann–Whitney) (**f**). **g**–**h** Placental *11βhsd*$_2$ was overall higher in males (two-way ANOVA $F_{(1,46)} = 188.59$, $p = 0.000$) but was reduced by PNS only in females (interaction effect $F_{(1,46)} = 5.85$, $p = 0.020$, $N = 11$–12, from 5,6 different dams) (**g**) resulting in high fetal CORT in PNS females ($F_{sex(1,24)} = 5.28$, $p = 0.032$, $N = 12$) (**h**). **i** The placental miRNA array performed on females revealed downregulation of miR-340 by PNS. **j** MiR-340 validation showed reduced levels in PNS females and males of both prenatal conditions (two-way ANOVA $F_{sex(1,41)} = 41.00$, $p < 0.0001$) and ($F_{prenatal\ (1,41)} = 6.51$, $p = 0.015$). **k** MiR-340 is expressed in the junctional zone of the placenta. **l** Schematic representation of the *Rnf130* gene and CpG areas analyzed. **m** 5-aza treatment of N42 cells at increasing concentrations upregulated miR-340 levels (one-way ANOVA $F_{(3,15)} = 18.79$, $p < 0.0001$, with Bonferroni post-hoc tests). **n** CpGs on the miR-340 sequence were highly methylated and CpG_2 was significantly more methylated in PNS female placentas (Mann–Whitney $U = 3.50$, $Z = -2.35$, $p = 0.015$). Data are presented in min. to max. **o** Global DNA methylation differed dramatically among the groups (Kruskal–Wallis $H = 18.31$, $p = 0.000$). Females showed higher global methylation than males, an effect increased even further by PNS ($N = 6$, from 5 to 6 different dams). Significance between groups and sexes based on Tukey's multiple comparison tests and Mann–Whitney post-hocs when relevant. GD gestation day, CTRL Control. Data are presented in mean and s.e.m. Scale bar: 1 mm

(Fig. 6b). MiR-340 OE transgenes collapsed more frequently toward the end of the food restriction period (Fig. 6c), displayed higher BW change (Fig. 6d) and showed circadian disruption as reflected by the distance run (km) in the light phase (Fig. 6e) compared to transgene controls. While food intake during FR was not significantly affected (Fig. 6f), miR-340 OE induced hyperactivity in both males and females (Fig. 6g). Taken together, these parameters exposed the significantly higher susceptibility to ABA in miR-340 OE transgenes of both sexes, as reflected by the higher ABA score compared both to wild type (WT) and CV controls (Fig. 6h). Finally, hypothalamic assessment of AN candidate genes in these groups revealed long-lasting down-regulation of *AgRP* and upregulation of *Htr1a*, resembling the expression patterns found in the original control ABA group (Fig. 6i and Fig. 1j) and further confirming the central role played by the hypothalamic melanocortin and serotonin systems in anorexia. Altogether, these findings translated into higher percentages of animals being prone to ABA as a result of miR-340 OE (Fig. 6j).

Taken together, we propose that placental miR-340, through the regulation of genes known to be involved in placental structure and function, such as *GR*, *Cry2* and *H3f3b* and downstream nutrient transporters, can change the fetal environment and hypothalamus to induce later life susceptibility or resistance to ABA (Fig. 7).

Discussion

In the current set of studies, we have identified, for the first time, a potential mechanism of ABA gestational programming. It appears that early life variables that affect placental gene expression may play a crucial role in this predisposition. These findings are supported by the genetic epidemiology of AN, which indicates strong evidence for familial contribution but does not

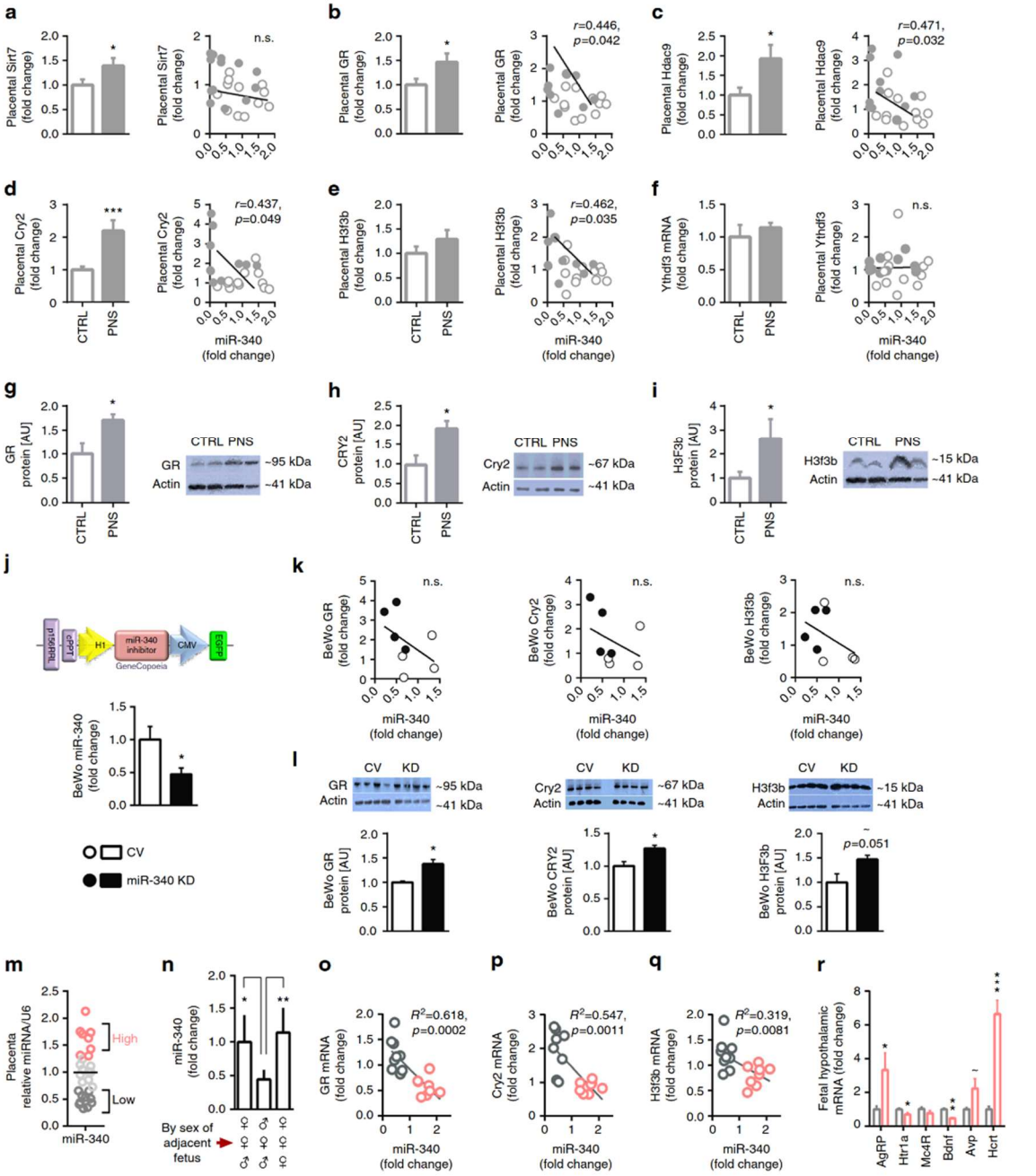

Fig. 3 MiR-340 exerts its effects through targeting of GR, Cry2, and H3f3b. **a**–**f** Validation of potential miR-340 target in prenatal stress (PNS) vs. control female placentas showed that *Sirt7* and *Ythdf3* were not significantly correlated with miR-340 (**a**, **f**). **b**–**e** In contrast, *GR*, *Hdac9*, *Cry2*, and *H3f3b* expression was significantly higher in PNS and inversely correlated with miR-340. **g**–**i** Placental GR, CRY2, and H3F3b protein levels were increased by PNS ($N = 4$). **j** Lentiviral KD of miR-340 in BeWo choriocarcinoma cells reduced the expression of miR-340 ($F_{(1,7)} = 5.654$, $p = 0.050$, $N = 4$). **k** MiR-340 KD did not significantly affect mRNA levels of the target genes. **l** At the protein level, miR-340 KD increased GR ($t_{(6)} = 3.687$, $p = 0.010$) and CRY2 ($t_{(6)} = 3.156$, $p = 0.0197$), and tended to increase H3F3b. **m** Within the control group, miR-340 expression shows great endogenous variability ($N = 28$, from six dams). **n** Female fetuses surrounded by two males in the uterus show lower levels of placental miR-340 compared to females surrounded by females or mixed sexes (one-way ANOVA $F_{(2,23)} = 9.31$, $p = 0.0013$). Data are presented in mean and s.e.m. and Tukey's multiple comparison tests. **o**–**q** The "high" and "low" subgroups included samples above 1.3 and below 0.70 relative to the groups' average respectively. The expression of *GR*, *Cry2*, and *H3f3b* inversely correlated with the endogenous levels of miR-340. Data are presented as mean and s.e.m. **r** Fetal hypothalamic gene expression of AN candidate genes differed between the "high" and "low" subgroups ($F_{(6,5)} = 13.1$, $p = 0.006$). Data are presented in mean and s.e.m. ($N = 6$)

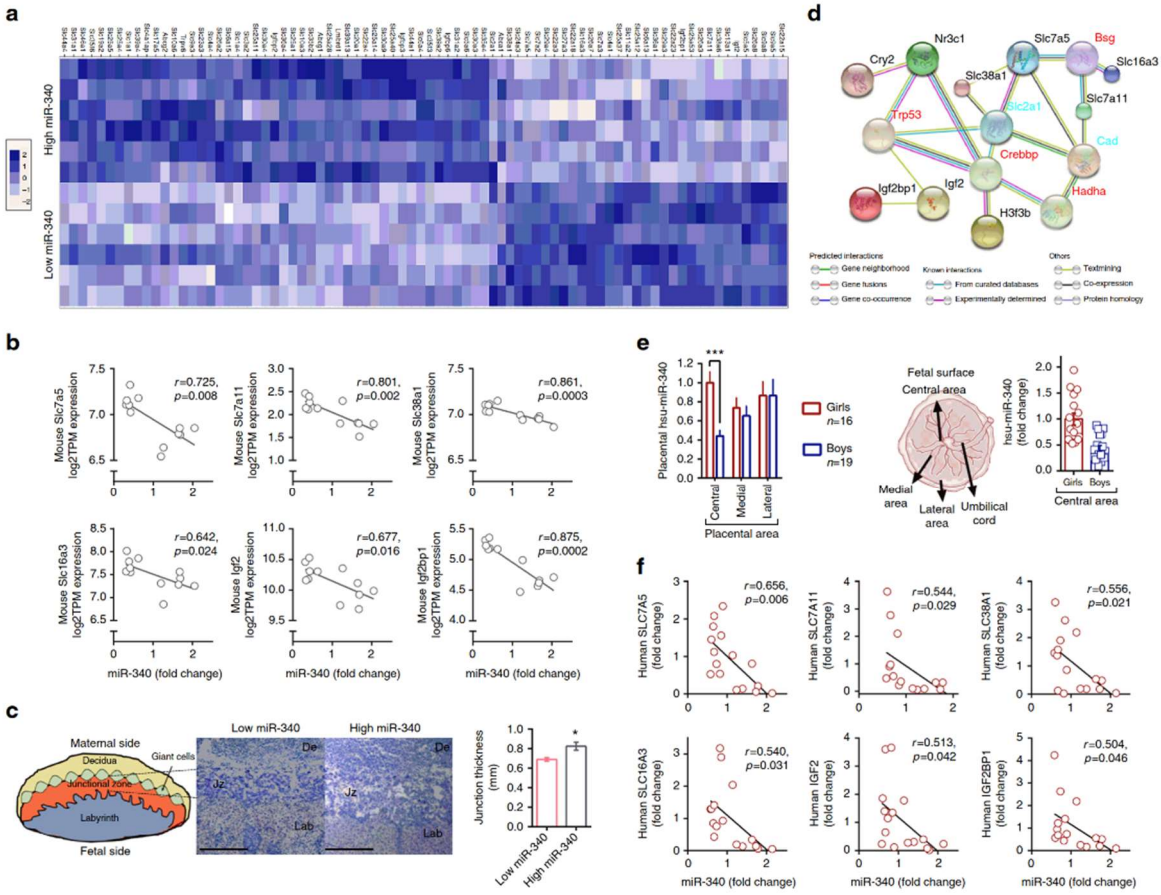

Fig. 4 MiR-340 is associated with differential expression of nutrient transporters both in mouse and human female placenta. **a** Heat-map comparing placental nutrient transporters between female mice endogenously expressing high or low levels of miR-340. **b** The expression of *Slc7a5*, *Slc7a11*, *Slc38a1*, *Slc16a3*, *Igf2*, and *Igf2bp1* is inversely correlated with miR-340 in mice. **c** Eosin-hematoxylin staining of the mouse placenta show a thicker junctional zone in the high miR-340 group ($t_{(6)} = 3.07$, $p = 0.022$). **d** STRING pathway analysis linking the miR-340 targets *Nr3c1*, *Cry2*, and *H3f3b* with selected nutrient transporters (https://string-db.org). **e** Expression of miR-340 in the human placenta in central, medial, and lateral areas. Girls present higher levels in the central area compared to boys (two-way ANOVA $F_{(1,104)} = 14.78$, $p < 0.0001$). Data are presented as mean and s.e.m. **f** The expression of *SLC7A5*, *SLC7A11*, *SLC38A1*, *SLC16A3*, *IGF2*, and *IGF2BP1* are inversely correlated with miR-340 expression in the central area of human samples. Scale bar: 1 mm

always provide convincing evidence of hereditability according to population-based homozygous twin studies[40,41]. When it comes to gestational programming, the placenta plays a central part in shaping the fetal environment[42]. Placentas exhibit pronounced sexual dimorphism in response to variation in the maternal milieu both in humans[43] and mice[31,44], which appears to be the case for miR-340 in the junctional zone of the mouse placenta. This zone contains zygote-derived cytotrophoblasts, which have direct access to the maternal blood flow[45]. Two types of cytotrophoblasts exist in this zone at GD17.5 in mice, spongiotrophoblasts and trophoblast glycogen cells, both of which synthesize protein hormones such as IGF_2, a key growth and nutrient supply gene[46]. The human and mouse placentas share a similar function, but are structurally quite different. The corresponding region to the murine junctional zone in humans is the basal plate, which differently from mice presents multi-layered cytotrophoblastic columns with a morphological gradient of cells. Despite this difference, in both species this region does not contain any fetal blood, but is traversed by maternal blood channels lined by zygote-derived trophoblast cells, through which maternal blood flows into and out of the fetal placenta/labyrinth[45].

The placental responses to stress include adaptations at multiple epigenetic levels, which affect molecular processes on a global scale. Abnormal DNA methylation is one of these processes[47], that in turn shapes placental morphology with far-reaching implications including impairments in placental development and nutrient supply. Maternal stress during pregnancy broadly influences the placenta, inducing the very well documented and varied negative effects in the offspring such as anxiety, depression, cognition, memory[48,49], and metabolism[50]. When PNS is limited to the last week of gestation, unlike our protocol, susceptibility to ABA appears to increase in a subset of rats[30]. A similar finding was recently reported for binge eating disorder using a different stress model but the same window of intervention[51]. Thus, ABA resistance resulting from chronic PNS may represent a beneficial side effect of an otherwise negative overall outcome.

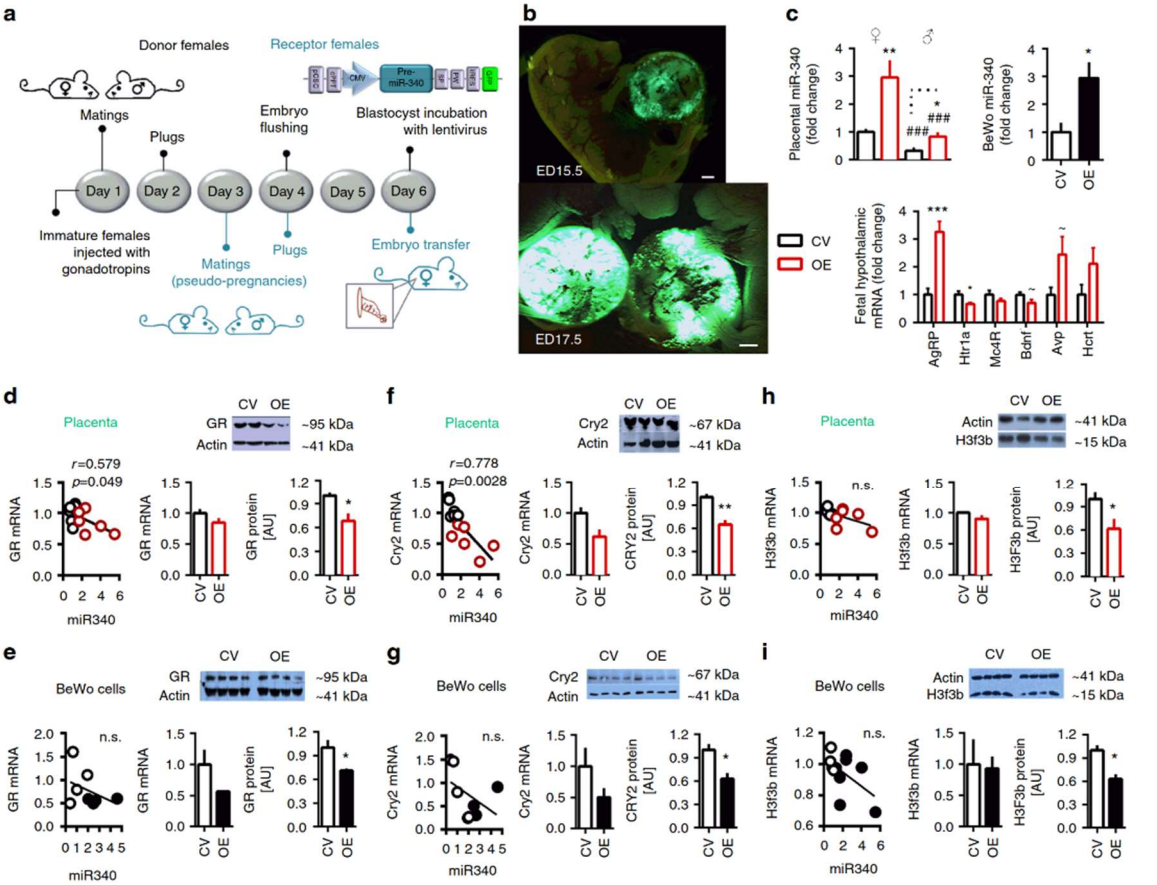

Fig. 5 MiR-340 overexpression (OE) decreases GR, CRY2, and H3F3b protein in the placenta and in BeWo cells. **a** Experimental design for generation of placenta-specific transgenes. **b** Representative pictures out of about 20 transfers of placenta-specific infection. **c** Placental miR-340 was highly expressed in the female transgenes of both groups compared to males (two-way ANOVA $F_{sex(1,23)} = 47.39$, $p < 0.0001$) and was increased by the miR-340 OE lentivirus in both sexes ($F_{treatment(1,23)} = 28.78$, $p < 0.0001$, $N = 6$). Infection of BeWo cells with the miR-340 OE lentivirus led to increase in miR-340 expression levels (Unpaired *t*test $t_{(6)} = 1.77$, $p = 0.019$). Fetal hypothalamic gene expression of anorexia candidate genes differed between the CV and miR-340 OE groups (MANOVA $F_{(6,5)} = 7.08$, $p = 0.024$), with high expression of *AgRP*and low expression of *Htr1a*. **d** In miR-340 OE transgenes, placental *GR* mRNA inversely correlated with miR-340 ($N = 6$) and placental protein tended to be reduced ($t_{(6)} = 2.414$, $p = 0.052$, $N = 4$). **e** In BeWo cells, *Nr3c1/GR* mRNA x miR-340 correlation showed a similar pattern to the placenta and miR-340 OE decreased GR protein levels ($t_{(6)} = 3.09$, $p = 0.011$, $N = 4$). **f** Placental *Cry2* mRNA inversely correlated with miR-340 ($N = 12$) and showed decreased protein levels after miR-340 OE (Unpaired *t*test $t_{(6)} = 2.451$, $p = 0.049$, $N = 4$). **g** In BeWo cells, miR-340 OE significantly decreased CRY2 protein levels ($t_{(6)} = 3.381$, $p = 0.0148$). **h–i** MiR-340 OE did not affect *H3f3b* mRNA expression but decreased H3F3b protein levels in the placenta ($t_{(6)} = 2.452$, $p = 0.0451$, $N = 4$) (**h**) and in BeWo cells ($t_{(6)} = 4.25$, $p = 0.0054$, $N = 4$) (**i**). Data presented as mean and s.e.m. CV control virus. Scale bar: 1 mm

Overexpression of GR, as seen in our placental PNS samples, induced multiple neuroendocrine changes that have been shown to result in a blunted response to restraint stress and to endotoxic shock in a different animal model[52]. Accordingly, high maternal cortisol in utero and/or inhibition of 11βHSD$_2$ are associated with programmed outcomes in childhood including higher blood pressure, behavioral disorders, and altered brain structure[53]. Given the remarkable resistance of males to ABA, a potential mechanism of ABA prevention in females by PNS may be related to its well-known masculinizing effects. PNS increases anogenital distance, which is a sexually dimorphic biomarker of prenatal androgen exposure in many species[54]. We noticed that females were undistinguishable from males in the PNS group at birth due to larger than usual anogenital distance. This effect resembles prenatal testosterone exposure, which was shown to masculinize the food intake pattern of female offspring[55]. Moreover, disorganized eating in girls may be improved by prenatal androgen exposure, as shown in a twin study in which female pairs had significantly higher disordered-eating scores than girls with male twins[56]. This "prenatal androgen exposure hypothesis" has been more frequently linked to autism spectrum disorders[57], but could also be involved in determining the level of predisposition to ABA in females. This is particularly likely given the well-documented effects of uterine position on the fetuses: females developing between two males are more likely to show masculinized behavioral, anatomical physiological traits due to the transfer of testosterone from the adjacent fetuses[58]. This could be a potential source of the great variability adolescent WT females show in their response to ABA. Thus, females surrounded by other female fetuses may be more vulnerable to ABA as suggested by human

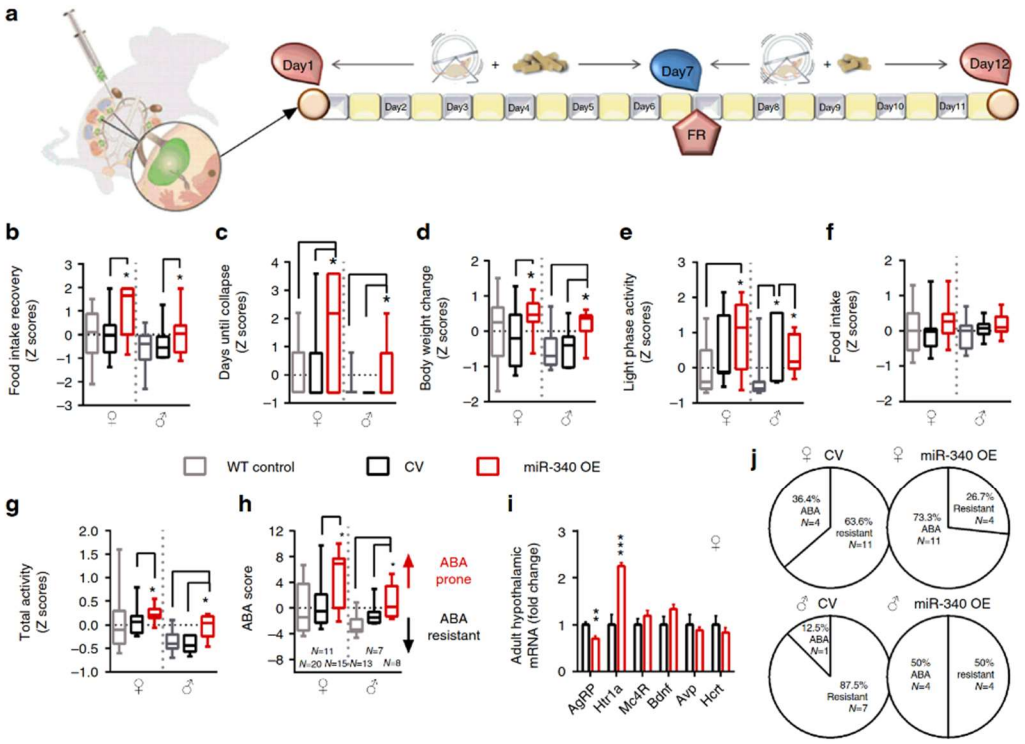

Fig. 6 Placental miR-340 overexpression (OE) robustly increases the susceptibility to activity-based anorexia (ABA) in both sexes. **a** Transgene animals of both sexes were exposed to the ABA protocol. **b**–**g** MiR-340 OE transgenes of both sexes scored higher than controls in food intake recovery (one-way ANOVA $F_{(5,68)} = 4.49$, $p = 0.0014$) (**b**), days until collapse ($F_{(5,68)} = 5.36$, $p = 0.0003$) (**c**), body weight (BW) change ($F_{(5,68)} = 3.99$, $p = 0.003$) (**d**), circadian disruption (light phase activity) ($F_{(5,68)} = 5.01$, $p = 0.0006$) (**e**) and total activity ($F_{(5,68)} = 6.81$, $p < 0.0001$) (**g**) during the food restriction part of the protocol. In contrast, food intake during food restriction did not significantly differ between the groups (**f**). **h** Altogether, placental miR-340 OE robustly increased the susceptibility to ABA in both sexes compared to both WT controls and CV animals ($F_{(5,68)} = 6.83$, $p < 0.0001$). Data presented as min to max with median. Differences between the groups are based on Tukey's multiple comparisons test. $^*p < 0.05$. **i** Hypothalamic gene expression of anorexia candidate genes differed between CV and miR-340 OE females (MANOVA $F_{(6,5)} = 53.83$, $p < 0.000$), with low expression of *AgRP* and high expression of *Htr1a*. Data are presented in mean and s.e.m. ($N = 6$). **j** MiR-340 OE increased the susceptibility to ABA in both sexes. CV control virus

twin studies[56,59]. While the sex-specific physiological mechanism through which placental miR-340 methylation and expression is determined under both stressful and normal conditions remains unclear, hormonal alterations in utero may represent a potential candidate as suggested by Rnf130 regulation by LH/hCG in Leydig cells in rats[60]. Finally, the fact that ABA and AN are typically triggered during adolescence may further suggest that the prenatal hormonal effects on female offspring may form a platform for a later triggering or protective effect of gonadal steroids on this phenotype.

The modulation of the targets identified here, and potentially dozens of further targets by miR-340, likely affect nutrient transporters and growth factors, which may have in turn a pivotal influence on fetal development and programming. The ability of a single miR molecule to affect the functional levels of multiple proteins/pathways supports therefore their possible involvement in complex disorders, such as EDs, which are suggested to be polygenic by nature and influenced by gene × environment interactions[61]. Similarly to miRs, transcription factors like GR[62] are highly involved in the regulation of gene expression. GR is widely expressed both in the labyrinth and the junctional zone of the murine placenta[63]. It is involved in the expression and alteration of a great number of placental genes including the regulation of trans-placental glucose transfer, through modulation of the glucose[64] and amino transporters. It is therefore a crucial factor for sustaining fetal life and securing its normal development[65] affecting the newborns' neurobehavior[66]. GR interacts with Cry2, a key component of the circadian core oscillator complex that regulates the circadian clock and has been detected both in the labyrinth and the junctional zone in rats[67]. The clock genes are widely involved in the regulation of placental function, suggesting that normal circadian variations may be involved in a healthy placental phenotype[67]. Finally, H3f3b, one of the replication-independent variants of the Histone 3 mammalian isoform, is enriched in coding regions and at specific chromatin landmarks in mouse somatic and embryonic cells[68]. While its role in placental structure and functioning is largely unknown, it is suggested to affect chromatin architecture changing the regulation of epigenetic mechanisms during development[69]. Given their function, it is not surprising that the miR-340 targets may affect the transfer of nutrients to the fetus by regulating selective transporters. In particular, less transfer of amino acids to the fetus, as reflected by lower expression of three key transporters, and Igf2, which can affect the thickness of the junction hindering the transfer of nutrients[70].

Overall, we have identified a placental mechanism through which miR-340 mediates vulnerability to ABA, likely through influencing placental function. MiR-340 presents clear sexual

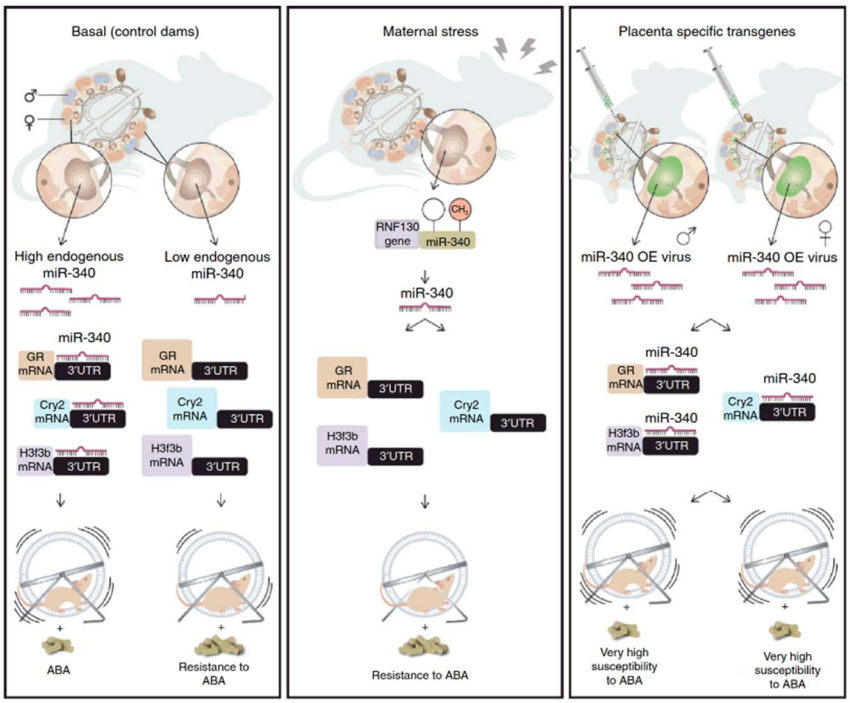

Fig. 7 Summary scheme comparing placental miR-340 expression and the adult outcome in the different experiments. Female offspring born from control dams present high levels of placental miR-340, while the male levels are endogenously low. MiR-340 targets *Nr3c1/GR*, *Cry2*, and *H3f3b* programming susceptibility to activity-based anorexia (ABA) specifically in females (left panel). Prenatal stress downregulated miR-340 through gene-body DNA methylation, upregulating *Nr3c1/GR*, *Cry2*, and *H3f3b*, thus are protecting the female offspring from sensitivity to ABA (central panel). Upregulation of placental miR-340 through lentiviral infection of blastocysts reduced GR/CRY2/H3F3b protein levels, and robustly increased ABA susceptibility in both sexes (right panel). CV control virus, GR glucocorticoid receptor, OE overexpression

dimorphism and is downregulated by PNS inducing a "protective" effect against ABA. Placenta-specific OE of miR-340 in transgene mice exposed its role in the regulation of placental functioning through GR/Cry2//H3f3b and its involvement in gestational programming of ABA, potentially influencing fetal brain development. Our findings directly link, for the first time, the variability in the expression of a placental miR with fetal programming and later vulnerability to AN and provide important insights into the ontogeny of this poorly understood ED.

Methods

Animal care. ICR/CD1 mice (Harlan Sprague Dawley Inc., Indianapolis, IN) were maintained in a pathogen-free temperature-controlled (22 ± 1 °C) mouse facility on a reverse 12 h light−dark cycle at the Weizmann Institute of Science, according to institutional guidelines. Food (Teklad Global, Harlan Sprague Dawley Inc., Indianapolis, IN) and water were given ad libitum (apart from during FR). All experimental protocols were approved by the Institutional Animal Care and Use Committee of the Weizmann Institute of Science.

Breeding. Female ICR mice were mated at 11−13 weeks of age. Two or three females were housed with one male (minimum age 12 weeks) at the beginning of the dark period and were examined for the presence of a vaginal copulation plug at the end of the dark period. Presence of a copulation plug denoted day 0.5 of gestation. After breeding, the females were individually housed.

Experimental groups. Females with plugs were randomly assigned to the control or PNS treatment. From day 18.5 of gestation, females were checked twice a day for the presence of a litter (0900−1000 hours, 1700−1800 hours). Newborn litters found by 1800 hours were designated as born on that day—postpartum day 0 (PPD 0). On PPD 1, pups were counted and litters were culled to ten pups (with sex distribution kept as equal as possible in each litter). Litters with less than seven pups were excluded.

PNS protocol. From gestation day (GD) 1.5 until GD16.5, pregnant females were exposed to a chronic variable mild stress protocol, including two short manipulations during the dark phase and a further overnight (ON) manipulation during the light phase. The chosen stressors did not induce pain and did not directly influence maternal food intake or weight gain and were repeated on a weekly basis. The short stressors included multiple cage changes, cage tilt, white noise, water in cage or no bedding for two periods of 2 h, immobilization in a tube or elevated platform for 30 min and swim stress in warm water for 15 min. Overnight manipulations included illumination, saturated bedding (with water), novel object (marbles), and overcrowding.

Activity-based anorexia model. On PPD 21−22, pups were weaned and offspring were group housed until PPD 30, where they were randomly designated to one of two experimental groups (using a randomized complete block design to avoid potential litter effects): (1) Control group (free food access, no RW); (2) Food-restricted group (FR group): Free food the first week, FR the second week, no RW; (3) RW group (free food access in the first week, FR in the second week, free RW). On PND 30, which is considered the onset of adolescence in mice as determined by the time of the first estrous[70], ICR mice in the ABA groups were placed in an RW system in order to record running pattern (diameter 115 mm, TSE-Systems, Bad Homburg, Germany). The protocol lasted for 11 days during which food intake and BW were measured daily. The first week was defined as a "training period", during which food and water were given ad libitum. On the first day of the second week food access was limited to 4 h, and on the following days the food access was limited to 3 h. Animals were defined as anorexic in retrospect by cluster analysis according to the following criteria, which was based on previous studies[21–24] and our preliminary findings: (1) Percentage weight loss; (2) Food intake during FR; (3) Food intake recovery (%) during the FR period; (4) Circadian disruption (km ran during the light phase); (5) Days until collapse (faint and become hypothermic) and (6) Total running distance (km) when FR. Animals that developed ABA were

removed from the RW cage once they collapsed and were subsequently given food ad libitum and monitored until fully recovered. The predictive strength of the six ABA parameters was determined by two-step cluster analysis and was used to calculate the *Z* scores.

Production of lentiviral vectors. MiR-340 was PCR amplified from mouse genomic DNA, using the following oligonucleotide primers, both carrying restriction sites for *Age*I :5′-TCTTCAAGAGGGAGCCTCAG-3′ and 3′-AACAGGCATGATCTGTGGTG-5′. The purified PCR product (~175 bp) was digested using *Age*I enzyme and ligated to pCSC-SP-PW-IRES-GFP plasmid. MiR-340 sequence was confirmed by DNA sequencing. High titer lentiviruses expressing miR-340 and green fluorescent protein (GFP) were produced by transient transfection in HEK293T cells. Infectious particles were harvested at 48 and 72 h post-transfection, filtered through 0.45 µm-pore cellulose acetate filters (Sigma-Aldrich), concentrated by ultracentrifugation, re-dissolved in sterile HBSS, aliquoted and stored at −80 °C. Vector concentrations were analyzed using eGFP fluorescence in HEK293T cells infected with serial dilutions of the recombinant lentivirus[71,72].

Generation of placenta-specific lentiviral system. Three-week-old female mice were hyper-ovulated with gonadotropins (PMSG) (Sigma-Aldrich) followed 48 h later by hCG (5 IU each) and were then mated with males. Two days after the detection of a copulation plug, oviducts were dissected (Embryonic day (ED) 2.5) and flushed with M2 medium (M7167, Sigma-Aldrich, St. Louis, MO), using a syringe with 30-gauge blunt hypodermic needle. Embryos at their morula stage (ED2.5) were collected and rinsed through several drops of M2 medium. The zona pellucida was then removed by rinsing with Tyrode's solution (M8410, Sigma-Aldrich, St. Louis, MO). Denuded embryos were re-washed with M2 medium and placed in 50 µl drops of M16 medium (M7292, Sigma-Aldrich, St. Louis, MO) on a 35-mm tissue culture plate. They were then incubated for 2 nights at 37 °C and 5% CO_2 for further development. Embryos at their blastocyst stage (ED4.5) were then incubated in 30 µl drops of M16 + 3 µl concentrated lentivirus for 6 h. Using a stripper micropipette (Cat# MD-MXI.3-SRT-CGR; Zotal Ltd, Tel Aviv, Israel), infected blastocysts were then transferred into fresh drops of M2 medium and then into ED2.5 pseudo-pregnant females' uterus for further development[38,39]. This technique is highly specific to the transduction of the junction, therefore making vesicular transfer highly unlikely.

Generation of pseudopregnant females. The pseudo-pregnant females were produced by mating with sterilized males. Vasectomies were performed on 2-month-old males by making an incision across the lower abdomen, at the midline of the scrotal sac, under Ketamine:Xylazine (1:1 20% in saline) anesthesia. Then, a section of the vas deferens (0.5 cm) was bilaterally removed. Males were allowed 2 weeks to recover and were mated with females to confirm sterilization before the beginning of the protocol.

Embryo tissue collection. On GD17.5, pregnant females were anesthetized with an overdose of Ketamine-Xylazine (1:1, 20% in saline) and through cesarean section both the embryos and placentas were excised. Embryos were weighed and decapitated, the brain was extracted and the hypothalamus was removed, immediately frozen on dry ice and stored at −80 °C. Trunk blood was collected in EDTA-coated tubes (MiniCollect, Greiner bio-one, Austria). Placentas were also weighed and immediately stored at −80 °C. A portion of the embryos' tail was removed for later DNA extraction and sex genotyping. For analyses comparing between groups, only one fetus per litter (per sex) was used. These were chosen from the central uterinal location, with one male and one female as adjacent fetuses. Males chosen had one male and one female as adjacent fetuses. When the focus was intra-litter variability, the fetuses located at the extremes of the uterus were excluded.

Adult tissue collection. Adult animals were killed at the age of 3 months, 4 weeks after the end of the ABA protocol and when fully recovered. After decapitation, the hypothalamus was dissected and immediately frozen. Trunk blood was collected, immediately centrifuged and plasma samples were and stored at −80 °C.

Genotyping. Sex of the embryo was determined by Sry genotyping (forward 5′-TCATGAGACTGCCAACCACAG-3′ and reverse 5′-CATGACCACCACCAC-CACCAA-3′)[73]. Amplification product was detected by 2% gel electrophoresis.

Offspring physiological measurements. Pregnant and lactating dams underwent weekly follow-up of body weight and food intake. For pre-weaning weights, total litter weights were averaged (males and females apart). Post-weaning, pups were weighed individually and food intake was monitored weekly.

Plasma corticosterone measurement. Corticosterone levels were analyzed using radioimmunoassay (MP Biomedicals, Solon, Ohio, USA).

Mouse RNA extraction and real-time PCR. For placental tissue, purification of total RNA containing miRNAs and DNA was done using Tri Reagent (MRC Inc., Cincinnati, OH) according to the manufacturer's recommendations. gDNA was removed using Turbo DNAse digestion in solution, followed by heat deactivation (#AM2238, Thermo Fisher Scientific). Hypothalamic RNA was extracted using the miRNeasy Mini Kit (#217004, Qiagen) in conjunction with on column digestion of gDNA using Turbo DNAse (see above). RNA preparations were reverse transcribed to generate cDNA using miScriptII Reverse transcription kit for miRNAs/mRNA (QIAGEN, #218160, Hilden, Germany). Quantitative mRNA/miRNA expression were done using a SYBR®Green PCR kit (QIAGEN, Hilden, Germany) and miScript SYBR (#204057 QIAGEN, Germany) respectively, according to the manufacturer's guidelines and a StepOnePlus® Real time PCR system (Applied Biosystems, Waltham, MA), using specific primers. U6 snRNA was used as internal control for the miRs and Tbp was used as internal control for mRNA in placental samples.

MicroRNA Agilent array. MiRNA array of the placenta was performed using Agilent's microarray (SurePrint G3 Unrestricted GE 8*60k, G4872A; Agilent Technologies, Santa Clara, CA). The bioinformatic analysis was performed using the Limma (Liniar Models for MicroArray Data) package which is part of the Bioconductor software (http://bioconductor.org). We corrected the background with the Normexp method, used the Loess method for the within arrays normalization and the Aquantile for between arrays normalization. A linear model was applied in order to find the differentially expressed genes (a simple Bayesian model). Gene ontology analysis was performed using WebGestalt 58. (http://bioinfo.vanderbilt.edu/webgestalt/) (Supplementary Data 1).

Taqman array. Placental gene expression of potential miR-340 targets was analyzed by a Taqman fast small RNAs assay (Applied Biosystems, Waltham, MA) (Supplementary Table 1).

Mouse and human RT-PCR primers. See Supplementary Tables 4 and 5.

5-aza functionality assay of methylation. N42 immortalized hypothalamic cells were plated into 35 mm plates and treated for four days with different concentrations (0, 0.5, 2, 10 µM) of 5-Aza-2′-Deoxycytidine (Sigma-Aldrich, St. Louis, MO). Every day in the evening, medium was replaced with fresh growth medium containing fresh 5-Aza. Cells were then lysed and RNA was extracted using the miRNeasy mini kit (QIAGEN, Hilden, Germany). RNA was reverse transcribed to cDNA using miScript Reverse transcription kit (QIAGEN, Hilden, Germany).

Global DNA methylation. Global methylation of the placenta was done using the MethylFlash Methylated DNA Quantification ELISA kit (Epigentek Group Inc., Farmingdale, NY) according to the manufacturer's instructions.

DNA methylation of Rnf130 promoter and miR-340 sequences. Methylation analysis by pyrosequencing of bisulfite-treated genomic DNA was performed by Varionostic GmbH (http://www.varionostic.de/). Genomic DNA was bisulfite converted using the EZ DNA Methylation Gold Kit (Zymo Research, Irvine, CA). Amplicons were generated from bisulfite DNA covering 134 CGs in the CpG island located in the promoter region of the *Rnf130* gene and the sequence coding for miR-340 on intron 2 (Fig. 2 and Supplementary Fig. 3). Sequencing was performed on the Q24 System with PyroMark Q24 analysis software in CpG (QIAGEN, Hilden, Germany). Data were analyzed using SPSS Statistics, Version 17 (SPSS Inc., Chicago, IL) as indicated.

Western blot. Placental protein was purified in RIPA buffer, centrifuged for 10 min at 4 °C, separated in a 10% polyacrylamide gel by electrophoresis and transferred onto nitrocellulose membranes. The transfer was performed at 100 v, 350 mAmp for 1 h. After washes with PBST (PBS + 20% Tween20), membrane was blocked with 10% skimmed milk in PBST for 1 h. The primary antibodies anti-H3F3B (1:10,000, #GTX115549 GeneTex, Irvine, CA), anti-NR3C1 (GR) (1:200, (M-20) sc-1004; Santa Cruz Biotechnology), anti-CRY2 (abcam 1:500 ab38872), anti HDAC9 (1:500, B-1, sc-398003, Santa Cruz Biotechnology) and anti-Actin (1:1000, sc-1616; Santa Cruz Biotechnology) were added to PBST and placed on constant shaking at 4 °C overnight. After several washes with PBST, the secondary antibodies (Cell Signaling Technology, Beverly, MA) were added for 1 h incubation at RT. Finally, the membranes were visualized using ECL (Thermo Fisher Scientific, Waltham, MA) and film (Fujifilm, Tokyo, Japan). For tests and membranes, see Supplementary Fig. 8.

Gross placental structure analysis. The thickness of the placental section occupied by the junctional zone (Jz) was determined on an M205C stereo microscope (Leica, Wetzlar, Germany) and the Leica Application Suite X software (LAS X) following eosin−hematoxylin staining by averaging three measurements in the central area ($N = 4$).

Libraries and RNAseq. Libraries were prepared with the Illumina TruSeq Stranded Total RNA Library Preparation kit with Ribo Zero Gold (Illumina, #RS-122-2301) according to the instructions, using 1000 ng total mouse placenta RNA as starting material. Libraries were quantified on a Qubit fluorometer and by qPCR with a KAPA Library Quantification Kit for Illumina libraries (# KK4828). Size distribution was checked using the Agilent High Sensitivity DNA Assay (#5067-4626) on an Agilent Bioanalyzer. Samples were denatured using 1 N NaOH, diluted to a concentration of 3 nM with ExAMP mastermix and loaded onto a HiSeq 4000 machine (Illumina, San Diego, CA; #SY-401-4001) with 1% PhiX control (Illumina, #FC-110-3001) spiked in. HiSeq 3000/4000 flow cells and HiSeq 3000/4000 SBS sequencing chemistry were used for paired-end sequencing with a read length of 100 bp for each direction. Sequencing was performed at the Helmholtz Center (Munich, Germany).

RNAseq analysis. The quality of sequencing reads was verified using FastQC 0.11.5 (http://www.bioinformatics.babraham.ac.uk/projects/fastqc). Adapters were trimmed using cutadapt v.1.9.1[74] in paired-end mode. For quantification of gene expression, kallisto 0.43.1[75] was employed using the mouse Ensembl annotation v79 (downloaded from http://bio.math.berkeley.edu/kallisto/transcriptomes/). The 100 bootstaps sleuth 0.28.1[76] was used for the analysis of differentially expressed genes in gene aggregation mode, requiring q-values of <0.05 for both Wald and likelihood ratio tests, with a beta value cut-off 0.25. For KEGG pathway analysis, GAGE 2.24.0[77] was used with log2 transformed, filtered and normalized TPM values extracted from sleuth. An FDR of 0.1 was applied as cut-off for significance.

BeWo cell culture. BeWo choriocarcinoma immortalized cells were plated into 35 mm plates with F12 medium with 2 mM L-glutamine, fetal bovine serum (10%) and penicillin streptomycin solution (10,000 units/ml Penicillin GSodium Salt, 10 mg/ml Streptomycin Sulfate) (Thermo Fisher Scientific, Waltham, MA, USA) at 37 °C in a 5% CO_2 humidified incubator. BeWo cells were treated for 48 h with lentiviral vectors to overexpress or knockdown miR-340. Cells were then lysed and RNA was extracted using the miRNeasy mini kit (QIAGEN, Hilden, Germany) or were lysed using RIPA buffer for protein extraction.

Body composition. Body composition was assessed using Echo-MRI-100™ (Echo Medical Systems, Houston, TX, USA).

Metabolic assessment. Indirect calorimetry, food and water intake were measured using the LabMaster system (TSE-Systems, Bad Homburg, Germany). The LabMaster instrument consists of a combination of sensitive feeding and drinking sensors for automated online measurement. The calorimetry system is an open-circuit system that determines O_2 consumption, CO_2 production, and respiratory exchange ratio. Data were collected for five consecutive days after 24 h of adaptation for the apparatus.

Maternal behavior. On days 6/7 and 17/18 postpartum, patterns of undisturbed nocturnal maternal behavior were observed during 160 min sessions. Each mother was observed every 15 min, for 1−3 s. This allowed the identification of the ongoing maternal behavior at the observation time. Various maternal and non-maternal behaviors were recorded in every observation. The score was "1" if the behavior occurred and "0" if it did not occur. Maternal behavior measures were based on existing literature[78] and included both self-(grooming, eating) and pup-directed behaviors (nursing, licking/grooming) and activity measures.

Human placental tissue collection. Placental tissues were collected after obtaining informed consent from pregnant women at the Division of Gynecology and Obstetrics of the Lindenhofgruppe, Bern, Switzerland. The studies were approved by the cantonal ethic commission of the canton of Bern (KEK), # 2016-00250. Term placentas (38−40 weeks) were collected from uncomplicated pregnancies after elective cesarean section without prior labor symptoms upon patients' request or due to breech presentation ($n = 35$) (Supplementary Table 2). Placental tissues were collected from the villous tree within 1 h of delivery. To minimize blood contamination, each piece of tissue was intensively washed in Dulbecco's phosphate-buffered saline. Tissue samples were then immediately snap-frozen in liquid nitrogen and stored at −80 °C until RNA isolation. As placenta is a heterogeneous tissue, and physiological differences in gene expression may occur depending on the sampling site, we standardized the sampling protocol and routinely collected tissue samples from three different locations within the placenta: central (C), paracentral/medial (M) and peripheral/lateral (L) parts. Total RNA was isolated similarly to the mouse samples, using cold Trizol reagent (Invitrogen Life Technologies, Carlsbad, CA) and approximately 50 mg of frozen placental specimens on wet ice[79].

Statistical approach. Data were expressed as mean ± standard error of the mean (SEM). For the Z scores data were presented in min. to max. Statistical analyses were performed using Statistical Package for the Social Sciences (SPSS) software, Version 20.0 (SPSS Inc., Chicago, IL) and GraphPad Prism 6 (GraphPad Software, Inc., La Jolla, CA). Tests included repeated measures ANOVA, $t$tests or one-way ANOVA when relevant. Differences between the groups were assessed using Tukey's multiple comparisons post hocs. When appropriate, non-parametric tests such as Mann–Whitney and Kruskal−Wallis were used. Linear regression and r values were determined in GraphPad Prism 6 (GraphPad Software, Inc., La Jolla, CA).

Data availability. The Agilent miR microarray data have been deposited with GEO-NCBI under the accession number GSE110597 and the Illumina RNA-seq data have been deposited in the Sequence Read Archive (SRA), using the NCBI portal, under the BioProject accession number PRJNA434509 and SRA accession number SRP133035.

Received: 4 October 2017 Accepted: 15 March 2018
Published online: 23 April 2018

References

1. Smink, F. R. E., van Hoeken, D. & Hoek, H. W. Epidemiology of eating disorders: incidence, prevalence and mortality rates. *Curr. Psychiatry Rep.* **14**, 406–414 (2012).
2. Franko, D. L. et al. A longitudinal investigation of mortality in anorexia nervosa and bulimia nervosa. *Am. J. Psychiatry* **170**, 917–925 (2013).
3. Hudson, J. I., Hiripi, E., Pope, H. G. & Kessler, R. C. The prevalence and correlates of eating disorders in the National Comorbidity Survey Replication. *Biol. Psychiatry* **61**, 348–358 (2007).
4. Keating, C. Sex differences precipitating anorexia nervosa in females: the estrogen paradox and a novel framework for targeting sex-specific neurocircuits and behavior. *Curr. Top. Behav. Neurosci.* **8**, 189–207 (2011).
5. Favaro, A., Tenconi, E. & Santonastaso, P. The interaction between perinatal factors and childhood abuse in the risk of developing anorexia nervosa. *Psychol. Med.* **40**, 657–665 (2010).
6. Rayworth, B. B., Wise, L. A. & Harlow, B. L. Childhood abuse and risk of eating disorders in women. *Epidemiology* **15**, 271–278 (2004).
7. St-Hilaire, A. et al. A prospective study of effects of prenatal maternal stress on later eating-disorder manifestations in affected offspring: preliminary indications based on the project ice storm cohort. *Int. J. Eat. Disord.* **48**, 512–516 (2015).
8. Su, X. et al. Prenatal and early life stress and risk of eating disorders in adolescent girls and young women. *Eur. Child. Adolesc. Psychiatry* **25**, 1245–1253 (2016).
9. Favaro, A., Tenconi, E. & Santonastaso, P. Perinatal factors and the risk of developing anorexia nervosa and bulimia nervosa. *Arch. Gen. Psychiatry* **63**, 82–88 (2006).
10. Bronson, S. L. & Bale, T. L. The placenta as a mediator of stress effects on neurodevelopmental reprogramming. *Neuropsychopharmacology* **41**, 207–218 (2015).
11. Davis, E. P. & Pfaff, D. Sexually dimorphic responses to early adversity: implications for affective problems and autism spectrum disorder. *Psychoneuroendocrinology* **49**, 11–25 (2014).
12. Schroeder, M. et al. A methyl-balanced diet prevents CRF-induced prenatal stress-triggered predisposition to binge eating-like phenotype. *Cell Metab.* **25**, 1269–1281.e6 (2017).
13. Nugent, B. M. & Bale, T. L. The omniscient placenta: metabolic and epigenetic regulation of fetal programming. *Front. Neuroendocrinol.* **39**, 28–37 (2015).
14. Gabory, A., Attig, L. & Junien, C. Sexual dimorphism in environmental epigenetic programming. *Mol. Cell. Endocrinol.* **304**, 8–18 (2009).
15. Rosenfeld, C. S. Sex-specific placental responses in fetal development. *Endocrinology* **156**, 3422–3434 (2015).
16. Tarrade, A., Panchenko, P., Junien, C. & Gabory, A. Placental contribution to nutritional programming of health and diseases: epigenetics and sexual dimorphism. *J. Exp. Biol.* **218**, 50–58 (2015).
17. Walker, C. K. et al. Preeclampsia, placental insufficiency, and autism spectrum disorder or developmental delay. *JAMA Pediatr.* **169**, 154–162 (2015).
18. Mouillet, J.-F., Ouyang, Y., Coyne, C. B. & Sadovsky, Y. MicroRNAs in placental health and disease. *Am. J. Obstet. Gynecol.* **213**, S163–S172 (2015).
19. Zhao, Z., Moley, K. H. & Gronowski, A. M. Diagnostic potential for miRNAs as biomarkers for pregnancy-specific diseases. *Clin. Biochem.* **46**, 953–960 (2013).
20. Hall, J. F., Smith, K., Schnitzer, S. B. & Hanford, P. V. Elevation of activity level in the rat following transition from ad libitum to restricted feeding. *J. Comp. Physiol. Psychol.* **46**, 429–433 (1953).
21. Pjetri, E. et al. Identifying predictors of activity based anorexia susceptibility in diverse genetic rodent populations. *PLoS ONE* **7**, e50453 (2012).
22. Barbarich-Marsteller, N. C. et al. Identifying novel phenotypes of vulnerability and resistance to activity-based anorexia in adolescent female rats. *Int. J. Eat. Disord.* **46**, 737–746 (2013).

23. Chowdhury, T. G., Wable, G. S., Sabaliauskas, N. A. & Aoki, C. Adolescent female C57BL/6 mice with vulnerability to activity-based anorexia exhibit weak inhibitory input onto hippocampal CA1 pyramidal cells. *Neuroscience* **241**, 250–267 (2013).
24. Klenotich, S. J. & Dulawa, S. C. The activity-based anorexia mouse model. *Methods Mol. Biol.* **829**, 377–393 (2012).
25. Vink, T. et al. Association between an agouti-related protein gene polymorphism and anorexia nervosa. *Mol. Psychiatry* **6**, 325–328 (2001).
26. Gutiérrez, E. et al. High ambient temperature reverses hypothalamic MC4 receptor overexpression in an animal model of anorexia nervosa. *Psychoneuroendocrinology* **34**, 420–429 (2009).
27. Haleem, D. J. Serotonin neurotransmission in anorexia nervosa. *Behav. Pharmacol.* **23**, 478–495 (2012).
28. Brandys, M. K., Kas, M. J. H., van Elburg, A. A., Campbell, I. C. & Adan, R. A. H. A meta-analysis of circulating BDNF concentrations in anorexia nervosa. *World J. Biol. Psychiatry* **12**, 444–454 (2011).
29. Gold, P. W., Kaye, W., Robertson, G. L. & Ebert, M. Abnormalities in plasma and cerebrospinal-fluid arginine vasopressin in patients with anorexia nervosa. *N. Engl. J. Med.* **308**, 1117–1123 (1983).
30. Boersma, G. J. et al. Failure to upregulate Agrp and Orexin in response to activity based anorexia in weight loss vulnerable rats characterized by passive stress coping and prenatal stress experience. *Psychoneuroendocrinology* **67**, 171–181 (2016).
31. Pankevich, D. E., Mueller, B. R., Brockel, B. & Bale, T. L. Prenatal stress programming of offspring feeding behavior and energy balance begins early in pregnancy. *Physiol. Behav.* **98**, 94–102 (2009).
32. Rodriguez, A., Griffiths-Jones, S., Ashurst, J. L. & Bradley, A. Identification of mammalian microRNA host genes and transcription units. *Genome Res.* **14**, 1902–1910 (2004).
33. Das, S. et al. Modulation of neuroblastoma disease pathogenesis by an extensive network of epigenetically regulated microRNAs. *Oncogene* **32**, 2927–2936 (2013).
34. Lou, S. et al. Whole-genome bisulfite sequencing of multiple individuals reveals complementary roles of promoter and gene body methylation in transcriptional regulation. *Genome Biol.* **15**, 408 (2014).
35. Lager, S. & Powell, T. L. Regulation of nutrient transport across the placenta. . *J. Pregnancy* **2012**, 1–14 (2012).
36. Fowden, A. L., Forhead, A. J., Sferruzzi-Perri, A. N., Burton, G. J. & Vaughan, O. R. Review: Endocrine regulation of placental phenotype. *Placenta* **36**, S50–S59 (2015).
37. Szklarczyk, D. et al. The STRING database in 2017: quality-controlled protein-protein association networks, made broadly accessible. *Nucleic Acids Res.* **45**, D362–D368 (2017).
38. Georgiades, P., Cox, B., Gertsenstein, M., Chawengsaksophak, K. & Rossant, J. Trophoblast-specific gene manipulation using lentivirus-based vectors. *Biotechniques* **42**, 317–318 (2007).
39. Okada, Y. et al. Complementation of placental defects and embryonic lethality by trophoblast-specific lentiviral gene transfer. *Nat. Biotechnol.* **25**, 233–237 (2007).
40. Bulik, C. M. et al. Prevalence, heritability, and prospective risk factors for anorexia nervosa. *Arch. Gen. Psychiatry* **63**, 305–312 (2006).
41. Walters, E. E. & Kendler, K. S. Anorexia nervosa and anorexic-like syndromes in a population-based female twin sample. *Am. J. Psychiatry* **152**, 64–71 (1995).
42. Sferruzzi-Perri, A. N. & Camm, E. J. The programming power of the placenta. *Front. Physiol.* **7**, 33 (2016).
43. Sedlmeier, E.-M. et al. Human placental transcriptome shows sexually dimorphic gene expression and responsiveness to maternal dietary n-3 long-chain polyunsaturated fatty acid intervention during pregnancy. *Bmc Genom.* **15**, 941 (2014).
44. Mao, J. et al. Contrasting effects of different maternal diets on sexually dimorphic gene expression in the murine placenta. *Proc. Natl. Acad. Sci. USA* **107**, 5557–5562 (2010).
45. Georgiades, P., Ferguson-Smith, A. C. & Burton, G. J. Comparative developmental anatomy of the murine and human definitive placentae. *Placenta* **23**, 3–19 (2002).
46. Redline, R. W., Chernicky, C. L., Tan, H. Q. & Ilan, J. Differential expression of insulin-like growth factor-II in specific regions of the late (post day 9.5) murine placenta. *Mol. Reprod. Dev.* **36**, 121–129 (1993).
47. Jensen Peña, C., Monk, C. & Champagne, F. A. Epigenetic effects of prenatal stress on 11β-hydroxysteroid dehydrogenase-2 in the placenta and fetal brain. *PLoS ONE* **7**, e39791 (2012).
48. Glover, V. & Hill, J. Sex differences in the programming effects of prenatal stress on psychopathology and stress responses: an evolutionary perspective. *Physiol. Behav.* **106**, 736–740 (2012).
49. Davis, E. P., Glynn, L. M., Waffarn, F. & Sandman, C. A. Prenatal maternal stress programs infant stress regulation. *J. Child. Psychol. Psychiatry* **52**, 119–129 (2011).
50. Moisiadis, V. G. & Matthews, S. G. Glucocorticoids and fetal programming part 1: Outcomes. *Nat. Rev. Endocrinol.* **10**, 391–402 (2014).
51. Reichardt, H. M., Umland, T., Bauer, A., Kretz, O. & Schütz, G. Mice with an increased glucocorticoid receptor gene dosage show enhanced resistance to stress and endotoxic shock. *Mol. Cell. Biol.* **20**, 9009–9017 (2000).
52. Reynolds, R. M. Glucocorticoid excess and the developmental origins of disease: two decades of testing the hypothesis—2012 Curt Richter Award Winner. *Psychoneuroendocrinology* **38**, 1–11 (2013).
53. Barrett, E. S. et al. Prenatal exposure to stressful life events is associated with masculinized anogenital distance (AGD) in female infants. *Physiol. Behav.* **114–115**, 14–20 (2013).
54. Bánszegi, O., Altbäcker, V., Dúcs, A. & Bilkó, A. Testosterone treatment of pregnant rabbits affects sexual development of their daughters. *Physiol. Behav.* **101**, 422–427 (2010).
55. Culbert, K. M., Breedlove, S. M., Burt, S. A. & Klump, K. L. Prenatal hormone exposure and risk for eating disorders: a comparison of opposite-sex and same-sex twins. *Arch. Gen. Psychiatry* **65**, 329–336 (2008).
56. Mouridsen, S. E., Rich, B. & Isager, T. Sibling sex ratio of individuals diagnosed with autism spectrum disorder as children. *Dev. Med. Child. Neurol.* **52**, 289–292 (2010).
57. Ryan, B. C. & Vandenbergh, J. G. Intrauterine position effects. *Neurosci. Biobehav. Rev.* **26**, 665–678 (2002).
58. Culbert, K. M., Breedlove, S. M., Sisk, C. L., Burt, S. A. & Klump, K. L. The emergence of sex differences in risk for disordered eating attitudes during puberty: a role for prenatal testosterone exposure. *J. Abnorm. Psychol.* **122**, 420–432 (2013).
59. Guais, A., Solhonne, B., Melaine, N., Guellaen, G. & Bulle, F. Goliath, a ring-H2 mitochondrial protein, regulated by luteinizing hormone/human chorionic gonadotropin in rat leydig cells. *Biol. Reprod.* **70**, 204–213 (2004).
60. Issler, O. & Chen, A. Determining the role of microRNAs in psychiatric disorders. *Nat. Rev. Neurosci.* **16**, 201–212 (2015).
61. Cuffe, J. S. M., O'Sullivan, L., Simmons, D. G., Anderson, S. T. & Moritz, K. M. Maternal corticosterone exposure in the mouse has sex-specific effects on placental growth and mRNA expression. *Endocrinology* **153**, 5500–5511 (2012).
62. Thompson, A. Spatial and temporal patterns of expression of 11 -hydroxysteroid dehydrogenase types 1 and 2 messenger RNA and glucocorticoid receptor protein in the murine placenta and uterus during late pregnancy. *Biol. Reprod.* **67**, 1708–1718 (2002).
63. Kipmen-Korgun, D. et al. Triamcinolone up-regulates GLUT 1 and GLUT 3 expression in cultured human placental endothelial cells. *Cell. Biochem. Funct.* **30**, 47–53 (2012).
64. Bivol, S., Owen, S. J. & Rose'Meyer, R. B. Glucocorticoid-induced changes in glucocorticoid receptor mRNA and protein expression in the human placenta as a potential factor for altering fetal growth and development. *Reprod. Fertil. Dev.* https://doi.org/10.1071/RD15356 (2016).
65. Conradt, E., Lester, B. M., Appleton, A. A., Armstrong, D. A. & Marsit, C. J. The roles of DNA methylation of NR3C1 and 11β-HSD2 and exposure to maternal mood disorder in utero on newborn neurobehavior. *Epigenetics* **8**, 1321–1329 (2013).
66. Waddell, B. J., Wharfe, M. D., Crew, R. C. & Mark, P. J. A rhythmic placenta? Circadian variation, clock genes and placental function. *Placenta* **33**, 533–539 (2012).
67. Szenker, E., Ray-Gallet, D. & Almouzni, G. The double face of the histone variant H3.3. *Cell Res.* **21**, 421–434 (2011).
68. Bush, K. M. et al. Endogenous mammalian histone H3.3 exhibits chromatin-related functions during development. *Epigenetics Chromatin* **6**, 7 (2013).
69. Fowden, A. L., Coan, P. M., Angiolini, E., Burton, G. J. & Constancia, M. Imprinted genes and the epigenetic regulation of placental phenotype. *Prog. Biophys. Mol. Biol.* **106**, 281–288 (2011).
70. vom Saal, F. S., Pryor, S. & Bronson, F. H. Effects of prior intrauterine position and housing on oestrous cycle length in adolescent mice. *J. Reprod. Fertil.* **62**, 33–37 (1981).
71. Naldini, L., Blömer, U., Gage, F. H., Trono, D. & Verma, I. M. Efficient transfer, integration, and sustained long-term expression of the transgene in adult rat brains injected with a lentiviral vector. *Proc. Natl. Acad. Sci. USA* **93**, 11382–11388 (1996).
72. Tiscornia, G., Singer, O. & Verma, I. M. Production and purification of lentiviral vectors. *Nat. Protoc.* **1**, 241–245 (2006).
73. Petropoulos, S., Gibb, W. & Matthews, S. G. Breast cancer-resistance protein (BCRP1) in the fetal mouse brain: development and glucocorticoid regulation. *Biol. Reprod.* **84**, 783–789 (2011).
74. Martin, M. Cutadapt removes adapter sequences from high-throughput sequencing reads. *EMBnet. J.* **17**, 10 (2011).
75. Bray, N. L., Pimentel, H., Melsted, P. & Pachter, L. Near-optimal probabilistic RNA-seq quantification. *Nat. Biotechnol.* **34**, 525–527 (2016).
76. Pimentel, H., Bray, N. L., Puente, S., Melsted, P. & Pachter, L. Differential analysis of RNA-seq incorporating quantification uncertainty. *Nat. Methods* **14**, 687–690 (2017).

77. Luo, W., Friedman, M. S., Shedden, K., Hankenson, K. D. & Woolf, P. J. GAGE: generally applicable gene set enrichment for pathway analysis. *BMC Bioinform.* **10**, 161 (2009).
78. Schroeder, M., Zagoory-Sharon, O., Lavi-Avnon, Y., Moran, T. H. & Weller, A. Weight gain and maternal behavior in CCK1 deficient rats. *Physiol. Behav.* **89**, 402–409 (2006).
79. Huang, X. et al. RNA degradation differentially affects quantitative mRNA measurements of endogenous reference genes in human placenta. *Placenta* **34**, 544–547 (2013).

Acknowledgements

We thank Mr. Sharon Ovadia for his devoted assistance with animal care. We also thank Lisa Tietze for her help with in situ hybridization; Daniela Harbich, Andrea Parl, and Carola Eggert for their help with western blots/stainings; Michael Lüthi for help in human placental RNA isolation and qPCR measurements and Stoyo Karamihalev for help with the graphic images. The authors also wish to express their gratitude to the patients, physicians, and midwives from the Lindenhofgruppe, Bern, for participating in this study. This work was supported by: an FP7 Grant from the European Research Council (260463, A.C.); a research grant from the Israel Science Foundation (1565/15, A. C.); the ERANET Program, supported by the Chief Scientist Office of the Israeli Ministry of Health (3-11389, A.C.); the project was funded by the Federal Ministry of Education and Research under the funding code 01KU1501A (A.C.); research support from Roberto and Renata Ruhman (A.C.); research support from Bruno and Simone Licht; I-CORE Program of the Planning and Budgeting Committee and The Israel Science Foundation (grant no. 1916/12 to A.C.); the Nella and Leon Benoziyo Center for Neurological Diseases (A.C.); the Henry Chanoch Krenter Institute for Biomedical Imaging and Genomics (A.C.); the Perlman Family Foundation, founded by Louis L. and Anita M. Perlman (A.C.); the Adelis Foundation (A.C.); the Marc Besen and the Pratt Foundation and the Irving I. Moskowitz Foundation (A.C.). C.A. was supported by the Swiss National Science Foundation (SNSF) through the National Center of Competence in Research (NCCR) TransCure, University of Bern, Switzerland, and the Swiss National Science Foundation (Grant No. 310030_149958). M.J. was supported by a NARSAD young investigator grant.

Author contributions

M.S. designed the experiments and prepared the manuscript. A.C. supervised the project. M.S. performed the embryo transfers. M.S. and T.P. performed the behavioral experiments, RNA, DNA and protein extractions. T.P. and Y.D. killed the animals. M.S. performed the in vitro experiments. M.J. constructed the libraries and performed NGS. S. R., M.J. and S.B.-D. performed the bioinformatic predictions and analysis. C.A. and J.Z. organized the collection of the human placenta samples and J.Z. and A.L. performed gene expression analysis.

Additional information

Supplementary Information accompanies this paper at https://doi.org/10.1038/s41467-018-03836-2.

Competing interests: The authors declare no competing interests.

9.1.6 Published by Frontiers Cell and Developmental Biology (18 Sep 2020)

frontiers in Cell and Developmental Biology

ORIGINAL RESEARCH
published: 18 September 2020
doi: 10.3389/fcell.2020.574034

Dynamics of Tryptophan Metabolic Pathways in Human Placenta and Placental-Derived Cells: Effect of Gestation Age and Trophoblast Differentiation

*Rona Karahoda[1†], Cilia Abad[1†], Hana Horackova[1], Petr Kastner[2], Jonas Zaugg[3,4], Lukas Cerveny[1], Radim Kucera[2], Christiane Albrecht[3,4] and Frantisek Staud[1]**

[1] Department of Pharmacology and Toxicology, Faculty of Pharmacy in Hradec Kralove, Charles University, Hradec Kralove, Czechia, [2] Department of Pharmaceutical Chemistry and Pharmaceutical Analysis, Faculty of Pharmacy in Hradec Kralove, Charles University, Hradec Kralove, Czechia, [3] Institute of Biochemistry and Molecular Medicine, University of Bern, Bern, Switzerland, [4] Swiss National Centre of Competence in Research (NCCR) TransCure, University of Bern, Bern, Switzerland

OPEN ACCESS

Edited by:
Maria Barile,
University of Bari Aldo Moro, Italy

Reviewed by:
Luc Maroteaux,
INSERM U839 Institut du Fer à Moulin (IFM), France
David W. Walker,
RMIT University, Australia

***Correspondence:**
Frantisek Staud
frantisek.staud@faf.cuni.cz

[†]These authors have contributed equally to this work

Specialty section:
This article was submitted to Cellular Biochemistry, a section of the journal Frontiers in Cell and Developmental Biology

Received: *18 June 2020*
Accepted: *21 August 2020*
Published: *18 September 2020*

Citation:
Karahoda R, Abad C, Horackova H, Kastner P, Zaugg J, Cerveny L, Kucera R, Albrecht C and Staud F (2020) Dynamics of Tryptophan Metabolic Pathways in Human Placenta and Placental-Derived Cells: Effect of Gestation Age and Trophoblast Differentiation. Front. Cell Dev. Biol. 8:574034. doi: 10.3389/fcell.2020.574034

L-Tryptophan is an essential amino acid and a precursor of several physiologically active metabolites. In the placenta, the serotonin and kynurenine metabolic pathways of tryptophan metabolism have been identified, giving rise to various molecules of neuroactive or immunoprotective properties, such as serotonin, melatonin, kynurenine, kynurenic acid, or quinolinic acid. Current literature suggests that optimal levels of these molecules in the fetoplacental unit are crucial for proper placenta functions, fetal development and programming. Placenta is a unique endocrine organ that, being equipped with a battery of biotransformation enzymes and transporters, precisely orchestrates homeostasis of tryptophan metabolic pathways. However, because pregnancy is a dynamic process and placental/fetal needs are continuously changing throughout gestation, placenta must adapt to these changes and ensure proper communication in the feto-placental unit. Therefore, in this study we investigated alterations of placental tryptophan metabolic pathways throughout gestation. Quantitative polymerase chain reaction (PCR) analysis of 21 selected genes was carried out in first trimester (n = 13) and term (n = 32) placentas. Heatmap analysis with hierarchical clustering revealed differential gene expression of serotonin and kynurenine pathways across gestation. Subsequently, digital droplet PCR, Western blot, and functional analyses of the rate-limiting enzymes suggest preferential serotonin synthesis early in pregnancy with a switch to kynurenine production toward term. Correspondingly, increased function and/or protein expression of serotonin degrading enzyme and transporters at term indicates efficient placental uptake and metabolic degradation of serotonin. Lastly, gene expression analysis in choriocarcinoma-derived cell lines (BeWo, BeWo b30, JEG-3) revealed dissimilar expression patterns and divergent effect of syncytialization compared to primary trophoblast cells isolated from human term placentas; these findings show that the commonly used *in vitro* placental

models are not suitable to study placental handling of tryptophan. Altogether, our data provide the first comprehensive evidence of changes in placental homeostasis of tryptophan and its metabolites as a function of gestational age, which is critical for proper placental function and fetal development.

Keywords: fetal programming, trophoblast, tryptophan metabolism, placenta–brain axis, kynurenine pathway, serotonin pathway

INTRODUCTION

Placenta is a multifunctional organ providing the fetus with optimal conditions for its growth, development, and programming (Staud and Karahoda, 2018). As a continuously maturing organ, it undergoes structural (Kingdom et al., 2000), epigenetic, and transcriptomic (Uuskula et al., 2012; Cox et al., 2015) changes to adapt to its own as well as maternal and fetal demands. Correspondingly, a wide number of biological processes and molecular and metabolic pathways are differentially affected during gestation (Mikheev et al., 2008; Sitras et al., 2012).

Tryptophan (TRP) is an important amino acid necessary for protein synthesis as well as a precursor of several biologically active metabolites. During pregnancy, TRP and its metabolites are of crucial importance for placentation, fetal development, and immune regulation (Sedlmayr et al., 2014; Laurent et al., 2017). In the placenta, two main TRP metabolic pathways have been identified: the serotonin (5-HT) (Bonnin et al., 2011) and kynurenine (KYN) pathways (Sedlmayr et al., 2002; Goeden et al., 2017). The rate-limiting enzyme of the 5-HT pathway, tryptophan hydroxylase (TPH), gives rise to 5-HT, an important trophic factor early in gestation (Bonnin et al., 2011). Within the placenta a fraction of 5-HT is additionally metabolized to melatonin (Lanoix et al., 2008), which is involved in circadian rhythmicity, fetal growth, and placental function regulation (Iwasaki et al., 2005; Nagai et al., 2008; Seron-Ferre et al., 2012). Several studies have shown that maternal 5-HT also contributes to fetal 5-HT levels (Cote et al., 2007; Gleason et al., 2010; Muller et al., 2017). While early in pregnancy the fetus is dependent on placental/maternal 5-HT, from midgestation it synthesizes its own 5-HT from maternally derived TRP (Arevalo et al., 1991; Sano et al., 2016) suggesting that placental/maternal 5-HT is no longer needed. Indeed, in our latest study (Karahoda et al., 2020) we observed that at term, rat and human placenta does not provide 5-HT to the fetus; in contrast, it takes up fetal 5-HT across the basal membrane of the syncytiotrophoblast (STB) for subsequent degradation by monoamine oxidase-A (MAO-A). Together these findings indicate that placental handling of 5-HT changes throughout gestation.

The KYN pathway generally accounts for most of the TRP degrading activity via the rate-limiting enzymes, indoleamine 2,3-dioxygenase-1/2 (IDO1/2), and tryptophan 2,3-dioxygenase (TDO) (Sedlmayr et al., 2014). In the placenta, this pathway plays a crucial role in preventing fetal rejection by the maternal immune system (Munn et al., 1998). Extensive studies have been carried out to evaluate IDO1 expression/localization in the placenta, indicating that IDO1 expression/function increases during gestation (Sedlmayr et al., 2002; Ligam et al., 2005; Blaschitz et al., 2011; Murthi et al., 2017; Wakx et al., 2018), yet the exact localization in the placenta remains contradictory (Sedlmayr et al., 2014). Contrary to other studies (Sedlmayr et al., 2002; Honig et al., 2004; Kudo et al., 2004), it has been recently observed that IDO1 is not expressed in villous or extravillous trophoblast and the increasing IDO activity at term is exclusively due to expression in endothelial cells (playing a role in immunosuppression and placental tone relaxation) (Blaschitz et al., 2011). KYN is further metabolized to kynurenic acid (KYNA) and quinolinic acid (QUIN), which have neuroprotective and neurotoxic properties, respectively (Foster et al., 1984; Schwarcz et al., 2012). However, the importance of placental KYNA and QUIN remains to be fully elucidated. Recent studies in mouse term placenta report minimal placental contribution to fetal KYNA levels (Goeden et al., 2017; Notarangelo et al., 2019). Importantly, little is known about the effects of gestational age on expression and function of the enzymes down the KYN metabolic pathway, particularly those responsible for production of KYNA and QUIN.

Recently, the importance of gut microbiome metabolism of TRP for gut–brain axis has been described (Kaur et al., 2019; Gao et al., 2020). Similarly, placental metabolism of TRP might form a crucial component of the placenta–brain axis (Rosenfeld, 2020a,b). Considering the large spectrum of TRP metabolites and their roles in pregnancy, it is important to elucidate and understand the shifts in enzyme/transporter expression/activity occurring during gestation. Knowledge on the interplay between enzymes and transporters could provide a better understanding on the significance of a specific pathway at a certain point in pregnancy. Thus, in our study we investigated how advancing gestation affects expression and function of selected enzymes/transporters involved in placental homeostasis of TRP and its metabolites. In addition, we analyzed the effect of cell/trophoblast differentiation on gene expression patterns in isolated primary trophoblast cells and placenta-derived cell lines (BeWo, BeWo b30 clone, JEG-3) to assess their suitability for designated studies.

MATERIALS AND METHODS

Chemicals and Reagents

Serotonin hydrochloride, L-Tryptophan, and phenelzine (MAO inhibitor) were purchased from Sigma–Aldrich (St. Louis, MO, United States). Forskolin (proliferation-activating agent) was obtained from Scintila, s.r.o. (Jihlava, CZ). Bicinchoninic acid

assay (BCA assay) reagents were purchased from Thermo Fisher Scientific (Waltham, MA, United States). All other chemicals were of analytical grade.

Human Placenta Sample Collection

First-trimester placentas (n = 13) were obtained after elective interruption of healthy pregnancy between 8 and 11 weeks of gestation. Term placentas (n = 32 for mRNA/protein/functional analysis and n = 5 for primary trophoblast isolation) were obtained from uncomplicated pregnancies at 38 to 40 weeks of gestation immediately after delivery. Samples were collected at the University Hospital in Hradec Kralove, Czech Republic or at the Division of Gynecology and Obstetrics, Lindenhofgruppe, Bern, Switzerland. All experiments were performed in accordance with the Declaration of Helsinki and human placenta samples were obtained upon women's written informed consent and with the approval of the University Hospital Research Ethics Committee (201006 S15P) and Ethics Committee of the Canton of Bern (Basec No. 2016-00250).

Choriocarcinoma-Derived Cell Cultures

The human choriocarcinoma-derived BeWo and JEG-3 cell lines were obtained from the European Cell Culture Collection (ECACC; Salisbury, Wiltshire, United Kingdom). BeWo cells were cultured in Ham F-12 medium supplemented with 10% fetal bovine serum (FBS), whereas JEG-3 cells were cultured in MEM medium supplemented with 10% FBS.

The human choriocarcinoma-derived BeWo b30 cell line (known to form integral monolayers) was obtained from Dr. A. Schwartz (Washington University, St. Louis, United States). Cells were cultured in Dulbecco modified eagle medium (high glucose) supplemented with 10% FBS.

All cell lines were cultivated without antibiotics at 37°C/5% CO_2. For differentiation induction, BeWo b30 cell line was treated with 100 μM forskolin for 72 h with daily change of medium.

Isolation and Characterization of Primary Trophoblast Cells

Villous cytotrophoblast cells (CTBs) were isolated from term placental tissue by enzymatic digestion and Percoll gradient separation, as previously described, with minor modifications (Kallol et al., 2018). In brief, approximately 50 g of villous tissue was washed in 0.9% NaCl (Sigma–Aldrich) four times for 5 min. Thereafter, the tissue was minced and digested three times with 0.25% trypsin (Sigma–Aldrich) and 300 IU/mL deoxyribonuclease I (Sigma–Aldrich) at 37°C (20 min each). The cell suspension was filtered and overlaid on FBS (Seraglob, Switzerland). After centrifugation at 1,000 × g for 15 min at 10°C, the cell pellet was collected in Dulbecco modified eagle medium (high glucose) basic medium (without FBS) and filtered through 100-μm strainer (BD Biosciences, San Jose, CA, United States). Next, cells were overlaid on a discontinuous Percoll® (Sigma–Aldrich) density gradient. After centrifugation, CTBs were located at the layer corresponding to 1.046–1.065 g/mL (35–50%) density (Petroff et al., 2006). The isolated CTBs were cultured at a density of 1 × 10^6 cells/cm^2 in 6-well CellBIND® plates (Corning, New York, NY, United States) in Dulbecco modified eagle medium (high glucose) supplemented with 10% FBS and 1% antibiotic–antimitotic (Thermo Fisher Scientific). Cells were cultured for 12 h (CTB stage) or 72 h (STB stage).

Flow Cytometry Analysis of Primary Trophoblast Cell Purity

The purity of the isolated trophoblast (PHT) cells was evaluated by staining with specific cell markers followed by flow cytometry analysis as previously described with minor modifications (Kallol et al., 2018). Cells were grown on CellBIND® plates, detached by Accutase® (Sigma–Aldrich), and fixed in 4% formaldehyde (Thermo Fisher Scientific) for 10 min on ice. After washing with Dulbecco phosphate-buffered saline (DPBS; Sigma–Aldrich) cells were centrifuged at 200 g for 10 min at 4°C and then permeabilized with 0.5% Tween-20 (wt/vol) (Sigma–Aldrich) in DPBS for 15 min at room temperature. For evaluation of cell purity, dual staining of CTB and STB with directly labeled antibodies (Novus Biologicals, CO, United States) prepared in staining buffer (5% FBS, 0.1% Tween-20 (wt/vol) in DPBS), was performed. Antibody cocktails comprised (1) anti–cytokeratin 7 (CK-7; AF 488®) plus anti-vimentin (Vim; AF 647®); (2) anti–E-cadherin (E-cad; AF 488®) plus anti-von Willebrand Factor (vWF; AF 647®). Cells were incubated with the respective antibody cocktail for 45 min on ice, followed by two times washing in DPBS (1 min each). After centrifugation at 200 g for 10 min at 4°C, pelleted cells were suspended in DPBS and acquired by flow cytometry (BD FACS LSRII; BD Biosciences). Data acquisition and analysis for each staining were based on at least 10,000 events and performed by using BD FACSDiva™ (BD Biosciences) and FlowJo® software version 10 (FlowJo LLC, Ashland, OR, United States). Because CTB and STB are epithelial cells, staining for CK-7 and E-cad served as positive cell markers (Maldonado-Estrada et al., 2004; Li and Schust, 2015). Anti-vim, known to predominantly stain mesenchymal cells, fibroblast, and stromal cells and anti-vWF staining endothelial cells (Zanetta et al., 2000; Maldonado-Estrada et al., 2004; Li and Schust, 2015) served to quantify potential cellular contaminations by other cell types.

RNA Isolation, Reverse Transcription, and Quantitative Polymerase Chain Reaction Analysis

RNA isolation was performed using Tri Reagent (Molecular Research Centre, Cincinnati, OH, United States) or Trizol (Invitrogen, Carlsbad, CA, United States) according to the manufacturer's instructions. RNA concentration was calculated by measuring absorbance (A) at 260 nm and purity by the A260/280 and A260/230 ratios measured on NanoDrop™ 1000 Spectrophotometer (Thermo Fisher Scientific). RNA integrity was confirmed by electrophoresis on a 1.5% agarose gel. 1 μg of total RNA was reversely transcribed to cDNA in a total volume of 20 μL using the iScript cDNA Synthesis Kit (Bio-Rad, Hercules,

CA, United States) on a Bio-Rad T100™ Thermal Cycler; for primary trophoblast cells using oligo(dT)15 primers and GoScript™ Reverse Transcriptase System (Promega, Madison, WI, United States) according to the manufacturer's instructions.

cDNA (12.5 ng/μL) was amplified in QuantStudio™ 6 (Thermo Fisher Scientific) using the TaqMan® Universal Master Mix II without UNG (Thermo Fisher Scientific) and predesigned TaqMan® Real Time Expression polymerase chain reaction (PCR) assays (listed in **Supplementary Table 1**, Additional File 1). PCR analysis was run in 5 μL volume, in 384-well plate format. Each sample was amplified in triplicate, following the thermal conditions according to the manufacturer's instructions.

Prior to quantitative analysis, we evaluated several reference genes for their stable expression during gestation/upon differentiation. Target gene expression in choriocarcinoma-derived cell cultures and primary trophoblast cells was normalized against the predesigned reference gene tyrosine 3-monooxygenase/tryptophan 5-monooxygenase activation protein zeta (*YWHAZ*; Thermo Fisher Scientific) using the $2^{\Delta\Delta Ct}$ method, whereby $\Delta Ct = Ct_{ref} - Ct_{target}$ and $\Delta\Delta Ct = \Delta Ct_{differentiated} - \Delta Ct_{undifferentiated}$. On the other hand, gene expression of target genes in human placenta samples was normalized against the predesigned reference gene TATA-box binding protein (*TBP*; Thermo Fisher Scientific) using the ΔCt method, whereby $\Delta Ct = Ct_{ref} - Ct_{target}$. These values were used to generate a gene expression heat map, through the freely available web server Heatmapper[1] (Babicki et al., 2016). Hierarchical clustering (Average linkage, Euclidean distance) was applied to group samples with similar expression levels. The scatter plot was constructed in GraphPad Prism 8.3.1 software (GraphPad Software, Inc., San Diego, CA, United States) using the average $2^{\Delta Ct}$ values for first-trimester and term placentas.

Droplet Digital PCR Assay

Absolute quantification of *SLC6A4*, *SLC22A3*, *MAO-A*, *TPH1*, *TPH2*, *IDO1*, and *IDO2* in human first-trimester and term placentas was performed using duplex droplet digital PCR (ddPCR) analysis, as described previously (Karahoda et al., 2020). Briefly, the duplex reaction mixture consisted of 10 μL of ddPCR™ Supermix for Probes (Bio-Rad), 1 μL of each of the predesigned probe assays (target – FAM and reference – HEX) (listed in **Supplementary Table 1**, Additional File 1), and 0.5 μL of cDNA (50 ng/μL), in a total volume of 20 μL. Droplets were generated using QX200 Droplet Generator and subsequently amplified to end-point using T100™ Thermal Cycler following the thermal conditions recommended by the manufacturer. Droplet counting was performed in QX200™ Droplet Reader and the concentration of the target gene was calculated using the QuantaSoft™ Software. For final data evaluation, only wells in which the number of droplets obtained was higher than 13,000 were used. Expression levels are reported in number of transcripts/ng of transcribed RNA. The QX200™ Droplet Digital™ PCR System, T100™ Thermal Cycler, and all consumables and reagents were obtained from Bio-Rad (unless otherwise stated).

[1]http://www.heatmapper.ca/

Preparation of Human Placenta Homogenates

Human first-trimester and term placentas were washed with 0.9% NaCl at 4°C. After weighing and cleaning, the decidua and the chorionic plate were removed, and the placentas were cut in small pieces and homogenized at 4°C in a buffer containing 50 mM Tris-HEPES (pH 7.2), 5 mM EGTA, 5 mM EDTA, 1 mM phenylmethylsulfonyl fluoride, and 250 mM sucrose. The homogenates were filtered through gauze and centrifuged at 15,000 *g* for 10 min. The supernatant was collected and stored in the freezer at −80°C until use. Protein concentration was determined using the BCA protein assay kit.

Western Blot Analysis

Aliquots of placenta homogenates (30 μg total protein) were mixed with loading buffer under reducing conditions (Laemmli, 1970), heated at 96°C for 5 min, and separated by SDS-PAGE on polyacrylamide gels (10% for SLC6A4, SLC22A3, and MAO-A; 15% for IDO and TPH). Electrophoresis was performed at 150 V and proteins were transferred to polyvinylidene fluoride (PVDF) membranes (SERVA, Heidelberg, DE). The membranes were blocked in 20 mM Tris-HCl pH 7.6, 150 mM NaCl, 0.1% Tween 20 (TBS-T) containing 5% non-fat milk for 1 h at room temperature and washed with TBS-T buffer. Incubation with primary antibodies against SLC6A4, SLC22A3, MAO-A, IDO, and TPH (listed in **Supplementary Table 2**, Additional File 1) was performed overnight at 4°C. After washing with TBS-T buffer, the membranes were incubated with a specific secondary antibody (listed in **Supplementary Table 2**, Additional File 1) for 1 h at room temperature. Membranes were developed using Chemiluminescence HRP Substrate Kit (SERVA Light Vega). Band intensity was visualized and quantified by densitometric analysis using ChemiDoc MP, Imaging system™ (Bio-Rad). To ensure equal loading of proteins, membranes were probed for β-actin and specific secondary antibody (listed in **Supplementary Table 2**, Additional File 1).

5-HT Metabolism by MAO-A in Human Placenta Homogenates

MAO-A activity was determined by the method of Carrasco et al. (2000). Briefly, 180 μL placenta homogenate (1.5–2 mg/mL) was pre-incubated with or without MAO-A inhibitor, phenelzine (100 μM) for 5 min at 37°C, and then the reaction was initiated by incubation with 20 μL of 5-HT (0.5 mM) for an indicated time period. The reaction was stopped by adding 40 μL of $HClO_4$ (3.4 M) and placed on ice for 5 min. Samples were centrifuged at 5,000 *g* for 10 min, and the supernatant was used for 5-HT determination by high-performance liquid chromatography (HPLC).

IDO Enzymatic Activity

IDO activity was determined by the method of Takikawa et al. (1988). The incubation media (50 mM potassium phosphate buffer pH 6.5, 20 mM ascorbate, 0.01 mM methylene blue, 100 units/mL catalase) was pre-incubated for 5 min at 37°C, with or without 0.4 mM TRP. The reaction was initiated by

adding the placenta homogenate and terminated after 30 min with 200 μL of trichloroacetic acid 30%. Samples were further incubated for an additional 30 min at 50°C to assure complete hydrolysis of N-formyl KYN to KYN. The reaction mixture was then centrifuged for 20 min at 3,000 *g*, 20°C and supernatant was collected for HPLC measurement of KYN. The IDO enzymatic activity was calculated as the difference between the amount of KYN produced in the media with and without TRP. The results are expressed as nmol KYN/μg protein per min.

TPH Enzymatic Activity

TPH enzymatic activity was determined by the method by Goeden et al. (2016). Human placenta homogenates were supplemented with 1 mM dithiothreitol as a reducing agent ensuring complete enzymatic activity (Fitzpatrick, 1999). The enzymatic reaction was carried out at 37°C, pH 7.5, with ∼1.5 to 2 mg protein/mL. The incubation media contained (final concentrations): 50 mM Tris buffer, 1 mM EGTA, 100 units/mL catalase, 0.1 mM ammonium iron (II) sulfate, 0.1 mM tetrahydrobiopterin (BH4, a cofactor required for TPH activity), either in the absence or in the presence of 0.25 mM TRP. Briefly, placenta homogenate was incubated with the incubation media for 30 min at 37°C. Reaction was terminated by adding 200 μL of $HClO_4$ with 100 μM EDTA. Samples were incubated on ice for 15 min for complete protein denaturation and then centrifuged for 15 min at 21,000 *g*. Supernatants were collected for determination by HPLC of 5-hydroxytryptophan (5-OH-TRP), a metabolic intermediate in 5-HT synthesis. The results were calculated as the difference between the amount of 5-OH-TRP liberated in samples with and without TRP and are expressed as nmol 5-OH-TRP/μg protein per min.

HPLC Analysis of TRP Metabolites in Placental Homogenates

The HPLC analyses were performed using Shimadzu LC20 Performance HPLC chromatograph (Shimadzu, Kyoto, Japan) equipped with UV and fluorescence detector. For simultaneous chromatographic separation of all tested compounds, Phenomenex Kinetex 5 μm EVO C18 100 A 150 × 3 mm with a guard column was used. An isocratic elution, at a flow rate of 0.5 mL/min, was performed with mobile phase consisting of 0.1 M acetic acid, pH 4.5 (adjusted with NaOH), and methanol 97 + 3. All analytes were eluted within 8.5 min.

Excitation and emission wavelengths of fluorescence detector were set for individual compounds: 275/333 nm for 5-OH-TRP from 0 to 3.1 min and 280/334 nm for 5-HT and TRP from 3.1 min. KYN was detected by UV detection with wavelength set to 369 nm. Additionally, in cases of TRP concentrations higher than the range of fluorescence detection, UV detection was used with wavelength set to 300 nm.

Statistical Analysis

Quantitative PCR (qPCR) results were assessed using Mann–Whitney tests. ddPCR analyses, protein expression, and functional studies were evaluated using unpaired *t*-test. All statistical analyses were implemented in GraphPad Prism 8.3.1 software (GraphPad Software, Inc.). Asterisks in the figures indicate significance levels: $^{*}p \leq 0.05$, $^{**}p \leq 0.01$, and $^{***}p \leq 0.001$.

RESULTS

Clinical Characteristics

Characteristics of the first-trimester and term pregnancies are listed in **Table 1**. No statistical differences were found in the mean maternal age and maternal BMI before pregnancy between the two groups. In the term group ($n = 32$) only healthy, non-medicated and non-smoking mothers were included. On the other hand, 5 of 13 women from the first trimester samples were smokers (frequency: three women < 10 cigarettes/day; two women > 10 cigarettes/day). Placenta samples from these women were included in the PCR analysis only if no association between smoking and gene expression was found. These samples have been marked with an asterisks (*) in the heatmap representing gene expression data (**Figure 1**).

Relative Gene Expression Analysis of TRP Metabolic Pathways in Human First-Trimester and Term Placenta

Human placenta fully expresses the enzymatic machinery for TRP metabolism to 5-HT and KYN pathways. A heatmap with hierarchical clustering revealed sample distribution into three main clusters, whereby the first-trimester placentas were clustered predominantly into one cluster, whereas term placenta samples were distributed into the remaining two clusters (**Figure 1**); the pattern of distribution indicated differential expression of the pathways across gestation. Subsequently, individual analysis of genes in first-trimester and term placentas showed several enzymes/transporters to be significantly up- or down-regulated at term.

TABLE 1 | Clinical characteristics of first-trimester and term pregnancies involved in the study.

Parameter	First trimester ($n = 13$)	Term ($n = 37$)
Maternal age (years)	27.91 ± 8.04	32.24 ± 5.07
Gestational age (weeks)	9.62 ± 1.19	39.57 ± 1.03
Smoking (Y:N)	5:8	0:37
Maternal BMI before pregnancy (kg m^{-2})	24.48 ± 3.31	24.67 ± 4.59
Maternal BMI at delivery (kg m^{-2})	NA	29.28 ± 4.30
Labor (NSVD:CS)	NA	21:16
Birth weight (kg)	NA	3.30 ± 0.44
Birth height (cm)	NA	49.94 ± 1.93
Fetal sex (M:F)	NA	20:17

Parameters are expressed as mean ± SD. CS, cesarean section; F, female; M, male; NA, not applicable; N, no; NSVD, normal spontaneous vaginal delivery; Y, yes.

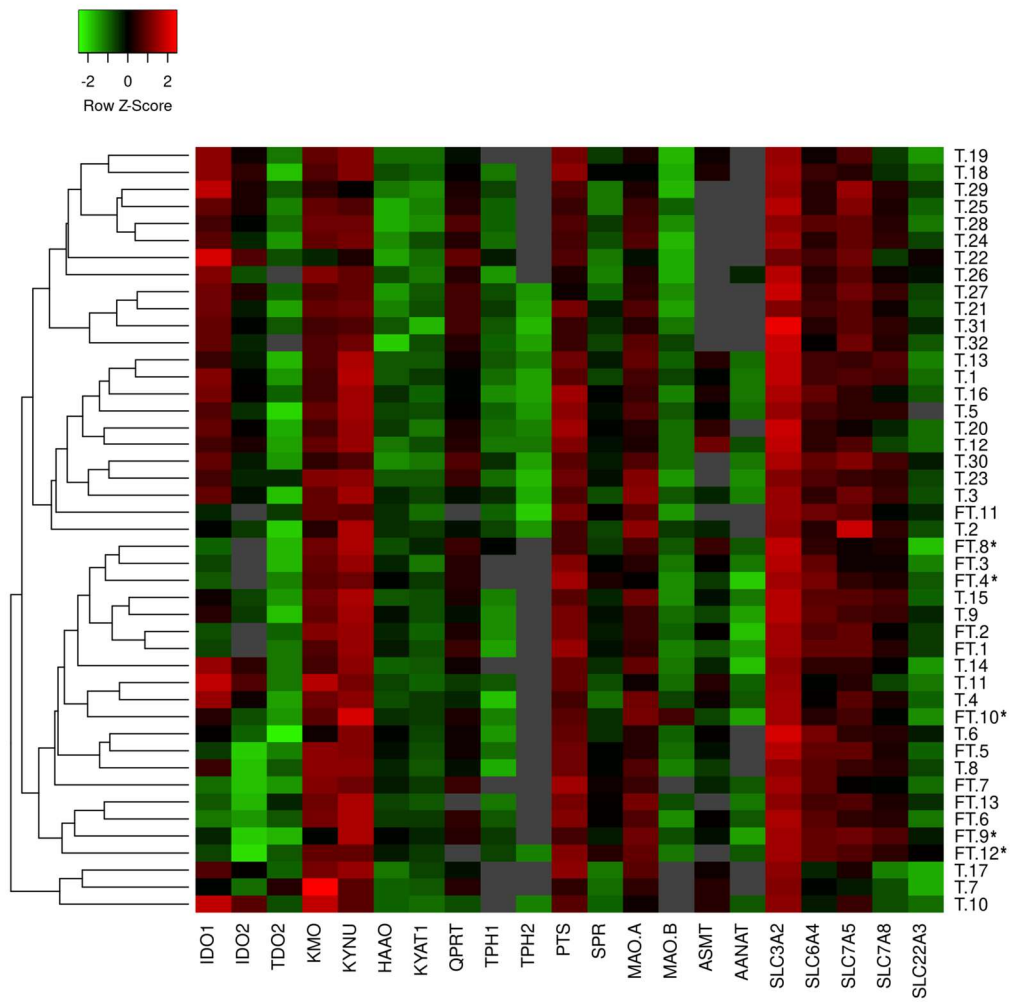

FIGURE 1 | Heatmap generated from qPCR gene expression analysis of TRP pathway in human placenta. Expression of 21 key transporters/enzymes was analyzed in first trimester (FT; $n = 13$) and term (T; $n = 32$) human placenta samples. Hierarchical clustering (average linkage, Euclidean distance) was applied to group samples with similar expression levels, emphasizing the overall changed expression during gestation. The color intensity indicates expression levels; red: up-regulation, green: down-regulation, gray: not detected. *Placentas from smokers.

Of the 5-HT pathway, gene expression of the main enzymes (*PTS*, *SPR*) responsible for BH4 production, a co-factor necessary for TPH function, were found to be significantly decreased at term, compared with first-trimester placenta. On the other hand, the rate-limiting enzymes of the KYN pathway, *IDO1/2*, were negligibly expressed in the first-trimester placenta, whereas we observed significant expression at term. Interestingly, the subsequent enzymes of the KYN pathway (specifically *KMO*, *KYNU*, *HAAO*, *KYAT1*, *QPRT*) were found to be expressed in lower amounts at term, compared with first-trimester placenta. Lastly, of the transport proteins tested, *SLC3A2*, *SLC6A4*, and *SLC7A8* revealed higher expression in the first-trimester placenta. Scatter plots of the $\log_{10}$-expression in first-trimester and term placenta were used to display the data and visualize the gene expression differences (**Figure 2**).

ddPCR Quantification of TPH1, TPH2, MAO-A, IDO1, IDO2, SLC6A4, and SLC22A3 Transcripts

ddPCR analysis was conducted in 13 first-trimester and 25 term placentas for absolute quantification of transcripts of the rate-limiting enzymes and main transporters of 5-HT

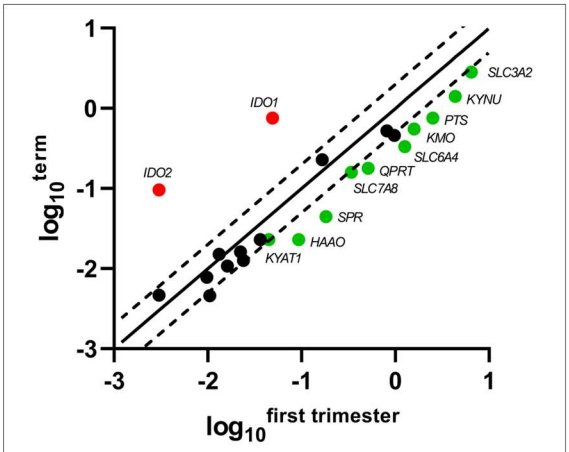

FIGURE 2 | Scatter plot of the TRP pathway enzymes/transporters showing significant changes in gene expression during gestation. Log_{10} of each gene-specific $2^{\Delta Ct}$ in the first-trimester placenta is plotted against those of term placenta. The central diagonal line shows unchanged gene expression, whereas the dotted lines depict the upper and lower limit of the threshold fold regulation, which was set to 2. Data were further evaluated using non-parametric Mann–Whitney test on ΔCt values, and those that exceed the threshold fold regulation and were statistically significant ($p \leq 0.05$) are named and shown in color: red – up-regulation, green – down-regulation.

and KYN pathways in the human placenta. We observed statistically significant down-regulation of *TPH1* (**Figure 3A**), *MAO-A* (**Figure 3B**), and *SLC6A4* (**Figure 4A**) at term, whereas *IDO1* (**Figure 3C**) and *IDO2* (**Supplementary Figure 1B**, Additional File 1) gene expression was up-regulated. *SLC22A3* (**Figure 4B**) and *TPH2* (**Supplementary Figure 1A**, Additional File 1) expression remained unchanged during gestation.

While human placenta expresses both isoforms (1 and 2) of *TPH* and *IDO* (Sedlmayr et al., 2014; Laurent et al., 2017; Ranzil et al., 2019), we found that *TPH1* and *IDO1* are predominant throughout gestation. Specifically, *IDO1* (**Figure 3C**) levels in the first-trimester and term placenta exceeded those of *IDO2* (**Supplementary Figure 1B**, Additional File 1) by 30- and 11-fold, respectively. On the other hand, *TPH1* (**Figure 3A**) showed three to six times higher expression compared to *TPH2* (**Supplementary Figure 1A**, Additional File 1), during gestation.

Moreover, we observed that *MAO-A* transcripts outnumbered those of *TPH1* transcripts by more than 1,000-fold in the first trimester and almost 700-fold at term (**Figures 3A,B**). On the other hand, while *TPH1* expression remained unchanged during pregnancy, we observed a 20-fold increase in *IDO1* transcripts at term (**Figure 3C**), suggesting a shift/preferential TRP metabolism toward the KYN pathway at term.

Protein Analysis

To investigate the expression at protein level, western blot analysis using specific antibodies for TPH, MAO, IDO, SLC6A4, and SLC22A3 was performed in homogenates from first-trimester (n = 3) and term (n = 3) human placenta samples. We observed no difference in MAO-A and TPH1 protein expression during gestation (**Figures 3D,E**). On the other hand, IDO1 protein band (45 kDa) was clearly detected in term placenta homogenates, whereas it was not visible in first trimester samples (**Figure 3F**), indicating that IDO1 protein is not expressed at early stages of pregnancy. As for the transport proteins, both SLC6A4 (**Figure 4C**) and SLC22A3 (**Figure 4D**) showed a significantly increased protein expression in term placentas compared with the first trimester ones.

Functional Analysis

TPH Activity

TPH activity was evaluated in first-trimester and term placenta homogenates, using TRP as a substrate and measuring the production of 5-OH TRP. As shown in **Figure 3G**, TPH activity ranged between 2 and 3 nmol 5-OH TRP/μg protein per min, and it was not affected by gestational age.

MAO Activity

MAO enzymatic activity was determined in first-trimester and term placenta homogenates by measuring the amount of 5-HT metabolized in the placental homogenate after 60 min of incubation with 5-HT. As shown in **Figure 3H**, after 60 min of incubation, 45% of 5-HT was metabolized by first-trimester placenta and nearly 75% by term placenta. Metabolism of 5-HT was completely inhibited by addition of phenelzine (100 μM) (Karahoda et al., 2020), indicating that 5-HT was metabolized specifically by MAO. These data suggest that placental metabolism of 5-HT increases towards the end of pregnancy.

IDO Activity

IDO activity in first-trimester and term placentas was evaluated using TRP as a substrate. IDO activity showed a significant increase during human pregnancy, with levels as low as 29 nmol KYN/μg protein per min (±17.3) in the first-trimester placenta to 7-fold higher activity at term (193 ± 32.3 nmol KYN/μg protein per min) (**Figure 3I**).

Gene Expression of TRP Metabolic Pathways in Placental-Derived Cells

Choriocarcinoma-derived cell lines (BeWo, BeWob30, JEG-3) and PHT cells isolated from human term placentas, were analyzed for expression of the main enzymes/transporters of the TRP pathway. Out of 21 genes tested, only 10 were found to be co-expressed in all cell types, with the PHT and BeWo b30 cells showing the highest similarity in gene expression (**Figure 5A**). Nonetheless, none of the choriocarcinoma-derived cell lines expressed the rate-limiting enzyme of the KYN pathway, *IDO1* or the 5-HT uptake transporter (OCT3/*SLC22A3*), making the PHT cells the only suitable *in vitro* model for studies of the respective pathways.

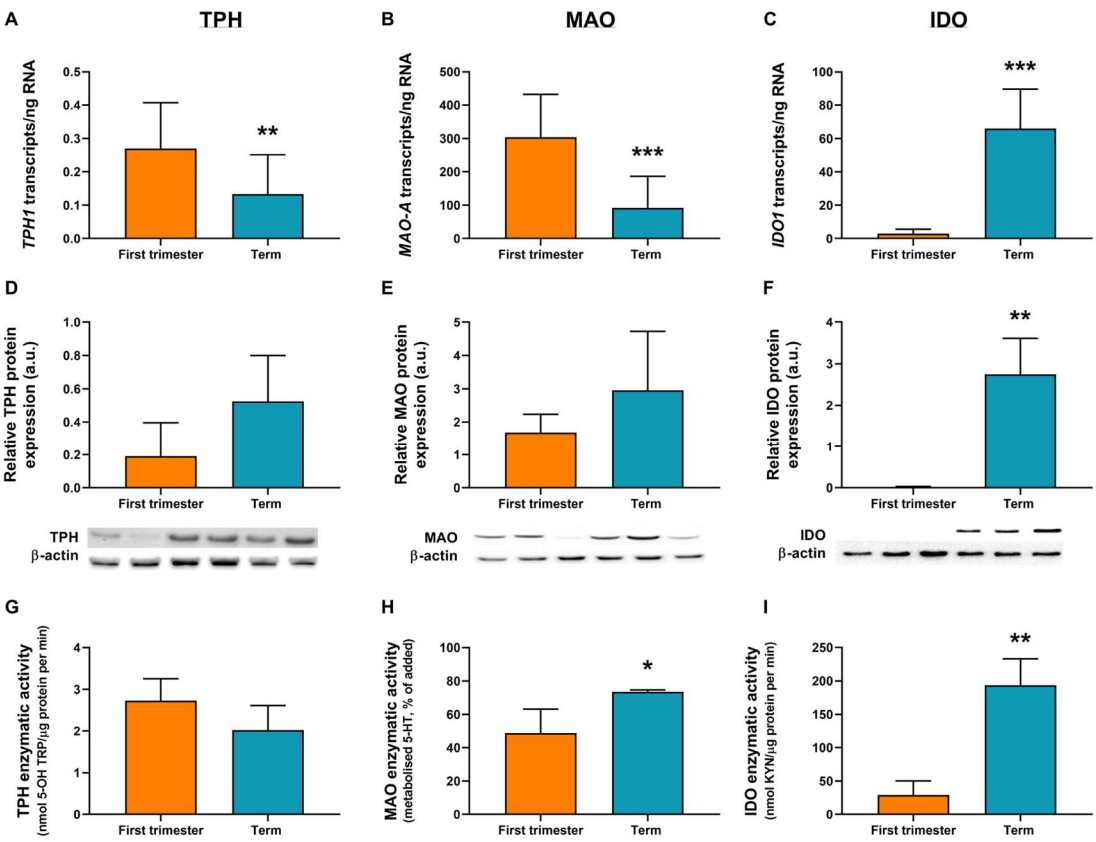

FIGURE 3 | Gene/protein expression and functional analyses of the rate-limiting enzymes of 5-HT and KYN pathways. Expression and function of tryptophan hydroxylase-1 (*TPH1*/TPH1), monoamine oxidase-A (*MAO-A*/MAO-A), and indoleamine 2,3-dioxygenase-1 (*IDO1*/IDO1) between the first-trimester and term human placenta was analyzed by digital droplet PCR **(A–C)**, Western blot **(D–F)**, and enzymatic activity **(G–I)** analyses. Protein expression was normalized to β-actin as a loading control; representative immunoblots for target proteins and β-actin are shown. For ddPCR analysis $n = 13$ (first trimester) and $n = 25$ (term placentas); for protein/functional analysis $n = 3$ for each. Data are presented as mean ± SD and statistical significance was evaluated using unpaired *t*-test; $^{*}p \leq 0.05$, $^{**}p \leq 0.01$, $^{***}p \leq 0.001$.

Effect of Differentiation on Gene Expression Profile in BeWo Cells and Human Primary Trophoblast Cells

Since the PHT and BeWo b30 cells shared the highest homology in genes expressed at mRNA level, we further studied the effect of differentiation in these cells. While CTB spontaneously syncytialized within 48–72 h, BeWo cell differentiation was induced with forskolin over a 72-h period. Only two of the tested genes (*SLC6A4* and *SPR*), revealed similar gene expression changes, specifically up-regulation, in BeWo and PHT cells upon differentiation. However, altogether, we observed that the differentiation process in BeWo cells affects the gene expression of TRP pathway enzymes/transporters in a more profound manner than in PHT cells (**Figures 5B,C**). Specifically, in PTH cells *IDO1* and *KYNU* were found to be down-regulated, whereas *MAO-A* and *QPRT* up-regulated (**Figure 5B**). Conversely, in BeWo cells we observed up-regulation for the following genes: *TPH2*, *KYNU*, *KMO*, *TDO2*, *SLC3A2*, *SLC7A5*, and *SLC7A8* (**Figure 5C**).

DISCUSSION

In our recent study (Karahoda et al., 2020) we demonstrated that the term placenta no longer provides 5-HT to the fetus. In contrast, it extracts it from the fetal circulation via OCT3-mediated process for subsequent degradation by MAO-A. We thus hypothesized that fetoplacental homeostasis of TRP and 5-HT changes throughout gestation. In this follow up study, we investigated the gene expression of 16 enzymes and 5 transporters involved in the metabolism and transport of TRP and its metabolites in human placenta (first trimester and term) and placental-derived cells. Moreover, using a combination of

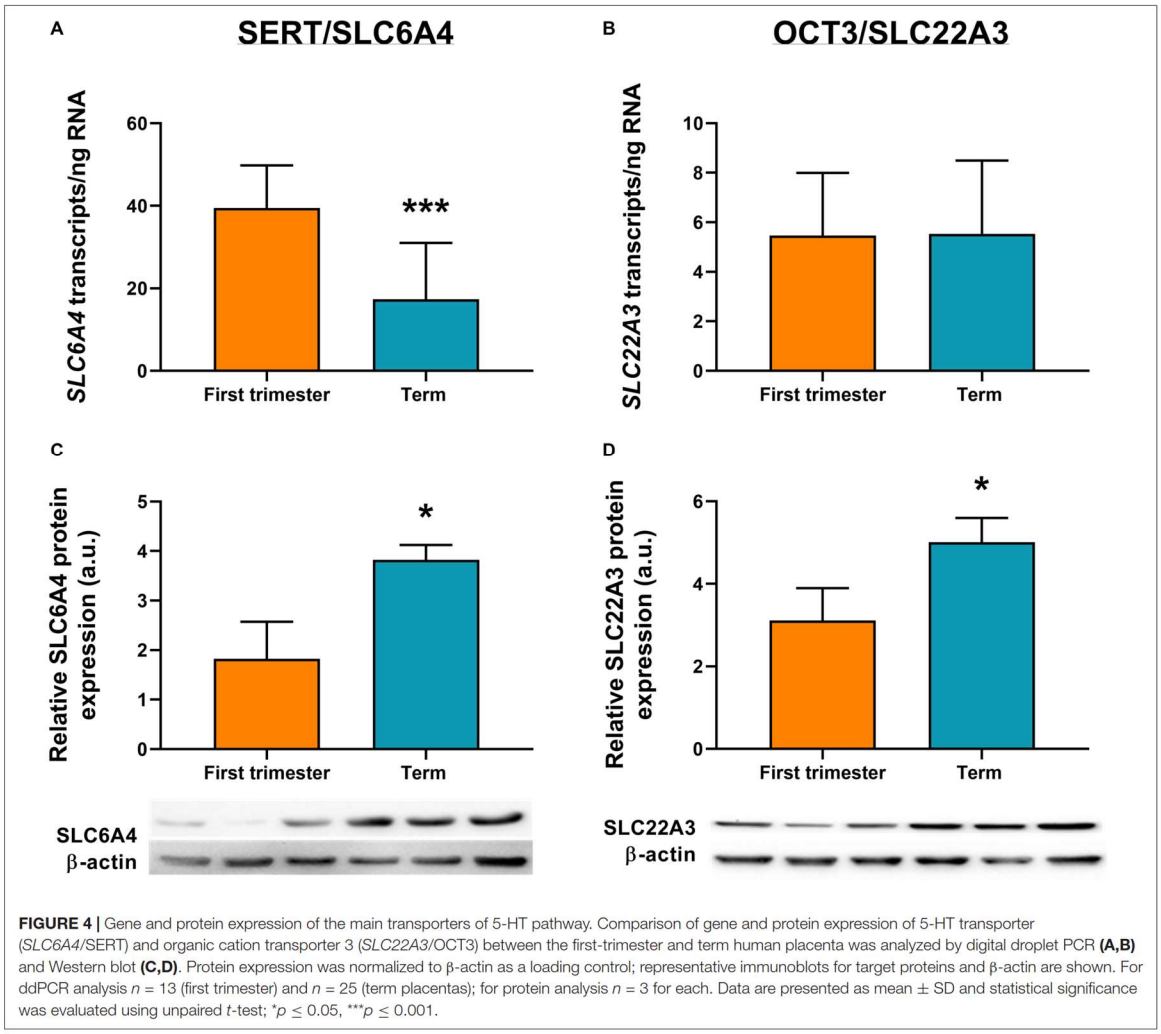

FIGURE 4 | Gene and protein expression of the main transporters of 5-HT pathway. Comparison of gene and protein expression of 5-HT transporter (*SLC6A4*/SERT) and organic cation transporter 3 (*SLC22A3*/OCT3) between the first-trimester and term human placenta was analyzed by digital droplet PCR **(A,B)** and Western blot **(C,D)**. Protein expression was normalized to β-actin as a loading control; representative immunoblots for target proteins and β-actin are shown. For ddPCR analysis $n = 13$ (first trimester) and $n = 25$ (term placentas); for protein analysis $n = 3$ for each. Data are presented as mean ± SD and statistical significance was evaluated using unpaired *t*-test; $^{*}p \leq 0.05$, $^{***}p \leq 0.001$.

gene/protein expression and functional analyses, we further report that the key enzymes and transporters involved in placental homeostasis of TRP, 5-HT, and KYN exhibit changes throughout gestation, likely as a result of adaptation to meet different placental/fetal needs with time.

Placental expression of several enzymes involved in TRP metabolism has been investigated before (Ligam et al., 2005; Lanoix et al., 2008; Bonnin et al., 2011; Laurent et al., 2017) and related to pathological conditions such as fetal growth restriction and preeclampsia (Carrasco et al., 2000; Murthi et al., 2017; Ranzil et al., 2019). Nevertheless, comprehensive characterization of the metabolic pathways in human placenta and physiological changes that may occur during gestation are poorly understood. As TRP is an essential amino acid, the placenta and fetus are dependent on maternal intake and placental transport from the maternal to fetal circulation. Therefore, apart from the metabolizing enzymes, it is also important to study the expression and function of placenta membrane transporters responsible for fetoplacental handling of TRP and its metabolites.

TRP is a substrate of L-type amino acid transporter-1 (LAT1/*SLC7A5*) on the maternal-facing membrane and L-type amino acid transporter-2 (LAT2/*SLC7A8*) on both maternal- and fetal-facing membranes; LAT1/2 functional activity is dependent on heterodimerization with the 4F2 heavy chain (*SLC3A2*) (Gaccioli et al., 2015). We observed that placental expression of *SLC3A2* and *SLC7A8* is down-regulated at term, which contrasts with a recent examination of publicly available gene expression array data, reporting no change at any stage of pregnancy for these transporters (Simner et al., 2017). However, it should be noted that the small sample size ($n = 4$ per gestational age) compared with our cohort ($n = 13$ for first-trimester and $n = 32$ for term placenta) could account for the different outcomes.

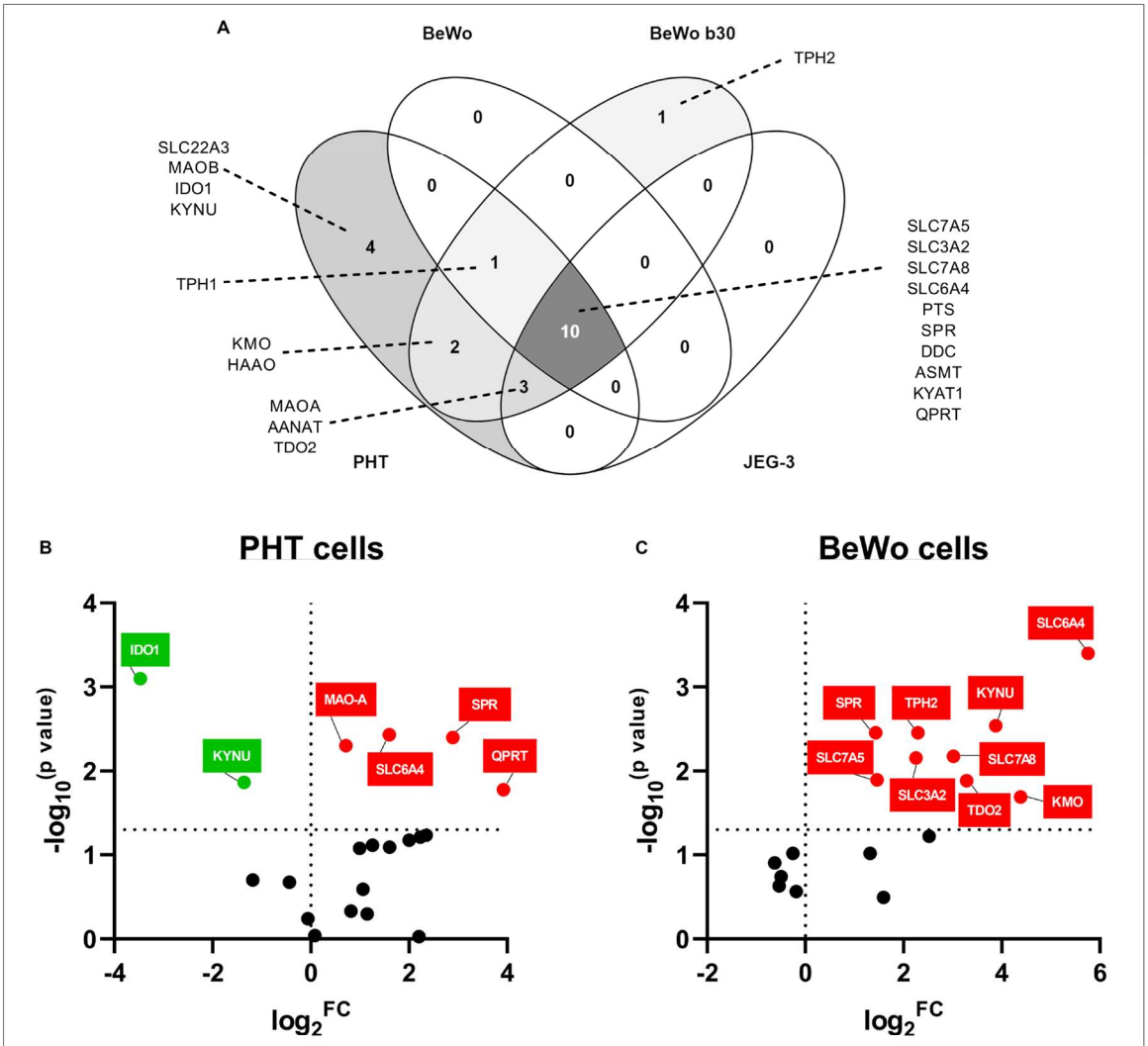

FIGURE 5 | Gene expression of TRP pathway-related enzymes and transporters in placental-derived cells. Placental-derived cells were obtained from three different passages of BeWo, BeWo b30, and JEG cells and five isolations of primary human trophoblast cells (PHT). **(A)** Venn diagram of the overlap in gene expression among four cell lines. PHT and BeWo b30 cells share the highest gene homology, with the PHT cells additionally expressing four important genes, including the rate-limiting enzyme, *IDO1*, and the polyspecific organic transporter, *SLC22A3*. Subsequently, effect of differentiation in these two cell lines was tested, revealing dissimilarity between spontaneous syncytialization **(B)** and forskolin-induced differentiation **(C)**. Data are visualized as volcano plots of fold changed expression in the differentiated cells, compared to the undifferentiated counterpart. Color indicates statistically significant changes: red – up-regulation, green – down-regulation. Statistical significance was evaluated using Mann–Whitney test.

TRP metabolism to 5-HT is mediated by TPH, whose activity depends on tetrahydrobiopterin (BH4) as a cofactor (Mckinney et al., 2005). Two mechanisms of BH4 synthesis in the human placenta have been suggested, *de novo* synthesis and/or salvage pathway (Iwanaga et al., 2004). We observed that the expression of 6-pyruvoyltetrahydropterin synthase (PTS), involved in *de novo* synthesis, and of sepiapterin reductase (SPR), involved in both pathways, decreased significantly at term, which corresponds nicely with previous reports on decreased SPR activity with increasing gestational age (Iwanaga et al., 2004). With the importance of BH4 as a cofactor for endothelial nitric oxide synthase (necessary for nitric oxide production), we speculate that decreasing SPR expression and activity at term may decrease the availability of BH4 for TPH activity, thus 5-HT synthesis at term.

Interestingly, we demonstrate that the first-trimester placentas show preferential expression of downstream enzymes of the KYN pathway, specifically *KMO*, *KYNU*, *HAAO*, and *QPRT* [involved in generation of 3-hydroxy-L-KYN (3-HK), 3-hydroxy anthranilic acid (3-HAA), and QUIN] and *KYAT1* (involved in generation of KYNA). This was unexpected because the rate-limiting enzyme IDO1 is, in contrast, only modestly expressed in the first-trimester placenta. While in 1998, Munn et al. (1998) suggested IDO1-based suppression of immune reactions to mediate fetomaternal tolerance, in a follow-up study, they reported that pregnancy success rate is not affected in the IDO-deficient mouse model (Baban et al., 2004). The authors proposed involvement of alternative processes, such as TDO, which may compensate for IDO activity when low or absent. In our study, we observed that *TDO* expression, although at relatively low levels, remains stable throughout gestation. Our results thus support a concept proposed by Badawy (2015) in which TRP degradation in early-to-mid pregnancy is catalyzed by TDO, with IDO gaining a partial/transient role in midgestation. We speculate that in the first trimester, KYN synthesis via TDO serves mainly as a precursor of 3-HK, 3-HAA, QUIN, and KYNA. QUIN is important for NAD^+ synthesis, necessary for numerous redox reactions and DNA repair. Similarly, 3-HK and 3-HAA are important metabolites with antioxidant and immunosuppressive properties. Lastly, KYNA, apart from its immunosuppressive function, plays a role in neuroprotection, probably through its action on the NDMA receptor (Foster et al., 1984). In accordance with our qPCR data, recent studies in mouse placenta showed limited placental KYNA synthesis at term (Goeden et al., 2017; Notarangelo et al., 2019). Thus, we believe that the impact of these metabolites may be of higher importance in the first trimester when the pro-inflammatory environment is less pronounced (Hannan et al., 2014; Holtan et al., 2015). On the other hand, the significant increase in IDO1 at term could account for high KYN production involved in the immune related activities. Indeed, this concept was previously discussed

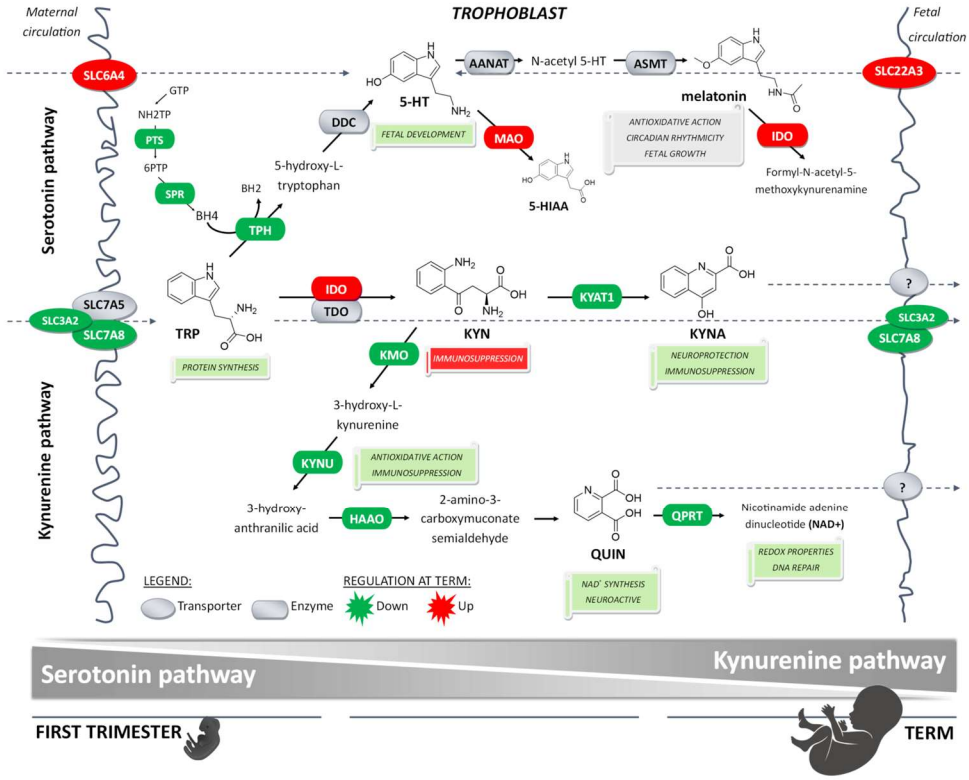

FIGURE 6 | Proposed gestational age-dependent changes in placental TRP metabolic pathways. The schematic illustration is based on gene expression studies and, in the case of rate-limiting enzymes/key transporters, also on protein, and/or functional activity. The first-trimester placenta preferentially utilizes TRP for generation of 5-HT involved in fetal development and synthesis of KYN metabolites implicated with neuroprotection, antioxidative and redox effects, and DNA repair. On the other hand, the term placenta synthesizes significant amounts of KYN important for immune regulation activities. Collectively, our findings strongly indicate gestational age-related changes in placental handling of TRP and its main metabolites, 5-HT and KYN. This may reflect the changes in placental and fetal demands for metabolites of either pathway to ensure proper embryonic and fetal development throughout pregnancy.

by Badawy who suggests preferential TRP utilization for protein, 5-HT and NAD^+ synthesis in early pregnancy (Badawy, 2015).

Therefore, we investigated the expression profiles and metabolic activity of the rate-limiting enzymes of the 5-HT and KYN pathways, TPH and IDO, respectively, early in pregnancy and at term. Our results indicate that during the first trimester, placenta may preferentially metabolize TRP to 5-HT, an important trophic factor for fetal development. Indeed, Bonnin et al. (2011) showed that placental 5-HT synthesis occurs as early as E10.5 in mice and week 11 in humans. It is during this period when the fetus is not capable of synthesizing 5-HT, yet serotonergic neurons and receptors have been identified (Bonnin and Levitt, 2011). As the immature fetal blood–brain barrier is not fully functional (Daneman et al., 2010), it has been well-established that the placenta serves as the main source of fetal 5-HT in early gestation (Bonnin and Levitt, 2011; Bonnin et al., 2011). However, later in gestation, the fetus gains the capability of 5-HT synthesis (Arevalo et al., 1991; Sano et al., 2016). With increased IDO expression/activity at term, also reported before (Blaschitz et al., 2011; Murthi et al., 2017; Wakx et al., 2018), it seems plausible that at later stages of gestation, TRP is preferentially utilized for KYN production.

In our previous study (Karahoda et al., 2020) we described the importance of membrane transporters (SERT/OCT3) and metabolizing enzyme (MAO-A) for placental 5-HT homeostasis at term. Here we reveal that, at protein levels, both transporters and the metabolizing enzyme are up-regulated at term. Increased OCT3 protein expression in human term placenta was also described by Lee et al. (2013). These findings suggest that towards term, placental capacity to take up 5-HT from both maternal and fetal circulations increases. The parallel increase in MAO-A expression and activity toward term strengthens our hypothesis that an orchestration between SERT, OCT3, and MAO-A activity serves as a 5-HT detoxification mechanism, protecting the term placenta and the fetus from high 5-HT circulating levels.

In vitro cell-based approaches (e.g., BeWo, BeWo b30, and JEG-3) are often applied as alternative methods to investigate placental physiology. However, these cells are derived from first trimester choriocarcinoma and, correspondingly, we show that gene expression of TRP metabolic pathways differs largely from that of primary trophoblast cells isolated from human term placenta. Specifically, BeWo and JEG-3 cells lack expression of crucial proteins, *IDO1* and *SLC22A3*; lack of *IDO1* in BeWo cells was also reported before (Entrican et al., 2002). In contrast, isolated PHT cells show expression pattern similar to that of term placenta. Another advantage of isolated PHT cells is their spontaneous fusion in culture to form the syncytium (Huang et al., 2016) while in BeWo cells, syncytialization must be provoked by modulators of cAMP metabolism such as forskolin (Jiraskova et al., 2018) which, in the present study, resulted in a non-physiological up-regulation of several genes (see **Figures 5B,C**). Taken together, these results indicate that placenta-derived carcinoma cells, BeWo, BeWo b30, and JEG-3, are not optimal *in vitro* models for TRP-related placental research; instead, use of primary human trophoblast cells is recommended.

Inconsistency exists in the current literature on IDO1 localization in the placenta and its expression in trophoblast cells (Sedlmayr et al., 2014). In the present study, we observed higher expression of *IDO1* in isolated CTB when compared to STB stage. While several studies report IDO1 in STB (Sedlmayr et al., 2002; Honig et al., 2004; Kudo et al., 2004) and CTB (Dong et al., 2008; Cvitic et al., 2013), recent papers (Ligam et al., 2005; Blaschitz et al., 2011) propose exclusive localization in vascular endothelium arguing that previous findings of IDO1 in trophoblast are a result of contaminating endothelial cells in isolated PHT cells (Sedlmayr et al., 2014). However, in our preparations, contamination with endothelial cells is routinely less than 1%, reflecting solely *IDO1* expression in CTBs. Moreover, for a long time it was believed that as pregnancy proceeds, the CTB layer gradually disappears (Benirschke et al., 2016); however, latest research reveals increasing number of CTBs at term (Mori et al., 2007) and designates them as the most metabolically active cells in human term placenta (Kolahi et al., 2017). Thus, for certain enzymes such as IDO1, CTB layer may be more active in metabolism than STB, and functional studies in isolated CTB cells should not be neglected.

In conclusion, here we report that placental homeostasis of TRP is subject to strictly regulated developmental changes during pregnancy (**Figure 6**). Considering the manifold role of TRP metabolites in placenta function, fetal development, and programming, tight regulation is necessary to maintain its homeostasis in the fetoplacental unit and ensure optimal communication on the placenta–brain axis. Subsequently, any internal or external insults, such as polymorphisms, epigenetics, pharmaceuticals or diseases, may compromise this harmonized interplay of enzymes and transporters, and result in suboptimal *in utero* conditions, and subsequently poor pregnancy outcomes. Importantly, timing of these insults is critical for fetal development (Barker et al., 2010); thus, knowledge of TRP catabolic pathways in the placenta during pregnancy aids in understanding the biological roots of fetal programming.

DATA AVAILABILITY STATEMENT

The original contributions presented in the study are included in the article/**Supplementary Material**, further inquiries can be directed to the corresponding author.

ETHICS STATEMENT

The studies involving human participants were reviewed and approved by the University Hospital Research Ethics Committee (201006 S15P) and the Ethics Committee of the Canton of Bern (Basec No. 2016-00250). The participants provided their written informed consent to participate in this study.

AUTHOR CONTRIBUTIONS

RKa, CAb, and FS participated in the study concept and design. RKa, CAb, HH, PK, and JZ participated in the data acquisition.

RKa, CAb, HH, PK, LC, RKu, CAl, and FS performed the data analysis and participated in interpretation of the results. RKa, CAb, and FS wrote the article. All authors contributed to the article and approved the submitted version.

FUNDING

This study was financially supported by the Czech Science Foundation (Grant No. 20/13017S), by the Grant Agency of Charles University (SVV 2020/260414), and the EFSA-CDN project (No. CZ.02.1.01/0.0/0.0/16_019/0000841), which was co-funded by the ERDF. CAl and JZ were supported by the Swiss National Centre of Competence in Research, NCCR TransCure, University of Bern.

ACKNOWLEDGMENTS

We would like to thank Prof. Marian Kacerovsky, Ph.D., Dr. Tomas Faist, Dr. Jaroslav Stranik, and Martina Hudeckova from the Department of Obstetrics and Gynecology, Faculty Hospital in Hradec Kralove for providing us the placental tissues as well as gathering all the available patient information data; physicians and midwives from the Lindenhofgruppe, Bern, Switzerland, are further acknowledged.

SUPPLEMENTARY MATERIAL

The Supplementary Material for this article can be found online at: https://www.frontiersin.org/articles/10.3389/fcell.2020.574034/full#supplementary-material

REFERENCES

Arevalo, R., Afonso, D., Castro, R., and Rodriguez, M. (1991). Fetal brain serotonin synthesis and catabolism is under control by mother intake of tryptophan. *Life Sci.* 49, 53–66. doi: 10.1016/0024-3205(91)90579-z

Baban, B., Chandler, P., Mccool, D., Marshall, B., Munn, D. H., and Mellor, A. L. (2004). Indoleamine 2,3-dioxygenase expression is restricted to fetal trophoblast giant cells during murine gestation and is maternal genome specific. *J. Reprod. Immunol.* 61, 67–77. doi: 10.1016/j.jri.2003.11.003

Babicki, S., Arndt, D., Marcu, A., Liang, Y., Grant, J. R., Maciejewski, A., et al. (2016). Heatmapper: web-enabled heat mapping for all. *Nucleic Acids Res.* 44, W147–W153.

Badawy, A. A. (2015). Tryptophan metabolism, disposition and utilization in pregnancy. *Biosci. Rep.* 35:e00261.

Barker, D. J. P., Eriksson, J. G., Kajantie, E., Alwasel, S. H., Fall, C. H. D., Roseboom, T. J., et al. (2010). "The maternal and placental origins of chronic disease," in *The Placenta and Human Developmental Programming*, eds G. J. Burton, D. J. P. Barker, A. Moffett, and K. Thornburg (Cambridge: Cambridge University Press), 5–17.

Benirschke, K., Kaufmann, P., and Baergen, R. (2016). *Pathology of the Human Placenta*. New York, NY: Springer.

Blaschitz, A., Gauster, M., Fuchs, D., Lang, I., Maschke, P., Ulrich, D., et al. (2011). Vascular endothelial expression of indoleamine 2,3-dioxygenase 1 forms a positive gradient towards the feto-maternal interface. *PLoS One* 6:e21774. doi: 10.1371/journal.pone.0021774

Bonnin, A., Goeden, N., Chen, K., Wilson, M. L., King, J., Shih, J. C., et al. (2011). A transient placental source of serotonin for the fetal forebrain. *Nature* 472, 347–350. doi: 10.1038/nature09972

Bonnin, A., and Levitt, P. (2011). Fetal, maternal, and placental sources of serotonin and new implications for developmental programming of the brain. *Neuroscience* 197, 1–7. doi: 10.1016/j.neuroscience.2011.10.005

Carrasco, G., Cruz, M. A., Dominguez, A., Gallardo, V., Miguel, P., and Gonzalez, C. (2000). The expression and activity of monoamine oxidase A, but not of the serotonin transporter, is decreased in human placenta from pre-eclamptic pregnancies. *Life Sci.* 67, 2961–2969. doi: 10.1016/s0024-3205(00)00883-3

Cote, F., Fligny, C., Bayard, E., Launay, J. M., Gershon, M. D., Mallet, J., et al. (2007). Maternal serotonin is crucial for murine embryonic development. *Proc. Natl. Acad. Sci. U.S.A.* 104, 329–334. doi: 10.1073/pnas.0606722104

Cox, B., Leavey, K., Nosi, U., Wong, F., and Kingdom, J. (2015). Placental transcriptome in development and pathology: expression, function, and methods of analysis. *Am. J. Obstet Gynecol.* 213, S138–S151.

Cvitic, S., Longtine, M. S., Hackl, H., Wagner, K., Nelson, M. D., Desoye, G., et al. (2013). The human placental sexome differs between trophoblast epithelium and villous vessel endothelium. *PLoS One* 8:e79233. doi: 10.1371/journal.pone.0079233

Daneman, R., Zhou, L., Kebede, A. A., and Barres, B. A. (2010). Pericytes are required for blood-brain barrier integrity during embryogenesis. *Nature* 468, 562–566. doi: 10.1038/nature09513

Dong, M., Ding, G., Zhou, J., Wang, H., Zhao, Y., and Huang, H. (2008). The effect of trophoblasts on T lymphocytes: possible regulatory effector molecules–a proteomic analysis. *Cell Physiol. Biochem.* 21, 463–472. doi: 10.1159/000129639

Entrican, G., Wattegedera, S., Chui, M., Oemar, L., Rocchi, M., and Mcinnes, C. (2002). Gamma interferon fails to induce expression of indoleamine 2,3-dioxygenase and does not control the growth of Chlamydophila abortus in BeWo trophoblast cells. *Infect. Immun.* 70, 2690–2693. doi: 10.1128/iai.70.5.2690-2693.2002

Fitzpatrick, P. F. (1999). Tetrahydropterin-dependent amino acid hydroxylases. *Annu. Rev. Biochem.* 68, 355–381. doi: 10.1146/annurev.biochem.68.1.355

Foster, A. C., Vezzani, A., French, E. D., and Schwarcz, R. (1984). Kynurenic acid blocks neurotoxicity and seizures induced in rats by the related brain metabolite quinolinic acid. *Neurosci. Lett.* 48, 273–278. doi: 10.1016/0304-3940(84)90050-8

Gaccioli, F., Aye, I. L. M. H., Roos, S., Lager, S., Ramirez, V. I., Kanai, Y., et al. (2015). Expression and functional characterisation of System L amino acid transporters in the human term placenta. *Reproduct. Biol. Endocrinol.* 13, 57–57.

Gao, K., Mu, C. L., Farzi, A., and Zhu, W. Y. (2020). Tryptophan metabolism: a link between the gut microbiota and brain. *Adv. Nutr.* 11, 709–723. doi: 10.1093/advances/nmz127

Gleason, G., Liu, B., Bruening, S., Zupan, B., Auerbach, A., Mark, W., et al. (2010). The serotonin1A receptor gene as a genetic and prenatal maternal environmental factor in anxiety. *Proc. Natl. Acad. Sci. U.S.A.* 107, 7592–7597. doi: 10.1073/pnas.0914805107

Goeden, N., Notarangelo, F. M., Pocivavsek, A., Beggiato, S., Bonnin, A., and Schwarcz, R. (2017). Prenatal dynamics of kynurenine pathway metabolism in mice: focus on kynurenic acid. *Dev. Neurosci.* 39, 519–528. doi: 10.1159/000481168

Goeden, N., Velasquez, J., Arnold, K. A., Chan, Y., Lund, B. T., Anderson, G. M., et al. (2016). Maternal inflammation disrupts fetal neurodevelopment via increased placental output of serotonin to the fetal brain. *J. Neurosci.* 36, 6041–6049. doi: 10.1523/jneurosci.2534-15.2016

Hannan, N. J., Bambang, K., Kaitu'u-Lino, T. U. J., Konje, J. C., and Tong, S. (2014). A bioplex analysis of cytokines and chemokines in first trimester maternal plasma to screen for predictors of miscarriage. *PLoS One* 9:e93320. doi: 10.1371/journal.pone.0093320

Holtan, S. G., Chen, Y., Kaimal, R., Creedon, D. J., Enninga, E. A., Nevala, W. K., et al. (2015). Growth modeling of the maternal cytokine milieu throughout normal pregnancy: macrophage-derived chemokine decreases as inflammation/counterregulation increases. *J. Immunol. Res.* 2015:952571.

Honig, A., Rieger, L., Kapp, M., Sutterlin, M., Dietl, J., and Kammerer, U. (2004). Indoleamine 2,3-dioxygenase (IDO) expression in invasive extravillous

trophoblast supports role of the enzyme for materno-fetal tolerance. *J. Reprod. Immunol.* 61, 79–86. doi: 10.1016/j.jri.2003.11.002

Huang, X., Luthi, M., Ontsouka, E. C., Kallol, S., Baumann, M. U., Surbek, D. V., et al. (2016). Establishment of a confluent monolayer model with human primary trophoblast cells: novel insights into placental glucose transport. *Mol. Hum. Reprod.* 22, 442–456. doi: 10.1093/molehr/gaw018

Iwanaga, N., Yamamasu, S., Tachibana, D., Nishio, J., Nakai, Y., Shintaku, H., et al. (2004). Activity of synthetic enzymes of tetrahydrobiopterin in the human placenta. *Int. J. Mol. Med.* 13, 117–120.

Iwasaki, S., Nakazawa, K., Sakai, J., Kometani, K., Iwashita, M., Yoshimura, Y., et al. (2005). Melatonin as a local regulator of human placental function. *J. Pineal Res.* 39, 261–265. doi: 10.1111/j.1600-079x.2005.00244.x

Jiraskova, L., Cerveny, L., Karbanova, S., Ptackova, Z., and Staud, F. (2018). Expression of concentrative nucleoside transporters (SLC28A) in the human placenta: effects of gestation age and prototype differentiation-affecting agents. *Mol. Pharm.* 15, 2732–2741. doi: 10.1021/acs.molpharmaceut.8b00238

Kallol, S., Moser-Haessig, R., Ontsouka, C. E., and Albrecht, C. (2018). Comparative expression patterns of selected membrane transporters in differentiated BeWo and human primary trophoblast cells. *Placenta* 7, 48–52. doi: 10.1016/j.placenta.2018.10.008

Karahoda, R., Horackova, H., Kastner, P., Matthios, A., Cerveny, L., Kucera, R., et al. (2020). Serotonin homeostasis in the materno-fetal interface at term: role of transporters (SERT/SLC6A4 and OCT3/SLC22A3) and monoamine oxidase A (MAO-A) in uptake and degradation of serotonin by human and rat term placenta. *Acta Physiolo.* 229:e13478.

Kaur, H., Bose, C., and Mande, S. S. (2019). Tryptophan metabolism by gut microbiome and gut-brain-axis: an in silico analysis. *Front. Neurosci.* 13:1365. doi: 10.3389/fnins.2019.01365

Kingdom, J., Huppertz, B., Seaward, G., and Kaufmann, P. (2000). Development of the placental villous tree and its consequences for fetal growth. *Eur. J. Obstet. Gynecol. Reprod. Biol.* 92, 35–43. doi: 10.1016/s0301-2115(00)00423-1

Kolahi, K. S., Valent, A. M., and Thornburg, K. L. (2017). Cytotrophoblast, not syncytiotrophoblast, dominates glycolysis and oxidative phosphorylation in human term placenta. *Sci. Rep.* 7:42941.

Kudo, Y., Boyd, C. A., Spyropoulou, I., Redman, C. W., Takikawa, O., Katsuki, T., et al. (2004). Indoleamine 2,3-dioxygenase: distribution and function in the developing human placenta. *J. Reprod. Immunol.* 61, 87–98. doi: 10.1016/j.jri.2003.11.004

Laemmli, U. K. (1970). Cleavage of structural proteins during the assembly of the head of bacteriophage T4. *Nature* 227, 680–685. doi: 10.1038/227680a0

Lanoix, D., Beghdadi, H., Lafond, J., and Vaillancourt, C. (2008). Human placental trophoblasts synthesize melatonin and express its receptors. *J. Pineal Res.* 45, 50–60. doi: 10.1111/j.1600-079x.2008.00555.x

Laurent, L., Deroy, K., St-Pierre, J., Cote, F., Sanderson, J. T., and Vaillancourt, C. (2017). Human placenta expresses both peripheral and neuronal isoform of tryptophan hydroxylase. *Biochimie* 140, 159–165. doi: 10.1016/j.biochi.2017.07.008

Lee, N., Hebert, M. F., Prasad, B., Easterling, T. R., Kelly, E. J., Unadkat, J. D., et al. (2013). Effect of gestational age on mRNA and protein expression of polyspecific organic cation transporters during pregnancy. *Drug Metab. Disposit.* 41, 2225–2232. doi: 10.1124/dmd.113.054072

Li, L., and Schust, D. J. (2015). Isolation, purification and in vitro differentiation of cytotrophoblast cells from human term placenta. *Reprod. Biol. Endocrinol.* 13:71.

Ligam, P., Manuelpillai, U., Wallace, E. M., and Walker, D. (2005). Localisation of indoleamine 2,3-dioxygenase and kynurenine hydroxylase in the human placenta and decidua: implications for role of the kynurenine pathway in pregnancy. *Placenta* 26, 498–504. doi: 10.1016/j.placenta.2004.08.009

Maldonado-Estrada, J., Menu, E., Roques, P., Barre-Sinoussi, F., and Chaouat, G. (2004). Evaluation of Cytokeratin 7 as an accurate intracellular marker with which to assess the purity of human placental villous trophoblast cells by flow cytometry. *J. Immunol. Methods* 286, 21–34. doi: 10.1016/j.jim.2003.03.001

Mckinney, J., Knappskog, P. M., and Haavik, J. (2005). Different properties of the central and peripheral forms of human tryptophan hydroxylase. *J. Neurochem.* 92, 311–320. doi: 10.1111/j.1471-4159.2004.02850.x

Mikheev, A. M., Nabekura, T., Kaddoumi, A., Bammler, T. K., Govindarajan, R., Hebert, M. F., et al. (2008). Profiling gene expression in human placentae of different gestational ages: an OPRU Network and UW SCOR Study. *Reproduct. Sci. (Thousand Oaks Calif).* 15, 866–877. doi: 10.1177/1933719108322425

Mori, M., Ishikawa, G., Luo, S. S., Mishima, T., Goto, T., Robinson, J. M., et al. (2007). The cytotrophoblast layer of human chorionic villi becomes thinner but maintains its structural integrity during gestation. *Biol. Reprod.* 76, 164–172. doi: 10.1095/biolreprod.106.056127

Muller, C. L., Anacker, A. M., Rogers, T. D., Goeden, N., Keller, E. H., Forsberg, C. G., et al. (2017). Impact of maternal serotonin transporter genotype on placental serotonin, fetal forebrain serotonin, and neurodevelopment. *Neuropsychopharmacology* 42, 427–436. doi: 10.1038/npp.2016.166

Munn, D. H., Zhou, M., Attwood, J. T., Bondarev, I., Conway, S. J., Marshall, B., et al. (1998). Prevention of allogeneic fetal rejection by tryptophan catabolism. *Science* 281, 1191–1193. doi: 10.1126/science.281.5380.1191

Murthi, P., Wallace, E. M., and Walker, D. W. (2017). Altered placental tryptophan metabolic pathway in human fetal growth restriction. *Placenta* 52, 62–70. doi: 10.1016/j.placenta.2017.02.013

Nagai, R., Watanabe, K., Wakatsuki, A., Hamada, F., Shinohara, K., Hayashi, Y., et al. (2008). Melatonin preserves fetal growth in rats by protecting against ischemia/reperfusion-induced oxidative/nitrosative mitochondrial damage in the placenta. *J. Pineal Res.* 45, 271–276. doi: 10.1111/j.1600-079x.2008.00586.x

Notarangelo, F. M., Beggiato, S., and Schwarcz, R. (2019). Assessment of prenatal kynurenine metabolism using tissue slices: focus on the neosynthesis of kynurenic acid in mice. *Dev. Neurosci.* 41, 102–111. doi: 10.1159/000499736

Petroff, M. G., Phillips, T. A., Ka, H., Pace, J. L., and Hunt, J. S. (2006). "Isolation and culture of term human trophoblast cells," in *Placenta and Trophoblast: Methods and Protocols*, eds M. J. Soares and J. S. Hunt (Totowa, NJ: Humana Press).

Ranzil, S., Ellery, S., Walker, D. W., Vaillancourt, C., Alfaidy, N., Bonnin, A., et al. (2019). Disrupted placental serotonin synthetic pathway and increased placental serotonin: potential implications in the pathogenesis of human fetal growth restriction. *Placenta* 84, 74–83. doi: 10.1016/j.placenta.2019.05.012

Rosenfeld, C. S. (2020a). The placenta-brain-axis. *J. Neurosci. Res.* doi: 10.1002/jnr.24603 [Epub ahead of print].

Rosenfeld, C. S. (2020b). Placental serotonin signaling, pregnancy outcomes, and regulation of fetal brain development†. *Biol. Reprod.* 102, 532–538. doi: 10.1093/biolre/ioz204

Sano, M., Ferchaud-Roucher, V., Kaeffer, B., Poupeau, G., Castellano, B., and Darmaun, D. (2016). Maternal and fetal tryptophan metabolism in gestating rats: effects of intrauterine growth restriction. *Amino Acids* 48, 281–290. doi: 10.1007/s00726-015-2072-4

Schwarcz, R., Bruno, J. P., Muchowski, P. J., and Wu, H. Q. (2012). Kynurenines in the mammalian brain: when physiology meets pathology. *Nat. Rev. Neurosci.* 13, 465–477. doi: 10.1038/nrn3257

Sedlmayr, P., Blaschitz, A., and Stocker, R. (2014). The role of placental tryptophan catabolism. *Front. Immunol.* 5:230–230.

Sedlmayr, P., Blaschitz, A., Wintersteiger, R., Semlitsch, M., Hammer, A., Mackenzie, C. R., et al. (2002). Localization of indoleamine 2,3-dioxygenase in human female reproductive organs and the placenta. *Mol. Hum. Reprod.* 8, 385–391. doi: 10.1093/molehr/8.4.385

Seron-Ferre, M., Mendez, N., Abarzua-Catalan, L., Vilches, N., Valenzuela, F. J., Reynolds, H. E., et al. (2012). Circadian rhythms in the fetus. *Mol. Cell Endocrinol.* 349, 68–75.

Simner, C., Novakovic, B., Lillycrop, K. A., Bell, C. G., Harvey, N. C., Cooper, C., et al. (2017). DNA methylation of amino acid transporter genes in the human placenta. *Placenta* 60, 64–73. doi: 10.1016/j.placenta.2017.10.010

Sitras, V., Fenton, C., Paulssen, R., Vårtun, Å, and Acharya, G. (2012). Differences in gene expression between first and third trimester human placenta: a microarray study. *PLoS One* 7:e33294. doi: 10.1371/journal.pone.0033294

Staud, F., and Karahoda, R. (2018). Trophoblast: The central unit of fetal growth, protection and programming. *Int. J. Biochem. Cell Biol.* 105, 35–40. doi: 10.1016/j.biocel.2018.09.016

Takikawa, O., Kuroiwa, T., Yamazaki, F., and Kido, R. (1988). Mechanism of interferon-gamma action. Characterization of indoleamine 2,3-dioxygenase in cultured human cells induced by interferon-gamma and evaluation of the enzyme-mediated tryptophan degradation in its anticellular activity. *J. Biol. Chem.* 263, 2041–2048.

Uuskula, L., Mannik, J., Rull, K., Minajeva, A., Koks, S., Vaas, P., et al. (2012). Mid-gestational gene expression profile in placenta and link to pregnancy complications. *PLoS One* 7:e49248. doi: 10.1371/journal.pone.0049248

Wakx, A., Nedder, M., Tomkiewicz-Raulet, C., Dalmasso, J., Chissey, A., Boland, S., et al. (2018). Expression, localization, and activity of the aryl hydrocarbon receptor in the human placenta. *Int. J. Mol. Sci.* 19:3762. doi: 10.3390/ijms19123762

Zanetta, L., Marcus, S. G., Vasile, J., Dobryansky, M., Cohen, H., Eng, K., et al. (2000). Expression of Von Willebrand factor, an endothelial cell marker, is up-regulated by angiogenesis factors: a potential method for objective assessment of tumor angiogenesis. *Int. J. Cancer* 85, 281–288. doi: 10.1002/(SICI)1097-0215(20000115)85:23C281::AID-IJC213E3.0.CO;2-3

Conflict of Interest: The authors declare that the research was conducted in the absence of any commercial or financial relationships that could be construed as a potential conflict of interest.

Declaration of Originality

Last name, first name: Zaugg, Jonas

Matriculation number: 09-488-784

I hereby declare that this thesis represents my original work and that I have used no other sources except as noted by citations.

All data, tables, figures and text citations which have been reproduced from any other source, including the internet, have been explicitly acknowledged as such.

I am aware that in case of non-compliance, the Senate is entitled to withdraw the doctorate degree awarded to me on the basis of the present thesis, in accordance with the "Statut der Universität Bern (Universitätsstatut; UniSt)", Art. 69, of 7 June 2011.

Place, date

Bern, 1.12.2020

Signature